THE UNIVERSITY *of* EDINBURGH

On the Re-creation of Site-Specific Directional Wave Conditions

Samuel Draycott

A thesis submitted in partial fulfilment of the requirements for the award of an Engineering Doctorate

THE UNIVERSITY OF EDINBURGH

August 2016

IDCORE

This thesis is submitted in partial fulfillment of the requirements for the award of an Engineering Doctorate, jointly awarded by the University of Edinburgh, the University of Exeter, and the University of Strathclyde. The work presented has been conducted under the industrial supervision of FloWave TT Ltd. as a project within the Industrial Doctoral Centre for Offshore Renewable Energy (IDCORE).

THE UNIVERSITY *of* EDINBURGH

UNIVERSITY OF EXETER

University of Strathclyde Engineering

To my dog,

Mojo

Abstract

Wave tank tests facilitate the understanding of how complex sea conditions influence the dynamics of man-made structures. If a potential deployment location is known, site data can be used to improve the relevance and realism of the test conditions, thus helping de-risk device development. Generally this data is difficult to obtain and even if available is used simplistically due to established practices and limitations of test facilities. In this work four years of buoy data from the European Marine Energy Centre is characterised and simulated at the FloWave Ocean Energy Research Facility; a circular combined wave-current test tank. Particular emphasis is placed on the characterisation and validation processes, aiming to preserve spectral and directional complexity of the site, whilst proving that the defined representative conditions can be effectively created.

When creating representative site-specific sea states, particular focus is given to the application of clustering algorithms, which enable the entire spectral (frequency or directional) form to be considered in the characterisation process. This enables the true complex nature of the site to be considered in the data reduction process. Prior to generating and measuring the resulting sea states, issues with scaling are explored, the facility itself is characterised, and emphasis is placed on developing measurement strategies for the validation of directional spectra. Wave gauge arrays are designed and used to characterise various elements of the FloWave tank, including reflections, spatio-temporal variability and wave shape. A new method for directional spectrum reconstruction (SPAIR) is also developed, enabling more effective measurement and validation of the resulting directional sea states.

Through comparison with other characterisation methods, inherent method-induced trade-offs are understood, and it is found that there is no absolute favourable approach, necessitating an application specific procedure. Despite this, a useful set of ‘generic’ sea states are created for the simulation of both production and extreme conditions. For sea state measurement, the SPAIR method is proven to be significantly more effective than current approaches, reducing errors and introducing additional capability. This method is used in combination with a directional wave gauge array to effectively measure, correct, and validate the resulting directional wave conditions. It is also demonstrated that site-specific wave-current scenarios can be effectively re-created, thus demonstrating that truly complex ocean conditions can be simulated at FloWave. This ability, along with the considered characterisation approach used, means that representative site-specific sea states can be simulated with confidence, increasing the realism of the test environment and helping de-risk device development.

Acknowledgements

Funding from the Energy Technologies Institute (ETI) and the RCUK Energy Programme for the Industrial Doctoral Centre for Offshore Renewable Energy (Grant number EP/J500847/1) is gratefully acknowledged.

This EngD research would not have been possible without the help of my IDCORE academic supervisory team. As such, I would like to thank Prof. Sandy Day, Prof. Lars Johanning, and in particular my lead supervisor Prof. David Ingram for their guidance throughout the project. I would also like to acknowledge the IDCORE programme itself, for providing me the opportunity to carry out what I have found to be truly stimulating research in an area I am passionate about.

My experience carrying out research at FloWave has been amazing, and the whole team there have been very supportive and great to work with. I would particularly like to acknowledge the help of my industrial supervisor, Dr Thomas Davey, whose guidance and perspective have helped me immensely in completing the EngD. In addition I would like to thank the help of Dr Jeffrey Steynor, Rebecca Greener and Donald Noble, who have all been a great help in getting me over the finish line. Jeff and Donald have entertained my ramblings about waves on a daily basis for over three years, and I doubt many of the interesting areas in this thesis would have been explored if they hadn't.

A big thank you is owed to my parents, family and friends for being supportive throughout this and every path I have chosen to take. Lastly, I would like to give a special acknowledgement to my loving girlfriend Rhiannon, for it is her unwavering support which has kept me sane (ish) throughout these past years.

Declaration

I declare that that the work has not been submitted for consideration as part of any other degree or professional qualification. The journal and conference papers in Appendix C are my own work, unless otherwise stated. Furthermore, I declare that this thesis was composed by myself and that the material presented is my own work, except the following:

- Section 7.3 is part of a joint piece of work between myself and Donald Noble (IDCORE and FloWave). The research into theoretical wave-current interactions has been carried out by Donald, and the test design implementation and write-up has been carried out jointly. I took the lead on the obvious applications of my work including sea state measurement, analysis and implementation. Further detail on how this is attributed is outlined in Section 7.3.

Samuel Draycott

Contents

Figures and Tables

Figures

Tables

Chapter 1

Introduction

1.1 Motivation

Wave tank tests play an important role in understanding how devices such as Wave Energy Converters (WECs) respond to ocean conditions. If a deployment location is known, the test conditions can be chosen to represent the site, thus helping quantify device behaviour in the conditions of most relevance. Historically, however, this data has been difficult to obtain, and wave tanks have had limited capability to properly re-create the complexity of sea conditions. The aim of this project is to make use of directional buoy data to demonstrate that truly realistic conditions can be re-created for tank testing, thus helping to de-risk device development. Particular focus is given to the inclusion and reproduction of sea state directionality, enabling more detailed site representation whilst taking advantage of the capabilities of the FloWave Ocean Energy Research Facility (FloWave).

1.2 EMEC Wave Test Site: Billia Croo

The European Marine Energy Centre (EMEC) operates full-scale grid-connected facilities for the testing of wave and tidal energy converters, as well as two scale test sites. Based in Orkney, UK, both the Billia Croo wave site, and the Fall of Warness tidal site boast a large resource; creating a representative and challenging environment for device assessment. The locations of these test sites relative to the UK and Orkney Isles are shown in Fig. 1.1.

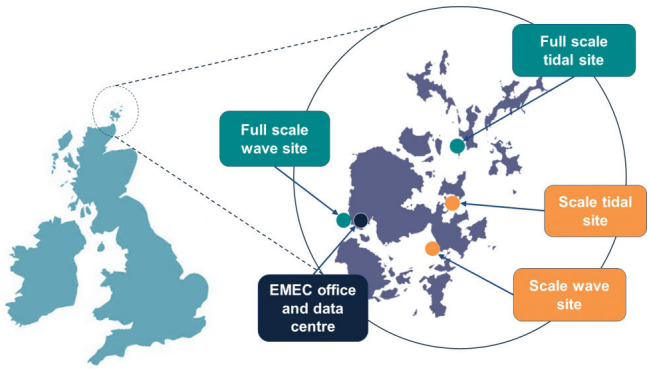

Figure 1.1: The European Marine Energy Centre test sites, relative to the Orkney Isles and the British Isles (EMEC, 2015)

(a) (b)

Figure 1.2: (a) Waverider buoy deployed at the European Marine Energy Centre, (b) Aerial view of EMEC's Billia Croo full-scale grid-connected wave test site (EMEC, 2016)

EMEC has been operational since 2003, gaining vast experience in both device installation and resource measurement. In this time many well-known wave energy developers such as Pelamis Wave Power and Aquamarine Power have trialled their devices in these Orkney waters, in addition to a large range of tidal energy developers including Alstom, Atlantis and Open Hydro.

The expertise of EMEC in measuring the wave climate has enabled large quantities of high quality directional wave data to be gathered over the years, using a number of Datawell Directional Waverider Buoys as shown in Fig. 1.2a. As part of a collaboration agreement roughly four years of this data have been made available to this project for the purpose of re-creating the Billia Croo wave conditions in the FloWave Ocean Energy Research Facility.

1.3 The FloWave Ocean Energy Research Facility

All experiments conducted throughout this research were carried out at the FloWave Ocean Energy Research Facility (Figs. 1.3 to 1.5), located at the University of Edinburgh, UK. Primarily designed for 1:20 to 1:40 scale model tests for offshore renewable energy devices, this 'large-scale' test facility provides an important intermediate stage between small scale (e.g. 1:100) tank testing and real sea prototypes. This results in significant reductions in scaling errors compared with small-scale, and cost in comparison with sea trials.

The facility itself is comprised of a circular 25m diameter, 2m depth combined wave and current test basin which is encircled by 168 active-absorbing force-feedback wavemakers. A re-circulating flow system is created using 28 impeller units mounted in a plenum chamber beneath the floor. These unique design features remove any inherent limitation on both wave and

Figure 1.3: The FloWave Ocean Energy Research Facility

Figure 1.4: The FloWave concentric wave spike 'party trick'. Demonstrates accuracy of circular generating capability

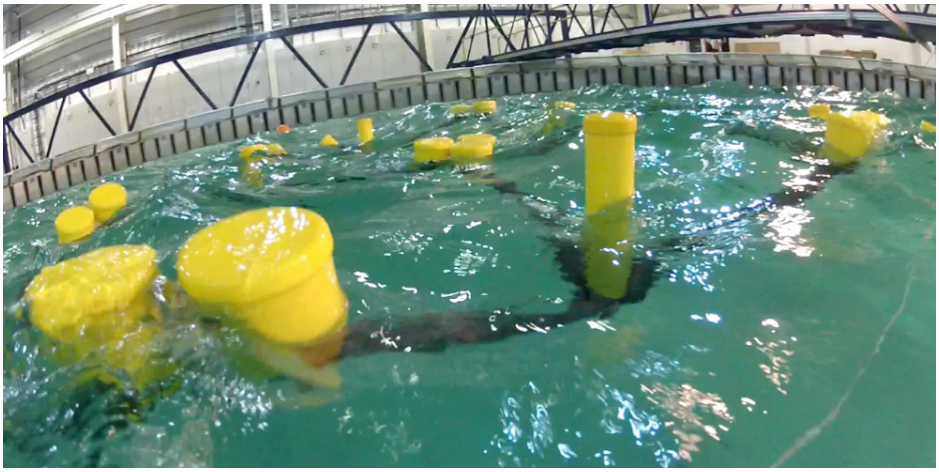

Figure 1.5: The Albatern WaveNET device being tested at FloWave (screen-grab from video available at Albatern (2016))

current direction, enabling complex wave, current, and wave-current scenarios to be simulated. The circular design also gives a large test area, and as such is well suited to testing arrays and array effects.

A computer sketch (2D CAD) of the FloWave facility is shown in Fig. 1.6, which highlights some of the other design features. A 15 m diameter raisable floor, accessible from the gantry, enables easy installation of models and equipment on one of the many fixing holes. Both the gantry and crane can traverse the tank hall (see Fig. 1.3), which facilitates transportation whilst also enabling installation of measurement equipment from the gantry.

For this research the capability of FloWave enables the re-creation of complex multi-directional wave conditions, and as such has the ability to mimic observed site-specific wave directionality. The current generating capability also opens up the possibility of creating site-specific wave current scenarios, enabling full simulation of observed sea conditions. For such conditions to be generated with confidence the facility must be understood, necessitating tank characterisation, and for sea state validation directional spectrum reconstruction strategies must be developed.

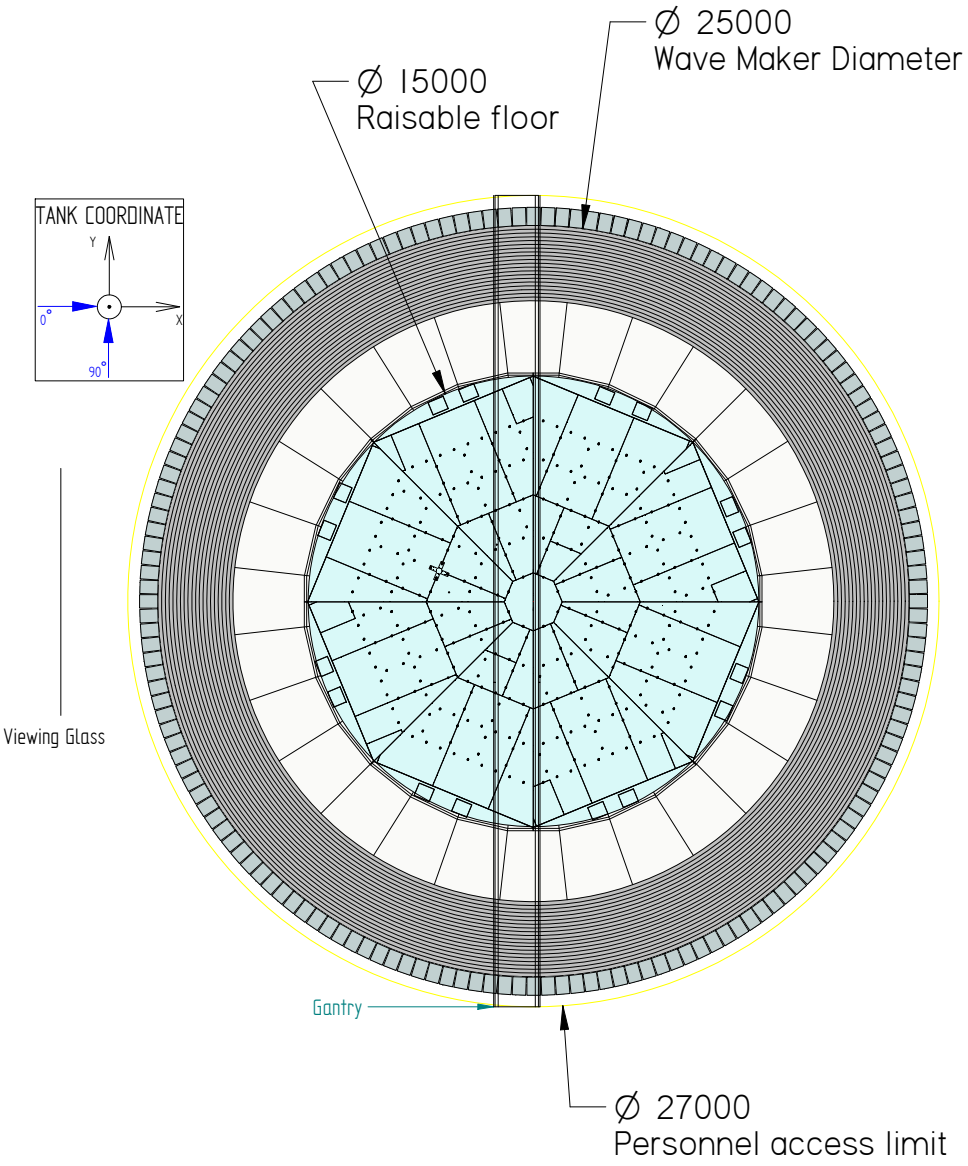

Figure 1.6: Detailed 2D CAD model of the facility. Shows raisable floor and floor fixings, gantry, turning vanes for current, along with basic dimensions and co-ordinate system. Origin is at the tank centre

1.4 Thesis Overview

The aim of this research is to develop methodologies for creating realistic and representative site-specific wave tests from buoy data, and demonstrate the capability to produce them at scale. This is carried out using buoy data from EMEC, and simulated at the FloWave test tank. Generally wave data is used simplistically for this purpose due to established practice and limitations of test facilities. In this work one of the main aims is, therefore, to develop and explore the use of more sophisticated site characterisation methodologies, whilst taking advantage of the capability of FloWave to simulate more realistic representative sea states.

To characterise the EMEC wave site particular emphasis is placed on the use of clustering algorithms, which can consider the entire spectral (frequency or directional) form in order to preserve observed site complexity. A number of different methodologies are explored and trialled to produce 20 and 40 representative 'production' sea states, and compared with more established approaches. After assessing the characteristics of each method a favourable 'generic' methodology is developed and used to create 41 representative directional spectra. Methodologies for creating extreme directional sea states are also explored, using bivariate probability distributions to create 1:10 and 1:50 year extreme directional sea states.

In order to demonstrate that the resulting site-specific sea states can be created at FloWave they need to be scaled, generated, measured and validated. As FloWave was still in the commissioning phase at the beginning of the project, prior to generating these complex wave conditions the facility itself was characterised. This enables generation and absorption limitations to be identified along with the assessment of the quality and characteristics of various wave fields. To infer such details wave gauge arrays were designed, suitable for analysing reflections, spatial variability and importantly, the reconstruction of directional spectra. A new method is also developed for directional spectrum reconstruction in this work, reducing errors and introducing additional capability. This method enables increased certainty in the validation process for directional sea states, whilst enabling effective characterisation of directional wave conditions at FloWave.

1.4.1 Outline of Thesis

An outline of how the research components are sorted into chapters is detailed here. The way these elements are interlinked to serve the main project path is shown in Fig. 1.7.

- **Chapter 2: Literature Review**
  An overview and assessment of relevant literature is detailed, establishing the key work conducted in this area, along with the context of the research presented here.
- **Chapter 3: Wave Measurement**
  The wave measurement system at FloWave is detailed along with the wave gauge array design methodologies. Non-conventional approaches are used to create effective arrays

for reflection analysis and directional spectrum measurement, as well as for the creation of spatial maps. These arrays are shown in their configurations and referred to throughout the text.

- **Chapter 4: Wave Characterisation and Tank Performance**
  The wave performance and characteristics at FloWave are assessed for a range of regular, uni-directional irregular and directional sea states. Numerous features are assessed including wave shape, reflections, and spatio-temporal variability. This helps identify favourable locations for testing, along with informing test plans with knowledge of wave performance for a variety of conditions.

- **Chapter 5: The SPAIR Directional Spectrum Reconstruction Method**
  A new directional spectrum reconstruction method is described, designed specifically for the tank environment. The method reduces uncertainty, as well as enabling isolation of incident and reflected time-series and spectra over 360°. In this chapter the method is demonstrated for the directional sea states tested in Chapter 4, and performance, sensitivities and limitations are assessed.

- **Chapter 6: Site Specific Resource Characterisation**
  The Billia Croo full-scale wave test site is analysed, with methods of creating representative extreme and production sea states explored. Inherent trade-offs are understood resulting from the constrained nature of the problem and the many variables that can be considered. Example directional spectra are created for both extreme and production conditions, with the aim of including spectral realism whilst simultaneously covering a wide range of wave height and period.

- **Chapter 7: The Re-creation of Site-Specific Sea States**
  The non-parametric sea state outputs from Chapter 6 are scaled, generated and corrected. Particular focus is given to scaling considerations, and alternative approaches are described. Finally, it is shown that corrected wave-current scenarios can be created, demonstrated with regular, uni-directional irregular and directional wave conditions with a variety of current velocities and relative angles.

- **Chapter 8: Conclusions and Further Work**
  Conclusions are made about the presented research, before detailing what further work could be carried out to further the findings.

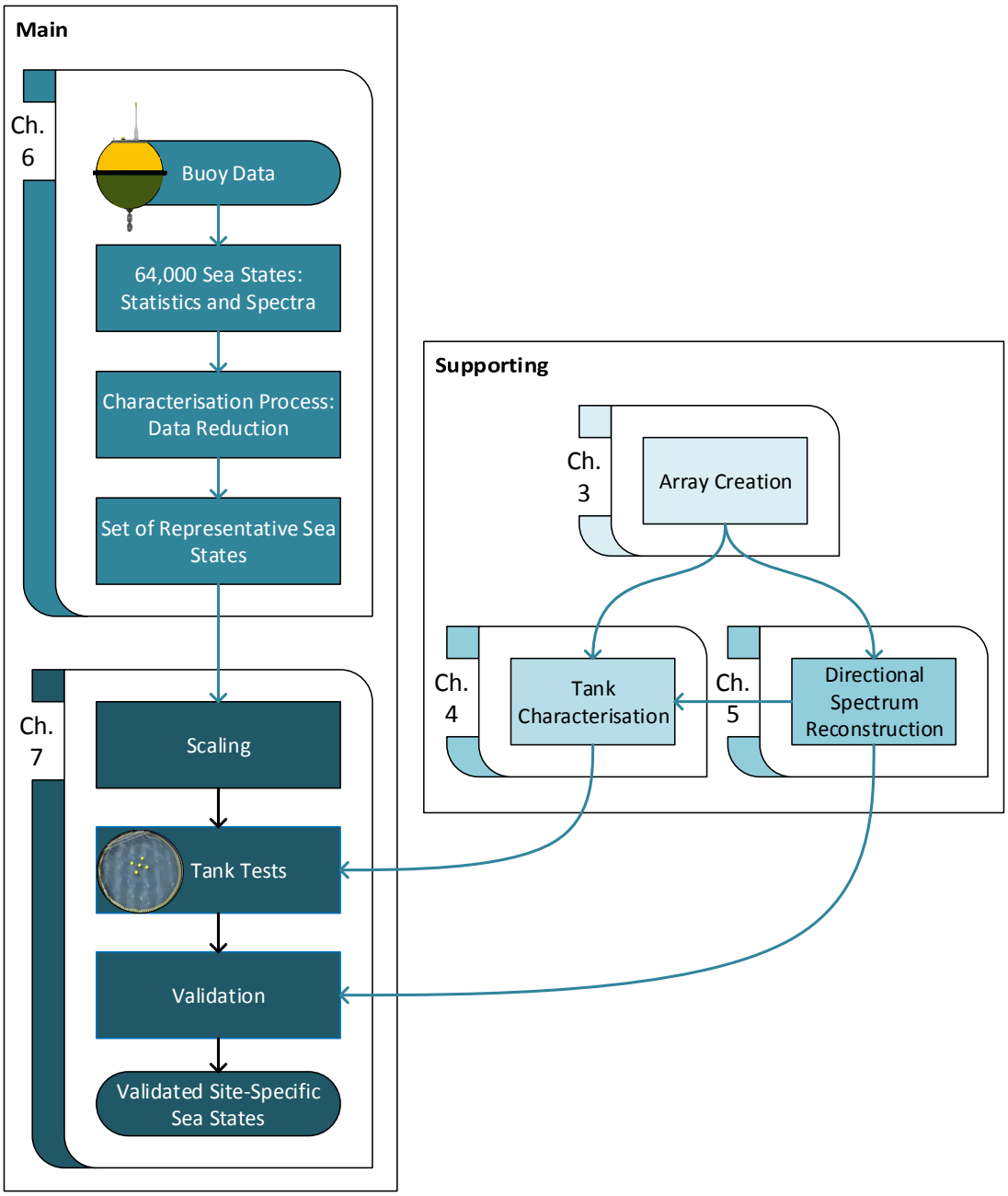

Figure 1.7: Overview of project and chapters, detailing how chapters are inter-linked to serve the main process path

1.5 Research Outcomes

1.5.1 Main Contribution to Knowledge

1. Established that Golomb rulers and Costas arrays can be used as effective, arbitrary number array layouts, for reflection and directional spectrum reconstruction respectively.
2. Characterised the wave generation and absorption performance of the unique FloWave tank, including detailed assessment of the wave field under a range of wave conditions.
3. A new tank-specific directional spectrum reconstruction method has been developed, reducing errors and increasing capabilities.
4. A simple method of creating realistic extreme directional seas from observed spectra is described based on I-FORM environmental contours.
5. Thorough numerical and observational performance assessment of a variety of non-conventional and conventional site classification methodologies was carried out, once applied to the problem of creating a small set of representative sea conditions.
6. Demonstrated that Froude scaling cannot truly be achieved at non-depth ratios, resulting in power and wavelength errors. Alternative scaling approaches based on preserving the power and wavenumber spectrum are detailed.
7. Showed that correct wave-current conditions can be obtained with complex directional spectra and non-collinear current, using linear amplitude based correction factors.

1.5.2 List of Publications

- Draycott, S., Davey, T., Ingram, D. M., Day, A., and Johanning, L. The SPAIR method: Isolating incident and reflected directional wave spectra in multidirectional wave basins. *Coastal Engineering*, 114:265–283, 2015a. ISSN 03783839. doi: 10.1016/j.coastaleng.2016.04.012
- Draycott, S., Davey, T., Ingram, D. M., Day, J. L. a., and Johanning, L. Using a Phase-Time-Path-Difference Approach to Measure Directional Wave Spectra in FloWave. *EWTEC Conference Proceedings*, pages 1–7, 2015b
- Draycott, S., Davey, T., Ingram, D. M., Lawrence, J., Day, A., and Johanning, L. Applying Site-Specific Resource Assessment : Emulation of Representative EMEC seas in the FloWave Facility. *Proceedings of the 25th (2015) International Ocean and Polar Engineering Conference*, pages 815–821, 2015c. ISSN 15551792
- Draycott, S., Davey, T., Ingram, D. M., Lawrence, J., Johanning, L., Day, A., Steynor, J., and Noble, D. Applying site specific resource assessment: methodologies for replicating real seas in the FloWave facility. *ICOE Conference Proceedings*, 44(November), 2014

Chapter 2

Literature Review

This research is concerned with both site characterisation and tank testing, with the aim of reproducing realistic ocean conditions in the FloWave tank. The measurement and representation of ocean conditions are discussed in Section 2.1, in order to understand the tools available to represent and condense wave data. Wave tanks and tank testing methodologies are focussed on in Section 2.2, where techniques for tank characterisation and wave measurement are assessed. Finally, in Section 2.3, the current uses of site data for tank testing is reviewed. Knowledge of these three areas will enable high quality site-specific sea states to be produced by a considered site classification methodology, which can be simulated in a well understood and characterised test facility, with a coherent measurement approach on hand to validate the results.

2.1 Describing and Measuring Ocean Waves

The random properties of ocean waves famously led Lord Rayleigh to state, in the late 19th century, that "The basic law of the seaway is the apparent lack of any law" (Denis and Pierson, 1953). Despite this early outlook, people have been quantifying the statistical nature of ocean surface waves since Munk (1944); Sverdrup and Munk (1947) introduced the idea of "significant waves", denoting the average height and periods of the highest one-third of the waves. This description roughly relates to the height and period values that would be estimated by a trained observer, and significant wave height, H_s, is still a term widely used to describe sea states today. Typically, however, this has been replaced by a spectral approximation, H_{m0}, defined as four times the standard deviation of the surface elevation (e.g. IAHR (1990)).

Wave energy spectra provide an effective means to describe the nature of stochastic wave fields, under the assumption that the sea surface can be described by a sum of sinusoidal wave components. Much of the effort in this area dates to the early 1950s (Mitsuyasu, 2002), culminating in the famous comparison study carried out by Pierson *et al.* (1955). One of the earliest and still most recognised formulations is the two-parameter formulation presented in Bretschneider (1959), however it was the Pierson and Moskowitz (1964) (PM) spectrum that has historically been used as a standard reference (Michel, 1999). This may largely be down to

being used in recommendations around the same time, such as those of the International Ship Structures Congress (Warnsinck, 1964).

The PM spectrum is a useful sea state description, yet is limited to fully developed single-peaked sea states. Developing seas have a more peaked spectrum, leading to a peak enhancement factor being incorporated in the well known JONSWAP spectral formulation described in Hasselmann *et al.* (1973). This spectrum is one of the most widely used to inform design and carry out laboratory experiments (Reeve *et al.*, 2004). Sea states composed of two or more wave systems cannot be effectively described by any of the aforementioned spectral forms, leading to efforts to rectify this. The most recognised of these is probably the Ochi and Hubble (1976) spectrum, which uses a six-parameter formulation to describe bi-modal sea states, although other more recent formulations exist such as those presented in Guedes Soares (1984) and Torsethaugen (1993).

The idea of multi-modal seas immediately introduces the possibility that these systems are propagating in different directions, and indeed even single wave systems contain a spread of directions. To more completely describe a sea state it is therefore required to define the directional spectrum; describing the energy distribution across both frequency (or wavenumber) and direction. The directional spectrum concept i.e. a surface made up of various regular waves with different amplitudes, directions and phases, was first introduced in Longuet-Higgins (1957). Longuet-Higgins *et al.* (1963) detail how directional spectra can be described as a directional Fourier series for each frequency component and how the first five Fourier coefficients can be inferred from data obtained from heave-pitch-roll buoys.

2.1.1 Measurement Approaches

There are now numerous methods to measure waves and infer directional spectra. The technologies available broadly fall into three categories: co-located gauges, spatial arrays and remote-sensing systems (Benoit and Teisson, 1994). In addition to the classical methods of heave-pitch-roll buoys (co-located) and spatial gauge/transducer arrays, there are now more recent approaches including using displacement-GPS buoys, Acoustic Doppler Current Profilers (ADCPs) and numerous radar technologies (Barstow *et al.*, 2005). Despite these advances, none of these instruments can provide enough data to obtain robust estimates of the directional spectrum, resulting in an "awkward inverse problem" (Benoit and Teisson, 1994). As such, assumptions are required about the spectral form in order to obtain estimates, which are instrument dependent (Barstow *et al.*, 2005).

Wave buoys are the most commonly used method for ocean wave measurement (Holthuijsen, 2007), with moored buoys being deployed since the 1950s (Meindl, 1996). Barber (1946) was the first to describe the principle of how directional wave spectra could be obtained from buoy motions, with this concept later becoming reality, as detailed in Longuet-Higgins *et al.* (1963).

As the data available for this research is from a wave buoy, methods of obtaining directional spectra from wave buoys will be focussed on.

2.1.1.1 Directional Spectrum Estimation from Buoy Data

There are many methods to estimate the directional spectrum, with the majority focussing on the idea of a Directional Spreading Function (DSF), describing the directional spread of wave energy in each frequency bin. These are generally created by starting with directional Fourier coefficients, which can be obtained from any set of independent measurements e.g. spatial arrays of gauges, pressure sensors, accelerations etc. as described in detail in Benoit *et al.* (1997). Directional wave buoys, including the Datawell Directional Waverider buoys deployed at EMEC, typically measure heave, pitch and roll. Cross-correlation between these three signals is used to infer directional information, with the co-spectra and quadrature-spectra providing the first five directional Fourier coefficients for each frequency band (Longuet-Higgins *et al.*, 1963).

Directional Fourier coefficients are provided with the EMEC data for this research. These cannot, however, be used directly to reconstruct the directional spectrum as they tend to produce negative values, leading Longuet-Higgins *et al.* (1963) to propose the Weighted Fourier Series (WFS) method. This approach has historically been the most widely used method for representing directional spectra (Earle *et al.*, 1999), however more advanced methods have since been developed with better directional resolution. Each method is based on different assumptions and give vastly differing results and as such it is important to make an informed decision when assuming the form of the directional spectrum.

There are multiple methods that take advantage of Fourier coefficients or cross-spectra to infer the directional spectrum, which are detailed in numerous papers including Earle *et al.* (1999); Benoit (1992) and Benoit *et al.* (1997). In addition to the Fourier series expansion approaches like the WFS, there are parametric models such as the widely used $\cos^{2s}$ spreading function detailed in Mitsuyasu *et al.* (1975) and Longuet-Higgins *et al.* (1963).

Despite parametric models being used extensively to define and simulate directional seas for testing and design purposes, the two most common approaches to infer directional distributions from single-point data are based on Maximum Likelihood Methods (MLM) and the Maximum Entropy Methods (MEM). The MLM, introduced by Capon *et al.* (1967), is a popular method and can be easily implemented assuming that the DSF can be estimated by a linear combination of cross-spectra (Benoit *et al.*, 1997). This approach has been built on in Oltman-Shay and Guza (1984) to improve consistency between cross-spectra from the estimate and from wave signal, in which they define the Iterative Maximum Likelihood Method (IMLM). MEM methods are always consistent with cross-spectra, and have been adapted from probability theory, treating the DSF as a Probability Density Function (PDF) (Benoit *et al.*, 1997). First introduced for single-point systems by Lygre and Krogstad (1986), an alternative MEM approach often called

the Maximum Entropy Principle (MEP), or MEM2, was applied in Nwogu *et al.* (1987) and has been shown to provide favourable results (Benoit *et al.*, 1997).

There are numerous less commonly used approaches, including the Bayesian Directional Method (BDM) described in Hashimoto and Kobine (1988) and Hashimoto (1997) and the Phase-Time-Path-Difference (PTPD) method outlined in Esteva (1976) and Fernandes *et al.* (2000). The BDM is considered the most powerful method for spatial arrays of gauges (see Section 2.2.3.2), however, is not recommended for single-point systems (Benoit *et al.*, 1997; Benoit, 1992), whilst the PTPD approach only obtains 'mean' directions for each frequency band rather than the nature of the directional spread.

In order to get reliable and robust estimates of directional spectra for the EMEC buoy data it is important to choose the most favourable approach for the application. It is suggested in Nwogu *et al.* (1987); Benoit (1992); Benoit *et al.* (1997) and Kim *et al.* (1994) that the MEM2/MEP method is the most reliable for estimates from single-point measuring systems like buoys. Despite this, the solution to the MEP is non-linear, computationally challenging and does not always converge. This led Hashimoto (1997) to propose using Newton's method of local linearisation to help the convergence and Kim *et al.* (1994) to suggest approximate solutions to the problem. Some of these directional spectrum reconstruction methods are trialled in Section 6.1.3, before a method is chosen to create approximately 65,000 directional spectra required for this research.

2.1.2 Site Characterisation

Site characterisation enables both the magnitude of the resource (i.e. energy available), along with the nature of the resource to be determined. Detailed studies into wave site characterisation largely date back to the 1950s, where work such as that carried out in Bretschneider (1959) began to assess statistics of site and wave characteristics to aid coastal engineering problems. Although historically not focussed on assessing the resource (Folley *et al.*, 2009), this sort of approach, particularly in measuring and analysing the energy spectra, is vital for understanding site wave power and characteristics.

With the notable resurgence of interest in wave energy converters in the 1970s, and again more recently, a focus on measuring and analysing the suitability of wave sites for energy extraction purposes has emerged. Although using some of the classical techniques, the emphasis has shifted to focus on different statistics, with the aim of using the resource assessment to predict expected energy yield at a site for a given technology. In addition to helping assess economic viability, importantly this feeds into engineering design and marine operations decisions as discussed in the EquiMar protocols (Davey *et al.*, 2010).

In-situ measurements are still used to obtain wave data, however since the development of 3^{rd} generation wave models starting in the 1980s (Mitsuyasu, 2002), spectral wave models

are frequently being used for this purpose. These models still require validation against in-site measurement such as buoys, as carried out in Wolf *et al.* (2000); Bunney (2011); Neill *et al.* (2014); Van Nieuwkoop *et al.* (2013); Lawrence *et al.* (2009); Gonçalves *et al.* (2014) and many others, but have the significant advantage of being able to obtain hindcast data over long timeframes; obtaining longer term variability and statistics (Emec, 2009). Extrapolation of extreme events can be carried out with reduced uncertainty, enabling site-specific extreme loads to be inferred through numerical modelling or tank testing with the defined conditions.

With many resource assessments being carried out for individual locations, such as those mentioned, guidance has recently become available from a number of sources including EMEC (Emec, 2009), the EquiMar protocols (Davey *et al.*, 2010), as well as earlier guidelines from individuals such as Mollison (1994) and Saulnier and Pontes (2006). Both the EMEC and EquiMar guidance describe resource assessment procedures, methods of measurement, spectral analysis and key parameters, and the role of wave models. Emphasis is placed on the use of scatter diagrams of significant wave height and energy period (H_{m0} and T_E) to assess resource, and the combination with device specific power matrices to assess expected productivity. Despite the focus on height and period metrics, the EMEC guidance discusses the potential of using other parameters to further split up energy matrices such as mean direction and directional spreading. This enables further partitioning of the data so that key parameters affecting device performance can be isolated and used to refine production estimates if combined with device performance knowledge under these conditions. The EquiMar guidance discusses the potential for more accurate power production estimates if directional spectra are used. Both sets of guidance discuss how to obtain the directional spectra from data, yet both somewhat confusingly suggest using the MEM approach. This is despite many comparison studies (as discussed in Section 2.1.1.1) showing that the MEM consistently produces artificially narrow peaks, results in spurious multi-modal estimates and is outperformed by the MEP approach (Earle *et al.*, 1999; Benoit *et al.*, 1997). It is likely that this recommendation is based on ease of application rather than performance.

Using spectra in site characterisation enables a more thorough, low-level assessment of the nature of the resource, which can be used to more effectively explore expected device behaviour. Detailed studies of site directional spectra are carried out, such as in Saulnier *et al.* (2012) and Alves and Melo (1999), where in Saulnier *et al.* (2012) it is noted that:

> "the fact a set of overall parameters – though straightforward to compute (e.g. H_{m0}, f_p) – is not sufficient (not to say misleading) to describe the actual sea complexity"

Other work such as that presented in Van Nieuwkoop *et al.* (2013) assesses the spectral variability observed within H_{m0}-T_E partitions, providing an example of the range of spectra that are essentially grouped together in this process. In certain sites multi-modal seas are prevalent, with 22% of North Atlantic spectra being multi-modal (Guedes Soares, 1984). These mixed seas can represent vastly differing conditions than uni-modal spectra with the same statistics,

leading to a need to identify such sea states so that more effective characterisation procedures can be carried out. Rodríguez and Guedes Soares (1999) presents a method for doing this, with Ewans *et al.* (2006) applying the procedure whilst fitting JONSWAP spectra to each mode.

To reduce datasets down to characteristic or representative sea states it is typical to create scatter diagrams as described in Davey *et al.* (2010) & Emec (2009). Bins can be defined on statistics such as $H_{m0}, T_E, \bar{\theta}$, before using parametric spectra to represent each bin (Boukhanovsky *et al.*, 2007). As mentioned in Saulnier *et al.* (2012) and others this does not necessarily provide a good representation of the underlying conditions and will lead to an incomplete or poorly detailed site description being fed into numerical models or tank tests. In Mansour and Ertekin (2003) it is noted that:

> "Structures with dynamic response require a representation of wave systems more detailed than a mere couple of significant wave height and period, and that requirement is usually satisfied with spectra".

Although spectra will be created and used for testing purposes, if they are not considered in the characterisation then the resulting 'representative' spectra will not correlate well to observed conditions.

Some effort in recent years has gone into characterising wave sites by their spectral similarity, rather than the typical proxy set of height and period parameters derived from such spectra. Boukhanovsky *et al.* (2007) created five climatic classes of directional wave spectra for the North Sea, based on varying 'degrees of multi-modality', where the relative abundance of each class was identified for a range of North Sea locations. Despite being an interesting and useful classification in some respects, Hamilton (2010) notes that the approach is "rather crude as a spectral classification". Hamilton (2010) implements a statistical clustering algorithm to effectively and automatically create (frequency) spectral classes. This approach means that no curve-fitting or parametrisation of spectra is required prior to classification and as such no information is lost in the grouping methodology itself, enabling multi-modal spectra, or indeed any spectral shape, to be considered and classified.

The types of more detailed characterisation work carried out by Boukhanovsky *et al.* (2007) and Hamilton (2010) demonstrate that spectra can be considered when carrying out site characterisation, and may be used to create more representative sea conditions suitable for tank testing or numerical modelling. Part of this thesis aims to assess this potential, exploring the use of clustering algorithms with directional spectra, along with the trade-offs introduced with respect to other parameters when applied to the constrained problem of creating a small set of statistical representative site-specific tank tests.

2.1.2.1 Obtaining Extremes

Characterising a site based on observed or hindcast data enables a detailed understanding to be gained about the nature of the site conditions which can be used to predict expected performance under the conditions, which have been observed. For survivability, however, it is paramount to identify the expected extreme conditions, which primarily focusses on the identification of extreme wave heights. This is achieved using extreme value distributions to extrapolate the observed data to the desired return period and is suggested by Goda (2010) to be the first step in coastal structure design.

To infer the expected extreme significant wave heights (return values) for a given return period, a distribution model must be fitted to those wave heights considered to be extreme. This is typically done using a Block Maxima (BM) or Peaks Over Threshold (POT) approach, although occasionally an r-largest methodology is used (Caires, 2011). Generalised Extreme Value (GEV) distributions (von Mises, 1936) describe data obtained using a block maxima approach (Caires, 2011), where block lengths can be chosen based on the length of the dataset and resulting fit (e.g yearly, monthly, weekly). Despite suggestions by Goda (2000) that "there is no theoretical ground to recommend any distribution function *a priori* to samples collected by POT", it is shown by Leadbetter (1983) that a Generalised Pareto Distribution (GPD) should be used for threshold derived extreme data.

Both Caires (2011) and Teena *et al.* (2012) give good overviews of the approaches available and when they are most applicable, whilst Coles (2001) goes into more detail about the development and derivation of such theories. It is recommended by Caires (2011) that if the dataset is relatively small (a few years) then a POT approach should be taken. Additionally, if multiple storm events occur within relatively small time-frames, it is recommended in Teena *et al.* (2012) to use this POT method to include all the extreme events in the analysis. As both of these criteria apply to the EMEC dataset obtained for this work a POT-GPD analysis will be carried out (see Section 6.3). To implement this approach and to ensure the POT data fits a GPD distribution, these data points should be approximately independent (Caires, 2011). In relation to wave data this essentially means ensuring each 'point' under consideration should be the maximum from each distinct storm event. The threshold choice is also important and is key to providing reasonable estimates of extreme event return values. This choice is essentially a trade-off between bias and variance (Teena *et al.*, 2012) and must be small enough to ensure there are sufficient points to determine the GPD parameters, but also must be large enough so that the data is truly capturing extreme events, and as such converges to a GPD (Abild *et al.*, 1992).

One of the issues with univariate extreme analysis, based solely on H_{m0}, is that appropriate wave period values are still required before extreme sea states can be created. From this univariate analysis, however, the wave period values for the specified return period are unknown. To calculate these values a joint extreme probability distribution must be obtained for wave

height and period. As recommended by Prevosto (2011), the Inverse First Order Reliability Method (I-FORM) can be used, which provides environmental contours at the desired return periods. A 3-parameter Weibull distribution fitted to significant wave heights is recommended by DNV (DNV, 2014) and is implemented either for all or just the extreme wave heights in Winterstein *et al.* (1993); Haver and Nyhus (1986) and Berg (2011). However, this is unlikely to fit the extreme data well, and it is shown in Doherty and Folley (2011) that the GPD POT-based distribution may be used effectively with this I-FORM method to describe just the extreme environmental contours. The resulting height-period combinations chosen from this analysis can be used to create extreme sea states that can be implemented in tank testing or numerical models.

2.2 Wave Tank Testing

William Froude in the early 19th century successfully pioneered the idea of tank testing to test scale models (Martins, 2009), developing scaling laws enabling similitude to be gained between full and model scale. This similitude is gained by preserving the Froude (Fr) number, defining the ratio between inertial and gravitational forces (Steen, 2014). It is these forces that are dominant in free-surface waves, so if all elements of a model and wave test conditions are Froude scaled then accurate conclusions about full-scale behaviour can be drawn from scaled test results. Wave tanks operate tests on this principle and exist globally to assist in a wide range of naval, ocean and coastal engineering problems.

Nowadays numerical modelling techniques can be used to assess the behaviour of, and loads on, offshore structures and devices, with many of these techniques well described in the recently published book by Folley (2016). Potential flow (e.g. Boundary Element Method (BEM)) solvers and Computational Fluid Dynamics (CFD) are commonly being used for this purpose (Nematbakhsh, 2015). Potential theory is reliable only when structure motion is linear and is being excited far from the natural frequency (Nematbakhsh, 2015), and as such is limited for assessing WECs as they are essentially tuned to have natural frequency modes near that of dominant wave energy peaks. CFD has been implemented to assess WECs, enabling a more complete consideration of the physical problem, however is typically limited to fairly simple geometry and is associated with large computational cost. Many studies have been completed, including Agamloh *et al.* (2008) where CFD is implemented to assess a simple cylindrical buoy and Westphalen *et al.* (2014) where another point-absorber type with simple geometry is used. Both studies conclude that although CFD applied to these simple cases provide good results, computational time is high and thus limits the application for real ocean conditions (Nematbakhsh, 2015), with Agamloh *et al.* (2008) noting that more work and significant computational time is required to assess more complex scenarios such as arrays of devices. Coe and Neary (2014) also highlight other difficulties in generating steep non-linear waves in CFD codes and

the fact that CFD results still require validation against physical model tests. Although these computational tools will continue to be developed and improved, currently physical modelling remains the most reliable way to obtain information about complex fluid-structure interactions.

2.2.1 Test Facilities

To aid in the variety of ocean and coastal engineering problems, tanks are designed with different purposes in mind. The types of facility typically useful for testing offshore renewables are ocean basins, coastal basins and towing tanks, and to a lesser extent flumes. Some of the earliest test tanks were towing tanks, characterised as long narrow facilities with carriages to tow models (typically ships), enabling assessment of ship resistance and propulsion. The carriage additionally enables tidal turbines to be tested, with the speed of the carriage defining the relative velocity of the incoming flow-field, as in Doman *et al.* (2015) and others. These are typically also fitted with a wavemaker on one end to assess device/ship motions in defined wave conditions (e.g. Cherneva and Guedes Soares (2011)), and have been used to test wave energy converters in uni-directional sea states (e.g. O'Reilly *et al.* (2011)). Ocean basins, defined as having width comparable to length, are more typically suited for renewable energy devices, however some devices designed for shallower water may utilise coastal basins. Coastal basins, like some of those operated by HR Wallingford (2016), tend to have piston-type wavemakers rather than the flap-type wavemakers used for ocean basins to better simulate the elliptical particle motions associated at shallower depths and are often used to study sediment transport and other coastal phenomena.

There are a great number of test centres with ocean basins, with several test facilities standing out as being particularly active and useful for the renewables sector. There are a number of large European institutions that fit into this category. The Norwegian Marine Technology Research Institute (MARINTEK), has an ocean wave basin ($80\times50\times10$ m with current capability), three towing tanks and a cavitation tunnel (Steen, 2014; MARINTEK, 2016). MARIN (Maritime Research Institute Netherlands) also has a number of facilities, operating six tanks (including an offshore basin with wave and current capability, $170\times40\times5$ m) and a cavitation tunnel (MARIN, 2016). Whilst in France, Ecole Centrale de Nantes (ECN) have a towing tank and a large basin ($50\times30\times5$ m) (Fremondiere, 2016), and IFREMER have three tanks including a deep water basin ($50\times12.5\times20$ m) (Ifremer, 2016). Further afield in Japan the National Maritime Research Institute (NMRI) has some very large towing tanks, an ocean engineering basin ($40\times27\times2$ m) and a circular deep-sea basin (14×5 m) (NMRI, 2016). The ocean and deep-sea basins present at these facilities can be used to test individual devices or small arrays of typical WECs, however have not been purpose built for this application.

Focussing on the UK, where a lot of the early work on tank testing WECs has been carried out, there are a number of tanks available that are suitable for tank testing renewable energy devices, most of which are university owned. Some of these facilities are primarily research

focussed, such as tanks owned by Imperial College London (2016), who operate a wave basin and multiple other facilities, whilst others are also available for commercial use such as the COAST laboratory operated by Plymouth University (2016). The COAST laboratory consists of a coastal basin, a sediment wave basin and an ocean basin ($35\times15.5\times3$ m) with current capability (0.2m/s) and adjustable floor depth.

The University of Edinburgh has a history of developing wave basins with the sole focus of testing wave energy devices. The 'Wide Tank', built in 1977, was the first multi-directional wave tank with absorbing wavemakers (Edinburgh Wave Power Group, 2009a), and was designed specifically to test wave energy converters between 1:150 & 1:100 scale, particularly the Edinburgh duck. The force-feedback mechanism implemented in this tank enables active absorption, which was pioneered by Salter (1981), and is used in many of the aforementioned tanks to improve the quality of the obtained wave fields. This tank was decommissioned in 2001, and harvested to build the 'Curved Tank' which was subsequently commissioned in 2003 (Pascal *et al.*, 2009). This unique facility was designed with wavemakers in a 90° arc to increase the available angular spread and hence the realism of directional sea states (Edinburgh Wave Power Group, 2009b). This facility is still in use today offering scale model testing in the 1:100 – 1:70 region.

More recently in Edinburgh the FloWave Ocean Energy Research Facility has been constructed and was commissioned in 2013/2014 (Ingram *et al.*, 2014). As detailed in Section 1.3 this is a circular combined wave-current tank, making it a one-of-a-kind facility that has the ability re-create multi-directional waves with currents at any relative angle. The tank is larger than other circular wave basins (NMRI deep-sea basin and AMOEBA - Advanced Multiple Organized Experimental BAsin) making it suitable for array testing, and has a larger current generation capability that other combined wave-current tanks. These features, according to Ingram *et al.* (2014), makes FloWave the first facility where *"realistic ocean conditions, typical of those found at marine energy deployment sites, can be created"*, thus making it well suited for effective testing of wave and tidal energy devices. Being a new and unique facility the tank must be characterised and understood, so that the complex sea conditions FloWave has the potential to create can be achieved with confidence.

2.2.2 Wave Tank Characterisation

There has been little published work specifically on the detailed characterisation of wave tank test facilities, however there are some studies published on the Edinburgh Curved Tank and the circular wave basins of NMRI and AMOEBA. Cruz *et al.* (2006) characterises the spatial variability of measured wave heights in the Edinburgh curved tank for regular and irregular seas and results of frequency and directional spectra are presented. The spectral outputs in this work seem quite poor, however it appears that this may be more a result of careless spectral analysis and array design due to the apparent spectral leakage and 'flat' DSF

outputs. This highlights that the correct tools and methodologies need to be used if meaningful results are to be inferred. In this instance, ensuring wave generation frequencies matched those of the FFT would improve the frequency spectrum outputs by reducing spectral leakage. Additionally, consideration of the vector wave gauge separations relative to wavelengths and angular components could dramatically improve the directional spectrum calculations.

Lucas *et al.* (2008) presents reflection analysis for a variety of regular waves highlighting the sensitivity to wave frequency of the passive beach and shows incident and reflected spectra before and after a location-specific correction procedure. Other work has been carried out on this facility, including that by Pascal *et al.* (2009), where wave reflections are assessed as a function of steepness, frequency and amplitude, and correctness of angle is analysed. Gyongy *et al.* (2014b) created a hydrodynamic Boundary Element Method (BEM) model for the curved tank and validated against measurement. This was achieved by assessing variation of wave height across the tank area compared with those predicted by the model, showing favourable results.

More analogous to FloWave, due to the tank being circular and completely relying on active absorption is the 14 m diameter Deep-sea basin at NMRI, which is assessed in Maeda *et al.* (2004). Wave height variations are measured over the tank area, demonstrating that the 'regular' wave fields are not spatially homogeneous and that in general, only a small central area obtains the desired wave heights. In this area, however, spectra with various directional distributions are shown to be reproduced well. Assessment of the temporal variability of both regular and irregular wave fields provide limits on the validity of the generated sea states, with conclusions that sea states are stable for a maximum of 7 - 20 minutes depending on frequency content.

Martins (2015) assesses the results from Maeda *et al.* (2004), whilst also considering the circular 1.6 m diameter AMOEBA tank. Comparisons are made between the areas where the wave field can be considered regular, concluding that the NMRI basin is irregular ($> 5\%$ deviation) outside 1 m radius (14%) for all frequencies other than 1 Hz, where a 4 m radius is deemed acceptable. For the AMOEBA tank it is suggested that this is true for a 0.35m radius, or 44% of the tank area. Other work assessing the AMOEBA tank includes Martins *et al.* (2007) and Martins (2009) where deviations from target spectra are assessed along with spatial variability of wave height. This variability is largely attributed to reflection as a result of improper absorption from the paddles.

There are various other observations of laboratory generated waves in other facilities which can aid somewhat in understanding quality metrics and observation methods, yet are more focussed studies in quite dissimilar wave tanks, so are somewhat less applicable. Spectral methods and observations are carried out in numerous papers, including Zhang (2011); Cherneva and Guedes Soares (2011) and Daoud and Kobus (1995). Interesting observations on the spatial evolution of spectra at MARINTEK is carried out by Cherneva and Guedes Soares (2011), giving some indication to the level of spectral spatial variability that may be expected in a basin, whilst

Daoud and Kobus (1995) assess the spectral characteristics at the ECN tank. In this work correction procedures are carried out, and it is noted that reflections cause the wave field to degrade rapidly, highlighting that temporal variability is important to understand and quantify. Other observations focussing on specific phenomena exist in numerous papers such as Westhuis *et al.* (2001) and Onorato *et al.* (2009), where bi-chromatic wave groups and non-linearities are assessed at MARIN, and the effect of angular distribution on statistics of waves at MARINTEK are looked at representatively. These sort of works are interesting and give an insight into some of the more specific considerations, yet would not typically be part of any general tank characterisation work.

Numerical analysis of wave basins, such as the work in Gyongy *et al.* (2014b) has also been conducted to assess the theoretical performance of test tanks. Newman (2010) applies potential theory to wave basins in order to assess control schemes and the resulting wave field, whilst similar analysis has been performed in Gyongy *et al.* (2014a) for the FloWave facility. Comparisons between measurements would be highly interesting, yet the nature of the results shown make them somewhat difficult to compare. Some of the techniques shown in these works are applied to assess the FloWave tank in Chapter 4, whilst additional approaches and techniques are used to assess other interesting elements of the wave fields generated at FloWave.

2.2.3 Measurement

To enable effective assessment of the generated wave fields at FloWave, various measurement strategies and techniques will need to be used. In addition to characterising the tank and assessing performance, measurement approaches are required to validate complex site-specific sea states. Wave gauge arrays and analysis techniques are therefore required to measure directional spectra, infer reflections and assess spatial variability.

2.2.3.1 Reflection Analysis

Historically there have been two dominant methods for the calculation of the reflection coefficient (ratio of reflected to incident wave amplitude), the Goda and Suzuki (1976) method and the method of Mansard and Funke (1980). The Goda method is a frequency domain method, correlating the Fourier coefficients from two points with a known separation. The Mansard and Funke method is an extension of this, using three points and a least squares method to resolve reflected spectra.

More recently an extension on the Mansard and Funke method has been formulated by Zelt and Skjelbreia (2011), extending the least squares method so that it can be applied to an arbitrary number of gauges. This method is discussed in more detail, with modifications proposed in Section 5.1.2. The Zelt and Skjelbreia (2011) approach enables all array separations less than half a component wavelength to be used for the estimation. Suryanto (2006) also essentially

presents this method, with a focus on extracting and assessing the resulting phase shift as a result of the reflection. Gronbech *et al.* (1996) develop a reflection analysis approach using a similar principle, whilst additionally isolating the cross-modes present in the data. The influence cross-modes have on the effectiveness of the standard Zelt and Skjelbreia (2011) implementation is also highlighted, showing the importance of isolating these modes if they are both present and significant.

Other, less commonly applied, methods exist such as the time-domain approach detailed by Frigaard and Brorsen (1995) and a neural network method is presented by Zanuttigh *et al.* (2013). For three-dimensional experiments, different approaches are required. Wang *et al.* (2008) present a method of isolating reflected spectra when incident waves are oblique and undergo refraction on a sloping bottom, whilst Das and Bora (2014) also details an approach for isolating reflected oblique waves under differing conditions. For fully 3D reflections, with directionally spread incoming wave fields, directional spectrum analysis is generally performed, using a defined incident and reflected range for the analysis. Zanuttigh and Andersen (2010) uses the BDM method to do this, whilst Huang *et al.* (2003) implement the MLM and Extended Maximum Entropy Principle (EMEP, see Section 2.2.3.2) approaches, concluding that the EMEP performs most favourably of the two. The problem with using directional spectrum analysis to assess reflection levels is that its effectiveness is dependent on the method's ability to fit two or more 'modes' at each frequency and limited by the necessity to define incident and reflected angular ranges. A tank-specific approach to resolving 3D phase-locked reflections at FloWave is developed and detailed in Chapter 5, whilst also reducing the uncertainty in the directional spectrum reconstruction (see Section 2.2.3.2).

2.2.3.2 Directional Spectrum Reconstruction Methods

To reconstruct directional spectra from tank data the methods discussed in Section 2.1.1.1 can be used, generally by using spatial arrays of gauges to infer the DSF by cross-correlation between the signals. As it is possible to increase the number of independent signals by deploying more gauges, a greater number of directional Fourier coefficients can be obtained. To infer these, however, modifications or extensions must be made to the formulations for co-located buoy signals.

Isobe *et al.* (1984) presents the extension to the MLM, defining the EMLM, which is implemented accordingly in Krogstad (1988) and Tsanis and Brissette (1991). The extension to the MEP approach is detailed in Nwogu (1989) and Hashimoto *et al.* (1994), whilst the IMLM (Oltman-Shay and Guza, 1984) and BDM (Hashimoto and Kobine, 1988) can also be used with spatial arrays of arbitrary number. As mentioned in Section 2.1.1.1 the BDM method is considered to be the most powerful method for reconstructing any shape of directional spectra for spatial arrays of gauges (Benoit *et al.*, 1997; Benoit, 1992), however it requires a minimum of four gauge elements to be considered favourable (Hashimoto and Kobine, 1988).

The EMLM, IMLM, EMEP and BDM approaches are implemented in the DIWASP (2015) MATLAB toolbox, however, after using the tools there seems to be an error in the BDM implementation. The BDM method is, however, readily available for this work through Aalborg University's WaveLab software, where the BDM approach is implemented correctly along with the EMLM approach. Despite the availability of such tools, inherent uncertainty in these DSF-based methods makes directional sea state validation somewhat challenging, hence the development of a new method in Chapter 5.

2.2.3.3 Wave Gauge Arrays

Reflection Analysis Arrays

To perform reflection analysis an array of gauges must be used, with gauge separations key to obtaining reliable data. For the Goda and Suzuki (1976) two-gauge method it is recommended that gauge separations are between 0.05 and 0.45 of the wavelengths of interest, as defined in Eqs. (2.1) and (2.2). For a given separation this gives the maximum and minimum wavelengths that can be resolved and hence the frequency range where reflections can be effectively isolated. For the least-squares three-gauge method presented in Mansard and Funke (1980), the recommendations are shown in Eqs. (2.3) and (2.4), with desired separations relative to the peak wavelength. The Zelt and Skjelbreia (2011) method, despite not having official recommendations, will also benefit from having multiple separations in a similar range.

Goda and Suzuki Limits:

$$Upper\,Limit(f_{max}) : \frac{x_{1,2}}{L_{min}} \cong 0.45 \tag{2.1}$$

$$Lower\,Limit(f_{min}) : \frac{x_{1,2}}{L_{max}} \cong 0.05 \tag{2.2}$$

Mansard and Funke Recommendations:

$$x_{1,2} = \frac{L_p}{10} \tag{2.3}$$

$$\frac{L_p}{6} < x_{1,3} < \frac{L_p}{3} \tag{2.4}$$

Ideally a single gauge array will be used to effectively isolate reflections for the entire frequency range of interest at FloWave. The separation recommendations and understanding of the methods available make this possible and an array is designed for this purpose in Section 3.3, before being used to help characterise the facility.

Directional Spectrum Reconstruction Arrays

To infer directional spectra through a spatial array of gauges it is important to consider the vector separations between all points. This is defined as the co-array, and in order to obtain meaningful results should be as uniform as possible (Haubrich, 1968) whilst not containing duplicate separations, thus maximising the availability of useful information. For directional spectrum reconstruction it is also important to consider the absolute separation magnitudes relative to the wavelengths present, analogous to the reflection array requirements described in Section 2.2.3.3. Specific guidance for directional spectrum arrays is discussed in Goda (2010) which stresses this further, stating that co-array points should be unique, distributed uniformly, and not too large as to create aliasing (i.e. less than half the wavelengths of interest).

There are many standard arrays used for this purpose, with some 'optimum' arrays detailed in Goda (2010), including the delta array (triangle), star array and a six-gauge array defined as 'Haubrich's Array', as published by Haubrich (1968). Arrays of five gauges have also been implemented in Panicker and Borgman (1970) and Nwogu (1989) to good effect, whilst Young (1994) trials a number of geometric arrays ranging from four to seven gauges, concluding that increasing the number of gauges improves the resulting estimates. Indeed, it seems logical that having more gauges would improve estimates, minimising errors, increasing directional resolution and widening the effective frequency and directional ranges. Although there are some arrays with greater than seven gauges presented in Haubrich (1968) these don't seem to have been implemented for directional spectrum reconstruction and there seems to be no standard arrays used with many gauges. Pascal (2012) takes a non-deterministic approach to array design, using a statistical method to choose a favourable seven-gauge layout from a set of randomly generated arrays. This sort of approach may offer a relatively simple route to obtaining effective arrays with an arbitrary number of gauges without the mathematical rigour required to deterministically obtain such arrays. Directional array design is explored further in Section 3.4.

2.3 Site Simulation in a Tank

The aim of this work is to simulate and validate site-specific directional sea states, in a well-characterised FloWave tank. Many tank tests simply explore parameter influence on device response, with tests not aiming to correlate to real world locations e.g. Pascal *et al.* (2012); Zurkinden *et al.* (2014), or test various regular waves to get an understanding of basic hydrodynamic response such as in Zhang *et al.* (2013) and others. It is known, however, that tank tests often aim to represent site conditions and it is recommended to use site specific data to select spectra in the EMEC tank testing guidance (Holmes, 2009). Davey *et al.* (2012) also stresses the importance of using site data for tank testing and in particular site-specific directional spectra to

incorporate true site complexity, noting that the capability of FloWave enables these observed seas to be simulated and how this is a "vital component of the tank's offering". How people choose/create sea states for this purpose, considering the parameters of interest and reducing the dataset down to a small yet meaningful set of test,s remains largely undocumented and seems to be fairly crude at present.

Various design work and tank tests have been performed with site relevance in mind. Goggins and Finnegan (2014) use site data to help optimise the shape of a WEC numerically, using the annual mean spectra from the Atlantic Marine Energy Test Site. Design optimisation based on a mean wave specification that may not actually occur has obvious downfalls and will not result in the optimal shape to maximise power output over the true range of expected sea states. More effective tests are carried out, aiming to cover the expected range, such as in Haller *et al.* (2011) where tests are designed to represent the 'full' range of expected conditions in Oregon. It is unclear, however, what has been considered to define the sea state classes, although various values of H_{m0}, T_p, θ_p and s are used to create a large number of parametric 'real seas'. Some consideration to spectral shape at site is carried out in works such as Lee *et al.* (2013) and Rhinefrank *et al.* (2010). The former eventually use JONSWAP equivalents to represent a small number of site relevant spectra, whilst the latter appear to use these observed spectra in numerical and experimental tests, yet show no information about the choice of sea state, sea state parameters, or results in the real sea conditions.

This thesis explores ways of creating truly representative directional sea states suitable for tank testing, that capture a range of conditions and site complexity and as such will use and build upon the literature discussed in this chapter. Representing the site complexity is important initially and as such, reliable directional spectrum estimates will be required using methods discussed in Section 2.1.1.1. Site characterisation methods detailed in Section 2.1.2 have been explored, built upon and trade-offs understood, with a shift in focus imposed in this case due to the constraint of having to create these seas in a defined time period (with cost implications). Methods of generating and validating the resulting complex sea states have been developed, using wave gauge arrays and directional spectrum reconstruction methodologies (as mentioned in Sections 2.2.3.2 and 2.2.3.3). This work has required a characterised tank to ensure knowledge is gained about the facility and the quality of the conditions generated therein and as such has utilised tools and methods researched in Section 2.2.2.

Chapter 3

Wave Measurement

This chapter describes the wave measurement strategies developed for the FloWave tank, focussing on the experimental configurations designed and used for this work. The design of, and the reasoning behind, various wave gauge arrays are explored and the tools developed are discussed. These array layouts are then shown in their various configurations and are referred to throughout the text when they are used for a set of experiments.

Highlights:

- Arrays created to measure spatial variability, reflections and directional spectra
  - Golomb ruler re-purposed as an effective array for reflection analysis
  - Re-configurable rig designed and built for housing directional spectrum array designs
  - Costas array layouts shown to be effective for directional spectrum reconstruction
  - 'Random' gauge placement tool detailed which chooses array based on co-array uniformity
    - Resulting from a numerical study an eight gauge array using this tool is chosen for directional wave analysis

3.1 Wave Gauges and Data Acquisition

Wave surface elevations are measured within the FloWave facility using multiplexed two-wire resistance type wave gauges, each providing a point measurement with a sample frequency of up to 128 Hz. These gauges create a simple, reliable and cost-effective solution to wave measurement and according to Massel (1996) provide a suitable resolution of $\pm$ 0.1 mm. For these reasons, resistance type gauges are exclusively used at the facility, with different gauge designs being utilised for particular applications.

Fig. 3.1 shows a simple diagram of a two-wire resistance type gauge. For a design of desired height, H, the wire diameter, d, will be adjusted to ensure the correct stiffness and natural frequency. This in turn defines the required separation distance, w. Once designed, the effective resistance between the two wires is proportional to the submerged length of of the wires. This

is an extremely linear relationship, allowing surface elevations to be effectively and easily obtained by recording the measured voltage.

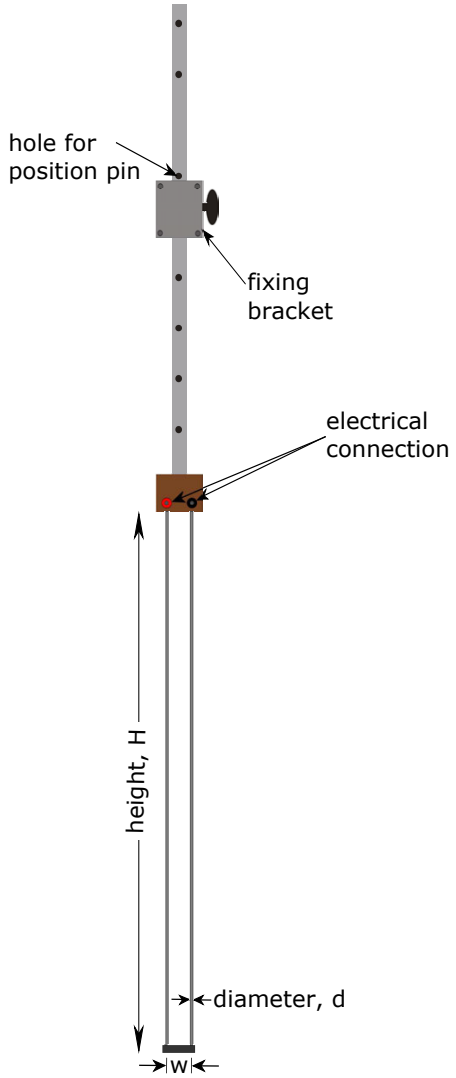

Figure 3.1: Diagram of a two-wire resistance type wave gauge showing key dimensions and features. Diagram based on wave gauges sold by Edinburgh Designs Ltd.

The wave generation and data acquisition are synchronised using a common clock, and are controlled using a single interface provided by Edinburgh Designs. Wave gauge controller 'boxes' manage eight gauges simultaneously, multiplexed so that each gauge is monitored separately, which ensures cross-talk of less that 0.1% (Edinburgh Designs, 2013). Overall, this forms an effective measurement approach, providing high quality data that is synchronised with the wave generation.

Surface elevations obtained from a single wave gauge can be used to calculate wave energy spectra and wave statistics at the gauge location. Deploying gauges in an array enables under-

standing of the wave field over a larger area and more detailed characteristics of the wave field to be inferred, such as reflections or directionality.

3.2 Spatial Mapping Array

3.2.1 Array Requirements

Variations in the wave field occur over the tank area, mostly due to the presence and build up of reflections. The detailed spatial and temporal characteristics of this effect can be identified through analysing the variation in wave height for individual frequency components, easily visualised through the measurement of regular waves.

Ideally the resulting 'spatial maps' will cover the entire 2D area of interest. This area has been taken as the blue floor shown in Fig. 1.6, roughly representing the operational region of the facility. To cover this area it is possible to move the available eight gauges to multiple locations. This, however, is very time consuming and difficult to achieve the desired positions accurately. If it is assumed the tank is rotationally symmetrical, this *effective* area can be created by rotating the waves around the gauges, rather than vice versa. The latter has been chosen for this work as it enables the rotational symmetry of the wave generation to be assessed, whilst also being easier to carry out; enabling the entire test plan to be programmed and run without intervention. The eight gauges have therefore been used in 1.1 m spacings from $(x,y) = (0,0) - (0,7.7)$.

3.2.2 Layout and Methodology

The chosen array layout, Spatial Array 1 (SA1) is shown in Fig. 3.2. The majority of tests that use this array layout assume reflective symmetry for the variations about the centreline of the tank. In these cases only half a rotation is used, covering 180° in 10° intervals. The resulting effective test configuration, Spatial Configuration 1 (SC1), is displayed in Section 3.5, detailing the relative measurement points achieved via this methodology.

The assumption of reflective symmetry may not always be appropriate due to certain random discrepancies in the wave generation and absorption and as such some spatial mapping tests are completed using 360° rotation. For these more detailed spatial maps the array is additionally shifted 550 mm out from the centre and the tests re-generated with a 5° offset. This relative configuration, Spatial Configuration 2 (SC2) shown in Section 3.5, provides a much higher resolution output.

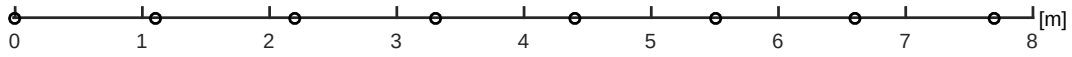

Figure 3.2: Spatial array (SA1) layout

3.3 Reflection Analysis Array

3.3.1 Array Requirements

As mentioned in Section 2.2.3.1 there are numerous methods that can be used to isolate incident and reflected spectra. Array spacing requirements are known for the Goda and Suzuki (1976) two-gauge method and Mansard and Funke (1980) three-gauge approaches from Section 2.2.3.3. For this array, it is desirable to isolate the incident and reflected spectra over the full frequency range of interest and as such a variety of gauge spacings are required, so greater than three gauges will need to be deployed. An array will therefore be designed with the Zelt and Skjelbreia (2011) method in mind, noting that the separation of cross-modes should not be of importance due to the active absorption.

In array design it is important to consider the co-array of the configuration (see Section 2.2.3.3). If a wave gauge configuration is developed that has good co-array properties, the range of separations available should enable reflections to be effectively calculated for a wide range of frequencies (and wavelengths) and have redundancy in all cases to enable error reduction. A summary of the design requirements for an array that can be used for a wide range of tests is shown in Table 3.1. At the time of designing the array eight gauges were available. The length of the array was chosen to be 3 m, as it enables five in-line reflection coefficient calculations to be achieved over the 15 m floor diameter, (for tests detailed in Sections 4.5.1.2 and 4.5.2), whilst additionally incorporating effective separations for the frequency range of interest, 0.2–1.2 Hz (L = 20.95–1.08 m respectively).

Table 3.1: Reflection wave gauge array design requirements

Constraint	Value(s)
Number of gauges	8
Length of array [m]	3
Frequency range [Hz]	0.2–1.2

3.3.2 Array Design and Layout

In this work, Golomb rulers, typically used for information theory and communications, have been re-purposed and explored for use as reflection array layouts. Golomb rulers, by definition, are a set of integer points whereby no pairs of points are the same distance apart (Meyer and Papakonstantinou, 2009). This means there are automatically no duplicate separations. In addition, if *optimal* Golomb rulers are used, there are no shorter rulers of that order, meaning that there will be a minimum number of integer gaps in the co-array. This also means that the co-array will be highly uniform and if scaled to cover the desired length range, should provide an ideal array candidate. For 8^{th} order i.e. eight gauges, there exists only one optimal Golomb ruler, shown in Eq. (3.1).

$$8^{th} \text{ order optimal Golomb ruler (RA1)} = \left| \begin{array}{cccccccc} 0 & 1 & 4 & 9 & 15 & 22 & 32 & 34 \end{array} \right| \tag{3.1}$$

The array and co-array of this Golomb ruler once it has been scaled to the desired array length (3m), is shown in Fig. 3.3. The resulting co-array, as expected, is highly desirable, meaning it is easy to choose suitable separations for the Goda, and Mansard and Funke methods. There are numerous useful separations available when using the approach taken by Zelt and Skjelbreia. This makes the array ideal for all potential reflection approaches applied to 2D problems.

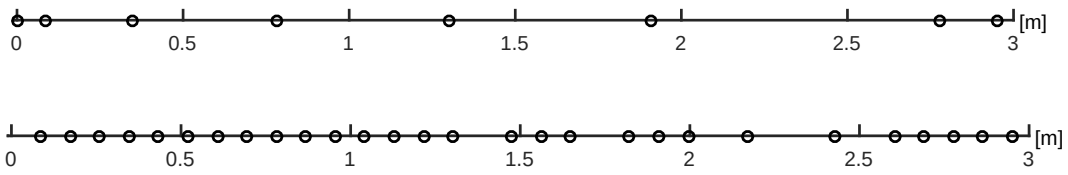

Figure 3.3: Array and Co-array of 8^{th} order Golomb Ruler (RA1) scaled to 2.95 m

The Zelt and Skjelbreia method has been implemented and used in combination with this Golomb-ruler-based array for all uni-directional reflection analysis. The array is used in two configurations, one at the centre of the tank, denoted Reflection Configuration 1 (RC1), and one at five in-line positions, RC2. Both of these configurations are shown in Section 3.5.

3.4 Directional Spectrum Array

3.4.1 Array Requirements

To estimate directional spectra a wave gauge array is required, in combination with a reconstruction method. Although all methods discussed in Sections 2.1.1.1 and 2.2.3.2 utilise the phase differences between gauges to infer directionality, their approaches differ and so

array suitability is slightly method specific. This means that a coherent directional array-methodology has to be formed in combination, to create an overall directional spectrum reconstruction strategy.

As the previously mentioned DSF-based approaches have significant uncertainty associated with them, an alternative approach has been developed in Chapter 5. This approach, called the Single-summation PTPD Approach with In-line Reflections, or SPAIR, works on the principle that each frequency component only has one direction. In Chapter 5 it is found to be significantly more effective for use in FloWave. However, in order to test this numerically over a large range of conditions, various arrays are assessed with a variety of reconstruction methods.

Similar to the reflection array requirements shown in Section 3.3.1, it is important to consider the co-array properties of the array configuration. However, for directional spectrum analysis it is important to consider the co-array uniformity in two dimensions. A range of separation magnitudes is required to deal with the variety of potential wavelengths, but these separations also need to span a range of angles to provide adequate angular resolution.

Table 3.2: Directional wave gauge array design requirements

Constraint	Value(s)
Number of gauges	8
Maximum length of array [m]	2
Maximum width of array [m]	1.3
Angular range of consideration [°]	360
Frequency range [Hz]	0.2–1.2

The nominal wave gauge array constraints are shown in Table 3.2. The array design is constrained to eight gauges at present and must fit onto the directional wave gauge array rig shown in Section 3.4.2.1. The final array will need to incorporate separations small enough to resolve the smaller wavelengths without aliasing (i.e. $< \frac{L_i}{2}$), but large enough to limit the influence of noise and position error on the perceived phase differences.

In order to create an effective array a numerical study has been performed. Two wave gauge array tools have been developed with the co-array uniformity in mind, both of which capable of creating effective arrays with an arbitrary number of gauges, shown in Section 3.4.2.2. In Appendix B the outputs of these tools, for 8 and 16 gauge arrays, have been compared with classical array layouts under a range of simulated sea state scenarios. A final array design from this analysis is chosen and scaled for the FloWave facility.

3.4.2 Array Design

3.4.2.1 Directional Array Rig

In order to mount wave gauges in various configurations, a reconfigurable array rig has been designed and built (with support from Dr Jeffrey Steynor, FloWave) (Fig. 3.4). The rig is 1.3 m $\times$2 m, which is large enough to house arrays suitable for the operational wavelength range, yet small enough to be relatively easy to transport.

Hooks are mounted on the gantry with 180 mm vertical separations, visible in Fig. 3.4. This enables calibration to be carried out over five points (for a 1 m long gauge), leaving a 140 mm gap on either side. The facility's overhead crane is used to lift the rig into these set positions prior to testing, enabling calibration to be carried out for all gauges simultaneously.

Two rows of moveable bars, shown in Fig. 3.5, allow wave gauges to be mounted anywhere within the 1.3 m $\times$ 2 m area, as well as any point on the outer frame. This gives flexibility to trial various wave gauge configurations, as well as enabling the use of test specific arrays, or easy redesign and reconfiguration if some of the gauges are required elsewhere.

The random array probe placement tool (Section 3.4.2.2) allows arrays to be visualised and tested for feasibility for placement on the rig. Examples of this for a number of array configurations are shown in Fig. 3.6.

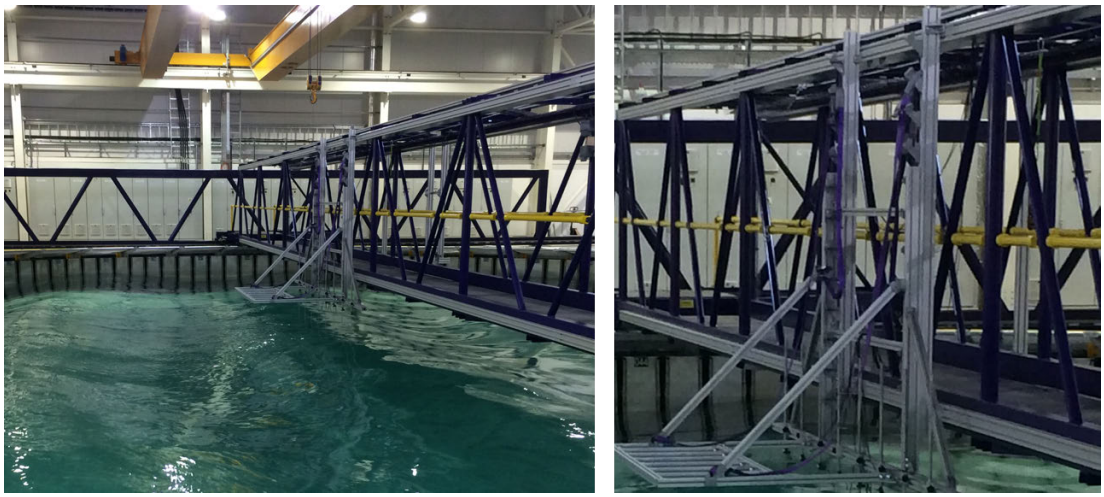

Figure 3.4: Pictures of directional array rig mounted on the FloWave gantry, and enlargement showing vertical hooks for rig calibration and support

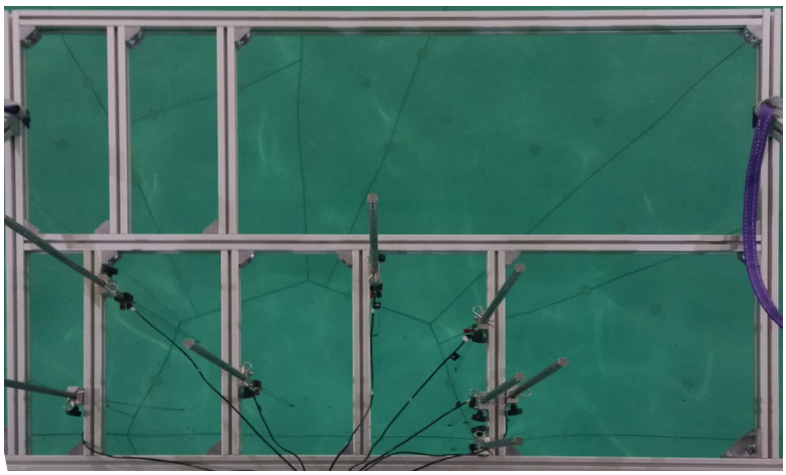

Figure 3.5: Picture of directional array rig showing how two rows of short (600 mm) vertical bars are able to re-configured to place wave gauges

3.4.2.2 Array Tools

Costas Arrays

Costas arrays are permutation matrices that are essentially the two-dimensional equivalent of Golomb rulers (Section 3.3.2), and have been identified as being potentially high performing directional array layouts. Costas arrays differ from other permutation matrices in that all vector distances between points are unique, with the result that the co-array will not contain duplicate separations. In addition, the fact that gauge locations are spaced in every column and row on a square grid means that Costas co-arrays are highly uniform. This makes them ideal candidates for directional wave gauge arrays aiming to resolve over 360°.

A database of Costas arrays, available online (Beard, 2015), provides all known Costas arrays for $N = 3 - 100$, enabling suitable arrays to be identified for an arbitrary number of gauges. As some orders contain a large number of known Costas arrays, a method of choosing the most favourable array layout needs to be defined.

To choose an array, the co-array separations have been binned into twelve directional and five magnitude bins. The co-array with the minimum standard deviation between the number in the bins is then chosen as the favourable array. Sixty bins have been used as an eight gauge array will have $8 \times 7 = 56$ co-array points. Although the number of bins should potentially be a function of the number of gauges, it appears to make little difference on the outputs, providing similar candidates for arrays with significantly more or less gauges. Example outputs of this are shown in Fig. 3.7 for 3, 5, 8 and 16 gauges, showing that as expected, the resulting co-arrays display a high degree of uniformity.

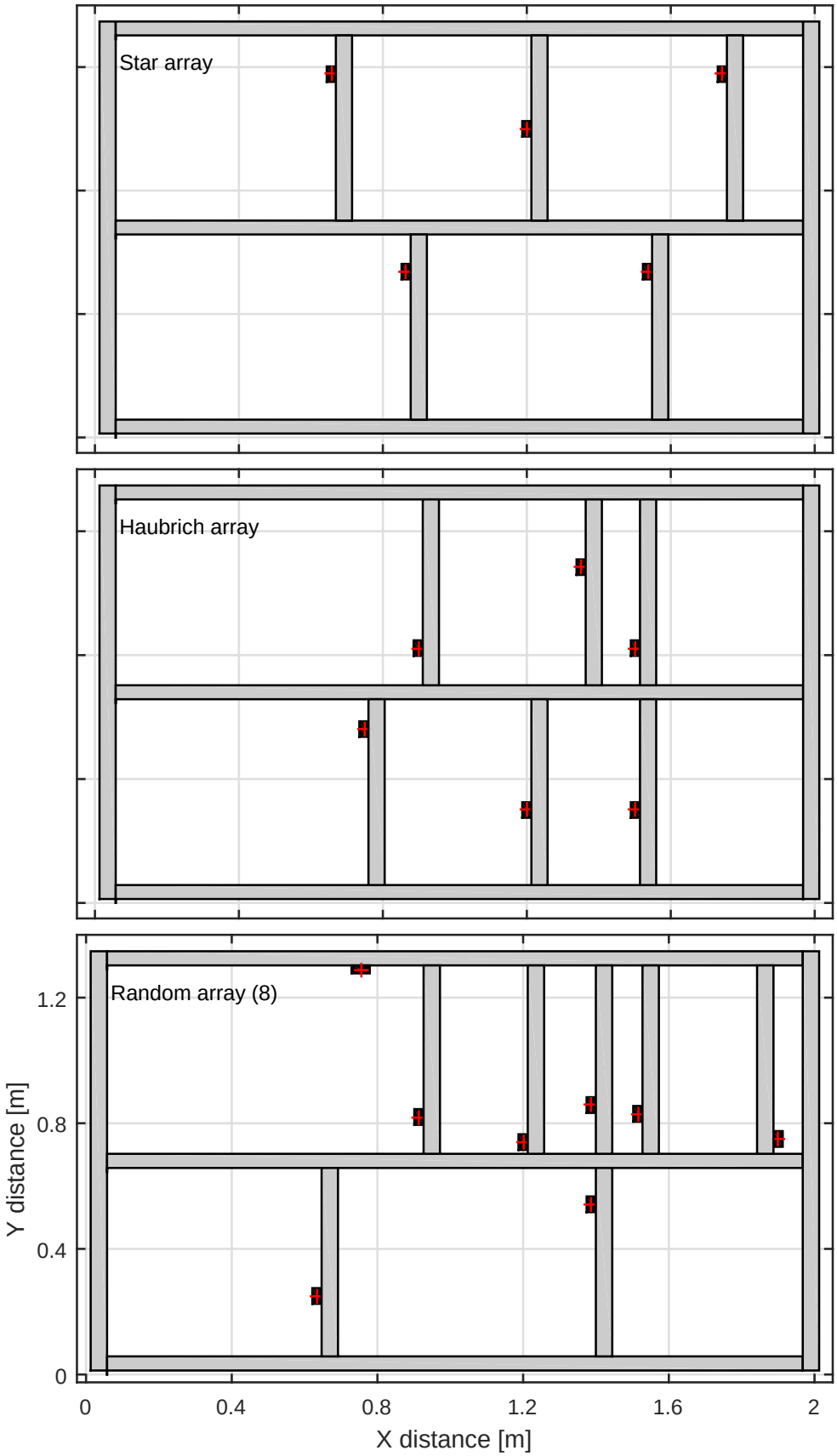

Figure 3.6: Example configurations with directional array rig. Nwogu (1989) star array, Haubrich (1968) six gauge array and a 'random' eight gauge array shown

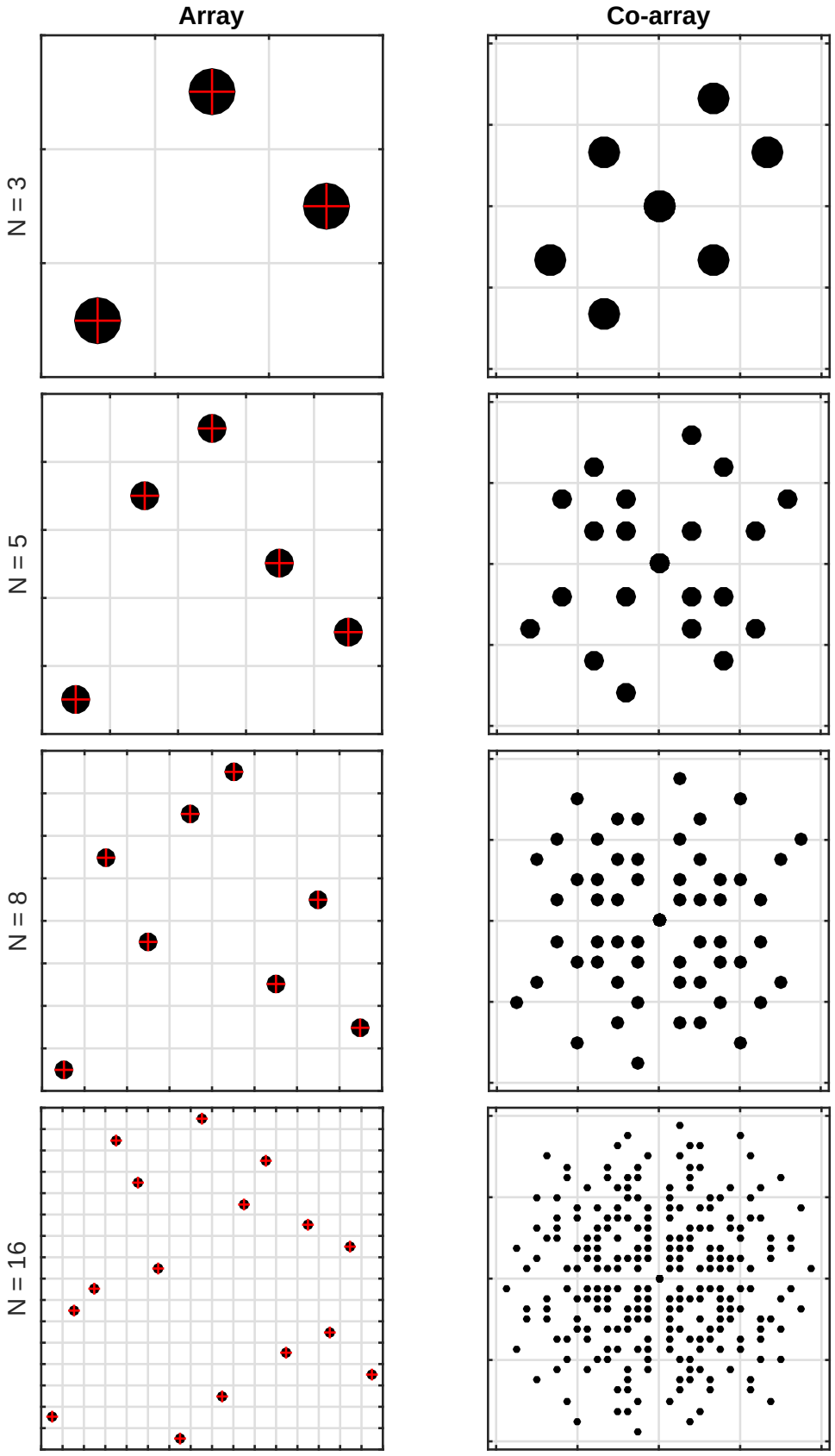

Figure 3.7: Costas array tool outputs for N = 3, 5, 8 and 16, with their respective co-arrays shown

Random Gauge Placement Tool

Pascal (2012) used a statistical approach to select an array from a range of randomly generated array configurations. This tool builds on this random approach, additionally considering wave gauge rig constraints in the array generation and choosing the array based on co-array uniformity.

The aim of this tool, much like the Costas array tool (Section 3.4.2.2), is to enable effective array creation with an arbitrary number of gauges. The procedure is detailed in Algorithm 1. For the required number of gauges, N_{gauges}, the tool creates the desired number of randomised solutions, $N_{iterations}$. The most favourable array is then chosen using the same co-array binning approach detailed in Section 3.4.2.2.

Algorithm 1 Pseudo code for 'random' array generation

procedure RANDOMARRAY($N_{gauges}, N_{iterations}$)
  for i = 1 $\rightarrow$ $N_{iterations}$ **do** ▷ Usually $10^3 \rightarrow 10^5$
    for j = 1 $\rightarrow$ N_{gauges} **do**
      Randomly generate (x_j, y_j) position
      GaugeBreach = BreachGauge($x_1 : x_j$, $y_1 : y_j$) ▷ Check if too close to other gauge (<50 mm)
      while GaugeBreach==true **do**
        Randomly re-generate (x_j, y_j) position
        GaugeBreach = BreachGauge($x_1 : x_j$, $y_1 : y_j$)
      end while
      BarBreach = BreachBar(x_j , y_j) ▷ Check if breach bar
      while BarBreach==true **do**
        (x_j, y_j) = (x_b, y_b) ▷ Move to closest edge of bar
        GaugeBreach = BreachGauge($x_1 : x_j$, $y_1 : y_j$)
        while GaugeBreach==true **do**
          Randomly re-generate (x_j, y_j) position
          GaugeBreach = BreachGauge($x_1 : x_j$, $y_1 : y_j$)
        end while
        BarBreach = BreachBar(x_j , y_j)
      end while
    end for
    Calculate co-array object, $CoArray_i$
    Bin angle and magnitude information of $CoArray_i$ to obtain $Bins_i$
    Calculate standard deviation of $Bins_i$: $SDEV_i$
  end for
  Choose most favourable array based on $min(SDEV)$
  return $(x_{min(SDEV)}, y_{min(SDEV)})$
end procedure

Example outputs of the random array generation tool are shown in Fig. 3.8, along with their respective co-arrays. The co-arrays are relatively uniform, however, as the tool is not limited

to integer positions, the separations are not as regular as the co-arrays created using the Costas array tool. This means, in places, there is higher co-array density, which may or may not be beneficial depending on the array size and application.

3.4.2.3 Array Layout

A numerical study has been carried out to determine the most favourable array and directional spectrum reconstruction method, included in Appendix B. In this work ten array candidates are trialled under a variety of wave conditions aimed at representing the entire range of conditions expected in the facility. From the resulting analysis an array generated using the “random gauge placement tool" was deemed favourable. This array can be found in Fig. 3.9 and is only deployed at the centre of the tank, in the configuration shown in Fig. 3.12.

The combination of this array with the SPAIR method, detailed in Chapter 5, has been found to be the most effective solution considered for the measurement of directional spectra. This combination of array and method then defines the overall directional spectrum reconstruction strategy used throughout this work.

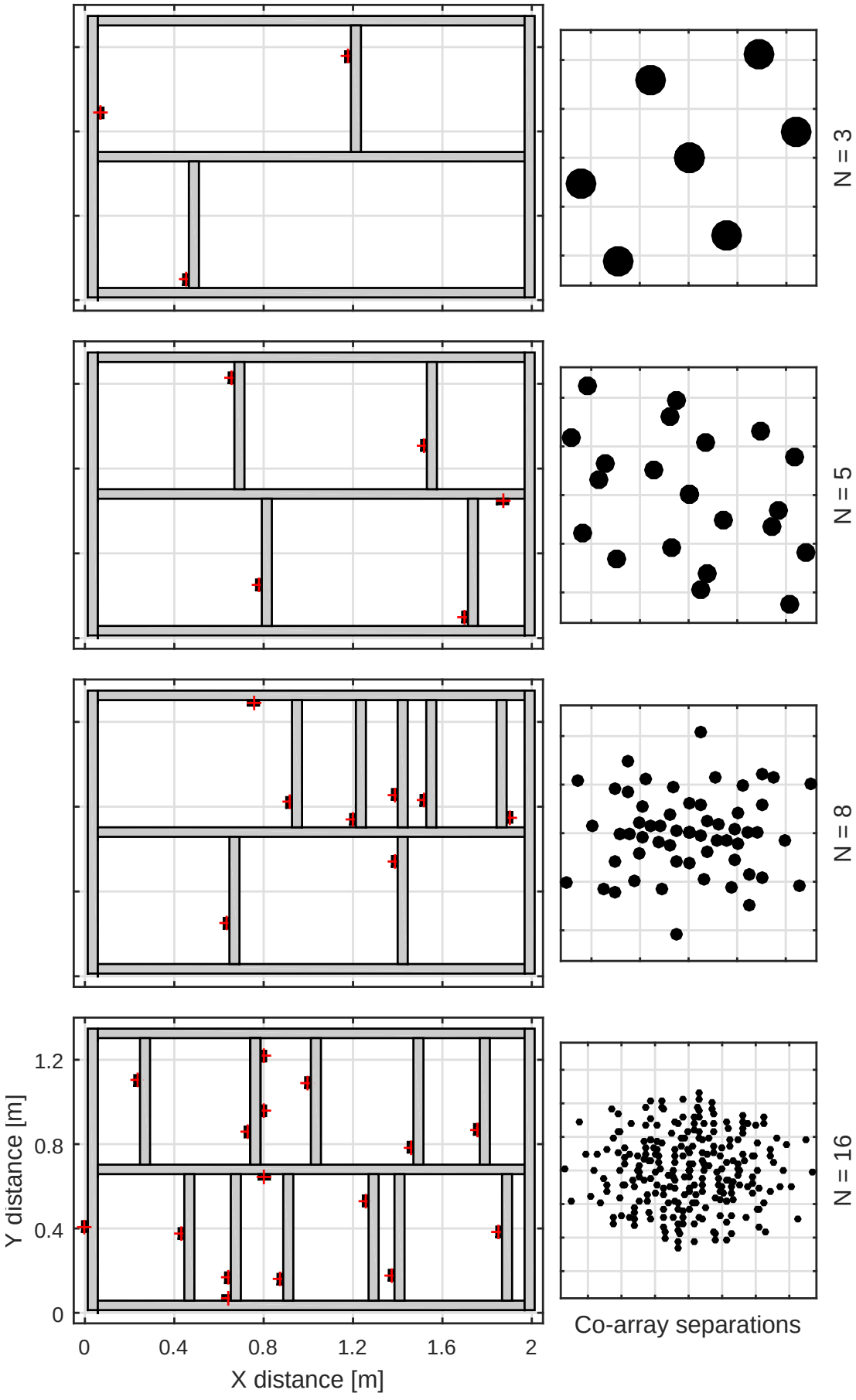

Figure 3.8: Random array tool outputs for N = 3, 5, 8 and 16, with their respective co-arrays shown

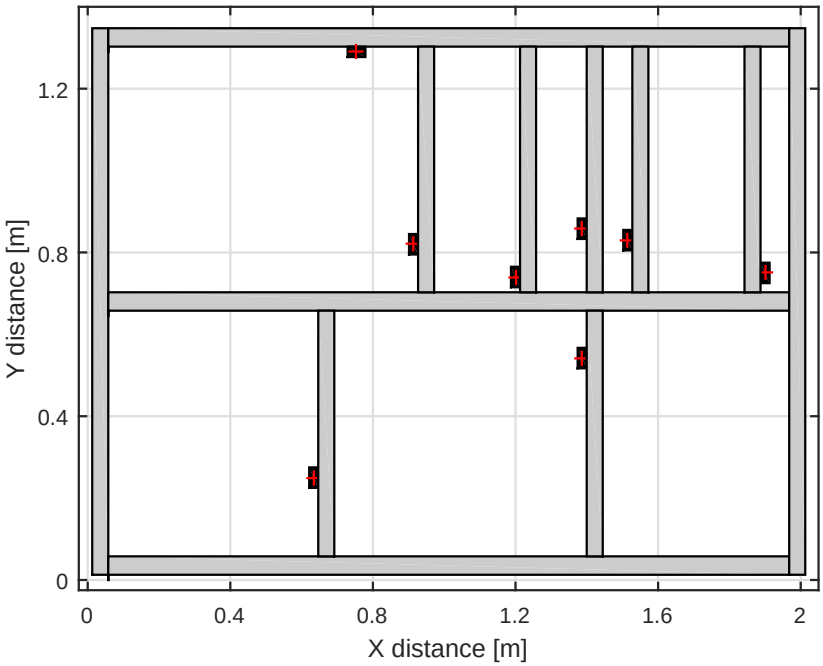

Figure 3.9: Directional Array 1 (DA1): Final eight gauge scaled array generated using random probe placement tool

3.5 Array Configurations

This section shows the arrays in their various configurations and is intended to be a convenient location for referencing experimental configurations used throughout the testing. For the spatial map tests, the configuration is essentially the resulting relative points obtained through the wave rotation, whilst for the reflection and directional spectrum arrays the configurations are in absolute (x, y) space. Spatial map configurations are shown in Fig. 3.10, and the reflection and directional configurations are shown in Figs. 3.11 and 3.12 respectively.

3.6 Implications for Testing

For FloWave the specific arrays designed are very useful for inferring important details about generated wave fields, and as such are vital elements in the tank characterisation and sea state validation work carried presented in this thesis. For users of other facilities the identification of Golomb rulers and Costas arrays as effective reflection and directional spectrum reconstruction arrays respectively is a useful finding. These known arrays provide an easy and effective method of choosing array layouts with an arbitrary number of gauges for a given application, and as such should improve both speed of array design and quality of results.

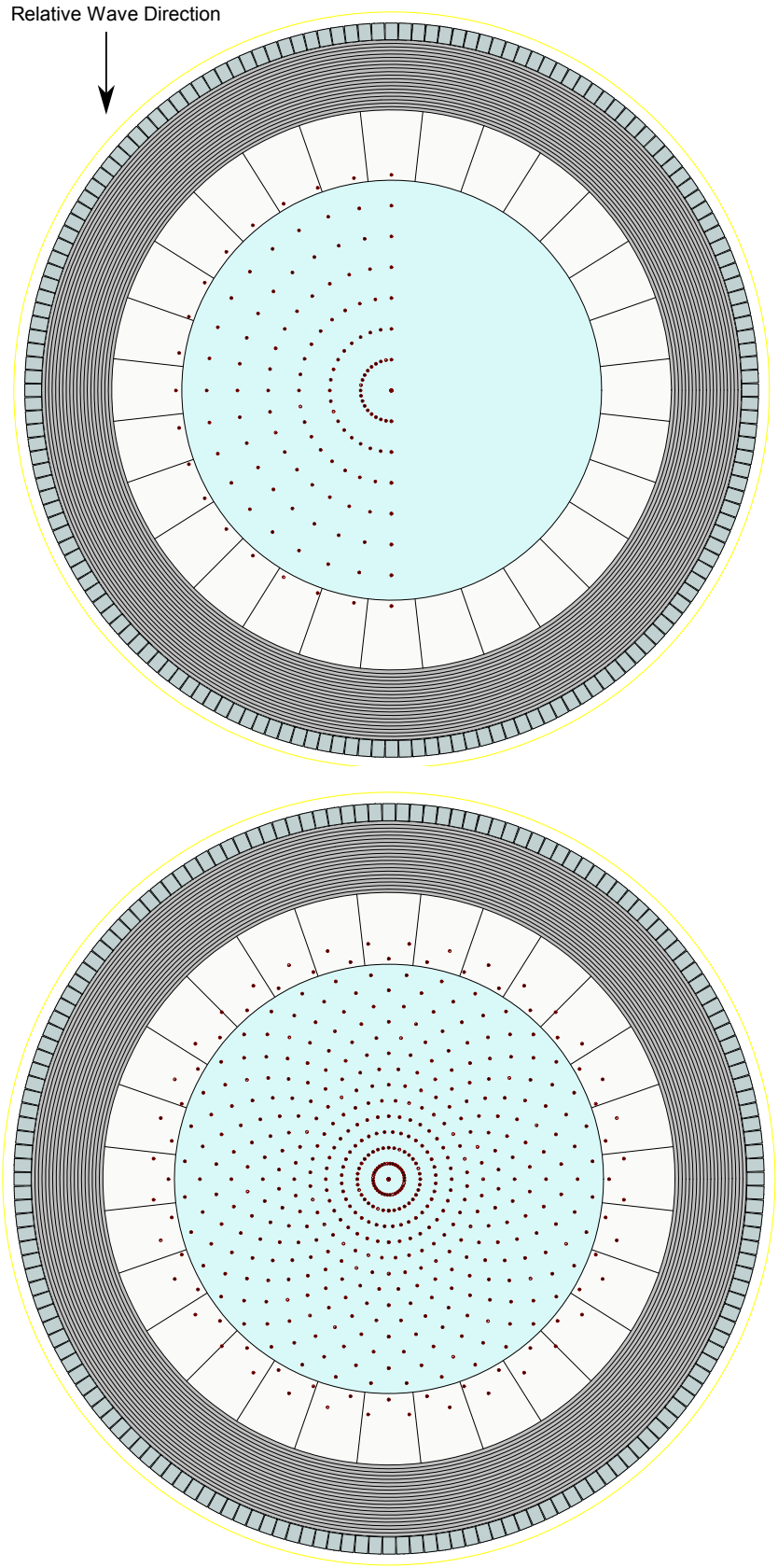

Figure 3.10: Spatial configuration 1 and 2 (SC1/SC2): half and full tank rotations. Measurement points shown relative to wave direction

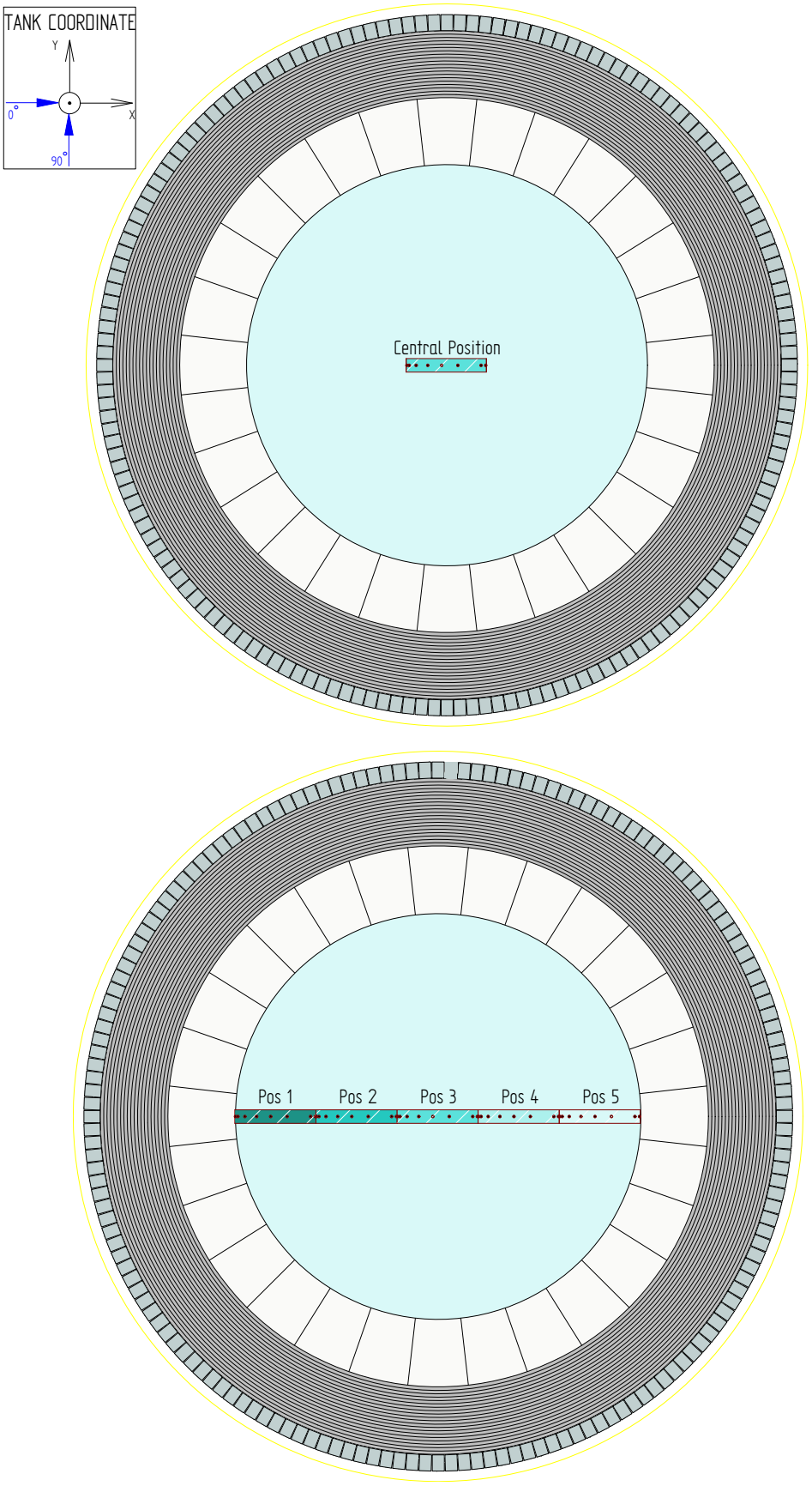

Figure 3.11: Reflection configuration 1 and 2 (RC1/RC2): Golomb ruler based array in centre and in various in-line positions. Waves are generated to propagate in the positive x-direction

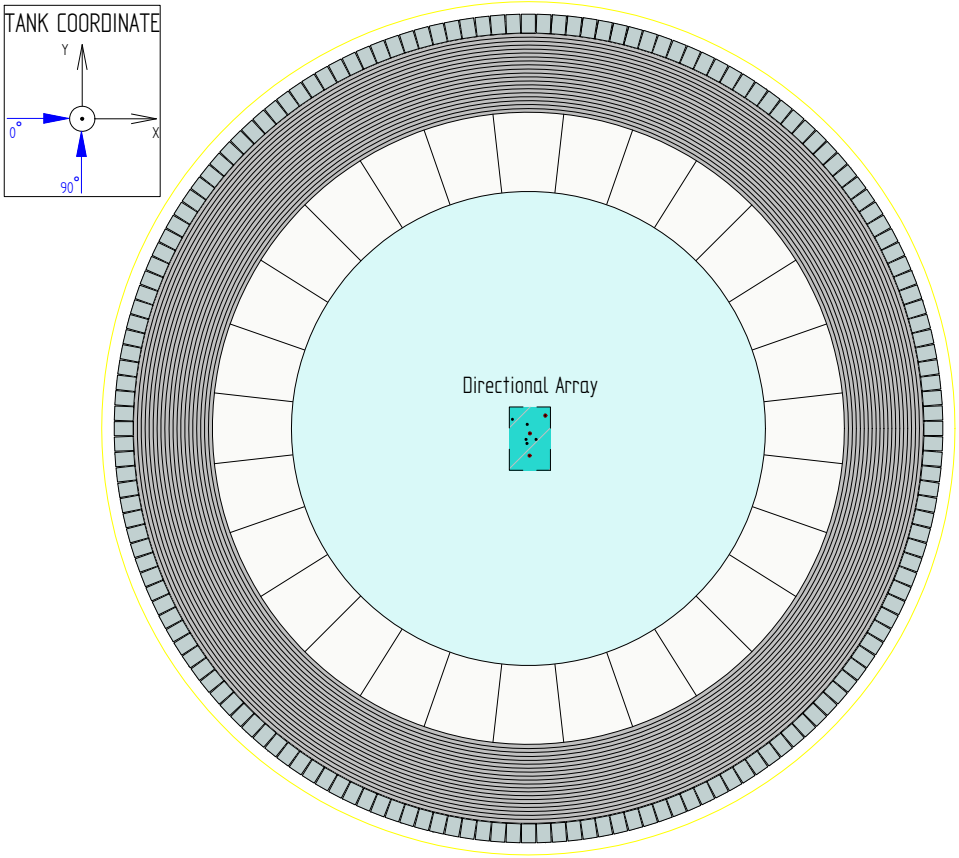

Figure 3.12: Directional Configuration 1 (DC1): Wave gauge array configuration for directional spectrum analysis

Chapter 4

Wave Characterisation and Tank Performance

This chapter discusses the characterisation of the wave field in the FloWave tank under various input conditions. The tank's performance is assessed, and the unique features arising from the tank's design and control are explored. This will inform testing procedures, as well as provide valuable specifics on the characteristics of sea states prior to generation.

Various elements of the wave characteristics are considered including; wave shape (curvature and non-linearity), reflection and absorption characteristics and spatial-temporal variability. The outputs of this analysis will feed into the site specific wave re-creation work (Chapter 7), providing a thorough understanding of the facility in well defined conditions, before more complex sea states are re-created.

Highlights:

- Incident wave curvature found to be negligible, correct wave angles appear to be produced and regular waves are well described by Stokes 2^{nd} order theory
- Reflection analysis carried out for regular and irregular waves, including directional spectra using the SPAIR method (see Chapter 5). These reflections are shown to be curved and found to be larger in high frequency-low steepness wave conditions. Absorption effectiveness is found to decrease rapidly above 1 Hz
- Ideal location for testing is found to be far from the 'absorbing' paddles boundary and off-centre
- Peculiar spectral content is observed in the reflected spectra, which may be attributed to harmonic generation

4.1 Wave Simulation and Generation

4.1.1 Wave Generation

4.1.1.1 Deterministic Wave Generation

In common with most tanks, FloWave uses software which produces pseudo-random deterministic waves. This type of wave generation should precisely reproduce the desired wave energy distribution, $S(f)$ or $E(f,\theta)$, within the specified repeat time of the test, T_r. In addition to ensuring the desired energy distribution, the force-feedback absorbing wave-makers create a precisely controllable wave field and combined with deterministic wave generation provide a very high degree of repeatability (Ingram *et al.*, 2014). Importantly, this enables device alterations to be assessed independently of sea state variations, whilst additionally enabling wave-by-wave comparisons to be made of devices in the time domain.

The chosen repeat time defines the generation frequencies used in increments of $\Delta F = \frac{1}{T_r}$. For each frequency increment, f_i, component amplitudes, A_i, are calculated and assigned a random phase, Φ_i. Component amplitude, frequency, phase and directional information are then provided to the tank, which through a tank transfer function determines the signals to be sent to the wave-makers; creating the desired wave spectrum across the tank after T_r. Running sea state instances for T_r with discrete generation frequencies means that, if performed properly, little to no spectral leakage occurs in frequency domain analysis. This removes the necessity for windowing functions, whilst also meaning that individual component amplitudes can be analysed and corrected effectively.

The repeatability and guaranteed spectral energy content make deterministic wave generation favourable, which is why it has been used exclusively at FloWave. However, it is worth noting that deterministic waves will not exhibit identical statistical properties to the waves they aim to re-create (Pascal, 2012). This is a result of not simulating a truly random Gaussian process and means that the statistics of wave groups may not be reproduced properly (Tucker *et al.*, 1984).

4.1.1.2 The Single-summation Method of Directional Spectrum Generation

A large part of this thesis is concerned with the effective generation and measurement of both parametric and site-specific directional spectra and as such, it is important to identify a suitable generation method.

When aiming to deterministically generate a directional spectrum, there are two main approaches. The first is to mimic the form of the directional spectrum, assigning each generation frequency multiple wave components with differing directions. This approach is called the double-summation method and is demonstrated by Eqs. (4.1) and (4.2). This generation procedure, however, leads to a phenomenon called phase-locking (Miles and Funke, 1989), which occurs when waves at the same frequency but different directions interact and cause

spatial patterns across the tank. These spatial patterns essentially create a non-ergodic wave field, undesirable for tank testing as a consistent wave field will not be obtained over a model location.

To limit the influence of phase-locking, the initial frequency increments, ΔF, can be split up further to create sub-frequency increments $\delta f = \Delta F / N_\theta$. These new frequency increments, still within the original frequency bins, are assigned a unique wave propagation direction. This approach is called the single-summation method, described by Eq. (4.3).

If using the single-summation method there still remains a choice over how to assign directions to the sub-frequency increments. For this work the same approach has been taken as Pascal (2012), whereby equivalent sub-frequencies within each initial frequency increment gets assigned the same direction, as shown in Fig. 4.1. Due to the likelihood of adjacent frequency bands having similar directional distributions ($DSF(f)$) wave components, and in particular the energetic wave components, are distributed as far as possible in frequency. This is important as it limits the effect of 'tooth-breeding', shown in Salter (1981) with reference to an experiment carried out by Glenn Keller. Tooth-breeding is the formation of new wave components, arising due to interaction between existing components very close in frequency. This would lead to spatially variable deviation from the desired energy spectrum and hence its effect should be mitigated.

Fig. 4.1 depicts the single-summation method used in this work. In addition to limiting the effect of phase-locking and tooth-breeding, this method of wave generation is key to the application of the SPAIR directional spectrum reconstruction method described in Chapter 5.

4.1.2 Sea State Simulation

The ability to simulate the wave field over the tank area allows time domain comparisons to be made between theoretical and measured surface elevations. Additionally, simulations of waves over the tank domain may be carried out, enabling theoretical studies to be completed prior to being used or trialled at the facility.

To calculate surface elevations under the assumption of linear wave theory, a summation of the wave components must be carried out. This requires consideration of frequency component phase and direction relative to the co-ordinates of the simulation point. For a directional spectrum described using the double-summation method, this can be calculated using Eq. (4.1) and Eq. (4.2), whilst the single-summation equivalent is shown in Eq. (4.3). When calculating location dependent surface elevations for uni-directional and regular waves this reduces down to Eqs. (4.4) and (4.6) respectively.

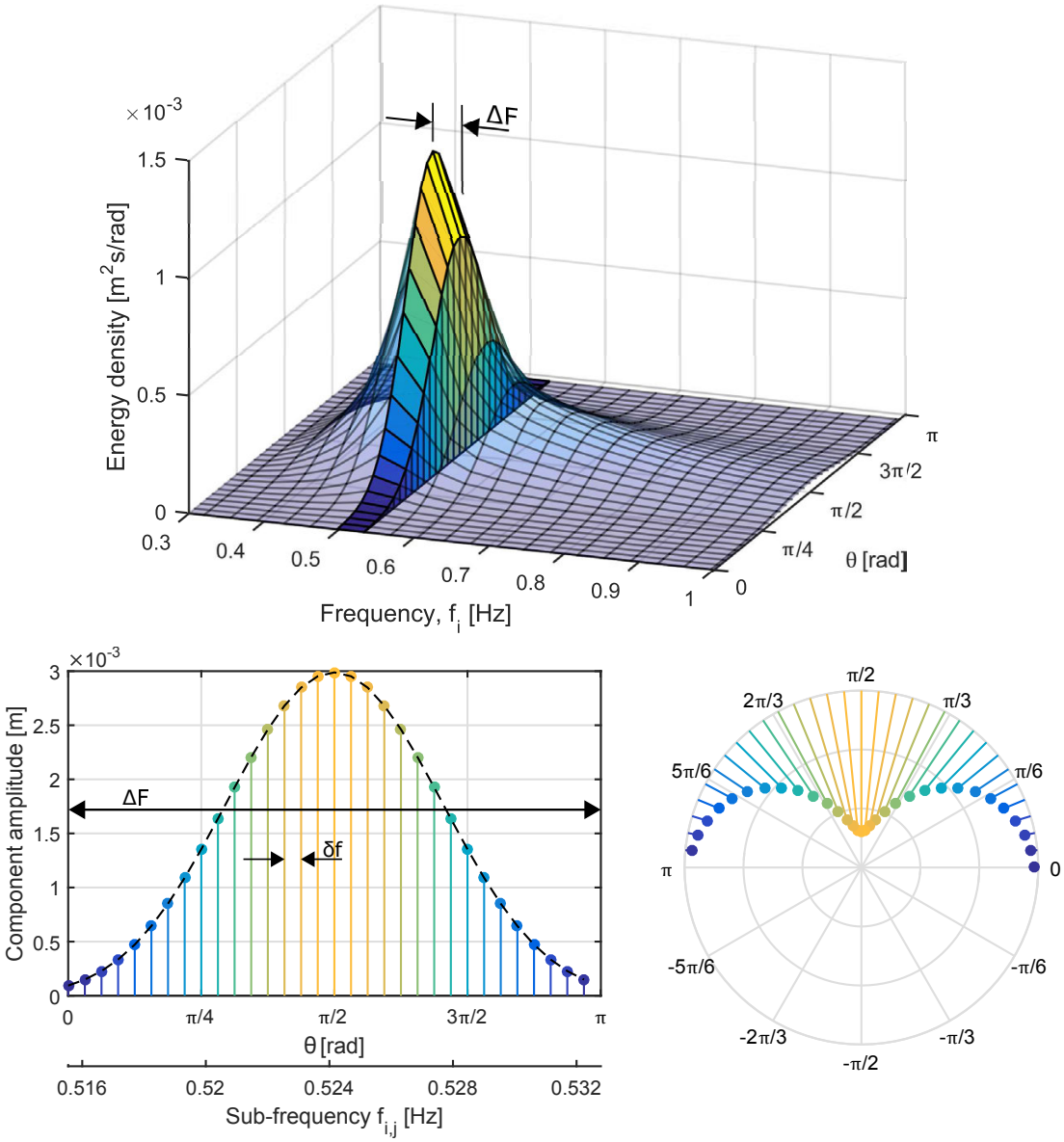

Figure 4.1: Schematic of discretisation of a directional spectrum using the single summation method and subsequent recreation in the tank. The panels show (top) the directional spectrum highlighting the frequency bins ΔF, (bottom left) how the sub-frequency bins δf are split across direction for each ΔF frequency bin, and (bottom right) how this directional spread is created in the tank

Directional Spectra (double-summation):

$$\eta(x,y,t) = \sum_{i=0}^{N_f} \sum_{j=0}^{N_\theta} A_{i,j} \cos\left(-\omega_i t + k_i \left[x\cos\alpha_j + y\sin\alpha_j\right] + \Phi_{i,j}\right) \tag{4.1}$$

$$A_{i,j} = \sqrt{2E_{i,j}df d\theta} \tag{4.2}$$

Directional Spectra (single-summation):

$$\eta(x,y,t) = \sum_{i=0}^{N_f} A_i \cos\left(-\omega_i t + k_i\left[x\cos\alpha_i + y\sin\alpha_i\right] + \Phi_i\right) \tag{4.3}$$

Uni-directional Spectra:

$$\eta(x,t) = \sum_{i=0}^{N_f} A_i \cos(-\omega_i t + k_i x + \Phi_i) \tag{4.4}$$

$$A_i = \sqrt{2S_i df} \tag{4.5}$$

Regular Waves:

$$\eta(x,t) = A\cos(-\omega t + kx + \Phi) \tag{4.6}$$

Computing surface elevations by summation is computationally inefficient and as such an Inverse Fast Fourier Transform (IFFT) has been used throughout this work. To compute the IFFT, the complex amplitude spectrum, $Z(f)$, must be formulated from the desired wave spectrum. $Z(f)$ should be in the same form as the equivalent Fast Fourier Transform (FFT) output from the time series. The amplitude spectrum for directional wave spectra can be calculated using Eq. (4.7) or Eq. (4.8), with the uni-directional equivalent shown in Eq. (4.9). The wave component amplitudes, $A_{i,j}$ and A_i, are calculated as shown in Eqs. (4.2) and (4.5).

Directional Spectra (double-summation):

$$Z_i = \sum_{j=0}^{N_\theta} A_{i,j} e^{i(k_i[x\cos\alpha_j + y\sin\alpha_j] + \Phi_{i,j})} \tag{4.7}$$

Directional Spectra (single-summation):

$$Z_i = A_i e^{i(k_i[x\cos\alpha_i + y\sin\alpha_i] + \Phi_i)} \tag{4.8}$$

Uni-directional Spectra:

$$Z_i = A_i e^{i(k_i x + \Phi_i)} \tag{4.9}$$

The surface elevations at (x,y) can now be calculated using $IFFT(Z)$, however it is usually necessary to use $real(IFFT(Z))$ due to the presence of an imaginary component existing as a result of round-off errors.

Specific (x,y) points of interest can be computed to give point measurements. Additionally, whole grids can be calculated to visualise the specified wave field across the tank area. Fig. 4.2 shows example point measurements whilst Figs. 4.3 to 4.5 show surface elevation examples across the whole tank area for the same time period.

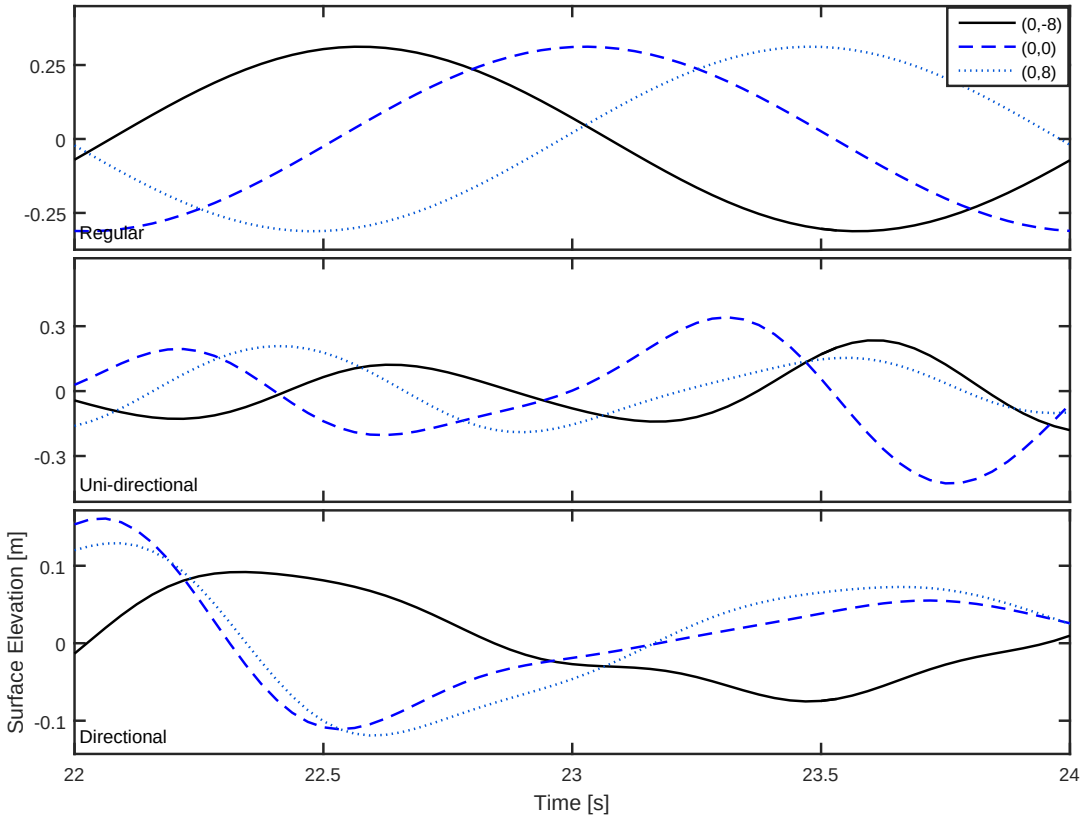

Figure 4.2: Example simulated point measurements at (0,-8), (0,0) and (0,8) for the regular, irregular and directional wave fields shown in Figs. 4.3 to 4.5

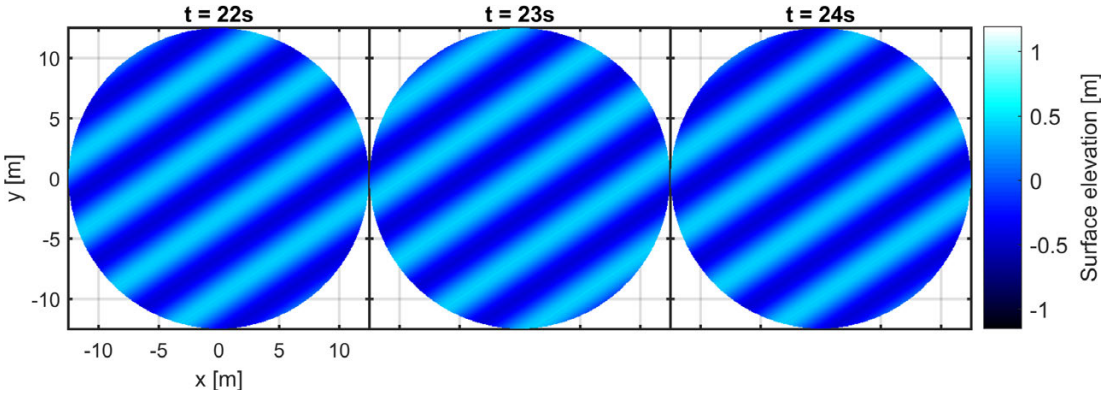

Figure 4.3: Simulated regular wave field over the FloWave tank. A=0.3 m, f=0.5 Hz, θ=-56.25°

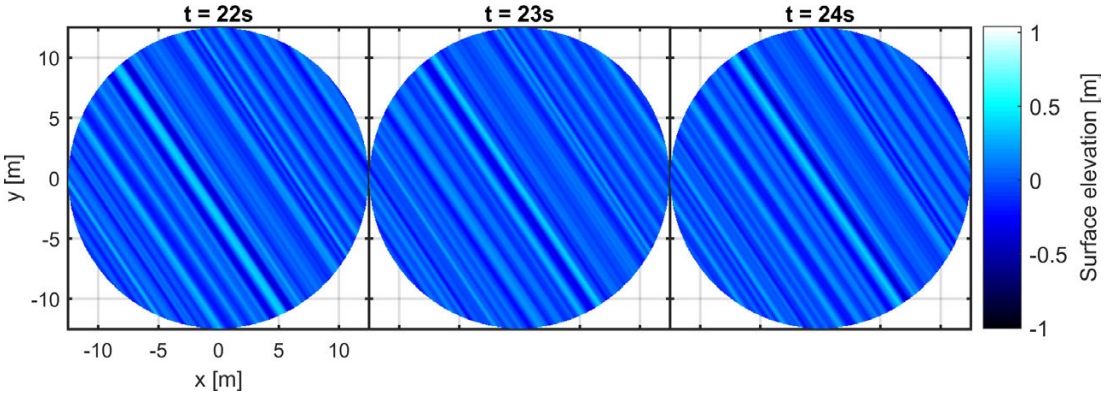

Figure 4.4: Simulated long-crested irregular wave field over the FloWave tank. H_{m0}=0.5 m, f_p=0.9 Hz, θ=-146.25°, γ=4

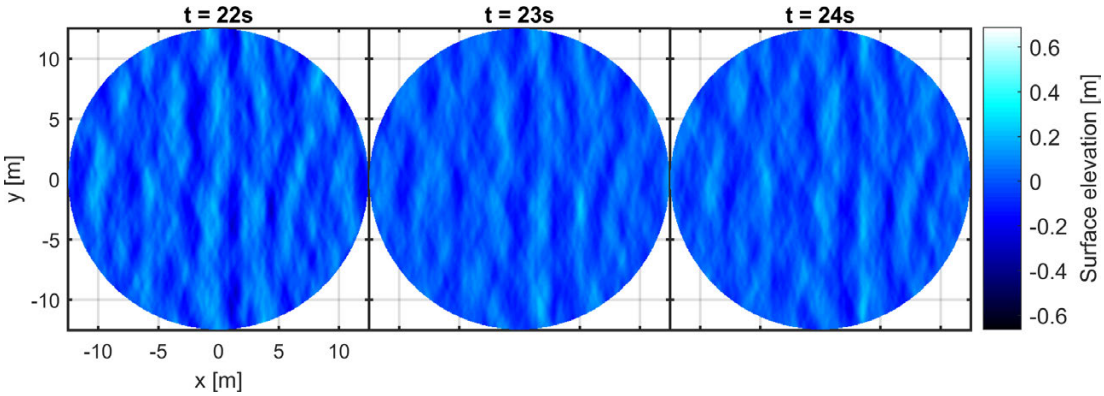

Figure 4.5: Simulated directional wave field over the FloWave tank. H_{m0}=0.3 m, f_p=0.6 Hz, $\bar{\theta}$=180°, γ=3.3, s=25

4.2 Wave Characterisation: Test Matrix and Test Plan

In order to practically characterise the wave performance in the FloWave facility, a consistent set of wave parameters have been explored. This allows comparisons to be made between regular, long-crested irregular and directional seas and enables isolation of the influence of key variables.

The default sea states have been defined in terms of frequency and steepness, covering the typical range of sea states used in the facility. For regular waves steepness is defined as H/L, whilst for irregular waves significant steepness, S_p, has been used and is defined as H_{m0}/L_p. Irregular waves have been created using parametric JONSWAP spectra each with γ value of 3.3 and the directionality of sea states has been explored by using cos^{2s} spreading values of 5, 10 and 25. JONSWAP spectra have been used exclusively with a constant (and typically used) γ, in order to limit the number of variables and hence time required to obtain a useful understanding of the facility. The combinations of these sea state parameters define the overall test matrix, which can be found in Table 4.1. Due to frequency dependent wave height limits it is not possible to carry out the 2% and 4% steepness scenarios for the 0.3 Hz sea states.

Table 4.1: Wave characterisation test matrix: sea state parameters used for wave characterisation. All combinations in each row are used, along with the regular wave equivalents (no γ or spreading)

Frequency [Hz]	Steepness [%]	Height [m]	γ	cos^{2s} spreading value
0.3	1	0.130	3.3	Inf, 5, 10, 25
0.45	1, 2, 4	0.072, 0.145, 0.290	3.3	Inf, 5, 10, 25
0.6	1, 2, 4	0.043, 0.086, 0.172	3.3	Inf, 5, 10, 25
0.75	1, 2, 4	0.028, 0.056, 0.111	3.3	Inf, 5, 10, 25
0.9	1, 2, 4	0.019, 0.039, 0.077	3.3	Inf, 5, 10, 25

The sea state combinations from Table 4.1 result in 13 regular waves and 52 irregular sea states for exploration. These sea states are generated in the tank with different array configurations in order to assess a variety of wave and tank characteristics. The array configurations defined in Section 3.5, along with the sea states used and the inferred wave characteristics, are shown in Table 4.2.

Table 4.2: Array configurations, associated sea states and inferred wave characteristics

Array configuration	Sea states	Wave characteristics inferred	Section
SC1 (Fig. 3.10)	all regular	wave shape, spatial and temporal variability	Sections 4.3 and 4.5
SC2 (Fig. 3.10)	regular waves: 0.3 Hz: 1% 0.45–0.9 Hz: 2%	wave shape, detailed spatial and temporal variability	Sections 4.3 and 4.5
RC1 & RC2 (Fig. 3.11)	all regular and unidirectional irregular	reflection analysis, in-line variation of apparent reflections, spatial variation (irregular)	Sections 4.4 and 4.5
DC1 (Fig. 3.12)	all irregular	reflection analysis, directional reflection analysis, sea state deviation and correction	Sections 4.4 and 4.6

4.3 Wave Shape

4.3.1 Curvature

It order to understand whether the circular FloWave tank is creating high quality long-crested waves it is important to quantify whether they are truly long-crested. This can be assessed through the measured wave curvature, which can be inferred from test data gathered using the SC1 and SC2 array configurations (Fig. 3.10). When gauges are in a line perpendicular to the wave propagation direction, curvature and skewness (correctness of angle) can be inferred through the phase difference between waves passing adjacent gauges.

Using the SC1 data, the analysis can be carried out for half the tank i.e. -7.7–0 m for all regular waves. The SC2 data additionally enables curvature to be calculated for both sides of the tank i.e. -7.7–7.7 m. This, however, has only been implemented for a single steepness value for each frequency, as defined in Table 4.2.

The analysis has been performed by using cross-correlation between all gauge time-series, relative to a base signal: gauge 1, based at $(0,0)$ (intended, although some error occurred). The lag at which this cross-correlation is a maximum then provides the perceived time difference between gauges, which can be converted to space if desired, through knowledge of the wavelength. This cross-correlation function is shown in Eq. (4.10), and has been implemented using the Matlab `xcorr` function.

Cross-correlation between gauges p and q:

$$(p \star q)(\tau) = \int_{-\infty}^{\infty} p^*(t) q(t+\tau) dt \tag{4.10}$$

The calculations have been carried out over the 'first' 1 and 20 waves, to enable assessment of initial wave curvature and 'apparent' wave curvature once reflections are present. The frequency dependent start and end times to achieve this are defined in Eqs. (4.11) and (4.12). This includes the tank ramp up time, along with the time taken for the waves to reach the centre of tank as a function of the group velocity. The first wave is then ignored due to potential shape abnormalities and the next n waves considered for analysis.

$$T_{start,i} = T_{ramp-up} + \frac{0.5 D_{tank}}{C_{g,i}} + T_i \tag{4.11}$$

$$T_{end,i} = T_{start,i} + nT_i \tag{4.12}$$

Where:

$$C_{g,i} = \frac{C_i}{2}\left(1 + \frac{2k_i h}{sinh(2k_i h)}\right) \tag{4.13}$$

$$C_i = \frac{L_i}{T_i} \tag{4.14}$$

$$w = \sqrt{gk \tanh kh} \tag{4.15}$$

The wave gauge data from the SC1 and SC2 tests are sampled at 128 Hz, for 128 s. Prior to analysis the data is up-sampled (interpolated) by a factor of 10 before carrying out cross-correlation for phase differences to appear less quantised. However, as the original data is in time increments of $\Delta t = \frac{1}{128}$ s, this is the minimum time difference that can be effectively inferred. This time difference as a proportion of the wave periods used is shown in Table 4.3, enabling measured time lags to be put into perspective.

Table 4.3: Smallest proportion of a wave period that can be inferred when using 128 Hz data

Frequency [Hz]	Δt_{min} [% of wave period]
0.3	0.23
0.45	0.35
0.6	0.47
0.75	0.59
0.9	0.70

The results of this analysis can be visualised in Figs. 4.6 to 4.7 in terms of percentage of wave period (noting that results shown in terms of metres or absolute time show the same line order i.e. is not same Δt for all frequencies distorted by use of percentage). The 'first' generated wave as defined in Eq. (4.11) shows that there is very little initial wave curvature. This suggests that, at least initially, the programmed timing between adjacent paddles is correct, producing good quality long-crested waves.

When calculated over the first 20 waves, the lags and *apparent* (phase-inferred) curvature increase significantly. This must be attributed to the effect of reflections. These reflections are highly curved, as shown in Section 4.5.1.1, and as such would introduce a phase difference across the gauges as a function of the reflection curvature, amplitude, position and period. Section 4.4 shows that higher frequency and lower steepness waves introduce larger reflections in general, and these larger relative amplitudes would introduce increased phase differences. This is what Figs. 4.6 to 4.7 appear to show, with the higher frequency, low steepness waves producing the larger phase differences.

The analysis carried out over 20 waves therefore does not really represent wave curvature, instead displaying the phase effect introduced by curved reflections. This becomes obvious when looking at Fig. 4.7, for the analysis over 20 waves. For some of the higher frequencies, the apparent curvature is in the opposite direction for the other half of the tank (noting that the data is built up of two tests rotated 180°). This appears to be the result of a relatively small position error, O(cm), in the direction of wave propagation. If this observation was indeed curvature related, the phase differences would have the same sign and it would not matter at which point in the tank the array was placed. However, as they are reflection induced, the slight

position change means that the incident and reflected waves have a different phase relationship at the new gauge locations (for the higher frequency, smaller wavelength conditions).

To assess the true wave curvature, only the first few waves can be analysed before reflections alter the phase. Re-visiting the 'first' generated wave it can be seen that the true wave curvature is negligible, with the only noticeable lags being just one or two time steps at 128 Hz, as defined in Table 4.3. This demonstrates that the generated wave curvature is negligible. Additionally, as there is no skew in the phase differences, this also demonstrates that the desired input angle was generated correctly.

4.3.2 Non-linearity

When simulating waves and sea states in Section 4.1.2, the assumption is that the waves can be represented by linear wave theory. However, this assumption is only valid when wave amplitudes are small relative to the wavelength and wavelengths are small compared with the water depth. If this is not the case then the wave profiles are better described by a non-linear wave theory, accounting for the non-sinusoidal shape of the waveform. For deep and intermediate water a Stokes expansion provides reasonable estimates, however for shallow water waves a different approach is required (Dalrymple and Dean, 1984).

Considering the tank water depth of 2 m, the waves used for the characterisation (Table 4.1) should be reasonably described by Stokes' 2^{nd} order wave theory. This is shown in Fig. 4.8, where the characterisation waves are shown relative to regions where certain wave theories are assumed valid, according to Mahaute (2014). This means that the linear approximations used for sea state simulations, along with those implied by the use of spectral analysis, will be somewhat invalid.

To assess how well Stokes' 2^{nd} order wave theory describes the waves in FloWave, measured regular wave profiles are compared to the expected Stokes waves, along with the equivalent linear wave theory profile. This is carried out by initially considering the first four measured waves, identified using the equations shown in Eqs. (4.11) to (4.14). The mean amplitude is taken from this portion to allow theoretical formulations to be based on generated amplitude rather than the desired amplitude, and the wave profiles are calculated for both linear and Stokes' theory using Eqs. (4.16) and (4.17):

Linear:

$$\eta_{lin}(x,t) = A_i cos(k_i x - w_i t) \tag{4.16}$$

Stokes 2^{nd} order:

$$\eta_{Stokes_2}(x,t) = A_i(cos(k_i x - w_i t) + k_i A_i \frac{3 - (tanh(k_i h))^2}{(4tanh(k_i h))^3} cos(2(k_i x - w_i t)) \tag{4.17}$$

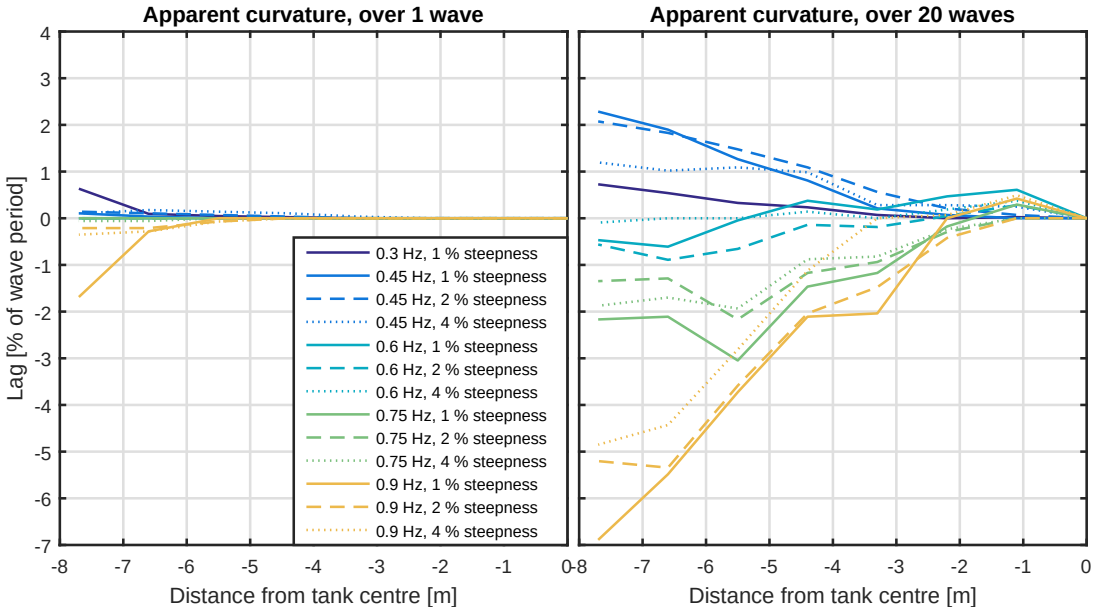

Figure 4.6: Apparent wave curvature inferred through cross-correlation. Calculated over 1 and 20 waves for -7.7–0 m

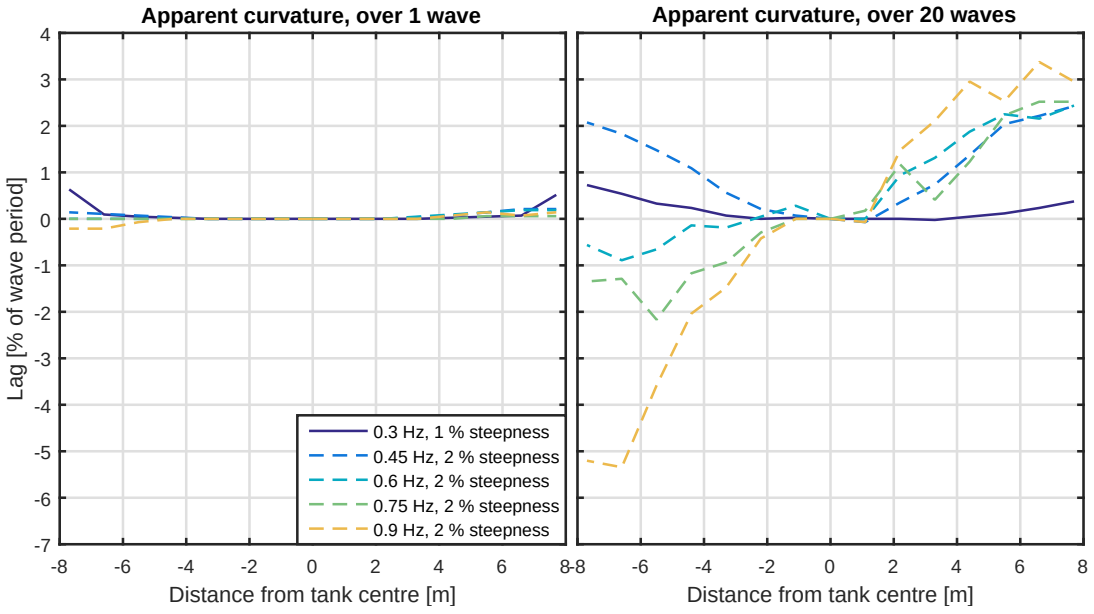

Figure 4.7: Apparent wave curvature inferred through cross-correlation. Calculated over 1 and 20 waves for -7.7–7.7 m

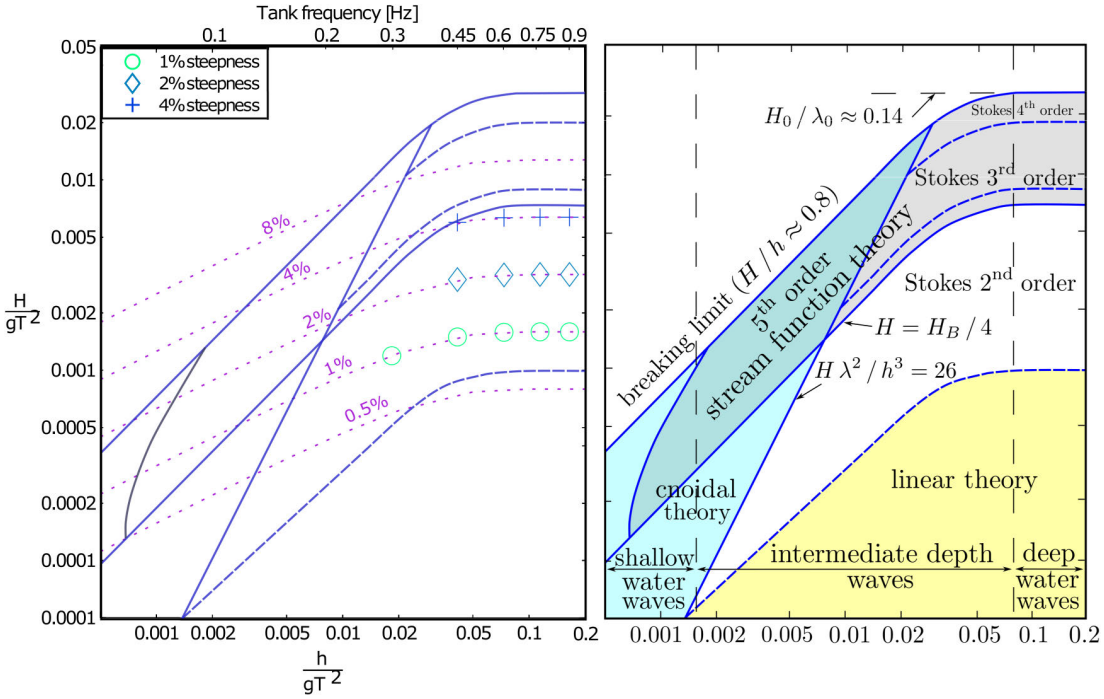

Figure 4.8: (Right) graph showing normalised water depth and wave height along with the regions where different wave theories are applicable (according to Mahaute (2014)).(Left) default sea states used for wave characterisation shown on the same axes, with tank frequency calculated

Any remaining phase differences between theory and measurements are calculated using cross-correlation, before being removed to allow fair comparison. An example time series comparison is shown in Fig. 4.9 and the coefficients of determination for all of the regular waves are shown in Fig. 4.10. It is evident that the 2^{nd} order model describes the measured wave profile more effectively in all cases. However, a mean coefficient of determination of 0.996 rather than 0.993 shows a modest improvement overall and put into the context of other errors incurred through scaled physical model testing, it seems quite insignificant. This means that although non-linear models will describe the wave field more effectively, a linear assumption is justified. This is particularly compelling when considering the ease and effectiveness of using spectral methods and enables an objective assessment of the inaccuracies arising as a result of the underlying, linear, assumptions.

Once reflections build up, the wave profiles will become more irregular. This results in wave statistics varying between samples. On average, however, they should still exhibit the expected non-linear properties. To assess what happens over many wave periods, each wave — as defined by a zero-crossing analysis — has been analysed. The time-series analysis throughout this work was carried out using FloWave internal Matlab code, which applies the Matlab polynomial interpolation tools to identify crests, troughs and zero-crossings (implemented in Davey *et al.* (2008)). This polynomial fitting approach avoids spurious identification of waves. Crest and

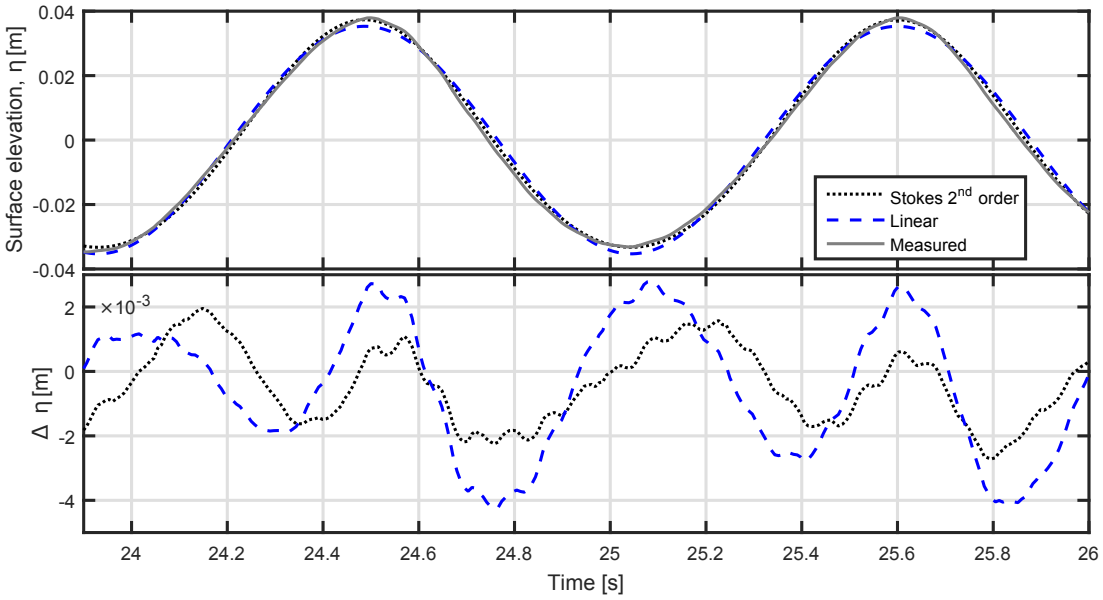

Figure 4.9: Example measured wave profile for 0.9 Hz–4% steepness regular waves. Shown compared to linear and Stokes' 2^{nd} order wave theories, with deviations shown underneath

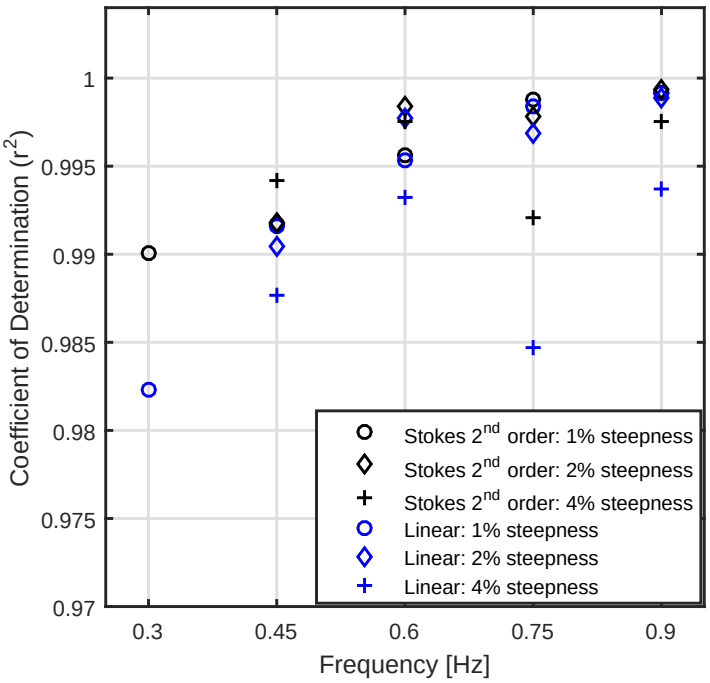

Figure 4.10: Coefficient of determination (r^2) indicating how well Stokes' 2^{nd} order wave theory and linear wave theory describe the measured wave profiles

trough times, T_{crest}, and T_{trough} have then been extracted, before fitting a multivariate kernel density estimate to the resulting data. The results of this are shown in Fig. 4.11, providing a good indication of the expected non-linearity and variability between waves.

As expected it appears that the variability is directly related to the magnitude of the reflection coefficient (see Fig. 4.12). In general the peak of the kernel density estimate shows good agreement with the expected Stokes values, however, it may be suggested that a higher order theory be more appropriate for certain wave conditions. From Fig. 4.8 it may be suggested that Stoke's 3^{rd} order theory may be more applicable.

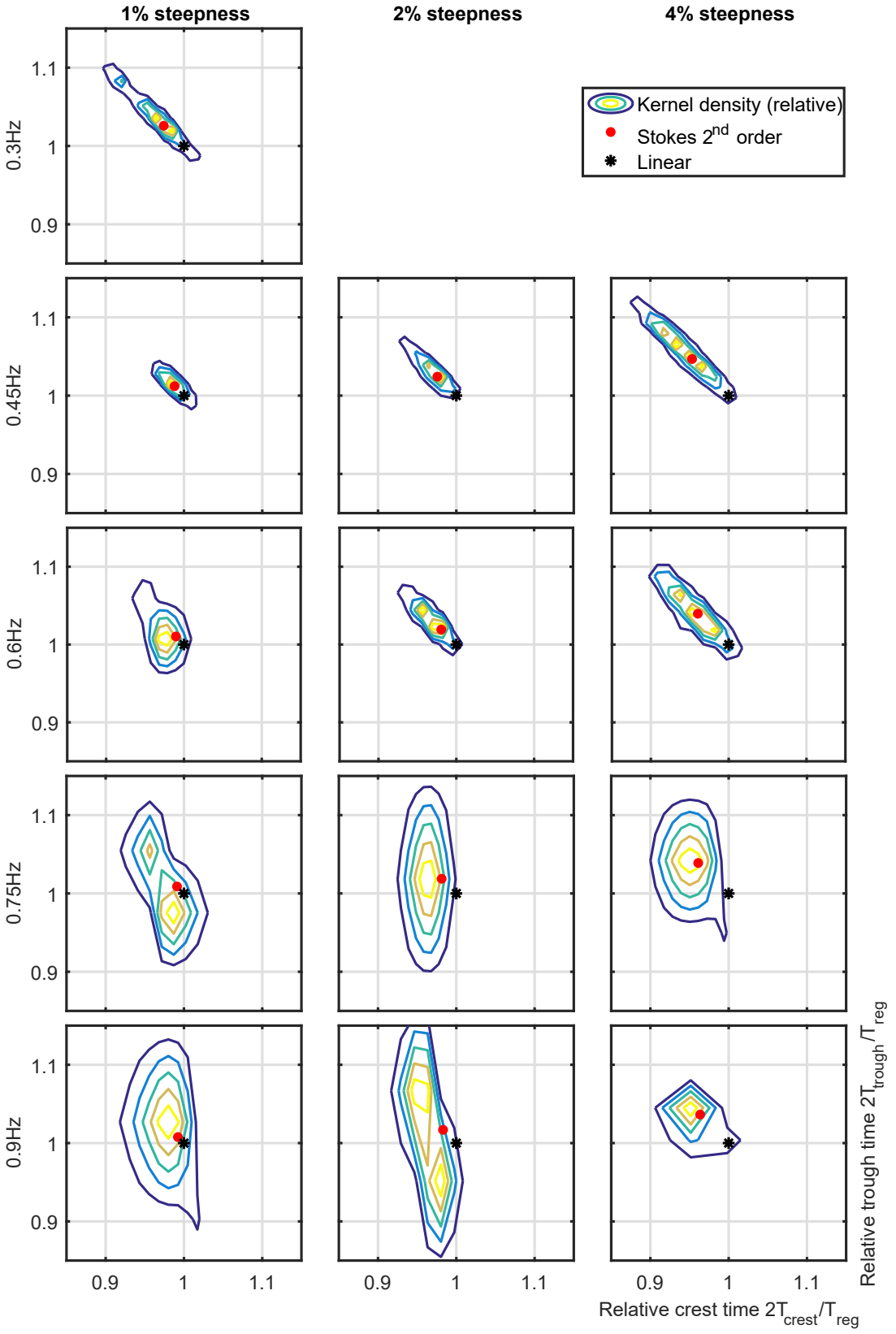

Figure 4.11: Kernel density plots (scaled to max of each frequency-steepness value) of relative crest and trough times for every wave recorded during the regular wave tests (Table 4.1). Shown with expected linear and Stokes' 2^{nd} order values

4.4 Reflection Analysis

In order to understand the absorption characteristics of the tank and how this influences the wave field, a reflection analysis procedure must be carried out. Throughout this work the Zelt and Skjelbreia (2011) frequency domain method has been used, which is described in Section 5.1.2, where it is modified to form part of the SPAIR method, enabling reflections to be calculated for directional sea states.

4.4.1 Effective Reflections at Tank Centre

As most models will be placed at or around the tank centre this is the most important area to characterise. For reasons discussed in Section 5.3.3.2, this location is also the only place where reflections for directional sea states can be reliably calculated at present, enabling comparisons to be drawn between regular, uni-directional irregular and directional sea states. Further analysis is carried out on the spatial variation of reflection coefficients, along with incident and reflected spectra in Section 4.5.

4.4.1.1 Regular Waves

The reflection analysis for regular waves has been done using array RC1 (Fig. 3.11). As there is only one input (forcing) frequency and the Zelt and Skjelbreia (2011) method provides a frequency domain solution, it is easy to identify the presence and magnitude of any free harmonics generated during the attempted absorption process. This analysis has shown that there are significant 2^{nd} order harmonics generated, however the magnitude of any higher order harmonics are negligible.

Fig. 4.12 presents the resulting 'reflection coefficients' for the 1^{st} and 2^{nd} harmonics, where the reflection coefficients for harmonics are defined by Eq. (4.18). This approach is clearly only valid when there are no input waves at the harmonic frequencies being considered. The reflection coefficient for harmonic, n, of frequency (forcing) component, i, is given by Eq. (4.18).

$$Kr_{n,i} = \frac{A_{n\times i}}{A_i} \tag{4.18}$$

It can be seen that the absorption effectiveness is generally increased at lower wave frequencies, likely a function of the paddle's shape characteristics. Somewhat counter-intuitively, it also appears that relative absorption effectiveness is improved in steeper waves. One may expect that the increased non-linearity of high steepness waves would increase the difficulty of effective absorption. It appears, however, that the force-feedback system is not as effective at measuring the low wave forces associated with these low steepness, low amplitude waves and as such the opposite effect is observed.

The relative contribution of the 2^{nd} order harmonic is in general minimal, however in some circumstances is comparable, or larger than, the fundamental reflection. It appears that the relative magnitude of this 2^{nd} harmonic is generally larger with increased wave steepness. This may suggest that its generation is a function of the wave non-linearity, and the increased mismatch between assumed (linear wave theory) and actual wave profile.

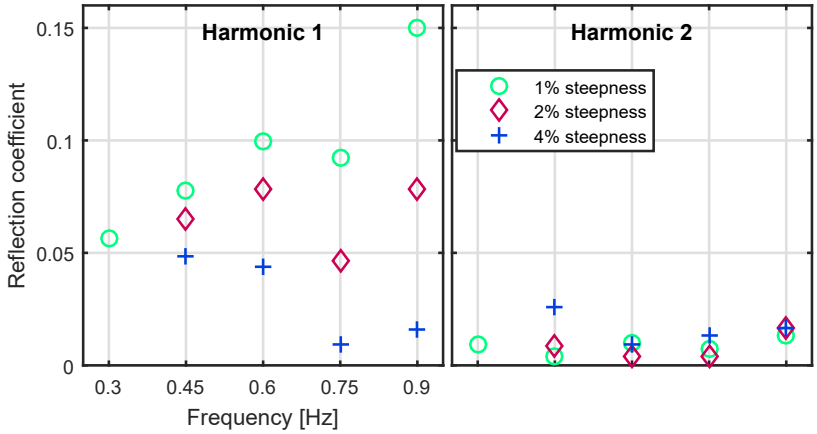

Figure 4.12: 1^{st} and 2^{nd} harmonic reflection coefficients for a range of regular waves, with various peak frequency and steepness values

4.4.1.2 Irregular Waves

Reflection analysis has been carried out for the all the irregular sea states, using the directional array configuration DC1 (Fig. 3.12). The SPAIR method developed in Chapter 5 enables reflections to be assessed for all irregular sea states using the same approach, regardless of directionality. Overall reflection coefficients for these spectra have been calculated, using the spectral density to create weighted averages of the frequency dependent reflection coefficients (Eq. (4.19)).

$$Kr_{overall} = \frac{\sum_{i=0}^{i=nf} S(f_i).K_{r,i}}{\sum_{i=0}^{i=nf} S(f_i)} \tag{4.19}$$

Assessing the resulting overall reflection coefficients, shown in Fig. 4.13, it can be seen that the same general trend is observed that was present for regular waves. Increased frequency and reduced steepness appear to give rise to larger reflections. It is clear, however, that the reflection coefficients in irregular sea states are consistently larger than their regular wave counter-parts.

The reasons why overall reflection coefficients are larger can be explained with the aid of the calculated frequency dependent reflection coefficients. Due to the use of the single summation method, Section 4.1.1.2, some frequency components (f_i) have no or little energy content and thus some reflection coefficients are essentially meaningless. To enable visualisation, a weighted binned reflection coefficient has been used for each of the 'original' frequency bins,

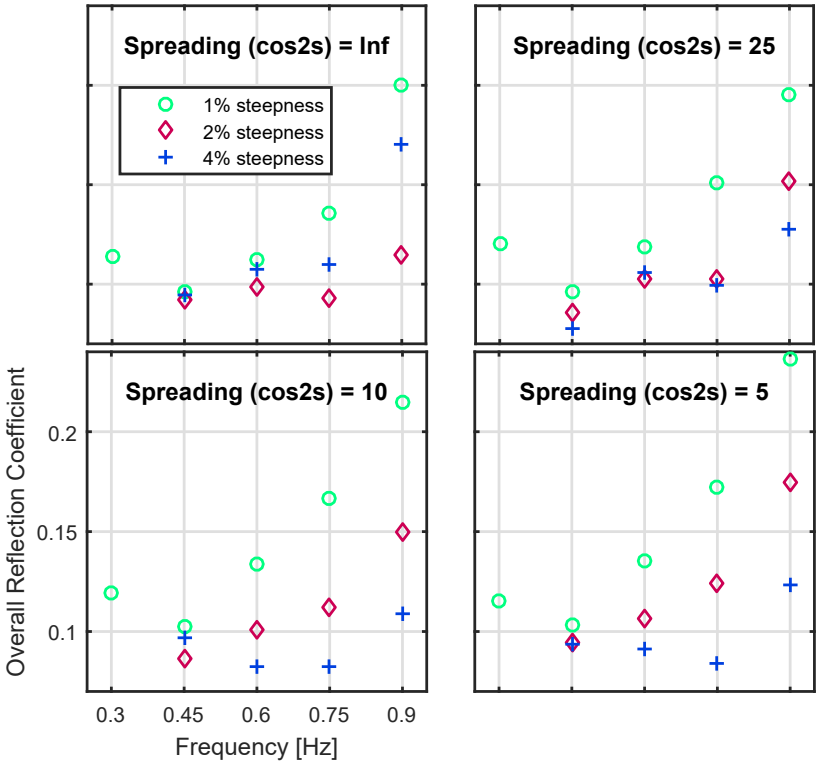

Figure 4.13: Overall reflection coefficient for a range of JONSWAP wave spectra, with various peak frequency, steepness and directional spreading values, ($\gamma = 3.3$). Note: Spreading = Inf is uni-directional

F_I. This is calculated using Eq. (4.20), with the results shown in Fig. 4.14. It is observed that the reflection coefficients increase dramatically at the high frequency part of the spectrum, where f > 1 Hz; suggesting this is probably the practical limit for effective absorption under the current control scheme. In contrast to the regular waves, these spectra all have some high frequency energy content, and thus have a contribution to the overall reflection coefficient (Eq. (4.19)) resulting from this poor absorption region.

$$Kr_{bin,j} = \frac{\sum_{i=N_\theta(j-1)+1}^{N_\theta j} S(f_i).K_{r,i}}{\sum_{i=N_\theta(j-1)+1}^{N_\theta j} S(f_i)} \tag{4.20}$$

In general, wave absorption has been shown to be highly effective up to around 1 Hz, giving low reflection coefficients at the tank centre for most frequency components. It is clear that wave frequency and steepness are the key parameters for absorption effectiveness, as altering the directional spreading appears to have little predictable influence over the resulting reflections.

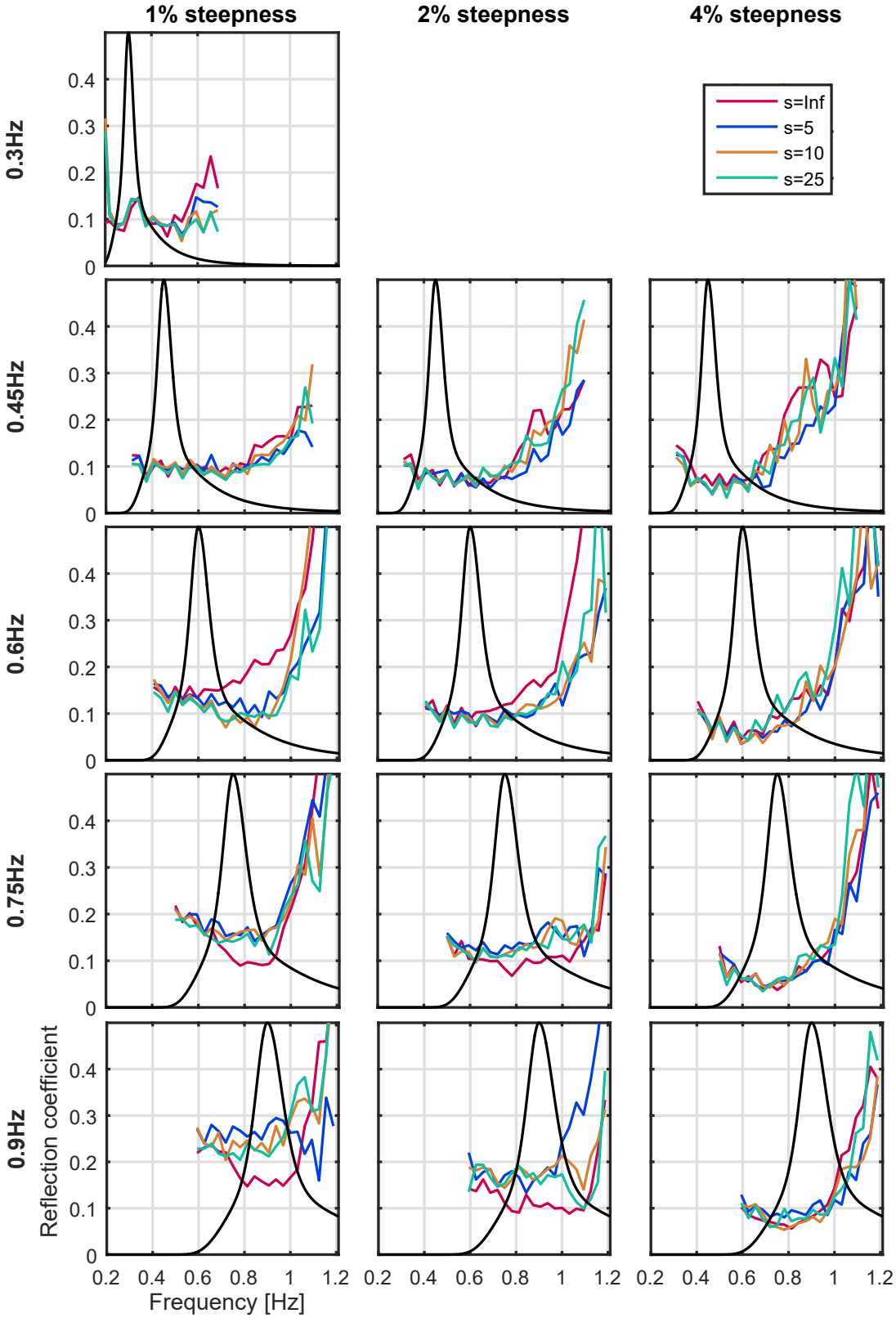

Figure 4.14: Frequency dependent binned reflection coefficients for a range of irregular spectra, with various peak frequency, steepness and directional spreading values, ($\gamma = 3.3$). Spectral shape overlaid to provide understanding of where the energy lies.

4.5 Spatial and Temporal Variability

The assessment of spatial and temporal variability enables quantification of the variation in wave characteristics over the tank area and over the duration of a sea state. The results from this can help identify the ideal locations for testing, in addition to helping gain a more detailed understanding of the facility.

The main source of the undesired variability arises from incomplete absorption. In this section, analysis is performed on measured wave heights, reflections and incident and reflected spectra in order to assess how this manifests in the resulting wave fields.

4.5.1 Regular Waves

4.5.1.1 Spatial Maps of Measured Wave Heights

Wave reflections cause spatial patterns of wave height deviation. In FloWave these are driven by curved reflected waves interacting with the incoming wave field. These patterns will exist as a complex type of partial standing wave and will fundamentally exist in both regular waves and in irregular sea states, for every frequency component. In order to easily visualise these variations spatially, the analysis is performed with regular waves and enables the assessment of the effect of wave frequency and steepness on the resulting deviations.

Using a circular tank removes limitations on the desired incident wave angle, which means that any wave component can be rotated by an arbitrary amount. Under the assumption that the tank is rotationally symmetrical in both generation and absorption effectiveness, a single array (SA1) can be used to build up a spatial map of the entire 'relative' tank area; combining multiple test runs at different angles. To achieve this, the absolute gauge locations, (x,y), are transformed using the rotation matrix shown in Eq. (4.21), so that they are relative to the wave propagation direction. This approach then enables the effective measurement points shown in arrays SC1 and SC2 (Fig. 3.10) to be achieved in a convenient manner.

$$\begin{bmatrix} x' \\ y' \end{bmatrix} = \begin{bmatrix} \cos(\theta) & -\sin(\theta) \\ \sin(\theta) & \cos(\theta) \end{bmatrix} \begin{bmatrix} x \\ y \end{bmatrix} \tag{4.21}$$

Wave-by-wave zero-down-crossing analysis in the time domain has been carried out for each of the rotational test runs, which identifies individual wave statistics along with the associated time stamp. Once these are calculated, the time-series database created can be probed for values closest to a time of interest. This, along with the transformed gauge locations, enables a close to simultaneous view of the state wave field to be obtained; enabling wave height variation to be assessed in both space and time.

Spatial maps are created by interpolating between measured points and displaying the relative wave height by variation in a colour map. Fig. 4.15 shows these spatial maps at a query time

of 128 s i.e. the end of the test, where the variation has been observed to be stable for all frequencies. It is clear that the resulting wave height variation is larger for low steepness–high frequency waves, correlating with the reflection analysis findings shown in Section 4.4. Also notable is the curvature of the 'hot-spots' (constructive interference locations), clearly resulting from curved reflected waves interacting with the incident wave field, known to be long crested (Section 4.3.1). The tank geometry is responsible for the circular focussing effect of these reflected components, which causes much greater variability near to the reflecting boundary. This results in the magnitude of the effective in-line reflections varying, which is assessed further in Sections 4.5.1.2 and 4.5.2.

In general, the resulting variations appear relatively symmetrical, suggesting that the assumption of rotational symmetry in the analysis is valid. For the high frequency data (0.75 and 0.9 Hz) there appears to be larger discrepancy and a less regular pattern. The irregularity is due to the fact that the gauge spacings were too large to effectively capture spatial variation for these small wavelengths. This has caused a form of spatial aliasing which in turn results in unrepresentative interpolated values. This is discussed further in Section 4.5.1.2, where an attempt is made to calculate the true expected centreline variation.

Using various time query points, the spatial variation of wave height through time can be assessed. This is shown in Figs. 4.16 to 4.18 for query points of 10, 20, 64 and 128 s, with these points showing initial wave propagation whilst also highlighting when the differing wave frequencies produce stable wave fields. This analysis has only been shown for the waves where a full rotation of measurements has been carried out (defined in Table 4.2 and seen in Fig. 4.15), as the higher resolution and full rotation enables a more detailed assessment of hot-spot development.

Due to the higher group velocity of low frequency waves, the wave fields stabilise much more quickly. This has implications for testing, as the desired (input) wave field will persist for less time, however a stable, less transient wave field is obtained more quickly. Despite the differing lengths of time required, it is apparent that all of the spatial maps appear stable after 64 s, and little change is observed between 64 and 128 s.

It appears that regardless of the wave input, there exist overall favourable locations for testing. Placing a model far from the reflection boundary and away from the centreline will result in sea states having less undesired spatial and temporal variability. It may be suggested that remaining a couple of meters closer to the generation side from tank zero will provide the best wave conditions, and would benefit from being 1 or 2 metres away from the centreline. For regular waves and uni-directional irregular seas this is easily achievable and will provide more desirable test outputs. For directional waves, however, this is not possible, as there are multiple effective reflected boundaries, potentially spanning the entire tank circumference. For this reason it seems that testing in the tank centre will provide the best compromise for directional sea states, however a location further from the absorbing walls and off-centre from

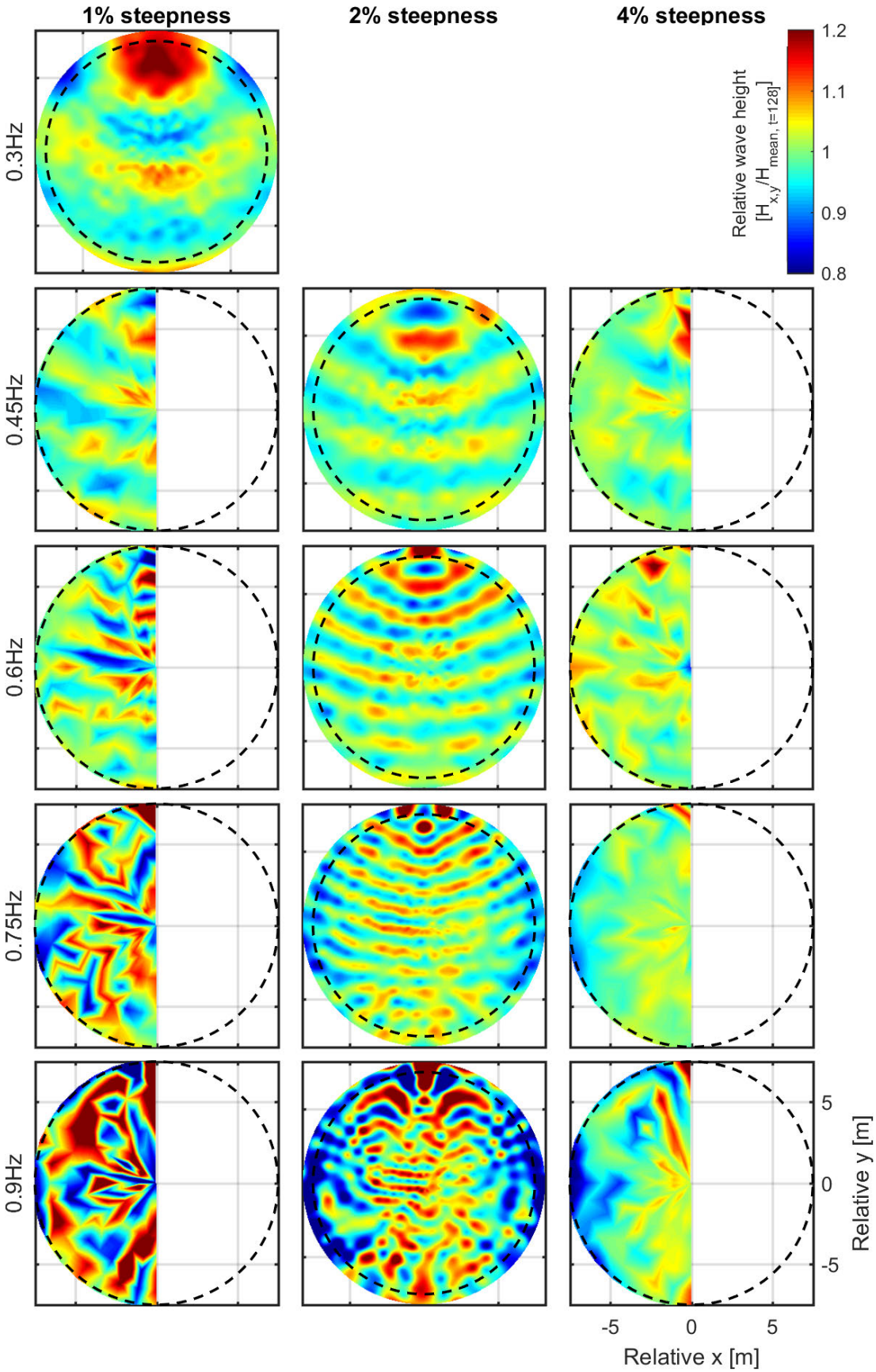

Figure 4.15: Spatial variation of relative wave height. Shown for all frequency and steepness values tested, at a query time of 128 s. Deviations in measured wave heights attributed to incident wave field interference with curved reflected waves.

the mean wave propagation direction may also be advantageous in some circumstances (e.g. low spread sea states, with all test runs having the same mean direction).

4.5.1.2 Spatial Variability of Reflections

Effective 1^{st} and 2^{nd} order reflection coefficients at various in-line positions have been calculated using the reflection array configuration RC2 (Fig. 3.11). These are shown in Fig. 4.19 and re-iterate the findings that effective reflections are larger with increased frequency and reduced steepness, regardless of the location in the tank. The measured reflection coefficients are found to increase dramatically near the reflected boundary, a function of the circular focussing effects observed in Section 4.5.1.1.

The 2^{nd} harmonic is also generally larger near the reflected boundary, although displays a less clear correlation. The generation of this harmonic content appears not to be so frequency dependent and seems to be increased with increased (1^{st} order) steepness. This agrees with the initial findings at the centre of the tank and suggests its generation is likely to be a complex function of the control system response to various wave forces, along with the non-linearity of the wave shape.

As guidelines, it can be inferred that for these regular waves, the reflection coefficients for 0.3-0.75 Hz are below 10% at the tank centre (0, 0) and can be reduced to around 5% 6 m further away from the reflecting boundary. For the 0.9 Hz waves this (-6 m) location is required to obtain less than 10% reflection for all steepness values.

4.5.1.3 Correcting Apparent Wave Height Variation

In Section 4.5.1.1 it was demonstrated that the gauge spacings are too large to effectively observe the spatial variation of wave heights for high frequency waves. This is because the interaction between incident and reflected components causes hot-spots to form in spatial intervals of $L/2$, requiring gauge spacings to be less than $L/4$ in order to avoid spatial aliasing. Noting that wavelengths for 0.75 Hz and 0.9 Hz waves are 2.77 and 1.93 m respectively (at 2 m water depth), it is clear that the gauge separations of 1.1 m is insufficient to capture the variation in the wave field.

Using the spatial variability of reflection coefficients obtained in Section 4.5.1.2, it should be possible to make reasonable predictions of the expected in-line variation of wave height. To this end Eq. (4.22) has been formulated, enabling an x-dependent interpolated reflection coefficient to be imported from the measured data (Fig. 4.19), whilst accounting for the locations of interaction. If the phase change at the reflecting wall is π, the first constructive interaction will exist at $L/4$ before the boundary. Where (0, 0) is the tank centre, the equation should be a maximum, i.e. a hot-spot location, at every valid $x = \frac{D}{2} - \frac{L}{4} - \frac{n_j L}{2}$. This has been ensured in

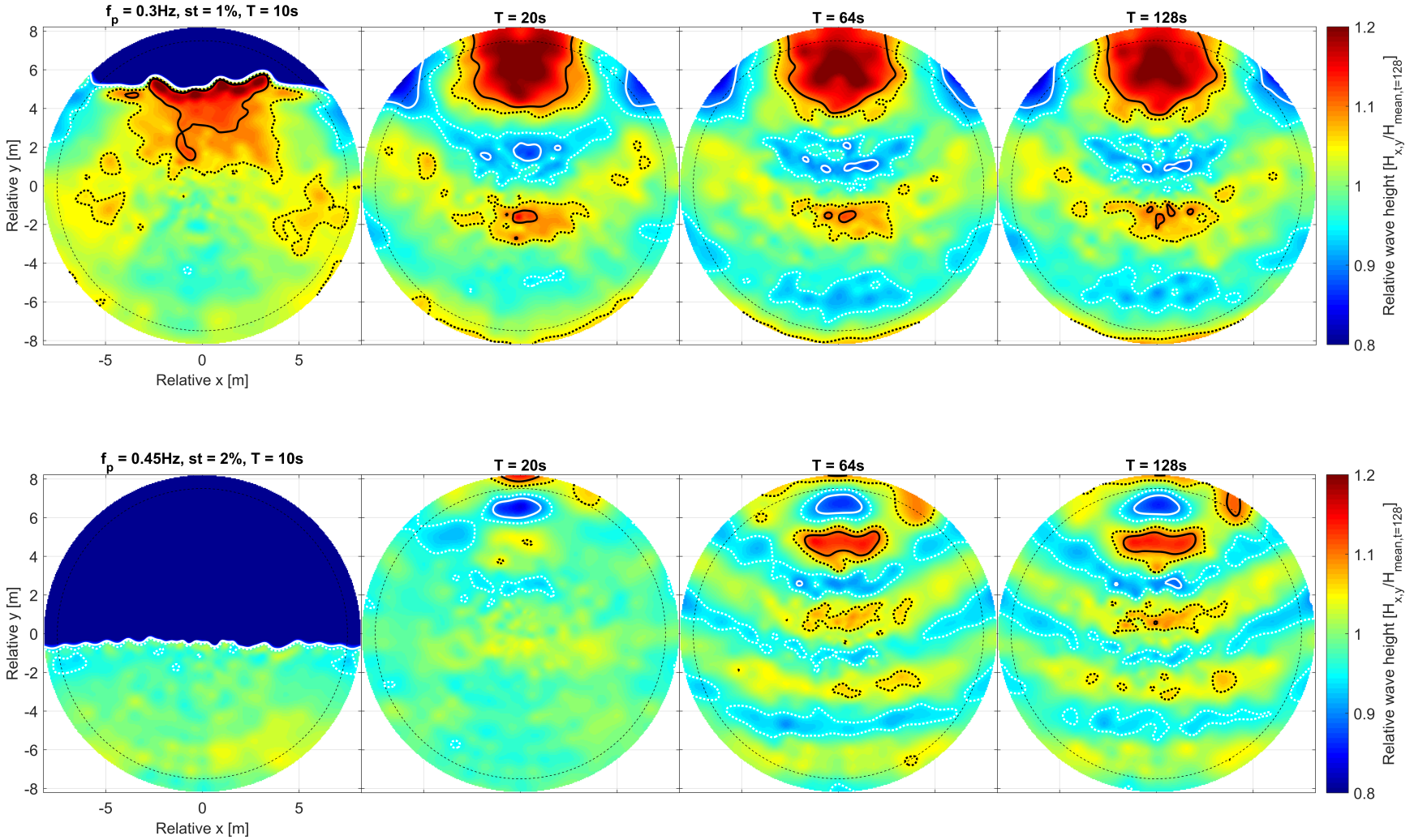

Figure 4.16: Spatial variation of wave height with time for 0.3Hz [1% steepness] (top) and 0.45Hz [2% steepness](bottom) regular waves. Contour lines: white= 0.9, white (dotted)= 0.95, black= 1.1, black (dotted)= 1.05. Black dashed line shows floor area. Dark blue initially indicates that no wave has arrived at the location

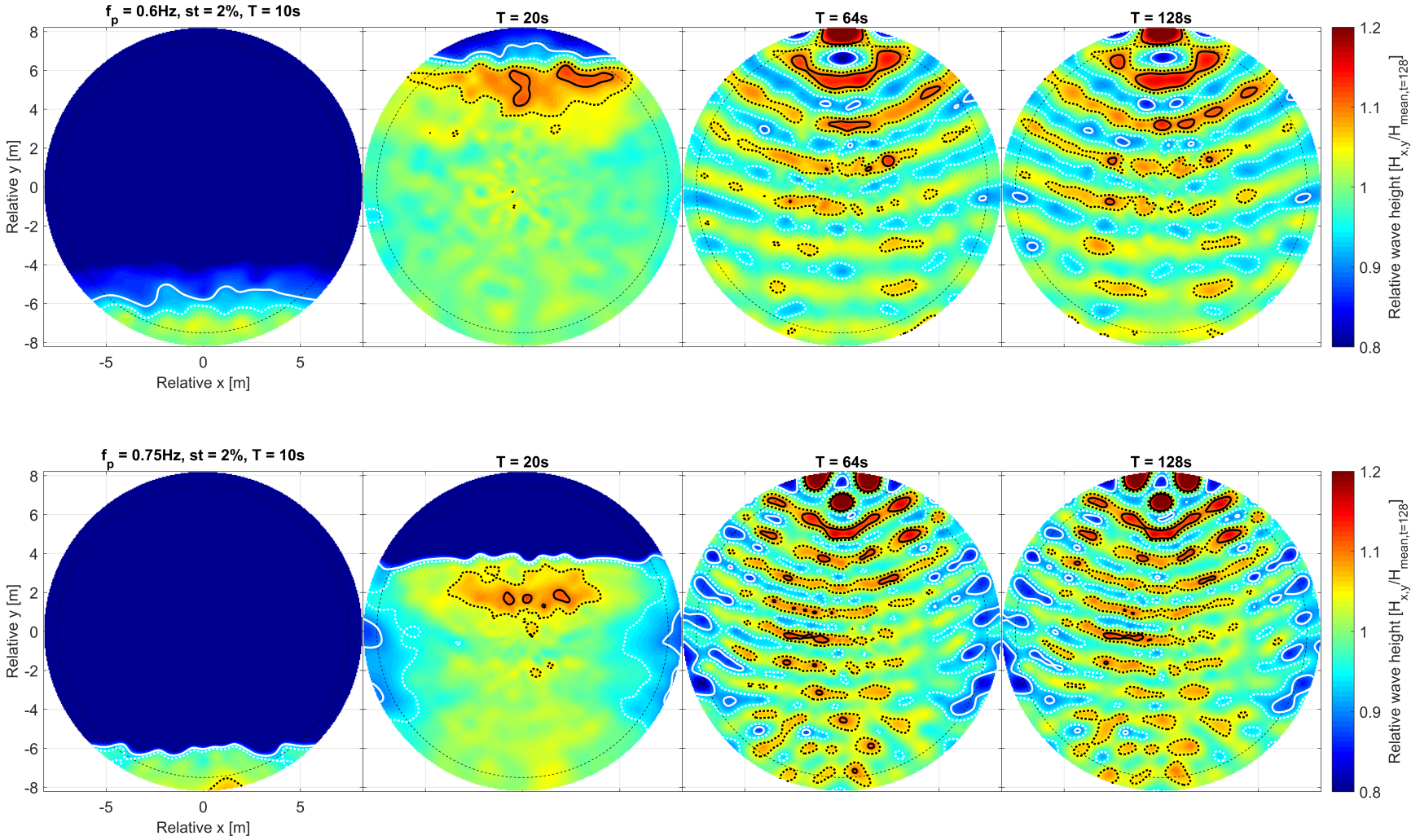

Figure 4.17: Spatial variation of wave height with time for 0.6Hz [2% steepness] (top) and 0.75Hz [2% steepness](bottom) regular waves. Contour lines: white= 0.9, white (dotted)= 0.95, black= 1.1, black (dotted)= 1.05. Black dashed line shows floor area. Dark blue initially indicates that no wave has arrived at the location

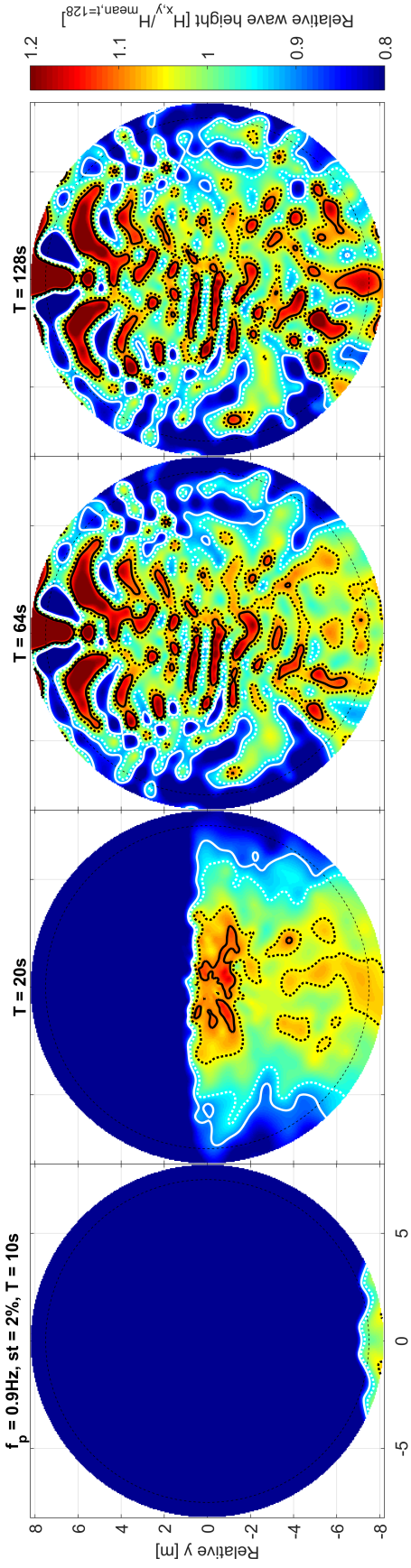

Figure 4.18: Spatial variation of wave height with time for 0.9Hz, 2% steepness regular waves. Contour lines: white= 0.9, white (dotted)= 0.95, black= 1.1, black (dotted)= 1.05. Black dashed line shows floor area. Dark blue initially indicates that no wave has arrived at the location

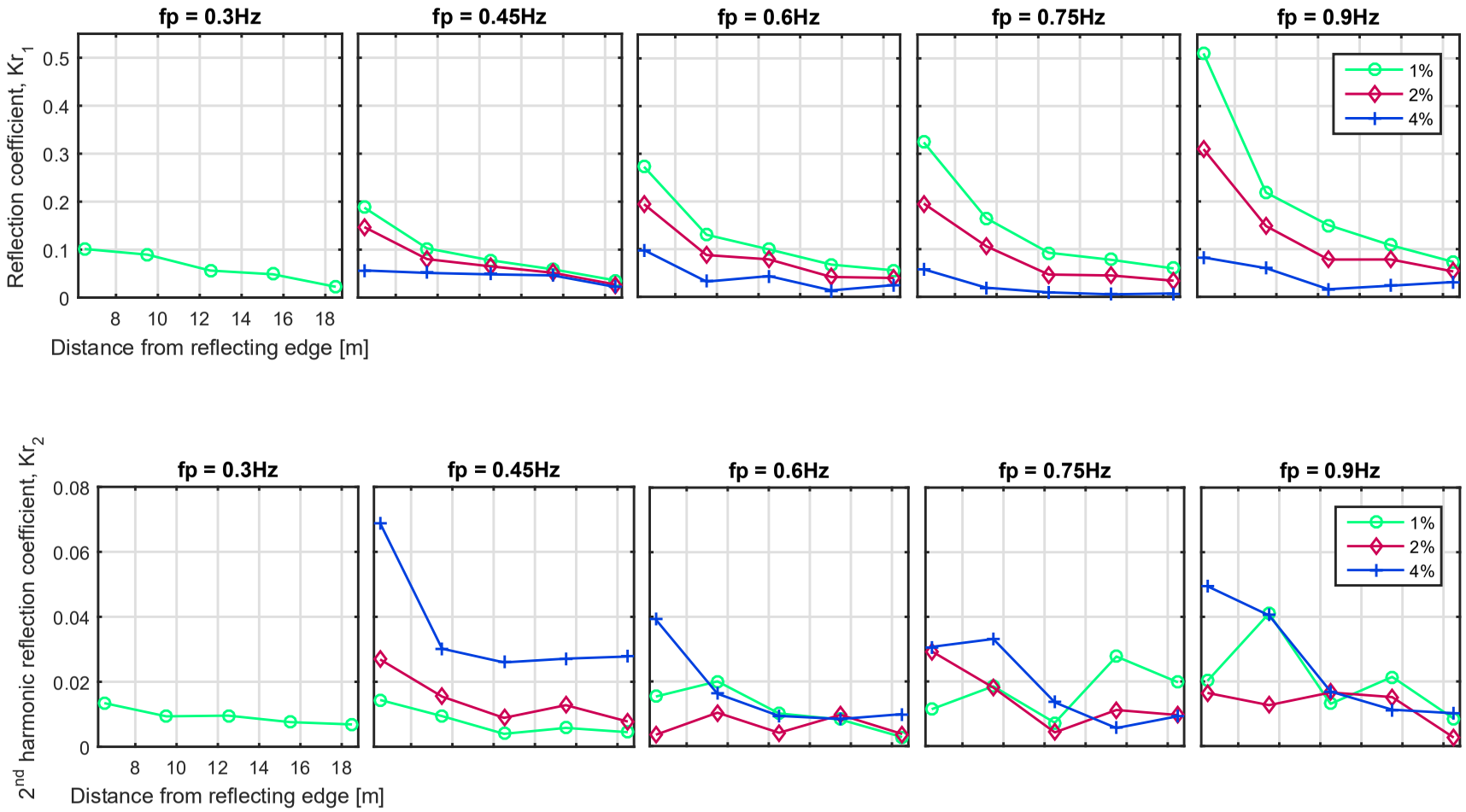

Figure 4.19: In-line variation of reflection coefficient and 2^{nd} harmonic generation

Eq. (4.22), whilst additionally allowing for an alternative phase change from reflection, Φ_{ref}.

$$\begin{aligned} H(x) &= \bar{H} + \bar{H}K_r(x)\cos(2kx - 2k(\frac{D}{2} - \frac{L}{4}) + \Phi_{ref}) \\ &= \bar{H} + \bar{H}K_r(x)\cos(2kx - 25k + \pi + \Phi_{ref}) \end{aligned} \tag{4.22}$$

Φ_{ref} has been 'solved' for by minimising the difference between the aliased measurements and the prediction at the gauge locations. The results of applying this are shown in Fig. 4.20. It is evident that the model wave heights at the gauge locations agree reasonably well with the measurements, showing particularly good agreement for the 0.45 and 0.6 Hz waves. Although not perfect agreement is observed with the aliased measurements at 0.75 and 0.9 Hz, it still provides reasonable 'best-guess' estimates until more data can be collected. The extent of the aliasing for these frequencies is also highlighted and it is clear that there is much greater variation than is portrayed by the spatial maps shown in Section 4.5.1.1.

4.5.1.4 Temporal Variability of Reflections

In addition to assessing the spatial variability of effective reflection coefficients, the change through time was also analysed. Reflection array RA1 has been used, but only in the tank centre i.e. configuration RC1 (Fig. 3.11). A single 160 s test for each frequency-steepness combination has been split into 5×32 s sections for both spectral, and reflection analysis.

The resulting temporal variability in the reflection coefficients are shown in Fig. 4.21. In common with the spatial map observations, it appears that the reflections for all cases are stable after 128 s. In most cases the reflections at the tank centre are stable after 64 s, however, due to the lower group velocity of the high frequency waves, the 0.75 and 0.9 Hz waves require a minimum of 96 s.

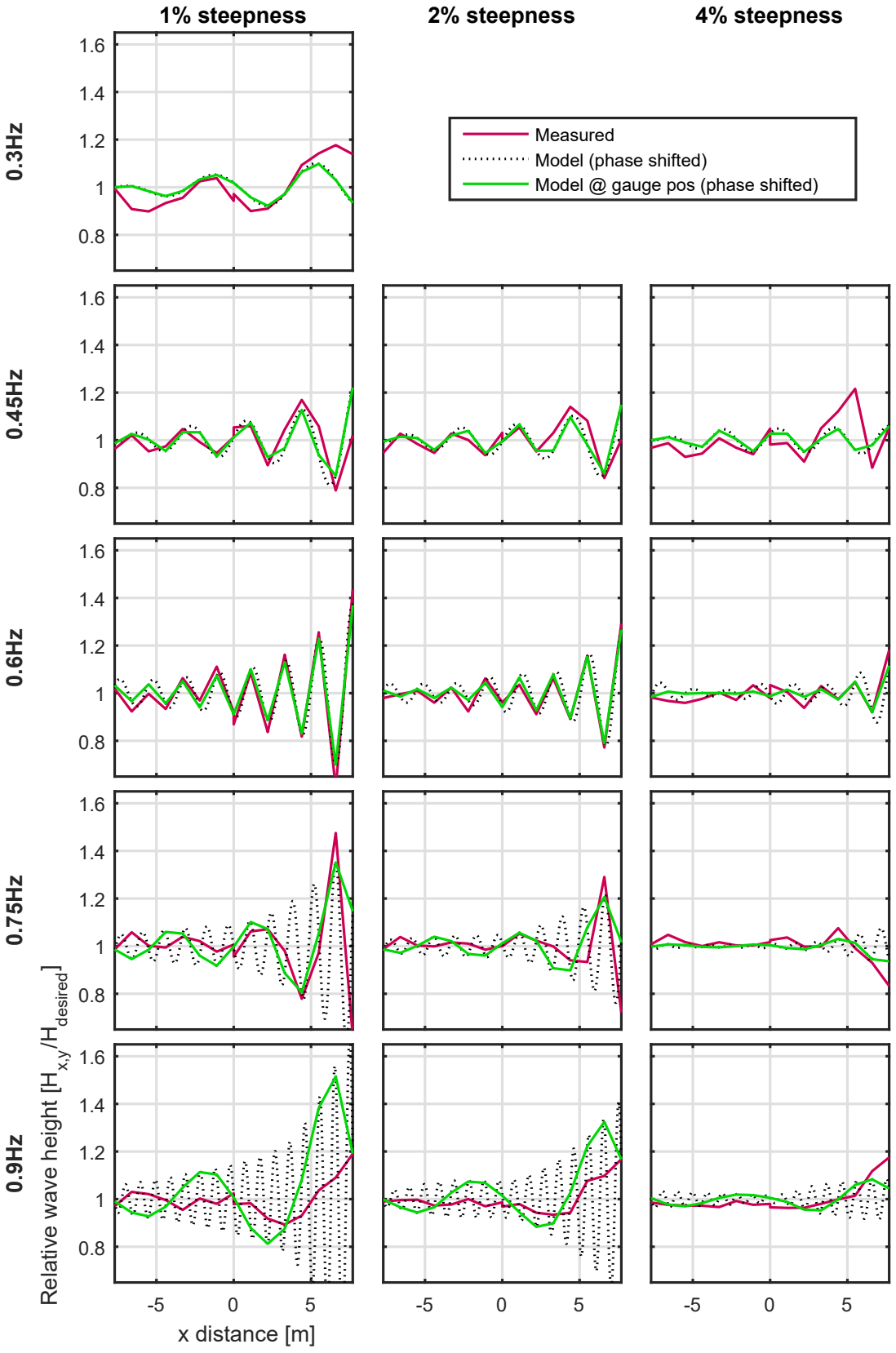

Figure 4.20: In-line variation measured with gauges compared with model prediction from Eq. (4.22). Highlights the extent of the spatial aliasing observed for the high frequency waves

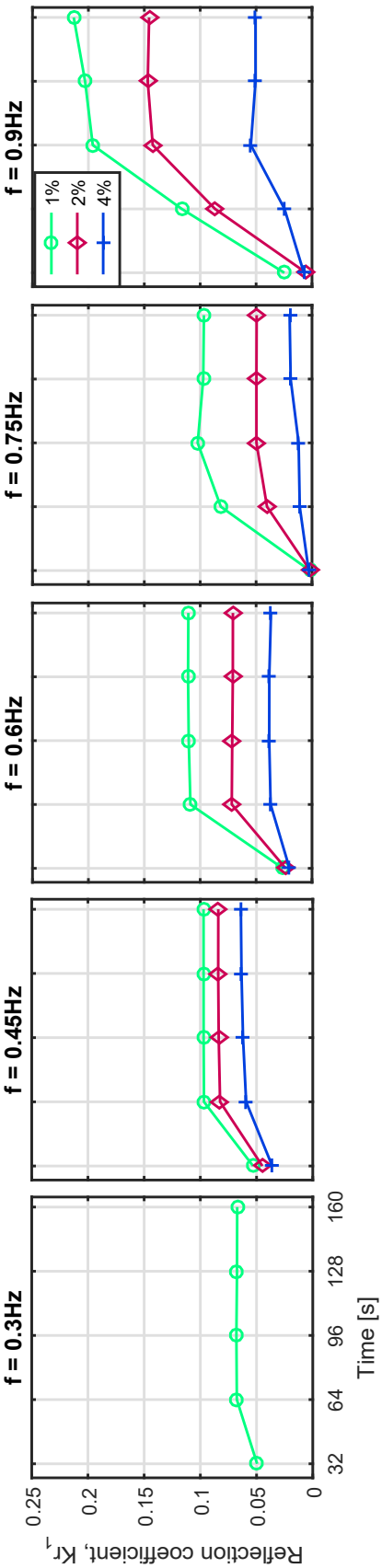

Figure 4.21: Temporal variability of reflection coefficient at tank centre for regular waves defined in Table 4.1. Indicates how reflections build up and at what point wave field is stable

4.5.2 Irregular Waves

4.5.2.1 Spatial Variability of Reflection Coefficient

Overall reflection coefficients (Eq. (4.19)) have been calculated for the irregular sea states (Table 4.1) at the five in-line positions shown in reflection array configuration RC2 (Fig. 3.11). Similar to the equivalent regular wave analysis, the effective reflection coefficients increase dramatically near the reflecting boundary, as can be seen in Fig. 4.22.

Noticeably, for f_p = 0.9 Hz, S_p = 1% waves near to the reflecting boundary, the overall 'effective' reflection coefficient reaches up to 0.75. This is clearly not the actual reflection coefficient and occurs because the array is at the focal point of the circular focussing effect observed. Nevertheless this location is obviously very poor for testing these high frequency waves. In general, it is clear that testing too close to an absorbing/reflecting wall of the tank will provide a poorer quality test environment and should be avoided unless absolutely necessary. More specifically it can be inferred that overall reflection coefficients are generally less than 10% at the tank centre for peak frequencies of 0.3-0.6 Hz (other than 1% steepness 0.6 Hz waves), whilst for 0.75 Hz it is less than 20% at the tank centre and usually less than 10% for the -6 m location. For f_p = 0.9 Hz, overall reflections of less than 20% for all steepness values are only gained once 6 m away from the reflecting boundary. These observations of reflection coefficients are reduced in higher steepness wave conditions and can be effectively decreased by moving away from the tank centreline.

4.5.2.2 In-line Variation of Incident and Reflected Spectra

From the spatial information in Fig. 4.22 it is clear that the effective reflections are larger near the reflecting boundary. In order to assess the more detailed characteristics of this, the reflected spectra can be isolated at each of the in-line positions. This has been achieved using the Zelt and Skjelbreia (2011) method. In doing this the incident spectrum can also be assessed to view whether there are any discrepancies in the apparent incoming wave field.

Figs. 4.23 and 4.24 show the isolation of incident and reflected spectra respectively. Although there are some differences in the various in-line incident spectra, it appears that the discrepancy is fairly minimal, particularly for the higher steepness conditions. This suggests that the tank is *generating* a reasonably spatially uniform wave field and that the array and measurement approach are providing consistently good data.

As expected, the apparent increase in magnitude of the reflected spectra near the boundary is clearly visible. The shape of the resulting spectra, however, is somewhat perplexing. Although for most spectra the dominant peak is at the peak frequency of the input spectrum, this is clearly not always the case. For some spectra it appears there is significant generation of harmonics and even non-harmonic components from the actively absorbing paddles. Of these, the appearance of a peak at 1.2 Hz seems particularly prevalent, and is difficult to explain It appears that it

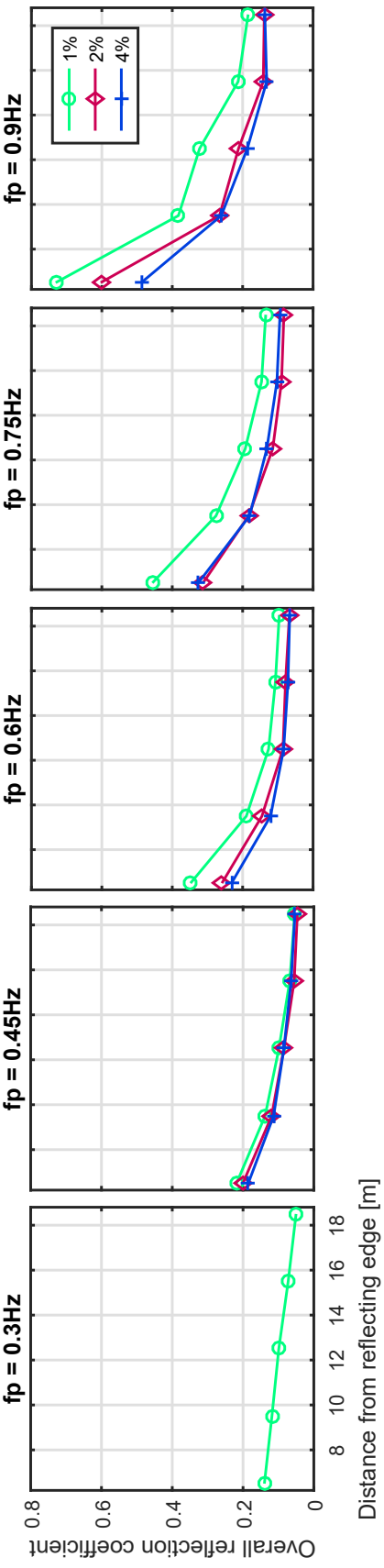

Figure 4.22: In-line variation of overall reflection coefficient for irregular uni-directional sea states defined in Table 4.1. Shows that the same circular focussing effects are occurring for irregular sea states that have been observed in Section 4.5.1.2 and Section 4.5.1.1

must be a complex function of the absorption control system dealing with various incident wave fields. Why there would be a particularly common response at this frequency however, remains unknown.

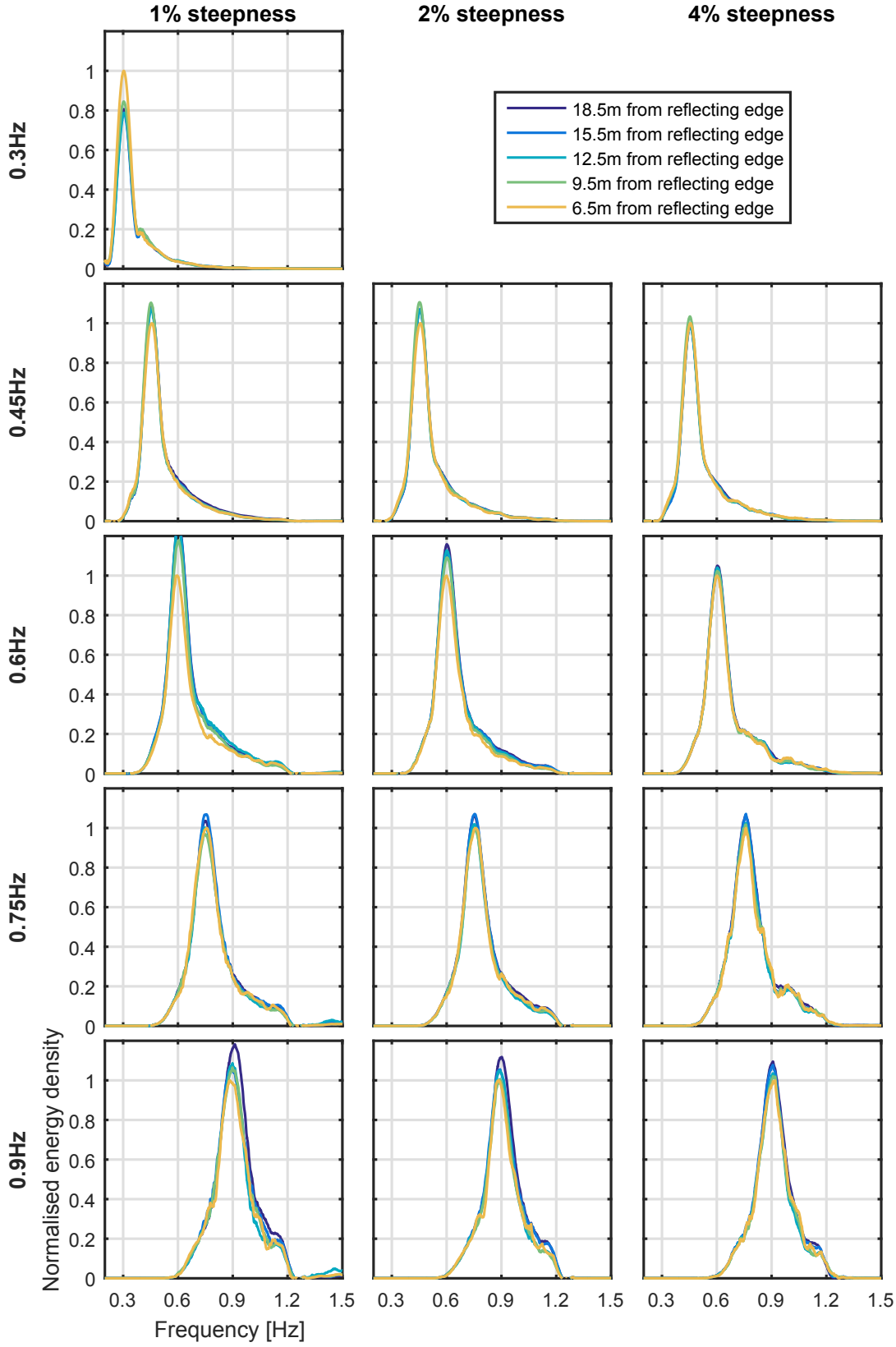

Figure 4.23: In-line variation of incident spectra for all irregular uni-directional sea states. Shown relative to 6.5m location. Smoothed to aid visibility

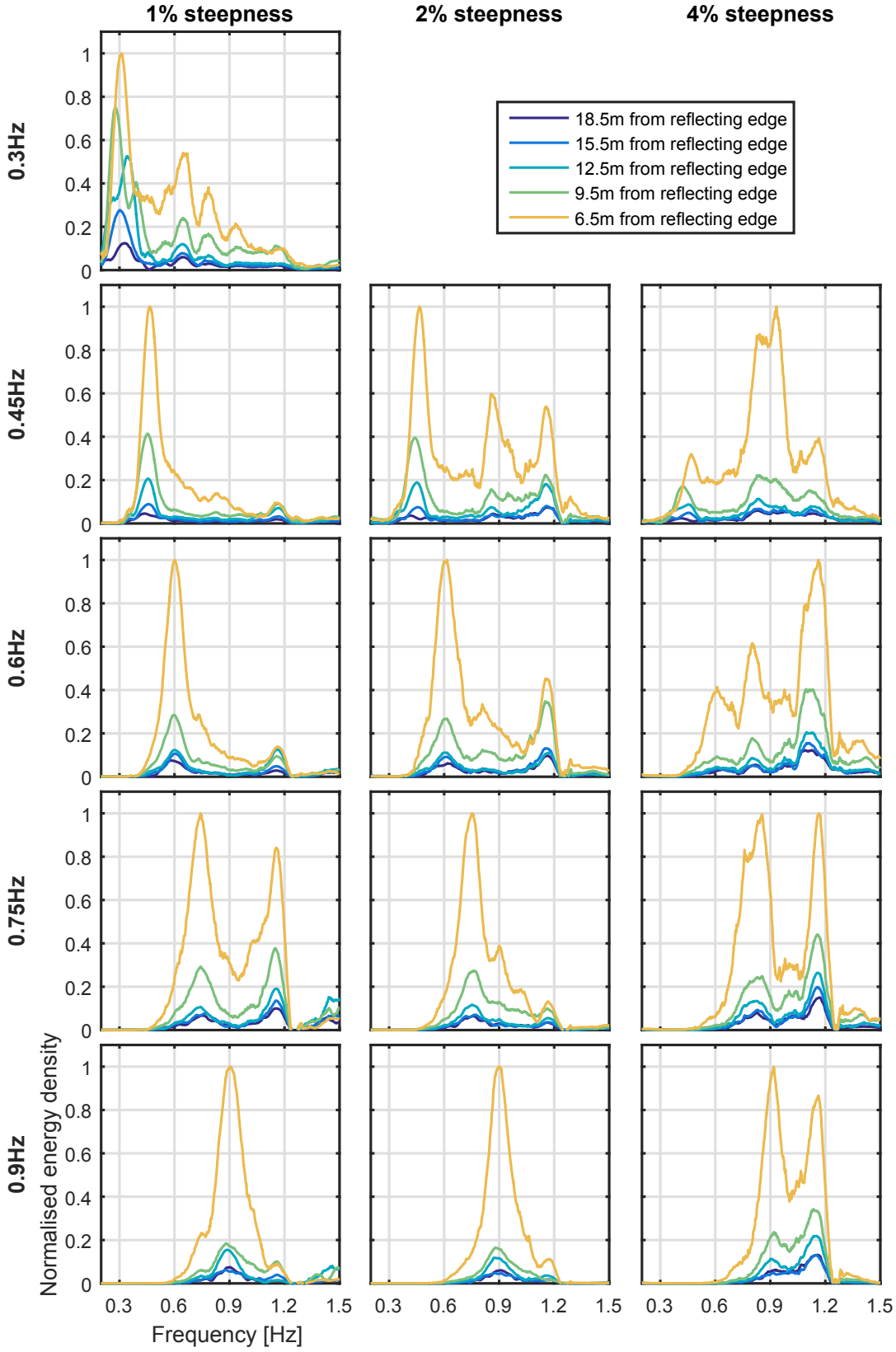

Figure 4.24: In-line variation of reflected spectra for all irregular uni-directional sea states. Smoothed to aid visibility. Shown relative to 6.5m location, to infer absolute reflection values see Fig. 4.22

4.6 Deviation, Correction and Validation

Throughout the characterisation tests it was noticed that the measured spectra, incident or total, did not match that of the desired; in general being under-produced. This suggests that the tank transfer function, which at present is solely based on theoretical wavemaker theory, needs some form of correction. Linear amplitude based correction factors have been calculated using Eq. (4.23) for all characterisation spectra, shown in Fig. 4.25.

$$CF_i = \frac{A_{i,desired}}{A_{i,measured}} \tag{4.23}$$

The frequency dependent correction factors are almost exclusively over one, for all peak frequency, steepness and spreading values. Similar to the reflection coefficients, the required correction factors are larger for higher frequencies, suggesting that the tank is less effective at both generating and absorbing these high frequency components. Overlaid in Fig. 4.25 is a weighted mean correction factor, which would be a potential solution for a pre-emptive correction procedure. It is evident from the discrepancy for individual spectra that despite providing better outputs in general, this would be an ineffective approach to apply to every sea state.

This simple way of formulating correction factors assumes that a linear change to the input amplitude will provide the desired output. To test whether or not this linear assumption is valid, an attempt has been made to correct all of the characterisation spectra, the measurements of which are shown in Fig. 4.26. Most spectra are corrected very effectively in a single iteration. Notably, however, the 0.9 Hz–1% steepness spectrum appears to still have significant deviations from the desired distribution. This may show the limit of this linear assumption. A small change in a non-linear process may be approximated as linear, however a larger change may not. The larger required correction factors (Fig. 4.25) for this spectrum may mean that this approach becomes somewhat inappropriate; necessitating a two-stage linear correction.

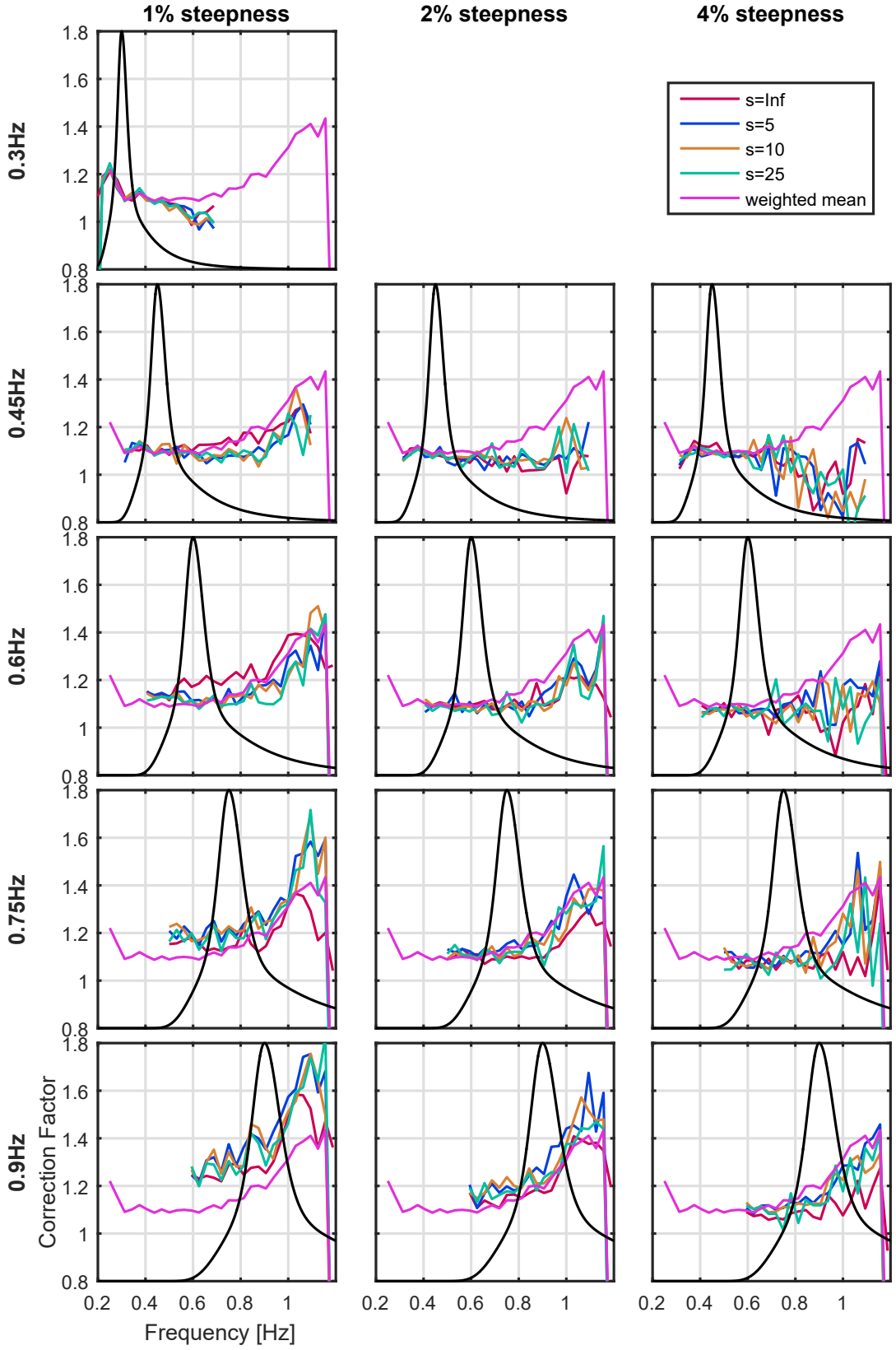

Figure 4.25: Amplitude correction factors for all irregular sea states. Normalised spectra overlaid to aid visualisation of energy distribution. Demonstrates that there is under-generation occurring, particularly affecting the higher frequencies

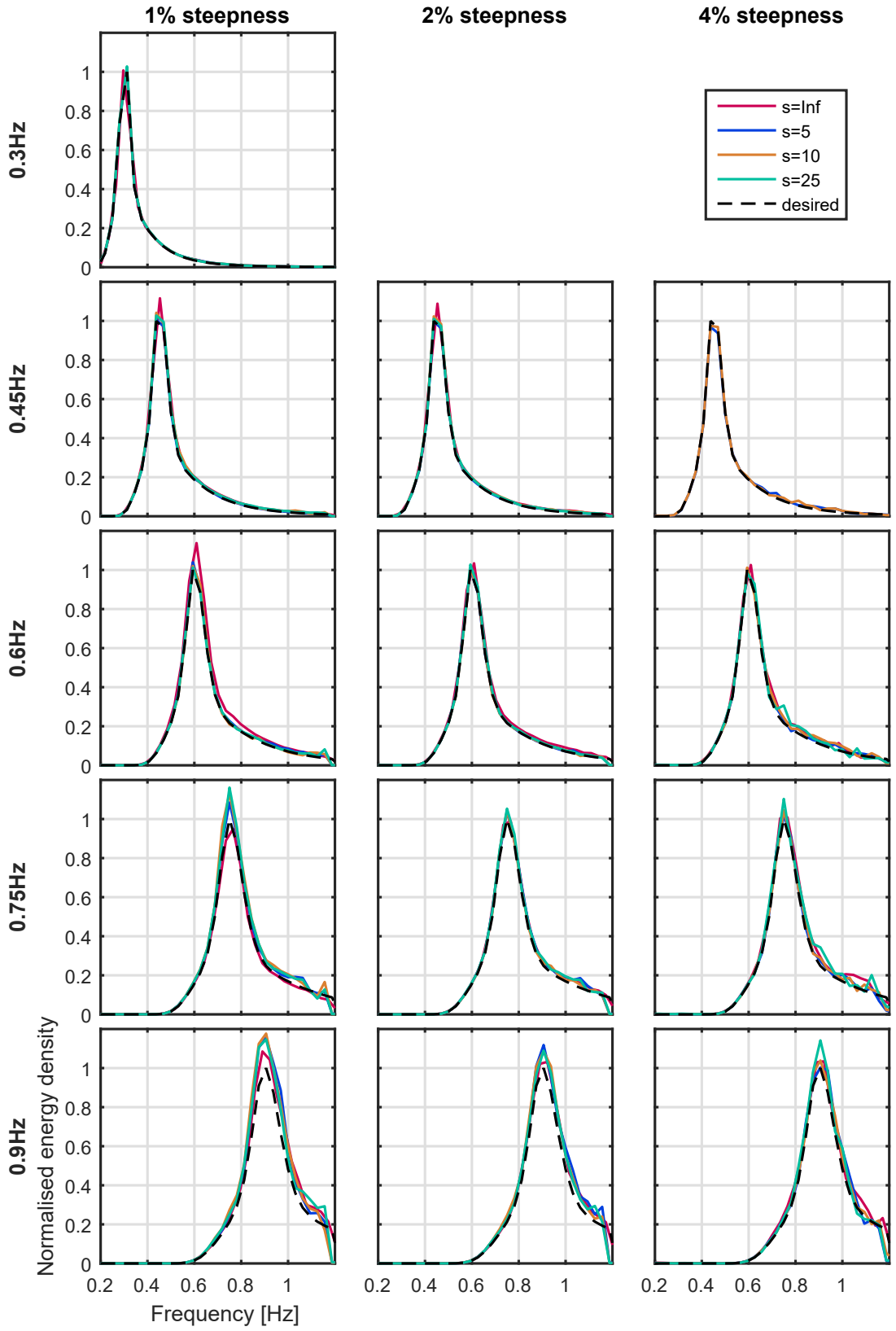

Figure 4.26: Resulting normalised spectra after linear amplitude correction factors applied. Demonstrates that the correction procedure is effective apart from when initial deviation from desired is large

4.7 Implications for Testing

The findings in this chapter provide valuable information which have implications for testing approaches and procedures at FloWave. Through knowledge of the negligible curvature and correct angle production, confidence is obtained in certain elements of the incident wave conditions (which can additionally help with measurement strategies, see Sections 5.4 and 7.2). It is known, however, that at present, correction factors must be applied to obtain the correct input spectrum, whereby a linear approach is proven to be effective unless the correction required is very large.

The sensitivity of the absorption effectiveness has been assessed, showing that peak frequency and steepness are the key parameters and that directional spreading has little effect. It is also found that the practical limit for effective absorption is around 1 Hz. This helps understand the facility characteristics, but also enables estimates of the likely reflection coefficients and quality of the wave field to be inferred prior to a prospective test. The change in the resulting reflections both spatially and temporally help identify favourable locations for testing, whilst additionally determining how long a given location is unaffected by reflections and when the wave field will become stable. This information will inform model location, but also the likely wave field variation over the model itself, along with the time-period associated with the highest quality data.

In addition to helping inform test procedures this chapter has helped contextualise some of the approaches used. For example it has been found that the waves generated at FloWave are typically non-linear and are best described by Stokes' 2^{nd} order theory. However, the improved description compared with linear theory is fairly modest, at least compared with other 'errors' incurred through scaling methods and wave field variations. Assessing this improvement, it is clear that linear methods are a reasonable approach. When the the spectral and time-series simulation methods detailed here are used they can be done so with confidence, yet with perspective and appreciation of the errors incurred.

Chapter 5

The SPAIR Directional Spectrum Reconstruction Method

To confidently re-create site specific wave conditions in FloWave (the aim of Chapter 7), it is necessary to validate the resulting directional spectra. Unfortunately, as mentioned in Section 2.2.3.2 and shown in Appendix B, Directional Spreading Function (DSF)-based methods such as EMEP and BDM have significant uncertainty associated with them, consistently resulting in apparent errors over 20%. The method developed in this chapter is therefore proposed as a wave-tank-specific alternative to standard DSF-based directional spectrum reconstruction methods; aimed at reducing the errors in the measurement and validation of directional spectra. This method has been published for a different set of sea states in Draycott *et al.* (2015a), which builds on work from Draycott *et al.* (2015b).

The proposed approach takes advantage of the single-summation method of wave generation (Section 4.1.1.2), ensuring each frequency component only has one incident wave direction. Meaningful frequency-dependent wave directions can be inferred using the Phase-Time-Path-Difference (PTPD) approach first described by Esteva (1976). The Single-summation PTPD Approach with In-line Reflections, or SPAIR method, uses these angles to calculate projected in-line gauge positions for each frequency enabling a modified version of the Zelt and Skjelbreia (2011) reflection analysis procedure to be carried out. Under the assumption that reflections have a mean direction opposing the incident wave components this enables the reflected spectrum to be isolated, with phase information, enabling both incident and reflected time-series to be reconstructed.

Highlights:

- Novel directional wave spectrum reconstruction method presented. Improvements over currently adopted methods include:
  - Ability to isolate incident and reflected time-series
  - Enables separation of incident and reflected directional spectra over 360°
  - Provides increased accuracy and reliability
- Example outputs shown and performance compared with EMEP, EMLM and BDM approaches. The SPAIR method is shown to reduce reconstruction errors significantly

- Sensitivity analysis performed, assessing effect of reflection level and angle, along with the influence of mean direction. The method is found to be only slightly affected by the level of in-line reflections, but at present cannot cope with oblique reflections.

5.1 Methodology

5.1.1 Input Angle Calculation using PTPD Approach

The commonly used methods of calculating directional spectra in tanks have been developed for ocean measurement and subsequently utilised for wave tank analysis. Similarly, the PTPD approach was also initially developed for use in ocean measurement (Esteva, 1976; Fernandes *et al.*, 2000). This technique has not however made the transition to the tank environment for the routine reconstruction of directional spectra. This is likely because of the method's inability to effectively resolve directional spectra in the ocean.

The PTPD approach uses the phase difference between triads of gauges to infer the wave direction. In the ocean, and when using the double-summation method in tanks, the phase differences in a given frequency band will encompass a range of wave components travelling in different directions. In practice the result is that the PTPD outputs essentially give a representative angle for that frequency band and cannot be used to create a full directional spectrum. When using the single-summation method of wave generation, however, there are many discrete frequency components, each of which propagates in a single direction. This should enable the method to calculate the actual directions at each sub-frequency (see Section 4.1.1.2), thereby allowing effective reconstruction of a directional spectrum when re-considering the desired, original frequency bins.

The present work uses the eight wave gauge array, DA1 (Fig. 3.9), to improve the propagation direction estimate, as previously described by Draycott *et al.* (2015b). The method is implemented as follows:

1. Obtain Fourier coefficients, $a_{i,n}$, using an FFT for each gauge, n. Calculate amplitudes, $A_{i,n}$, and absolute phases, $\Phi_{i,n}$
2. Find all three gauge combinations for N gauges, i.e. ${}^{8}C_{3} = 56$
   For every triad and all frequency components:
3. Ensure relative separations $D_{1,2}$, $D_{1,3}$ and $D_{2,3}$ are all $> 0.05L_i(f)$ and $< 0.45L_i(f)$ (analogous to spacing recommendations in Goda and Suzuki (1976))
   If so:
4. Calculate relative phases $\Phi_{1,2}$ and $\Phi_{1,3}$
5. Calculate perceived angle, α, by the method of Esteva (1976). The final equations of which are shown below:

$$\alpha = \tan^{-1} \frac{\left[(x_1 - x_2)\,\Phi_{1,3} - (x_1 - x_3)\,\Phi_{1,2}\right] / sign(P)}{\left[(y_1 - y_3)\,\Phi_{1,2} - (y_1 - y_2)\,\Phi_{1,3}\right] / sign(P)} \tag{5.1}$$

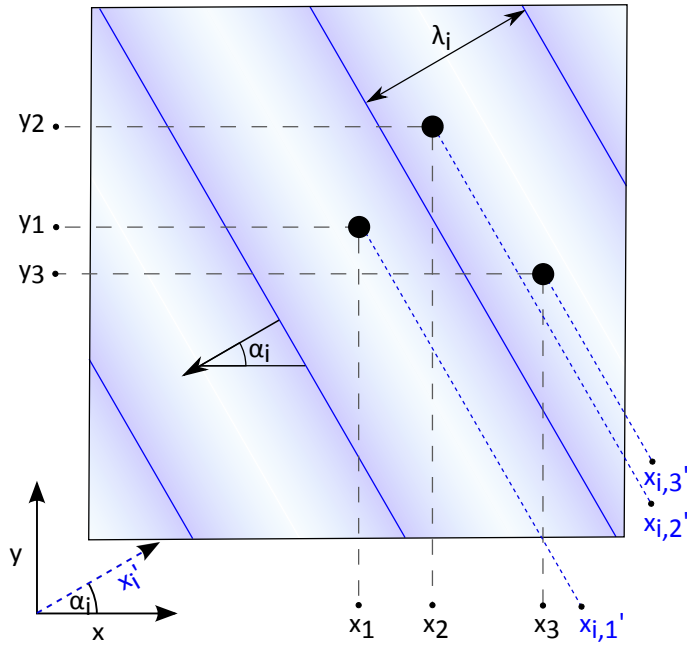

Figure 5.1: Example projected x values for a single frequency component and its associated propagation direction

$$P = [(x_1 - x_2)(y_1 - y_3) - (x_1 - x_3)(y_1 - y_2)] \tag{5.2}$$

6. Take the peak of a circular kernel density estimate over all valid triad combinations as the propagation direction for that frequency
7. Comparisons can now be made between the desired and measured angles, as per the single summation method. Additionally the data can be re-binned and compared with the desired directional spectrum

The PTPD approach relies on the fact that the phase difference between gauges is a function of the frequency-dependent wavelength and their relative positions. The phase difference between gauge n and gauge m, for a given frequency component, i, can therefore be represented as

$$\begin{aligned} \Phi_{i,nm} &= k_i \left[(x_n - x_m) \cos \alpha_i + (y_n - y_m) \sin \alpha_i \right] \\ &= k_i \left(x'_{i,n} - x'_{i,m} \right) \end{aligned} \tag{5.3}$$

The projected in-line x-positions for frequency i, $x'_{i,n}$, as a function of the measured wave direction, α_i, is shown in Fig. 5.1. Although only three gauges are required to get an estimate of the wave directions it is advantageous to have multiple estimates for the propagation direction at each frequency. This is because measurement noise, position error and the presence, or build-up of reflections, may result in errors in individual directional estimates.

In this work a maximum of 56 estimates are used to give a representative direction for each frequency, disregarding estimates derived from triads with inappropriate separation magnitudes.

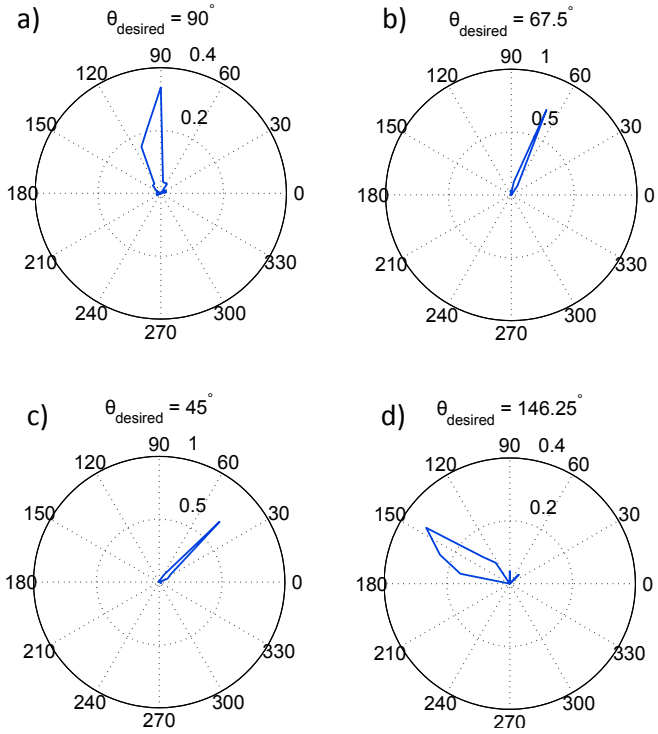

Figure 5.2: Example circular kernel density outputs showing a range of different spreads in the estimate

A circular mean, or circular median value may be used from these to estimate the true incident direction at this frequency, however, to limit the influence from rogue estimates a circular kernel density estimate has been used for this work. The peak of this kernel density estimate should generally represent the incident wave direction, with estimates lying either side of the peak being affected more strongly by reflections or position error. Mean or median values, however, may be used effectively with high order rotationally symmetric arrays, such as multiple high density 'circular' arrays. In this instance, the influence of reflections will roughly cause an equal number of over and under-estimates of wave direction, resulting from the cumulative triad orientations. However, as arrays have generally no, or low order, rotational symmetry there is typically a skewed distribution of estimates around the true incident value, as shown in Fig. 5.2.

Kernel density estimates are therefore calculated at each of the discrete frequency increments used for the sea state. Fig. 5.2 shows some example outputs of these estimates, highlighting the requirement to have multiple estimates in some scenarios, but not others. Fig. 5.2a and Fig. 5.2d highlight the advantage of using the peak of the kernel density estimates, rather than the mean, with Fig. 5.2a demonstrating this particularly well. It is clear here that using the circular mean value would have lead to a significant 'over-estimate' of the wave direction, amounting to around 10°.

5.1.2 Calculating In-line Reflections using Projected Gauge Positions

The PTPD approach used here takes advantage of the fact that the phase differences at a given frequency should be solely a function of the gauge positions, x_n, y_n, and the wave propagation direction, α_i. When using the single-summation method of wave generation this trait allows for the calculation of frequency dependent, in-line separations:

$$x'_{i,n} - x'_{i,m} = (x_n - x_m)\cos\alpha_i + (y_n - y_m)\sin\alpha_i \tag{5.4}$$

The complex amplitude spectra measured at each gauge, $a_{i,n}$, along with these assumed separations then allow a reflection analysis procedure to take place. The process in doing this essentially treats each frequency component as a uni-direction problem.

As mentioned in Section 2.2.3.1, typical uni-directional reflection analysis can be achieved with a small number of gauges, as demonstrated by Goda and Suzuki (1976), and Mansard and Funke (1980), for two and three gauges respectively. These methods require the gauge separations to be within a small range to give useful estimates. In this multi-directional work the effective in-line separations are highly variable, and as such require more gauges to ensure useful spacings are available. For this reason the Zelt and Skjelbreia (2011) method is used, with some slight modification. The three modifications made are as follows:

1. x-values are now frequency dependent in-line x-positions, based on the calculated α_i values.
2. Absolute phases are used rather than phase difference to gauge 1. This eventually allows reconstruction of total, incident and reflected time-series, and also direct use of the isolated Fourier coefficients.
3. As a weighting function the 'goodness' function presented in Zelt and Skjelbreia (2011) is used in conjunction with the coherence spectra between gauges (dot product). This should enable spacing considerations (goodness function) to be considered in conjunction with a measure of the consistency of the phase differences between gauges. In the results shown in Section 5.2 this has made little improvement (<2%). If, however, there are particularly noisy signals, or if complex reflections build up throughout a test this may prove more useful. The coherence spectra was calculated using the `mscohere` MATLAB function.

The final modified equations used to calculate the complex incident and reflected Fourier coefficients, a_{inc} and a_{ref} are

$$a_{inc,i} = \sum_{n=1}^{N} C_{i,n} a_{i,n} \tag{5.5}$$

$$a_{ref,i} = \sum_{n=1}^{N} C^*_{i,n} a_{i,n} \tag{5.6}$$

where $a_{i,n}$ is the *measured* Fourier coefficient with absolute phase (rather than with phases relative to gauge 1), $C^*_{i,n}$ is the complex conjugate of $C_{i,n}$ and

$$C_{i,n} = \frac{2iW_{i,n}}{D} \sum_{m=1}^{N} W_{i,m} \sin\left(\Delta\Phi_{i,nm}\right) e^{i\Phi_{i,m}} \tag{5.7}$$

$$D = 4 \sum_{n=1}^{N} \sum_{m<n} W_{i,n} W_{i,m} \left[\sin\left(\Delta\Phi_{i,nm}\right)\right]^2 \tag{5.8}$$

where

$$\begin{aligned} \Delta\Phi_{i,nm} &= k_i \left[(x_n - x_m)\cos\alpha_i + (y_n - y_m)\sin\alpha_i\right] \\ &= k_i \left(x'_{i,n} - x'_{i,m}\right) \end{aligned} \tag{5.9}$$

$$\Phi_{i,m} = k_i . x'_{i,m} \tag{5.10}$$

$W_{i,n}$ is the weighting function for gauge n and frequency i.

These equations allow the incident and reflected amplitude spectra to be resolved for single-summation generated directional spectra. The incident and reflected wave energy density spectra can now be calculated as

$$S_{inc,i} = \frac{\left|a_{inc,i}\right|^2}{2\delta f} \tag{5.11}$$

$$S_{ref,i} = \frac{\left|a_{ref,i}\right|^2}{2\delta f} \tag{5.12}$$

The frequency-dependent reflection coefficient, $K_{r,i}$, can also be readily calculated as

$$K_{r,i} = \frac{\left|a_{ref,i}\right|}{\left|a_{inc,i}\right|} \tag{5.13}$$

5.1.3 Calculating the Updated Incident and the Reflected Directional Spectrum

Knowledge of the incident and reflected wave frequency spectrum does not directly allow for an update to be made to the incident directional spectrum. The reflections present in the tank cause gauge dependent amplitude and phase deviations. The nature of the PTPD approach means that these can manifest themselves as a directional distribution error, rather than being isolated. This requires the incident propagation directions to be recalculated, using the already isolated incident Fourier coefficients.

In order to fix the measured incident directional spectrum, the isolated incident Fourier coefficients can be re-processed using the PTPD approach. This requires the phases for the 'base' Fourier coefficients, $a_{inc,i}$, at the origin (0,0), to be shifted to the in-line apparent gauge

positions. This is carried out noting that

$$a_{i,n} = a_{inc,i}e^{-i\Phi_{i,n}} + a_{ref,i}e^{i\Phi_{i,n}} \tag{5.14}$$

This defines the incident, position shifted Fourier coefficients to be

$$a_{inc,i,n} = a_{inc,i}e^{-i\Phi_{i,n}} = a_{inc,i}e^{-i\left(k_i.x'_{i,n}\right)} \tag{5.15}$$

These Fourier coefficients can now be used directly with the PTPD approach, enabling an estimate of the incident directional spectrum to be made with an attempt to remove the 'artificial' amplitude and phase deviations. The reflected directional spectrum can be calculated similarly, or more easily through knowledge of the reflection coefficients. In addition to this, the incident and reflected time series at the gauge positions can be estimated through an IFFT.

The nature of this combined approach means that incident and reflected spectra can be separated over all directions without requiring prior knowledge of the input angular range. Neither the BDM or EMEP approaches are capable of achieving this or the time-series reconstructions.

5.2 Example Results

The SPAIR method has been used to calculate the incident and reflected directional spectra and reflection coefficients for all of the characterisation sea states defined in Table 4.2. The resulting reflection coefficients are shown in Section 4.4 as part of the tank characterisation work.

In this section some of the other outputs of the SPAIR method are explored, looking particularly at the isolated incident and reflected directional spectra and time-series. A series of example sea states are shown, chosen to correspond to the sea state parameters explored in further detail in Chapter 4, with a variety of spreading values. These are defined in Table 5.1.

Table 5.1: Example sea states explored to assess SPAIR results

Sea State Reference	Frequency [Hz]	Steepness [%]	Spreading (cos^{2s})
1	0.3	1	5
2	0.45	2	10
3	0.6	2	25
4	0.75	2	10
5	0.9	2	5

5.2.1 Incident and Reflected Directional Spectra

Example directional spectra relating to the sea states defined in Table 5.1 are shown in Fig. 5.3. It is observed that the discrepancy between measured incident spectrum and desired spectrum is generally low, with the exception of sea state 5. Viewing the colour-scale-separated spectra (middle column of Fig. 5.3), it is apparent that the reflected spectrum has been effectively isolated, generally mirroring the form of the incident distribution.

Sea state 5 demonstrates much larger deviations that the other spectra. This sea state has the highest peak frequency and hence from the previously measured deviations (Fig. 4.25), is expected to have a larger deviation due to significant under-generation. This appears to be what is causing the majority of the perceived error here, rather than discrepancy in the generated directional distribution.

5.2.2 Time Series

Fig. 5.4 shows the example time series outputs for a single gauge in each of the sea states shown in Fig. 5.3. An IFFT of the complex input amplitude spectra, Eq. (4.8), enables the theoretical time series to be computed using linear wave theory, before being compared to the actual measurements. As detailed in Section 5.1.3, the presented method also allows for the separation of incident and reflected time series in the tank domain and as such these have been computed at the gauge locations for comparison.

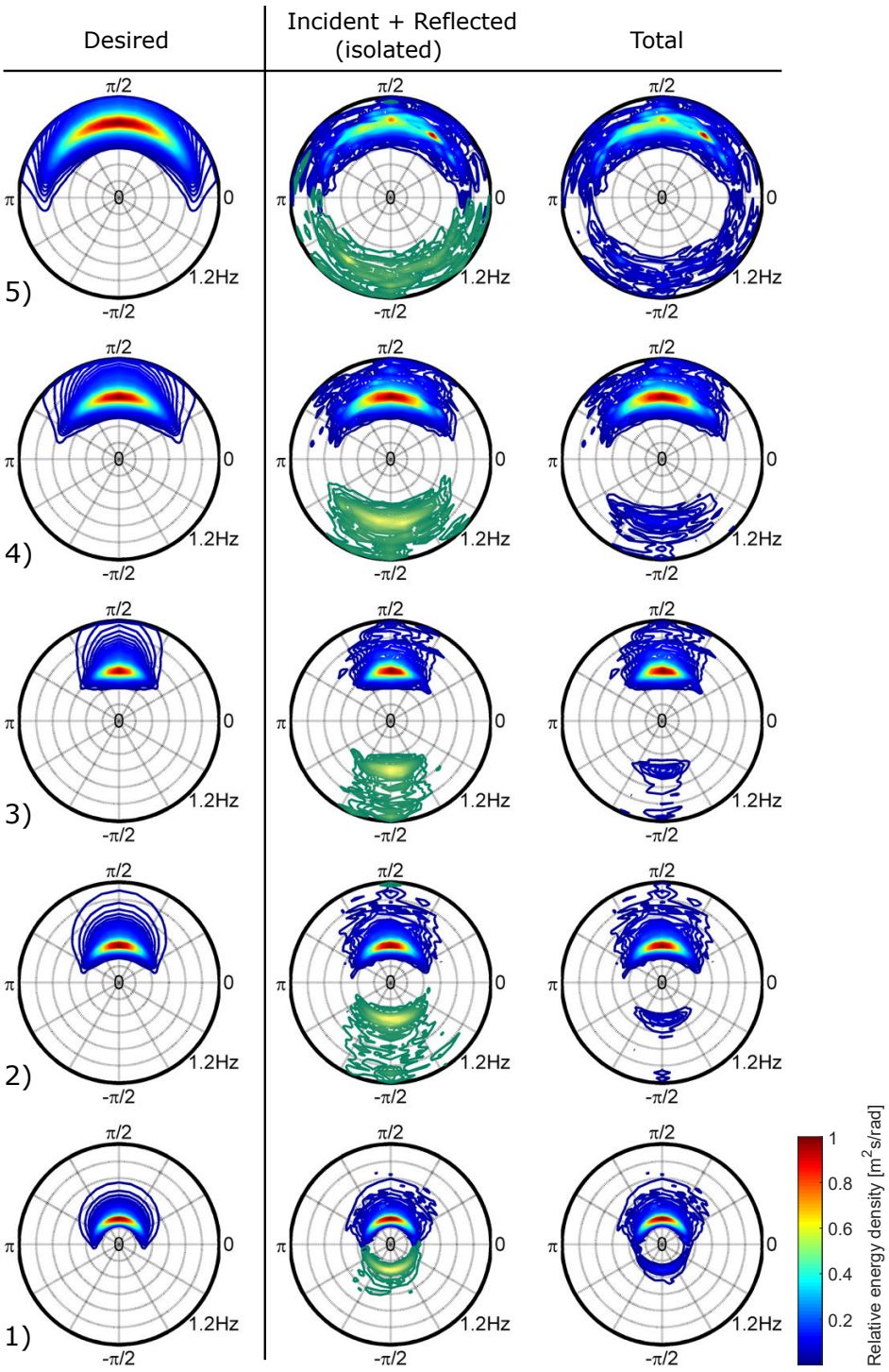

Figure 5.3: Example SPAIR reconstructed directional spectra outputs. Energy density $[m^2 s/rad]$ is shown by the colour, relative to the peak of the desired spectrum. 1) 0.3 Hz, $s = 5$, $st = 1\%$, 2) 0.45 Hz, $s = 10$, $st = 2\%$, 3) 0.6 Hz, $s = 25$, $st = 2\%$ 4) 0.75 Hz, $s = 10$, $st = 2\%$ 5) 0.9 Hz, $s = 5$, $st = 2\%$. The isolated spectra are shown on different colour scales to better illustrate the detail of the reflected spectrum

The computed lag resulting from cross-correlation, along with the coefficient of determination evaluated at this lag are also shown in Fig. 5.4. This has been carried out for both the measured and isolated incident time-series, with both providing reasonably good agreement with the theoretical (linear theory) expectation in the majority of cases. It is evident from this analysis that the removal of the reflected components generally provides a closer match, however, this is not always the case. Difficulty in isolating what is unaccounted reflections from non-linear behaviour, or simply mis-generation, means that it is hard to proportionally allocate the causes of the discrepancy.

Unsurprisingly, example sea state 5 shows the largest deviation from the theoretical target time series, agreeing with findings from Fig. 5.3. Also, as expected from the reflection analysis carried out in Section 4.4, it has the largest relative magnitude of reflected components.

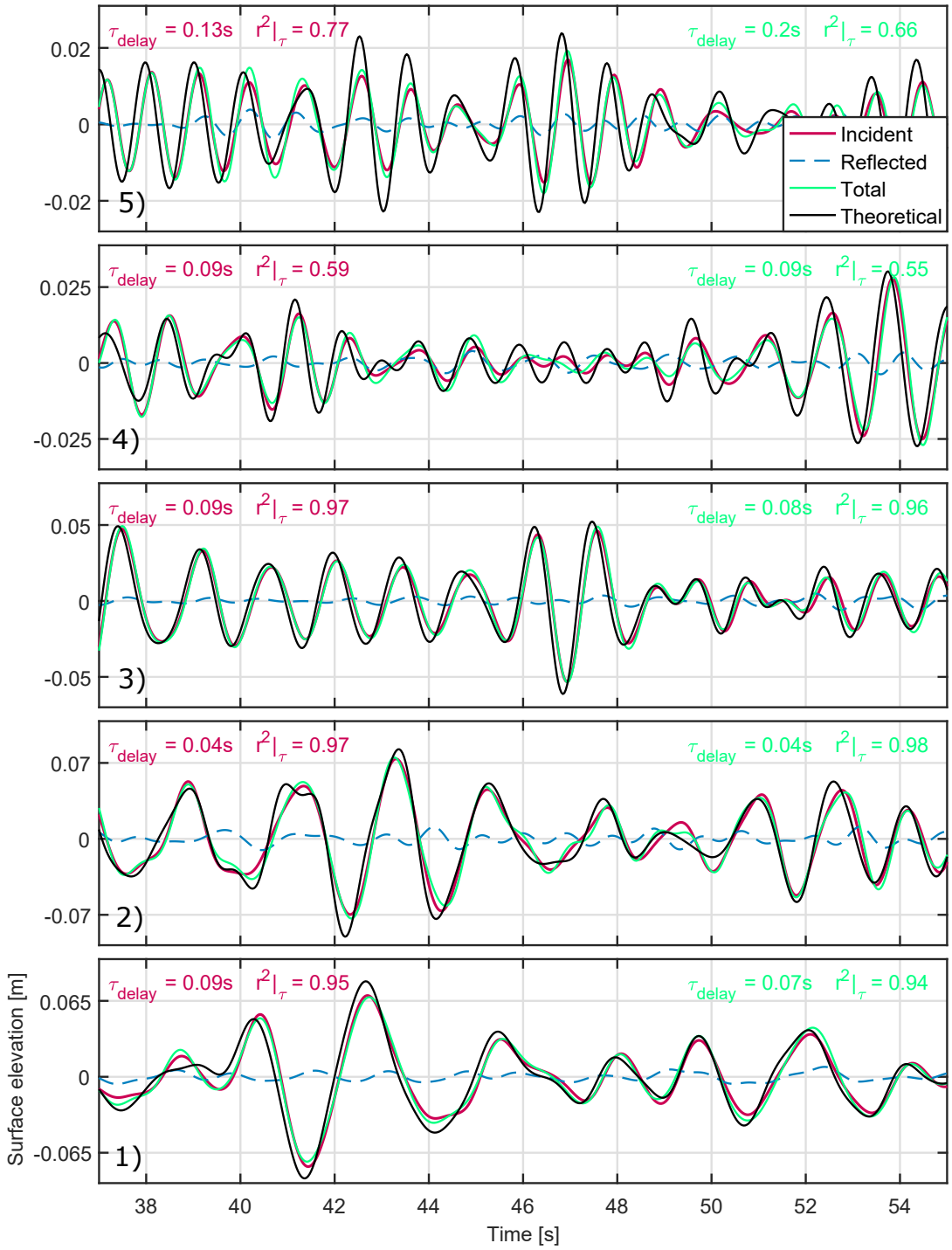

Figure 5.4: Example time series outputs for the example spectra shown in Fig. 5.3. Theoretical time series as well as measured are shown, in addition to the isolated incident and reflected components for a range of gauges. Sea state 1, gauge 1; sea state 2, gauge 2 etc. The computed cross-correlation lag and coefficient of determination evaluated at this lag are shown above each plot

5.3 Method Performance

5.3.1 Comparison to other Methods

5.3.1.1 Perceived Errors

In order to assess combined sea state and method performance, the Normalised Total Difference (NTD) between target (t) and measured (m) spectra can be assessed, defined as:

For directional spectra:

$$NTD_E = \frac{\sum_{p=1}^{N_f} \sum_{q=1}^{N_\theta} |E_{t,pq} - E_{m,pq}|}{\sum_{p=1}^{N_f} \sum_{q=1}^{N_\theta} E_{t,pq}} \tag{5.16}$$

For frequency spectra:

$$NTD_S = \frac{\sum_{p=1}^{N_f} |S_{t,p} - S_{m,p}|}{\sum_{p=1}^{N_f} S_{t,p}} \tag{5.17}$$

NTD_E provides assessment of the total deviation from target spectra, which includes:

- frequency spectrum error, NTD_S
- directional distribution error, NTD_D
- method reconstruction error, NTD_M
- miscellaneous (other) error, NTD_O e.g. noise, position error

Ideally the method reconstruction error, NTD_M, would be assessed to gauge method performance. It is not possible, however, to isolate this as the true directional distribution error is not known. From Section 4.6 it is known that the deviation from target frequency spectra, NTD_S, is mostly tank dependent and not a function of the methodology. As a result of this, to assess method performance, the metric NTD_E - NTD_S has been used, noting that it incorporates the method reconstruction error, along with the directional distribution error. As the true distribution error is constant this should allow effective comparisons to be made between methods.

Fig. 5.5 shows this comparison for all of the directional characterisation sea states (Table 4.1). The incident spectrum from the SPAIR method has been compared with those obtained using the BDM, EMEP and EMLM methods respectively (using a fixed input range of 0-180° for BDM, EMEP and EMLM methods). The SPAIR approach consistently performs better, with mean NTD_E - NTD_S values of 6.6%, compared with 20%, 14.9% and 38.7% for the BDM, EMEP and EMLM approaches respectively.

From these results is can safely be stated that the actual directional error is less than 6.6% on average and likely to be significantly smaller than this. This represents a significant improvement on what could be inferred from the use of other methods and will clearly help reduce uncertainty in the validation of directional sea states.

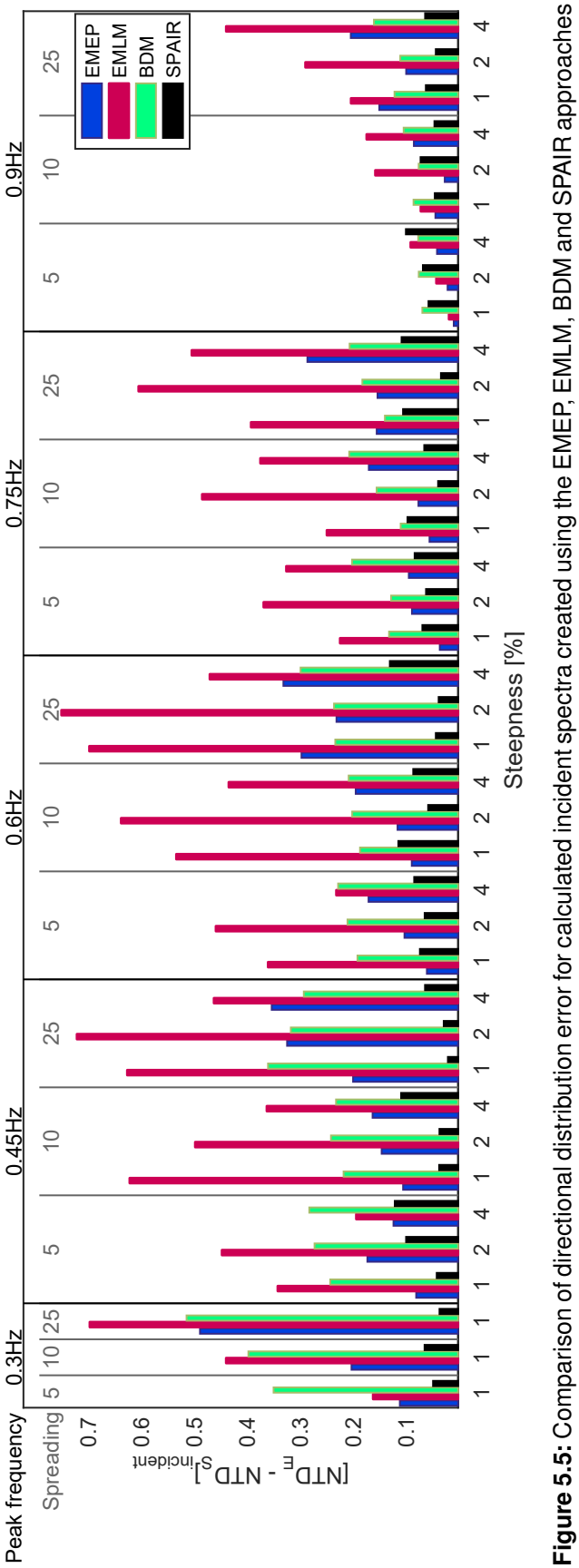

Figure 5.5: Comparison of directional distribution error for calculated incident spectra created using the EMEP, EMLM, BDM and SPAIR approaches

5.3.1.2 Comparison of Spectra

From Fig. 5.5 it is clear that the EMLM outputs for these sea states are very poor. This contradicts what may be expected from the wave gauge array study in Appendix B, where various directional spectrum reconstruction methods are assessed theoretically. Importantly, this highlights the differences between numerical studies and reality. For this reason (and space restrictions) the EMLM spectra have not been included in the comparison between spectra. The directional spectra for the remaining methods can be found in Fig. 5.6, for the same sea states shown in Fig. 5.3.

It is observed that neither the EMEP or BDM approaches consistently fit a DSF that incorporates reflected components. The EMEP approach appears to incorporate some reflected energy content, but the distribution seems incorrect, likely constrained by the inherent frequency-dependent 'curve-fitting' process.

Visually all of the methods perform reasonably well in terms of characterising the incident wave field, with the SPAIR approach demonstrating the best performance, as expected from the perceived error results. This is also apparent through visual observation, as the high energy components of the incident distribution match up very well with that of the desired. At low energy levels, however, the distribution does appear to be ill-defined, a function of the discretised nature of the solution and the low energy densities present at these frequencies.

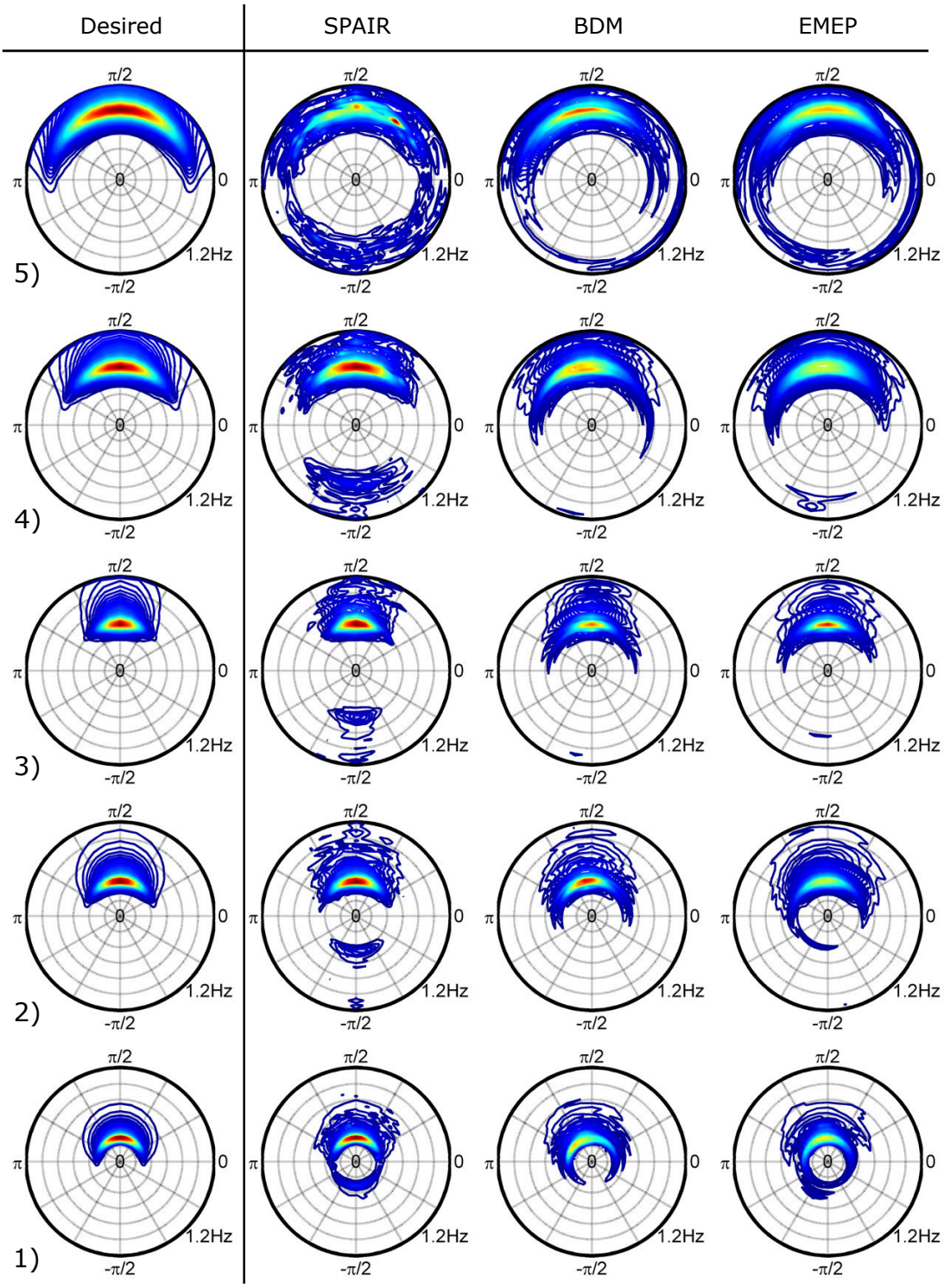

Figure 5.6: Comparison of example directional spectrum outputs from SPAIR, EMEP and BDM approaches. Energy density $[m^2 s/rad]$ is shown by the colour, relative to the peak of the desired spectrum. Same colour scale as Fig. 5.3

5.3.2 Performance with Complex Spectra

Complex yet well-defined sea states have been created to prove that the method can reconstruct such unconventional spectra, whilst additionally isolating the incident and reflected components over 360°. These sea states have been created using JONSWAP spectra with $\gamma = 3.3$, with the parameters defined in Table 5.2. The first spectrum is a multi-modal sea state consisting of two identical wave systems with the mean direction 120° apart, whilst the second spectrum is a single wave system with a very large directional spread, spanning 360°. Two completely opposing wave systems have been used for spectrum three, with a slight difference in peak frequency.

Table 5.2: Complex Spectra Tests. All with $\gamma = 3.3$

Wave Parameter	Spectrum a	Spectrum b	Spectrum c
peak frequency, f_p [Hz]	0.5, 0.5	0.45	0.45, 0.55
cos-2s spreading value, s	5, 5	0.5	20, 20
mean direction, $\bar{\theta}$ [deg]	45, 165	120	90, 270

It is often difficult to isolate the different incident modes of such spectra using conventional methods and the isolation of the incident and reflected spectra is not usually possible at all without a defined incident range. These tests therefore serve as a useful demonstration of the capability of the SPAIR method.

Fig. 5.7 shows the total reconstructed wave field using the three methodologies. It is clear that the EMEP and BDM approaches generally fail to capture the multi-modal and highly spread nature of the input sea states, other than perhaps the BDM approach reconstruction of spectrum c. The stochastic solution approach of the BDM (Benoit *et al.*, 1997) would typically mean that performance gains could be achieved with spectra a and b if longer run lengths were provided. However, given the constant inter-gauge phase relationships (at a given frequency) enforced by deterministic wave generation this may not have a significant impact for these tests.

Table 5.3: Directional distribution error, NTD_E - NTD_S, for complex spectra

NTD_E - NTD_S	Spectrum a	Spectrum b	Spectrum c
SPAIR	0.176	0.150	0.054
EMEP	0.332	0.224	0.445
BDM	0.405	0.340	0.315

The SPAIR approach enables a much more effective characterisation of the input conditions, as demonstrated in Fig. 5.7 and Table 5.3. The reflected spectrum and coefficients can also be calculated as no input angular range is required, with the result that the incident and reflected spectra can apparently overlap. The reflected spectra are shown in Fig. 5.8 and the total reflection calculated coefficients were found to be 8.33% , 8.63% and 8.10% respectively.

Each of the unusual spectra have peak frequencies of between 0.45 Hz and 0.5 Hz, around 2-3% steepness and large spreading. Despite having vastly different spectral forms they have near identical reflection coefficients, consistent with the results shown in Section 4.4. This supports previous findings that peak frequency and steepness are the main parameters driving absorption effectiveness at FloWave.

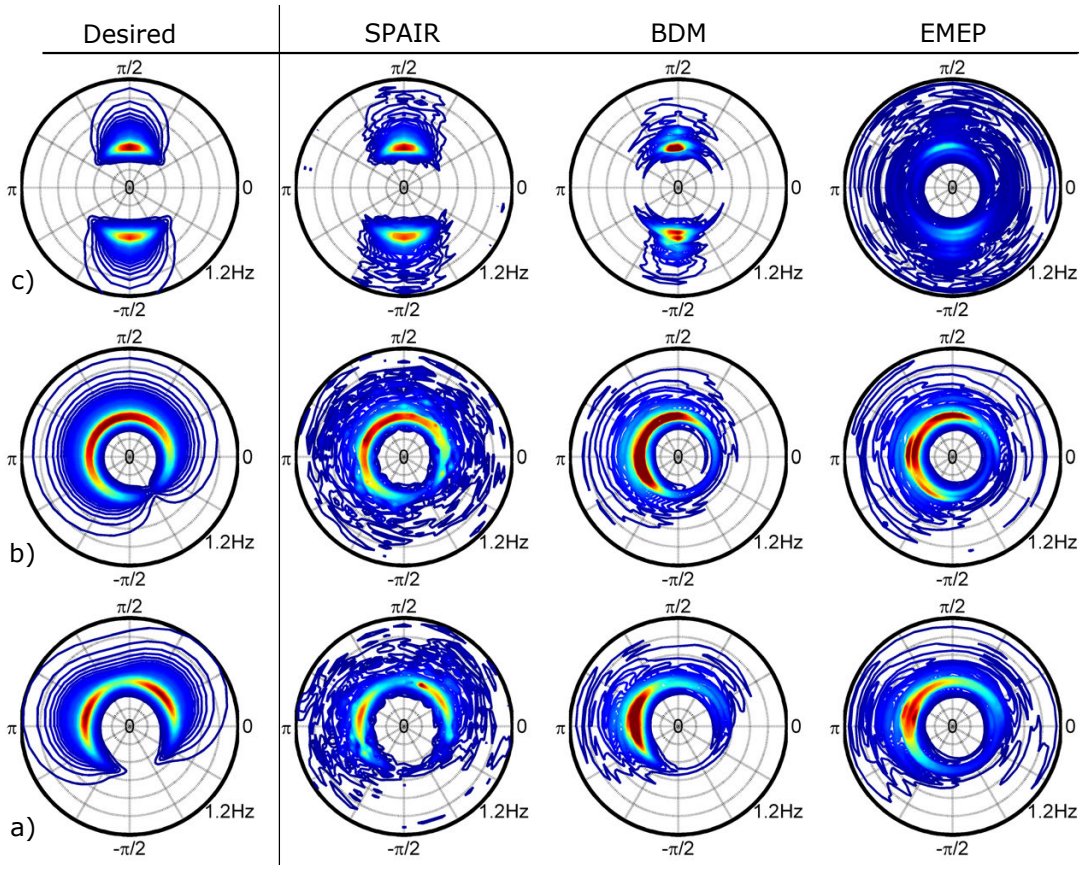

Figure 5.7: Complex directional spectra outputs (total) for SPAIR, BDM and EMEP approaches. Energy density $[m^2s/rad]$ is shown by the colour, relative to the peak of the desired spectrum. Same colour scale as Fig. 5.3

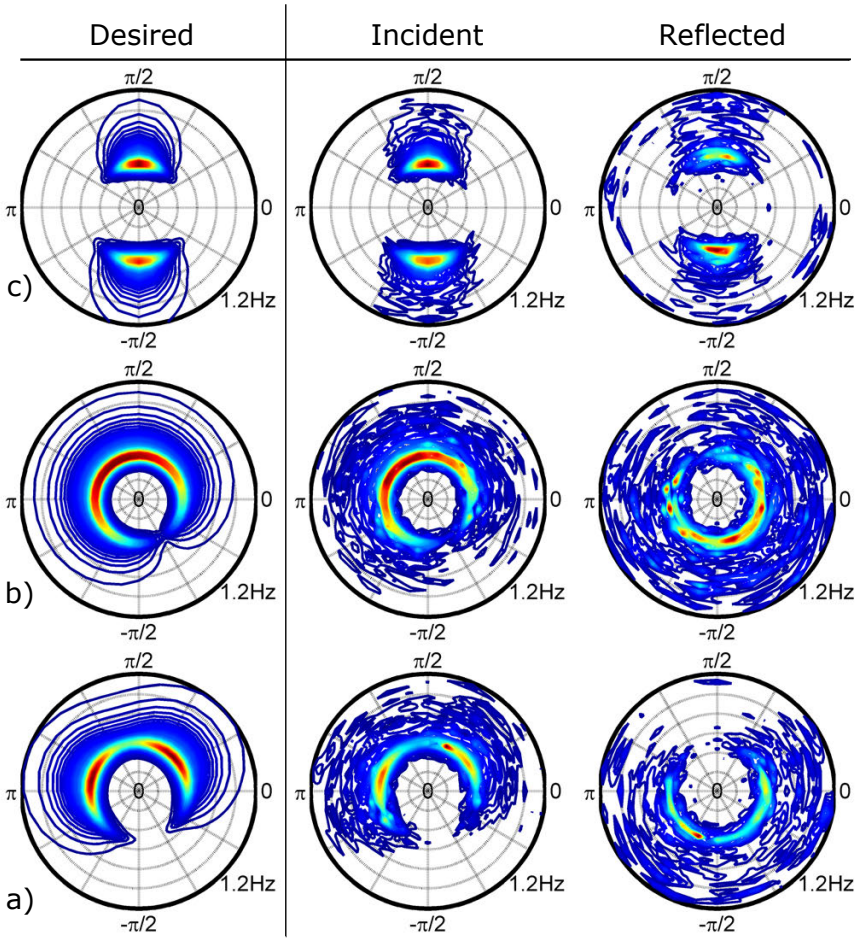

Figure 5.8: Incident and reflected directional spectrum outputs for complex spectra defined in Table 5.2. Energy density $[m^2s/rad]$ is shown by the colour, relative to the peak of each spectrum. Same colour scale as Fig. 5.3

5.3.3 Method Limitations and Sensitivity

5.3.3.1 Effect of In-line Reflection Level

The presence of in-line reflections alter the phases and phase differences measured at the gauges and hence causes an apparent angle estimation error through Eq. (5.1). The effect of this can be understood by looking at the resulting Fourier coefficients in the presence of such reflections.

Surface elevations in the presence of in-line reflections at (x,y), can be modelled as

$$\begin{aligned}\eta(x,y,t) = \sum_{n=1}^{N} & A_{inc,i}\cos\left(k_i(x\cos\alpha_{inc,i} + y\sin\alpha_{inc,i}) + \Phi_{inc,i} + \omega_i t\right) \\ & + K_{r,i}A_{inc,i}\cos\left(-k_i(x\cos\alpha_{inc,i} + y\sin\alpha_{inc,i}) + \Phi_{inc,i} + \Phi_{ref,i} + \omega_i t\right) \end{aligned} \quad (5.18)$$

Defining $k_{i,xy} = k_i(x_n\cos\alpha_{inc,i} + y_n\sin\alpha_{inc,i})$, and $k_{r,i} = K_{r,i}e^{i\Phi_{ref,i}}$, the resulting Fourier coefficients at gauge n can be expressed by

$$\begin{aligned} a_{i,n} &= a_{inc,i}e^{ik_{i,xy}} + a_{inc,i}k_{r,i}e^{-ik_{i,xy}} \\ &= a_{inc,i}[cos(k_{i,xy}) + isin(k_{i,xy})] + a_{inc,i}k_{r,i}[cos(k_{i,xy}) - isin(k_{i,xy})] \\ &= a_{inc,i}(1-k_{r,i})isin(k_{i,xy}) + a_{inc,i}(1+k_{r,i})cos(k_{i,xy}) \end{aligned} \quad (5.19)$$

The expected phase at gauge n is therefore

$$\Phi_{n,i} = \tan^{-1}\left[\frac{\tan k_{i,xy}(1-k_{r,i})}{(1+k_{r,i})}\right] \quad (5.20)$$

Apparent angle for each gauge triad is calculated using

$$\alpha_{apparent,i} = \tan^{-1}\frac{\left[(x_1-x_2)\Phi_{i,13} - (x_1-x_3)\Phi_{i,12}\right]/sign(P)}{\left[(y_1-y_3)\Phi_{i,12} - (y_1-y_2)\Phi_{i,13}\right]/sign(P)} \quad (5.21)$$

where

$$\Phi_{i,mn} = \Phi_{m,i} - \Phi_{n,i} \quad (5.22)$$

From Eq. (5.20) it can be seen that phases and phase differences at the gauge locations are heavily influenced by the magnitude of the reflection coefficient, $K_{r,i}$. However, the extent with which this alters the resulting angle estimation depends on the relative change in $\Phi_{i,13}$ to $\Phi_{i,12}$, which is a function of the angle relative to the triad orientation, along with the magnitude of the separations relative to the wavelength. Fig. 5.9 shows the expected angular error for a single equilateral gauge triad as a function of the reflection coefficient, incident angle and relative separation magnitude. K_r values between 0 to 10 have been used to assess whether the PTPD method presented identifies the 'reflected' component as the incident direction if $K_r > 1$. From Fig. 5.9 it is apparent that the method does find the correct 'dominant' angle when $K_r > 1$.

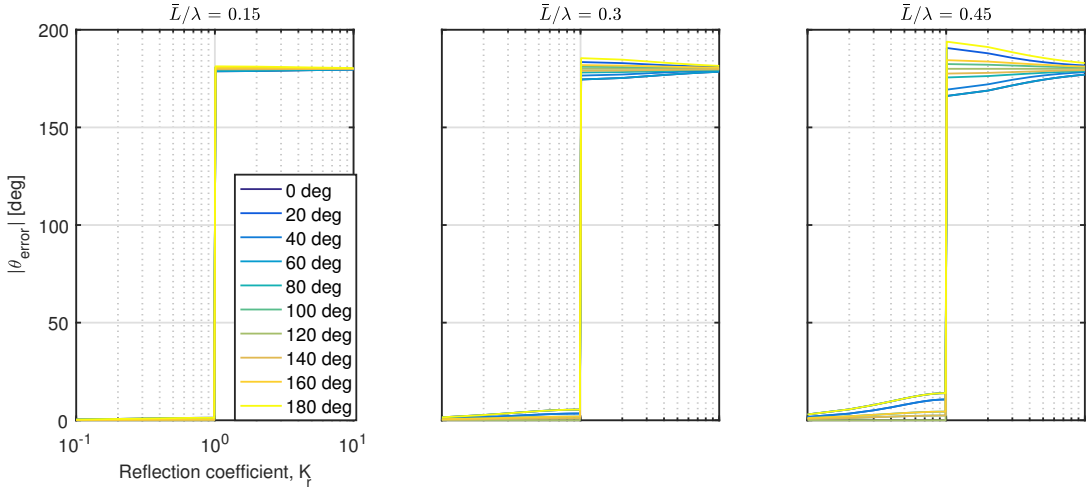

Figure 5.9: Effect of in-line reflection coefficient, wave angle and relative separation magnitude on apparent angle calculation

It is clear that if gauge separations are small then the angle calculation is relatively unaffected by the level of reflection. Practically, however, if gauge separations are *too* small relative to all frequency components, position error and noise will alter the measured phases more greatly and hence cause increased errors in the apparent angle estimates.

As expected, when reflection levels are low, the angular estimates are also largely unaffected. When reflections are large, however, the incident angle relative to the gauge triad orientation becomes important, highly influencing the values of individual angle estimates. Overall the effect of these poor individual estimates can be minimised by designing a wave gauge array so that for each frequency (wavelength) there is a uniform co-array distribution of valid separations. If this is the case, using all of the estimates, the kernel density estimate approach discussed in Section 5.1.1 should be able to isolate the correct incident angle.

To assess how the kernel density approach with the DA1 array configuration (Fig. 3.12) deals with different levels of reflection, a numerical simulation has been carried out, using a unidirectional broad-banded spectrum with various constant frequency independent reflection coefficients. This spectrum has been used as it covers the operational frequency range of the tank (0.2–1.2 Hz), whilst enabling easy analysis and viewing of results. This spectrum is shown in Fig. 5.10 and is also used for the sensitivity analysis shown in Section 5.3.3.2.

Fig. 5.11 shows the angular error resulting from the simulation. It is clear that the combination of the array and method used performs very well for frequencies up to 0.95 Hz, regardless of the level of reflection. The error shown is purely a function of the number of bins used for the kernel density estimate (250 in this case). When reflection is relatively low ($K_r < 0.5$) there is also no perceived error in the angle estimate at any frequency. This shows the array-method combination performs very well in general, especially for the level of reflection present in the

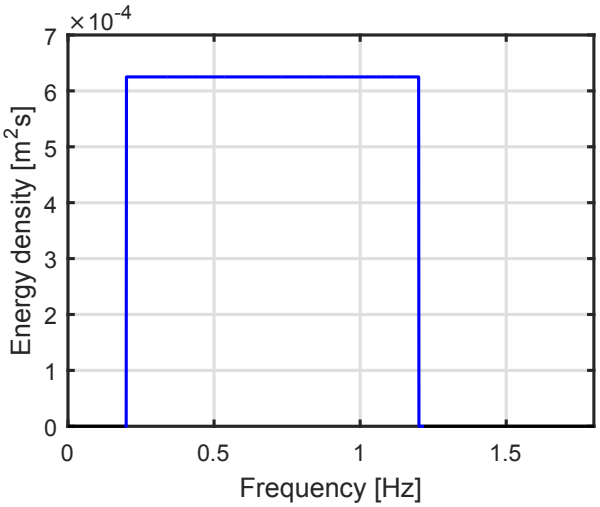

Figure 5.10: Uni-directional spectrum for numerical sensitivity analysis. H_{m0}= 0.2 m. For the simulations, an incident angle of $\theta = 22.5°$ has been used

FloWave basin (with no model present). Once this initial angle is effectively identified, the subsequent in-line reflection analysis will then be correct, which can be seen in Fig. 5.15 when the oblique reflection angle is 0°.

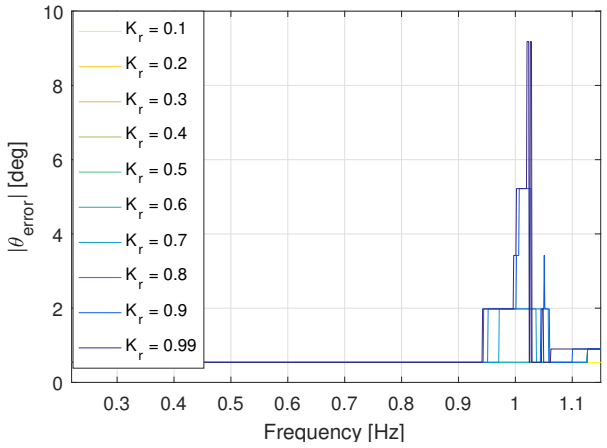

Figure 5.11: Angle error for broad-banded spectrum shown in Fig. 5.10 for various levels of in-line reflection

Errors arise from 0.95 Hz onwards when the reflection coefficient is over 0.5. This is due to the smaller number of valid gauge triads as shown in Fig. 5.12. This means that poor individual estimates have a greater effect on the final angle calculation; a result of the combined effect of larger reflections, triad orientation and large relative separations. Individual estimates for 1 Hz with a range of reflection scenarios are illustrated in Fig. 5.13, demonstrating how individual estimates are affected by reflection levels and how the kernel density estimate mitigates the effect of these on the final angle values.

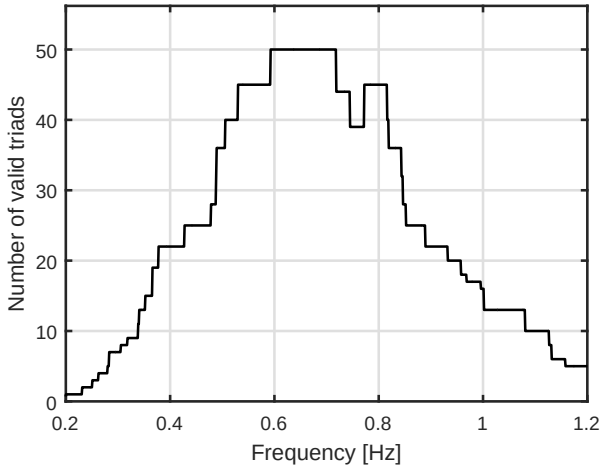

Figure 5.12: Number of valid gauge triads (all separations $> 0.05L_i$ and $< 0.45L_i$) as a function of frequency for the array shown in Fig. 3.9

Where large reflections and high wave frequencies are present, it may be necessary to use an array with additional gauges placed closer together. This would ensure there are enough gauge triads with separations less than $0.45L_i$, thus improving the high frequency estimates. For the levels of reflection present in the empty tank, the current array layout should be suitable for identifying the correct incident angle regardless of frequency. That is, under the assumption that position error and noise are negligible and more importantly, that reflections can be assumed to be in-line. This is discussed in Section 5.3.3.2.

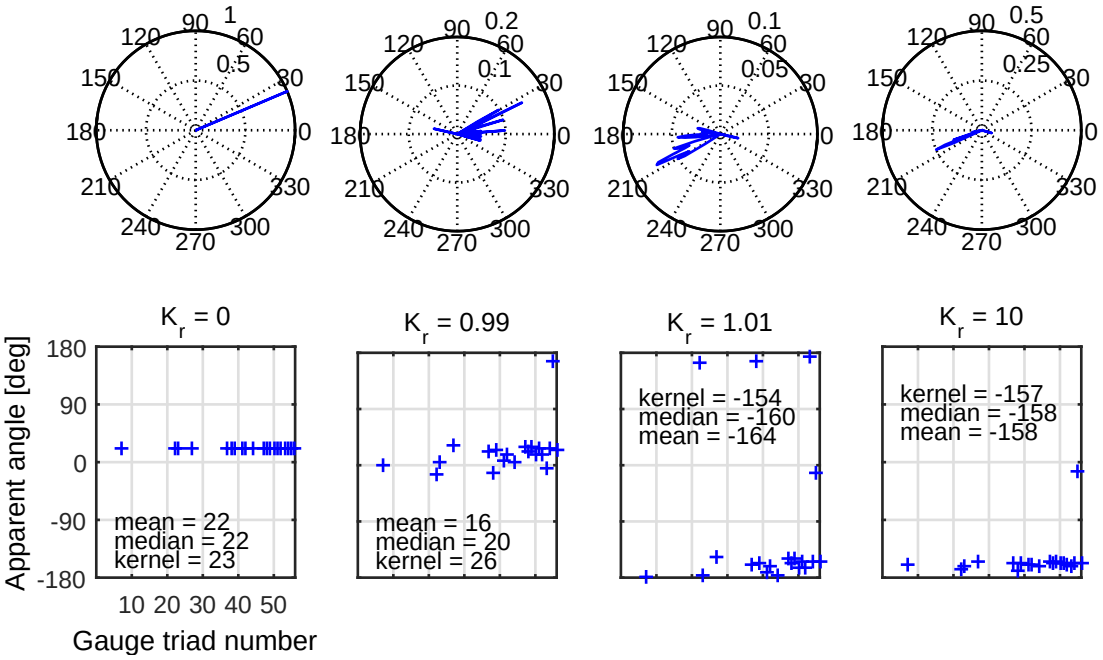

Figure 5.13: Individual angle estimates for 1 Hz components of spectrum shown in Fig. 5.10. Shown with in-line reflection levels of 0, 0.99, 1.01 and 10, along with the resulting kernel density estimates. Only valid triads of the 56 possible are included in the kernel density calculation and plotted

5.3.3.2 Effect of Reflection Angle and Curvature

Oblique Reflections

In Section 5.3.3.1 it was found that the level of in-line reflection does not greatly affect the correct identification of the incident angle when using the current implementation of the method in combination with the wave gauge array. This additionally enables a correct in-line reflection analysis to take place. If, however, the reflections are not in-line then this is no longer the case.

Introducing a change in reflected angle, $\Delta\alpha_{ref,i}$, the surface elevations become

$$\eta(x,y,t) = \sum_{n=1}^{N} A_{inc,i} cos(k_i(x\cos\alpha_{inc,i} + y\sin\alpha_{inc,i}) + \Phi_{inc,i} + w_i t)$$
$$+ K_{r,i} A_{inc,i} cos(-k_i(x\cos(\alpha_{inc,i} + \Delta\alpha_{ref,i}) + y\sin(\alpha_{inc,i} + \Delta\alpha_{ref,i})) + \Phi_{inc,i} + \Phi_{ref,i} + w_i t) \tag{5.23}$$

Defining $k_{i,\alpha,xy} = k_i(x\cos(\alpha_{inc,i} + \Delta\alpha_{ref,i}) + y\sin(\alpha_{inc,i} + \Delta\alpha_{ref,i})$, the resulting phases can be shown to be

$$\Phi_{n,i} = \tan^{-1}\left[\frac{a_{inc,i} sin(k_{i,xy}) - k_{r,i} a_{inc,i} sin(k_{i,\alpha,xy})}{a_{inc,i} cos(k_{i,xy}) + k_{r,i} a_{inc,i} cos(k_{i,\alpha,xy})}\right] \tag{5.24}$$

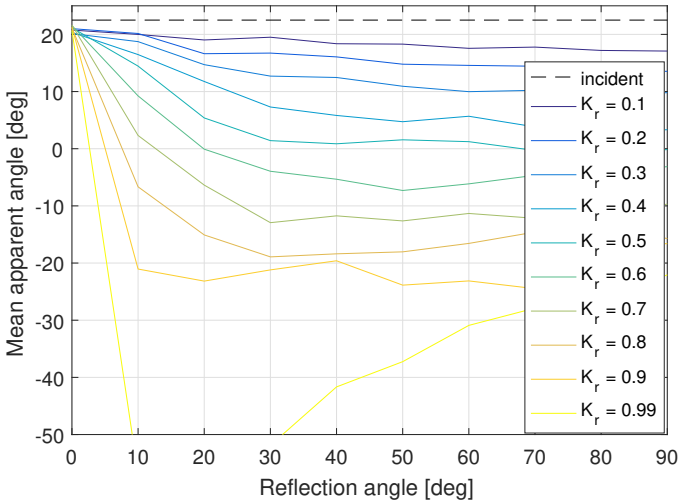

Figure 5.14: Effect of reflection level and angle on the mean apparent angle (over all frequencies)

It can be seen from Eq. (5.24) that the phase differences will be altered by the magnitude of $\Delta\alpha_{ref,i}$ in addition to the level of reflection and array layout. The difference here compared with the in-line reflection analysis, Eq. (5.20), is that when the angles are calculated using Eq. (5.1), the 'direction' of the angular error is now no longer solely a function of the triad layout and as such does not 'average' out over multiple estimates. All angle estimates now contain a consistent error as a function of $\Delta\alpha_{ref,i}$.

Using the spectrum shown in Fig. 5.10, and simulating the oblique reflections over the array, we can observe this consistent shift in angle estimate, shown in Fig. 5.14. This shows that if there are sizeable reflections with even a small reflection angle then the PTPD approach cannot be used to effectively identify the incident angle.

As discussed in Section 5.4.2 it is not always necessary to estimate the incident angle. To further assess how oblique reflections affect the method the incident angles are assumed to be known. Fig. 5.15 shows how the level and angle of reflection affect the isolation of incident and reflected spectra. As expected, this shows that it is not appropriate to use in-line reflection analysis when the reflections are oblique relative to the incident. This is because the phase differences are no longer a function of the 'in-line' gauge separations assumed in the analysis. It may however be suggested that results are still somewhat useful if the reflection angle is low, i.e. less than 20°.

Curved Reflections

When reflections are curved or directionally spread, there will be larger variation in the individual angle estimates generated using the gauge triad combinations. If the mean direction of

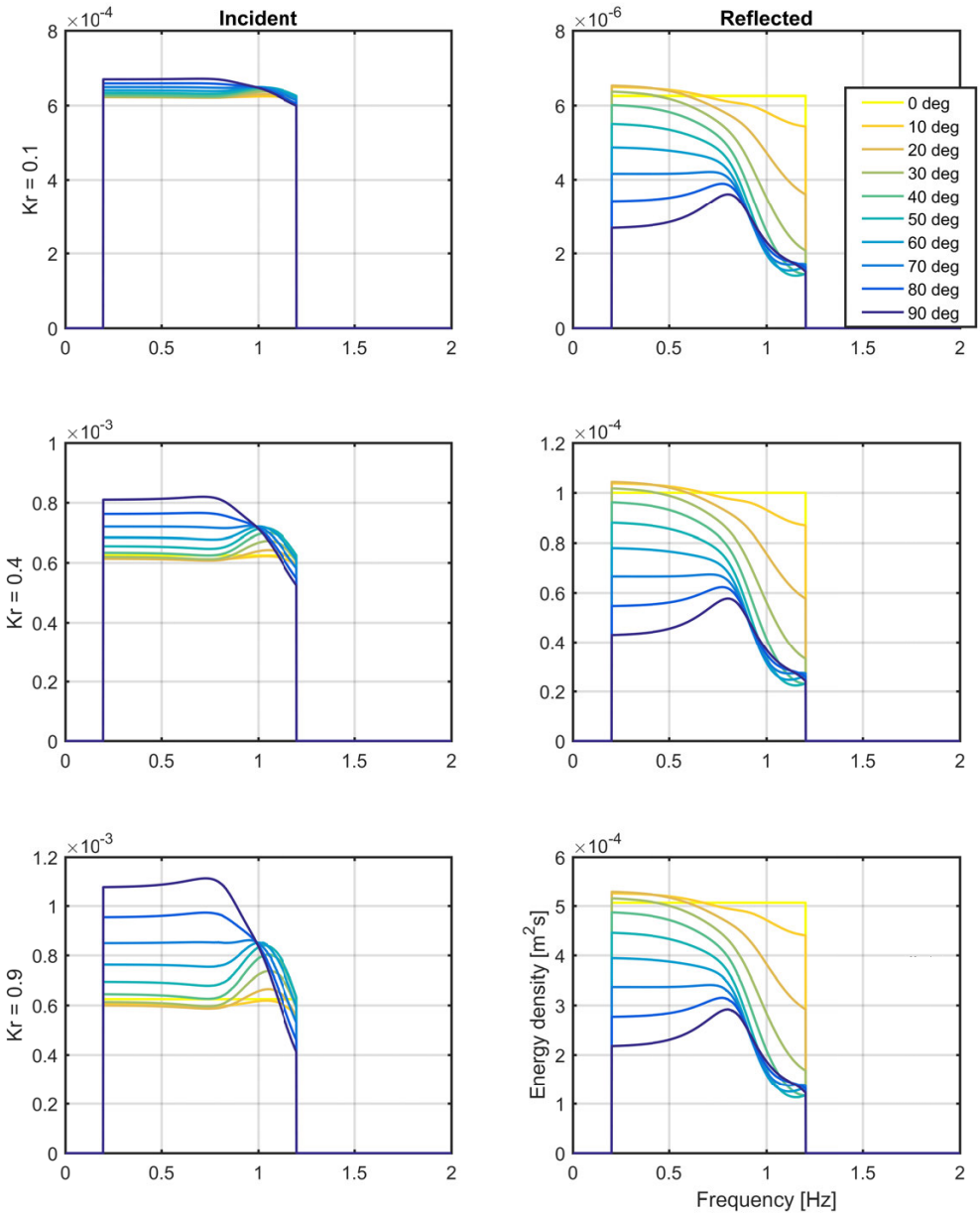

Figure 5.15: Effect of reflection level and angle on the separation of incident and reflected spectra

the curved waves is not opposite the incident, then similar behaviour is to be expected to the oblique wave analysis, but with additional scatter. If, however the mean direction of the curved waves opposes the incident, then the correct incident angle can be identified with an appropriate array and a meaningful representative in-line reflection analysis procedure can take place. This is the case at FloWave.

As shown in the spatial variation analysis, Section 4.5.1.1, the circular wave basin at FloWave ensures that the mean direction of reflected components oppose the incident, and are curved

as a function of the tank geometry. From Fig. 4.15 it appears that over the small array area (1 m^2), the assumption that curvature is negligible for the purpose of reflection analysis seems appropriate.

From the SPAIR method results, Section 5.2, it is evident that for the level of reflection and curvature present, the incident angle can be effectively identified using the PTPD approach with the DA1 array. Once these are identified, the co-array uniformity and least squares approach of the reflection analysis will ensure that the representative in-line reflection coefficients are valid despite these small levels of curvature. This will provide a very good estimate of the incident and reflected spectra and time-series over the array area. This approach means that sea states can be effectively characterised in a particular location (generally in the tank centre), prior to use in a test program with a model installed.

Revisiting Sections 4.5.1.2 and 4.5.2, it is apparent that the effective reflection coefficient is not constant and in fact varies in the in-line direction due to circular focussing effects. As a result of this, and the reflected wave curvature, it is clear that the reflected directional spectrum is spatially variable. This means that although the isolation of incident and reflected spectra and time-series over the array area gives reliable results, using this 2D approach to extrapolate far from the measurement area will not be accurate. Additionally, if the array is not central, the wave curvature will mean that some wave components cannot be well approximated as 'in-line', causing errors in the reflection analysis. This means the effective isolation of incident and reflected directional spectra can also only be calculated accurately at the tank centre (but can be inferred at other locations).

5.3.3.3 Influence of Mean Direction

The wave generating capability at FloWave is designed to be directionally independent, meaning that any change in mean wave propagation direction should not influence the sea state performance. The vast majority of any perceived changes should therefore be attributed to the array layout and the method itself. This is assessed by varying the mean direction for a single sea state, which is defined in Table 5.4.

Table 5.4: Directional sensitivity tests (10 tests in total)

Wave Parameter	Range of Value(s)
peak frequency, f_p [Hz]	0.6
cos-2s spreading value, s	10
significant steepness, S_p [%]	2
mean direction, $\bar{\theta}$ [°]	18, 35, 54, ... 180

Figs 5.16a and 5.16b show the perceived reflection coefficient and directional NTD variation incurred by varying the mean direction. It can be seen that when altering the mean direction,

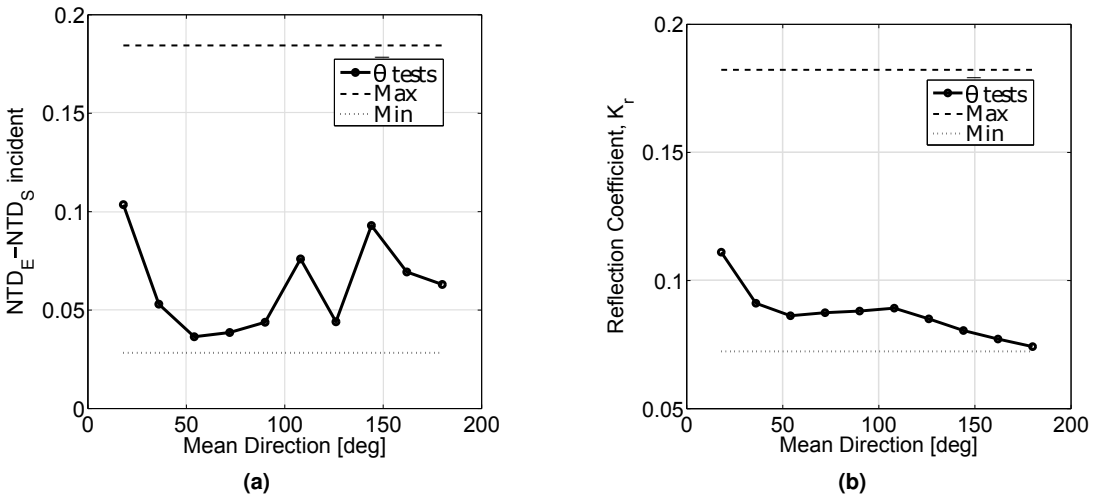

Figure 5.16: Effect of mean direction on perceived sea state performance (a) and reflection coefficient (b)

the perceived reflections also vary. This is coupled with variation in the perceived directional distribution error.

Without gauge position discrepancies, reflections, and noise there would be no error in the measured propagation directions, and hence no discrepancy in the directional distribution. Of these factors, the presence of reflections is probably the largest contributor in most circumstances. It is observed to have a consistent effect on both the relative phases and the amplitudes at the gauge locations.

As the mean direction changes, the array layout plays an important role, as the relative reflection and error-influenced phase differences are dependent on the projected in-line separations. These deviations cause differences in the perceived angles and hence incur a varied and largely unpredictable directional distribution error. A portion of the perceived directional deviation for any sea state is therefore a complex function of the induced phase errors (mostly reflection based) and the array layout.

5.4 Alternative Applications

5.4.1 No Reflection Analysis: PTPD Approach Only

As demonstrated in Draycott *et al.* (2015c), using the PTPD approach to reconstruct directional spectra at FloWave works effectively without the addition of reflection analysis. This works particularly well at the FloWave facility (or other circular wave basins with active absorption) as the reflections are low and can be approximated as in-line. It should also be effective for tanks with different geometry, providing reflections are relatively low, and the reflection angle isn't very large (see Fig. 5.14). If this is the case then the incident directions should be effectively identified and a more accurate representation of the incident directional spectrum should still be attained than using conventional methods.

5.4.2 No Angle Calculation: Assumed Incident Angles

Sections 5.3.3.1 and 5.3.3.2 show that under certain conditions the presence of reflections can introduce errors in the incident angle calculation. This, consequently, means that the projected in-line reflection analysis is carried out at a slightly incorrect angle thus meaning that the reflection coefficients themselves will be incorrectly calculated, along with the incident and reflected spectra. If it can be assumed that the incident wave propagation angles are known, and precisely produced, then reflection coefficients can be calculated more accurately, whilst giving a better representation of the reflected wave field. From the analysis of wave curvature, Section 4.3.1, it was inferred that the incident wave direction is indeed being generated correctly, hence proving it to be a valid approach to take in the FloWave facility. The method has been applied in this manner in Section 7.2 in order to obtain more accurate incident and reflected spectra.

5.5 Implications for Testing

The SPAIR method developed enables directional sea states to be reconstructed with a significant reduction in the perceived error. This means that directional sea states can be more effectively validated, enabling multi-directional wave basins to simulate realistic directional wave scenarios with increased confidence. This enables the complex site-specific directional seas defined in Chapter 6 and re-created in Chapter 7, to be implemented with increased certainty that the conditions are as specified.

The reflected directional spectrum and time-series obtained through this method provide valuable additional information about the re-created conditions. This enables effective characterisation of the tank's directional sea state generation performance, along with accurate specifics about a generated sea state. This more effective characterisation of a given sea state enables test outputs to be properly put into context.

Chapter 6

Site Specific Resource Characterisation

The aim of the work presented in this chapter is to use buoy data to produce representative site-specific sea states suitable for scale model testing at FloWave. Four years of data has been made available for this purpose by the European Marine Energy Centre (EMEC) for their full-scale grid connected wave site at Billia Croo. The site is initially assessed via its high level statistics and spectra in order to gain some understanding of its nature. Representative sea states are then created for both extreme and production conditions, with the aim of considering spectral form and directional complexity wherever possible, as to increase the realism of subsequent tests. The methods explored and detailed to create these sea states are applied to the Billia Croo wave site, yet are just as applicable to any dataset.

Extreme value analysis is carried out to provide wave height and periods associated with particular return periods. Extreme directional spectra are created for a variety of example conditions for 1:10 and 1:50 year events. This is done using parametric methods, before exploring the idea of 'scaling' the closest observed extreme sea state to the desired values. This provides a method of obtaining more realistic frequency spectra and directional distributions associated with extreme events at a site.

For the creation of production sea states the problem is more about classification of the data, rather than extrapolation for extreme seas. Classifying the data by similarity allows groups to be formed, which can be effectively represented by a single sea state with a known relative abundance. This enables the large dataset to be effectively represented by a smaller number of sea states, which can then be used for scaled power production tests to infer full scale site-specific device performance. The major issue in this process is which variables to use when considering similarity, along with the grouping methodology. Various binning and clustering approaches are trialled and assessed focussing on various parameters, and the inherent trade-offs are understood. Finally a generic set of sea states are created, focussing on obtaining a good range of H_{m0} and T_E values for power matrix contribution, whilst considering the form of the directional spectra in order to include spectral realism in the testing.

Highlights:

- I-FORM used to create bivariate H_{m0}-T_E contours for extreme value analysis, which are used to create parametric and scaled-observed extreme sea states
- For production sea state generation the use of clustering algorithms directly on the spectral (frequency or directional) form to group sea states is explored with the aim of including spectral complexity and hence sea state realism. The outputs and performance are assessed against other approaches including typical binning methods
- Trade-offs of classification methodologies are numerically assessed, highlighting the importance of focussing on particular parameters of interest for an application
- A combined binning-clustering method is chosen as a compromise and sea states are created from the resulting groups both parametrically and from the mean directional spectra. These sea states are ready to be scaled and reproduced to represent the site (Chapter 7)

6.1 The Site: Billia Croo

6.1.1 Summary Statistics

The buoy data from Billia Croo has been collected at a water depth of 52 m, which is considered intermediate water depth for the majority of wavelengths present. Roughly four years of half-hourly data at this site is available spanning from January 2010 to December 2013, which amounts to 64974 sea states after removing those identified as poor by the Quality Control (QC) files provided by EMEC. A time-series history of significant wave height and energy period over this time-frame is shown in Fig. 6.1. The data is observed to be generally good quality, possessing only a small number of brief gaps. It is also apparent that the resource is highly seasonally variable, displaying a clear increase in the winter months. Within these months there are a small number of extreme storm events, simultaneously showing very large wave heights and periods.

Table 6.1: Mean wave statistics at Billia Croo for each calender year (2010–2013)

	2010	2011	2012	2013
P [kW/m]	17.23	32.6	28.4	30.7
H_{m0} [m]	1.77	2.21	2.09	2.11
T_E [s]	8.12	8.57	8.10	8.51
T_p [s]	10.3	10.9	10.2	10.7
$\bar{\theta}[^\circ]$	305	293	306	296
ν	0.538	0.548	0.521	0.544
$\bar{\sigma_\theta}$ [rad]	0.601	0.597	0.597	0.606

Table 6.1 shows mean wave statistics for each of the calender years. From this, is it evident that the inter-annual variability between these years is quite low, with the exception of 2010

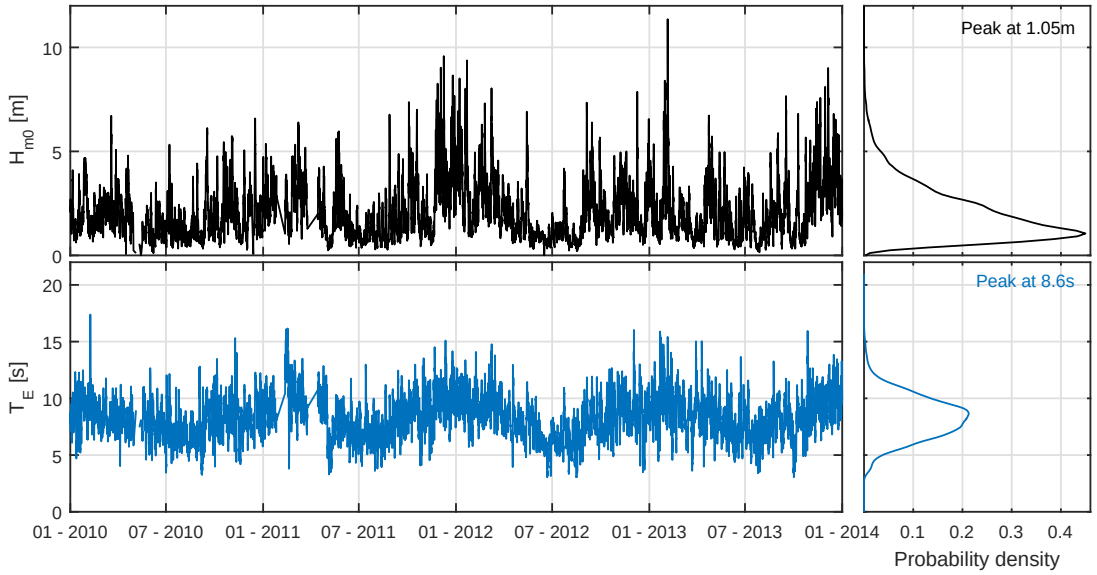

Figure 6.1: Time series of significant wave height and energy period for Billia Croo. Shown with corresponding kernel density estimates

which seems to have been an unusually calm year. 2011 displays the largest mean power, but from Fig. 6.1 it is clear that it does not contain the largest storm event. This event happens in 2013 with a significant wave height of around 11.5 m and an energy period of around 15 s (T_p = 20 s). This extreme storm condition is the only event in this time-series that is considered to be in the second highest category on both the Douglas and the Beaufort scales; described as 'Very high (8/9)' and 'Violent storm (11/12)' respectively.

Despite the occurrence of some very extreme sea conditions, it is clear that the majority of sea states at Billia Croo are much milder, with mean values of H_{m0} and T_E being 2.05 m and 8.33 s. In order to visualise the wave height-period combinations a scatter plot is shown in Fig. 6.2. A contour plot is overlaid, representing the bivariate kernel density estimate. This essentially shows an empirical form of the joint probability density, providing a good insight into likely combined conditions. The contour lines, describing equal likeliness, display the expected behaviour, centering on the most likely $H_{m0} - T_E$ combination of 0.97 m and 7.27 s. There is clearly a significant difference from the mean values. It is also interesting to note the reasonable discrepancy from the most likely value of the parameters individually, which can be seen in Fig. 6.1 to be 1.04 m and 8.56 s.

To visualise the (high-level) directionality of the sea states 'wave-rose' plots have been created for significant wave height, energy period and power. These are shown in Fig. 6.3, and show that the majority of sea states have a mean direction in the west-north-west and north-west regions. Additionally it can be inferred from the higher proportion of long wavelengths in this area that this is the direction swell sea states are originating from. This corresponds to swell generated from distant North Atlantic storms. It appears that sea states originating from other directions

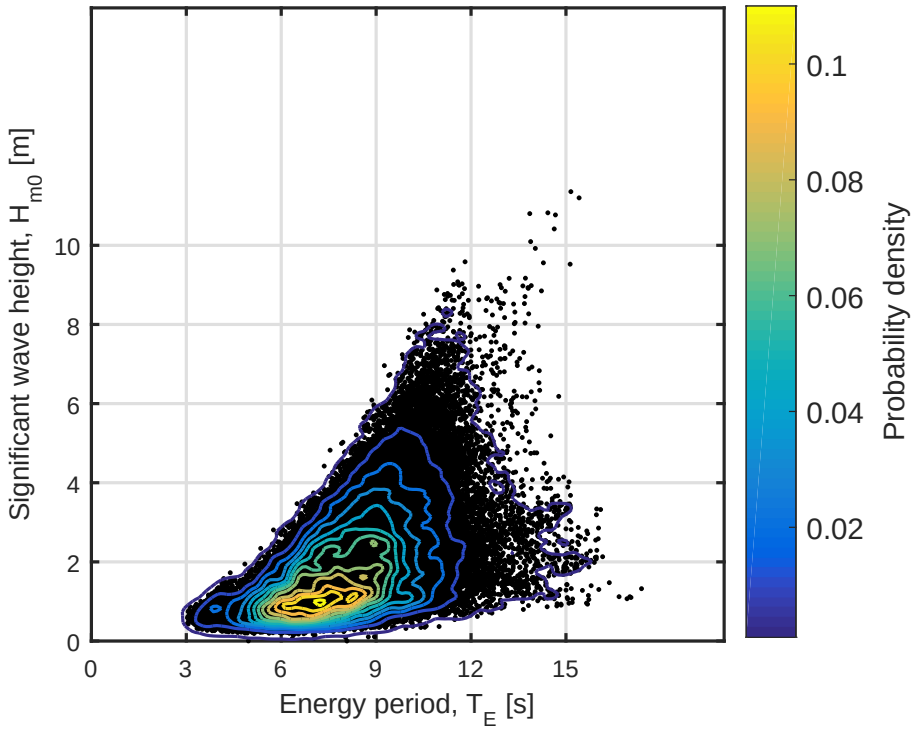

Figure 6.2: $H_{m0} - T_E$ scatter plot with bivariate kernel density estimate overlaid. Grid lines match up with the bins used in Figs. 6.5 and 6.6

typically tend to be of shorter wavelength and smaller wave height, suggesting that they are more locally generated 'wind-seas'. To infer more about the directionality and composition of the sea states the spectra need to be examined.

6.1.2 Spectral Information

Spectral information can aid in obtaining a more detailed understanding of the site's true characteristics. The mean frequency and directional spectrum (generated using MEP, see Section 6.1.3) have been shown in Fig. 6.4, along with the frequency-averaged DSF. This gives an indication of mean energy levels and range of directionality. However, as this is an average of many distinct sea states, the resulting spectra are likely to be unrepresentative of any realistic individual scenario.

To understand more about the actual spectral conditions at the site, all 64974 frequency spectra and frequency-averaged DSFs have been plotted, partitioned by H_{m0} and T_E (using the same bins as shown in Fig. 6.2). This is shown in Figs. 6.5 and 6.6, along with the mean spectrum/spreading function from each bin.

Taking the mean spectrum resulting from a binning approach is a potential method for creating representative sea states suitable for replication, as discussed in Section 6.4. It is clear that using this approach in this way results in very dissimilar spectra being grouped together ,with

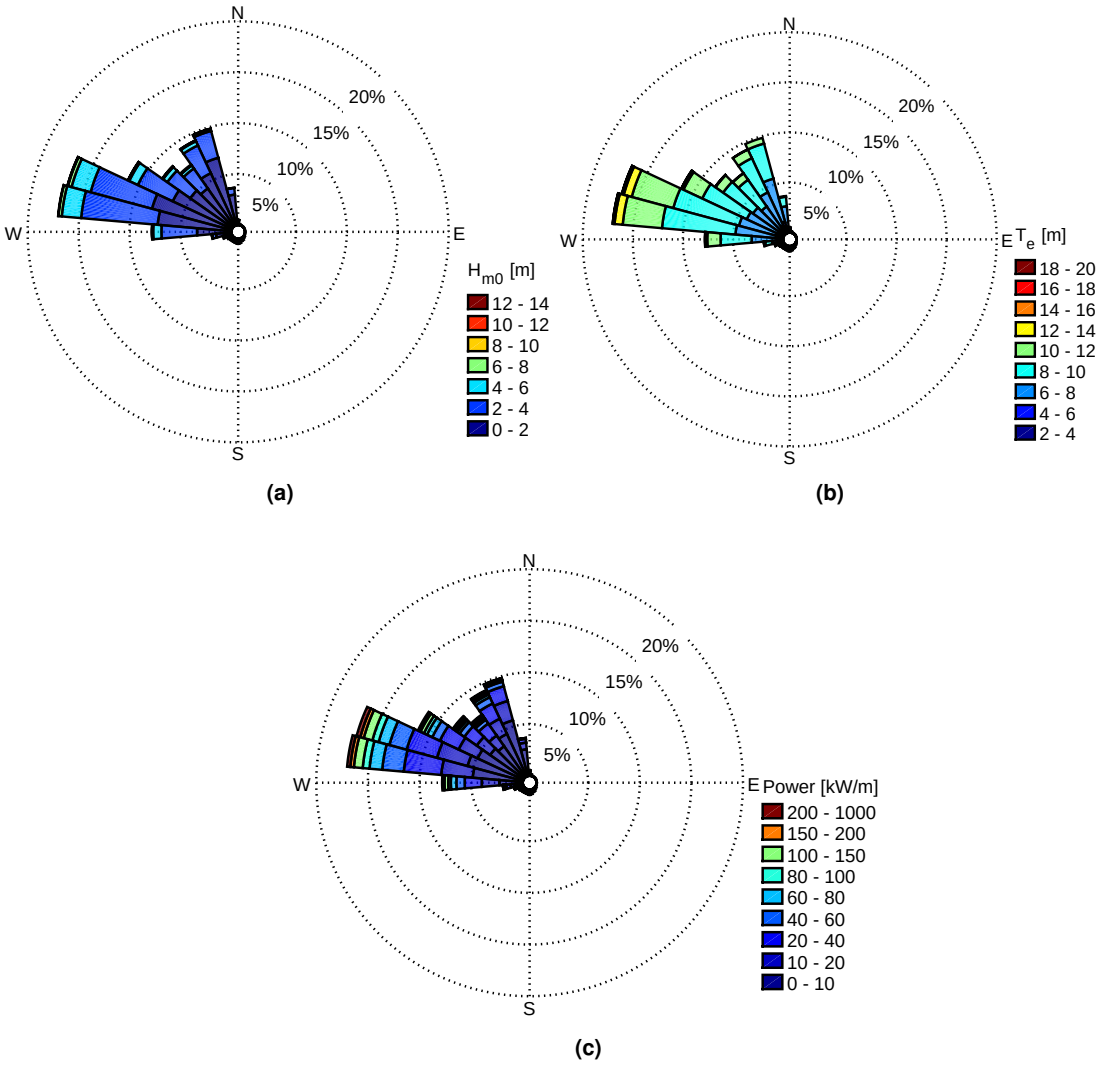

Figure 6.3: 'Wave-rose' plots showing sea state directionality and abundance of various a) significant wave heights b) energy periods and c) powers

potentially large differences in mean direction and directional spreading and that interesting 'characteristic' features are generally missed out or smoothed over. This may be expected as some bins have a large number of group members, for example the group containing all spectra with $0 < H_{m0} < 2$ and $6 < T_E < 9$ is made up of roughly 24,000 sea states. On the other hand some of the larger and more unusual sea states only have a handful of group members and so can be represented more accurately by a single 'representative' sea state. This demonstrates some of the difficulties and inherent trade-offs when trying to represent a large, complex, multivariate dataset by a small number of generic conditions. This will be explored in detail in Section 6.4 where attempts are made to include actual spectral shape and directionality into the classification process.

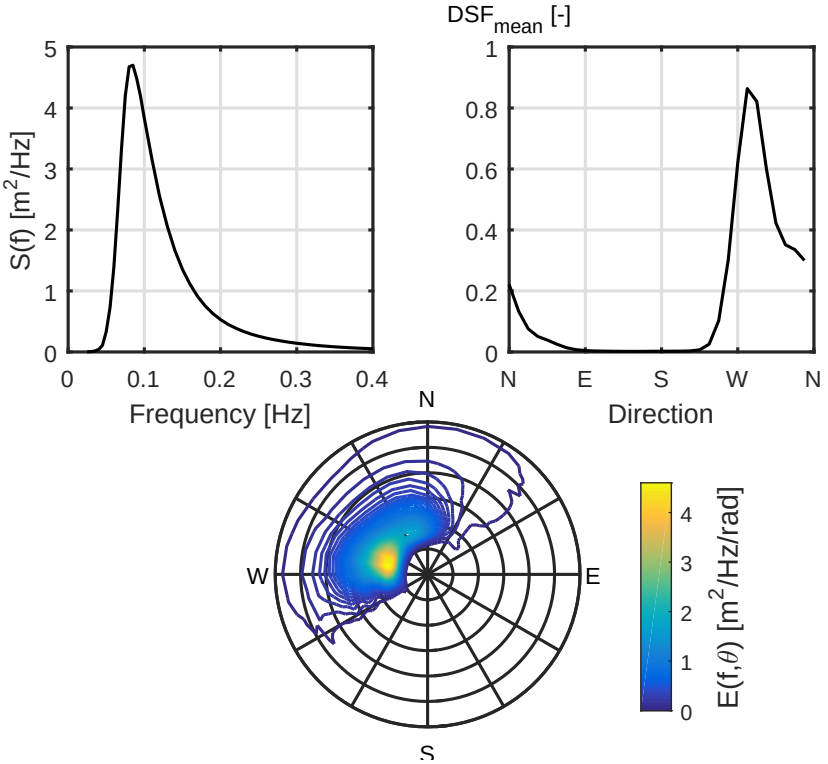

Figure 6.4: Mean frequency spectrum, directional spectrum and DSF_{mean} for Billia Croo

6.1.3 Directional Spectrum Creation

As discussed in Section 2.1.1.1 there are a variety of methods available for the reconstruction of directional spectra from directional Fourier coefficients. The different assumptions and formulations of these approaches lead to directional spreading functions that differ from each other significantly. This is demonstrated in Fig. 6.7 where the resulting DSF for six methods (TFS, $\cos^{2s}$, Gaussian, MEM, MLM and MEP) are shown for the peak frequency of an example Billia Croo spectrum.

From Fig. 6.7 it is clear that in this case the $\cos^{2s}$ and Gaussian methods produce similar broad spreading functions, with the MEM being significantly more 'peaky'. The MEP solutions appear to be somewhere in between, whilst the MLM outputs appear to give a multi-modal output, perhaps due to an error. The resulting directional spectrum for the same sea state is shown in Fig. 6.8, highlighting the eventual impact method choice has on the assumed energy distribution.

It has been shown by multiple authors that the Maximum Entropy Principal (MEP) provides the most reliable results from a single point measurement system (Benoit *et al.* (1997) and others, see Section 2.1.1.1). However, the solution to the MEP is non-linear, computationally challenging and often results in non-convergence (Kim *et al.*, 1994). To aid the convergence problem Newton's technique of local linearisation can be employed, outlined in Hashimoto

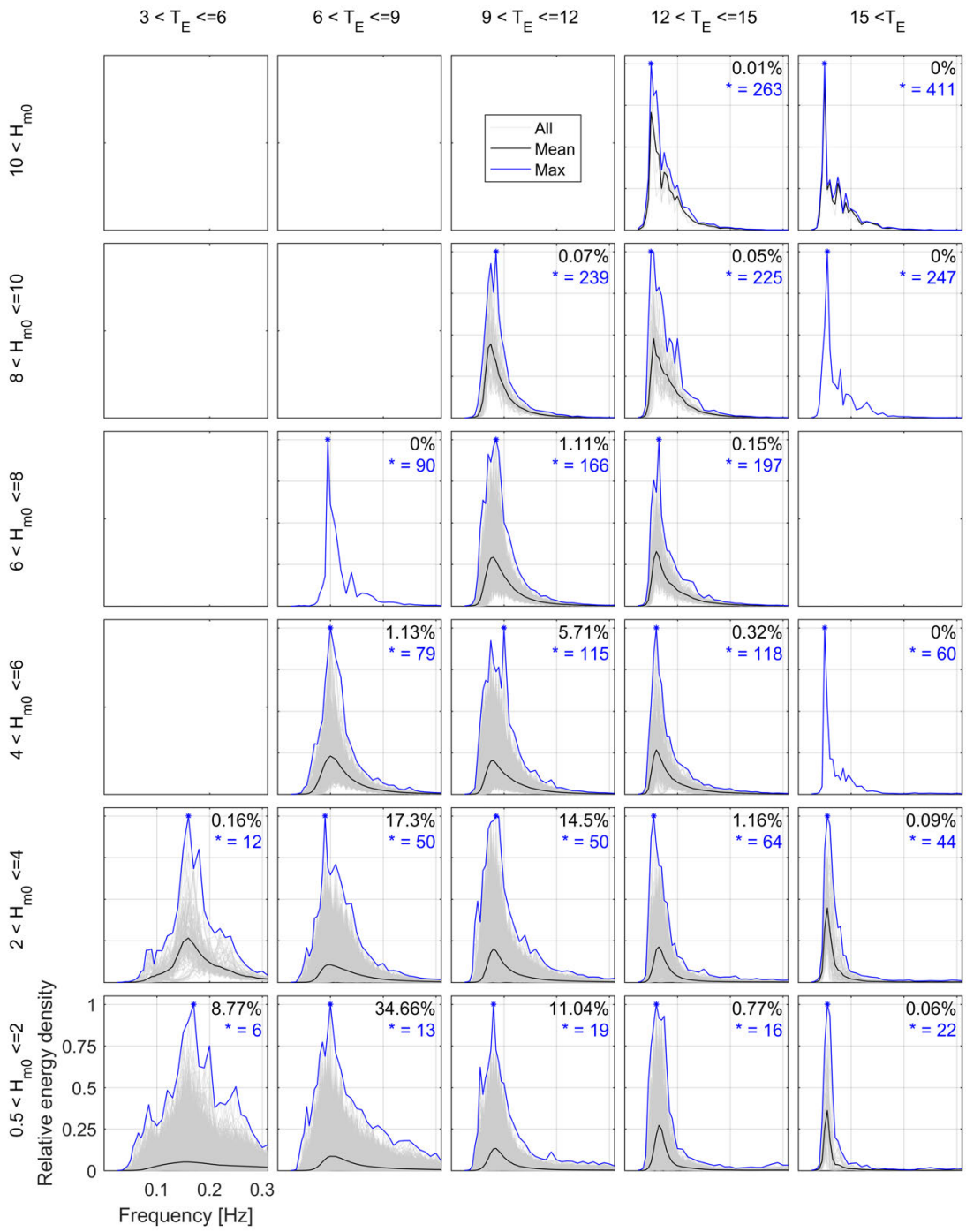

Figure 6.5: All half-hourly frequency spectra for four years at Billia Croo. Binned by H_{m0} and T_E with mean spectrum of each bin shown overlaid. The maximum envelope of all spectra is shown in blue. The peak of the largest spectrum is given in blue text, in m^2/Hz, to show relative magnitudes of the sub-plots. Sea states with $H_{m0} < 0.5m$ have been removed to aid visualisation

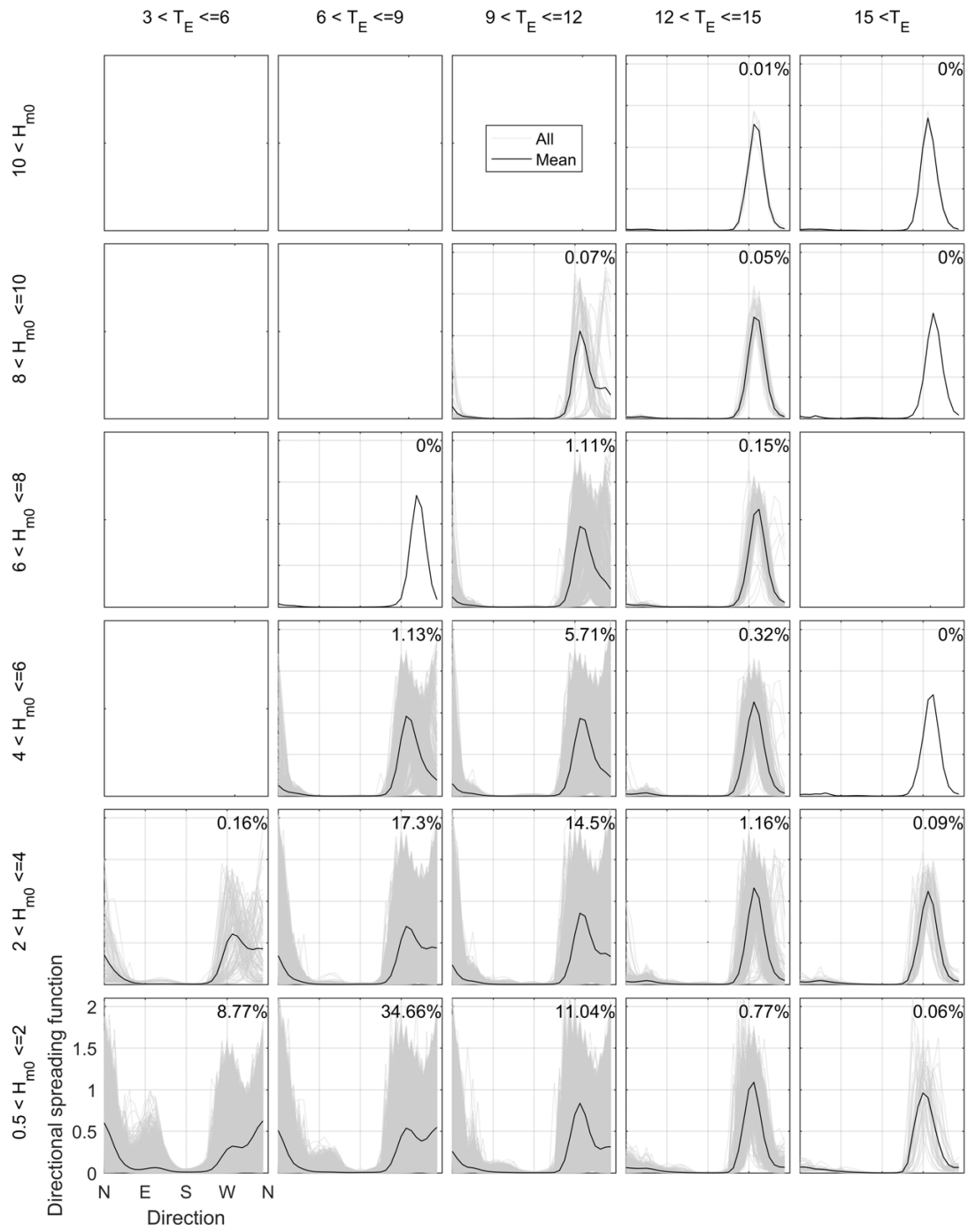

Figure 6.6: All frequency-averaged directional spreading functions for four years at Billia Croo. Binned by H_{m0} and T_E with mean DSF of each bin overlaid. Sea states with $H_{m0} < 0.5m$ have been removed. Sea states with $H_{m0} < 0.5m$ have been removed to aid visualisation

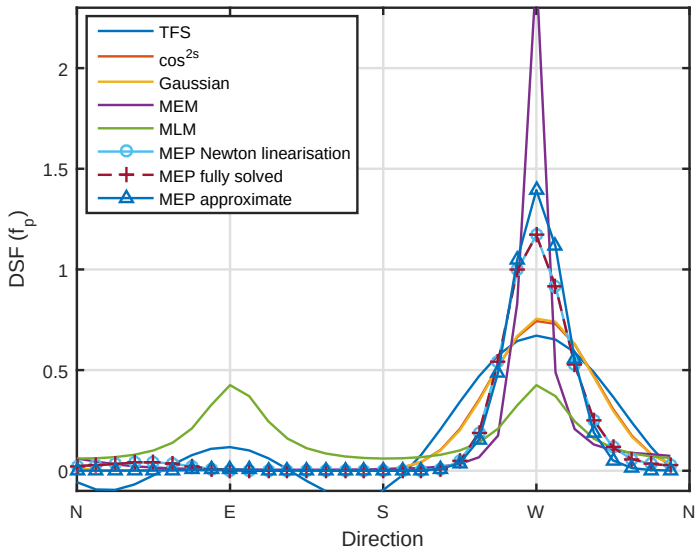

Figure 6.7: Example directional spreading functions generated by a variety of reconstruction methods. Shown for the peak frequency of one of the Billia Croo spectra

(1997). The outputs of this approach are also shown in Fig. 6.7 and agree exactly with the full MEP solution at the peak frequency. However, this method still fails to converge roughly 10% of the time on the dataset available and gives error prone results. This can be seen in Fig. 6.8 by the discrepancy between the Newton linearisation outputs and full solutions.

As a result of the time consuming nature of the full MEP solution and convergence issues with the Newton approach, approximate solutions have been used as described in Kim *et al.* (1994). The approximate MEP DSF generally shows good agreement with the full MEP solutions (as shown in Figs. 6.7 and 6.8) and as such has been deemed most effective for this work. It is, therefore, this approach that has been implemented to create the 64974 directional spectra used for this work.

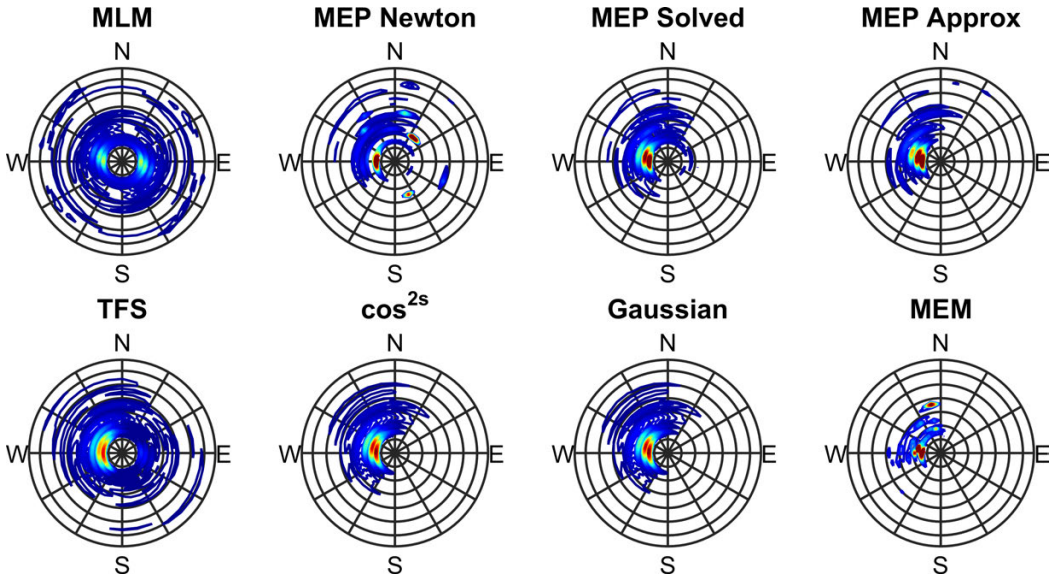

Figure 6.8: Example directional spectra generated by a variety of reconstruction methods. Shown for same Billia Croo spectrum as shown in Fig. 6.7

6.2 Classification Overview

The aim of the classification process is to look at methods of using buoy data to specify realistic site-specific sea states that cover the range of conditions present. This is carried out with particular focus on exploring the use of real spectral information and directionality wherever possible. This will be split up into extreme sea states and production sea states, relating to the extrapolation and characterisation of the data respectively.

A general overview of the classification process is shown in Fig. 6.9, along with some of the considerations at each of the identified stages. These will be discussed in detail in Sections 6.3 and 6.4, where the various options are explored. Reasonable examples are used for discussion where device considerations would clearly dominate any decision making process.

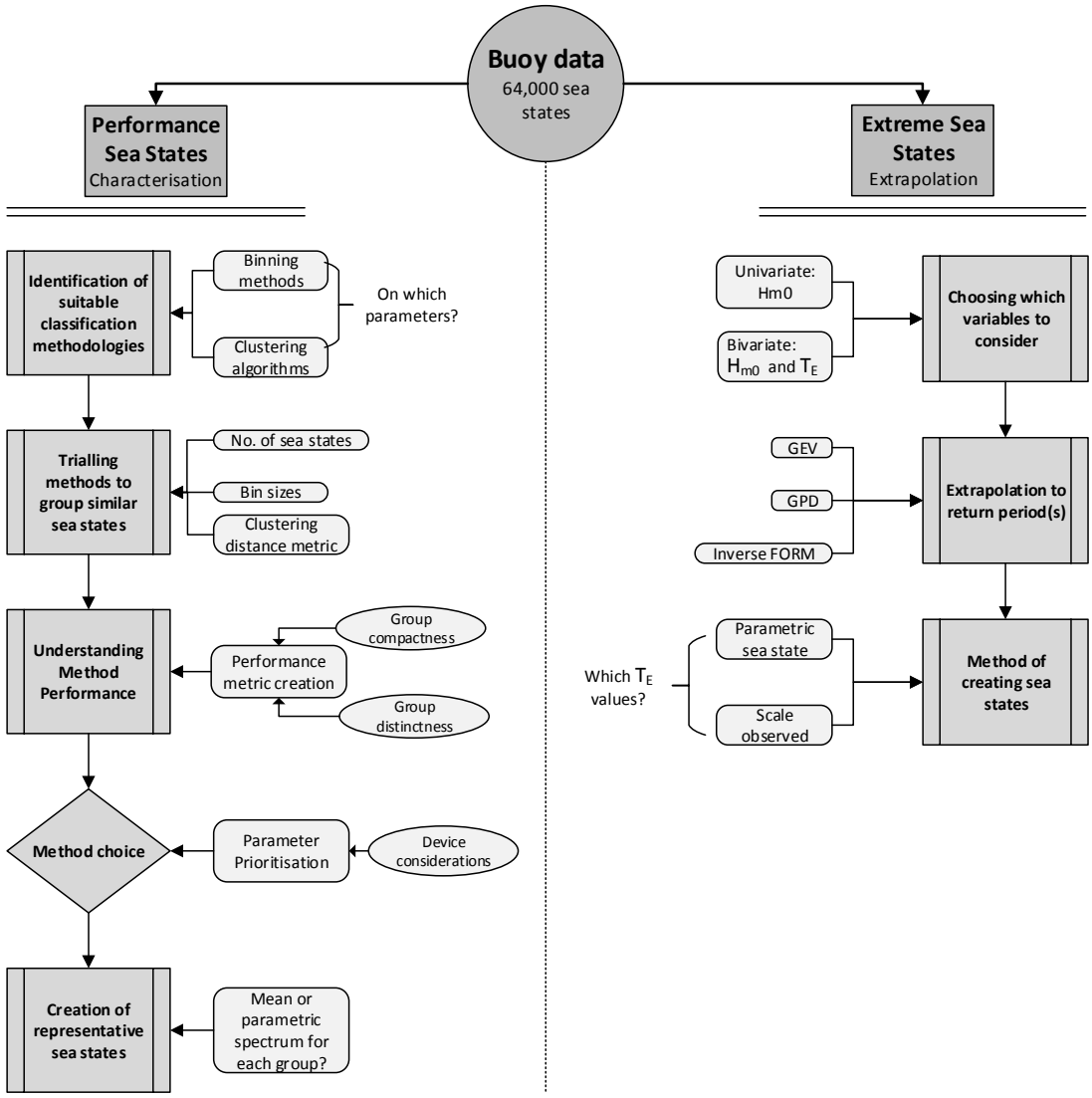

Figure 6.9: Overview of classification procedure for creation of extreme and production sea states. Shown with identified key stages and considerations

6.3 Classification 1: Survival Sea States

Physical model tests often aim to include simulated extreme events, enabling assessment of loading on the device or structure in these large wave conditions at scale, in a controllable and repeatable manner. If a deployment location is already known, site data (if available) can be used to infer the expected largest significant wave height in a specified return period. This enables sea states to be created corresponding to the extreme return values chosen, dependent on the expected deployment time-frame and approach to risk. In this section some fairly typical extreme value analysis techniques are carried out on the Billia Croo dataset. For the purpose of increasing realism, methods of creating extreme directional spectra are explored, including the possibility of 'scaling' observed sea states to the specified conditions.

6.3.1 Calculating Extreme Values

6.3.1.1 Univariate: H_{m0}

As discussed in Section 2.1.2.1, there are a number of approaches for inferring the largest expected wave heights in a given time frame, which is typically achieved using a block maxima or Peaks Over Threshold (POT) approach. As concluded in Section 2.1.2.1 from guidance in Caires (2011); Teena *et al.* (2012); Coles (2001), a GPD distribution fitted to POT data points is most appropriate for the EMEC dataset. The 1:m-year return value, z_m, resulting from a GPD model is given by either Eq. (6.1) or Eq. (6.2):

$$z_m = u + \frac{\sigma_u}{\xi}[(\lambda_u m)^{\xi} - 1] \qquad \text{for} \quad \xi \neq 0 \tag{6.1}$$

$$z_m = u + \sigma_u log(\lambda_u m) \qquad \text{for} \quad \xi = 0 \tag{6.2}$$

where: ξ = shape parameter, σ_u = scale parameter, λ_u = rate, u = threshold.

When implementing a POT extreme value analysis, only extreme occurrences over an appropriately high extreme threshold should be used, which should ensure they are distributed according to the GPD defined in Eqs. (6.1) and (6.2). Additionally, to ensure that the POT data does indeed fit a GPD distribution, these data points should be approximately independent (Caires, 2011) and as such only maximum values from distinct storm events should be used. To practically implement this, any given data point is only considered a POT-valid point if it is above the threshold, u, and is the largest H_{m0} value in the 24 hours preceding and following the event. The POT-valid points are shown for various threshold values for the H_{m0} time-series in Fig. 6.10. From this, it is clear that the implemented methodology is effective. For example, the 19 half-hourly sea states with $H_{m0} > 9$ m have been reduced to just five distinct POT-valid events.

In Section 2.1.2.1 the importance of threshold choice was discussed, noting that it should be small enough to ensure there are sufficient points to determine the GPD parameters, but also

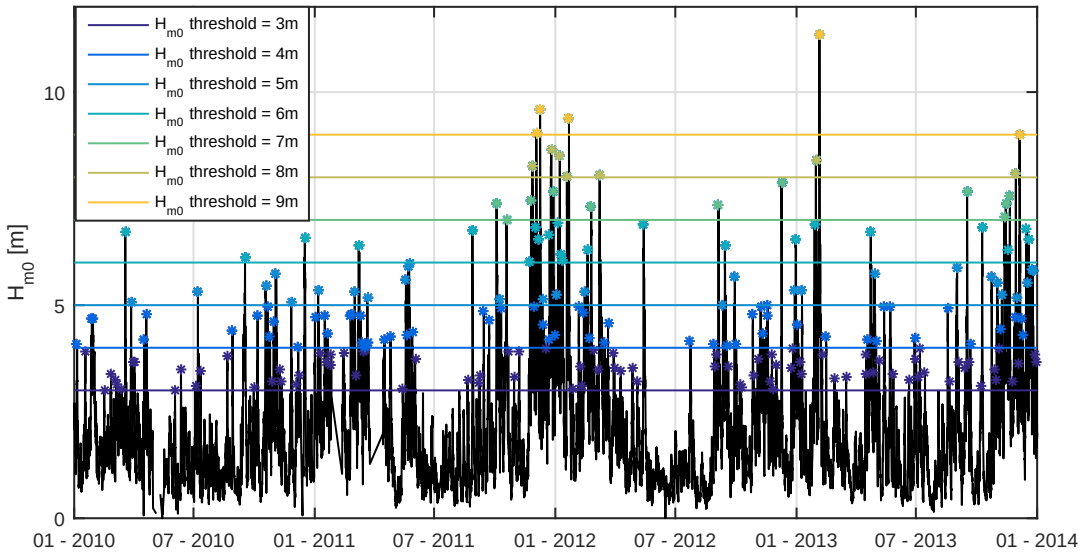

Figure 6.10: Demonstration of correct Peaks Over Threshold (POT) identification. To be considered a peak, each point over the threshold must be the maximum in the 24 hours preceding and after the point of interest

must be large enough so that the data is truly capturing extreme events, and as such converges to a GPD (Abild *et al.*, 1992). To identify an appropriate choice of threshold, the stability parameter defined in Caires (2011) has been used, defined as $\sigma^\star = \sigma_u - \xi u$. It is suggested that this parameter should be fairly constant with a small increase in u, when an appropriate threshold has been found. To assess this parameter, a GPD has been fitted using the Matlab in-house `gpfit` function for a variety of threshold values ranging from 3 to 8 m. The results, along with the number of POT-valid points, the coefficient of determination r^2 and expected return values, are shown in Fig. 6.11.

From Fig. 6.11 it is noted that the expected return values of H_{m0} are fairly consistent for most threshold values. Additionally, through comparison with analysis by Caires (2011) it is seen that the stability parameter is very constant up to a threshold of around 7 m. A value of 4 m was eventually chosen, considered large enough as to only consider extremes but include a sufficient number of points, whilst being associated with a 'stable' region of $\sigma^\star$, and with a high associated r^2 value.

The return value plot arising from the resulting distribution, along with the measured data (from an empirical CDF) is shown in Fig. 6.12. This correlates well with Lawrence *et al.* (2009), where an extreme H_{m0} distribution is obtained using a 20 year hindcast at the site. 1 : 10 and 1 : 100 extreme H_{m0} values of around 10.7 and 12 m respectively are found, which are very close to the 11 and 12.2 m values predicted from this analysis. These H_{m0} values can now be used as a basis for creating extreme sea states.

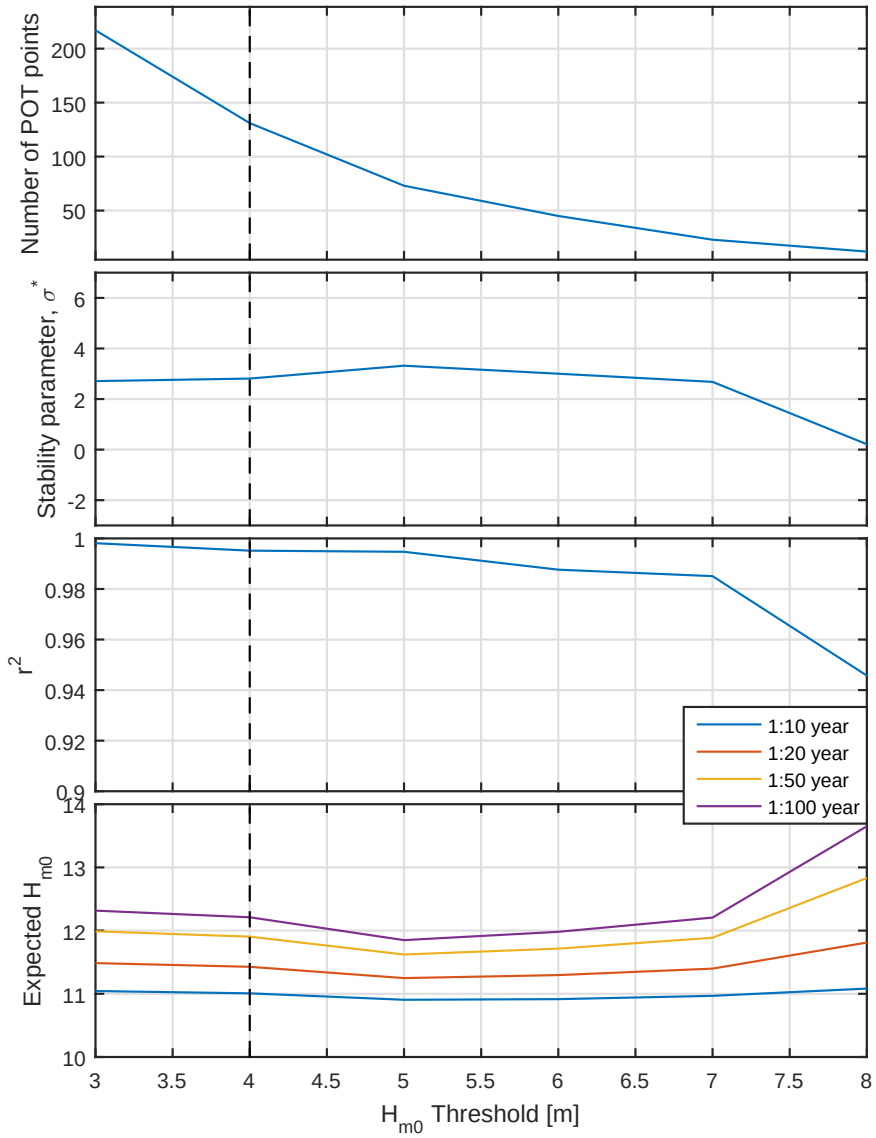

Figure 6.11: Effect of threshold choice on POT/GPD extreme value analysis results

6.3.1.2 Bivariate: H_{m0} and T_E

To create extreme sea states an associated measure of period is required along with the chosen wave height, and as such uni-variate extreme value analysis is insufficient. To obtain height-period combinations that relate to specific return periods a joint extreme probability distribution must be obtained. For this analysis energy period has been used, although the method can be applied to any wave period metric, or similarly for any number of dependent environmental variables.

The Inverse First Order Reliability Method (I-FORM) has been used, as recommended by Prevosto (2011), providing environmental contours at the desired return periods. This method

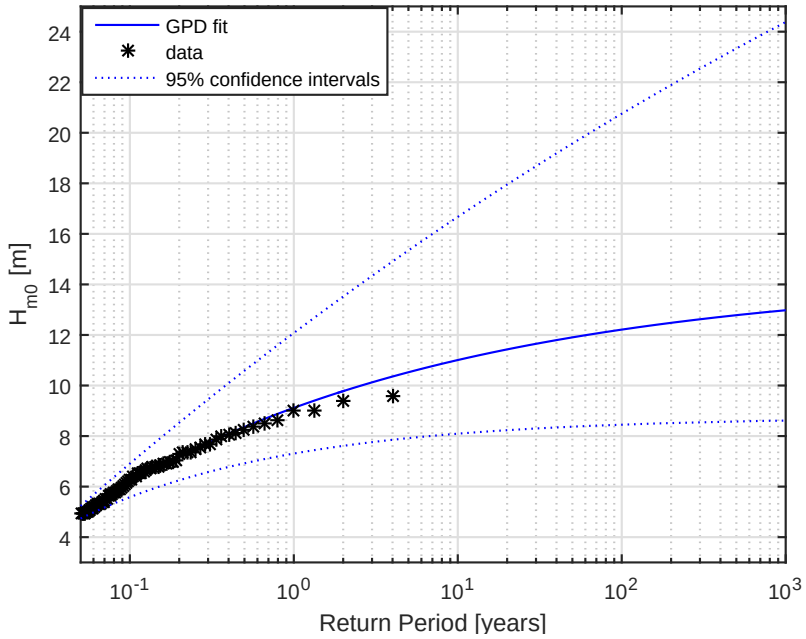

Figure 6.12: Resulting final GPD distribution for extreme significant wave heights using the chosen POT threshold of 4m

fits a marginal distribution of wave period conditioned on H_{m0}. Noting the relationship shown in Eq. (6.3), this enables the resulting probability distributions to describe the joint probability, before being transformed into $H_{m0} - T_E$ contours of equal probability.

$$F_{H_{m0},T_E}(H_{m0},T_E) = F_{T_E|H_{m0}}(H_{m0},T_E).F_{H_{m0}}(H_{m0}) \tag{6.3}$$

A log-normal distribution has been used for the conditional probability distribution for T_E, shown to effectively describe the wave period distribution by Burrows and Salih (1982) and others. Therefore a parameterised log-normal distribution has been implemented in a similar manner to Berg (2011), enabling the extrapolation of log-normal parameters μ and σ outside the observed range. This is described in Eqs. (6.4) to (6.6), where a least squares approach is taken to fitting the a and b values. The parameters have only been fitted for H_{m0} values roughly corresponding to those above the POT threshold, under the assumption that there may be a different relationship between wave period and extreme wave heights than for the total dataset. Bin sizes for the parameterisation are also increased for large values of H_{m0}, to ensure there is enough data in each bin to get meaningful standard deviations. The resulting fit is shown in Fig. 6.13.

$$P[T_E < t|h] = F_{T_E|H_{m0}}(t) = \Phi(\frac{ln\, t - \mu}{\sigma}) \tag{6.4}$$

$$\mu = E[ln\, T_E|h] = a_0 + a_1 h^{a_2} \tag{6.5}$$

$$\sigma = std[ln\, T_E|h] = b_0 + b_1 e^{b_2 h} \tag{6.6}$$

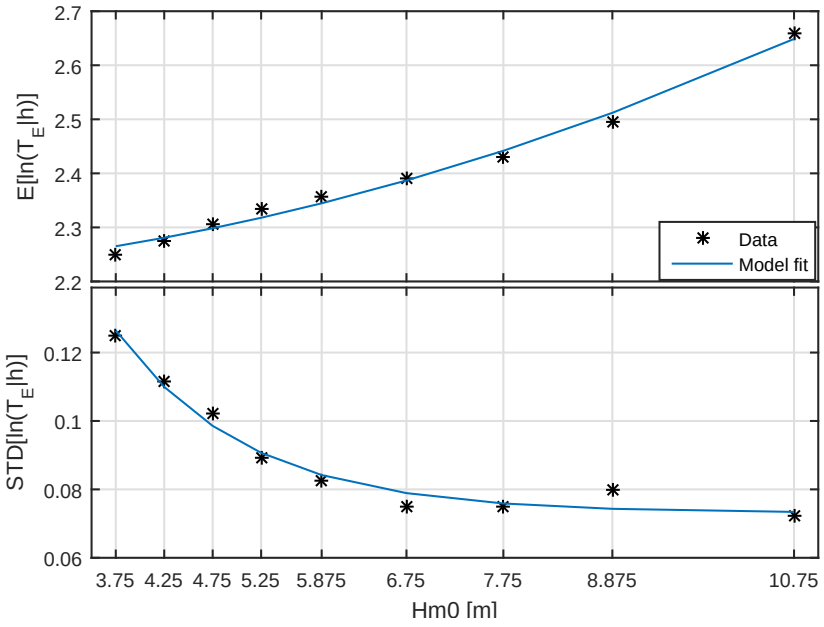

Figure 6.13: Fit of log-normal parameters for conditional probability distributions of T_E

The two probability distributions can now be used to create contours relating to a specified return period. This is achieved by defining β to be the exceedance value of a standard normal variable relating to the specified return period m. Two standard normal variables U_1 and U_2 are then defined along a circle so that their radius is equal to β. The standard normal probability of exceedance corresponding to the values of U_1 and U_2 can then be used to find the equivalent values of H_{m0} and T_E via the obtained distributions. As in Berg (2011), this is described formally in Eqs. (6.7) to (6.9).

$$\beta = \Phi^{-1}\left(1 - \frac{1}{\lambda_m m}\right) \tag{6.7}$$

$$\sqrt{U_1^2 + U_2^2} = \beta \tag{6.8}$$

$$H_{m0,m} = F_{H_{m0}}^{-1}(\Phi(U_1)); \quad T_{E,m} = F_{T_E|H_{m0}}^{-1}(\Phi(U_2)) \tag{6.9}$$

It is typical to inflate β to account for approximating true stochastic response by its median value. From Winterstein *et al.* (1993) and Berg (2011) it is suggested to inflate β using $\beta^\star = \beta/\sqrt{1-\alpha_0^2}$, with α_0 values of between 0.1 and 0.2. A value of 0.15 has therefore been chosen for this analysis, with the resulting contours for return periods of 1, 10, 50 and 100 years shown in Fig. 6.14. This I-FORM technique enables suitable combinations of H_{m0} and T_E to be obtained for specified return periods and may be used to inform extreme sea state creation.

It is worth noting that the H_{m0} and T_E values these contours are derived from have been based on 30 minute data samples (see Section 6.1.1). If these were based off longer time periods, such as the three hours sometimes used (and typically used in numerical models), then the observed extreme values would be slightly reduced. This would consequently provide

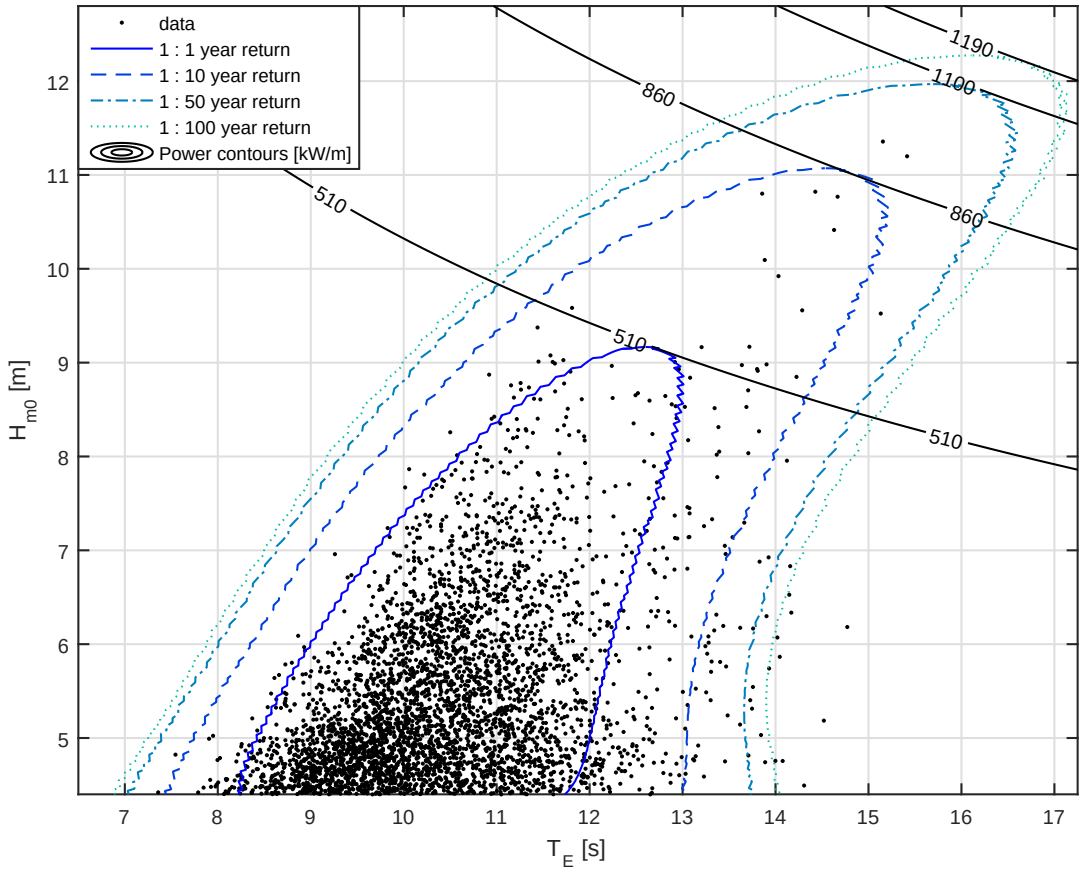

Figure 6.14: Resulting contours for bivariate probability density function

smaller estimates of the expected extreme wave conditions. Assessing the current dataset, using three hour moving averages causes the maximum H_{m0} to reduce from 11.36 m to 10.77 m, and maximum T_E down from 17.39 s to 16.79 s (for 3 hour blocks this becomes 10.34 m and 16.27 s respectively). This demonstrates the potential discrepancy caused by the sample length choice, whilst also highlighting one of the inherent difficulties in analysing ocean wave data. A compromise must be found so that the assumption of stationarity is valid, whilst simultaneously obtaining enough samples to have reasonably small uncertainty in spectral and statistical estimates. Whether 30 minute or longer samples are more appropriate for extreme value analysis is therefore a matter of debate, and is discussed further in Section 6.3.2.2 where the underlying uncertainty of spectral estimates is looked at.

6.3.2 Creating Extreme Conditions

6.3.2.1 Choosing Extreme Values

The choice of extreme H_{m0}–T_E combinations for tank testing, or numerical modelling, is dependent on the nature of the resulting probability distributions and the sensitivities of the device being tested. For a given return period it seems advantageous to choose a range of T_E values, enabling exploration of system response to extreme conditions at various dominant forcing frequencies. For example, developers may want to look at a large T_E value due to concerns over mooring loads, along with H_{m0}–T_E values associated with the largest power as to assess the largest expected structural loads. Additional lower period values may also be chosen, which may correspond to resonant conditions of the device, or the exploration of high wave steepness scenarios.

Without obtaining bivariate joint probabilities it seems highly likely that unsuitable T_E values would be chosen. For example, based on Fig. 6.11 alone, a 1 : 10 year storm condition may be initially defined by H_{m0} = 11 m. Logically one may then use multiple T_E values in combination, for example from 13 to 17 s. It is clear from Fig. 6.14 that this would lead to a number of conditions that are associated with significantly higher return periods, some of which over 100 years. For this reason it seems paramount that bivariate extreme value analysis be carried out for the purpose of creating realistic extreme sea states corresponding to specified return periods.

Using the extreme H_{m0}–T_E contours in Fig. 6.14, suitable H_{m0}–T_E combinations can now be chosen. Remaining device neutral, various points have been chosen for 1:10 and 1:50 year extremes, to serve as an example for further analysis. The 1:10 year extremes are used as they are probably sufficient for prototype devices with short deployments of a few years. Extreme 1:50 year events will be more representative of full deployment lifetimes in the region of 20 years or more, as recommended by IEC 61400-3 for offshore wind turbines (International Electrotechnical Commission, 2005) and used in Ruiz (2010) and Valamanesh *et al.* (2015).

Points have been chosen corresponding to locations on each contour for maximum energy period, maximum power and minimum T_E above a H_{m0} threshold (10 m for 1:10, and 11 m for 1:50). These could be seen as providing scenarios likely to give maximum mooring loads, maximum structural loads and maximum steepness conditions whilst ensuring wave height is still suitably large. The T_E conditions specified, in combination with the extreme contours, define the combined extreme H_{m0}-T_E values. These are shown in Table 6.2 and are highlighted in Fig. 6.15.

Table 6.2: Example extreme H_{m0}-T_E combinations for 1:10 and 1:50 year conditions

Extreme sea state	1 (1:10)	2 (1:10)	3 (1:10)	4 (1:50)	5 (1:50)	6 (1:50)
H_{m0}	10.65	11.05	10.01	11.45	11.86	11.02
T_E	15.21	14.78	11.86	16.61	16.32	12.66

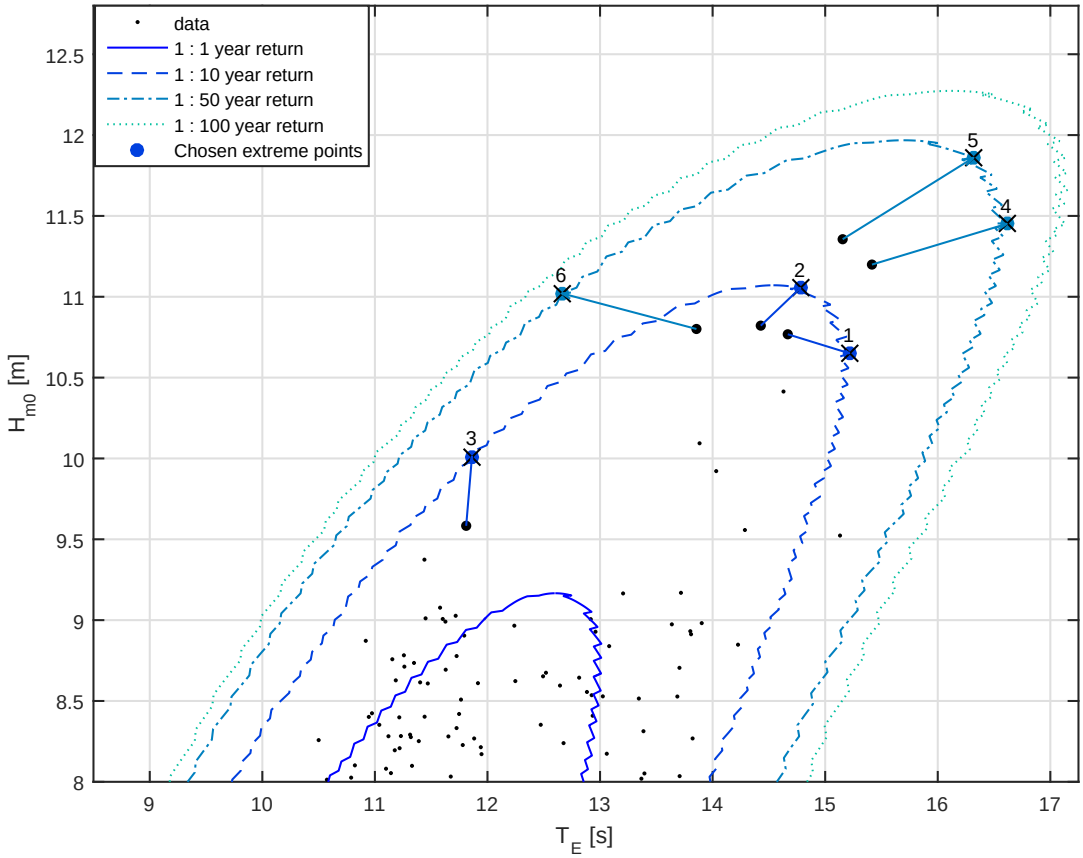

Figure 6.15: Bivariate extreme contours with example chosen points. Lines show observed sea states chosen to be scaled to match specified extreme conditions

6.3.2.2 Extreme Sea State Creation

Parametric

To create an extreme sea state suitable for numerical modelling or scaled tank testing, it is typical to use a parametric spectrum such as one created using the JONSWAP spectral model (Valamanesh *et al.*, 2015). It is possible to create JONSWAP frequency spectra corresponding to the H_{m0}-T_E combinations defined in Table 6.2. Typically these are created by defining H_{m0}, T_p, and γ. As such T_p and γ need to be defined for the extreme conditions.

In the JONSWAP formulation, T_E is essentially a function of T_p and γ. Although the γ value could simply be defined, only certain γ values are likely to be associated with these extreme

conditions, and as such should not be picked at random. To define γ, the formulation by Torsethaugen (1984) has been used, which is based on qualitative considerations of North Sea wave data. This formulation is shown in Eqs. (6.10) and (6.11). As γ is now defined as a function of T_p, yet T_p is a function of γ and T_E, this needs to be solved iteratively until T_E converges. The resulting values of T_p and γ can be found in Table 6.3, noting that 'typical' values of $\gamma = 1$ or 3.3 would not have been appropriate to use according to Torsethaugen (1984).

$$D = 0.036 - \frac{0.056\ T_p}{\sqrt{H_{m0}}} \tag{6.10}$$

$$\gamma = \exp \frac{3.484\ (1 - 0.1975\ D\ T_p^4)}{H_{m0}^2} \tag{6.11}$$

Table 6.3: Resultant T_p and γ values for JONSWAP spectra created for the extreme H_{m0}-T_E combinations defined in Table 6.2

Extreme sea state	1 (1:10)	2 (1:10)	3 (1:10)	4 (1:50)	5 (1:50)	6 (1:50)
H_{m0}	10.65	11.05	10.01	11.45	11.86	11.02
T_E	15.21	14.78	11.86	16.61	16.32	12.66
T_p (JONSWAP)	17.67	17.24	13.37	19.04	18.89	14.36
γ (JONSWAP)	1.135	1.021	2.178	1.474	1.212	1.909

As one of the objectives of this work is to incorporate improved directional complexity in tank testing, it is desirable to create directional spectra for the defined extreme sea states. This will typically be achieved using a frequency independent spreading function, defined using the cos^{2s} or Gaussian directional distributions. Both of these distributions are defined using the mean direction, $\bar{\theta}$, along with different metrics of directional spreading.

To obtain realistic directional parameters, complex multivariate forms of the I-FORM procedure, or other multivariate probability distribution techniques could be carried out. Yet as these are not the 'extreme' parameters of interest it is not so much a problem of extrapolation, but more a case of picking realistic values associated with hypothetical H_{m0}-T_E pairs. Fig. 6.16 shows the relationship between H_{m0}-T_E combinations and mean direction, whilst Fig. 6.17 shows the equivalent with the overall mean directional spreading (width), $\bar{\sigma_\theta}$ (as defined in Frigaard *et al.* (1997)). As expected, these figures show that mean direction tends towards West with increasing T_E, whilst for increasing H_{m0}-T_E values there is a tendency to have reduced spreading. This corresponds physically with large high period storms originating in the North Atlantic, and with the lower directional spreading associated with these sea states than with more 'choppy' seas.

The region with H_{m0}>8 s and T_E>10 s is assumed representative of the likely directionality of the extreme conditions, with associated mean values of $\bar{\theta} = 1.62\pi$ and $\bar{\sigma_\theta} = 0.506$ (mean of

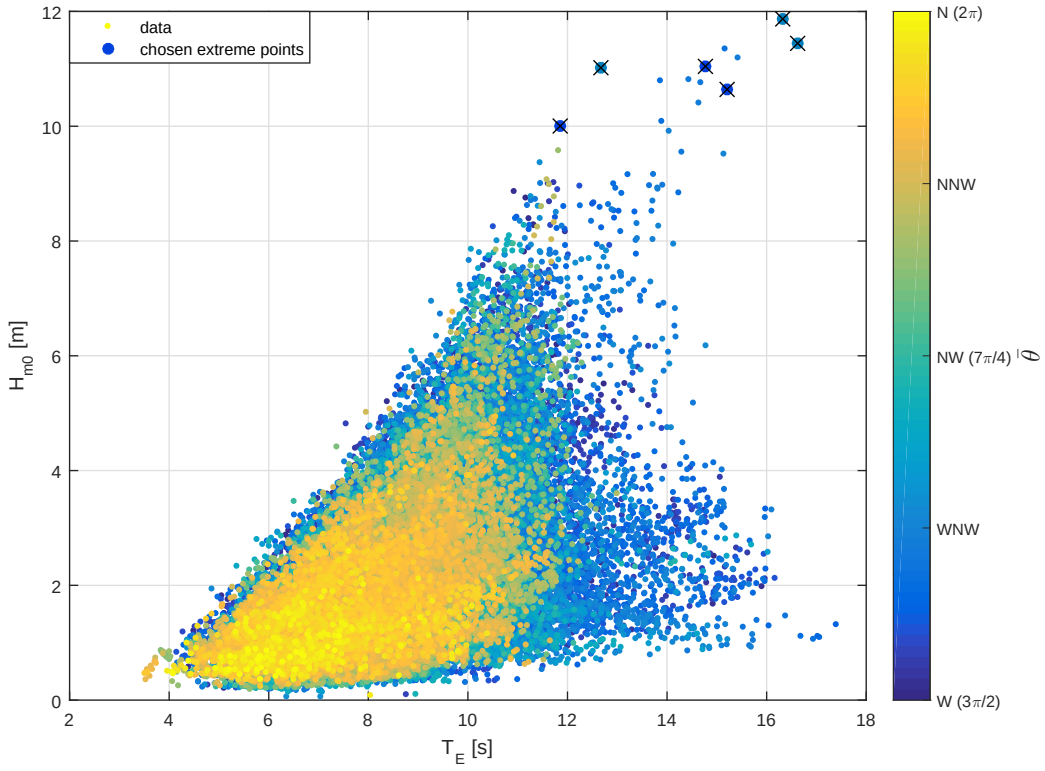

Figure 6.16: $H_{m0} - T_E$ scatter plot with mean direction, $\bar{\theta}$ shown as the colour scale. Note that there are roughly 64000 sea states, with higher values plotted last. This gives the impression that there are more northerly seas than is the case

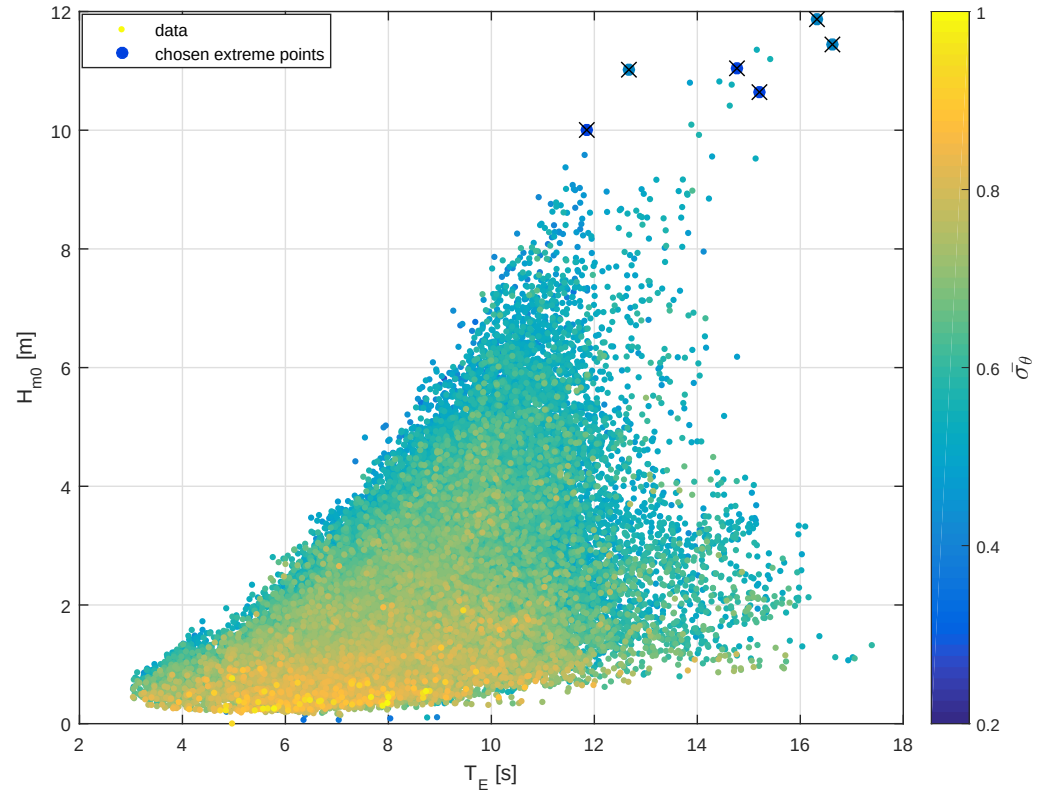

Figure 6.17: $H_{m0} - T_E$ scatter plot with mean spreading, $\bar{\sigma_\theta}$ shown as the colour scale

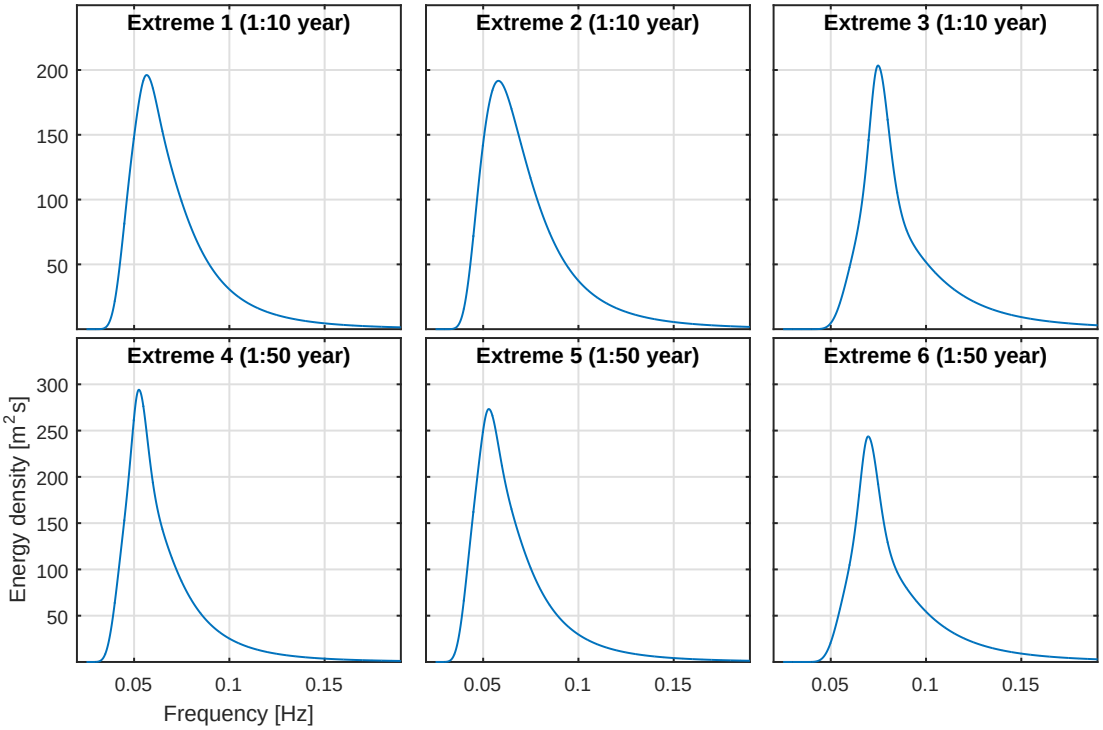

Figure 6.18: JONSWAP spectra for desired combined extreme conditions.

total dataset is 1.7π and 0.6 respectively). Directional spreading functions have been created with these values using a Gaussian directional distribution. The frequency spectra resulting from Table 6.3, along with the created directional spectra resulting from the DSF are shown in Fig. 6.18 and Fig. 6.19 respectively.

Scaling Observed Spectra

With the aim of using real spectral information wherever possible, the idea of 'scaling' observed spectra has been explored. This provides the possibility of using realistic energy distributions associated with extreme events at the site, thus increasing the realism of extreme device response. Clearly there is a question over the validity of scaling sea states along with the method of doing so and whether or not this will actually provide realistic, or even, possible conditions at a site. Equally, however, it may be suggested that JONSWAP spectral shapes for these extreme conditions are unlikely to occur.

To explore this idea, the closest sea state to the defined extreme H_{m0}-T_E points are identified, as defined in Eqs. (6.12) and (6.13). If a given observed sea state is the closest to multiple desired extreme points, distinct points are chosen that minimises the total distance. This enables the

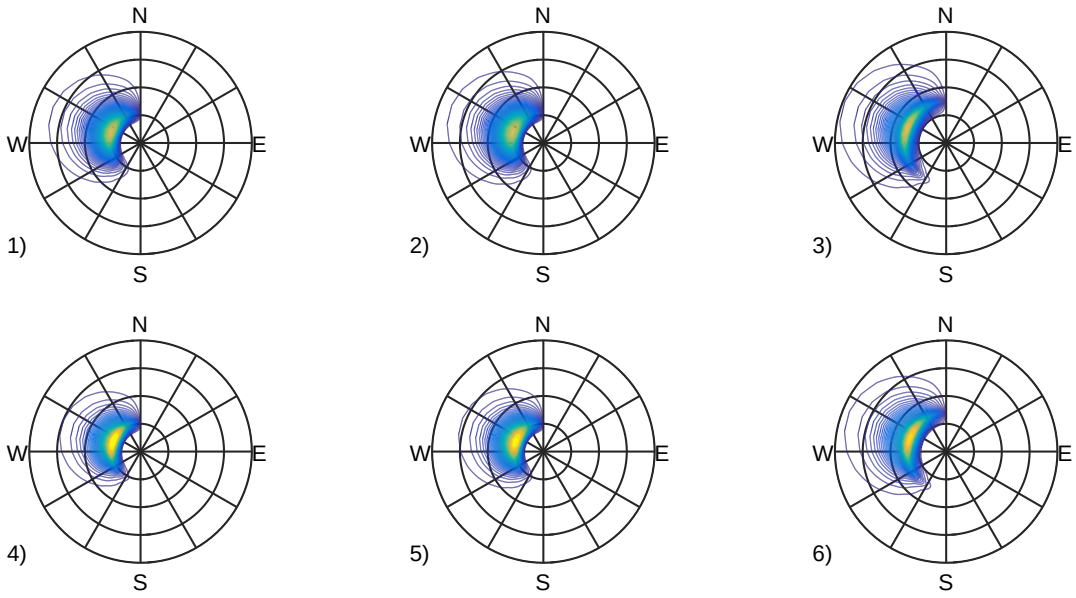

Figure 6.19: Directional spectra comprised of a JONSWAP frequency spectrum and Gaussian directional distribution for the desired combined extreme conditions. Contours relative to maximum of $200 m^2 s/rad$

inclusion of a variety of differing extreme conditions.

$$M_{seastate} = \sqrt{\Delta H_{m0,n}^2 + \Delta T_{E,n}^2} \tag{6.12}$$

$$\Delta H_{m0,n} = \frac{|H_{m0,obs} - H_{m0,des}|}{H_{m0,des}}; \quad \Delta T_{E,n} = \frac{|T_{E,obs} - T_{E,des}|}{T_{E,des}} \tag{6.13}$$

The resulting sea states identified using this procedure are indicated in Fig. 6.15. Extreme conditions 1 and 2, along with 4 and 5, each shared a 'closest' observed sea state. To avoid using duplicate sea states, 2 and 5 were allocated a different observed sea state for the purpose of scaling. From Fig. 6.15 it is clear that the extreme points identified on the 1:10 year contour are all reasonably close to observed conditions, whilst this is not evident for the 1:50 year conditions.

To scale the sea states to match the desired values of H_{m0} and T_E, the spectra have been be amplified and shifted in frequency. Noting that $S_i(f) \propto A_i(f)^2$, Eq. (6.14) can be used to get the correct H_{m0} by means of applying a single spectrum amplification factor. To obtain the correct T_E, the whole spectrum is first interpolated to give a large number of frequency values. The spectrum is then shifted on the frequency axis until the desired T_E is obtained. An iterative rather than analytic method was used as T_E is a function of m_{-1} (spectral moment) i.e. to find the shift, the desired energy distribution would need to be known, which remains a function of

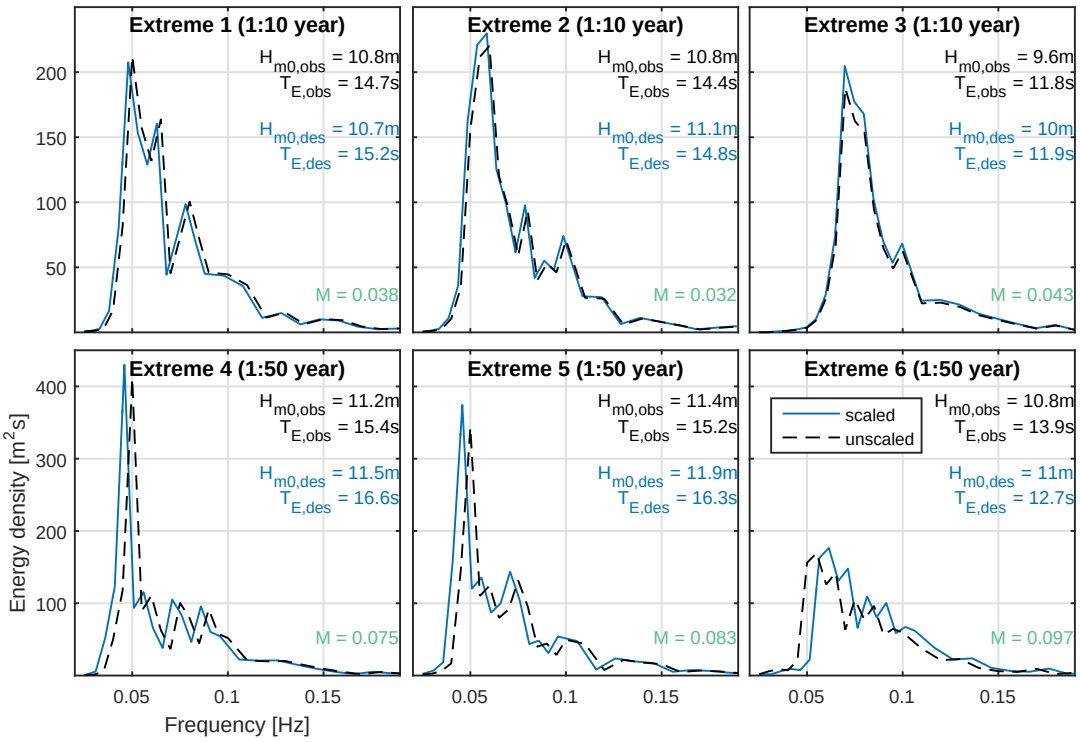

Figure 6.20: Frequency spectra for sea states identified in Fig. 6.15, scaled to desired extreme conditions. M value overlaid corresponding to Eq. (6.12)

the unknown frequency shift itself and the known spectral shape.

$$S_{scaled}(f) = S_{obs}(f)(\frac{H_{m0,des}}{H_{m0,obs}})^2 \tag{6.14}$$

The results from this scaling-shifting procedure for both the frequency and directional spectra are shown in Fig. 6.20 and Fig. 6.21 respectively. To assess the relative magnitude of the applied change, the recent transformations of the wave spectra can be assessed. Frequency spectra relating to the three hour periods prior to the identified events are shown in Fig. 6.22. Large changes in the spectral forms are observed within these short half hour periods, suggesting that the magnitude of the applied transformations may be reasonable, if not physically representative of wave energy transfer mechanisms. This aids somewhat in putting the proposed changes to the observed spectra into perspective.

This sort of extreme value analysis aims to identify and create improbable conditions, yet care must be taken to ensure the test spectra are not impossible. Despite the example transformations appearing somewhat feasible, it must be ensured that changes are not too large and do not breach any physical laws. In particular, if increasing H_{m0} significantly and/or reducing T_E, then the new steepness must be calculated to ensure that the proposed spectrum is still physically maintainable and wave steepness limits are not breached. Equally, shifting a spectrum to have

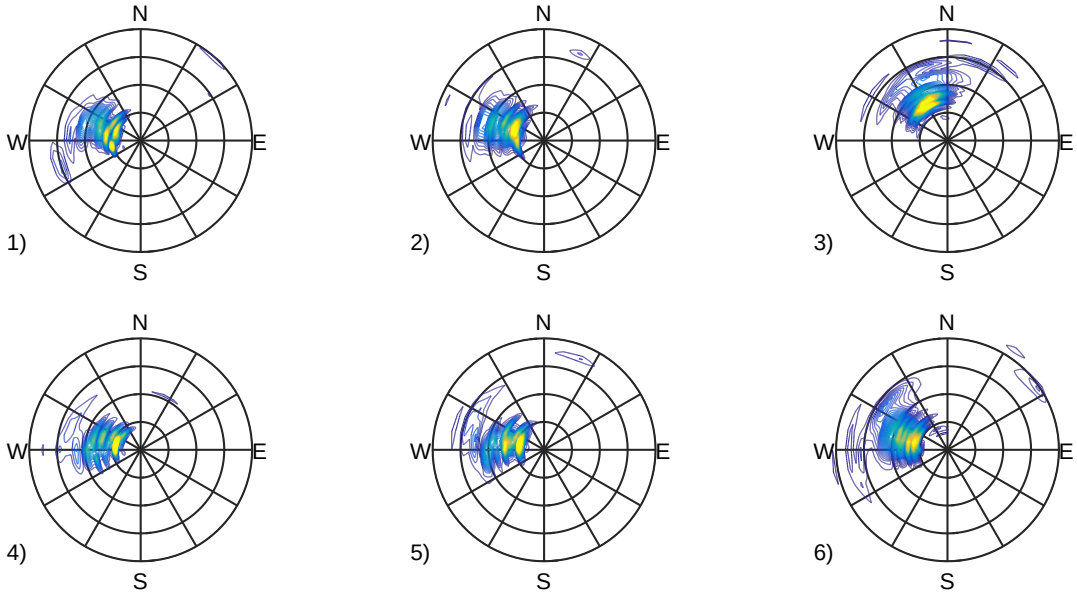

Figure 6.21: Directional spectra for sea states identified in Fig. 6.15, scaled to desired extreme conditions

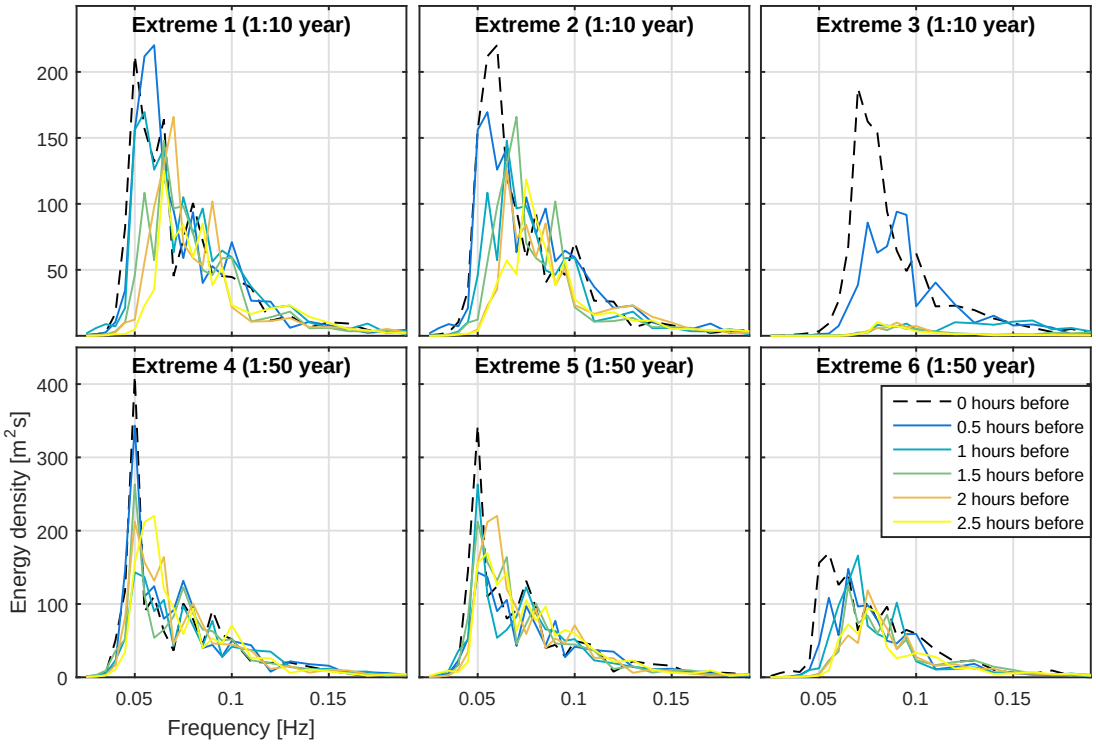

Figure 6.22: Frequency spectra change for the three hours prior to the extreme sea state identified

a much larger wave period may also represent an impossible energy distribution given the fetch

length available. Therefore, in addition to checking steepness, it seems that a limit should be placed on the overall transformation.

From observation of the transformed spectra in Fig. 6.20 it is suggested that the required scaling for the 1:10 year example events are very minor and hence represent a valid change. Relative to the large scale variations over short time frames demonstrated in Fig. 6.22, it also appears that scaling sea states for the 1:50 year events may also be reasonable. However, some of the large changes in the energy period required for some of these sea states, particularly Extreme 6, make this more questionable. Despite these concerns, the applied frequency shift seems to still create plausible conditions, due to the occurrence of many sea states with larger T_p values, up to 25 s (0.04 Hz).

On the basis of these observations, and noting the associated M values from Eq. (6.12), it seems reasonable to suggest that any M value of less than 0.05 would be a very minor required change and hence clearly acceptable. Care must be taken with M values greater than 0.05, although it is suggested that M values of less than 0.1 are potentially also acceptable, as long as it is ensured that both general and site-specific physical laws are not broken.

Potential Improvements if Hindcast Data is available

If hindcast data is available, then certain improvements can be made throughout the extreme sea state creation process. Assuming the hindcast data is reliable, the larger number of data points means that fitted distributions to H_{m0} will have significantly reduced uncertainty. Similarly there will also be increased certainty in the parameterised conditional T_E distributions, hence the resulting I-FORM contours should be more representative.

Having a greater number of points in H_{m0}-T_E space also means that if trying to scale spectra, it is highly likely that there will be points that are closer, thus reducing the M number and hence increasing the method validity. If there are a large number of similarly close data points, then one has the opportunity to choose various different observed extreme spectra with differing characteristics e.g. different directional spreads, spectral bandwidths and even multi-modal extremes. This, although a potentially difficult exercise, would provide tests with a better range of likely extreme conditions.

One of the main advantages of using real site data is to base tests on sea states which incorporate observed complexity in energy distribution, with respect to both frequency and direction. Although the sea states derived from hindcast data will not have been actually observed, to provide tests with a high amount of realism it seems important to properly incorporate directionality. In Lawrence *et al.* (2009) it is shown that forcing a hindcast model with directional spectra provides much improved results, resulting in detailed outputs. Additionally it is found that using coupled wave-tide models — incorporating the spatially variable wave-current interactions that occur at the site — is important to accurately predict observed conditions. This inclusion of tidal currents represents a significant advantage. Using buoy measurements without knowledge of the current field means that the spectra obtained can be misleading and estimates of the

wavelength, power and steepness will be incorrect. This has important consequences for both resource assessment and device testing, which is discussed and demonstrated in Section 7.3.

Inherent Uncertainty in Spectral Estimates

When scaling measured sea states to defined extreme conditions a lot of emphasis has been placed on trying to preserving observed spectral shape, or the estimates of. This approach was taken to preserve the 'best estimate' of the sea state as much as possible. It is to be noted, however, that there is significant uncertainty in these spectral estimates initially and the emphasis placed on such (frequency) spectral shapes should be put into context. To assess this, confidence intervals can be obtained for individual spectral estimates through a chi-squared distribution (χ^2) as described in Guedes Soares (1990), Earle (1996) and others. These bounds are shown in Eq. (6.15) for a given α value (e.g. for 90% confidence intervals, α = 0.9), and for a given Equivalent Degrees of Freedom (EDF). For non-segmented data the EDF are equal to twice the number of Fourier frequencies in each band (Earle, 1996).

$$\frac{S(f)EDF}{\chi^2(EDF, \frac{1+\alpha}{2})}; \qquad \frac{S(f)EDF}{\chi^2(EDF, \frac{1-\alpha}{2})} \tag{6.15}$$

The EMEC spectra provided has two differently sized frequency bins, which results in 90% confidence (assuming non-segmented: worst case) that individual spectral estimates lie within $0.62S(f)$ and $1.92S(f)$ below 0.1 Hz, and $0.71S(f)$ and $1.55S(f)$ above. This is fairly large uncertainty, highlighting that the true spectra may differ quite significantly from the estimates. To reduce these apparent uncertainties, averages over longer time periods can be used. To do this legitimately, however, relies on the sea state remaining stationarity, which as shown in Fig. 6.22 (particularly sea state 3) is often not the case for any significant length of time. For this work the 30 minute spectra provided, and typically used (Thomson *et al.*), have been used throughout as the assumption of stationarity appears invalid over much longer time frames. This 30 minute sample length is also widely suggested (e.g. in Euan *et al.* (2017) and Alvarez-Esteban *et al.* (2015)) to ensure that both the assumption of stationarity and ergodicity are reasonable.

In addition to the statistical uncertainty arising from approximating the spectral form from wave buoy heave time-series, it is worth assessing whether or not additional uncertainty exists when assuming this time-series is a good representation of the wave climate of interest. This, in part, relies on the hull-mooring response corrections being correct which may not always be the case if, for example, moorings snatch loads are induced in large waves. Additionally the presence of natural reflections, which result in non-ergodic wave fields may cause additional uncertainty. Spectra, that although estimate the surface variance at the buoy locations, will not give an accurate picture of the energy density at the site of interest (due to location relative to interference pattern between incident and reflected wave fields). It is not thought these issues

are too significant for the EMEC buoy data as the buoy is roughly 2km offshore, and quality control measures should have removed sea states with peculiar buoy dynamics. It is worth noting, however, that the uncertainties present in ocean wave data are not from the spectral estimation procedures alone, and there are many factors at play.

6.4 Classification 2: Representative (Production) Sea States

This section explores methods of creating a small set (K) of statistically representative directional sea states from the buoy data suitable for reproduction in the tank, which is essentially a data reduction exercise. The resulting combination of representative sea states should adequately describe the range of conditions at the site and hence result in effective site-specific test outputs. One of the aims in this work is to explore the merits of considering the whole spectral form (frequency or directional) in the characterisation, thus preserving sea state complexity and aiding in more realistic 'production' conditions.

A number of initial method ideas are assessed using binning and clustering techniques, grouping sea states by similarity, whether on statistical parameters or spectrally. The groups created then define the representative sea states. Mean spectra are used from each group, or parametric fitting to the mean is carried out to obtain the representative conditions. The effectiveness of each methodology is assessed both visually and through the use of a performance metric, which aims to quantify grouping effectiveness on a variety of sea state parameters (regardless of the number of dimensions), whilst considering both the inter-group distinctness and intra-group compactness.

Throughout the exploration process the inherent trade-offs are understood, along with the characteristics of the method types trialled. This helps in understanding which applications or devices they would be suitable for, enabling them to be used either as is, modified, or combined, to create suitable realistic site-specific tests for any wave site. With the aim of producing realistic directional spectra, but with a good range of key statistical parameters, a generic set of sea states are created for Billia Croo using a combined binning-clustering approach.

6.4.1 Classification Methodologies and Performance Metric

6.4.1.1 Binning Methods

High level resource assessment and site characterisation is typically carried out using a scatter diagram, which is essentially two-dimensional binning of wave period and significant wave height, showing abundance. It is recommended in Venugopal *et al.* (2011) to use bins of 0.5 m and 0.5 s, which is implemented accordingly in Lavelle and Kofoed (2011) and Pascal *et al.* (2015), whilst the IEC recommends bins of 0.5 m and 1 s. Assessing WEC performance, power matrices can be produced, denoting the mean device power capture measured in each bin, typically calculated using a combination of tank testing, site data and numerical modelling (Venugopal *et al.*, 2011). These combinations then enable estimations of energy production, taking into consideration the abundance of sea states in each bin and the assumed mean instantaneous power. It is well known, however, that the way the resource is represented and characterised in this manner introduces large uncertainties (Ricci *et al.*, 2011).

To create site specific tests, the data can be partitioned similarly using criteria imposed on the H_{m0}-T_E values, or indeed any number of key parameters. These can be regularly spaced bins, or may be irregular such as those implemented in Kofoed *et al.* (2013). Once the data is partitioned and the abundance is known, sea states can be created to represent each of these bins.

This sort of binning approach would be typical, and groups sea states effectively by the key statistical parameters defining device response and power available. Some of the issues with this approach are discussed in Section 2.1.2, with one of the issues being that highly dissimilar spectra can be combined together and represented by a single spectrum. Assessing Fig. 6.5, it can be seen that there are a variety of highly different spectral shapes in each of these bins, to which devices would respond dramatically differently. This is in addition to extremely varied associated directional spreading functions, shown in Fig. 6.6.

Statistics such as H_{m0}, T_E and $\bar{\theta}$ are essentially a proxy set of parameters derived from the observed spectra. Due to this, and the fact that true device response is really a complex function of these energy distributions, methods of considering the spectral shape are also explored and compared with binning outputs.

6.4.1.2 Clustering Methods

Cluster analysis is an unsupervised learning approach used to classify data objects into similar groups. This enables logical partitions to be made within datasets efficiently, allocating cluster membership to objects based on a user-specified distance metric. Importantly, clustering can be applied to multi-dimensional data and so can be used to group similar spectra together, or groups of key variables.

There are multiple forms of clustering algorithms. Some focus on hierarchical approaches, defining in stages the underlying natural relationships in the dataset and the logical partitions that can be made. Other approaches focus on partitioning itself, where the data is forced into a set number of groups. Although there are some natural hierarchies that will occur in the data due to sea state growth, transformation and decay, the data is fairly continuous in both the spectral shape and the resulting summary statistics. In addition, as it is desirable to specify the number of groups explicitly, the problem is essentially about forcing the data into distinct groups of similar objects which cover the defined variable space.

The K-means (partitioning) clustering algorithm has been chosen for this work, due to its simplicity and effectiveness at producing K distinct groups. K-means works by assigning data objects to K initial groups, calculating group means and re-assigning objects to the cluster with the 'nearest' centroid. This is done iteratively until objects cannot move to improve the objective function i.e. the sum of within cluster distances. For this work the Squared Euclidean distance is used, as defined in Eq. (6.16). Note that the distance is multidimensional (e.g. length

of frequency spectrum = p) describing the distance from object x to centroid c, in p-space.

$$d(x,c) = (x-c)(x-c)' \tag{6.16}$$

One of the issues with typical K-means is that the initial clusters are assigned randomly, which means that there is no guarantee that the resulting clusters are near optimal. To get around this it is typical to repeat the initial seeding process multiple times before choosing the best output. Alternatively one can use K-means++, which uses a careful seeding algorithm to increase both speed and accuracy of the clustering process (Arthur and Vassilvitskii, 2007). As a result of the performance increase the K-means++ seeding approach has been implemented in this work.

The K-means algorithm with K-means++ seeding will be used to assess the merits of using such algorithms to partition the wave data. This will focus on clustering the frequency spectra, directional spectra and normalised statistical parameters. Hamilton (2010) uses a CLARA clustering approach for characterising frequency spectra, but not for the purpose of creating sea states suitable for practical replication and as such, without the same constraints on the number of allowed groups (discussed in Section 6.4.2.1). This work aims to assess what will provide the overall best partitions, given the priorities for the testing and within the given constraints. If sea states are grouped by spectral similarity, then whether or not they are also automatically grouped well by the statistical parameters is of importance.

6.4.1.3 The Trialled Methods

A number of characterisation approaches have previously been trialled in Draycott *et al.* (2014) and Draycott *et al.* (2015c), for one and two years of the same dataset respectively. Here the whole dataset (four years) is used and a number of methodologies are re-assessed, along with some additional ones. The aim is to understand the fundamental characteristics and trade-offs introduced by adopting a certain characterisation approach and focussing on particular variables. The compromises introduced by focussing on many variables are also explored. Once these are understood a well-informed, tailored characterisation process can be devised, using these tools alone or in combination to provide desirable sets of sea states.

Eight methods in total have been trialled (A-H), aimed at assessing a variety of grouping methodologies with a range of considered variables. As mentioned in Ricci *et al.* (2011) other parameters such as $\bar{\theta}$ can be used to improve site characterisation by binning. This enables another level of specifics to be imposed and should therefore reduce the expected range of device response in each of the more refined bins. The use of two parameter H_{m0}-T_E binning (method A) and 3 parameter H_{m0}-T_E-$\bar{\theta}$ binning (method B) are therefore explored. However, as this process is constrained by the allowable number of total bins, increasing the number of parameters means that the bin resolution will drop significantly, hence will more poorly characterise with respect to individual parameters.

Clustering approaches have been used on both the frequency (method C) and directional spectra (method D) to assess the potential improvements in characterising spectral shape, along with the effect on the partitioning of the derived statistics. Clustering is also applied to normalised values of $[H_{m0}, T_E]$ (method E) to compare the outputs of this unsupervised approach with binning outputs. The clustering of normalised variables also opens up the possibility to consider many at once, so this same approach is explored with a vector consisting of $[H_{m0}, T_E, \nu, \bar{\theta}, P, S_p, \bar{\sigma_\theta}]$ (method F). It is thought this approach may enable characterisation of many key variables in combination, whilst avoiding what would effectively require a very low resolution with the comparable binning solution.

Finally, the idea of using combined statistical-spectral clustering methods are explored, grouping variables statistically before enabling the groups to be split up further by spectral shape. This may enable a completely unsupervised approach to the characterisation, whilst considering the statistics of interest, along with the spectral form. This is explored with $[H_{m0}, T_E]$ prior to $S(f)$ (method G), and $[H_{m0}, T_E, \nu, \bar{\theta}, P, S_p, \bar{\sigma_\theta}]$ prior to $E(f, \theta)$ (method H). These methods are summarised in Table 6.4.

Table 6.4: Methods trialled for sea state classification

Method	Binning (B)/ Clustering (C)	Variables considered
A	B	H_{m0}, T_E
B	B	$H_{m0}, T_E, \bar{\theta}$
C	C	$S(f)$
D	C	$E(f, \theta)$
E	C	H_{m0}, T_E
F	C	$H_{m0}, T_E, \nu, \bar{\theta}, P, S_p, \bar{\sigma_\theta}$
G	C	$H_{m0}, T_E, S(f)$
H	C	$H_{m0}, T_E, \nu, \bar{\theta}, P, S_p, \bar{\sigma_\theta}, E(f, \theta)$

6.4.1.4 Performance Metric

The identification of good or bad grouping can be a problematic and controversial issue (Rokach and Maimon, 2001), with Bonner (1964) being the first to argue that there is no all-encompassing criteria. In this work the 'good' or 'bad' can only really be assessed visually, or relative to the other methods trialled. To numerically compare between methods, a suitable metric must be used.

Generally, for a clustering output to be considered good the intra-group similarity is high i.e. small sum of within cluster distances, whilst the inter-group similarity is low. This is particularly applicable for this work. Inter-group similarity is required to be high to ensure any averaging within a group is carried out over similar values as to not distort the realism of the test conditions. Equally for tank testing, a wide range of conditions are desirable to understand performance and as such the inter-group distinctness should be high.

To get a measure of the group compactness and distinctness, the within-cluster and between-cluster scatter matrices can be used respectively. From Rokach and Maimon (2001), these are defined in Eqs. (6.17) to (6.20).

The within-cluster scatter matrix, S_W is

$$S_W = \sum_{k=1}^{K} S_k \tag{6.17}$$

where

$$S_k = \sum_{x \in C_k} (x - \mu_k)(x - \mu_k)^T \tag{6.18}$$

The between-cluster scatter matrix, S_B, can be calculated by

$$S_B = \sum_{k=1}^{K} N_k (\mu_k - \mu)(\mu_k - \mu)^T \tag{6.19}$$

where μ is the total mean vector, defined as

$$\mu = \frac{1}{N_{total}} \sum_{k=1}^{K} N_k \mu_k \tag{6.20}$$

To include both the compactness and distinctness of the resulting groups, the within-cluster and between-cluster scatter should be considered in combination. Using the invariant criterion from Rokach and Maimon (2001), good partitions are defined when the eigenvalues of $S_W^{-1} S_B$ are large. To infer this Eq. (6.21) is used, defining the absolute value of the performance metric for method m, and variable v.

$$p_{m,v} = tr[S_{W_{m,v}}^{-1} S_{B_{m,v}}] = \sum_{i=1}^{d} \lambda_{i_{m,v}} \tag{6.21}$$

6.4.2 Method Implementation and Results

6.4.2.1 Choice of Number of Sea States

Prior to implementing the chosen characterisation methods, the number of groups (equal to the number of resulting sea states) must be decided. The desired number of sea states, K, is a function of a number of considerations, however, is dominated for this application by the practical limit on the available number of days for tank testing. It is postulated that site-specific performance tests should take up no more than 1–2 days of a test programme. To determine the number of sea states that can be generated within the allocated days, the run-time of the sea states also needs to be defined, which is desired to be the same for all tests.

It is recommended in McCombes *et al.* (2010) that 500–1000 waves should be used to get a good representation of extremes. For the EMEC data the mean value of $T_{0,1}$ (mean wave period)

is calculated to be 6.89 s (max.=13.55 s, min.=2.46 s.) At tank scale (depth ratio = 1:26), to achieve 500 waves on average a repeat time of 676 s is required.

For ease of spectral analysis it is useful to have test lengths of power two and hence to achieve over 500 waves on average, 1024 s is preferable, or 2048 s to ensure that every sea state generated contains over 500 waves (1516 on average). Approximately 20 sea states can be generated at 1024 s within a day, meaning that over two days 40 sea states can be generated at this test length, or 20 using the longer repeat time of 2048 s.

There is a trade-off between the representation of individual extreme waves and the quality of the characterisation. Longer repeat times reduce the number of sea states that can be generated within the allowed time period, hence reducing the number of groups, or clusters that can be used to represent the site. To assess the influence the number of clusters has on the quality of the characterisation, the performance metrics are assessed for ten sea state parameters, for K values between 2 and 10,000. As an example, this is assessed with method C: clustering on $S(f)$. This is partly due to the ease of specifying K, but also to see if there is a clear point at which statistical parameters are partitioned well, whilst only considering spectral similarity. The outputs of this are shown in Fig. 6.23.

From Fig. 6.23 it is clear that for the majority of considered variables there is a significant increase in the invariant criterion, Eq. (6.21), between K=20 and K=40. This is mostly due to an increase in group compactness, shown by the reduction in intra-cluster scatter, however for some variables the inter-cluster scatter (distinctness of groups) also improved significantly. Due to this increase in characterisation performance, two sets of sea states for each of the exploration methods will be created with K=20 and K=40. This enables assessment of the influence of the number of sea states, within the allowable range, for a variety of methods and on a variety of sea state parameters. This also allows some level of understanding over the consequences of prioritising between the statistical representation of extremes within a test and the statistical representation of the site itself.

6.4.2.2 Method Implementation

To explore the performance of the various methods each approach has been tasked to produce 20 and 40 representative sea states from the data ($\pm$10% for methods where K can not be defined explicitly). As these sea states are designed for performance testing, the data has been filtered to only include sea states with significant wave heights under 7 m, with the process for extreme seas dealt with separately in Section 6.3. This value is meant to be a representative and conservative figure, however, if the generation limits are known for a specific device this could easily be included (and is likely to be lower). A minimum wave height could also be imposed if known.

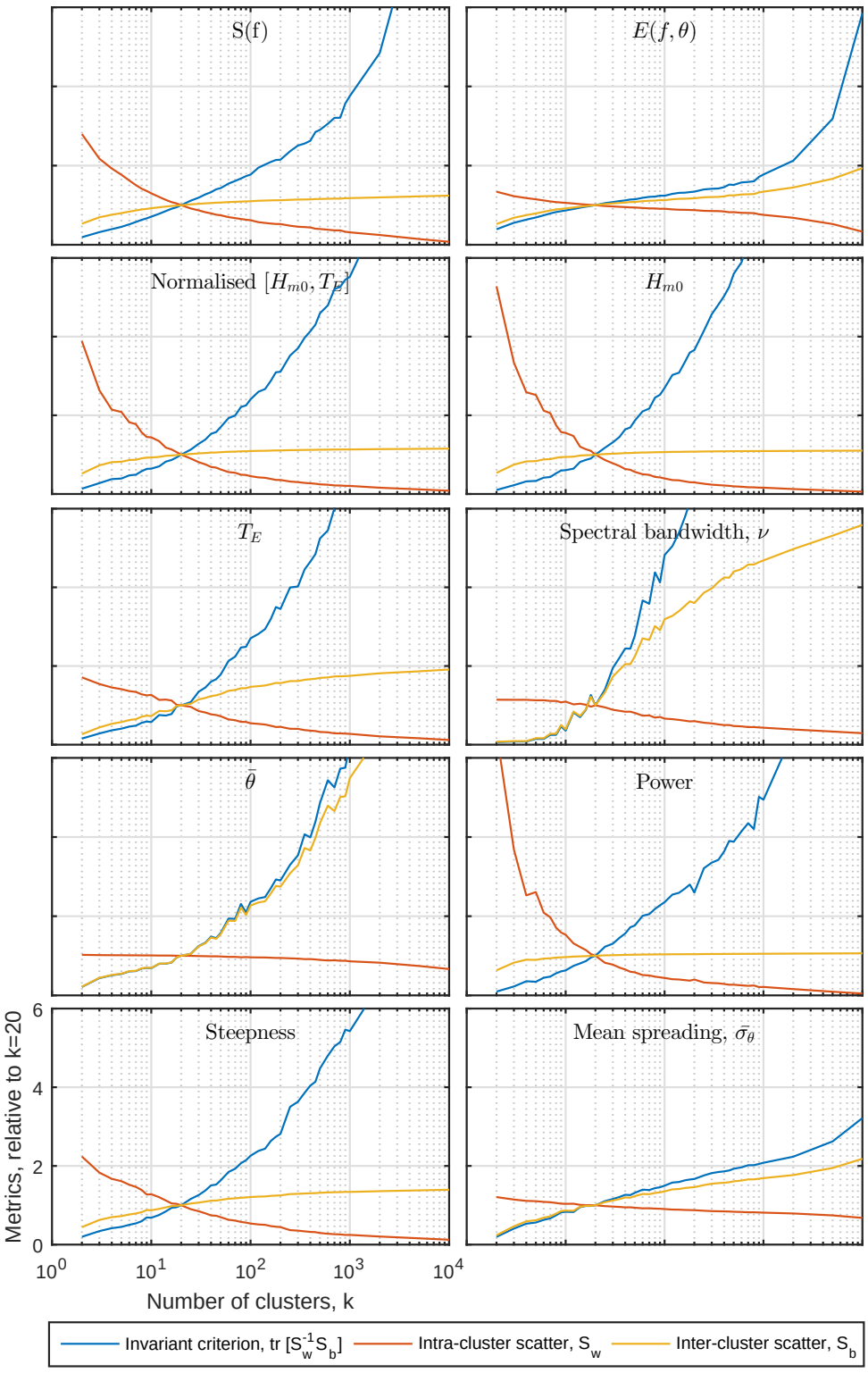

Figure 6.23: Influence number of clusters has on inter and intra-cluster scatter, along with the invariant criterion. Results shown for K-means++ clustering on S(f), relative to K=20

In order to obtain outputs from some of the methods, additional subjective decisions need to be made. These are essentially the relative number of bins for methods A and B and the relative number of statistical clusters to spectral sub-clusters in methods G and H. For methods C-F the number of clusters is simply specified and implemented. In order to assess the methods, sensible bin numbers were used, with a slightly higher emphasis on characterising H_{m0} (guided from IEC recommendations). These are detailed in Table 6.5, along with the resulting number of bins (allowing $\pm 10\%$).

Table 6.5: Relative number of bins for methods A and B

	No. of H_{m0} bins	No. of T_E bins	No. of $\bar{\theta}$ bins	Total no. non-empty bins
A_{20}	6	4	-	21
A_{40}	8	7	-	42
B_{20}	4	3	3	20
B_{40}	6	5	3	43

For methods G and H the view was taken to initially partition the data via statistical clustering using $K/2$ clusters, before splitting each of the statistical groups into two using the spectral form. This gives roughly equal emphasis on the spectral and statistical characteristics, yet does constrain the approach to having two different spectral shapes in each initial partition.

6.4.2.3 Method Results: Metric and Resulting Partitions

Methods A-H have been used to partition the EMEC data into roughly 20 and 40 sea states. Some of the outputs are shown here, with Section 6.4.3 addressing what can be inferred from these results. The invariant criterion performance metric for 10 key sea state variables, for each of the 8 methods and for K=20, and K=40 are shown in Fig. 6.24. This gives an indication as to how well the different methods are partitioning the data for a wide range of variables.

There are a large number of sea state outputs as a result of the characterisation methods and the partitions can be viewed in a number of ways. In this section only key variables are assessed, including H_{m0}-T_E partitions and some of the $S(f)$ partitions. Ideally the directional spectra partitions would be assessed, however, these are not easy to visualise. As mentioned in Section 6.4.1.1, depending on the aim of the testing, developers are typically interested in having a good range of H_{m0}-T_E combinations to contribute to conventional type power matrices. It is therefore important to assess these partitions to identify method suitability for these purposes. The H_{m0}-T_E partitions resulting from methods A-H, for 20 and 40 sea states are shown in Figs. 6.25 and 6.26 respectively.

The resulting mean frequency spectra from the characterisation methods are shown in Figs. 6.27 and 6.28, for K=20 and K=40 respectively. This gives an idea of the range of spectra resulting from each method type. To observe how similar the frequency spectra are in each group, all

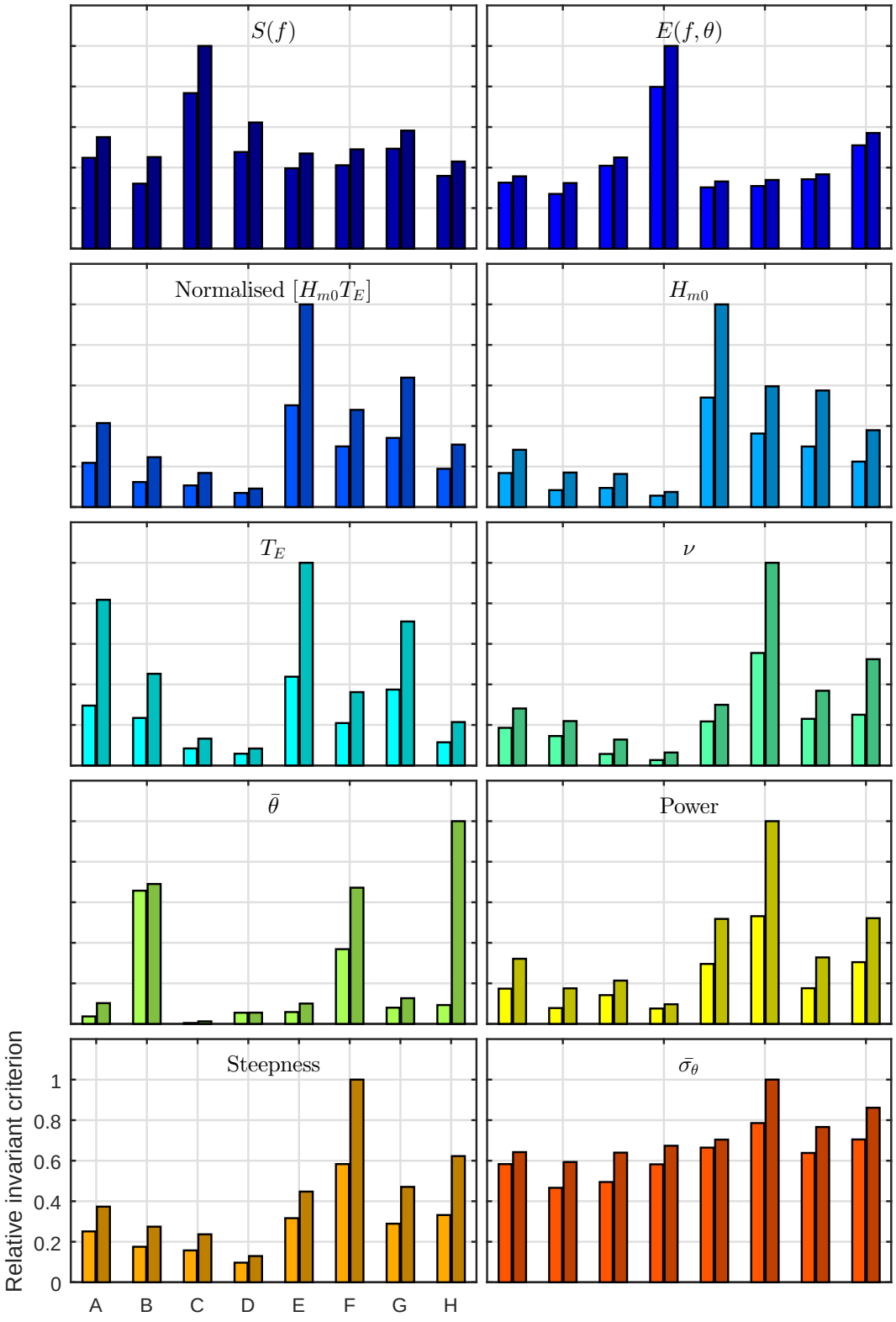

Figure 6.24: Performance metric for methods A-H, shown for 20 and 40 sea states, relative to the maximum metric obtained for each variable. K=40 is shown by the slightly darker colour

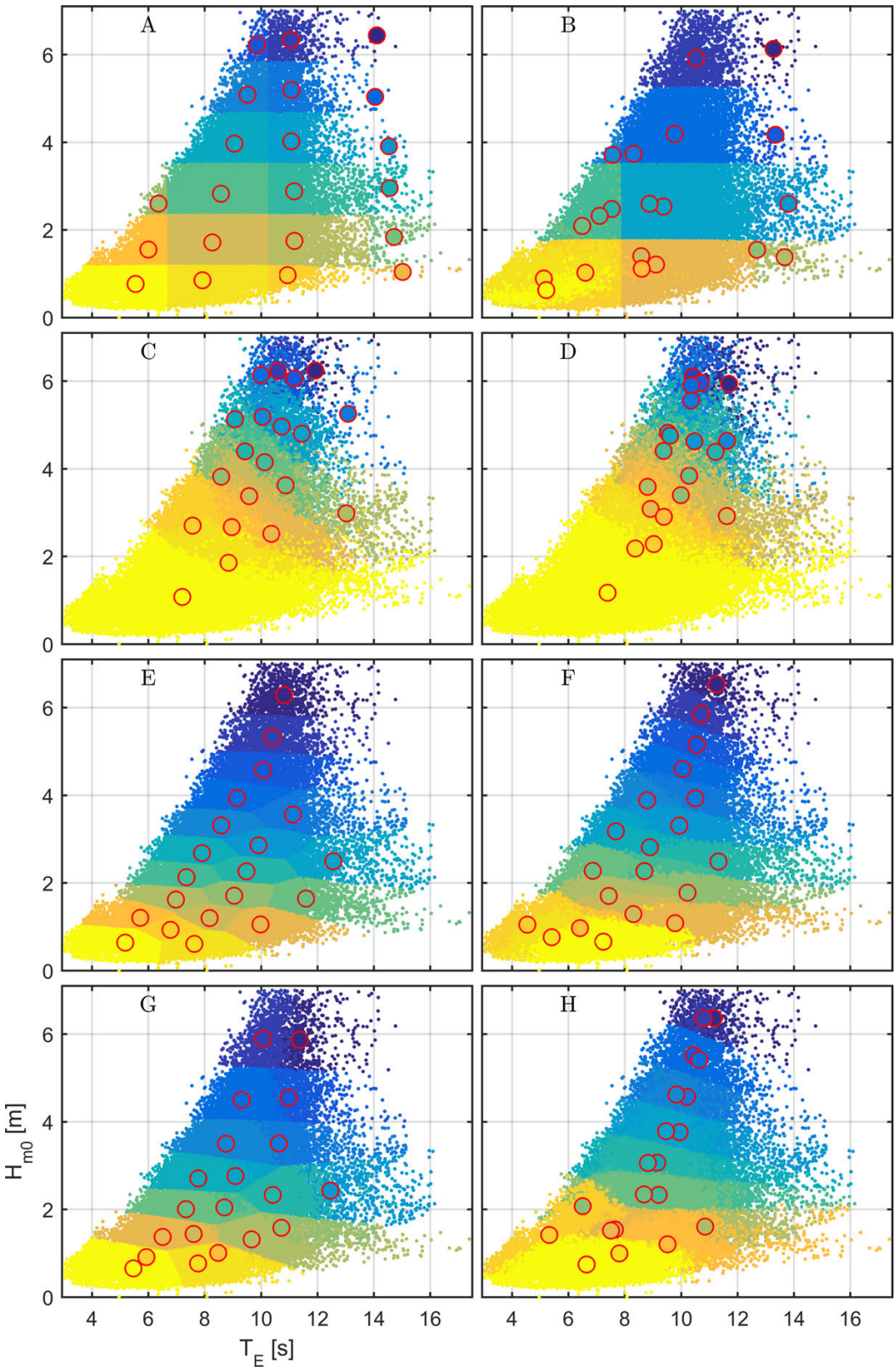

Figure 6.25: Resulting partitions in H_{m0}-T_E space for classification methods with K=20. Circles denote group centroids. Colour indicates sea state power from dark blue (highest) to bright yellow (lowest)

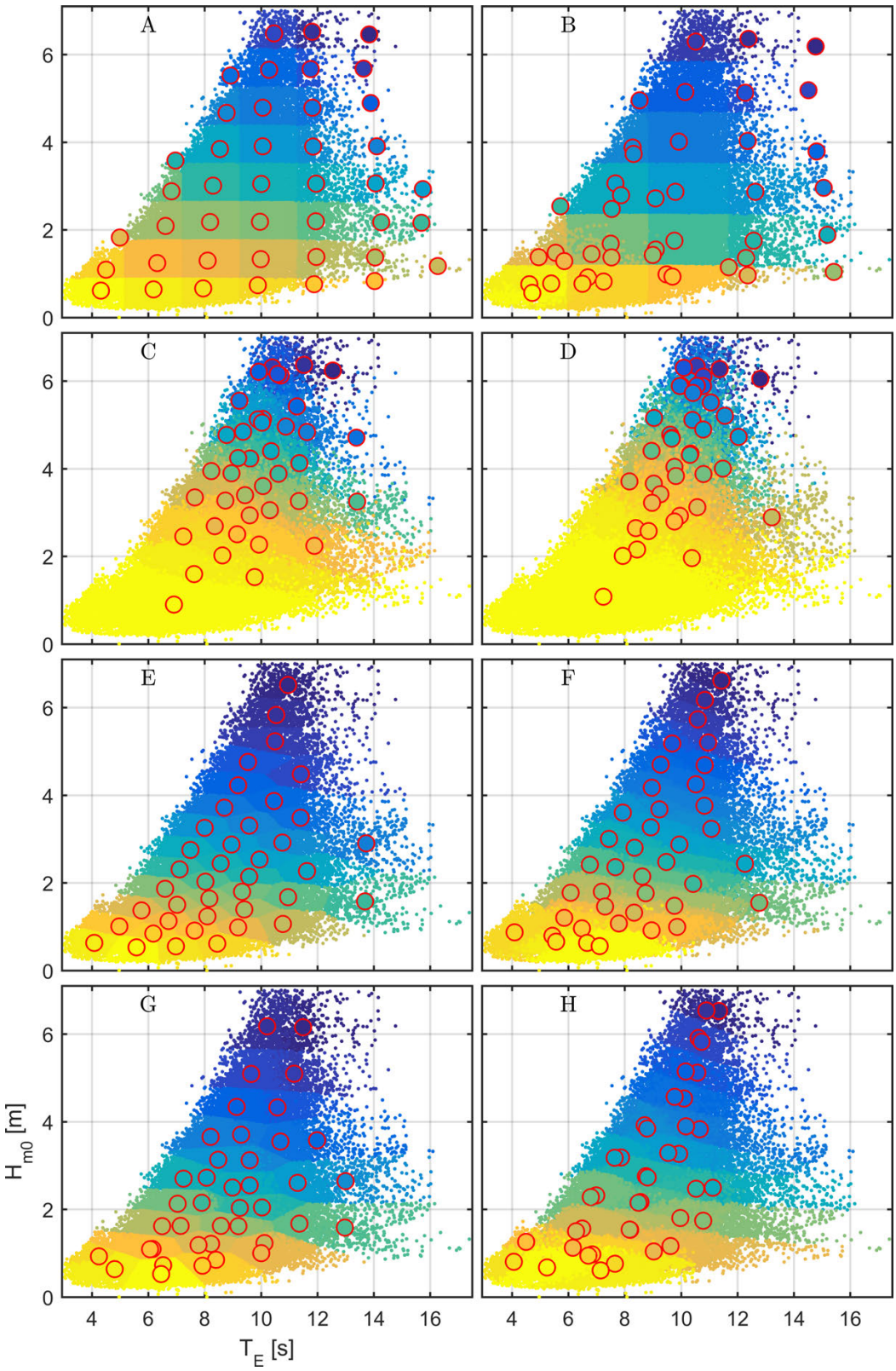

Figure 6.26: Resulting partitions in H_{m0}-T_E space for classification methods with K=40. Circles denote group centroids. Colour indicates sea state power from dark blue (highest) to bright yellow (lowest)

of the spectra in a particular group can be isolated and overlaid. This is shown for methods A (H_{m0}-T_E binning) and C (clustering on $S(f)$) in Figs. 6.29 and 6.30, to gauge how these two fundamentally different approaches partition spectral shape.

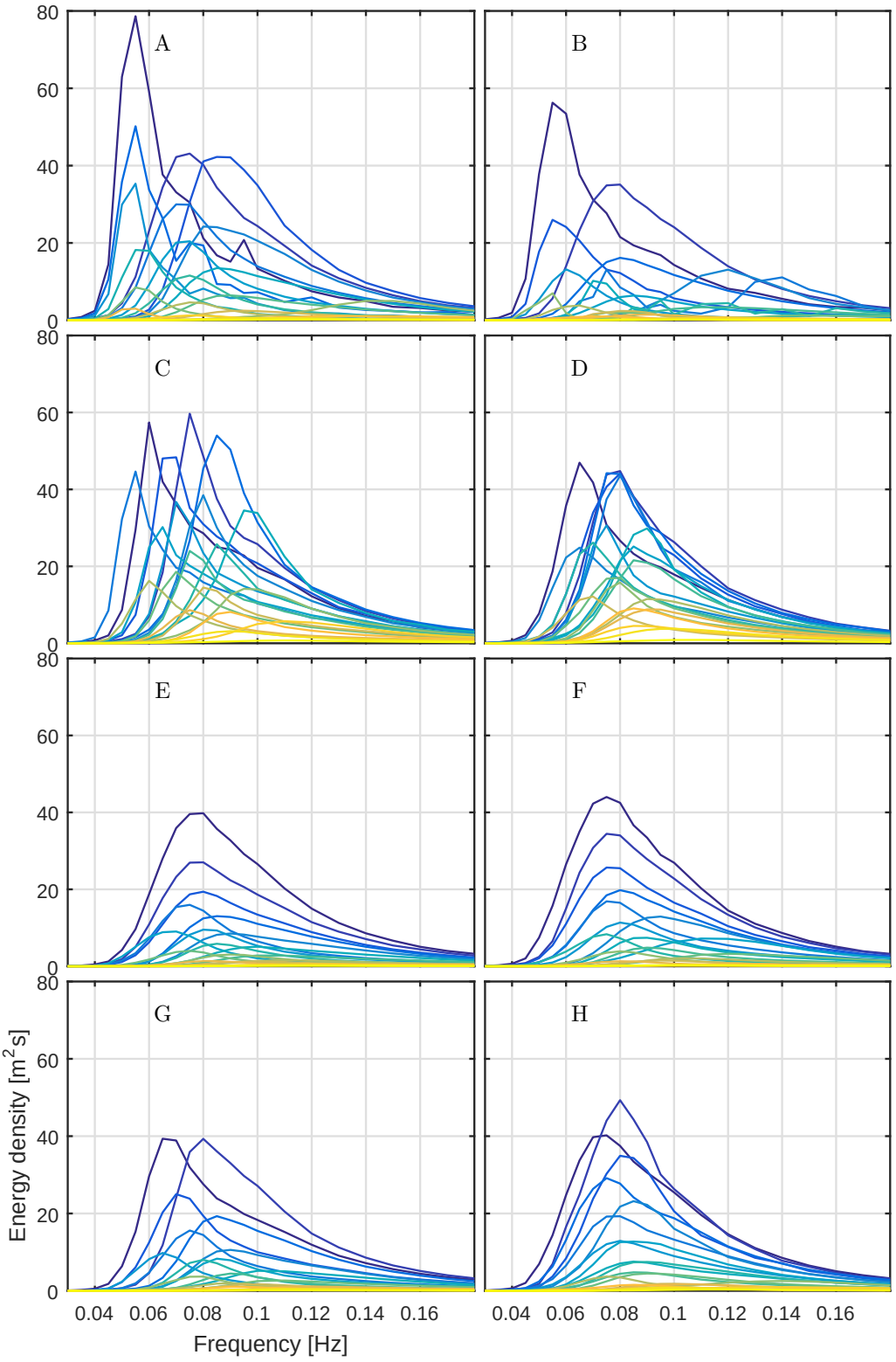

Figure 6.27: Resulting frequency spectra for classification methods for K=20. Colour indicates sea state power from dark blue (highest) to bright yellow (lowest)

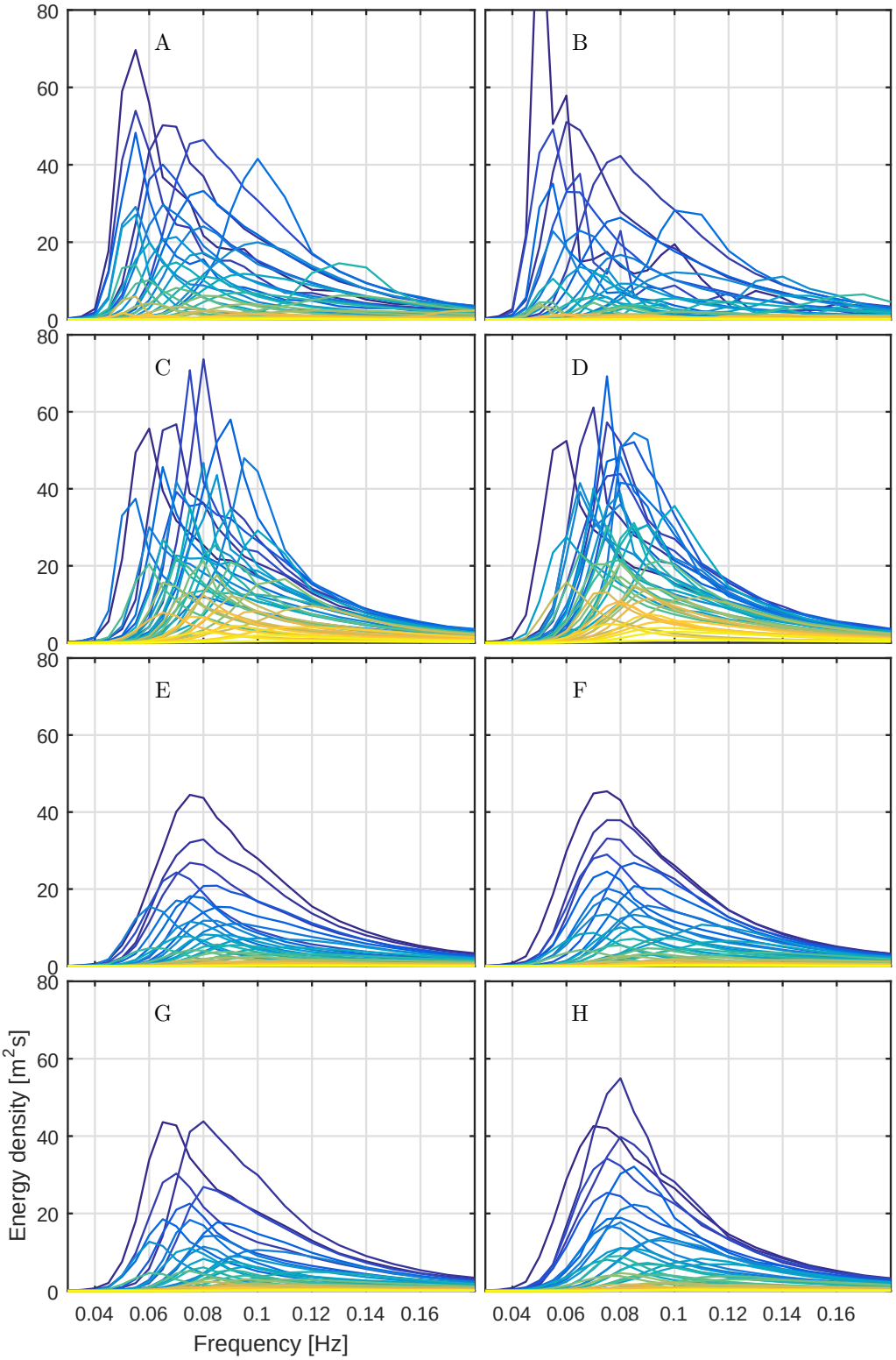

Figure 6.28: Resulting frequency spectra for classification methods for K=40. Colour indicates sea state power from dark blue (highest) to bright yellow (lowest)

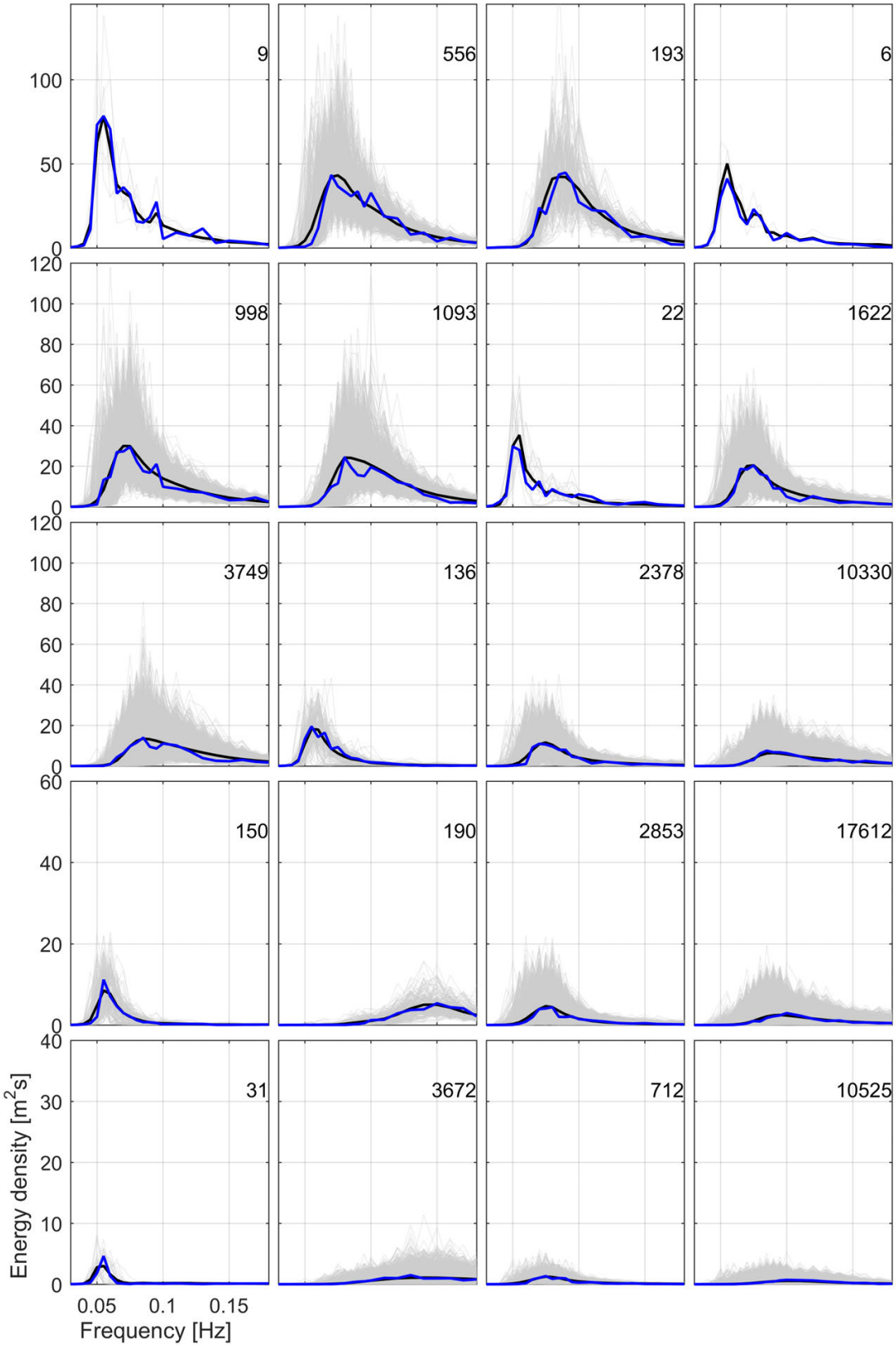

Figure 6.29: Resulting partitions in $S(f)$ space for method A with K=20. Mean spectrum shown in black, 'closest' spectrum to the mean shown in blue. Plots displayed in order of mean power in each group, from highest (top left) to lowest (bottom right).

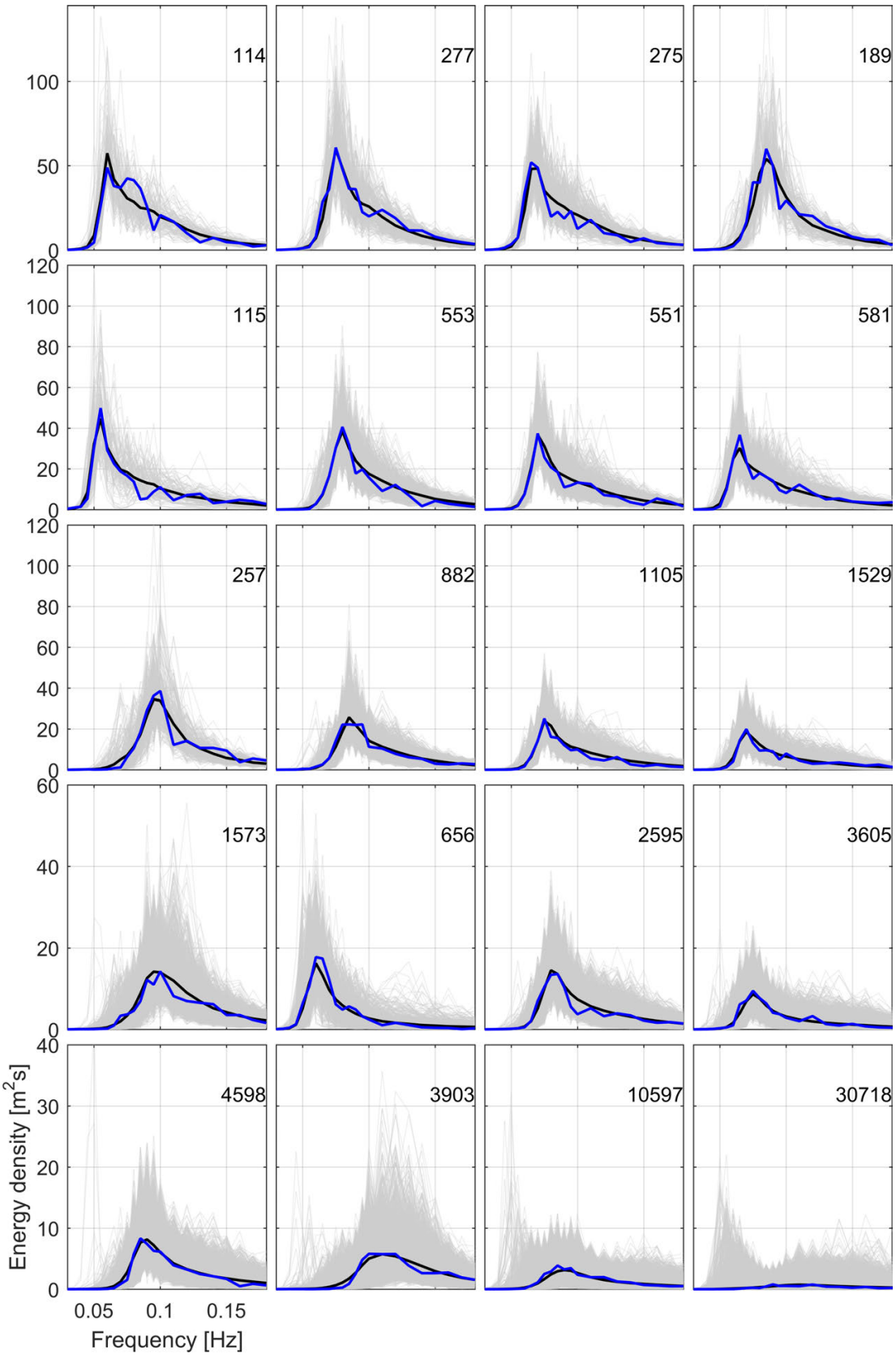

Figure 6.30: Resulting partitions in $S(f)$ space for method C with K=20. Mean spectrum shown in black, 'closest' spectrum to the mean shown in blue. Plots displayed in order of mean power in each group, from highest (top left) to lowest (bottom right).

6.4.3 Method Assessment & Discussion

6.4.3.1 Assessment of the Trialled Methods

There are 8 methods, 10 variables under consideration, and two outputs (K=20 and K=40) for each method type and as such there is a large amount of data resulting from this study, some of which are shown in Figs. 6.24 to 6.30. As one of the main aims is to assess the performance of clustering algorithms, this will be particularly focussed on, whilst trying to gain an understanding of the characteristics of the methods trialled. Of particular interest is the effect the characterisation focus and method of grouping has on the resulting partitions.

Performance Metric

As expected, from Fig. 6.24 it can be seen that for every method and all variables, increasing K from 20 to 40 causes an increase in the performance metric. Referring to Table 6.4 it can also be seen that those methods that focus on particular parameters, invariably perform well with respect to the parameters considered. The hypothesis that characterising the spectral form would automatically partition the derived statistical parameters does not appear to be the case, at least relative to other methods and for the K values used. Methods C and D perform very well with respect to the spectra under consideration, yet relatively poorly for practically all statistical parameters. It may be expected that by considering the shape of frequency spectra, that spectral bandwidth, ν, along with H_{m0} and T_E were bound to be well characterised. Equally, by considering the directional spectra it would seem likely that $\bar{\theta}$ and $\bar{\sigma}_\theta$ would be well characterised; yet in both cases this appears untrue. This is potentially due to an effective under-clustering, meaning that there is still too many dissimilar spectra in each group, which causes averaging over spectral detail and hence the resulting statistics. This highlights the inherent trade-offs present in such a constrained characterisation process.

Focussing on certain variables in the characterisation clearly improves their performance at the expense of others. Also significant, however, is the number of groups that are being created. Method E for example solely focusses on the joint values of H_{m0} and T_E, and proves to have significantly better performance metric than the other methods. However, method G, which applies the same approach before creating sub-clusters by $S(f)$, provides better performance for H_{m0} and T_E for K=40, than E with K=20, yet also has some consideration over spectral shape and hence will have much more realistic sea state outputs. A similar pattern is observed between F and H for a larger range of statistics and with $E(f,\theta)$ sub-clusters. This demonstrates that with more groups one can more effectively consider and categorise sea states using a greater number of variables. Without a limit on the number of sea states it would be possible to effectively characterise with respect to any number of variables, using a combination of methods.

As one of the key aims of this work is to produce realistic site-specific directional spectra, it is of interest how well each method performs with respect to the directional spectrum invariant criterion. As can be seen in Fig. 6.24, method D clearly provides a large increase in performance by considering the directional spectral form. This has implications over the validity of representative directional sea state creation, which is discussed in Sections 6.4.4 and 6.4.5.

Partitions

Assessing the H_{m0}-T_E partitions (Figs. 6.25 and 6.26), it is evident that methods C and D, clustering solely on spectra, have a tendency to focus on the high energy sea states and assign a large number of low energy sea states to a single group. This is a result of the units the clustering focusses on (energy density $\propto H_{m0}^2$), in addition to the nature of the K-means objective function. As the objective function aim to minimise the sum of the intra-cluster scatter, this causes a lower cost to the objective function to assign many low energy sea states in one group. High energy sea states are grouped more effectively as to avoid the higher numerical penalty if this is not achieved. This may be advantageous for certain applications, yet appears not to create tests that are automatically suitable for power matrix contribution.

Method E, which clusters on normalised H_{m0}-T_E pairs, visually provides very good irregularly sized partitions, explaining the high invariant criterion associated with it. This method, however, and indeed all of the clustering based methods, tend not to produce sea states with very high T_E values. This is again a result of the objective function response, this time to the much higher abundance of slightly lower period sea states. Methods F and G also provide reasonable partitions in H_{m0}-T_E space, despite having additional consideration of either frequency spectra, or extra statistics. This performance is again highlighted in the invariant criterion outputs (Fig. 6.24).

For both K=20 and K=40 the binning approach outputs are as expected. However, it seems fairly clear that the characterisation performed by method B for K=20, in H_{m0}-T_E space, is insufficient and that 40 sea states are required to obtain a useful distribution. For all methods there appears to be a large benefit in using 40 sea states, with practically all methods giving a desirable range of values, with the possible exception of methods C and D. Methods G and H do provide clustering outputs that, whilst consider the spectral form, also have the ability to provide good H_{m0}-T_E partitions. Interestingly, when K=40, method F provides good partitions in this space and as it considers a number of variables (Table 6.4) would be expected to partition similarly well with respect to all variables simultaneously.

Assessing the resulting frequency spectra in Figs. 6.27 to 6.28 it is evident that C and D cover the range of $S(f)$ space substantially, apparently providing an increase in spectra of any considerable magnitude. This ties up with the observations of Figs. 6.25 and 6.26, with the other methods tending to contain more low energy sea states, which on the displayed scale

renders them barely visible. Despite C and D apparently covering a better spectral range, it is methods A and B in this instance that provide the spectra with the largest peaks, and most unusual spectral detail. This is because the binning methodologies applied can result in bins with very small populations, thus averaging over a small number of spectra and preserving some of the apparent spectral complexity (although this may be an unrepresentative mean of dissimilar spectra). Mean and 'closest' to the mean spectra are shown in Figs. 6.29 and 6.30 for methods A and C to assess this. It is apparent that both methods provide mean spectra that correspond reasonably well to observed conditions.

In general it can be seen that there is a much larger deviation between the observed spectra in each of the method A partitions, compared with those from method C (Figs. 6.29 and 6.30). However, to achieve this method C 'dumps' over 30,000 spectra into a single highly-dissimilar group of low energy sea states. Method A also has some very large groups however, with three bins containing over 10,000 sea states, one of which contains over 17,000. This highlights a general problem with all of these approaches as implemented, in that some very large and dissimilar groups are likely to arise in this sort of over-constrained characterisation if abundance is not considered. Equally though, if abundance is considered in such a way as to ensure each group is not too large or small, then it is no longer purely driven by similarity, resulting in an overall reduction in intra-group compactness. This again highlights further trade-offs in this process, although these high abundances can be reduced as shown in Section 6.4.4.

Assessing the spectral shapes resulting from these characterisation processes (e.g. Figs. 6.29 and 6.30), it is evident that for the EMEC site this results in predominantly uni-modal frequency spectra. For groups with high abundance the averaging process also provides fairly typical spectral shapes, whereby parametric functions are likely able to approximate the majority quite effectively. For groups with low abundance more emphasis is placed on individual spectral estimates and as such these spectra are less typical. For the majority of sea states, however, it appears parametric functions may be sufficient to give a reasonable approximation of the underlying group frequency spectra. This suggests that considering the whole frequency spectral form is not always necessary, at least for this site where uni-modal spectra dominate. As shown in Fig. 6.35 and discussed in Section 6.4.5, the same cannot be said for the resulting directional spectra, suggesting that more attention may be required for the directional distributions.

6.4.3.2 Assessment of Performance Metric

Prior to using the proposed metric as an accurate measure of good grouping, one must question the validity of the metric for each particular application. The metric itself appears to provide sensible results, increasing with K and when parameters are particularly focussed on. For method B with K=20 and K=40 the number of directional bins remained constant and the mean direction metric remained very constant, also as would be expected. One surprising result,

however, was the apparently poor performance of H_{m0}-T_E binning (method A) for the H_{m0}, T_E and combined H_{m0}-T_E metrics relative to method E.

The metric includes both a measure of compactness, and distinctness, with equal emphasis placed on each. A high compactness metric, S_W^{-1}, ensures only similar sea states are grouped together, whilst a high distinctness, S_B, ensures resulting groups are dissimilar. From a site characterisation point of view it may be that group compactness is more important, ensuring that any mean spectra representing the group only averages over similar sea states, thus on average, more accurately representing individual groups. From a tank testing and device characterisation point of view however, it might be that distinctness is a higher priority, ensuring that the device is understood over a wide range of plausible conditions. This may be why the performance of method A is poorer than expected, in that the focus is on the distinctness whilst the compactness performance is essentially limited by the fairly large rectangular bins used. In the clustering approaches, however, the algorithm basically maximises the overall compactness and the distinctness arises from the best partitions that achieve this. Clearly weights could be placed on both compactness and distinctness if a clear preference was defined, however, it is suggested from this work that the metric be used more as an exploration tool rather than for numerical optimisation.

6.4.3.3 Methodology Assessment Summary

From the method assessments a number of conclusions can be drawn, which can help design a characterisation methodology fit for purpose. Some of the main outcomes are summarised below:

- As expected, focussing on a variable in the characterisation provides good grouping with respect to the variables considered.
  - This performance generally comes at the expense of other variables
- Unfortunately, clustering via the frequency or directional spectrum does not automatically provide good groupings with respect to the statistics derived from these spectra (i.e. all statistical parameters considered).
- Clustering on spectra, or statistics, tends not to provide sea states with high T_E, due to the relatively low abundance, yet a large range of T_E is potentially desirable to understand device response.
- It is possible to effectively consider a high number of statistical parameters in combination using clustering techniques on normalised statistical parameters.
- Increasing the number of sea states (K) invariably improves the grouping performance for all parameters and for every method. There is a significant increase in performance from K=20 to K=40.
  - Yet this means, for a fixed time-frame that sea states have to be shorter in length and as such have a poorer representation of extremes.

- None of the trialled methods provide a desirable range of H_{m0} and T_E whilst simultaneously providing good directional spectra groupings.

6.4.4 Generic Characterisation Choice: Realistic Directional Sea States with a good range of H_{m0} and T_E

The optimal choice of characterisation methodology will be application specific, dependent on the device in question, the purpose of the test regime and the stage of device development. These factors will massively influence which parameters are most desirable to preserve. It was thought, however, that it would to be useful to have a generic set of sea states that may suit a number of potential clients and tank users. Given the large performance increase of using 40 sea states, a value of K=40 will be aimed for, with 758 waves on average deemed acceptable for providing a good representation of extremes.

FloWave, being a circular combined wave and current test facility, tends to attract clients looking to assess their device in wave-current conditions, in directional waves, or both. Therefore it is desirable to include directionality, and in particular for site-specific tests, realistic directional distributions associated with observed directional spectra. Parametric seas will be able to include representative directional spreading functions (from mean $\bar{\theta}$ and $\bar{\sigma_\theta}$ values), yet to properly incorporate observed directionality a mean of the directional spectra in a group should be used. However, if the directional spectra itself is not considered in the characterisation process then this is likely not to be valid. If taking the mean spectrum when the spectral form has not been considered, artificial multi-modal seas will result along with smoothing out of features, which will create conditions that are highly unrepresentative of realistic scenarios.

In order to ensure that realistic representative directional spectra are created from the characterisation process, the directional spectrum will need to be considered. It is also thought, however, that clients will require a comprehensive range of H_{m0} and T_E so as to help contribute to power matrices, or to contextualise findings from these more realistic seas with respect to those already attained. From Figs. 6.25 and 6.26 it can be seen that clustering on directional spectra does not provide such a range and as such cannot be used alone. To rectify this, the sea states are initially binned by H_{m0} and T_E prior to creating sub-clusters of directional spectra within each bin. This will ensure a good range and distinctness of these primary sea state parameters, before also ensuring that each resulting group is similar in spectral form, thus picking out the main spectral shapes and allowing a more valid averaging procedure to take place.

To implement the proposed method the sea states are first binned into 21 H_{m0}-T_E bins (aiming for 20 non-empty bins) before clusters are created operating on the directional spectra within each bin. This was achieved using six bins of H_{m0} and four bins of T_E, guided by the higher emphasis placed on H_{m0} in the IEC guidelines. As discussed in Section 6.4.3 some of the resulting groups have a large number of sea state members and as such are likely to contain

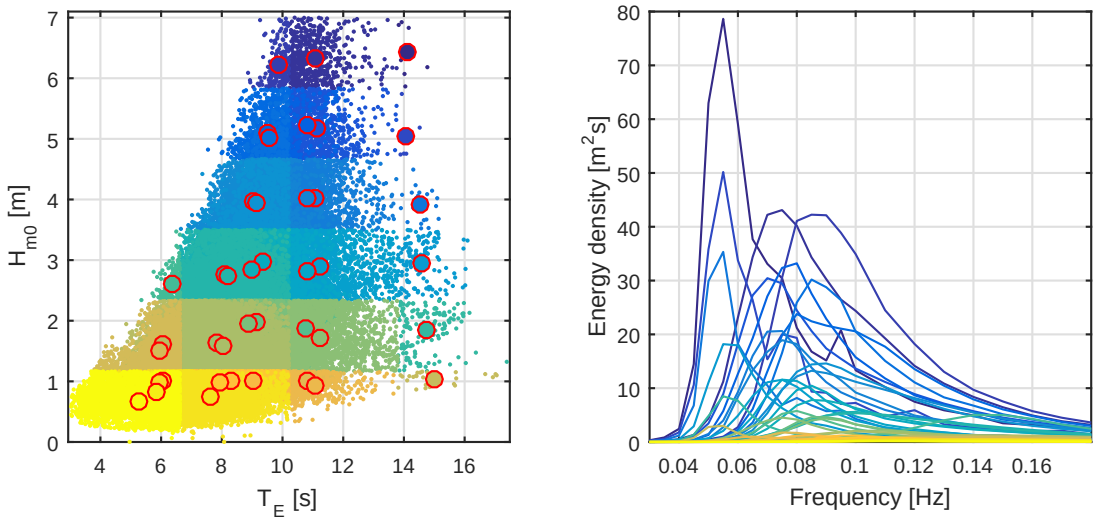

Figure 6.31: Outputs for generic characterisation in H_{m0}–T_E space, and resulting representative frequency spectra. Circles denote group centroids and are ordered by sea state power from dark blue (highest) to bright yellow (lowest)

an increased number of distinct directional spectrum classes. In an attempt to account for this effect somewhat and enable more classes to arise when there are a large number of seas, the number of sub-clusters in each bin is determined based on criteria imposed on the initial bin population. If a group contains over 10% of the population, four directional spectrum clusters are created, whereas if there are less that 1%, only one is created, with all others being split into two. This process forms 41 resulting groups.

The resulting partitions in H_{m0}-T_E space, along with the mean frequency spectra from each group are shown in Fig. 6.31. It is interesting to note that the resulting directional spectrum clusters in some of the bins result in very similar H_{m0}-T_E values. This demonstrates that there are highly different directional spectra in each bin, showing that the differences in spectral form dominate over the associated H_{m0}-T_E values and that there is a low local correlation between the directional spectral shape and these summary statistics.

Examples of the resulting directional spectra sub-clusters are shown in Figs. 6.32 and 6.33. It is evident that the methodology has enabled the isolation of highly distinct directional spectrum classes in each bin, differing in both mean direction and directional spread. It is clear that using the initial 21 bins to form representative seas would have resulted in unrepresentative conditions, highlighting further the value of creating more sea states and also the importance of considering the spectral form in the classification. These sea states provide a desirable range of primary sea state parameters, whilst simultaneously being representative of observed directional spectra. Parametric alternatives are created in Section 6.4.5, before the mean (non-parametric) spectra are scaled and generated in the FloWave tank in Chapter 7.

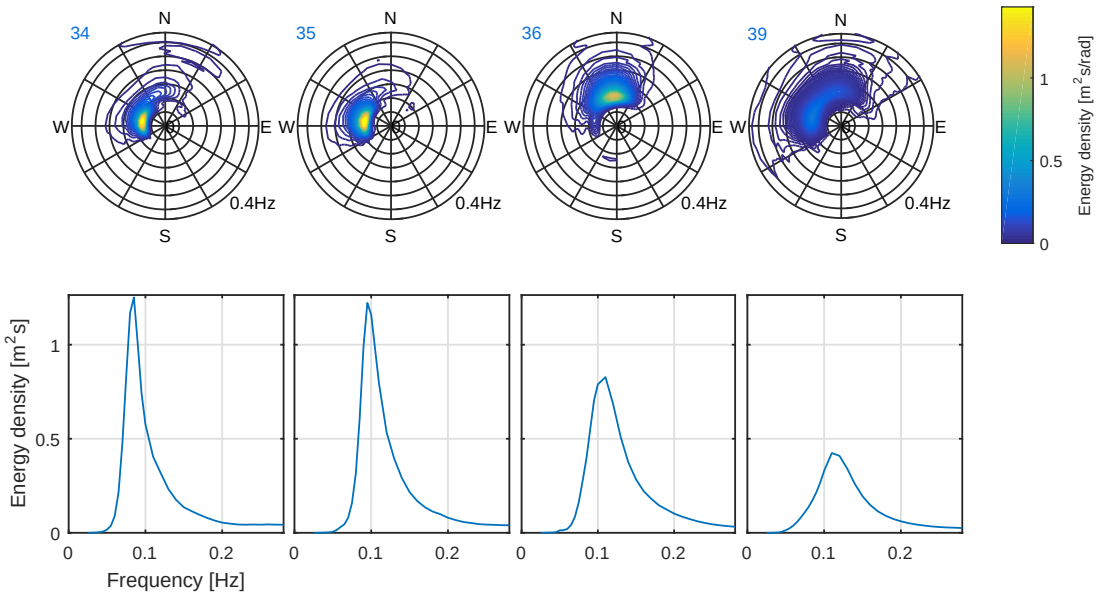

Figure 6.32: Mean frequency and directional spectra for the directional spectrum sub-clusters created within initial bins of 6.6 s<T_E<=10.2 s & H_{m0}<=1.17 m. Numbers relate to the power of the sea state from 1 (highest) to 41 (lowest) and correspond to numbers in Table 6.6

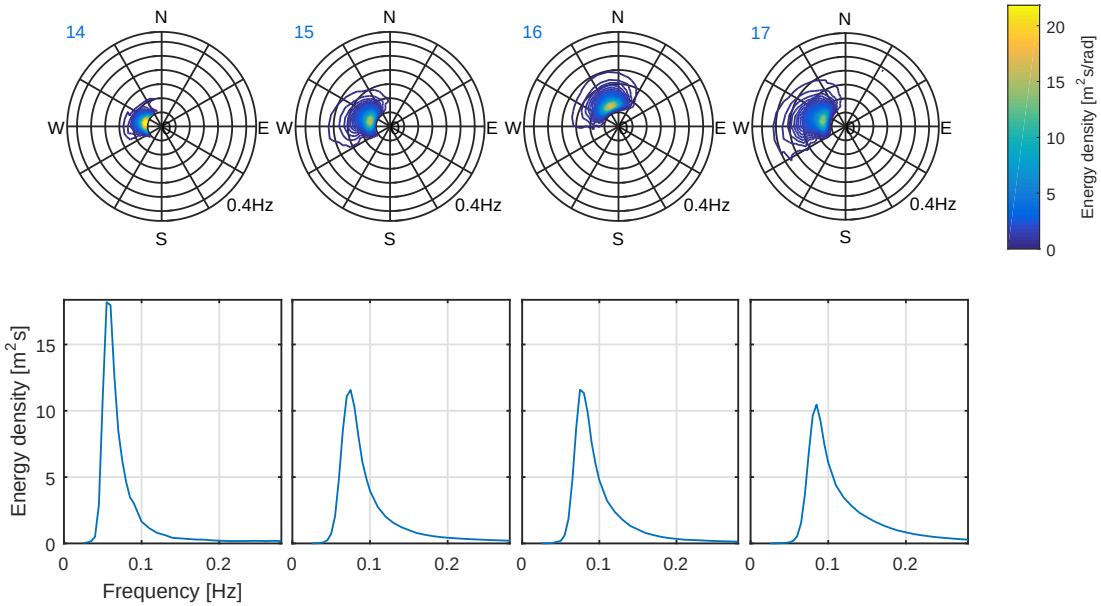

Figure 6.33: Mean frequency and directional spectra for the directional spectrum sub-clusters created within initial bins of 6.6 s<T_E<=10.2 s & 1.17 m<H_{m0}<=2.33 m. Numbers relate to the power of the sea state from 1 (highest) to 41 (lowest) and correspond to numbers in Table 6.6

6.4.5 Creating Representative Directional Sea States

To create representative directional spectra suitable for re-production in the tank the mean spectrum from each of the resulting groups can be used, as shown in Figs. 6.32 and 6.33. This should be reasonably valid given that the directional spectra has been considered in the characterisation (except potentially for when no sub-clusters have been created from the initial H_{m0}-T_E bins). These sea states should give realistic directional characteristics and frequency spectra. Additionally, as a mean has been taken, once abundance of each group has been considered, the resulting analysis of the device will be equivalent to being excited at every frequency and direction by the correct proportion of wave energy. This will enable more accurate power production estimates to be gathered than equivalent parametric approaches.

Some clients may require simpler spectral shapes, either for ease of understanding results, or so that they can be more easily replicated in numerical models. Some numerical models may have the ability to take in arbitrary directional spectra, yet it was thought necessary to have a simpler version of the representative seas, which can be described by a small number of parameters.

The parametric directional spectra have been created in two stages. First a JONSWAP spectrum has been fitted to the mean frequency spectrum, before a Gaussian directional distribution is created from the mean direction (circular mean) and mean directional spreading associated with each group. The JONSWAP spectra were fitted using a least squares approach, with limits of γ from 1–7 to ensure valid spectra are created. The fitted values, along with the mean directional parameters used and the relative abundance of each of the sea states are shown in Table 6.6. If these parametric sea states were to be used for testing this table could be provided to clients, enabling all information relating to the site characterisation and resulting test conditions to be communicated easily.

Some examples of the fitted JONSWAP spectra to the mean are shown in Fig. 6.34. The resulting parametric directional spectra are displayed in Fig. 6.35, along with the mean directional spectra from each group for comparison. It is apparent from Fig. 6.34 that the fitted JONSWAP can be used to quite effectively describe the mean frequency spectra for the instances shown. This is observed to be a representative selection, with an interesting finding being that almost all mean spectra are well described by JONSWAP spectral shapes.

Although some of the directional spectra are very similar for both the mean and parametric approaches, the same level of similarity observed with the frequency spectra is not present. As it is required to have a parameterised DSF, a frequency independent solution will be created. A Gaussian distribution was used for the DSF creation for these sea states. This is primarily because the data already contains calculated $\bar{\theta}$ and $\bar{\sigma}_\theta$ values which can be used directly as inputs. A cos^{2s} distribution could also be used for this purpose, but as shown in Fig. 6.7 the Gaussian and cos^{2s} approaches tend to give very similar results. As may be expected from Fig. 6.7, along with the knowledge that the EMEP approach has been used to create the

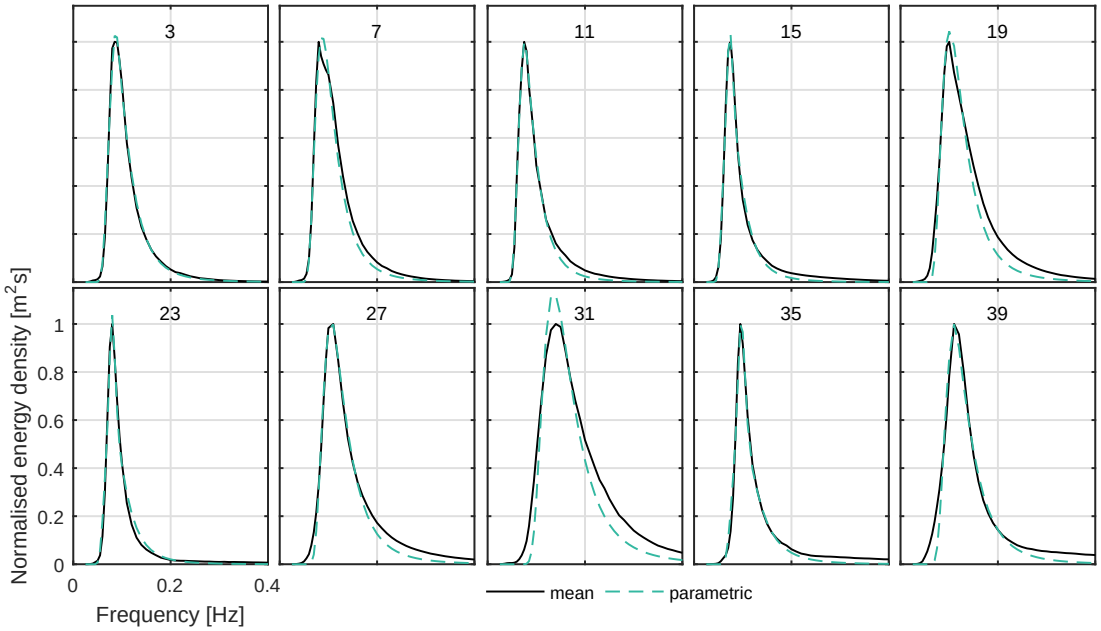

Figure 6.34: Example JONSWAP fit to mean frequency spectra, for directional spectra shown in Fig. 6.35

directional spectra initially, the parameterised directional spectra shown in Fig. 6.35 tend to be more directionally spread than the equivalent mean spectra. This in addition to being a symmetrical frequency independent distribution, means that any asymmetry and changes of spreading and mean direction with frequency are not effectively described. Clearly this would mean that creating parametric spectra for multi-modal systems would require partitioning and would be a difficult process, as explored in Ricci *et al.* (2011).

Despite the parametric sea states having some difficulty in describing some of the more detailed characteristics of the site, they still provide a useful alternative to the mean spectra when required. This provides two sets of generic spectra which can be used for site-specific testing, giving a good range of $H_{m0} - T_E$ values, whilst considering directional spectral similarity. These can be scaled and generated in the tank, as carried out in Chapter 7, and used to provide test outputs corresponding to realistic conditions at Billia Croo. A similar process could be applied to any dataset.

Table 6.6: Fitted values to mean spectra in each group. For use with JONSWAP frequency spectra and Gaussian directional distribution. Shown with relative abundance of each sea state from sea state with highest mean power (1) to lowest (41)

No.	H_{m0} [m]	T_p [s]	γ	$\bar{\theta}$ [deg]	$\bar{\sigma}_\theta$	Abundance [%]
1	5.94	18.1	1.60	291	0.54	0.01
2	5.97	13.5	1.00	295	0.53	0.86
3	6.22	11.5	1.15	296	0.51	0.30
4	4.63	18.1	1.63	287	0.50	0.01
5	4.78	14.0	1.10	286	0.55	1.33
6	5.00	13.0	1.21	324	0.55	0.21
7	4.87	11.5	1.00	285	0.53	1.33
8	4.89	11.4	1.40	323	0.53	0.36
9	3.57	18.8	2.40	284	0.56	0.03
10	3.78	13.7	1.33	287	0.55	2.22
11	3.85	13.2	1.11	325	0.53	0.29
12	3.70	11.2	1.00	286	0.55	4.57
13	3.82	11.1	1.00	328	0.55	1.22
14	2.91	17.5	1.86	285	0.55	0.21
15	2.80	13.6	1.40	286	0.56	3.08
16	2.79	12.8	1.57	328	0.52	0.59
17	2.79	11.7	1.44	285	0.56	3.96
18	2.71	11.1	1.08	333	0.54	2.66
19	2.57	9.9	1.00	281	0.57	4.48
20	2.54	10.0	1.00	314	0.59	4.88
21	1.83	17.7	2.37	284	0.59	0.23
22	2.58	7.0	1.38	291	0.56	0.29
23	1.92	12.6	1.72	329	0.56	0.63
24	1.88	11.3	1.58	286	0.57	4.69
25	1.86	11.0	1.43	332	0.57	2.96
26	1.71	13.5	1.52	287	0.59	3.79
27	1.56	9.5	1.05	330	0.59	7.55
28	1.47	10.1	1.00	287	0.62	12.03
29	1.50	7.3	1.00	280	0.61	2.59
30	0.96	19.0	4.04	293	0.66	0.05
31	1.31	7.4	1.00	322	0.59	3.08
32	1.01	12.8	2.04	288	0.63	0.57
33	0.82	14.9	1.08	298	0.69	0.53
34	0.90	12.0	1.79	287	0.66	1.96
35	0.96	10.3	1.81	288	0.63	2.13
36	0.94	9.6	1.17	335	0.61	3.15
37	0.94	7.3	1.00	340	0.58	1.18
38	0.87	7.5	1.00	286	0.65	1.60
39	0.70	9.1	1.07	306	0.68	9.04
40	0.72	7.4	1.00	335	0.63	2.48
41	0.43	9.4	1.00	248	0.68	6.86

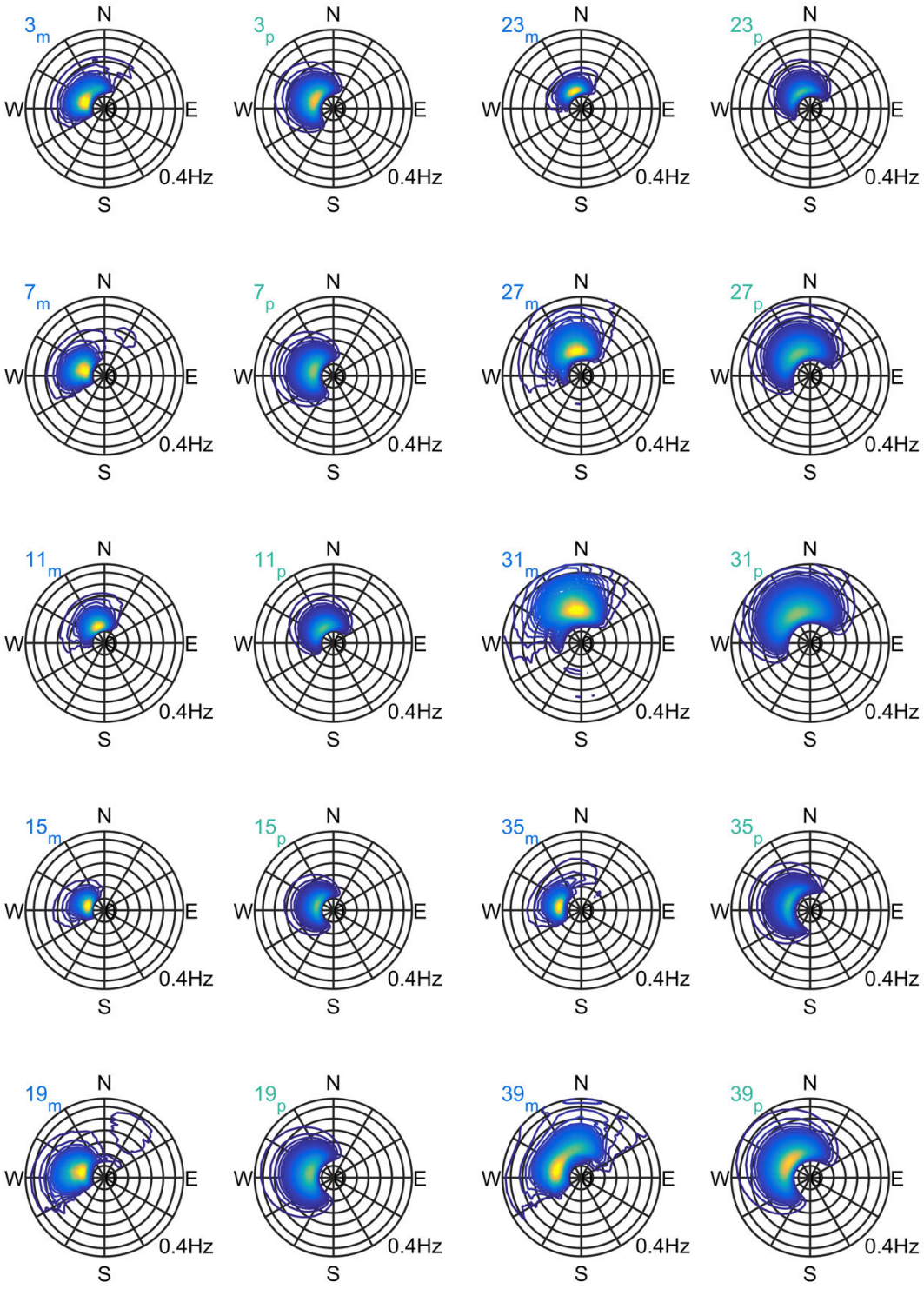

Figure 6.35: Example directional spectrum outputs for parametric and mean approaches.

6.5 Implications for Testing

A simple yet effective way of obtaining realistic extreme conditions from site data has been described, based on bivariate probability distributions and a scaling-shifting procedure applied to observed spectra. These sea states, when used for tank testing or numerical modelling, will increase the realism of extreme device response and hence from the subsequent analysis and knowledge gained should help reduce risk in device development.

Methods of creating characteristic/representative sea states have been assessed, exploring alternatives that can retain more detailed information, thus resulting in more realistic representative conditions. Due to the constrained nature of the problem it was found that there are large trade-offs introduced when particular variables are focussed on. This demonstrates that when creating these characteristic sea states, the aim of the testing should be explicitly considered. Using combinations of the methods trialled it is shown that spectral similarity can be considered whilst additionally maintaining a good range of the typically desired H_{m0} and T_E values. Although just an example output, it shows that large scale data reduction can be carried out whilst preserving at least some of the more detailed characteristics. These sort of more considered characterisation procedures should help increase test realism and similar to the extreme sea outputs, provide more realistic device response and more accurate site-specific findings prior to deployment.

One of the interesting outputs resulting from the Billia Croo site characterisation was that the resulting frequency spectra were reasonably well described by JONSWAP spectral shapes, however the directional distributions differed significantly from parametric alternatives. This is perhaps a site-specific outcome, however suggests that parametric spreading functions are not representative of real ocean distributions even when averaged over hundreds or thousands of sea states.

Chapter 7

The Re-creation of Site-Specific Sea States

This chapter takes the non-parametric representative site-specific directional sea state outputs from Chapter 6 and demonstrates that they can be scaled and generated at FloWave. The resulting spectra for both the extreme and production sea states are scaled, replicated, and corrected. Tank limits are considered in this process, whilst additionally focussing on the consequences of not scaling spectra to the desired ratio of site to tank depth. The wavelength and power errors incurred when this is required are assessed. When non-depth ratio scaling is necessary, the approach of scaling the wavenumber or power spectra rather than the frequency spectra is also explored; assessing and describing alternatives to the standard methodology. These approaches may be useful when devices are highly sensitive to wavelength and for instances where sea state power representation is paramount.

Additionally, it is demonstrated that correct site-specific directional spectra can be effectively created in a variety of current conditions. This is potentially important to ensure that wavelength, steepness and power are fully represented (along with direct current effects e.g. mooring loads). It is demonstrated that corrected site-specific directional spectra can be re-created with current, using three current velocities and five relative angles.

Highlights:

- Power and wavelength errors incurred through non-depth ratio scaling investigated for FloWave/Billia Croo. Alternative scaling approaches demonstrated with examples, showing that at non-depth ratio scales power *or* energy distribution can be ensured across frequency *or* wavenumber.
- Extreme and production Billia Croo derived sea states scaled, generated, corrected and validated at FloWave and show good agreement with the desired spectra. The SPAIR method is used for validation.
- Influence of current on wave parameters assessed, highlighting importance of inclusion in testing. This capability is demonstrated with a non-parametric directional Billia Croo sea state with a range of currents and relative angles, and measured using a PTPD approach. This demonstrates that the true complexity of combined conditions can be

simulated at FloWave, whilst additionally showing that the PTPD approach is significantly more effective at inferring directional characteristics in current.

7.1 Scaling

7.1.1 Issues To Consider

Froude scaling is used to scale sea states in order to obtain the correct ratio between inertial and gravitational forces, which are dominant for ocean waves (as discussed in Section 2.2). To achieve this properly there are multiple issues to consider, which are a function of the sea state in question along with the characteristics and limitations of the facility. Generally, frequency spectra are Froude scaled to produce model sea states. However, if they are scaled and reproduced at any ratio other than the depth ratio, there are potential wavelength and power discrepancies to consider, differing from the desired Froude scaled values. For all but deepwater conditions, non-depth ratio scaling makes it is impossible to Froude scale all elements of a sea state. As WECs are typically proposed for intermediate water depth due to mooring costs etc, these errors are particularly important to quantify.

In addition to pure scaling issues it is also important to consider additional 'model' effects introduced by carrying out scaled tests in a laboratory. Considering the laboratory itself there are considerations over the frequency limits of the tank, both the absolute limits (0.2–2 Hz), and the frequency dependent wave height limits. In some circumstances, dependent on spectral shape, it may not be possible to scale to the depth ratio whilst avoiding frequency limitations in the generation. One may also consider the quality of the conditions as a soft constraint in this process. In addition, constraints on the availability or type of model components (e.g. Power Take Off (PTO)) or facility limitations may necessitate physical models being built using non-depth-ratio dimensions, and hence tests will have to be generated at the required model scale.

7.1.1.1 Sea State Representation Issues due to Incorrect Scaled Depth

Fig. 7.1 shows the influence of scale on the wavelength discrepancy from the desired Froude scaled values, as a function of full scale frequency, for scaled Billia Croo frequency spectra being reproduced at FloWave (52 m to 2 m). Wavelength error is zero when scaled at the depth ratio, or for frequency components that were in deep water condition, and remain to be deep water in the 2 m depth FloWave tank, at the given scale. When neither of these conditions are true, it is clear that there are significant differences between the desired Froude scaled wavelength and that obtained by Froude scaling the frequency spectra. This could have large implications for devices which are highly sensitive to wavelength as the device response will not correlate with the equivalent full scale response in the same frequency spectrum. This is discussed further in Section 7.1.4.

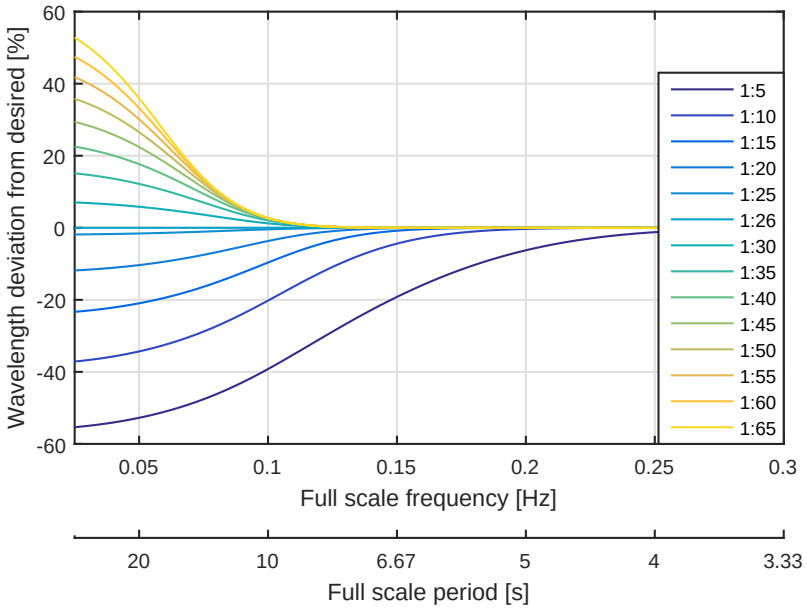

Figure 7.1: Effect of scale on wavelength discrepancy from desired Froude scaled value for a range of frequencies and scales. Shown for Billia Croo frequency spectra scaled to FloWave, with depths of 52 and 2m respectively

Errors in component wave power (from Eq. (7.1)) resulting from the group velocity discrepancy at non-depth ratios are shown in Fig. 7.2. Similarly to wavelength, large errors are possible when not scaled to the depth ratio. The discrepancy in power is more complex than that observed for wavelength, where for a given scale the sign of the discrepancy is now dependent on the frequency. As a result of this, if operating at a small scale (e.g. 1:60), swell components may increase in power, whilst higher frequency wind-seas will show a decrease from the desired. This discrepancy is clearly important to quantify, particularly if undertaking power production tests.

$$p(f) = S(f)\rho g C_g(f,k); \qquad P = \int_0^\infty p(f)\delta f \tag{7.1}$$

The alternative approach of Froude scaling wavenumber spectra rather than frequency spectra is explored in Section 7.1.4, which would ensure the correct distribution of energy with wavelength, but not frequency. Additionally power spectra are scaled, ensuring that the correct power is present at each frequency but both frequency and wavenumber spectra will now differ from the desired Froude scaled values.

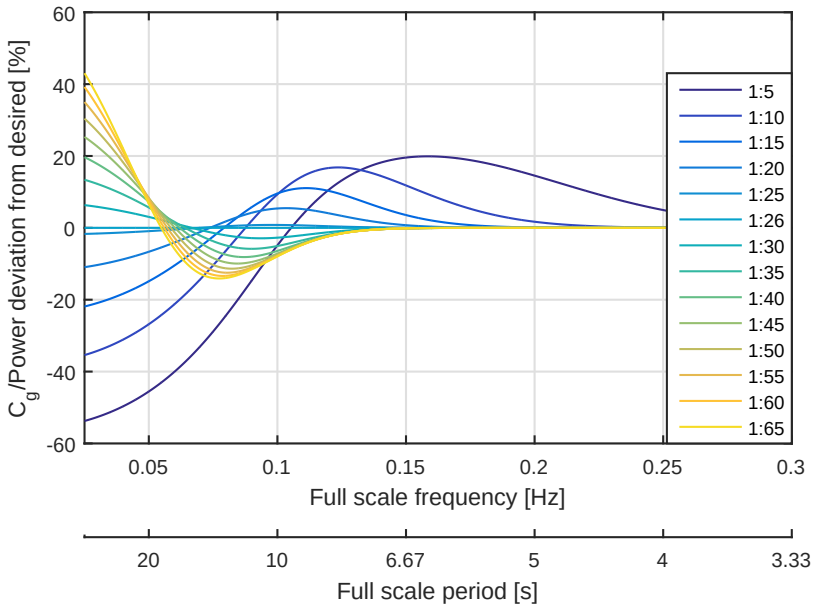

Figure 7.2: Effect of scale on power discrepancy from desired Froude scaled value for a range of frequencies and scales. Shown for Billia Croo frequency spectra scaled to FloWave, with depths of 52 and 2 m respectively

7.1.1.2 Tank Wave Generation Limits

If the correct depth ratio is used as the scale ratio, then sea state representation errors do not need to be considered, but some sea states may breach practical frequency and height limits associated with a test facility. At FloWave there are frequency limits imposed in the software of 0.2–2 Hz, meaning no components can be generated outside these limits. Clearly some energy falling out of these bounds would be acceptable up to a point, which can be specified separately for both high and low frequency breaches depending on the device sensitivity. More importantly in most cases is the wave height (f) limits, as if the tank cannot generate the sea state safely this cannot be negotiated.

There are essentially two methods for obtaining the wave generation limits for the FloWave facility. Limits can be calculated by the Edinburgh Designs Wave Synthesiser software, which is based on a combination of linear wave theory and wavemaker theory, calculating the required paddle motions to generate the specific wave field and assessing whether or not this is possible. Due to the assumptions made in this approach, sometimes it has been found that the practical limits are somewhat lower than predicted, affecting either wave quality or generation/absorption capability. There is therefore a separate set of somewhat more conservative recommended limits used at FloWave, which are based on well defined limits for regular waves. For irregular waves it is not possible to specify an absolute significant wave height limit for each peak frequency due to the effect of generating waves using a random phase method. Some random phases may produce ‘clipping’ whilst others may not, which is another reason for

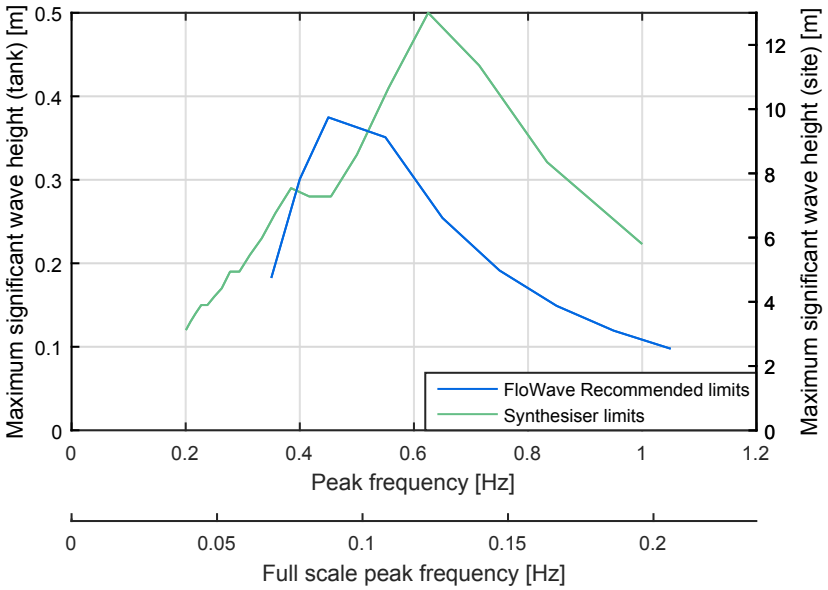

Figure 7.3: Wave height limits from Edinburgh Designs' Synthesiser, and recommended FloWave tank limits. Shown relative to equivalent full scale frequency and wave height (1:26 scale)

adopting more conservative limits. These two sets of limits are shown in Fig. 7.3. Due to the limited frequency range of the defined recommended limits, Wave Synthesiser limits will be used for prospective sea states with parameters outside this range.

7.1.2 Scaling Production Sea States

From dimensional analysis, Eqs. (7.2) and (7.3) can be used to Froude scale the production frequency (and directional) spectra created in Section 6.4.4 and Section 6.4.5. λ_s is the scale factor, which for 1:26 scale is defined as 1/26, with $_{fs}$ denoting full scale and $_s$ as Froude scaled.

$$S_s(f_s) = S_{fs}(f_{fs}).\lambda_s^2.\sqrt{\lambda_s} = S_{fs}(f_{fs}).\lambda_s^{2.5} \tag{7.2}$$

$$f_s = f_{fs}.\sqrt{\frac{1}{\lambda_s}} \tag{7.3}$$

To avoid the requirement for multiple test models of differing scale it is highly desirable to have all production sea states at a single scale. When scaling these production sea states it was found that there is not an individual scale factor that enables all sea states to not breach wave height limits or have significant energy outwith the hard frequency limits. Due to this and importantly to avoid wavenumber and power spectra errors, it was decided to generate these seas at the depth ratio i.e. 1:26 scale. If wave height limits are breached, they cannot be generated, and if they have a large proportion of the spectral energy outside the hard frequency limits, they are also not generated. For these sea states limits were set such that only 1% of energy can be

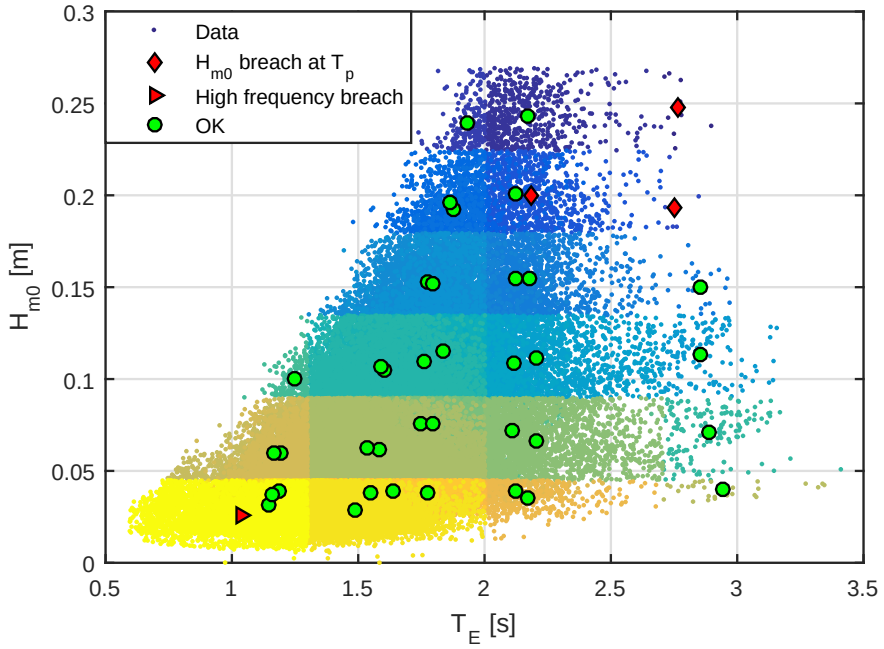

Figure 7.4: Scatter plot of production sea states scaled to 1:26 scale. Representative sea states that breach defined limits are highlighted in red

below 0.2 Hz and 10% above 2 Hz, on the assumption that the energy at these high frequencies is unlikely to affect device response significantly. This is defined in Eq. (7.4).

$$\frac{\int_0^{0.2} S_s(f)\delta f}{\int_0^{\infty} S_s(f)\delta f} < 0.01; \qquad \frac{\int_2^{\infty} S_s(f)\delta f}{\int_0^{\infty} S_s(f)\delta f} < 0.1 \tag{7.4}$$

The mean spectra resulting from the characterisation process (Section 6.4.4) have been scaled, and after applying the criteria, 37 of the 41 defined production sea states remain valid. Fig. 7.4 shows that three of these sea states cannot be generated due to breaching wave height limits, and an additional sea state cannot be generated as a result of having a large proportion of energy over 2 Hz (note that wave height limits are based on T_p not T_E). The scaled mean representative directional spectra associated with these spectra can now be generated, measured and validated, which is carried out in Section 7.2.

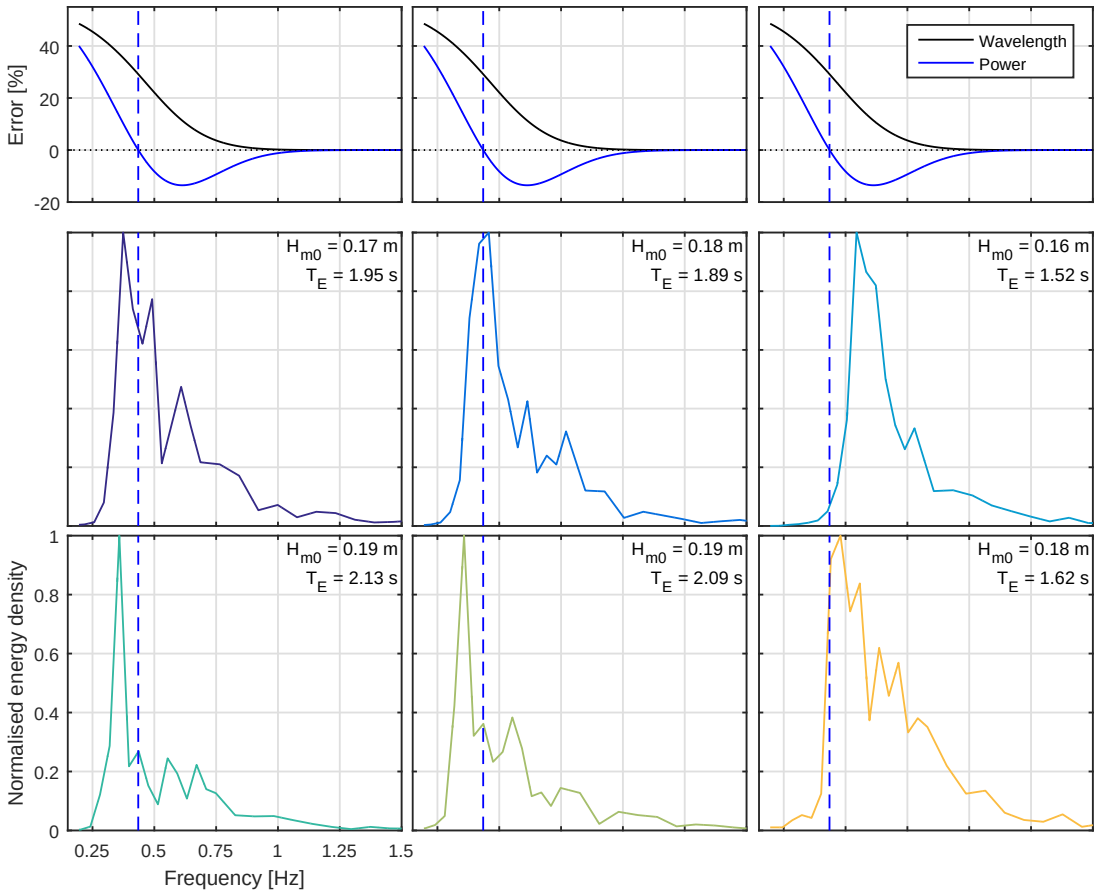

Figure 7.5: Extreme sea frequency spectra scaled to 1:61 scale. Resulting relative frequency dependent wavelength and power errors at this scale shown above

7.1.3 Scaling Extreme Sea States

Assessing the wave height limits in Fig. 7.3 and noting that the example extreme sea states identified have wave heights of between 10 and 12m full scale, it is clear that they will not be able to be generated at 1:26 scale. it is therefore not possible to test a single scale model in both the production and extreme sea states. The default extreme seas are scaled frequency spectra, as are the standard approach and hence will be more widely accepted. These sea states are, however, used in Section 7.1.4 to demonstrate other scaling approaches.

As in Section 7.1.2 it is desirable to generate all sea states at a single scale. The largest scale all of the extreme spectra can be generated at without breaching wave generation limits is 1:61, meaning that there will be significant power and wavelength errors associated. The scaled frequency spectra, along with these errors are shown in Fig. 7.5, demonstrating the areas of each spectra that are associated with both positive and negative deviations from the desired Froude scaled power, along with the extent of wavelength discrepancy.

7.1.4 Alternative Scaling Approaches

As discussed in Sections 7.1.1 to 7.1.3 there are potential wavelength and power errors incurred when Froude scaling frequency spectra. The production sea states have been scaled at the depth ratio and therefore frequency, wavenumber and power spectra are Froude scaled correctly. However, when models cannot be built to the desired scale, or when the desired sea states breach tank limits (e.g. the example extreme sea states), then another scale is required. When this is the case it is not possible to get the desired relationship between frequency and wavenumber (and group velocity etc.), but it is possible to obtain the correct energy *or* power distribution with respect to frequency *or* wavenumber.

If a device is seen to be more sensitive to frequency than wavelength, for example a point absorber, then it may be a good assumption that RAO's can describe the body motion and that the typical frequency scaling approach is acceptable. However, if a structure is comparable in size to wavelengths present, or is a multi-body device, then clearly these distances relative to the wavelengths are going to have a large influence over the response. In these instances there is influence from both frequency and wavelength, yet if the wavelength effects are seen to be dominant, wavenumber spectrum scaling may be more appropriate to simulate site conditions.

When not scaling to the depth ratio, frequency and wavenumber spectra will both produce incorrect power spectra i.e. wave power distribution across frequency or wavenumber. As shown in Fig. 7.2 at FloWave this discrepancy is a function of scale factor and frequency, as well as depth. Noting Eq. (7.1), the overall sea state power is also very likely to be incorrect and as such power production tests will be unrepresentative. It is suggested here that this can be corrected by scaling the power spectra, however wavenumber and frequency spectra will now be incorrectly Froude scaled. This will be shown here with the power frequency spectra, but an equivalent procedure for the distribution of power with wavelength could also be carried out with analogous results.

Table 7.1 details the values that can be guaranteed to be Froude scaled ($_s$) from the full-scale ($_{fs}$) values by each of the scaling approaches, along with the other values obtained ($_o$) from the approach. Defining an energy or power distribution across either frequency or wavenumber means that the other parameters are fixed via the dispersion and group velocity relationships. These will differ from their desired values depending on the discrepancy between the tank depth and the desired Froude scaled depth. Importantly, group velocities cannot be effectively Froude scaled when non-depth-ratio scaling as a result of being a function of both frequency and wavenumber.

Table 7.1: Effect of Various Scaling Methods on other Parameters (Froude scaled parameters shown in blue)

	$S(f)$ scaling	$S(k)$ scaling	$p(f)$ scaling
$S(f)$	$S_s(f_s) = S_{fs}\lambda_s^{2.5}$	$S_o(f_o) = \frac{S_s(k_s)2\pi}{C_g(k_s,f_o)}$	$S_o(f_s) = \frac{p_s(f_s)}{C_g(k_0,f_s)\rho g}$
$S(k)$	$S_o(k_o) = \frac{S_s(f_s)C_g(k_o,f_s)}{2\pi}$	$S_s(k_s) = S_{fs}(k_{fs})\lambda_s^3$	$S_o(k_o) = \frac{S_o(f_s)C_g(k_o,f_s)}{2\pi}$
$p(f)$	$p_o(f_s) = S_s(f_s)C_g(k_o,f_s)\rho g$	$p_o(f_o) = S_o(f_o)C_g(k_s,f_o)\rho g$	$p_s(f_s) = p_{fs}(f_{fs})\lambda_s^3$
f	$f_s = f_{fs}\sqrt{\frac{1}{\lambda_s}}$	$f_o = \frac{\sqrt{gk_s\tanh k_s h}}{2\pi}$	$f_s = f_{fs}\sqrt{\frac{1}{\lambda_s}}$
k	$2\pi f_s = \sqrt{gk_o\tanh k_o h}$	$k_s = k_{fs}\lambda_s$	$2\pi f_s = \sqrt{gk_o\tanh k_o h}$
C_g	$C_g(k_o,f_s)$	$C_g(k_s,f_o)$	$C_g(k_o,f_s)$

7.1.4.1 Effect of Different Scaling Approaches on Resulting Spectra

To assess how the different scaling approaches affect the resulting spectra, the extreme sea states will be used as examples. At 1:61 scale the resulting frequency, wavenumber and power spectra from each of the scaling approaches are shown in Fig. 7.6. From this it can be seen that for frequency and power(f) spectrum scaling, the effect of producing waves at too small a scale causes a wavelength increase as shown in Fig. 7.1. This results in the peak energy lying at higher wavelengths and hence lower wavenumbers than the desired Froude scaled values. Similarly, to obtain the correct wavenumber distribution, (S_k scaling), higher frequencies are required.

The power spectrum has been calculated with respect to frequency and as such the power and frequency spectrum scaling appear similar, only differing in magnitude rather than 'location' as a result of the discrepancy shown in Fig. 7.2. In all cases the total power is less than the desired when using wavenumber spectrum scaling (around 5-10%). This is to be expected as the higher frequencies used to obtain the desired, shorter wavelengths, are associated with lower C_g values at this depth and scale and hence cause a power decrease. For the frequency spectrum scaling, whether or not total power is above or below the desired value depends on the spectral shape.

Regardless of the scaling approach it is apparent that it is only possible to obtain energy or power correctly distributed across either frequency or wavenumber. The distribution across the unconsidered variable will differ significantly from the desired Froude scale values.

Although the scaled extreme frequency(-direction) spectra will be used as default, these additional sets are now available if desired and deemed appropriate. This sort of analysis also provides a means of quantifying inherent errors in wavenumber, power, wavenumber spectra

etc. and will be highly useful when model scale does not match the depth ratio of potential deployment sites (e.g. Billia Croo); helping contextualise results and understand discrepancies.

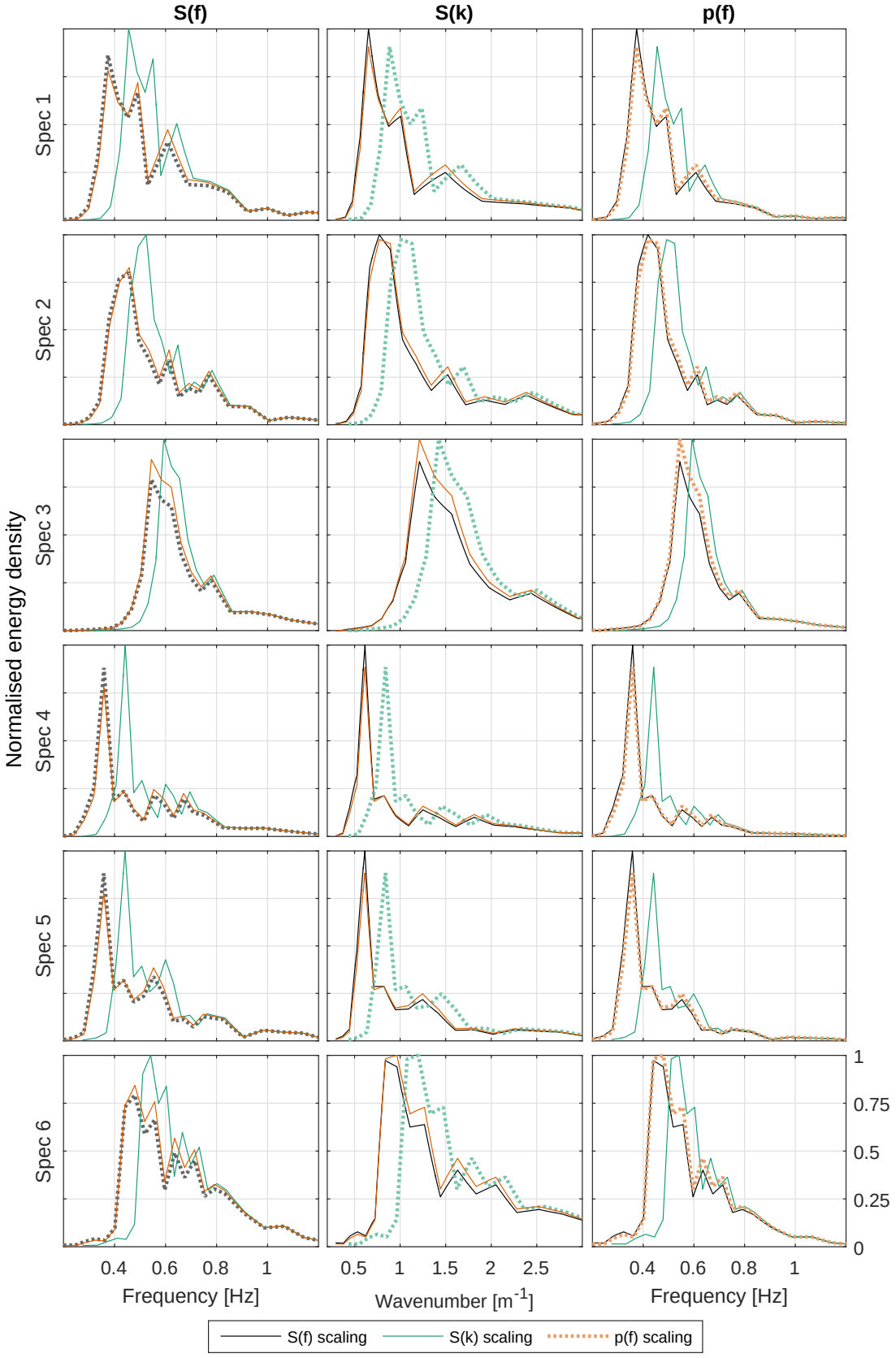

Figure 7.6: Effect of different scaling approaches on resulting spectra for extreme sea states. Scaled at 1:61 scale with 52m site depth and 2m tank depth. Desired Froude scaled spectra shown in bold with dotted lines

7.2 Re-creating Site Specific Wave Conditions

This section brings a number of outputs together, using the tools developed in combination with the sea state characterisation outputs to demonstrate the ability to reproduce representative site-specific directional wave conditions. The Froude scaled extreme and production directional spectra from Billia Croo (created using a combined binning-clustering approach in Section 6.4.4 and scaled in Section 7.1.2) are generated using a single summation approach (Section 4.1.1.2). The SPAIR method developed in Chapter 5 is used in combination with the directional array and rig designed in Section 3.4 to provide measurements of the incident and reflected directional spectra, frequency spectra and time series. This enables characterisation of the generated representative conditions, which is used to inform a correction and validation procedure to improve the outputs.

7.2.1 Production Sea States

The 37 Froude scaled production sea states that do not breach constraints (see Fig. 7.4) have been generated using repeat times of 1024 s. This has been achieved using the single summation method, with 32 directions from $-\frac{3\pi}{4}-\frac{\pi}{4}$ and 64 frequency increments from 0 to 2 Hz (with no energy below 0.2 Hz). Having the angular range over π rather that 2π means that the directional spectrum can have twice the directional resolution and with the chosen range, omits virtually no spectral energy for any of the sea states.

The directional sea states have been measured, and analysed using the SPAIR method (computational domain from 0 to 2π). Linear, amplitude based, correction factors have been identified (Section 4.6) based on the calculated incident spectrum, before being applied to the input spectra and re-generated. The final sea states for the example spectra in Fig. 6.35 are shown in Fig. 7.7, with the corresponding incident frequency spectra and reflection coefficients shown in Fig. 7.8. The final sea states shown have been analysed using the SPAIR method, but using pre-defined input angles as discussed in Section 5.4.2. This is because from Section 4.3.1 it is known that the incident wave angles are correct, and with this assumption more accurate directional spectra and reflection coefficients can be obtained which results in more accurate correction factors.

The directional distribution error approximation as defined in Section 5.3.1 ($NTD_E - NTD_S$) is shown in Fig. 7.9. For some sea states it is apparent that the discrepancy is very small, whilst for others there is still significant error/uncertainty associated. It is thought that the errors overall are higher (mean $NTD_E - NTD_S$ of 7.3%, with mean NTD_E of 13.19%) than observed in Fig. 5.5 due to a large number of very small amplitude sea states high peak frequencies. Sea states of this type are generally generated and absorbed more poorly, whilst measurement error is larger due to the relative effect of noise, vibration etc.

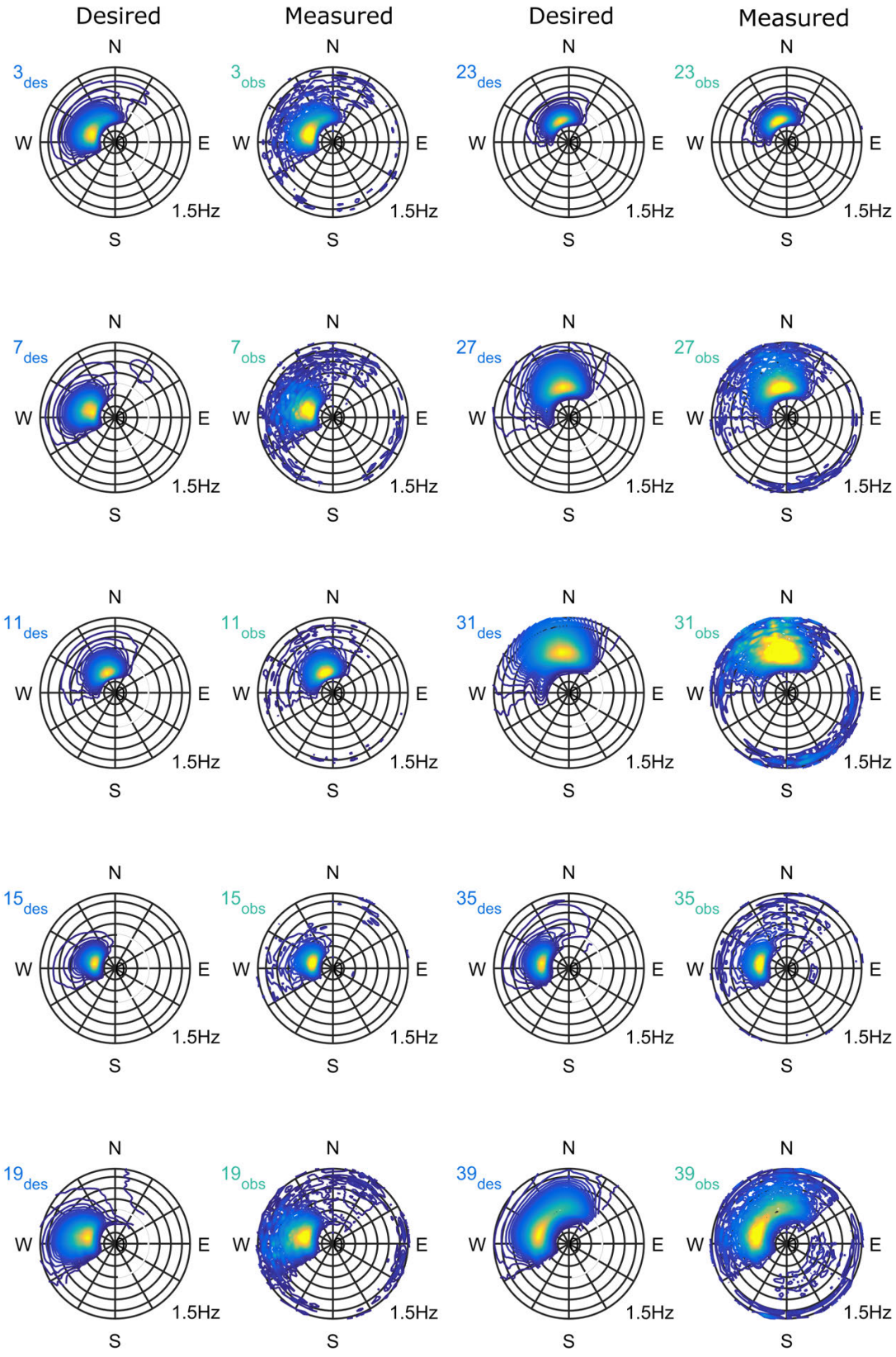

Figure 7.7: Example SPAIR method directional spectrum outputs for the example representative spectra shown in Fig. 6.35

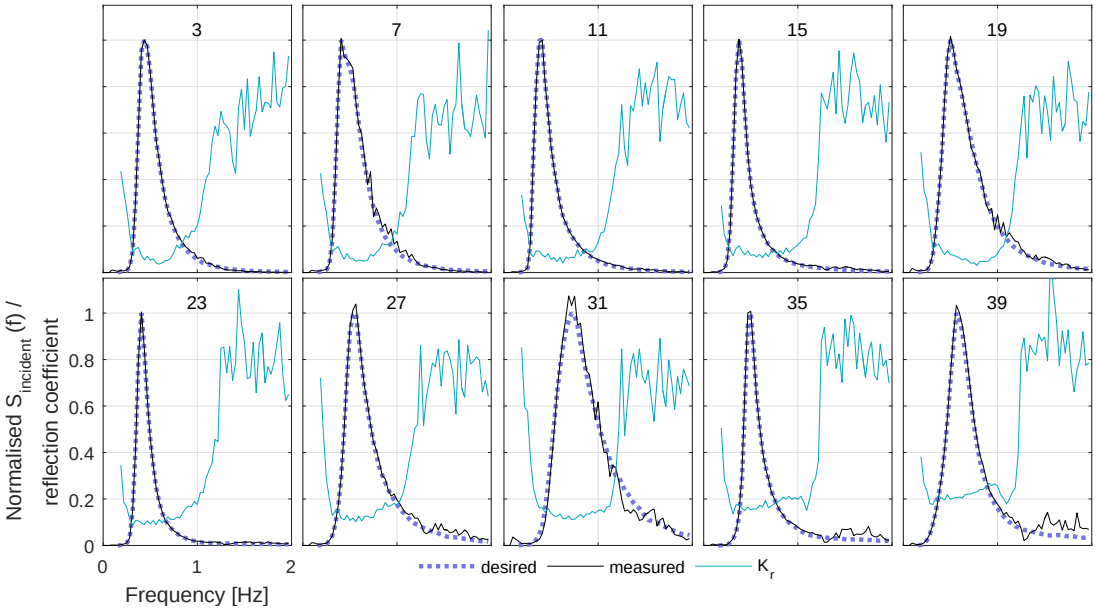

Figure 7.8: Example SPAIR method incident frequency spectrum outputs for the example representative spectra shown in Fig. 6.34

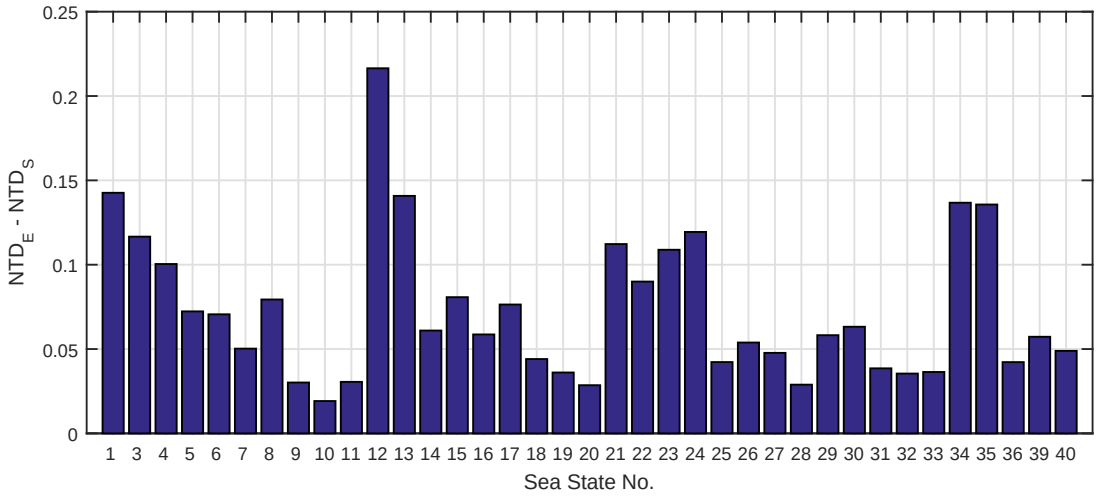

Figure 7.9: Final NTD_E-NTD_S values for representative production sea states

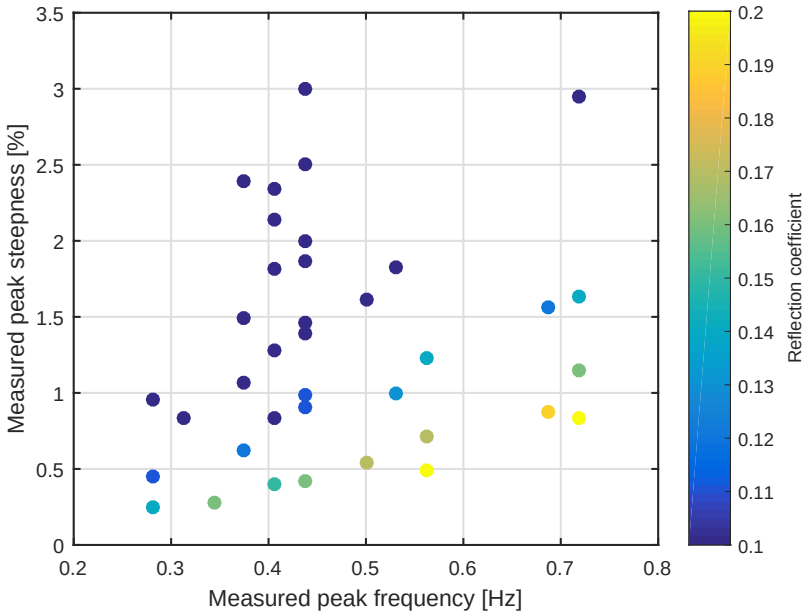

Figure 7.10: Calculated weighted reflection coefficients for measured f_p and steepness values

Details for all 37 final sea states can be found in Appendix A, including all directional and frequency spectra, and frequency-dependent reflection coefficients. The weighted total reflection coefficients are shown in Fig. 7.10 as a function of measured peak frequency and steepness. The same trend is observed for these sea states as in Section 4.4, with low steepness–high peak frequency sea states displaying larger reflection coefficients. This can also be inferred from assessing the frequency dependent reflection coefficients shown in Fig. 7.8 and Fig. A.5.

It is apparent from Figs. 7.7 and 7.8 that the final sea states have been very effectively created and corrected. With the relative abundance known, inferences can be made about how any device tested in such conditions would respond in the full-scale equivalent conditions, whilst quantifying and considering unavoidable discrepancy such as reflections. The considered characterisation approach (combined clustering and binning) to create these sea states should provide confidence that they are truly representative of the site's range of conditions and spectral complexity.

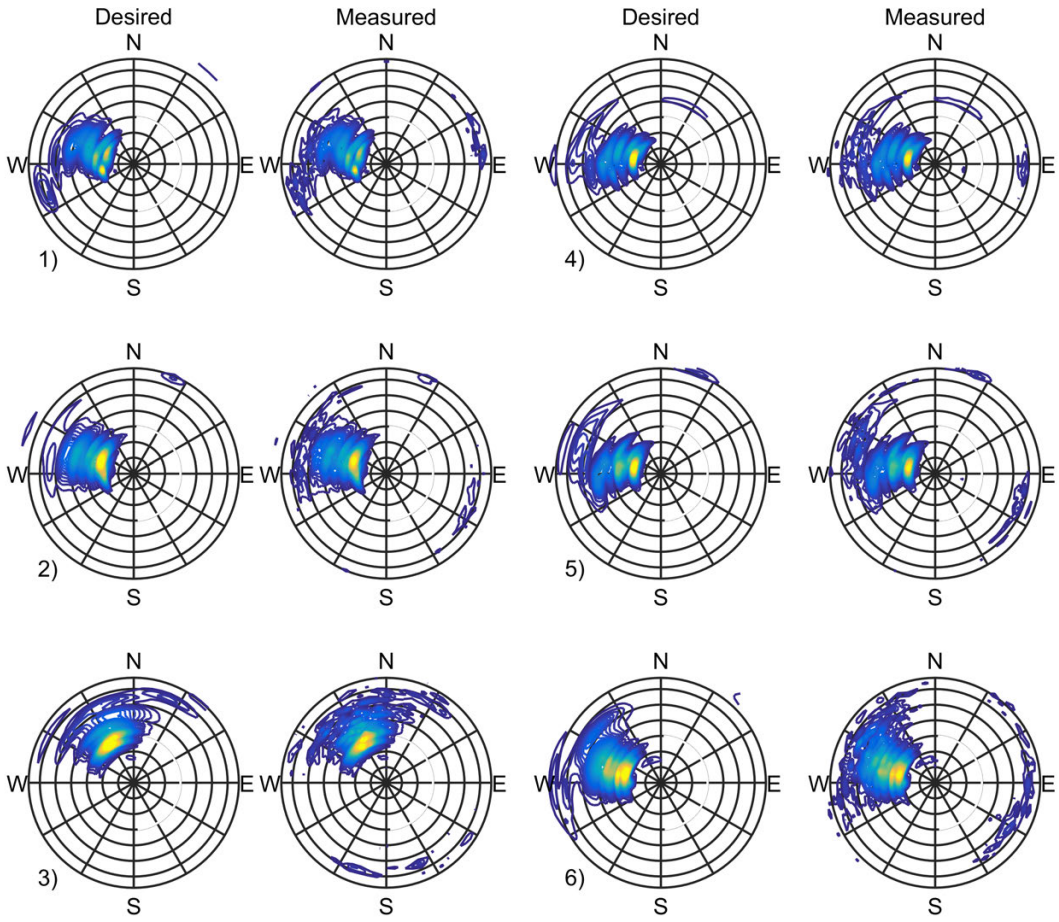

Figure 7.11: SPAIR method directional spectrum outputs for the example extreme spectra

7.2.2 Extreme Sea States

The same procedure carried out for the production sea states has been applied to the extreme frequency spectra at 1:61 Froude scale. The final corrected directional spectra are shown in Fig. 7.11, with the final incident frequency spectra and reflection coefficients in Fig. 7.12.

Similarly to the production sea states it is shown that the resulting corrected spectra are very close to the desired, with NTD_E values of 9.7, 8.6, 22, 8.3, 9.4 and 16% for sea states 1 to 6 respectively. These sea states, or similar, may be used for testing in extreme conditions at Billia Croo. However, if opting for this typical frequency-scaled approach the power and wavelength errors shown in Fig. 7.5 should also be noted to contextualise the findings.

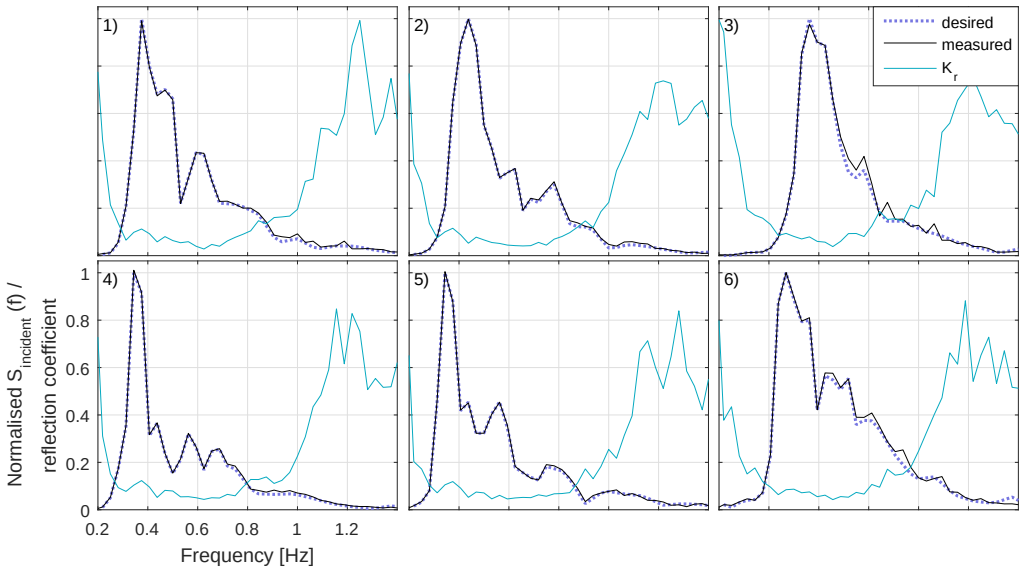

Figure 7.12: SPAIR incident frequency spectrum outputs for the extreme sea states, compared with desired. Shown with calculated frequency dependent reflection coefficients

7.3 Creating Site-Specific Wave-Current Conditions

This section is part of a joint piece of work carried out with Donald Noble (IDCORE and FloWave) and has been submitted as a paper, for publication in Ocean Engineering (Draycott *et al.*, 2017). This work has largely been a joint effort in terms of test design, implementation and write-up, and although text has been modified to fit with the thesis, much of this section has been jointly written. In addition to the joint work, there are also significant individual contributions that have been combined to create the work, namely:

Research into theoretical wave-current interaction theories was carried out by Noble, and all previous current characterisation at FloWave has been presented in Noble *et al.* (2015).

The theoretical analysis on changes to wavenumber spectra, power and steepness was carried out by the author of this thesis. The author also took the lead on the obvious applications of the previously presented research to this problem, including directional sea state measurement and analysis, as well as the implementation of correction procedures.

This section aims to demonstrate that site-specific directional wave–current scenarios can be re-created effectively. This is important as some wave site locations have non-negligible current velocities present, which alter both the form of the waves and the power available. This is in addition to the direct effects a current may have on any device/structure. If a current is present, then to truly replicate wave conditions it must be generated in the tank, because although the frequency spectrum and thus wave heights can be re-created, the relationship between wavenumber and frequency cannot (similar to non-depth ratio scaling in Section 7.1.4). This causes sea state power and steepness to be misrepresented.

Initially in this section the influence of current on the wave field is explored, before assessing what the assumed wave conditions would be without knowledge of this current (i.e. known frequency spectrum and assuming standard dispersion relation applies). This demonstrates the importance of measuring current at wave sites. It is then shown that if this current was known, then the correct combined conditions can be re-created at FloWave by means of correcting input amplitudes. This is carried out with regular waves, a long-crested JONSWAP, and a non-parametric representative EMEC directional spectra taken from Draycott *et al.* (2015c), all with comparable wave heights and frequencies. Each of the wave conditions are observed and corrected for a range of relative angles and for a range of current velocities, providing interesting non-collinear wave-current interactions in the process.

7.3.1 Effect of Current on the Wave Field, and the Assumed Wave Field

Current transforms the wave field, including wave height and length, which alters the form of the frequency and wavenumber spectra. Importantly this alters sea state power and steepness. Wave buoys, including the Datawell Waverider buoys deployed by EMEC, typically measure heave, pitch and roll. The resulting frequency spectra are calculated from the heave motions, whilst the directionality is inferred through cross-correlation of the three signals (Earle, 1996). If a current is present at the site, the sea surface elevations and hence calculated frequency spectrum will represent the altered wave field, but without knowing the corresponding change in wavelength.

If it is assumed there is no current, wavenumber spectra calculated for the recorded frequency spectra will be incorrect, as will steepness and power. This has large implications for the assumed resource available, along with the form of the waves. Additionally, if a spectrum is replicated in a test environment without current, this would fail to capture the true nature of the site conditions.

7.3.1.1 Transformation of Wave Spectra in the Presence of Current

For waves in the absence of current, wavenumbers can be calculated via Eq. (4.15), with corresponding wavenumber spectrum and group velocities calculated from Table 7.1 and Eq. (4.13), along with the measured frequency spectrum $S(f)$. Component and total power can then be calculated from Eq. (7.1).

Steepness for wave spectra is assessed by significant steepness, S_p^* (Eq. (7.5)), and for this work is calculated from the wavelength associated with the peak of the wavenumber spectrum, L_p^*, and . L_p^* has been defined thus, rather than from the wavelength associated with the peak frequency, for two reasons. Firstly, the wavelength associated with the peak of the wavenumber spectrum does not always equal that obtained from f_p, as discussed in Plant (2009). The peak energy lies at the wavelength associated with the wavenumber peak so using this value provides a more representative figure for the true steepness of a sea state. Secondly, this definition allows for a consistent comparison of steepness between cases with and without current.

$$S_p^* = \frac{H_{m0}}{L_p^*} \tag{7.5}$$

To assess the influence of current, a spectrum can be broken down into component amplitudes using Eq. (4.2) or Eq. (4.5), and operated on individually under the assumption of linear wave theory and linear wave-current interaction, before being reconstructed.

In the presence of current, wavelength is no longer related to frequency through the standard dispersion relation, Eq. (4.15), instead a modified relation, Eq. (7.6) is used (Jonsson, 1990). In the following equations, subscripts $_1$ and $_0$ refer to regions with and without current respec-

tively. Importantly, the wavenumber in the presence of a current, k_1, will differ from k_0.

$$\omega - k_1 U = \sqrt{g k_1 \tanh k_1 h} \tag{7.6}$$

The current modified component wave amplitudes can be calculated assuming conservation of 'wave action' (Jonsson, 1990):

$$\frac{\partial}{\partial x}\left(\frac{E\left(C_{gr}+U\right)}{\omega_r}\right) = 0 \tag{7.7}$$

Where E is the wave energy and x the direction of wave propagation. The subscript $_r$ denotes variables relative to the current, i.e. assuming a frame of reference moving at the same velocity as the current. The relative angular velocities and group velocities can be expressed as

$$\omega_r = \sqrt{g k_1 \tanh k_1 h} \tag{7.8}$$

$$C_{gr} = \frac{1}{2}\frac{\omega_r}{k_1}\left(1 + \frac{2k_1 h}{\sinh 2k_1 h}\right) \tag{7.9}$$

Equating wave action between regions with a steady current, U, and no current, Eq. (7.7) can be rearranged to relate wave amplitudes (Smith, 1997):

$$A_1 = A_0 \sqrt{\left(\frac{C_{g,0}}{C_{gr,1}+U}\right)\left(\frac{1}{1+\frac{U}{C_{gr,1}}}\right)} \tag{7.10}$$

The transformed frequency spectrum can be reconstructed using Eq. (7.11), noting this results in the same transformation as that formulated in Chakrabarti and Johnson (1995):

$$S_1(f) = \frac{\left(A_1(f)\right)^2}{2\Delta f} \tag{7.11}$$

The wavenumber spectra, available power and wave steepness in the presence of a current can be calculated via Table 7.1 and Eqs. (7.1) and (7.5) using the relevant terms with current as appropriate.

7.3.2 Assumed Power and Steepness if Current Modification Omitted

The calculation of power and steepness for waves in the presence of a current will give incorrect results if the wavenumber transformation described in Section 7.3.1.1 is not also included. This situation could arise when using measurements from a wave buoy where there is no knowledge of the current and thus the wavelength change. The measured transformed spectrum, $S_1(f)$, has associated wavenumbers $k_1(f)$. With the assumption of no current, wavenumbers $k_0(f)$ are calculated using Eq. (4.15), rather than using Eq. (7.6) to get $k_1(f)$. This assumption leads

to incorrect calculation of group velocities and wavenumber spectra, hence the power and steepness will also be incorrect.

To demonstrate the effect of current on both the transformed and assumed spectra, a Pierson Moskowitz (PM) spectrum with H_{m0} of 5 m and T_p of 8 s is used to show the effect over a wide range of frequencies. This has been analysed with both opposing and following current velocities of 0.25, 0.5 and 1 m/s. The significant wave height is found to increase to 6.38m with 1 m/s opposing current, and decrease to 4.14m for 1 m/s following current.

The transformation of frequency and wavenumber spectra are shown in Fig. 7.13, along with the wavenumber spectrum that would be assumed without the knowledge of the current present. In opposing flow, waves increase in steepness and thus spectral magnitude increases, with associated reduction in wavelength shown as a shift to higher wavenumbers. The opposite is true of the following current conditions.

For the assumed case with no current, there is no shift in wavenumber and hence the steepness change will be under-estimated. In addition, the group velocity is unaltered which causes an over-estimation of the change in power. This is shown in Fig. 7.14, where maximum discrepancy is the 1 m/s opposing case, under-estimating steepness by 18.6% and over-estimating power by 26.9%. This demonstrates the importance of measuring current at a site if it is expected to be significant, in order to obtain a realistic resource assessment and site characterisation.

When tank testing with realistic site conditions, the associated current should be included, so that conditions mimic the site and results inferred from the testing are representative. The correct wavenumber for each frequency component cannot be attained without the current, but are implicitly correct if the current and scaled depth are accurately reproduced. It is important the frequency spectrum is correct in order to obtain the desired wavenumber spectra, power and steepness. At FloWave this requires a correction procedure as a result of the current transformation, so input amplitudes must be altered. This process is detailed in Section 4.6 and demonstrated for a range of combined wave-current conditions in Section 7.3.4.

7.3.3 Combined Wave-Current Test Conditions

The wave current correction procedure was applied for wave conditions of varying complexity. Tests were conducted with regular waves, a long-crested parametric JONSWAP spectrum and the non-parametric directional sea state derived from the EMEC data. To facilitate comparison, the height and period of the initial waves were chosen to roughly match the representative EMEC sea state (see Table 7.2). Each of the wave cases were produced and measured in the tank with a range of representative currents.

The representative EMEC sea state was taken from the characterisation approach deemed most favourable from Draycott *et al.* (2015c). From this classification, a multi-modal sea state has

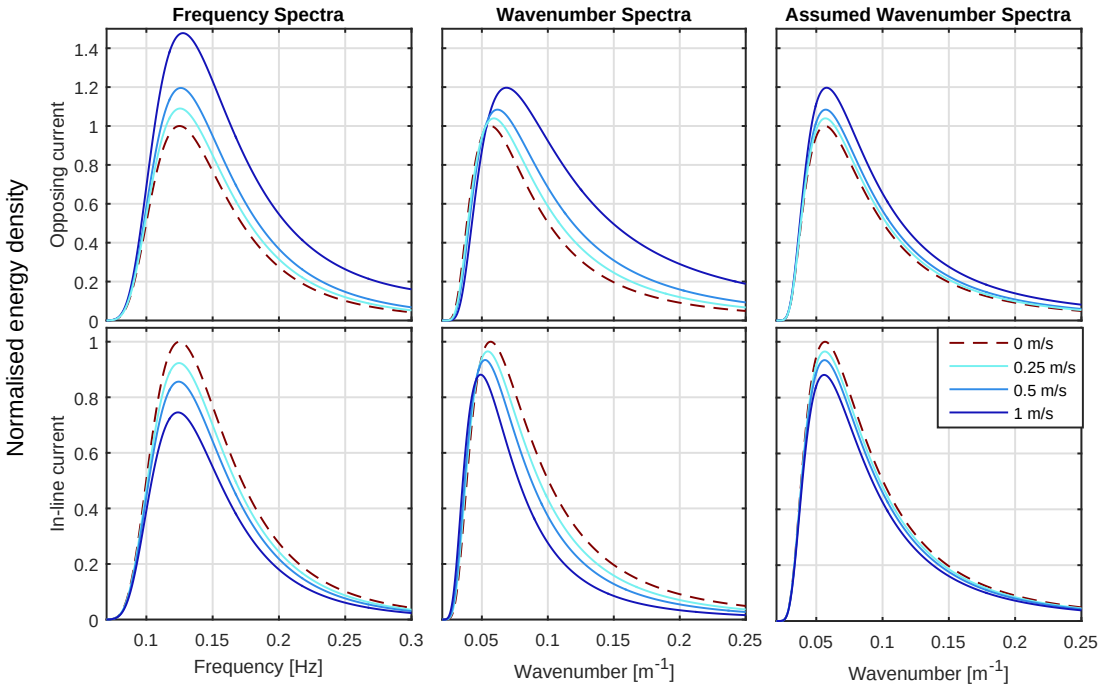

Figure 7.13: Change in example PM spectrum (H_{m0}=5 m, T_p=8 s) in the presence of in-line and opposing currents. Panels show the real frequency and wavenumber spectra, along with the wavenumber spectra assumed without knowledge of the change in wavelength resulting from the interaction with current.

been chosen, representing approximately 0.14% of the dataset. This representative sea state has a significant wave height, $H_{m,0}$ of 3.53 m, a peak period, T_p of 20 s and mean power, P of 87.6 kW/m. The frequency and directional spectra, along with the weighted Directional Spreading Function (DSF) are shown in Fig. 7.15. The sea state has been scaled to 1:26 scale as no wave height and frequency limits are breached (see Section 7.1.1.2).

Using the Atlas of UK Marine Renewable Energy (ABP MER, 2012), the peak tidal velocity at the Billia Croo site is expected to be between 0.5 and 1 knots which is approximately between 0.25 and 0.5 m/s. At 1:26 (Froude) scale, this corresponds to 0.05 and 0.1 m/s respectively in the tank. An additional velocity of 0.2 m/s was also used to demonstrate the method effectiveness in faster currents, where the wave-current interaction is greater and more non-linear.

Previous published work on wave-current interactions has largely focussed on collinear cases; waves either propagating in the same direction as the current, or directly opposing it. Thomas (1981), Kemp and Simons (1982a) and Kemp and Simons (1982b) made analogous observations of regular waves with collinear current, whilst Hedges *et al.* (1985) and Chakrabarti and Johnson (1995) carried out investigations with uni-directional spectra. Nwogu (1993); Guedes Soares *et al.* (2000) assessed directional spectra, although with a small set of conditions and limited presentation of results for oblique conditions. The capability of the FloWave facility permits the testing of non-collinear cases, with the waves at an arbitrary angle to the current

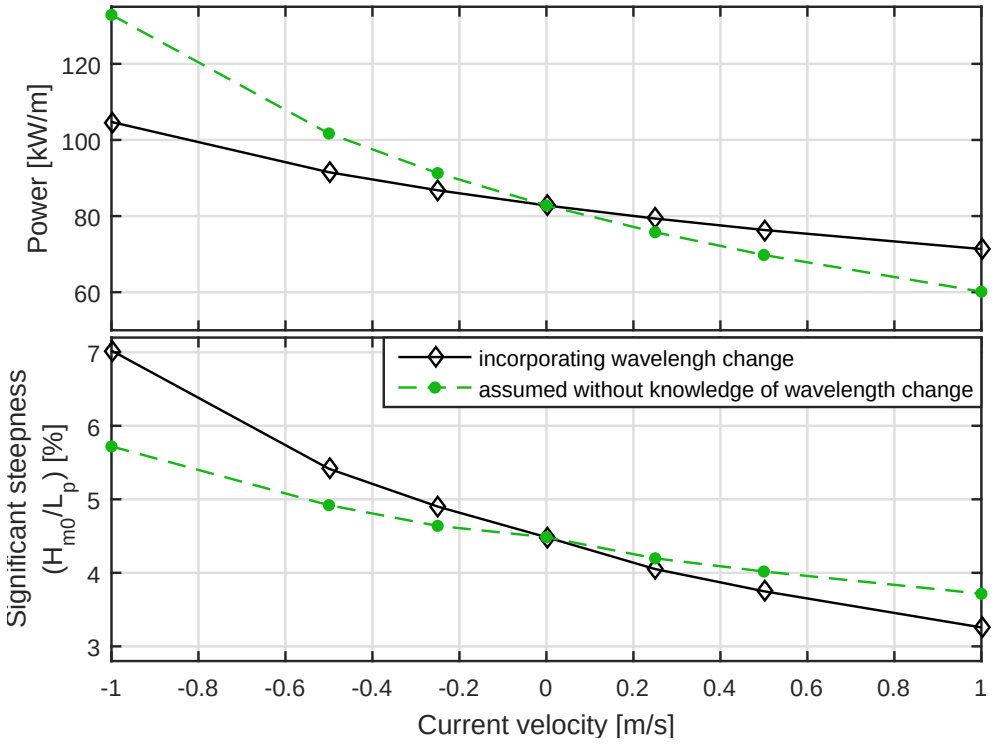

Figure 7.14: Change in power and significant steepness in the presence of in-line and opposing currents for cases incorporating wavelength change and that assumed without knowledge of wavelength change

direction. Waves were therefore run at relative angles to the current of 0 (following), $\pi/4$, $\pi/2$ (perpendicular), $3\pi/4$ and π (opposing). For the regular wave tests, an additional four intermediate angles were also measured. A range of angles were tested to demonstrate the applicability of the method, however when replicating a real site, these would be chosen based on the wave fetch and tide directions.

7.3.4 Observation and Correction

The sea states defined in Table 7.2 were initially validated in the tank without the presence of current. Subsequent correction and validation ensures that the desired spectra are effectively created in the absence of current, before observing and analysing the assumed transformations. At present it is not possible to isolate the incident and reflected wave spectrum in combined wave-current conditions and as such all corrections are made relative to the mean amplitudes measured over the array, rather than the incident spectrum (as applied in Section 7.2 and Section 4.6).

The current velocity was chosen based on a depth averaged calibration from measurements taken in the centre of the tank. It is noted that there is some spatial variation with reduced velocity towards the outside of the basin due to the method of producing current in the circular

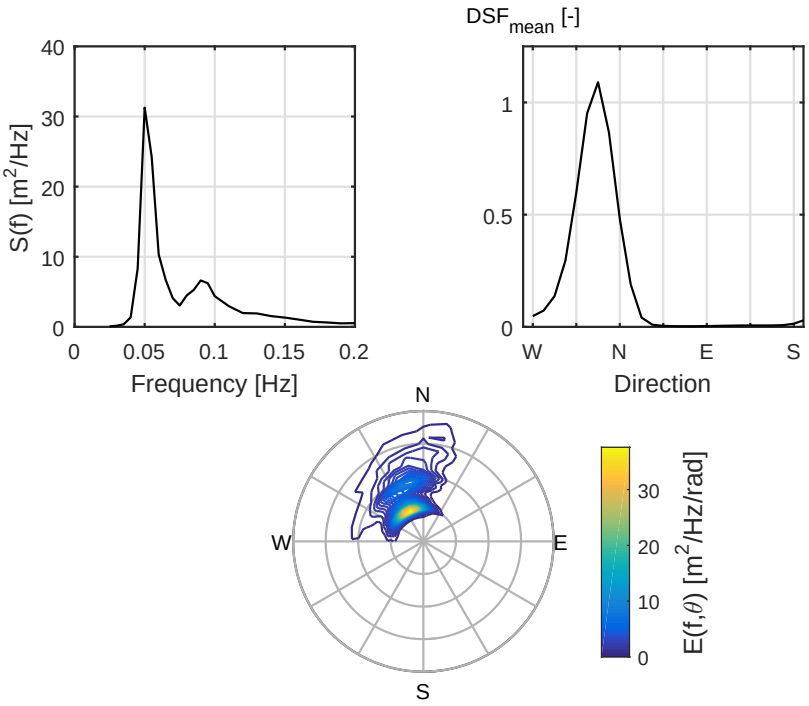

Figure 7.15: Representative complex sea state from Billia Croo. Subplots show the spectral density, S(f), weighted mean directional spreading function, DSF_{mean}, and directional spectrum, $E(f,\theta)$

Table 7.2: Wave-Current Test Conditions

Wave parameters	Wave angles relative to current	Currents [m/s]	Test length [s]
Long crested regular waves, T=3.3s, H=0.130m	9 angles: 0-π at π/8 increments	0.05, 0.1, 0.2	128
Long crested JONSWAP spectrum, T_p=3.3, H_{m0}=0.130m γ=3.3	5 angles: 0-π at π/4 increments	0.05, 0.1, 0.2	512
Measured EMEC directional sea, T_p=3.76, H_{m0}=0.128m	5 angles: 0-π at π/4 increments	0.05, 0.1, 0.2	2048

tank (Noble *et al.*, 2015). The potential implications of this are explored in Section 7.3.5. Velocity measurement using an Acoustic Doppler Velocimeter (ADV) ensured that the current had reached an equilibrium prior to wave generation.

The sea states have been generated using the single-summation method (Section 4.1.1.2), using the array DA1 (Fig. 3.9). Corrections are applied linearly, based on the discrepancy between measured and desired component amplitudes (Eq. (4.23)).

7.3.4.1 Regular Waves

The change in wave height as a function of relative angle and current velocity can be seen in Fig. 7.16. As expected, the observed transformation increases with larger current velocities, and for a given current, a larger relative angle corresponds to an increase in wave height. This change has been compared to wave-current interaction theories, both linear (Smith, 1997) and a non-linear 2^{nd} order (Baddour and Song, 1990; Hasanat Zaman and Baddour, 2011). The observed transformation is larger than predicted by either, as can be seen in Fig. 7.17. This highlights that applying pre-emptive theoretical correction factors in this context is not particularly effective. Another interesting observation is the reduction in wave height with increasing current velocity when waves and current are perpendicular, which is discussed further in Section 7.3.5.

Fig. 7.16 also shows the error in wave height once they have been empirically corrected, along with the *apparent* angular change. For all velocities and relative angles, the resulting measured wave heights were within 0.7% of the desired. The measured angular change is also relatively small, yet displays no obvious pattern with respect to relative angle and current velocity. The presence of a current reduces measurement accuracy (through gauge vibrations, bending etc.) making it difficult to isolate small refraction effects from this increased error. It is evident that any refraction effects are very small at these velocities and so have not been corrected for any of the sea states. This, along with other practical considerations are discussed further in Section 7.3.5.2.

7.3.4.2 Uni-directional Parametric Spectrum

The observed transformation of the parametric spectra is shown in Fig. 7.18, along with the deviation in energy density compared to the desired before and after correction. Clearly the same trend is seen as with the regular waves, with larger transformations in the presence of larger currents and larger wave heights with increasing angle.

Analysing this change in energy density, it is clear that although the majority of the change is a result of wave-current interaction, there is also significant variation due to reflections, particularly affecting the higher frequencies. The magnitude of these variations are a function of the reduced absorption effectiveness in the presence of larger currents. The cause of this 'spiky' variation at higher frequencies is the incident and reflected wave components at a given frequency being in or out of phase at the gauge array location.

Regardless of the source of the frequency dependent variation, the corrected deviation shows that the spectrum has been effectively corrected using a linear approach in a single iteration.

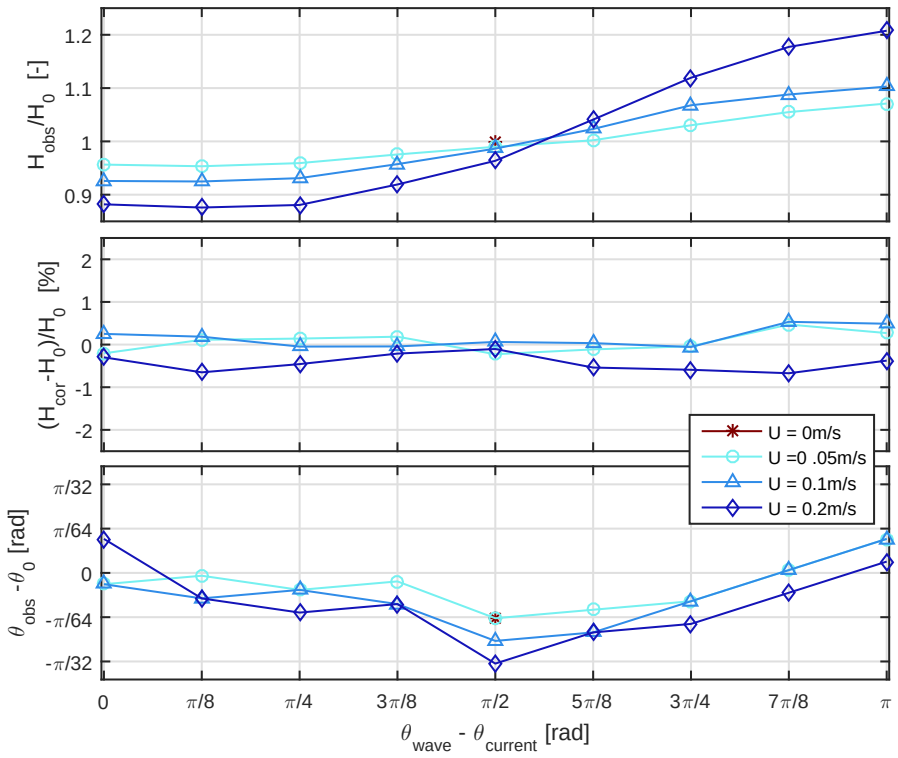

Figure 7.16: Observed change in wave height and direction for regular waves at various angles to the current direction. Top panel shows relative wave height, middle panel shows percentage discrepancy of corrected wave height, and bottom panel change in direction.

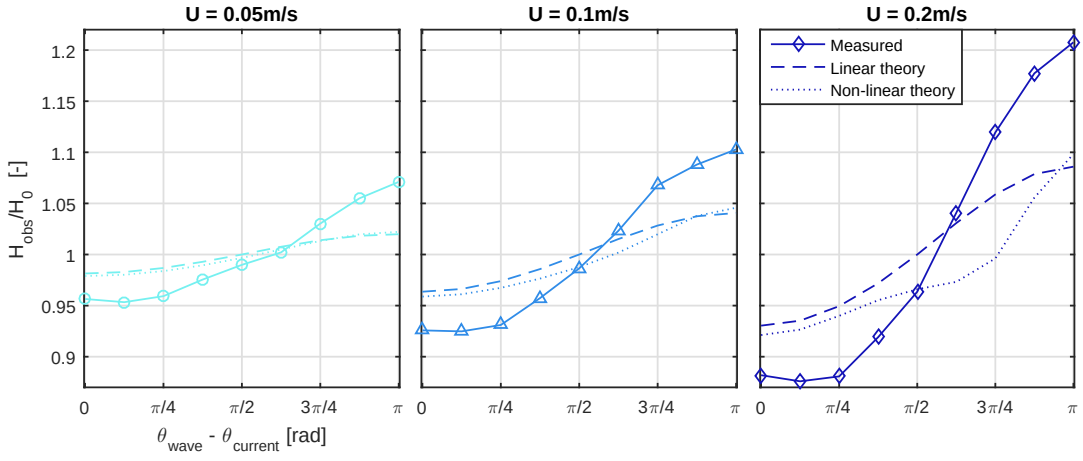

Figure 7.17: Observed change in wave height for regular waves at various angles to the current direction, with comparison to theory

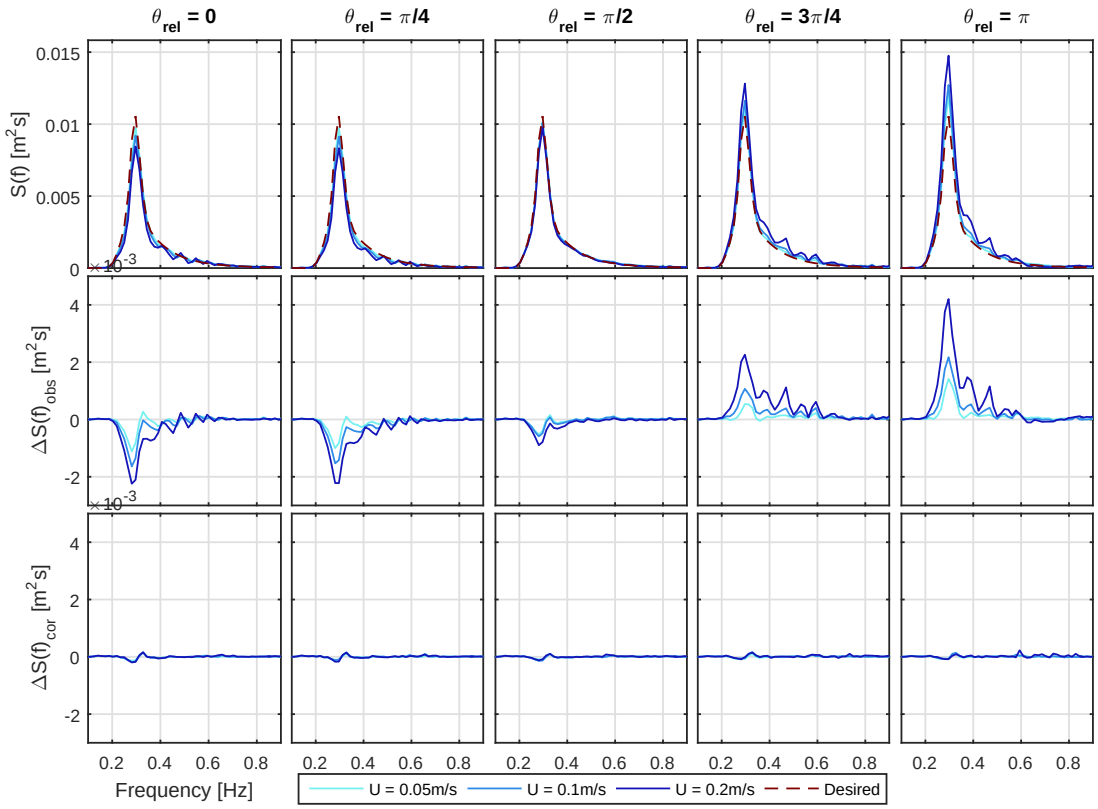

Figure 7.18: Results of parametric spectrum correction procedure, at 5 relative angles to current. Top row shows observed spectral density, middle row shows observed deviation from desired prior to correction, and bottom row shows deviation following correction.

All wave-current-angle scenarios were corrected to give a final weighted error (NTD_s) of less than 3%.

7.3.4.3 Non-parametric Directional Spectrum

Similar to the parametric outputs found in Fig. 7.18, the frequency spectrum transformation and correction for the non-parametric sea state recorded at EMEC is shown in Fig. 7.19. Despite this sea state having significant directional spreading, the magnitude of transformation is observed to be similar to the parametric case, along with analogous influence of reflections. The corrected frequency spectra are also all within 3% of the desired, demonstrating that the linear correction procedure applied to the sub-frequency angular components is equally effective.

Fig. 7.20 shows the final corrected sea states output. Frequency spectra along with weighted DSF are shown for each of the three velocities and at the five relative angles. The final directional spectrum output using the PTPD approach is shown for the base 0.1 m/s case, noting that the 0.05 m/s and 0.2 m/s results appear very similar.

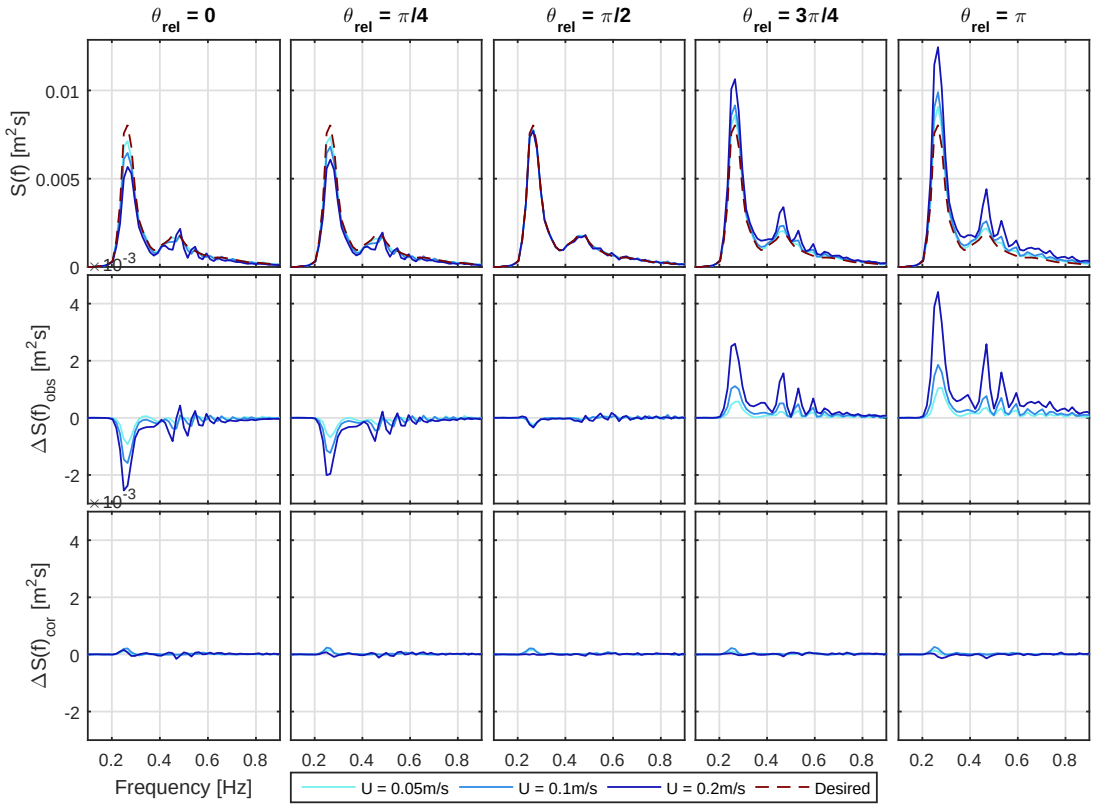

Figure 7.19: Results of non-parametric EMEC spectrum correction procedure, at 5 relative angles to current. Top row shows observed spectral density, middle row shows observed deviation from desired prior to correction, and bottom row shows deviation following correction.

The final sea states re-iterate that the frequency spectra have been effectively corrected for all velocity-angle combinations and in general so have the directional spectra and mean DSF. Directional errors are larger with increasing current velocity which is clear when assessing the weighted DSF errors. With zero current, the weighted DSF error was 6.95%, whereas in 0.05, 0.1 and 0.2 m/s current the mean errors over all angles are 13.3%, 14.3% and 18.5% respectively. Although this is a significant increase, it is felt that the majority of this increase is not refraction induced and instead is a product of increased measurement error combined with the manner in which the error is calculated. This is discussed further in Section 7.3.5.

7.3.5 Assessment of Results and Measurement/Correction Procedure

7.3.5.1 Observed Change in Wave Height and Spectra

Although the main aim of this section is to demonstrate the effective re-creation of directional spectra with current, one of the interesting outcomes is the observation of non-collinear wave current interactions. All results show larger wave transformation in the presence of higher current velocities and an increase in wave amplitude with increasing relative angle, as would be

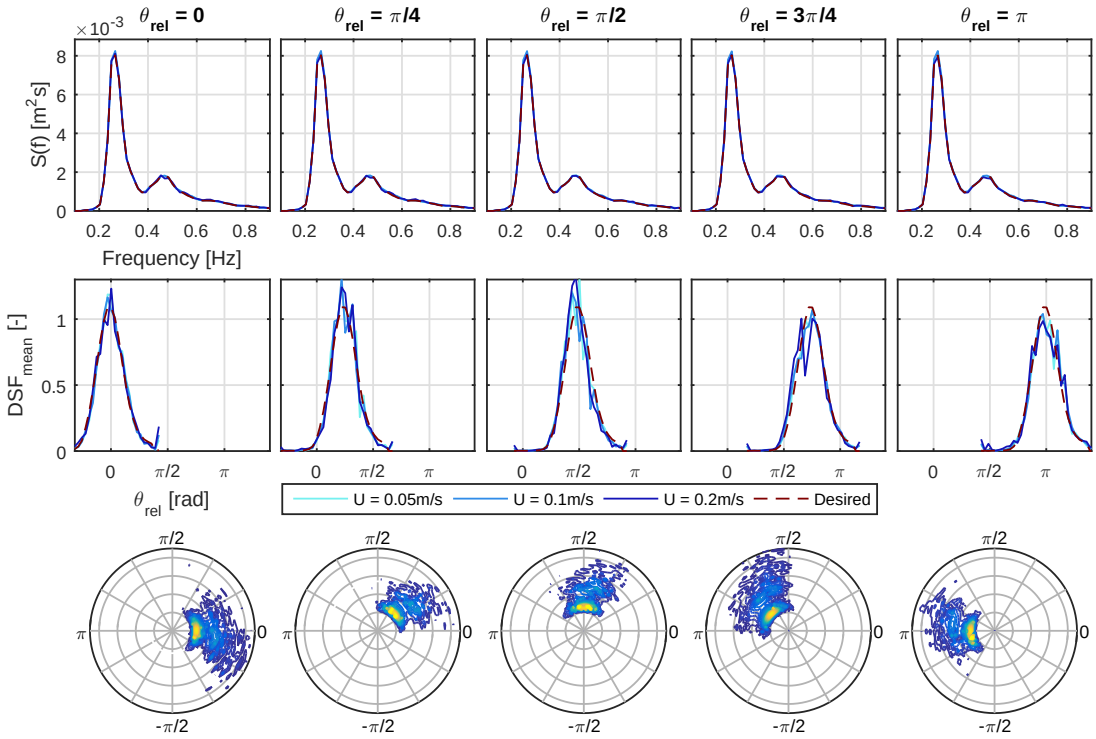

Figure 7.20: Final non-parametric EMEC spectra following correction, at 5 relative angles to current. Top row shows spectral density, S(f), middle row showss weighted mean directional spreading function, DSF_{mean}, and bottom row shows directional spectra, $E(f,\theta)$, for 0.1m/s current.

expected. The magnitude of the wave transformation, however, was much larger than predicted, as shown in Fig. 7.17. This may be a result of tank specific wave generation issues in the presence of a current (discussed further in Section 7.3.5.2), so caution must be applied before assuming that these results are representative of pure wave-current interaction.

The change in wave height (regular or significant) with respect to the current condition was observed to be comparable for each of the sea states. This is shown in Fig. 7.21, and is largely a result of all sea states having similar frequency and steepness values. It may be expected that the directional sea state would have a smaller range in measured wave heights due to different wave components propagating at different relative angles. However, this proved not to be the case, which is clear when assessing the observed wave height for the EMEC sea state in 0.2 m/s current at a relative angle of π. The cause of this is unknown, but may be a consequence of reflections causing a net constructive effect over the wave gauge array area. These reflections are dependent on frequency, flow velocity and angle.

Another interesting result was the apparent decrease in wave height in all cases when the mean wave angle is perpendicular to the current. The measured wave heights under this condition decrease with increasing current velocity and although it is a possibility that it is a paddle-

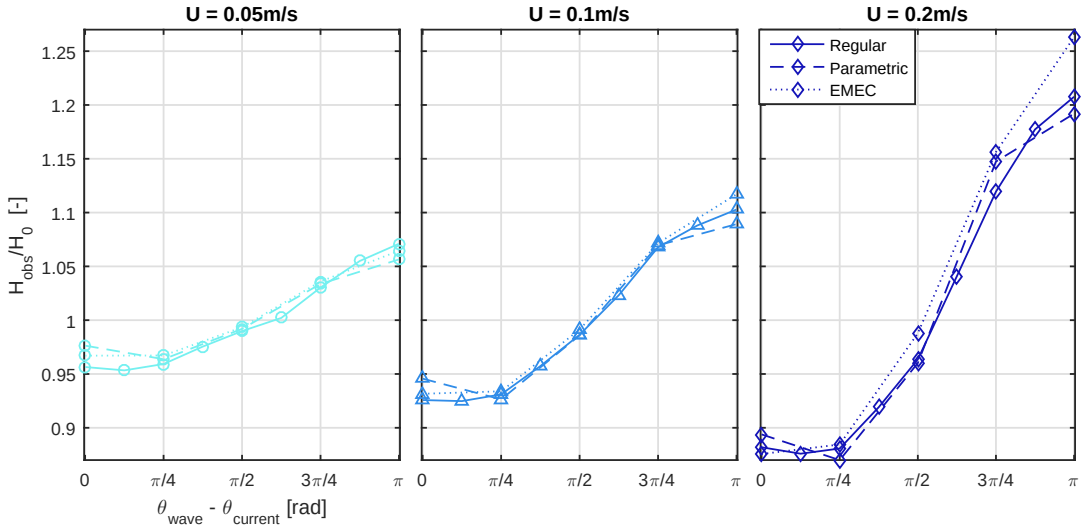

Figure 7.21: Observed change in wave height by relative wave angle for regular, parametric and site-specific EMEC sea for the three current velocities tested.

control system response to perpendicular current, it seems that it may be purely a wave-current effect. It appears to be analogous to having a finite crest length in open water, with the resulting current causing wave crests to 'stretch out' along their length. In the tank, waves are generated along the whole circumference, yet as water passes through the turning vanes, wave energy is lost via the current return path under the floor. Although the crest length appears to stay constant, energy is transferred perpendicular to the wave propagation direction, thus having the effect of reducing the crest height.

7.3.5.2 Assessment of correction procedure

The amplitude correction procedure applied has proven to be effective for all sea states, providing frequency spectrum errors of less than 3% in all cases. Consequently, the resulting wave heights were found to be very close to the desired. For the regular, uni-directional parametric and non-parametric EMEC sea states, the mean wave height discrepancy over all velocity-angle combinations were found to be 0.27%, 0.42% and 0.91% respectively (maximum errors of 0.67%, 1.11% and 1.38%).

The correction factor, although assumed linear, includes a number of different factors of which the proportional influence remains unknown. Namely:

1. Superposition of wave and current fields
2. Mass, momentum and energy conservation between wave and current fields
3. Increased reflections with larger currents, which is relative to the array location
4. Spatial variation of current in the tank
5. Paddle response to the presence of current

The favourable results show that, although current effects on the wave field at FloWave are inherently complex and non-linear, the variation in relative wave deformation as a result of a modest change in input wave amplitude can effectively be approximated as a linear process. This is a useful output from this work, although limits to the validity of this finding will need to be identified through additional testing with steeper waves and higher current velocities.

The wave-current interaction theories do not include all of these factors, which may account for the discrepancies in Fig. 7.17. The linear theory only accounts for the first, while the non-linear theory also partially accounts for the second. Factors 3-5 are facility specific, and cannot be dealt with by general theories.

7.3.5.3 Measurement of Wave Directionality

Measurement of component wave angles in current

Component angles are measured using the PTPD approach as implemented by Draycott *et al.* (2015a,b) and detailed in Chapter 5. Each gauge triad provides an estimate of wave angle for each of the frequency components based on the measured phase differences from an FFT. A circular kernel density estimate (250 bins) is then applied to the 56 individual triad estimates with an aim to identify the true incident angle for each component. This approach has been shown to provide very good estimates of incident wave angle without the presence of current, typically identifying the correct angle within $\pm\pi/90$. Noting the directional bin widths are $\pi/32$, this usually provides good resulting spectral estimates.

In the presence of currents, estimates of wave angle are not so accurate. This is partly due to additional measurement uncertainty from a number of sources; run-up on gauges, turbulence, and Vortex Induced Vibration (VIV). The presence of the current also causes inconsistent bending to occur in the gauges meaning the assumed gauge positions are somewhat inaccurate and importantly, wire separations can be variable. Additionally, reflection levels are higher in the presence of currents, which also alter the perceived phases, particularly when the reflections are not opposing the incident components. The cumulative effect of this is increased uncertainty in the angular estimates.

Fig. 7.22 shows the PTPD angle calculation outputs for the uni-directional parametric spectrum, noting that it is much easier to observe and analyse than the non-parametric directional sea state. It is clear that the overall sea state direction is generally identified well. Using a directional bin size of $\pi/32$, a measured deviation of just $\pi/64$ from the desired angle would result in the energy being attributed to a different directional bin for that frequency component. This happens relatively frequently in the presence of current as can be seen in Fig. 7.22, causing apparently large errors to arise through a measurement discrepancy of less than three degrees. This results in the DSF and directional spectrum in Fig. 7.20 showing significant deviation, even though the underlying errors themselves are quite minimal. To get an error metric not

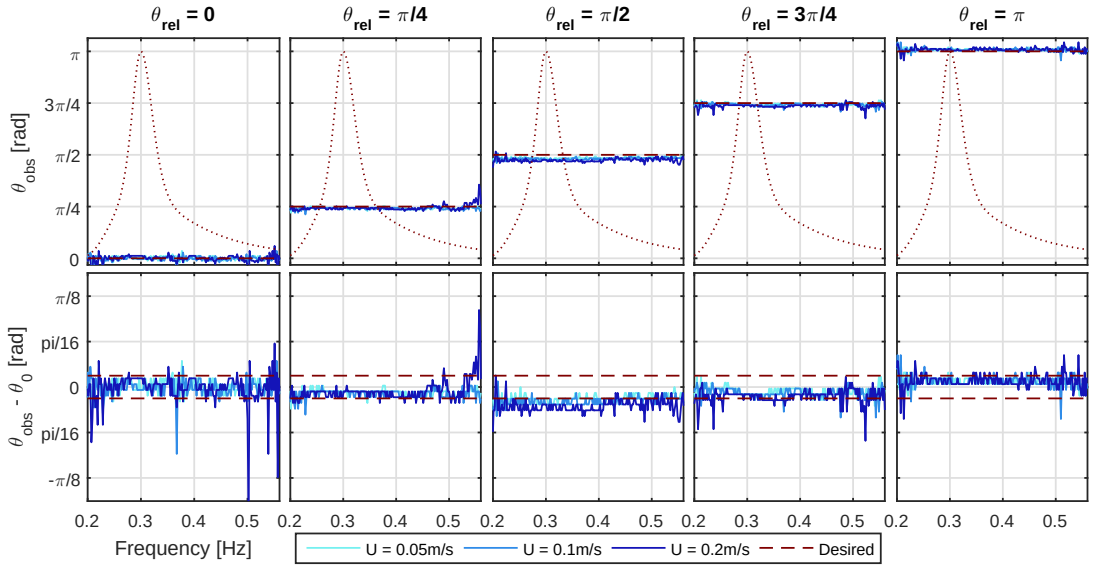

Figure 7.22: Observed wave component angles at different velocities (top) and discrepancy from desired (bottom). Amplitude spectrum shown dotted in top panels to highlight where energy content lies. Spacing between dashed lines in lower panels represents directional bin size.

related to bin size, a net weighted angular error has been defined in Eq. (7.12), with the observed outputs for both the parametric and non-parametric EMEC sea shown in Fig. 7.23.

$$\theta^{\star}_{error} = \frac{\sum(\theta_{obs,i} - \theta_{0,i})A_i}{\sum A_i} \tag{7.12}$$

As refraction levels are expected to be in the order of a few degrees, isolating what is refraction and what is simply increased measurement error has proved difficult. Any significant refraction should, however, manifest itself as a negative weighted angular change in Fig. 7.23 for all non-collinear cases. As there is no clear indication that this is the case, it is assumed that the refraction levels in these tests are low enough that they do not need to be corrected. If this work was to be extended to tests with larger currents it may be that the refraction cannot be ignored, requiring improvements to the measurement system. This may take the form of stiffer wave gauges (or an alternative measurement system) to reduce vibration and deflection in the presence of current. This would allow the implementation of an iterative procedure to correct for the observed refraction.

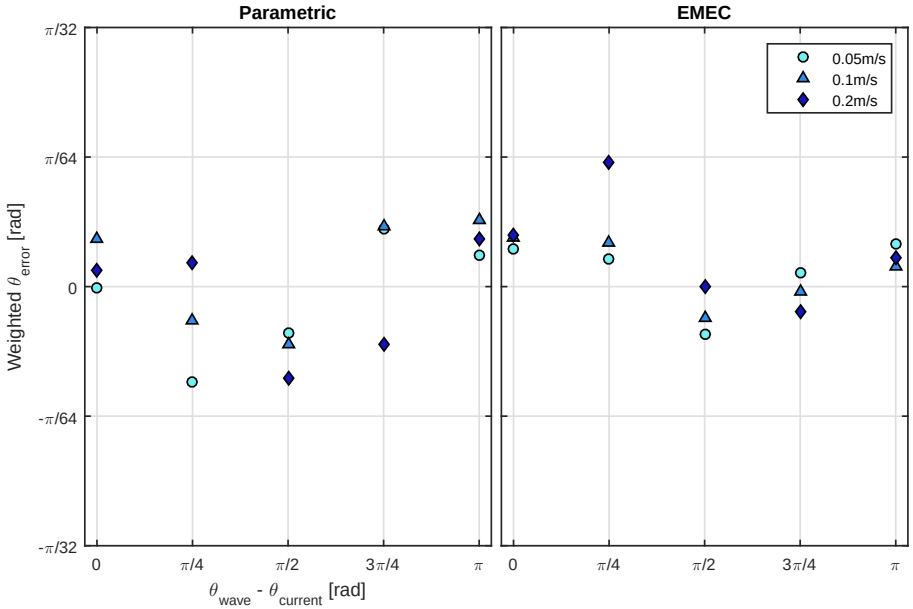

Figure 7.23: Net weighted error for parametric and non-parametric sea states for the combinations of current and relative wave angle tested, showing no significant deviation.

Relative Performance of PTPD Approach

In the presence of a current, the increased measurement errors mean that the PTPD outputs have some uncertainty associated. Although it has been inferred that the actual discrepancy is likely to be small, this still means that the true directional spectrum generated remains unknown. This uncertainty, however, is still significantly smaller than if typical directional spectrum reconstruction methods were used. This is demonstrated in Fig. 7.24, where the DSF outputs for the base 0.1m/s cases are shown for the PTPD, EMLM and EMEP approaches.

In Fig. 7.24 it appears that other than the EMEP reconstruction at $3\pi/4$, the EMEP and EMLM approaches fail to effectively characterise the DSFs; having a non-zero magnitude for all angles. This is clearly not the case and is likely due to the limitations of these 'curve-fitting' methods trying to fit to small reflections, along with additional reconstruction errors. As there is only significant energy within a range of $\pi/4$ and the array is in the tank centre (meaning component reflections are opposing incident), there should only be a very small DSF component (roughly 1-4% size of incident peak corresponding to 10-20% reflection) opposing the incident, rather than the observed constant energy content.

The poor performance of the EMEP and EMLM approaches in this case mean that the resulting reconstructions would clearly not be suitable to use as a basis for subsequent directional correction. Despite the PTPD approach reducing errors significantly, identification of refraction effects with these low velocities and wave gauges available is still error prone. It is thought, however, that using this approach with stiffer gauges will prove effective at measuring DSFs

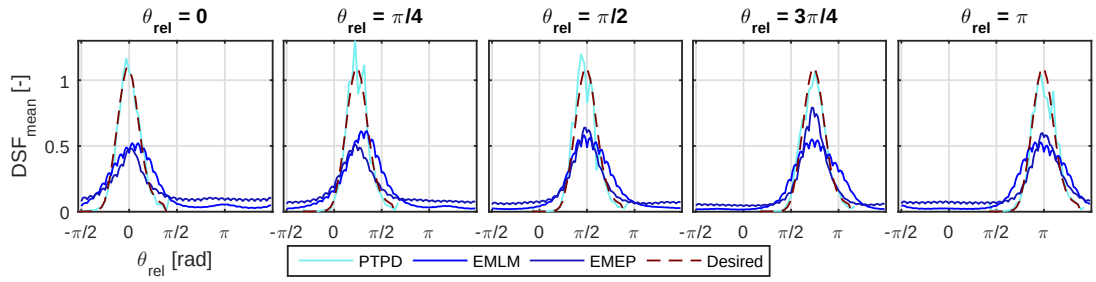

Figure 7.24: Comparative performance of three directional spectrum reconstruction approaches: Phase-Time Path Difference (PTPD), Extended Maximum Likelihood Method (EMLM) and Extended Maximum Entropy Method (EMEP)

accurately in current, with the additional advantage that component angles have been calculated and can now inform a correction procedure.

7.4 Implications for Testing

The level of sea state complexity generally increases as a concept advances through Technology Readiness Levels (TRLs). Early stage testing is typically limited to regular waves of varying frequency and height before advancing to standard parametric spectra (both long and short crested). The ability to produce complex site-specific conditions will usually apply more to devices at advanced TRLs where a particular deployment site has been identified. As such, this ability to produce site-specific combined sea states has the potential to extend and complement established development paths.

The results of this chapter demonstrate that site-specific directional spectra can be re-created with and without current at FloWave. This shows that true site complexity can be simulated effectively, capturing the nature of multi-directional wave-current ocean locations. The increased realism will aid in de-risking device development and in the case of wave-current conditions, will help explore the envelope of expected responses. This will in turn provide more insightful and realistic device and mooring loads, including both those incurred through the presence of the current directly, as well as those resulting from the influence of the current on the wave field. It also highlights the value in obtaining measurements of current velocity when carrying out resource assessment, or assessing the outputs of full scale testing.

Additionally, the errors in wavelength, steepness and power are assessed when scaling at non-depth ratio values, along with identifying the effect of omitting, or not knowing, the current conditions. This demonstrates the importance of scaling to depth ratios if possible and including current if known, whilst additionally quantifying the errors and uncertainty associated when these are not possible.

Chapter 8

Conclusions and Further Work

8.1 Conclusions

In this thesis methods of using buoy data to create validated site-specific directional wave conditions in test tanks have been explored for the first time. This has been approached by considering the whole process from sea state representation and characterisation, to the tank considerations of scaling, generation, measurement, and validation. Various methods of creating representative wave conditions from the EMEC Billia Croo wave test site have been trialled and assessed, with particular focus on using clustering algorithms to preserve spectral complexity. Prior to generating representative conditions at FloWave, the wave fields at the facility are characterised and emphasis is placed on developing measurement strategies for the validation of directional spectra. The final outcome is a set of statistically representative directional sea states, validated using a novel and effective suite of analysis tools. The methods explored and tools developed will enable realistic site-specific wave conditions to be implemented more effectively, thus helping reduce risk in device development.

The major contributions centre around novel site characterisation approaches (Chapter 6) and directional spectrum reconstruction methods (Chapter 5). However, there has also been progress made in the design of measurement arrays, the understanding and characterisation of the FloWave facility, alternative scaling methodologies and the effective re-creation of combined wave-current directional seas. Due to covering multiple topic areas the more detailed conclusions have been split into three sections.

8.1.1 Tank Characterisation and Wave Measurement

For the first time Golomb rulers and Costas arrays have been assessed for use as arbitrary number reflection and directional spectrum reconstruction arrays respectively. The properties for these are easily accessible from available databases and they have been shown to be instantly effective layouts due to their co-array properties, enabling tank test engineers to rapidly create suitable arrays given the number of gauges available. An alternative ‘random array design tool’ has also been developed for the creation of directional spectrum configurations and although

proven to be more effective than Costas arrays in the numerical study, requires more effort to ensure the array is suitable.

The waves at the unique FloWave Ocean Energy Facility have been assessed under a variety of wave conditions, gaining an understanding of the wave field properties and the tanks performance. From this analysis it is found that the incident wave curvature is negligible and angular generation is correct (at least for regular waves). Regular wave conditions are also found to be reasonably well described by Stokes' 2^{nd} order theory. It is concluded, however, that the difference between linear wave theory approximation and the 2^{nd} order formulation for the wave conditions at FloWave is small enough to warrant using the significantly more convenient linear approach for the purpose of wave simulation and spectral analysis.

The main area of interest explored in the tank characterisation was the wave field quality and characteristics, which is determined largely by the tank's absorption effectiveness and the effect the resulting reflections have on the wave field. It is found that FloWave has poorer absorption for high frequency–low steepness waves with a rapid decrease in effectiveness above 1 Hz. These reflections are curved as a result of the tank geometry and create circular focussing effects, resulting in larger deviations from desired near to the reflecting boundary and along the centreline of the tank relative to the generation angle. Various other specifics are gained over the characteristics of a variety of wave fields helping inform test design, but most influential is the understanding of the spatio-temporal variability introduced by these reflections. This work identifies the ideal testing location to be far from the reflecting boundary and off-centre, with knowledge over how long the wave field at a defined location will be within specified tolerances (dependent on frequency and steepness).

8.1.2 Directional Spectrum Reconstruction

A novel tank-based directional spectrum reconstruction method has been developed called the Single-summation PTPD Approach with In-line Reflections (SPAIR) (Draycott *et al.*, 2015a), based on knowledge of the method of sea state generation. This approach has been shown to reduce the apparent directional distribution error to 6.6% over a range of tests, down from 20%, 14.9% and 38.7% for the BDM, EMEP and EMLM approaches respectively. In addition, as the method resolves phase-locked reflections, it enables the isolation of incident and reflected directional spectra and time-series over 360°, providing additional capabilities. Sensitivity analysis shows that this method, in combination with the wave gauge array, is robust regardless of the magnitude of in-line reflection, particularly for the range expected at the FloWave facility. However, high sensitivity is displayed in the presence of oblique reflections, something which future work aims to deal with (see Section 8.2.2).

The SPAIR method as developed, or modified, will enable directional sea states to be validated with increased certainty, enabling multi-directional wave basins to simulate realistic directional wave scenarios with increased confidence. The additional specifics relating to the reflected

wave field and time-series also provides valuable information to help properly contextualise results from tank testing.

8.1.3 Site Characterisation and Emulation

The research into site characterisation and emulation represents the first time a wave site has been represented in such detail, simulated and validated. A variety of classification methodologies were explored, focussing particularly on the use of clustering algorithms on frequency spectra, directional spectra and statistics. These methods were compared both visually and numerically, via a performance metric, to a number of other methodologies including classical binning methods, in order to assess how well each method groups with respect to certain key variables. The knowledge gained about such methods applied to the EMEC dataset will be useful in identifying favourable characterisation approaches for any location. No overall favourable methodology was identified throughout this process. It was hoped that perhaps considering the whole directional or frequency spectral form in the classification would automatically partition well with respect to the statistics representing such spectra. Unfortunately, this proved impractical due to the constrained nature of the problem coupled with the vast amount of data and the high number of variables of interest. This highlighted, importantly, that the optimal solution is application driven, dependent on device characteristics and test purpose.

Despite no obvious overall favourable site characterisation method choice, a generic set of production sea states have been created from the EMEC data, aimed at serving the majority of clients interests. This is based on the rationale that clients tend to require a range of H_{m0}-T_E values in order to populate power matrices, but will also be interested in having spectral realism in the testing. Therefore a combined binning (H_{m0}-T_E)– clustering ($E(f,\theta)$) approach was used to create 41 sea states, 37 of which can be created at FloWave at the required scale. These have been generated, measured, corrected and validated using the SPAIR method, demonstrating that complex site-specific directional spectra can be effectively produced.

Extreme sea states have also been created for 1:10 and 1:50 year events using I-FORM contours to choose a range of extreme conditions. These spectra cannot be generated at the depth ratio due to breaching tank limits and as such the implications of this with respect to the wavelength and power of the resulting sea states are quantified. This analysis demonstrated that errors of up to around 40% can be expected for some low frequency components (at the scale and site considered). This work highlights that there are significant discrepancies which must be quantified and understood, both for site representation in the tank, and for tank outputs compared with eventual site trials. As a result of the large error potential in fixed depth tanks, alternative methodologies to scaling are then detailed, aimed at preserving the energy distribution with respect to wavelength, and the power distribution. It is demonstrated that these can easily be achieved and that for certain types of devices or tests, may be more beneficial than the conventional frequency spectrum scaling. It is expected that power production tests will aim

to actually preserve sea state power and that devices highly sensitive to wavelength may benefit from preserving the wavenumber spectrum rather than the frequency spectrum.

The last major output for the site replication work is an example of how site-specific directional wave-current conditions can be effectively created at FloWave. The importance of including representative current is highlighted, specifically assessing the effect on sea state power and steepness. The consequence of not knowing the current and the associated wavelength and group velocity effects are also explored, showing that power change will be over-estimated and steepness change under-estimated. This is shown to be in the order of 20% for 1 m/s current velocities. This demonstrates that site conditions (in locations with current) cannot be properly represented without current measurement (or additional wavelength measurement) and as such should be included in resource assessment and site characterisation. It is demonstrated that corrected site-specific directional spectra with currents of various velocities and relative angles can be achieved at FloWave. These experiments are carried out using the wave gauge array and SPAIR method developed to correct site-specific directional spectra from a characterisation methodology and demonstrates that true site complexity can be effectively captured, replicated and validated using the tools presented in this thesis.

8.2 Further Work

8.2.1 Tank Characterisation and Wave Measurement

The reasons behind the peculiar spectral content in the isolated reflected spectra (Section 4.5.2.2) should be resolved. This would involve identifying whether these are harmonics which can be explained using sum-difference terms applied to the incident spectrum, or are actually being generated from the mechanics of improper absorption. If the study is conclusive, this would progress the understanding of absorbing wavemakers, along with helping understand the effects of relying on active absorption alone to limit reflections in wave tanks.

8.2.2 Directional Spectrum Reconstruction (SPAIR Method)

- The SPAIR method developed is very effective at isolating incident and reflected directional spectra in an empty circular basin, however an extension to the method is required to enable more accurate isolation of reflected directional spectra with oblique incident angles. This extension will enable reflected/radiated spectra from models to be isolated with increased accuracy, thus providing valuable information about device behaviour.
- Another extension to the SPAIR method will enable the isolation of incident and reflected directional wave spectra in combined wave-current conditions. In Section 7.3 the mean spectra rather than the incident spectra was used to make sea state corrections, however, it is more accurate and useful to provide the correct incoming waves. The problem is

challenging due to the wavelengths not obeying the standard dispersion relation, and additionally differing between the incident and reflected waves due to their respective interaction with the current field. It should be possible to modify the reflection formulations with theoretical wavenumbers (see Section 7.3.1.1) resulting from modified dispersion relations, however these will need to be experimentally proven to be correct at FloWave before this approach can be taken. If successful, this will improve both the characterisation of wave-current scenarios and the effective re-creation of such conditions.

8.2.3 Site Characterisation and Emulation

- The wavenumber estimates obtained from directional wave buoys are typically replaced by standard dispersion relation values if they are found to disagree (Earle *et al.*, 1999). However, these calculated values may be highly useful in inferring the current velocity at a site through the observed wavelength change, and as such a study should be completed to assess this. This would have to be achieved by calculating the expected velocity from the observed wavenumber-frequency relationship (perhaps best fit across all frequencies) and comparing with a tidal model or in-situ measurement of current velocity. If this approach is found to give reliable estimates, directional wave buoys can be used to infer the concurrent current condition, thus providing a more accurate description of the sea state. This, as mentioned in Section 7.3.1, has significant implications for the assumed sea state power and steepness and should enable more reliable resource assessment and site characterisation to be carried out. Importantly this can be done using already deployed equipment, and as such, at low cost.
- Subjecting different device types to a few resulting representative sea states would help quantify the effect of the more sophisticated techniques developed in this thesis. This will highlight that parametric uni-directional spectra resulting from binning outputs are not sufficient to understand device performance. Similarly it would be interesting to trial the different scaling approaches identified for instances where depth-ratio scaling is not possible. Testing a device in frequency, wavenumber and power spectra scaled equivalents to assess survivability implications will confirm the issues raised for site replication in fixed depth tanks. For both studies test outputs such as device loadings, motion and power output would help quantify the expected differences.

Bibliography

Abild, J., Andersen, E. Y., and Rosbjerg, D. The climate of extreme winds at the great belt, Denmark. *Journal of Wind Engineering and Industrial Aerodynamics*, 41(1-3):521–532, 1992. ISSN 01676105. doi: 10.1016/0167-6105(92)90458-M.

ABP MER. Pentland Firth and Orkney Waters Strategic Area : Marine Energy Resources. Technical Report November, The Crown Estate, 2012.

Agamloh, E. B., Wallace, A. K., and von Jouanne, A. Application of fluid-structure interaction simulation of an ocean wave energy extraction device. *Renewable Energy*, 33(4):748–757, 2008. ISSN 09601481. doi: 10.1016/j.renene.2007.04.010.

Albatern. Technology Development, 2016. URL `http://albatern.co.uk/wavenet/technology-development/`.

Alvarez-Esteban, P. C., Euán, C., and Ortega, J. Time Series Clustering using the Total Variation Distance with Applications in Oceanography. *Environmetrics*, pages 1–23, 2015.

Alves, J. H. G. M. and Melo, E. On the measurement of directional wave spectra at the southern Brazilian coast. *Applied Ocean Research*, 21(6):295–309, 1999. ISSN 01411187. doi: 10.1016/S0141-1187(99)00019-X.

Arthur, D. and Vassilvitskii, S. K-Means++: the Advantages of Careful Seeding. *Proceedings of the eighteenth annual ACM-SIAM symposium on Discrete algorithms*, 8:1027–1025, 2007. ISSN 978-0-898716-24-5. doi: 10.1145/1283383.1283494.

Baddour, R. E. and Song, S. On the interaction between waves and currents. *Ocean Engineering*, 17(1-2):1–21, 1990. ISSN 00298018. doi: 10.1016/0029-8018(90)90011-T.

Barber, N. Measurements of sea conditions by the motion of a floating buoy. *Admiralty Res. Lab. Rep*, 103:N2, 1946.

Barstow, S., Bidlot, J., and Caires, S. Measuring and Analysing the directional spectrum of ocean waves. *COST Office*, 2005. URL `http://hal.inria.fr/hal-00529755/`.

Beard, J. K. Costas Arrays, 2015. URL `http://jameskbeard.com/jameskbeard/Costas{_}Arrays.html`.

Benoit, M. Practical comparative performance survey of methods used for estimating directional wave spectra from heave-pitch-roll data. *Coastal Engineering Proceedings*, 1 (23), 1992.

Benoit, M. and Teisson, C. Laboratory Comparison of Directional Wave Measurement Systems and Analysis Techniques. *24th Conference on Coastal Engineering*, 24:1–15, 1994.

Benoit, M., Frigaard, P., and Schaffer, H. A. Analyzing multidirectional wave spectra: a tentative classification of available methods. *Proceedings of the 1997 IAHR conference*, pages 131–158, 1997.

Berg, J. C. Extreme Ocean Wave Conditions for Northern California Wave Energy Conversion Device. *Sandia National Laboratories*, 2011.

Bonner, R. E. On Some Clustering Techniques, 1964. ISSN 0018-8646.

Boukhanovsky, A. V., Lopatoukhin, L. J., and Guedes Soares, C. Spectral wave climate of the North Sea. *Applied Ocean Research*, 29(3):146–154, jul 2007. ISSN 01411187. doi: 10.1016/j.apor.2007.08.004.

Bretschneider, C. L. Wave variability and wave spectra for wind-generated gravity waves. *Beach Erosion Board, Tech. Memo. US Army Corps of Engineers,*, Nº 113:192 pp., 1959.

Bunney, C. A High Resolution SWAN Model Assessment:North Norfolk to Humber. *Met Office*, (July), 2011.

Burrows, R. and Salih, B. a. Statistical Modelling of Long-Term Wave Climates. *Coastal Engineering*, pages 42–56, 1982. ISSN 08938717.

Caires, S. Extreme Value Analysis : Wave Data. *Joint WMO/IOC Technical Commission for Oceanography and Marine Meteorology (JCOMM) Technical Report 57 (2011)*, (57):33, 2011.

Capon, J., Greenfield, R., and Kolker, R. Multidimensional maximum-likelihood processing of a large aperture seismic array. *Proceedings of the IEEE*, 55(2):192–211, 1967. ISSN 0018-9219. doi: 10.1109/PROC.1967.5439.

Chakrabarti, S. K. and Johnson, J. G. Random wave-current interaction – Theory and experiment. *No. CONF-950695–. American Society of Mechanical Engineers, New York, NY (United States)*, dec 1995.

Cherneva, Z. and Guedes Soares, C. Evolution of wave properties during propagation in a ship towing tank and an offshore basin. *Ocean Engineering*, 38(17-18):2254–2261, dec 2011. ISSN 00298018. doi: 10.1016/j.oceaneng.2011.10.009.

Coe, R. G. and Neary, V. S. Review of Methods for Modeling Wave Energy Converter Survival in Extreme Sea States. *Proceedings of the 2nd Marine Energy Technology Symposium (METS2014)*, 2014.

Coles, S. *An Introduction to Statistical Modeling of Extreme Values*. Springer, 2001. ISBN 978-1-84996-874-4. doi: 10.1007/978-1-4471-3675-0.

Cruz, J., Pascal, R., and Taylor, J. Characterisation of the wave profile in the Edinburgh curved tank. In *Proceedings of the 25th International Conference on Offshore Mechanics and Arctic Engineering*, pages 1–10, 2006. ISBN 0791837777.

Dalrymple, R. A. and Dean, R. G. *Water wave mechanics for engineers and scientists*. 1984. ISBN 9810204205.

Daoud, B. and Kobus, J. IRREGULAR WAVE GENERATION METHOD WITH GIVEN CHARACIYERISTICS IN EXPERIMENTAL TANKS. *Ocean Engineering*, 22(4):387–410, 1995.

Das, S. and Bora, S. N. Reflection of oblique ocean water waves by a vertical rectangular porous structure placed on an elevated horizontal bottom. *Ocean Engineering*, 82:135–143, 2014. ISSN 00298018. doi: 10.1016/j.oceaneng.2014.02.035.

Davey, T., Bruce, T., and Allsop, W. Getting more from physical modelling - measuring extreme responses using importance sampling. In *Proceedings 31st International Conference on Coastal Engineering*, 2008.

Davey, T., Venugopal, V., Smith, H., Smith, G., Lawrence, J., Cavaleri, L., Bertotti, L., Prevosto, M., Girard, F., and Holmes, B. Equimar D2.7. Technical report, 2010.

Davey, T., Bryden, I. G., Ingram, D. M., Robinson, A., Sinfield, J. L., and Wallace, A. R. The All-Waters Test Facility âĂŞ a new resource for the marine energy sector. *4th International Conference on Ocean Energy*, pages 1–6, 2012.

Denis, M. S. and Pierson, W. J. On the Motions of Ships in Confused Seas. *Transactions Society of Naval Architects and Marine Engineers*, 61:280–357, 1953.

DIWASP. DIWASP: DIrectional WAve SPectrum analysis Version 1.4, 2015. URL `https://github.com/metocean/diwasp`.

DNV. Environmental Conditions and Environmental Loads. *RECOMMENDED PRACTICE DNV-RP-C205*, (October), 2014.

Doherty, K. and Folley, M. Extreme Value Analysis of Wave Energy Converters. *Proceedings of the 21st ISOPE Conference*, 8:557–564, 2011.

Doman, D. A., Murray, R. E., Pegg, M. J., Gracie, K., Johnstone, C. M., and Nevalainen, T. Tow-tank testing of a 1/20th scale horizontal axis tidal turbine with uncertainty analysis. *International Journal of Marine Energy*, 11:105–119, 2015. ISSN 22141669. doi: 10.1016/j.ijome.2015.06.003.

Draycott, S., Davey, T., Ingram, D. M., Day, A., and Johanning, L. The SPAIR method: Isolating incident and reflected directional wave spectra in multidirectional wave basins. *Coastal Engineering*, 114:265–283, 2015a. ISSN 03783839. doi: 10.1016/j.coastaleng.2016.04.012.

Draycott, S., Davey, T., Ingram, D. M., Day, J. L. a., and Johanning, L. Using a Phase-Time-Path-Difference Approach to Measure Directional Wave Spectra in FloWave. *EWTEC Conference Proceedings*, pages 1–7, 2015b.

Draycott, S., Davey, T., Ingram, D. M., Lawrence, J., Day, A., and Johanning, L. Applying Site-Specific Resource Assessment : Emulation of Representative EMEC seas in the FloWave Facility. *Proceedings of the 25th (2015) International Ocean and Polar Engineering Conference*, pages 815–821, 2015c. ISSN 15551792.

Draycott, S., Noble, D. R., Davey, T., Bruce, T., Ingram, D. M., Johanning, L., and Smith, H. C. M. Re-creation of Site-Specific Multi-Directional Waves with Non-Collinear Current. *Ocean Engineering*, pages 1–24, 2017.

Draycott, S., Davey, T., Ingram, D. M., Lawrence, J., Johanning, L., Day, A., Steynor, J., and Noble, D. Applying site specific resource assessment: methodologies for replicating real seas in the FloWave facility. *ICOE Conference Proceedings*, 44(November), 2014.

Earle, M. D. Nondirectional and directional wave data analysis procedures. *NDBC Tech. Doc. 96*, 002(January), 1996.

Earle, M. D., Steele, K. E., and Wang, D. W. C. Use of advanced directional wave spectra analysis methods. *Ocean Engineering*, 26(12):1421–1434, 1999. ISSN 00298018. doi: 10.1016/S0029-8018(99)00010-4.

Edinburgh Designs. Wave Gauges, 2013. URL `http://www.edesign.co.uk/product/wavegauges/`.

Edinburgh Wave Power Group. Wide Tank, 2009a. URL `http://www.homepages.ed.ac.uk/v1ewaveg/widetank/widetank.html`.

Edinburgh Wave Power Group. Curved Tank, 2009b. URL `http://www.homepages.ed.ac.uk/v1ewaveg/curvedtank/curvedtankworking.htm`.

EMEC. Facilities, 2015. URL `http://www.emec.org.uk/facilities/`.

EMEC. Gallery: EMEC Gallery, 2016. URL `http://www.emec.org.uk/about-us/media-centre/gallery/`.

Emec. *Assessment of Wave Energy Resource*. European Marine Energy Centre, 2009. ISBN 9780580656576. URL `www.emec.org.uk/standards/assessment-of-wave-energy-resource/`.

Esteva, D. Wave direction computations with three gage arrays. *Coastal Engineering Proceedings*, 1976.

Euan, C., Ortega, J., and Alvarez-esteban, P. C. DETECTING STATIONARY INTERVALS FOR RANDOM WAVES USING TIME SERIES. In *Proceedings of the ASME 2014 33rd International Conference on Ocean, Offshore and Arctic Engineering OMAE2014 June 8-13, 2014, San Francisco, California, USA*, 2017.

Ewans, K. C., Bitner-Gregersen, E. M., and Soares, C. G. Estimation of Wind-Sea and Swell Components in a Bimodal Sea State. *Journal of Offshore Mechanics and Arctic Engineering*, 128(November 2006):265, 2006. ISSN 08927219. doi: 10.1115/1.2166655.

Fernandes, A. A., Sarma, Y. V. B., and Menon, H. B. Directional spectrum of ocean waves from array measurements using phase/time/path difference methods. *Ocean Engineering*, 27 (4):345–363, 2000. ISSN 00298018. doi: 10.1016/S0029-8018(99)00024-4.

Folley, M. *Numerical modelling of wave energy converters : state-of-the-art techniques for single devices and arrays*. Elsevier, 2016. ISBN 9780128032107.

Folley, M., Elsaesser, B., and Whittaker, T. Analysis of the wave energy resource at the European Marine Energy Centre. *Renewable Energy*, 34(7):1709–1715, 2009.

Fremondiere, A. L. Ecole Centrale de Nantes - LHEEA - Research Laboratory in Hydrodynamics, Energetics and atmospheric environment, 2016. URL `http://www.ec-nantes.fr/version-anglaise/research/lheea-research-laboratory-in-hydrodynamics-energetics-and-atmospheric-environment-kjsp?RH=ENGLISH03`.

Frigaard, P., Helm-Petersen, J., and Klopman, G. IAHR List of Sea Parameters: an update for multidirectional waves. *The 27th IAHR Congress*, 1997.

Frigaard, P. and Brorsen, M. A time-domain method for separating incident and reflected irregular waves. *Coastal Engineering*, 24(3-4):205–215, 1995. ISSN 03783839. doi: 10.1016/0378-3839(94)00035-V.

Goda, Y. *Random seas and design of maritime structures*, volume 15. 2000. ISBN 981023256X. doi: 10.1017/S0022112089222437.

Goda, Y. *Random seas and design of maritime structures*. World Scientific, 2010.

Goda, Y. and Suzuki, T. Estimation of incident and reflected waves in random wave experiments. *Coastal Engineering Proceedings*, 1(15), 1976.

Goggins, J. and Finnegan, W. Shape optimisation of floating wave energy converters for a specified wave energy spectrum. *Renewable Energy*, 71:208–220, 2014. ISSN 09601481. doi: 10.1016/j.renene.2014.05.022.

Gonçalves, M., Martinho, P., and Guedes Soares, C. Wave energy conditions in the western French coast. *Renewable Energy*, 62:155–163, 2014. ISSN 09601481. doi: 10.1016/j.renene.2013.06.028.

Gronbech, J., Jensen, T., and Andersen, H. Reflection Analysis with Separation of Cross Modes. *Proceedings of the 25th International Conference on Coastal Engineering,*, pages 968–980, 1996. ISSN 2156-1028. doi: 10.1061/9780784402429.076.

Guedes Soares, C. Representation of double-peaked sea wave spectra. *Ocean Engineering*, 11 (2):185–207, 1984. ISSN 00298018. doi: 10.1016/0029-8018(84)90019-2.

Guedes Soares, C. Effect of spectral shape uncertainty in the short term wave-induced ship responses. *Applied Ocean Research*, 12(2):54–69, 1990. ISSN 01411187. doi: 10.1016/S0141-1187(05)80030-6.

Guedes Soares, C., Rodriguez, G. R., Cavaco, P., and Ferrer, L. Experimental Study on the Interaction of Wave Spectra and Currents. In *the 19th International Conference on Offshore Mechanics and Arctic Engineering, ASME, New York*, pages paper OMAE2000/S&R – 6133, 2000.

Gyongy, I., Bruce, T., and Bryden, I. Numerical analysis of force-feedback control in a circular tank. *Applied Ocean Research*, 47:329–343, aug 2014a. ISSN 01411187. doi: 10.1016/j.apor.2014.07.002.

Gyongy, I., Richon, J. B., Bruce, T., and Bryden, I. Validation of a hydrodynamic model for a curved, multi-paddle wave tank. *Applied Ocean Research*, 44:39–52, jan 2014b. ISSN 01411187. doi: 10.1016/j.apor.2013.11.002.

Haller, M. C., Porter, A., Lenee-Bluhm, P., Rhinefrank, K., and Hammagren, E. Laboratory Observations of Waves in the Vicinity of WEC-Arrays. *EWTEC 2011 Proceedings*, pages 3–9, 2011.

Hamilton, L. J. Characterising spectral sea wave conditions with statistical clustering of actual spectra. *Applied Ocean Research*, 32(3):332–342, jul 2010. ISSN 01411187. doi: 10.1016/j.apor.2009.12.003.

Hasanat Zaman, M. and Baddour, E. Interaction of waves with non-colinear currents. *Ocean Engineering*, 38(4):541–549, mar 2011. ISSN 00298018. doi: 10.1016/j.oceaneng.2010.11.015.

Hashimoto, N. Analysis of the directional wave spectra from field data. *Advances in coastal and ocean engineering*, 3:103–144, 1997.

Hashimoto, N. and Kobine, K. Directional Spectrum Estimation From a Bayesian Approach. *Coastal Engineering Proceedings*, pages 62–76, 1988.

Hashimoto, N., Nagai, T., and Asai, T. Extension of the maximum entropy principle method for directional wave spectrum estimation. *Coastal Engineering Proceedings*, pages 232–246, 1994. ISSN 2156-1028.

Hasselmann, K., Barnett, T. P., Bouws, E., Carlson, H., Cartwright, D. E., Enke, K., Ewing, J. A., Gienapp, H., Hasselmann, D. E., Kruseman, P., Meerburg, A., Muller, P., Olbers, D. J., Richter, K., Sell, W., and Walden, H. Measurements of Wind-Wave Growth and Swell Decay during the Joint North Sea Wave Project (JONSWAP). *Ergnzungsheft zur Deutschen Hydrographischen Zeitschrift Reihe*, A(8)(8 0):p.95, 1973. doi: citeulike-article-id:2710264.

Haubrich, R. A. Array design. *Bulletin of the Seismological Society of America*, 58(3):977–991, 1968. ISSN 0037-1106.

Haver, S. and Nyhus, K. A wave climate description for long term response calculations, 1986.

Hedges, T. S., Anastasiou, K., and Gabriel, D. Interaction of random waves and currents. *Journal of Waterway, Port, Coastal and Ocean Engineering*, 111(2):275–288, 1985. ISSN 01980254. doi: 10.1016/0198-0254(85)92681-0.

Holmes, B. *Tank Testing of Wave Energy Conversion Systems.* EMEC, 2009. ISBN 9780580672620.

Holthuijsen, L. H. *Waves in oceanic and coastal waters.* 2007.

HR Wallingford. HR Wallingford: Physical modelling, 2016. URL `http://www.hrwallingford.com/facilities/physical-modelling`.

Huang, W. P., Chou, C. R., and Yim, J. Z. Experiments on the reflection coefficients of a detached breakwater in a directional wave field. *Coastal Engineering*, 47(4):367–379, 2003. ISSN 03783839. doi: 10.1016/S0378-3839(02)00129-1.

IAHR. List of Sea State Parameters. *Ocean Engineering*, 115(6):793–808, 1990.

Ifremer. Marine Environment Tests and Research Infrastructure, 2016. URL `http://www.ifremer.fr/metri/pages{_}metri/infrastructure/brest{_}basin.htm`.

Imperial College London. Available laboratory facilities, 2016. URL `http://www.imperial.ac.uk/fluid-mechanics/hydrodynamics-laboratory/`.

Ingram, D., Wallace, R., Robinson, A., and Bryden, I. The design and commissioning of the first, circular, combined current and wave test basin. *Oceans 2014 - Taipei*, 2014. doi: 10.1109/OCEANS-TAIPEI.2014.6964577.

International Electrotechnical Commission. IEC 61400-3: Wind TurbinesâĂŞPart 1: Design Requirements. *International Electrotechnical Commission, Geneva*, 2005.

Isobe, M., Kondo, K., and Horikawa, K. Extension of MLM for estimating directional wave spectrum. *Symp. on Description and Modelling of Directional Seas. DHI & MMI*, A6:1–15, 1984. doi: citeulike-article-id:6354853.

Jonsson, I. G. Wave-current Interactions. In LeMehaute, B. and Hanes, D. M., editors, *The Sea, Ocean Engineering Science*, volume 9, chapter 7, pages 65–120. Wiley-Interscience publications, New York, 1990. ISBN 0471633933.

Kemp, P. H. and Simons, R. R. The interaction between waves and a turbulent current: waves propagating with the current. *Journal of Fluid Mechanics*, 116(-1):227–250, apr 1982a. ISSN 0022-1120. doi: 10.1017/S0022112082000445.

Kemp, P. H. and Simons, R. R. The interaction between waves and a turbulent current: waves propagating with the current. *Journal of Fluid Mechanics*, 116:227–250, apr 1982b. ISSN 0022-1120. doi: 10.1017/S0022112082000445.

Kim, T., Lin, L.-H., and Wang, H. Application of Maximum Entropy Method to the Real Sea Data. *24th Conference on Coastal Engineering*, 24:340–355, 1994. ISSN 08938717.

Kofoed, J. P., Pecher, A., Margheritini, L., Antonishen, M., Bittencourt, C., Holmes, B., Retzler, C., Berthelsen, K., Le Crom, I., Neumann, F., Johnstone, C., McCombes, T., and Myers, L. E. A methodology for equitable performance assessment and presentation of wave energy converters based on sea trials. *Renewable Energy*, 52:99–110, apr 2013. ISSN 09601481. doi: 10.1016/j.renene.2012.10.040.

Krogstad, H. E. Maximum likelihood estimation of ocean wave spectra from general arrays of wave gauges. *Modeling, Identification and Control*, 9(2):81–97, 1988. ISSN 03327353. doi: 10.4173/mic.1988.2.3.

Lavelle, J. and Kofoed, J. P. *Power Production Analysis of the OE Buoy WEC for the CORES Project*. PhD thesis, Aalborg University, 2011.

Lawrence, J., Kofoed-Hansen, H., and Chevalier, C. High-resolution metocean modelling at EMEC's (UK) marine energy test sites. *8th European Wave and Tidal Energy Conference, Uppsala, Sweden, 2009*, pages 1–13, 2009. doi: 10.1111/j.2007.0908-8857.03909.x.

Leadbetter, M. R. Extremes and local dependence in stationary sequences. *Zeitschrift f??r Wahrscheinlichkeitstheorie und Verwandte Gebiete*, 65(2):291–306, 1983. ISSN 00443719. doi: 10.1007/BF00532484.

Lee, B. C., Fan, Y. M., Feng, X., and Kao, C. C. Experimental study of the reverse conversion of wave spectra. *Journal of Marine Science and Technology (Taiwan)*, 21(1):51–57, 2013. ISSN 10232796. doi: 10.6119/JMST-011-0831-1.

Longuet-Higgins, M. S. The Statistical Analysis of a Random, Moving Surface. *Philosophical Transactions of the Royal Society A: Mathematical, Physical and Engineering Sciences*, 249 (966):321–387, 1957. ISSN 1364-503X. doi: 10.1098/rsta.1957.0002.

Longuet-Higgins, M. S., Cartwright, D., and Smith, N. D. Observations of the directional spectrum of sea waves using the motions of a floating buoy. *Ocean wave spectra*, pages 111–136, 1963. ISSN 00117471. doi: 10.1016/0011-7471(65)91457-9.

Lucas, J., Cruz, J., Salter, S., Taylor, J., and Bryden, I. Update on the Design of a 1:33 Scale Model of a Modified Edinburgh Duck WEC. *Volume 6: Nick Newman Symposium on Marine Hydrodynamics; Yoshida and Maeda Special Symposium on Ocean Space Utilization; Special Symposium on Offshore Renewable Energy*, 6:605–615, 2008. doi: 10.1115/OMAE2008-57230.

Lygre, A. and Krogstad, H. E. Maximum Entropy Estimation of the Directional Distribution in Ocean Wave Spectra, 1986. ISSN 1520-0485. URL `http://journals.ametsoc.org/doi/abs/10.1175/1520-0485{%}281986{%}29016{%}3C2052{%}3AMEEOTD{%}3E2.0.CO{%}3B2`.

Maeda, K., Hosotani, N., Tamura, K., and Ando, H. Wave making properties of circular basin. *Proceedings of the 2004 International Symposium on Underwater Technology (IEEE Cat. No.04EX869)*, 2004.

Mahaute, B. L. *An Introduction to Hydrodynamics and Waterwaves*, volume 53. Springer-Verlag, 2014. ISBN 9780874216561. doi: 10.1007/s13398-014-0173-7.2.

Mansard, E. P. D. and Funke, E. R. The Measurement of Incident and Reflected Spectra Using a Least Squares Method. *Proceedings of 17th Conference on Coastal Engineering, Sydney, Australia.*, pages 154–172, 1980. ISSN 08938717. doi: 10.1061/9780872622647.008.

Mansour, A. E. and Ertekin, R. C. Report of technical committee I.1 environment. *Proceedings of the 15th international ship and offshore structures congress*, 1, 2003.

MARIN. Basins, 2016. URL `http://www.marin.nl/web/Facilities-Tools/Basins.htm`.

MARINTEK. Marintek laboratories, 2016. URL `https://www.sintef.no/en/marintek/marintek-laboratories/`.

Martins, J. COMMENTS ON THE WAVE FIELD OF CIRCULAR TANK. 1, 2015. ISSN 1098-6596. doi: 10.1017/CBO9781107415324.004.

Martins, J., Naito, S., Minoura, M., and Shimakawa, Y. WAVE AND FORCE MEASUREMENTS IN CIRCULAR COMPACT BASIN. *Proceedings of the 20th Pan-American Congress of Naval Engineering. S{ã}o Paulo, Brasil*, 53(9):1689–1699, 2007. ISSN 1098-6596. doi: 10.1017/CBO9781107415324.004.

Martins, J. A. d. A. Measurements in Circular Wave Tank With Active Generators. *Volume 4: Ocean Engineering; Ocean Renewable Energy; Ocean Space Utilization, Parts A and B*, pages 629–637, 2009. doi: 10.1115/OMAE2009-80013.

Massel, S. R. *Ocean Surface Waves: Their Physics and Prediction (Advanced Series on Ocean Engineering)*. 1996. ISBN 9789810221096.

McCombes, T., Johnstone, C. M., Holmes, B., Myers, L. E., Bahaj, A. S., and Kofoed, J. P. Deliverable 3.4 - Best practice for tank testing of small marine energy devices. *EquiMar Project*, pages 1–48, 2010.

Meindl, A. Guide to moored buoys and other ocean data acquisition systems. *DBCP Technical Document*, 8:40, 1996.

Meyer, C. and Papakonstantinou, P. A. On the complexity of constructing Golomb Rulers. *Discrete Applied Mathematics*, 157(4):738–748, 2009. ISSN 0166218X. doi: 10.1016/j.dam.2008.07.006.

Michel, W. H. Sea spectra revisited. *Marine Technology*, 36(4):211–227, 1999.

Miles, M. D. and Funke, E. R. A Comparison of Methods for Synthesis of Directional Seas, 1989. ISSN 08927219.

Mitsuyasu, H. A historical note on the study of ocean surface waves. *Journal of Oceanography*, 58(1):109–120, 2002. ISSN 09168370. doi: 10.1023/A:1015880802272.

Mitsuyasu, H., Tasai, F., Suhara, T., Mizuno, S., Ohkusu, M., Honda, T., and Rikiishi, K. Observations of the directional spectrum of ocean waves using a coverleaf buoy. *Journal of Physical Oceanography*, 5(4):750–760, 1975. ISSN 0022-3670. doi: 10.1175/1520-0485(1975)005<0750:OOTDSO>2.0.CO;2.

Mollison, D. Assessing the wave energy resource (Chapter 11). *Statistics for the environment 2: water-related issues*, pages 205–221, 1994.

Munk, W. Proposed uniform procedure for observing waves and interpreting instrument records. *La Jolla, California: Wave Project at the Scripps Institute of Oceanography, Report*, (26), 1944.

Neill, S. P., Lewis, M. J., Hashemi, M. R., Slater, E., Lawrence, J., and Spall, S. A. Inter-annual and inter-seasonal variability of the Orkney wave power resource. *Applied Energy*, 132:339–348, nov 2014. ISSN 03062619. doi: 10.1016/j.apenergy.2014.07.023.

Nematbakhsh, A. Comparison of Experimental Data of a Moored Multibody Wave Energy Device With a Hybrid Cfd and. *Proceedings of the ASME 2015 34th International Conference on Ocean, Offshore and Arctic Engineering OMAE2015*, pages 1–10, 2015. doi: 10.1115/OMAE2015-41732.

Newman, J. N. Analysis of wave generators and absorbers in basins. *Applied Ocean Research*, 32(1):71–82, feb 2010. ISSN 01411187. doi: 10.1016/j.apor.2010.04.004.

NMRI. National Maritime Research Institute -Main facilities, 2016. URL `https://www.nmri.go.jp/main/overview/facilities/facilities{_}e.html`.

Noble, D. R., Davey, T., Smith, H. C. M., Kaklis, P., Robinson, A., and Bruce, T. Characterisation of spatial variation in currents generated in the FloWave Ocean Energy Research Facility. In *11th European Wave and Tidal Energy Conference, Nantes, France*, pages 1–8, Nantes, France, 2015.

Nwogu, O. Maximum entropy estimation of directional wave spectra from an array of wave probes. *Applied Ocean Research*, 11(4):176–182, 1989. ISSN 01411187. doi: 10.1016/0141-1187(89)90016-3.

Nwogu, O. Effect of steady currents on directional wave spectra. In *12th Intl Conf on Offshore Mechanics & Arctic Engng, OMAE 1993*, volume I, Offshor, pages 25–32, Glasgow, UK, jun 1993. ASME. ISBN 0791807835.

Nwogu, O., Mansard, E., Miles, M., and Isaacson, M. Estimation of directional wave spectra by the maximum entropy method. *Proceedings*, 1987.

Ochi, M. K. and Hubble, E. N. On six-parameter wave spectra. *Proceedings of the 15th International Conference on Coastal Engineering*, 1:301–328, 1976. ISSN 2156-1028.

Oltman-Shay, J. and Guza, R. T. A Data-Adaptive Ocean Wave Directional-Spectrum Estimator for Pitch and Roll Type Measurements. *Journal of Physical Oceanography*, 14(11):1800–1810, 1984. ISSN 0022-3670. doi: 10.1175/1520-0485(1984)014<1800:ADAOWD>2.0.CO;2.

Onorato, M., Cavaleri, L., Fouques, S., Gramstad, O., Janssen, P. a. E. M., Monbaliu, J., Osborne, a. R., Pakozdi, C., Serio, M., Stansberg, C. T., Toffoli, a., and Trulsen, K. Statistical properties of mechanically generated surface gravity waves: a laboratory experiment in a three-dimensional wave basin. *Journal of Fluid Mechanics*, 627(2009):235, 2009. ISSN 0022-1120. doi: 10.1017/S002211200900603X.

O'Reilly, O., Savas, Ö., Judge, C., and Namachchivaya, N. Preliminary Experimental Results for a Novel Wave Energy Converter. *Proceedings of 2011 NSF Engineering Research and Innovation Conference, Atlanta, Georgia*, pages 1–3, 2011.

Panicker, N. and Borgman, L. Directional Spectra From Wave-Gage Arrays. *Coastal Engineering Proceedings*, 1:117–136, 1970. ISSN 2156-1028. URL `https://journals.tdl.org/icce/index.php/icce/article/view/2612`.

Pascal, R., Payne, G., Theobald, C., and Bryden, I. Parametric models for the performance of wave energy converters. *Applied Ocean Research*, 38:112–124, oct 2012. ISSN 01411187. doi: 10.1016/j.apor.2012.06.003.

Pascal, R. Quantification of the influence of directional sea state parameters over the performances of wave energy converters. *Doctor*, page 260, 2012.

Pascal, R., Lucas, J., Ingram, D. M., and Bryden, I. Assessing and improving the Edinburgh curved wave tank. In *Proceedings of the 19th International Offshore and Polar Engineering Conference*, pages 269–276, 2009. ISBN 9781880653531.

Pascal, R., Torres Molina, A., and Gonzalez Andreu, A. Going further than the scatter diagram : tools for analysing the wave resource and classifying sites. In *Proceedings of the 11th European Wave and Tidal Energy Conference*, pages 5–12, 2015.

Pierson, W. J., Neumann, G., and James, R. W. Practical Methods For Observing And Forecasting Ocean Waves By Means Of Wave Spectra And Statistics. *Hydrographic Office under authority of the Secretary of the Navy*, page 284, 1955.

Pierson, W. J. J. and Moskowitz, L. A Proposed Spectral Form for Fully Developed Wind Seas Based on the Similarity Theory of S. A. Kitaigorodskii. *Journal of Geophysical Research*, 69(24):5181–5190, 1964. ISSN 0148-0227. doi: 10.1029/JZ069i024p05181.

Plant, W. J. The Ocean Wave Height Variance Spectrum: Wavenumber Peak versus Frequency Peak. *Journal of Physical Oceanography*, 39(9):2382–2383, 2009. ISSN 0022-3670. doi: 10.1175/2009JPO4268.1.

Plymouth University. Coastal, Ocean And Sediment Transport (COAST) laboratory, 2016. URL `https://www.plymouth.ac.uk/research/institutes/marine-institute/coast-laboratory`.

Prevosto, M. D2.6: Extremes and Long Term Extrapolation. Technical report, 2011.

Reeve, D., Chadwick, A., and Fleming, C. *Coastal Engineering: Processes, theory and design practice*. Spon Press, 2004. ISBN 0-203-64735-1.

Rhinefrank, K., Schacher, A., Prudell, J., Cruz, J., Jorge, N., Stillinger, C., Naviaux, D., Brekken, T., von Jouanne, A., Newborn, D., Yim, S., and Cox, D. Numerical and Experimental Analysis of a Novel Wave Energy Converter. *29th International Conference on Ocean, Offshore and Arctic Engineering: Volume 3*, pages 559–567, 2010. doi: 10.1115/OMAE2010-20901.

Ricci, P., Duperray, O., Torre-enciso, Y., Liria, P., and Villlate, J. L. Sea State Characterisation for Wave Energy Performance Assessment at the Biscay Marine Energy Platform. *EWTEC 2011 Proceedings*, (October), 2011.

Rodríguez, G. and Guedes Soares, C. A criterion for the automatic identification of multimodal sea wave spectra. *Applied Ocean Research*, 21(6):329–333, 1999. ISSN 01411187. doi: 10.1016/S0141-1187(99)00007-3.

Rokach, L. and Maimon, O. *Data Mining and Knowledge Discovery Handbook*, volume 40. mar 2001. ISBN 9780387098227. doi: 10.1002/1521-3773(20010316)40:6<9823::AID-ANIE9823>3.3.CO;2-C.

Ruiz, M. T. Dynamics and Hydrodynamics for Floating Wave Energy Converters. Technical report, Instituto Superior Técnico, Lisbon, Portugal, 2010.

Salter, S. H. Absorbing wave-makers and wide tanks. *Directional Wave Spectra Applications*, pages 182–202, 1981.

Saulnier, J. and Pontes, M. Guidelines for wave energy resource assessment and standard wave climate. *Proc. International Conference Ocean Energy ...*, 2006.

Saulnier, J. B., Maisondieu, C., Ashton, I., and Smith, G. H. Refined sea state analysis from an array of four identical directional buoys deployed off the Northern Cornish coast (UK). *Applied Ocean Research*, 37:1–21, aug 2012. ISSN 01411187. doi: 10.1016/j.apor.2012.02.001.

Smith, J. M. One-dimensional wave-current interaction. Technical Report 9, US Army Engineer Waterways Experiment Station, Coastal Engineering Research Center, ENGINEER RESEARCH AND DEVELOPMENT CENTER VICKSBURG MS COASTAL AND HYDRAULICS LAB., 1997.

Steen, S. P. Experimental Methods in Marine Hydrodynamics. (August), 2014.

Suryanto, A. Estimation of Incident and Reflected Waves in Random Wave Experiments. *Journal of the Indonesian Mathematical Society*, (April):644–657, 2006. doi: http://dx.doi.org/10.1016/B978-1-4160-2591-7.10048-7.

Sverdrup, H. and Munk, W. Wind, Sea, and Swell. Theory of Relations For FOrecasting. *Office*, (601):44, 1947.

Teena, N. V., Sanil Kumar, V., Sudheesh, K., and Sajeev, R. Statistical analysis on extreme wave height. *Natural Hazards*, 64(1):223–236, jun 2012. ISSN 0921030X. doi: 10.1007/s11069-012-0229-y.

Thomas, G. P. Wave-current interactions: an experimental and numerical study. Part 1. Linear waves. *Journal of Fluid Mechanics*, 110(-1):457, 1981. ISSN 0022-1120. doi: 10.1017/S0022112081000839.

Thomson, J., Brown, A., Ellenson, A., and Haller, M. Extreme Conditions at Wave Energy Sites. pages 8–11.

Torsethaugen, K. A two peak wave spectral model. *Omae*, 1993.

Torsethaugen, K. *Characteristica for extreme sea states on the Norwegian continental shelf*. Norwegian Hydrodynamics Laboratories Division River and Harbour Laboratory, Trondheim Norway, 1984.

Tsanis, I. K. and Brissette, F. P. A wave directional spectra program for wave gage arrays. *Environmental Software*, 6(3):151–160, 1991. ISSN 02669838. doi: 10.1016/0266-9838(91)90026-M.

Tucker, M. J., Challenor, P. G., and Carter, D. J. T. Numerical simulation of a random sea: a common error and its effect upon wave group statistics. *Applied Ocean Research*, 6(2):118–122, apr 1984. ISSN 01411187. doi: 10.1016/0141-1187(84)90050-6.

Valamanesh, V., Myers, A. T., and Arwade, S. R. Multivariate analysis of extreme metocean conditions for offshore wind turbines. *Structural Safety*, 55:60–69, 2015. ISSN 01674730. doi: 10.1016/j.strusafe.2015.03.002.

Van Nieuwkoop, J. C. C., Smith, H. C. M., Smith, G. H., and Johanning, L. Wave resource assessment along the Cornish coast (UK) from a 23-year hindcast dataset validated against buoy measurements. *Renewable Energy*, 58:1–14, oct 2013. ISSN 09601481. doi: 10.1016/j.renene.2013.02.033.

Venugopal, V., Davey, T., Smith, H., Smith, G., Holmes, B., Barrett, S., Prevosto, M., Maisondieu, C., Cavalieri, L., Bertotti, L., Lawrence, J., and Girard, F. Wave and Tidal resource characterisation. EQUIMaR Deliverable D2.2. *Equimar Protocols*, page 83, 2011.

von Mises, R. La distribution de la plus grande de n valeurs. *American Mathematical Society*, 2(1):271–294, 1936.

Wang, S. K., Hsu, T. W., Weng, W. K., and Ou, S. H. A three-point method for estimating wave reflection of obliquely incident waves over a sloping bottom. *Coastal Engineering*, 55(2):125–138, feb 2008. ISSN 03783839. doi: 10.1016/j.coastaleng.2007.09.002.

Warnsinck, W. Report of Committee 1 on Environmental conditions. *Proceedings 2nd International Ship Structures Congress (ISSC). Delft*, 1964.

Westhuis, J., van Groesen, E., and Huijsmans, R. Experiments and numerics of bichromatic wave groups. *Journal of Waterway, Port, Coastal, and Ocean Engineering*, 127(6):334–342, 2001. ISSN 0733950X. doi: 10.1061/(ASCE)0733-950X(2001)127:6(334).

Westphalen, J., Greaves, D., and Raby, A. Investigation of Wave-Structure Interaction Using State of the Art CFD Techniques. *Open Journal of Fluid ...*, (March):18–43, 2014. ISSN 2165-3852. doi: 10.4236/ojfd.2014.41003.

Winterstein, S. R., Ude, T. C., Cornell, C. a., Bjerager, P., and Haver, S. Environmental Parameters for Extreme Response: Inverse Form with Omission Factors. *Icossar-93*, (August):9–13, 1993.

Wolf, J., Hargreaves, J., and Flather, R. Application of the SWAN shallow water wave model to some UK coastal sites. (57), 2000.

Young, I. R. On the measurement of directional wave spectra. *Applied Ocean Research*, 16(5): 283–294, 1994. ISSN 01411187. doi: 10.1016/0141-1187(94)90017-5.

Zanuttigh, B. and Andersen, T. L. Wave reflection in 3D conditions. *Coastal Engineering*, 57 (5):531–538, may 2010. ISSN 03783839. doi: 10.1016/j.coastaleng.2009.12.006.

Zanuttigh, B., Formentin, S. M., and Briganti, R. A neural network for the prediction of wave reflection from coastal and harbor structures. *Coastal Engineering*, 80:49–67, oct 2013. ISSN 03783839. doi: 10.1016/j.coastaleng.2013.05.004.

Zelt, J. A. and Skjelbreia, J. E. Estimating Incident and Reflected Wave Fields Using an Arbitrary Number of Wave Gauges. *Coastal Engineering Proceedings*, 1:777–789, 2011. ISSN 2156-1028.

Zhang, D., Aggidis, G., Wang, Y., McCabe, A., and Li, W. Experimental results from wave tank trials of a multi-axis wave energy converter. *Applied Physics Letters*, 103(10):1–5, 2013. ISSN 00036951. doi: 10.1063/1.4820435.

Zhang, H. Analysis of Laboratory Generated Sea Waves. (December):76, 2011.

Zurkinden, A. S., Ferri, F., Beatty, S., Kofoed, J. P., and Kramer, M. M. Non-linear numerical modeling and experimental testing of a point absorber wave energy converter. *Ocean Engineering*, 78:11–21, 2014. ISSN 00298018. doi: 10.1016/j.oceaneng.2013.12.009.

Appendix A

Full Sea State Outputs

Example sea state outputs for the production EMEC sea states are provided in Section 7.2, along with the full extreme sea state outputs. The full set of directional and frequency spectra are shown here, along with frequency dependent reflection coefficients. Directional spectra are shown in Figs. A.1 to A.4, whilst the frequency spectra and reflection coefficients can be found in Fig. A.5

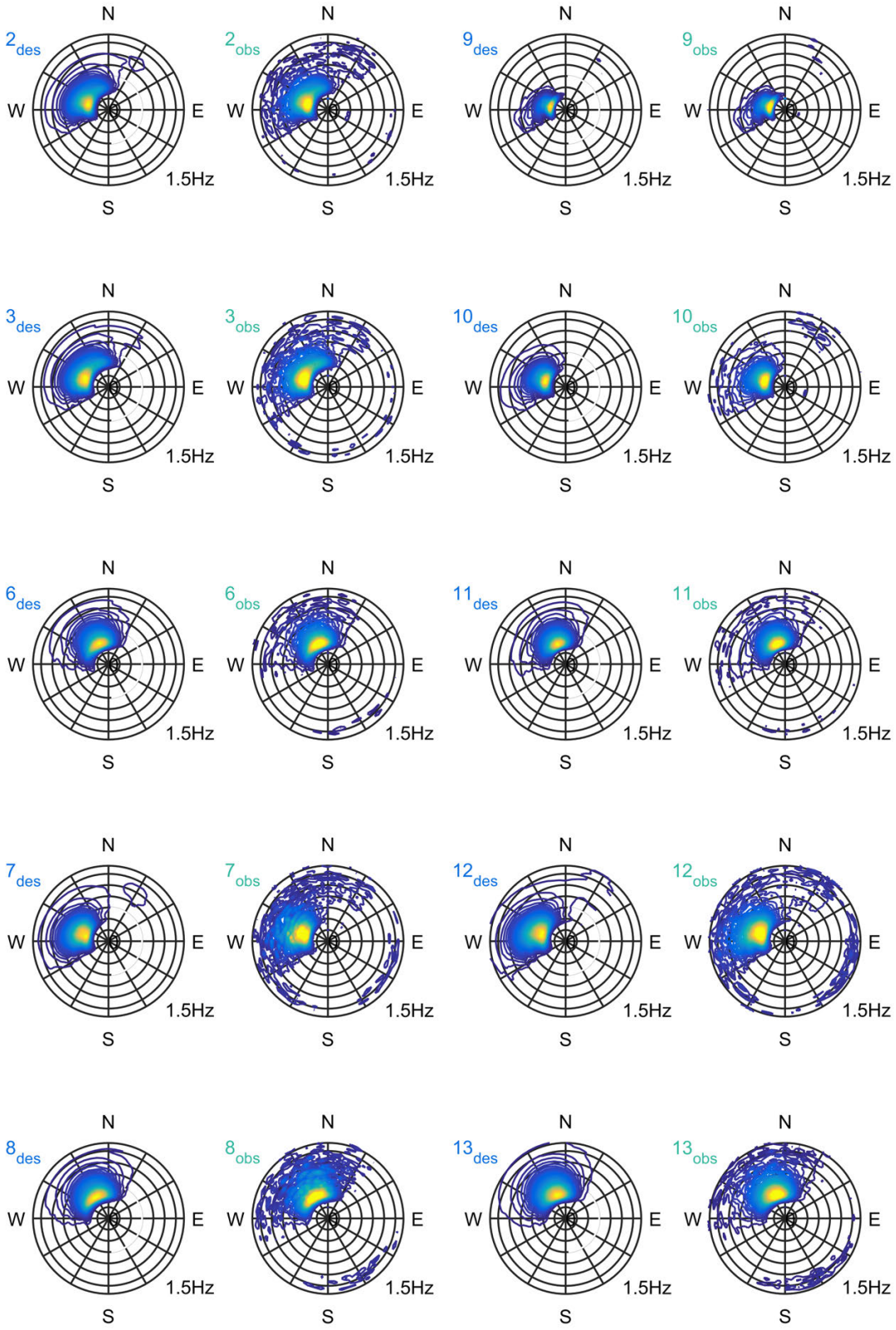

Figure A.1: SPAIR method directional spectrum outputs for sea states 2-13

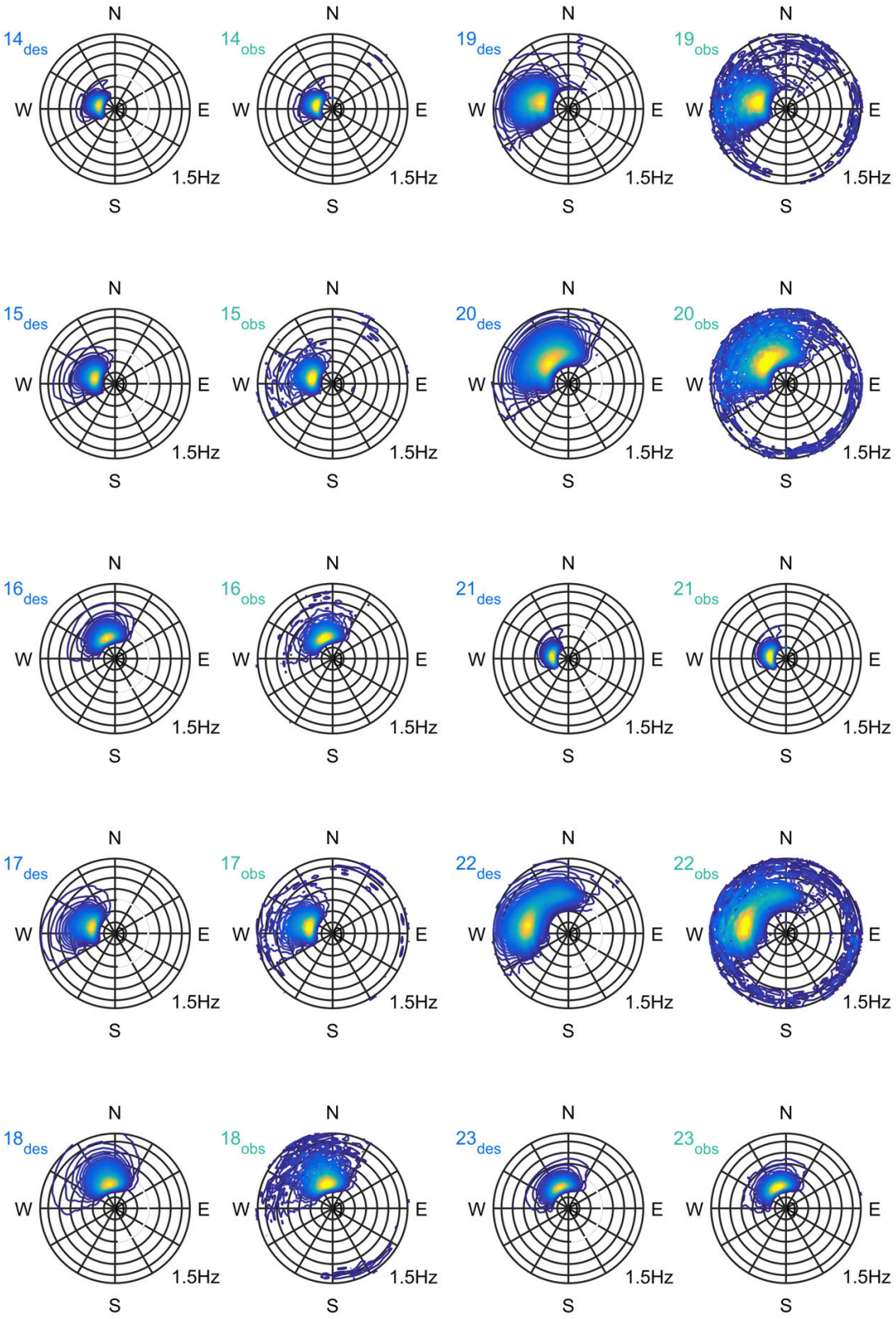

Figure A.2: SPAIR method directional spectrum outputs for sea states 14-23

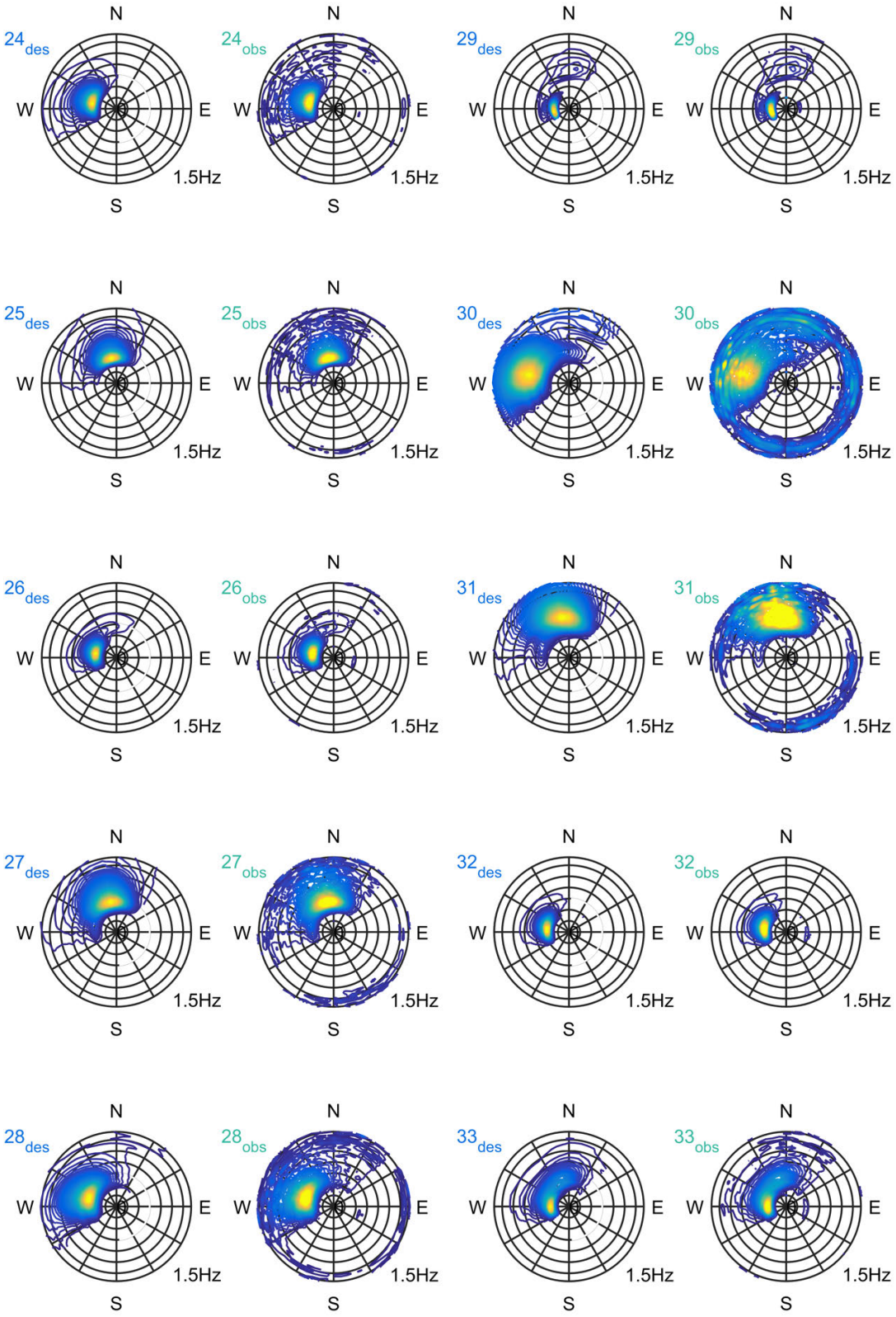

Figure A.3: SPAIR method directional spectrum outputs for sea states 24-33

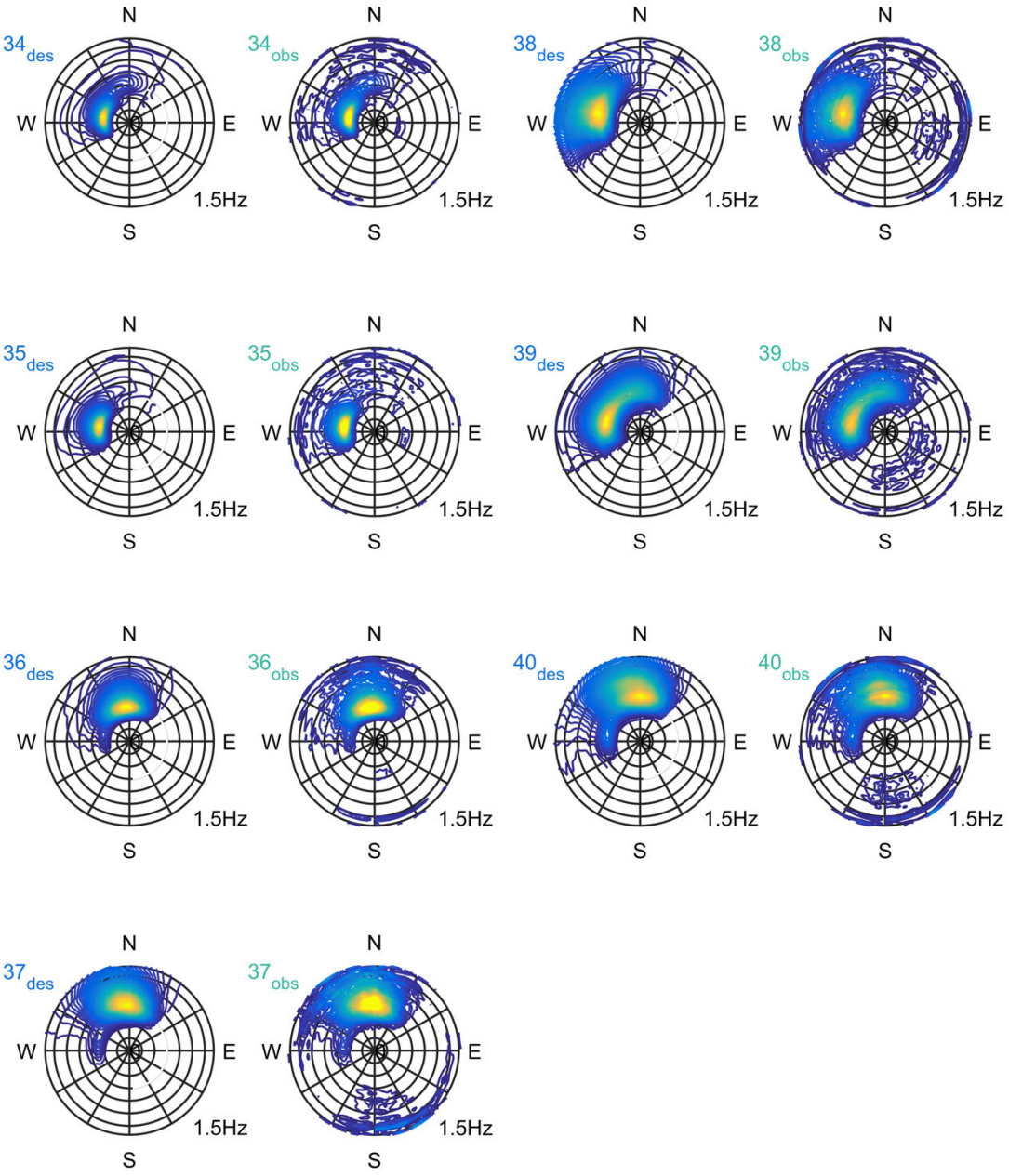

Figure A.4: SPAIR method directional spectrum outputs for sea states 34-40

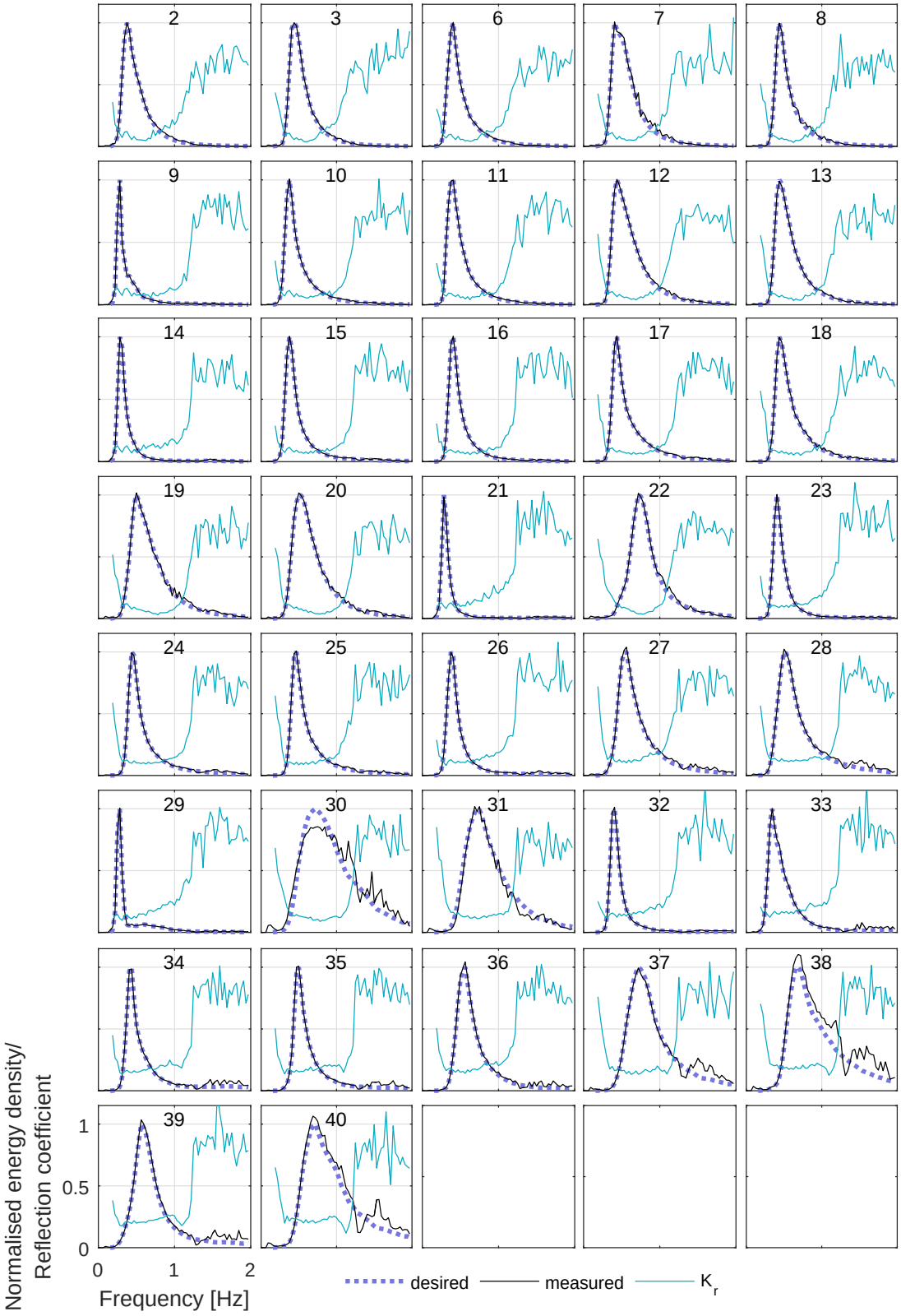

Figure A.5: SPAIR method incident frequency spectrum outputs for all sea states that can be generated

Appendix B

Directional Wave Gauge Array Study

In this appendix the study used to identify a favourable array layout for directional spectrum reconstruction is detailed, as referenced in Section 3.4.2.3. The aim is to produce a suitable wave gauge array that can be used for all sea state measurement and validation at FloWave. This will require an effective configuration to be decided upon, before being sized for the range of potential wavelengths. In addition it is important to identify a preferred reconstruction method as this will influence the array choice and performance. The aim of this study is therefore to create an overall directional spectrum measurement strategy, defining the array and reconstruction method to be used for further work.

To carry out this study 10 array candidates have been identified, detailed in Appendix B.1. These are then studied, looking at the array statistics along with sensitivities to signal noise, relative size, mean direction and directional spreading. A representative parametric sea state is created using a JONSWAP spectrum ($\gamma = 3.3$) with a cos^{2s} spreading factor applied. Sea state simulations are then carried out using an IFFT of Eq. (4.8).

Directional spectrum reconstruction is carried out using the EMLM, EMEP and SPAIR approaches. The BDM approach wasn't used in this study as there is an error in the DIWASP toolbox for this method, and the simulations are required to be in Matlab. The IMLM method was omitted due to the time taken to carry out the simulations, and that the outputs appear very similar to the EMLM approach.

As this is a high dimensional problem default values have been used once they have been seen to be representative. These are defined in Table B.1 and enable sensitivity to individual parameters to be isolated. The default spectrum resulting from these values is shown in Fig. B.1.

This initial study enables array and reconstruction sensitivities to be understood for typical sea states over a range of parameters. In Appendix B.4 two array candidates are chosen and a study on their performance in actual size (not relative to wavelength) is carried out. The size is a trade-off between noise influence and aliasing, and therefore three noise scenarios are used. A wide-band, wide-spread sea state is used as an indicator of the array performance over the directional and frequency range of interest. From this a final array configuration, size and reconstruction method is chosen.

Table B.1: Default values for array study

Parameter	Value
$\bar{\theta}$ [rad]	$\pi/2$
cos^{2s} spreading factor	10
Signal to noise ratio	10
$\bar{L}/L_p$	0.05
T_p [s]	2
H_{m0} [m]	0.2
γ	3.3

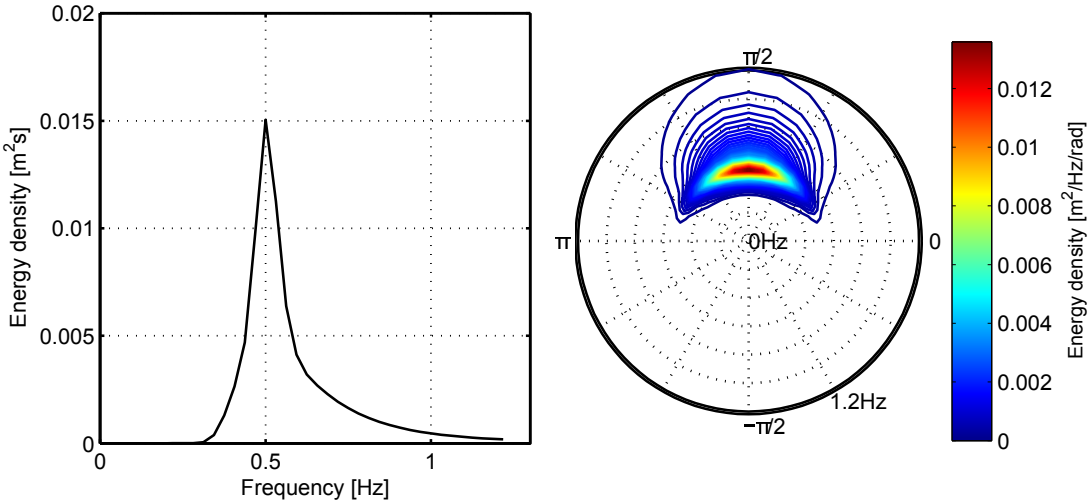

Figure B.1: Default frequency spectrum (left) and directional spectrum (right) used for directional array study

B.1 Array Candidates

Ten potential array candidates have been identified for study. Delta and star arrays as detailed in Goda (2010) are used, along with the 6 gauge Haubrich (1968) array and 5 gauge Nwogu (1989) array. Additional arrays have been created for 6 and 7 probes using a polygon and a circle, while the remaining 4 arrays are 8 and 16 gauge results from the random and Costas array tools developed in Sections 3.4.2.2 and 3.4.2.2. These arrays shown relative to their mean separation distance are shown in Fig. B.2.

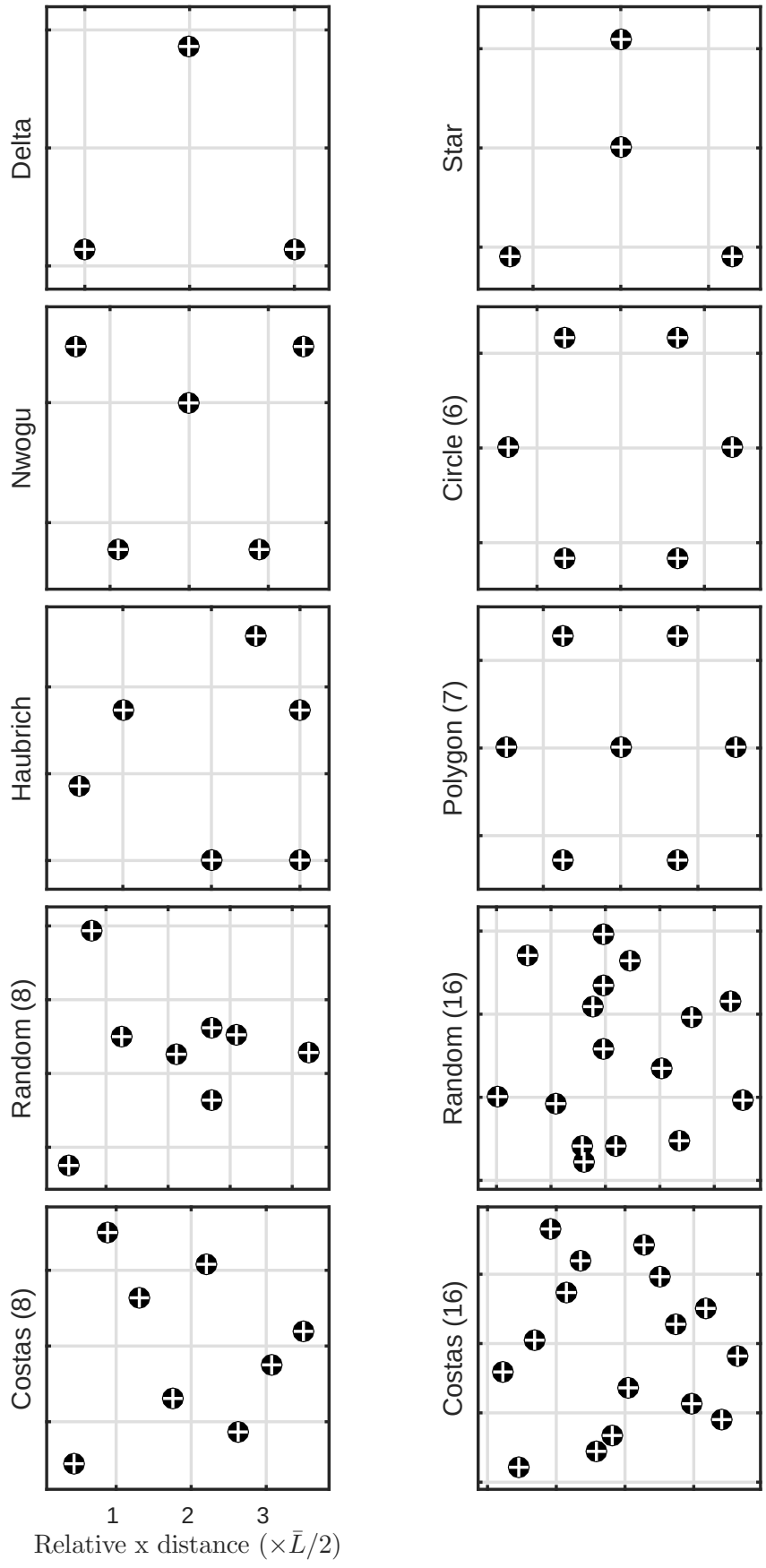

Figure B.2: Array candidates. Each grid line is half the mean separation distance for the array candidate, i.e. $\bar{L}/2$

B.2 Array Statistics

Non-dimensional array statistics (as used by Pascal (2012)) are shown in Figs. B.3 and B.4. Fig. B.3 shows how these statistics vary depending on the number of gauges, and the type of array. It can be seen that the separation standard deviation relative to the mean separation distance is generally lower with a low number of gauges, especially with 'standard' arrays, but any array with 6 gauges or more appears to have an $SDEV/\bar{L}$ value of around 0.45. This gives an indicator of how the spread of separations is different for small arrays. The dimensionless area tends to increase as the number of gauges increases, as does the relative maximum separation. It is interesting to note the delta array which contains separations with only one magnitude, has a standard deviation of zero and a relative maximum separation of 1.

Fig. B.4 shows the potential variability of the random and Costas array tool outputs. The variability shown for the random array tool is from 100 outcomes of the tool, with 1000 solutions per outcome. As the Costas array tool will always choose the same preferred array the variability shown here is between all known Costas arrays of that order.

The Costas array outputs tend to show less variability and also tend to show lower mean values in all of the array statistics. This is largely expected. This is because the random arrays are placed on a 1.2×2 m rig and therefore have the potential contain a small number of much larger separations along the 2 m dimension. This typically creates larger $max(L)/\bar{L}$ and $A/\bar{L}^2$ values. In contrast, the Costas arrays tend to be roughly square and so have smaller relative areas and maximum separations. Additionally, as they are placed on a regular grid, separations are regularly spaced leading to lower standard deviation.

It is clear for both tools that increasing the number of gauges reduces the relative standard deviations whilst increasing relative areas and maximum separations. There is, however, fairly significant variability in the outputs of the random array tool, especially for 8 gauges, suggesting that 1000 random solutions may not be enough iterations to guarantee similar solutions. The variability is lower for the Costas array tool, which may mean that the choice of Costas array is not so important.

B.3 Sensitivity

B.3.1 Effect of Noise

The effect of noise on the array candidates, for the three reconstruction methods is shown in Fig. B.5. Relatively speaking it can be seen that the SPAIR method is most affected by noise, however shows a lower error overall. The SNR level is likely to be around $10^2:1 \rightarrow 10^1:1$ in most cases, and in this region it can be seen that the SPAIR method is favourable, independent of the array choice.

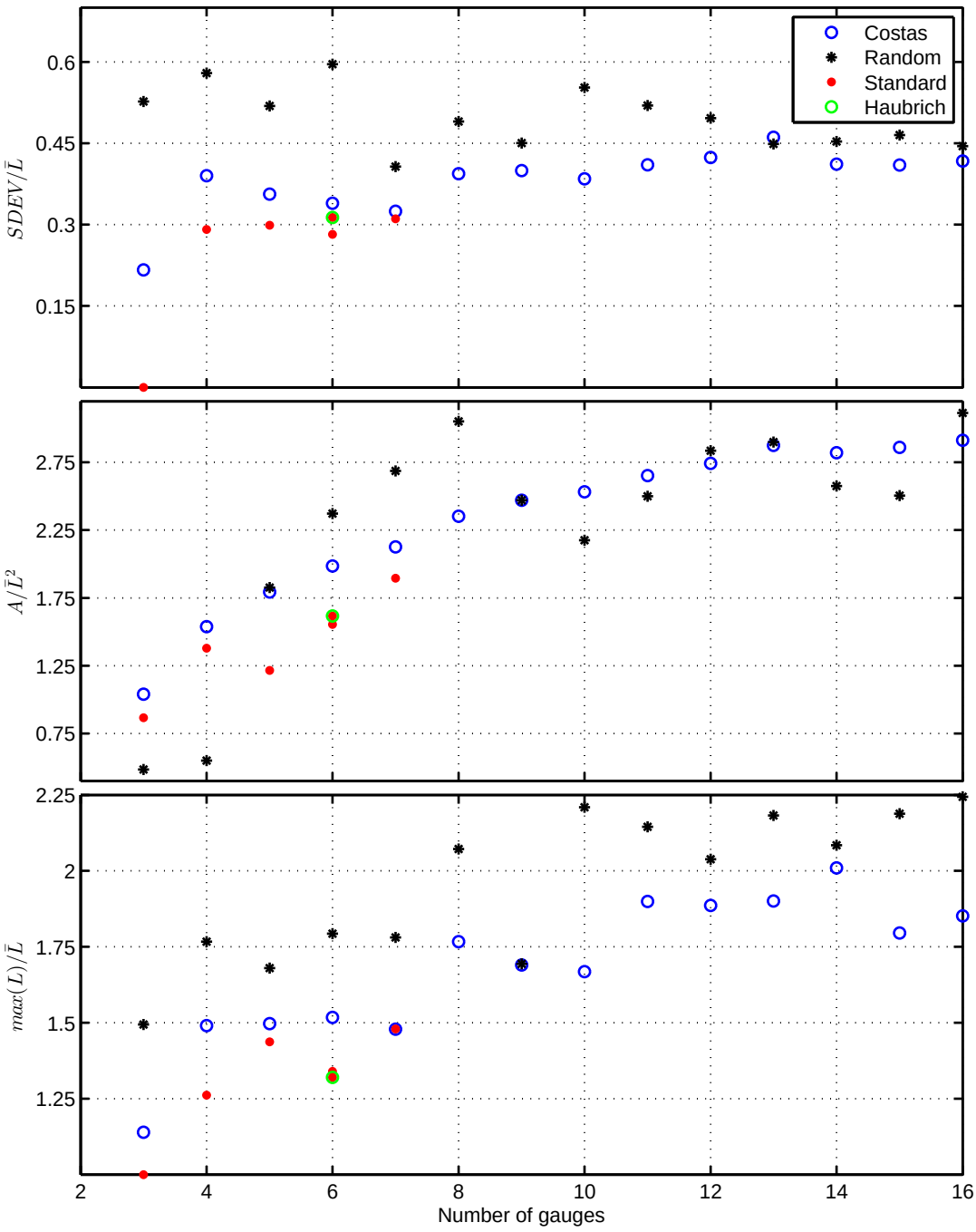

Figure B.3: Effect of number of gauges on array statistics for random and Costas array tools, and for the array candidates chosen. As there are two 'standard' arrays with 7 gauges the Haubrich array has been circled in green.

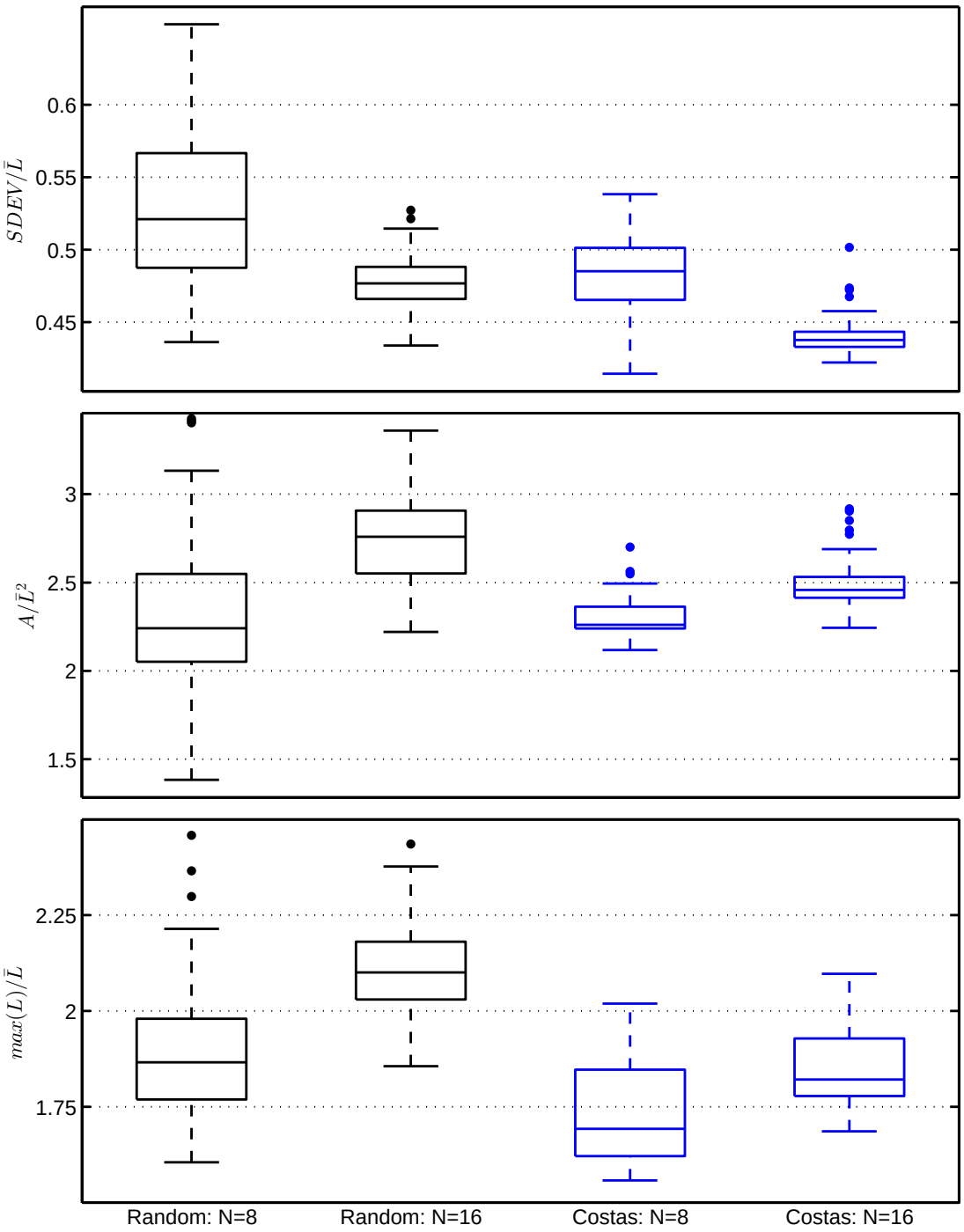

Figure B.4: Box-plots of array statistics between various potential array solutions. For the random probe placement tool the variation shown is from 100 different outcomes of the tool (1000 solution per outcome). The Costas array variation is between all Costas arrays of that order

Using the default size and sea state parameters defined in Table B.1, it is difficult to identify a favourable array. Interestingly and somewhat counter-intuitively it can be seen that for the EMLM method having 8 gauges performs favourably, however with 16 gauges (generated using either Costas or random tools) there are larger perceived errors. This suggests that the DIWASP implementation of the EMLM approach may have issues dealing with large numbers of separations.

B.3.2 Effect of Relative Size

Reconstruction performance is highly sensitive to the array size and incorporated separations relative the wavelengths present in the tank. This is due to the potential for aliasing if separations are greater than half a component wavelength.

It can be seen in Fig. B.6 that the SPAIR method is particularly sensitive to the relative size. This is because, at present, the SPAIR method uses triads of gauges, and requires all separations within a triad to be less than half a component wavelength for the estimate to be used. This means if the array is relatively large, there may not be separations small enough to resolve the angular information for some high frequency components. This leads to a largely predictable error increase with size, as a function of the proportion of energy above the limiting wave frequency. The SPAIR method be improved in future so that all separations less than half a wavelength can be used. Despite this it is clear that if the array is sized appropriately the method in its current form still provides the best, and most predictable outputs.

For all of the methods it proves beneficial to have more gauges when the array is large, due to having a greater number of useful, smaller separations. As a result of this, for the majority of relative array sizes the Costas and random array tool outputs give the most favourable results. The random arrays prove more effective over a larger relative size range than the Costas because they contain some gauge clusters with smaller separations than the Costas 'integer base unit' (see Fig. B.2).

B.3.3 Effect of Mean Direction

Fig. B.7 shows the effect of mean direction. As expected there is very little change in the performance of the SPAIR outputs. The EMLM outputs show some minor sensitivity, whilst the EMEP outputs display some peculiar and hard to explain issues at around $\pi/4$ for some of the Costas and random arrays. This further highlights the unpredictability of the EMEP method.

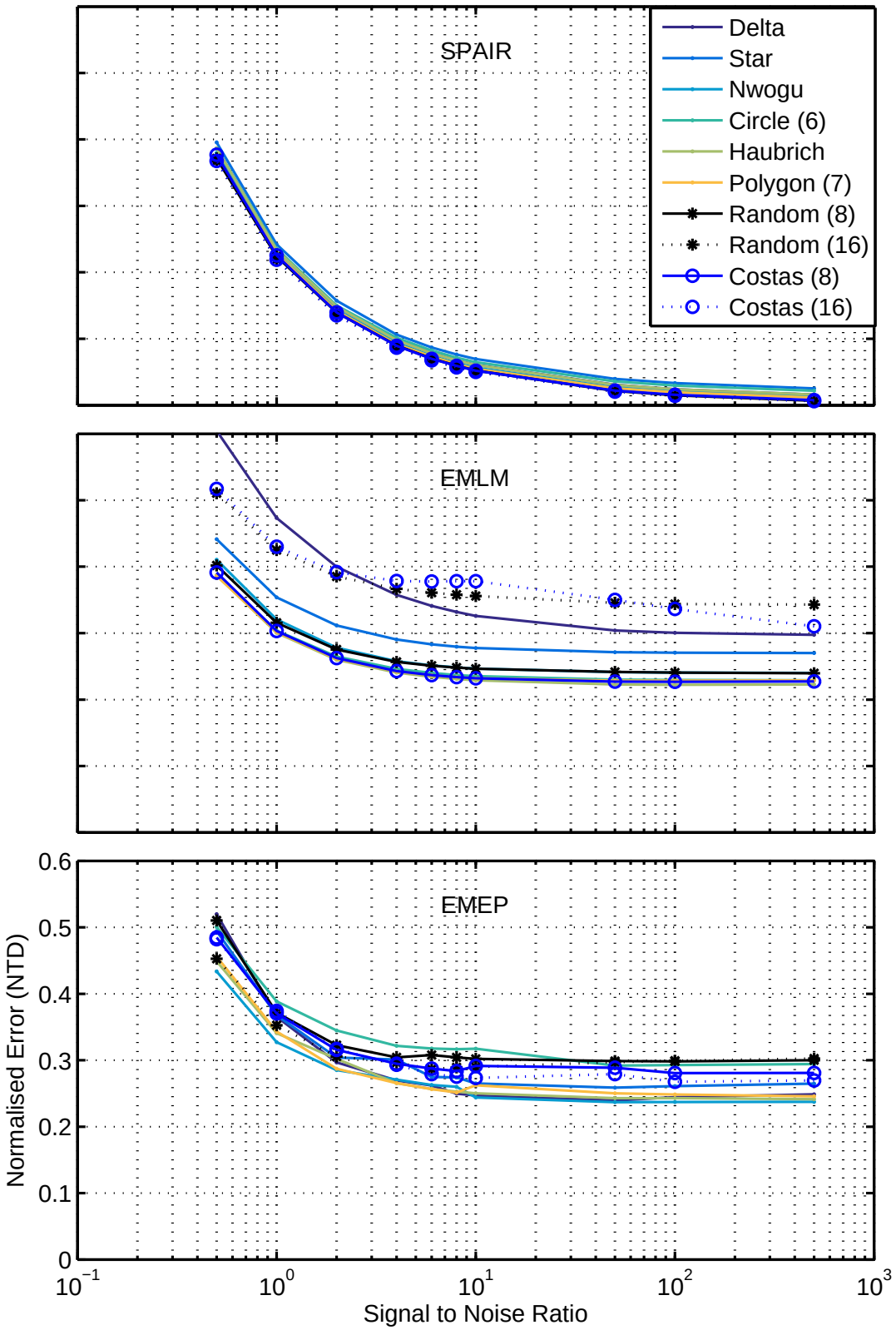

Figure B.5: Effect of noise on the array candidates for the default spectrum. Outputs shown using the SPAIR, EMLM and EMEP methods

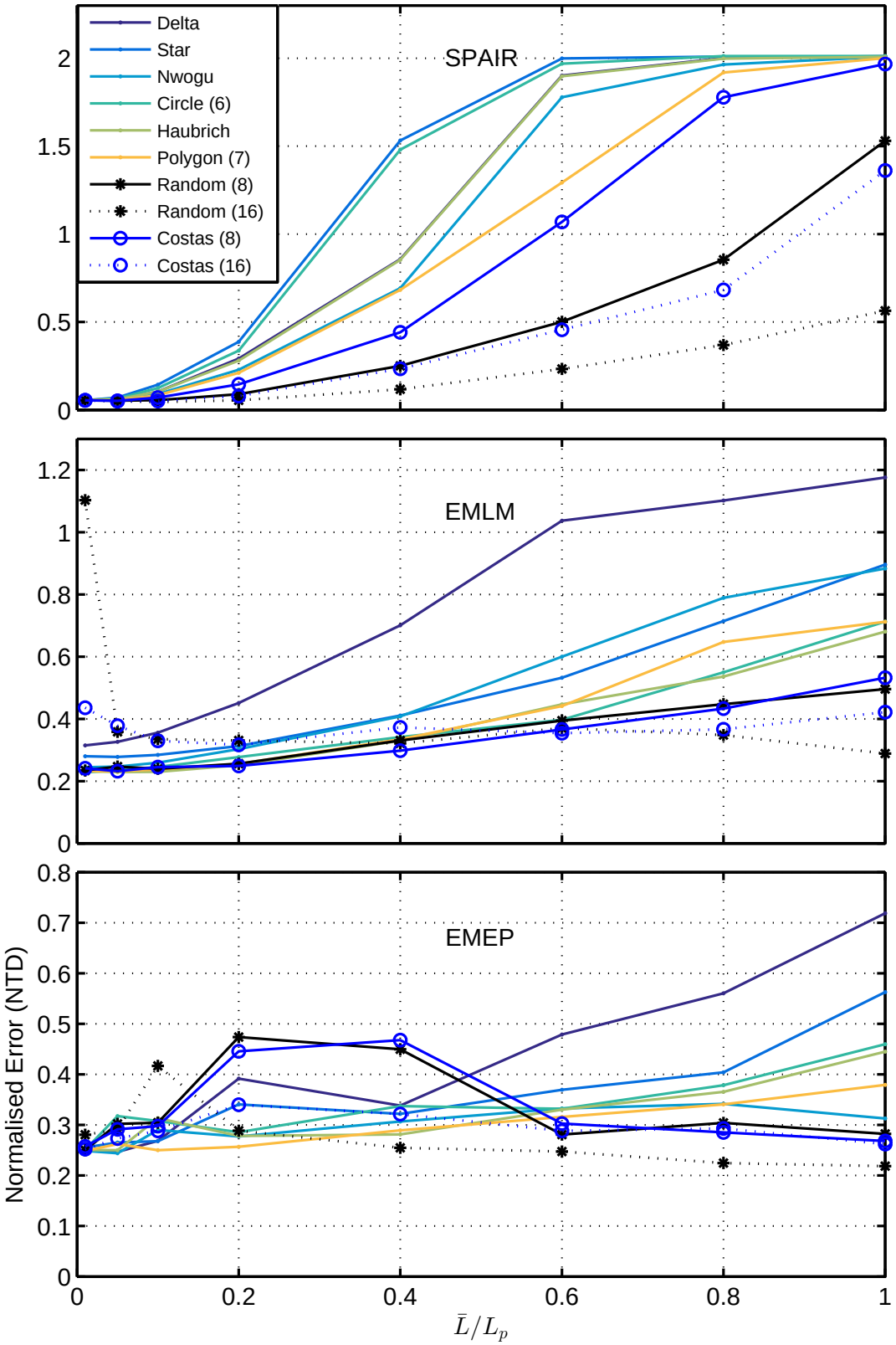

Figure B.6: Effect of relative size on the array candidates for the default spectrum. Outputs shown using the SPAIR, EMLM and EMEP methods

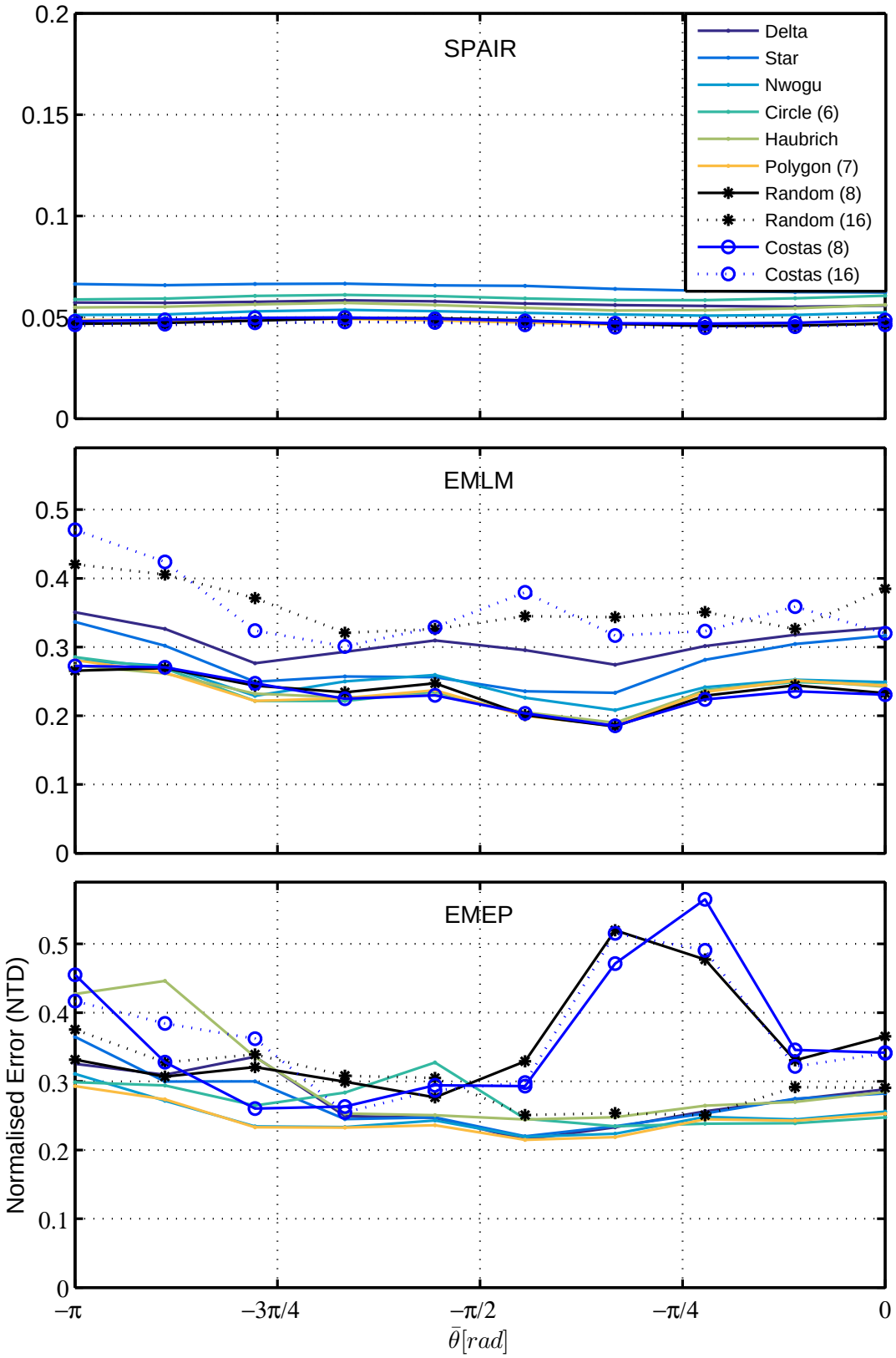

Figure B.7: Effect of mean direction on the array candidates for the default spectrum. Outputs shown using the SPAIR, EMLM and EMEP methods

B.3.4 Effect of Spreading

Spreading appears to have little effect on the reconstruction performance for any of the arrays or methods. Smaller cos^{2s} spreading values i.e. higher spreading, leads to slightly lower performance for the SPAIR method, however for the EMLM and EMEP methods it appears the opposite is true. These differences may be due to the relative number of useful in-line array separations differing as a function of angle, in combination with how the method utilises such separations. A greater spread therefore may increase or decrease the array-reconstruction performance depending on the reference mean direction and the reconstruction method.

B.4 Final choice of Array, Array Size and Reconstruction Method

The aim is to create an overall directional spectrum measurement strategy, defining the reconstruction method, whilst creating an array that is effective across the entire tank range of interest. From Appendix B.3 it is clear that the SPAIR method will provide the most accurate reconstructed directional spectra as long as the array is sized appropriately. The SPAIR method will therefore be used throughout this work and the array will be chosen based on its combined performance with this method. From Figs. B.5 to B.8 it is clear that the SPAIR method favours a larger number of gauges with the 16 gauge Costas and random array tool outputs proving to be most effective. Practical constraints meant that there were only 8 gauges available throughout this work and so the 8 gauges outputs from both the Costas and random array tools have been chosen for practical sizing in the facility.

Table 3.2 shows the tank range of interest to be 0.2→1.2 Hz, and over 360°. To test the array performance under these conditions many typical sea states could be simulated, covering this range. However, it was thought more effective to use a broad-banded, broad-spread spectrum covering the entire range, placing an equal weighting on all angles and all frequency components. This sea state has therefore been created, shown in Fig. B.9, and is used for the final sizing of the array.

In an idealised scenario, without noise or position error the array would be sized so that all separations are below half the smallest wavelength i.e. $\frac{L_{1.2Hz}}{2} = 0.5419$, meaning the phase information from all separations can be used to estimate component angles. However, in reality, signal noise and probe position error exist and with smaller arrays these introduce larger phase errors and hence angle estimation errors. For this reason 3 different noise scenarios ($10^2 : 1 \rightarrow 1 : 1$) have been simulated along with the generated wave field, and the array tested at various relative scales, this time defined relative to $L_{min} = L_{1.2Hz}$. The EMLM and EMEP results have been computed for comparison, and to check array performance in the event these methods were used at the request of a client.

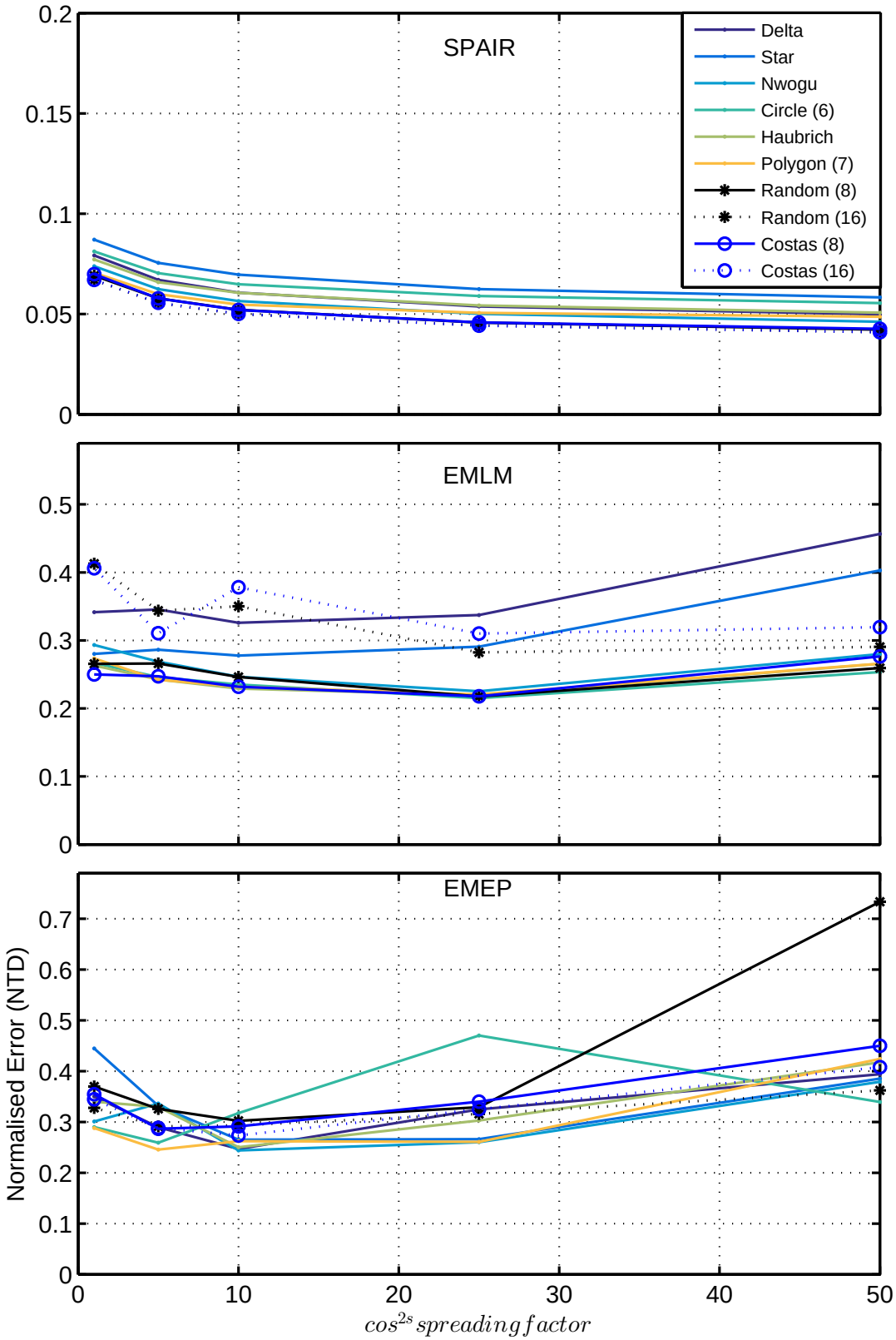

Figure B.8: Effect of directional spreading on the array candidates for the default spectrum. Outputs shown using the SPAIR, EMLM and EMEP methods

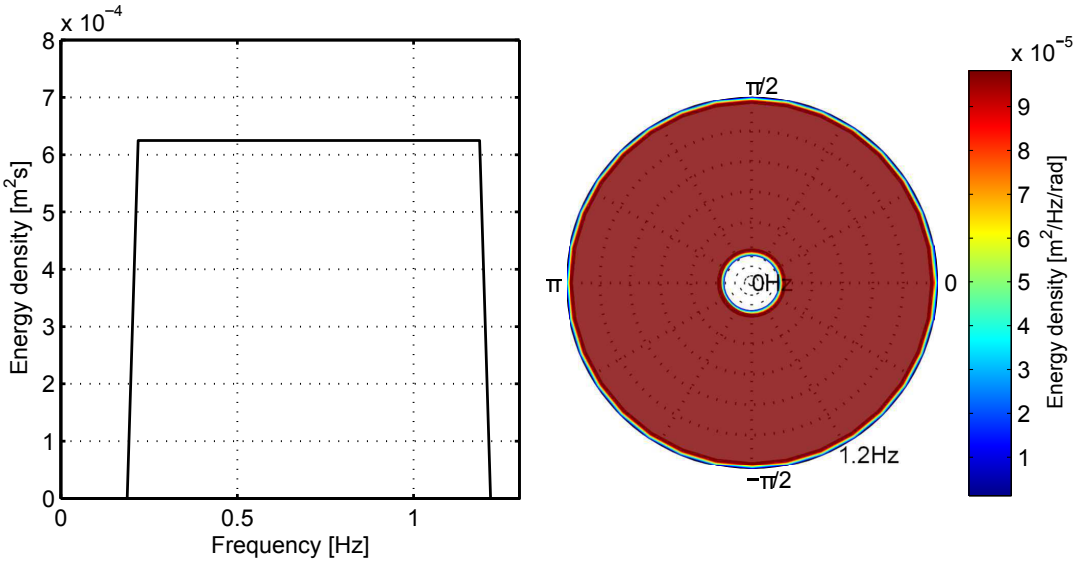

Figure B.9: Broad-band, broad-spread frequency spectrum (left) and directional spectrum (right) used for final array sizing

The perceived error results for the broad-banded broad-spread spectrum for the arrays at different sizes are shown in Fig. B.10. Concentrating on the SPAIR results it can be seen that the performance of the 8 gauge Costas and random arrays are identical up until values of $\bar{L}/L_{1.2Hz} = 0.6$. After this point the Costas array error increases because no gauge triads exist where all separations are below 0.542 m. This is not the case for the random array as it encompasses smaller clusters of gauges. Additionally, as expected, it can be seen that smaller arrays are affected more significantly by noise. This leads to optimal relative size values for the Costas and random arrays to be 0.6 and 1 respectively ($\bar{L}/L_{1.2Hz}$).

The final design was created using the 'random' 8 gauge array layout. Size constraints on the rig limit the relative $\bar{L}/L_{1.2Hz}$ to around 0.6 meaning the Costas and random arrays would perform very similarly up to 1.2 Hz. The random array was chosen as it has a larger range, enabling effective angle calculation up to around 1.6 Hz, whilst displaying similar performance for the EMEP and EMLM methods. The final array can be seen in therefore "Random (8)" from Fig. B.2, which is shown in Fig. 3.9 scaled to size.

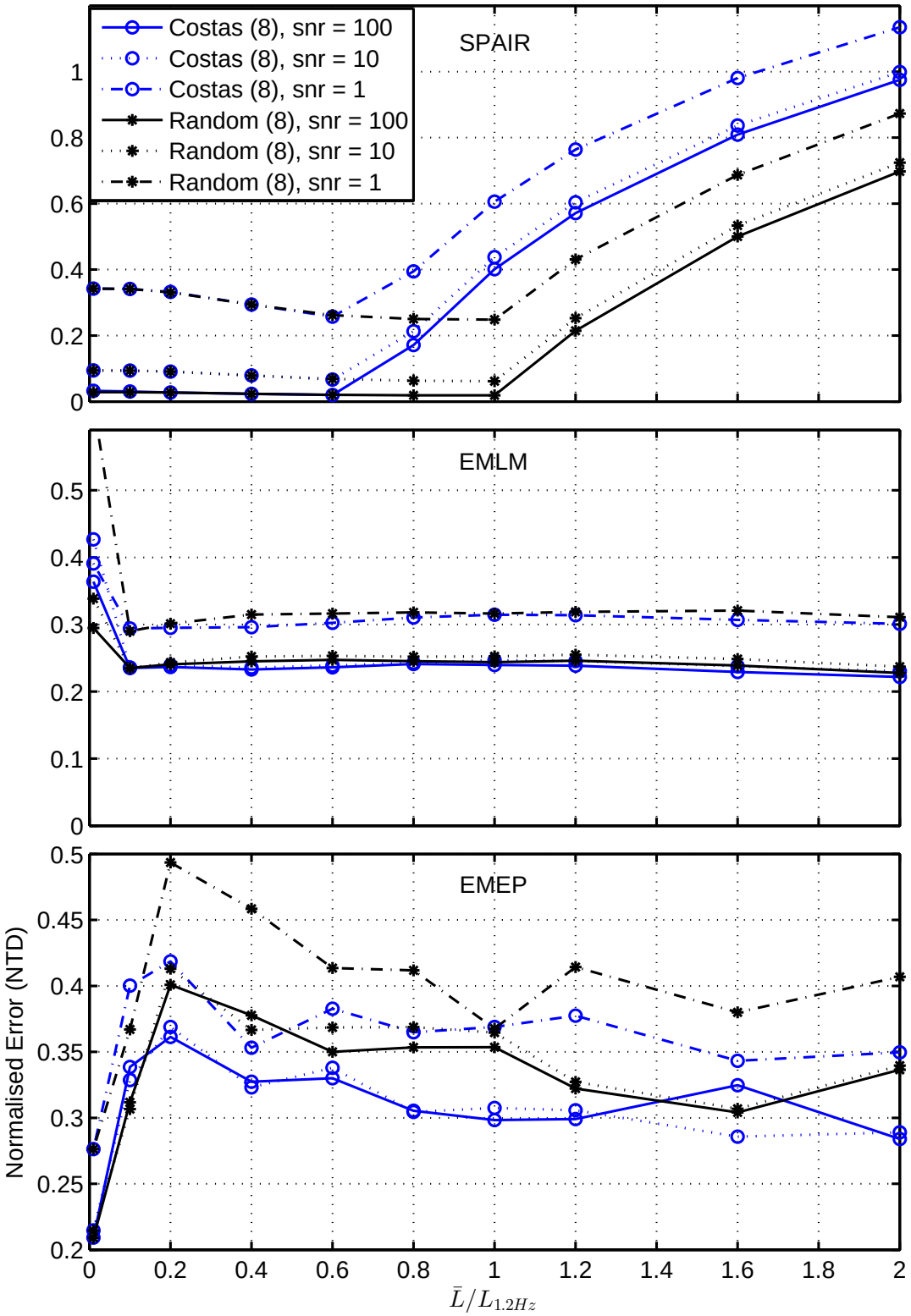

Figure B.10: Effect of noise on optimal array size for a broad banded, broad spread spectrum. Outputs shown using the SPAIR, EMLM and EMEP methods

Appendix C

Publications

In this appendix the publications resulting from the research are attached, in the following order:

- Draycott, S., Davey, T., Ingram, D. M., Day, A., and Johanning, L. The SPAIR method: Isolating incident and reflected directional wave spectra in multidirectional wave basins. *Coastal Engineering*, 114:265–283, 2015a. ISSN 03783839. doi: 10.1016/j.coastaleng.2016.04.012
- Draycott, S., Davey, T., Ingram, D. M., Day, J. L. a., and Johanning, L. Using a Phase-Time-Path-Difference Approach to Measure Directional Wave Spectra in FloWave. *EWTEC Conference Proceedings*, pages 1–7, 2015b
- Draycott, S., Davey, T., Ingram, D. M., Lawrence, J., Day, A., and Johanning, L. Applying Site-Specific Resource Assessment : Emulation of Representative EMEC seas in the FloWave Facility. *Proceedings of the 25th (2015) International Ocean and Polar Engineering Conference*, pages 815–821, 2015c. ISSN 15551792
- Draycott, S., Davey, T., Ingram, D. M., Lawrence, J., Johanning, L., Day, A., Steynor, J., and Noble, D. Applying site specific resource assessment: methodologies for replicating real seas in the FloWave facility. *ICOE Conference Proceedings*, 44(November), 2014

Coastal Engineering 114 (2016) 265–283

Contents lists available at ScienceDirect

Coastal Engineering

journal homepage: www.elsevier.com/locate/coastaleng

The SPAIR method: Isolating incident and reflected directional wave spectra in multidirectional wave basins

S. Draycott [a,*], T. Davey [a], D.M. Ingram [b], A. Day [c], L. Johanning [d]

[a] FloWave Ocean Energy Research Facility, Max Born Crescent, King's Buildings, Edinburgh EH9 3BF, UK
[b] Institute for Energy Systems, School of Engineering, The University of Edinburgh, Edinburgh EH9 3JL, UK
[c] Naval Architecture and Marine Engineering, The University of Strathclyde, Glasgow G4 0LZ, UK
[d] Renewable Energy Research Group, University of Exeter, TR10 9E, UK

ARTICLE INFO

Article history:
Received 3 June 2015
Received in revised form 6 April 2016
Accepted 9 April 2016
Available online 25 April 2016

Keywords:
SPAIR
Tank testing
Directional spectrum measurement
FloWave
Phase-Time-Path-Difference
Wave reflection
Single-summation method

ABSTRACT

Wave tank tests aiming to reproduce realistic or site specific conditions will commonly involve using directionally spread, short-crested sea states. The measurement of these directional characteristics is required for the purposes of calibrating and validating the modelled sea state. Commonly used methods of directional spectrum reconstruction, based on directional spreading functions, have an inherent level of uncertainty associated with them. In this paper we aim to reduce the uncertainty in directional spectrum validation by introducing the SPAIR (Single-summation PTPD Approach with In-line Reflections) method, in combination with a directional wave gauge array. A variety of wave conditions were generated in the FloWave Ocean Energy Research Facility, Edinburgh, UK, to obtain a range of sea state and reflection scenarios. The presented approach is found to provide improved estimates of directional spectra over standard methods, reducing the mean apparent directional deviation down to below 6% over the range of sea states. Additionally, the method isolates incident and reflected spectra in both the frequency and time domain, and can separate these wave systems over 360°. The accuracy of the method is shown to be only slightly sensitive to the level of in-line reflection present, but at present cannot deal with oblique reflections. The SPAIR method, as presented or with slight modification, will allow complex directional sea states to be validated more effectively, enabling multidirectional wave basins to simulate realistic wave scenarios with increased confidence.

1. Introduction

Wave tank tests facilitate the understanding of how complex sea conditions influence the dynamics of man-made structures. A key requirement for any test programme is the ability to create these conditions in a highly controlled and repeatable manner. To have such control, it is vital to be able to measure and validate the desired test conditions. Whilst this is a relatively simple task when generating uni-directional waves, the extension to the measurement and validation of directional spectra can be challenging.

The experimental measurements presented here were made at the FloWave Ocean Energy Research Facility, located at the University of Edinburgh (Fig. 1). The facility consists of a circular 25 m diameter, 2 m depth combined wave and current test basin which is encircled by 168 active-absorbing force-feedback wavemakers. This geometry and design are intended to remove any inherent limitation on wave direction and therefore allow the recreation of highly spread and highly complex directional spectra. As such, it presents an ideal environment to explore and demonstrate directional measurement methodologies.

To validate a directional spectrum, a method of reconstruction is required. Most of these methods aim to resolve the frequency-dependent Directional Spreading Function (DSF), thus describing the distribution of wave energy with direction. These methods use the measured cross-spectra between wave gauges, along with the known gauge positions, to fit a directional distribution. There are a number of approaches in doing this, with some commonly used approaches being the Bayesian Directional Method (BDM) (Hashimoto and Konbune, 1988), the Maximum Likelihood Method (MLM) (Benoit et al., 1997; Krogstad, 1988), and the Extended Maximum Entropy Principal (EMEP) (Hashimoto et al., 1994).

The nature of DSF-based reconstruction methods means that there is some uncertainty associated with the estimate. In this work we use a combined wave generation-measurement approach that enables the directional spectra to be estimated with increased certainty, whilst additionally enabling the isolation of incident and reflected components under certain conditions. This method has been named SPAIR, or the Single-summation PTPD Approach with In-line Reflections, and enables directional sea states to be validated with greater confidence.

* Corresponding author.
E-mail address: S.Draycott@ed.ac.uk (S. Draycott).

http://dx.doi.org/10.1016/j.coastaleng.2016.04.012

Fig. 1. The FloWave Ocean Energy Research Facility.

To generate the waves a single-summation method is used (Miles and Funke, 1989) ensuring that each discrete frequency component only has one propagation direction. This enables meaningful frequency dependent wave directions to be inferred from a wave gauge array, using a Phase-Time-Path-Difference (PTPD) approach (Esteva, 1976), providing an estimate of the directional spectrum. This approach is demonstrated by Draycott et al. (2015), and has been shown to be significantly more effective than both the EMEP and BDM methods at estimating directional spectra when combined with single-summation wave generation. In this paper the method is demonstrated over a larger test matrix, designed to explore the reconstruction effectiveness over a range of peak frequencies, directional spreading and peak steepness. Additional complex spectra are explored, which highlight the benefit of using this approach when analysing highly spread or multi-modal spectra.

The SPAIR method, as employed in FloWave, uses the PTPD approach and calculated directions to perform in-line reflection analysis using a least squares method, similar to Zelt and Skjelbreia (1992). Under the assumption that reflections mirror the incident, this enables the reflected directional spectrum to be isolated, with phase information, enabling both incident and reflected time-series to be reconstructed.

Limits of the method assumptions are explored, particularly relating how the magnitude and angle of reflections affect both the incident angle calculation, and on the separation of incident and reflected components. In addition, alternative uses of these single-summation based tools are discussed for different purposes, and for when the SPAIR method assumptions are inappropriate.

2. Methodology

2.1. Sea state input and generation

2.1.1. Input sea states

To examine the SPAIR method performance under a range of representative conditions, 27 parametric sea states were created and tested at the facility. These tests cover a range of peak frequencies, f_p, directional spreading, s, and peak wave steepness', s_p (defined as H_{m0}/L_p, where H_{m0} is the significant wave height, and L_p is the peak wavelength). All of the sea states were created using JONSWAP spectra with a constant gamma value of 3.3. In addition to this, a range of mean directions were then considered, examining the influence of the wave gauge orientation on the method performance. Finally three complex sea states were created, using combinations of parametric seas to provide unconventional wave conditions; both multi-modal and highly spread. The wave parameters for these sea states are shown in Tables 1, 2 and 3.

The complex sea states in Table 3 have been designed to prove that the method can reconstruct such spectra, whilst additionally isolating the incident and reflected components over 360°. The first spectrum is a multi-modal sea state consisting of two identical wave systems with the mean direction 120° apart, whilst the second spectrum is a single wave system with a very large directional spread, spanning 360°. Two completely opposing wave systems have been used for spectrum three, with a slight difference in peak frequency. These spectra are illustrated in Fig. 17. It is often difficult to isolate the different incident modes of such spectra using conventional methods, and the isolation of the incident and reflected spectra is not usually possible at all without a defined incident range. These tests therefore serve as a useful demonstration of the capability of the SPAIR approach used here.

Table 2
Directional sensitivity tests (10 tests in total).

Wave parameter	Range of value(s)
Peak frequency, f_p [Hz]	0.6
cos-2 s spreading value, s	10
Peak steepness [%]	2
Mean direction, $\bar{\theta}$ [deg]	18, 36, 54, … , 180

2.1.2. Wave generation

Deterministic waves are generated at FloWave using force-feedback wavemakers, providing a very high degree of repeatability (Ingram et al., 2014). This enables device alterations to be assessed independently of sea state variations, and allows wave-by-wave comparisons to be made of the device in the time domain.

Throughout this work the generation of directional wave spectra is achieved using the single-summation method, avoiding phase-locking (Miles and Funke, 1989). Phase-locking occurs when waves at the same frequency but different directions interact, causing spatial patterns across the tank, thus creating a non-ergodic wave field. To avoid this, the initial frequency increments, ΔF, can be split up further to create sub-frequency increments $\delta f = \Delta F/N_\theta$, as shown in Pascal (2012). These new frequency increments, still within the original frequency bins, now have a unique wave propagation direction associated with each of them. In addition to avoiding phase-locking, this method of wave generation is key to the application of the SPAIR method. This generation approach is demonstrated in Fig. 2.

Using the re-defined directional spectrum, the surface elevation can be calculated via an Inverse Fast Fourier Transform (IFFT), or summation. The surface elevation at point $[x,y]$, and time t can now be described by:

$$\eta(x,y,t) = \sum_{i=0}^{N_f \cdot N_\theta - 1} A_i \cos(-\omega_i t + k_i[x\cos\alpha_i + y\sin\alpha_i] + \Phi_i) \quad (1)$$

where:

A_i wave amplitude of frequency component i
ω_i angular frequency of component i, rad/s
k_i $= \frac{2\pi}{L_i}$, wavenumber of component i

Table 1
Main 3×3×3 test matrix (27 tests in total).

Wave parameter	Range of values		
Peak frequency, f_p [Hz]	0.45	0.6	0.75
cos-2 s spreading value, s	5	10	25
Peak steepness [%]	1	2	4

Table 3
Complex spectra tests.

Wave parameter	Spec 1	Spec 2	Spec 3
Peak frequency, f_p [Hz]	0.5, 0.5	0.45	0.45, 0.55
cos-2 s spreading value, s	5, 5	0.5	20, 20
Mean direction, $\bar{\theta}$ [deg]	45, 165	120	90, 270

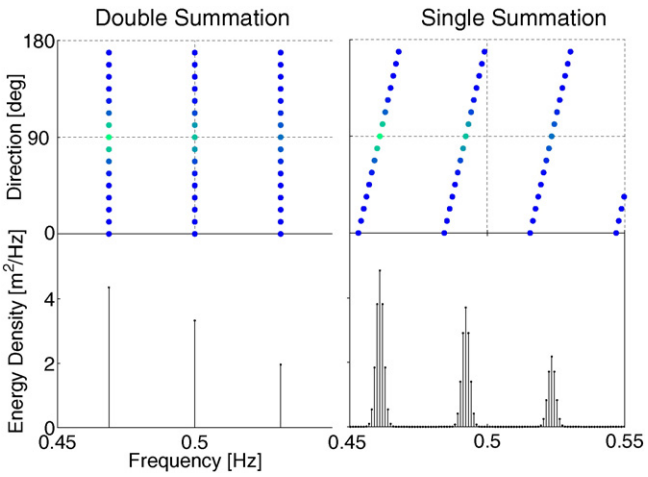

Fig. 2. The single (right) and double (left) summation methods of wave generation. This demonstrates how wave partitions made in the frequency domain are attributed unique directions (Draycott et al., 2015).

α_i wave direction of component i
Φ_i phase of component i at $x = y = t = 0$.

The sea states presented here have a repeat time, T, of 1024 s. This defines the frequency increments, δf, to be $\frac{1}{1024}$Hz, providing 2048 frequency components within the tank's nominal generation range, 0–2 Hz. For the simulation of directional spectra this was achieved using 64 frequency bins, and 32 directional bins ($N_f = 64, N_\theta = 32$). Re-defining the directional spectrum for use in the single-summation method gives the required frequency increments of:

$$\delta f = \frac{\Delta F}{N_\theta} = \frac{f_{max}}{(N_f \times N_\theta)} = \frac{1}{T} = \frac{1}{1024}\,[\mathrm{Hz}] \tag{2}$$

2.2. Experimental configuration

Wave surface elevations are measured within the facility using multiplexed two-wire resistance type wave gauges, each providing a point measurement with a sample frequency of 32 Hz. The wave generation and data acquisition (DAQ) are synchronised using a common clock, and are controlled using a single interface provided by Edinburgh Designs. Such synchronisation of DAQ and wavemaker system is expected to be needed for the application of the new method.

In order to estimate wave directionality these gauges must be deployed in an array. The wave directions will be inferred from the known array spacings, and as such it is important that these vector separations cover as many directions and magnitudes as possible relative to the wavelengths present in the tank. For DSF-based reconstruction methods this enables the directional distributions to be inferred at a range of frequencies with greater angular resolution. The PTPD method detailed in Section 2.3.1 only requires a minimum of 3 gauges, however a larger number of vector separations enables effective error reduction (see Fig. 8). In addition to this, the reflection analysis procedure shown in Section 2.3.2 benefits from having a range of projected in-line array separations for each calculated direction.

Inter-array gauge separations can be represented by their co-array, describing the vector separations between all points (Haubrich, 1968). Effective directional wave gauge arrays therefore have a uniform co-array, spanning the appropriate range of magnitudes. With this criteria in mind, an 8 gauge array layout was designed for installation on a re-configurable rig, shown in Fig. 3, with the co-array and projected in-line separations shown in Figs. 4 and 5 respectively.

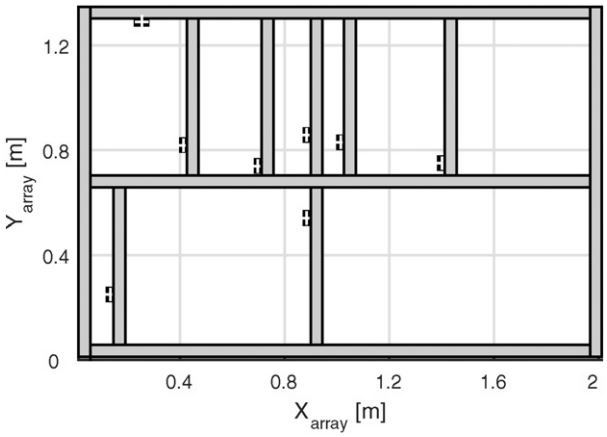

Fig. 3. Wave gauge array layout with bar positions for re-configurable rig.

It is observed that the co-array of the array design is largely uniform with no duplicate vector separations, and that there is a good range of projected in-line separations for every angle of incidence. The size of the array was chosen to ensure that there is a sufficient number of useful separations for the frequency range of interest, taken here to be 0.2 — 1.2 Hz. Analogous to the criteria proposed by Goda and Suzuki (1976) for reflection analysis, separations are considered useful for frequency component i if they are between $0.05\lambda_i$ and $0.45\lambda_i$. As $\lambda_{f\ =\ 1.2\ \mathrm{Hz}}$ is 1.08 m, and $\lambda_{f\ =\ 0.2\ \mathrm{Hz}}$ is roughly 21 m, the array has been designed so that there are a sufficient number of separations smaller than 0.49 m and larger than 1.05 m.

Gauges are used in groups of three to estimate wave angles, and so for a given frequency component the estimate is only assumed valid if all separations adhere to the separation criteria. The resulting number of valid gauge triads as a function of frequency is shown in Fig. 6, and it can be seen that for the frequency components of interest there are normally multiple useful gauge triads, and hence multiple valid angle estimates.

2.3. The SPAIR method applied to the FloWave Ocean Energy Research Facility

The SPAIR method as detailed in this section uses single-summation wave generation before estimating the frequency dependent incident angles. These angles provide projected in-line separations, which are used to perform a 2D reflection analysis for each frequency component. Under the assumption that this frequency dependent 2D approach is

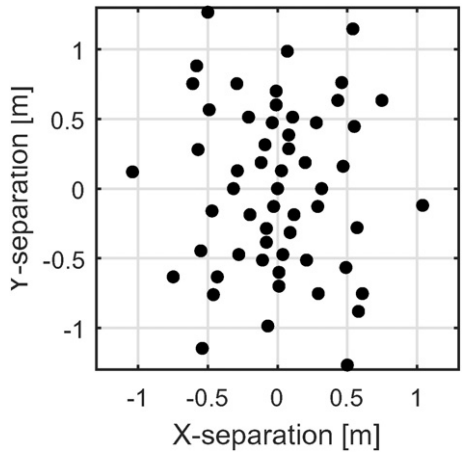

Fig. 4. Co-array separations for the wave gauge array layout shown in Fig. 3.

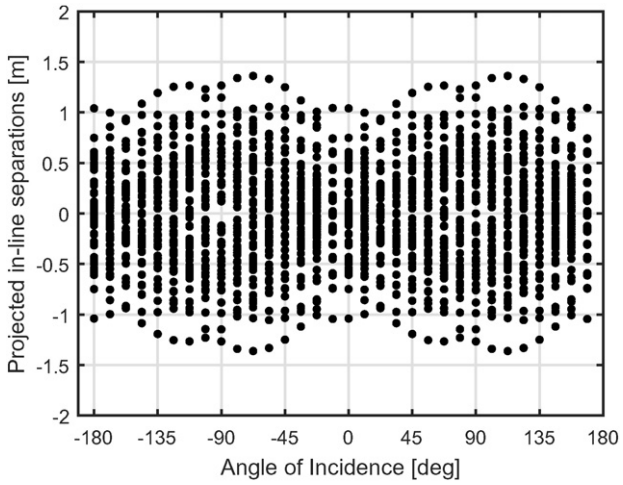

Fig. 5. Projected in-line wave gauge separations for a range of angles of incidence.

valid, this enables isolation of the incident and reflected directional spectra, and time-series.

The complete method works very well for sea state validation at the FloWave Ocean Energy Research Facility. However, the combined use of all the single-summation based tools present in the SPAIR method may not always be appropriate. For example, if it is known that the wave tank produces incident waves at the correct angle then the initial PTPD angle calculation is not required. Also if reflections are large, and not a mirror of the incident, the reflection analysis procedure will give unreliable results. The method limitations and sensitivity are detailed in Section 4.1, and alternative uses of the tools are discussed in Section 4.2.

2.3.1. Input angle calculation using PTPD approach

The current methods of calculating directional spectra in tanks, such as the EMEP and BDM approaches, have been developed for ocean measurement and subsequently utilised for wave tank analysis. Similarly, the PTPD approach was also initially developed for use in ocean measurement (Esteva, 1976; Fernandes et al., 2000). This technique has not however made the transition to the tank environment for the routine reconstruction of directional spectra. This is likely because of the method's inability to effectively resolve directional spectra in the ocean.

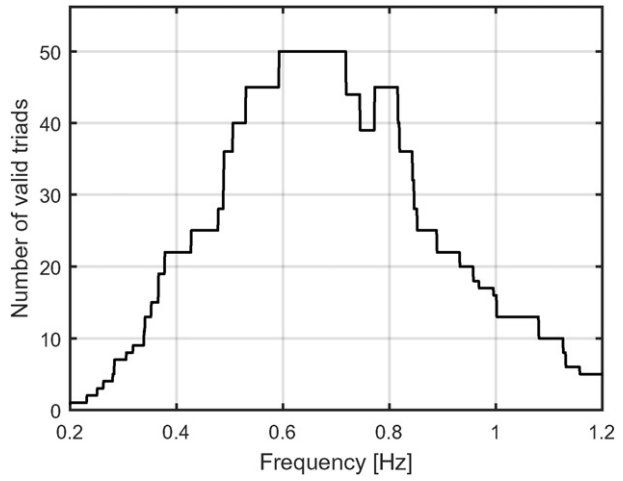

Fig. 6. Number of valid gauge triads (all separations $>0.05\lambda_i$ and $<0.45\lambda_i$) as a function of frequency for the array shown in Fig. 3.

The PTPD approach uses the phase difference between triads of gauges to infer the wave direction. In the ocean, and when using the double-summation method in tanks, the phase differences at a given frequency will encompass a range of wave components travelling in different directions. In practice the result is that the PTPD outputs essentially give a representative angle for that frequency band and cannot be used to create a full directional spectrum. When using the single-summation method of wave generation, however, there are many discrete frequency components, each of which propagates in a single direction. This should enable the method to calculate the actual directions at each sub-frequency, thereby allowing effective reconstruction of a directional spectrum when re-considering the desired, original frequency bins.

The present work uses 8 wave gauges to improve the propagation direction estimate, as previously described by Draycott et al. (2015). The method is implemented as follows:

1. Obtain Fourier coefficients $a_{i,n}$ using an FFT for each gauge n. Calculate amplitudes $A_{i,n}$ and absolute phases $\Phi_{i,n}$.
2. Find all 3 gauge combinations for N gauges, i.e. ${}^{8}C_3 = 56$.
   For every triad and all frequency components:
3. Ensure relative separations $L_{1,2}$, $L_{1,3}$ and $L_{2,3}$ are all $>0.05\lambda_i(f)$ and $<0.45\lambda_i(f)$.
   If so:
4. Calculate relative phases $\Phi_{1,2}$ and $\Phi_{1,3}$.
5. Calculate perceived angle, α, by the method of Esteva (1976). The final equations of which are shown below:

$$\alpha = \tan^{-1}\frac{\left[(x_1-x_2)\Phi_{1,3}-(x_1-x_3)\Phi_{1,2}\right]/sgn(P)}{\left[(y_1-y_3)\Phi_{1,2}-(y_1-y_2)\Phi_{1,3}\right]/sgn(P)} \tag{3}$$

$$P = [(x_1-x_2)(y_1-y_3)-(x_1-x_3)(y_1-y_2)]. \tag{4}$$

6. Take the peak of a circular kernel density estimate over all valid triad combinations as the propagation direction for that frequency.
7. Comparisons can now be made between the desired and measured angles, as per the single summation method. Additionally the data can be re-binned and compared with the desired directional spectrum.

   The PTPD approach relies on the fact that the phase difference between gauges is a function of the frequency-dependent wavelength and their relative positions. The phase difference between gauge n and gauge m, for a given Fourier coefficient, i, can therefore be represented as:

$$\begin{aligned}\Phi_{i,nm} &= k_i[(x_n-x_m)\cos\alpha_i + (y_n-y_m)\sin\alpha_i] \\ &= k_i\left(x'_{i,n}-x'_{i,m}\right).\end{aligned} \tag{5}$$

Fig. 7 shows the projected in-line x-positions for frequency i, $x_{i,n}'$, as a function of the measured wave direction, α_i. Although only 3 gauges are required to get an estimate of the wave directions it is advantageous to have multiple estimates for the propagation direction at each frequency. This is because measurement noise, position error and the presence, or build-up of reflections, may result in errors in individual directional estimates.

In this work a maximum of 56 estimates are used to give a representative direction for each frequency, disregarding estimates derived from triads with inappropriate separation magnitudes. A circular mean, or circular median value may be used from these to estimate the true incident direction at this frequency, however, to limit the influence from rogue estimates a circular kernel density estimate has been used for this work. The peak of this kernel density estimate should generally represent the

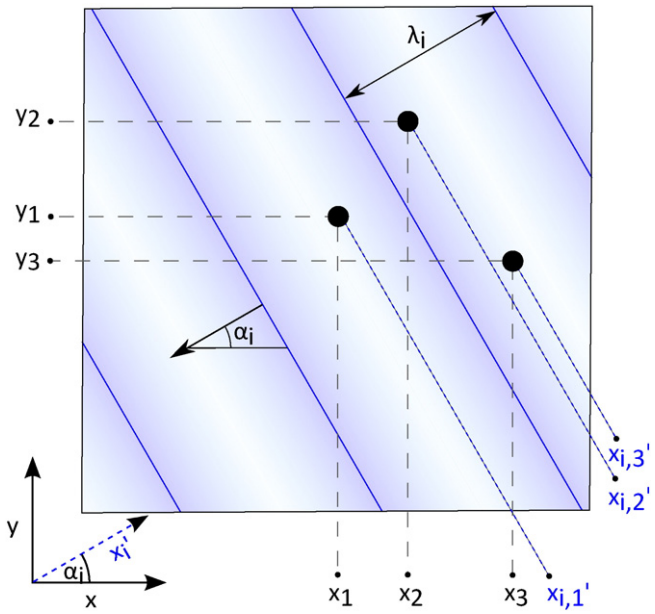

Fig. 7. Example projected x values for a single frequency component and its associated propagation direction.

incident wave direction, with estimates lying either side of the peak being affected more strongly by reflections or position error etc.

There are 2048 kernel density estimates for each sea state, corresponding to the discrete frequency increments used in these tests. Fig. 8 shows some example outputs of these estimates, highlighting the requirement to have multiple estimates in some scenarios, but not others. Fig. 8a and d highlights the advantage of using the peak of the kernel density estimates, rather than the mean, with Fig. 8a

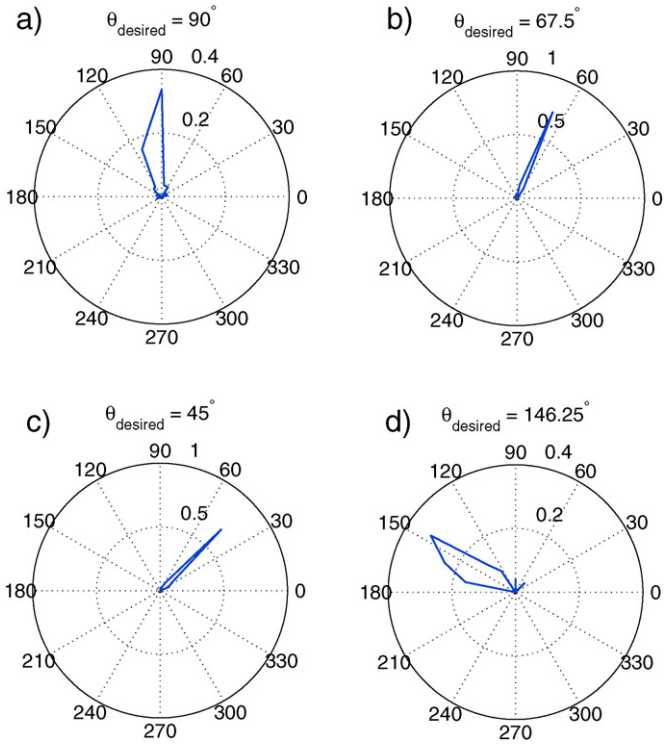

Fig. 8. Example circular kernel density outputs showing a range of different spreads in the estimate.

demonstrating this particularly well. It is clear here that using the circular mean value would have lead to a significant 'over-estimate' of the wave direction, amounting to around 10°.

2.3.2. Calculating in-line reflections using projected gauge positions

The PTPD approach used here takes advantage of the fact that the phase differences at a given frequency should be solely a function of the gauge positions and the wave propagation direction. This trait allows for the calculation of frequency dependent, in-line separations:

$$x'_{i,n} - x'_{i,m} = (x_n - x_m)\cos\alpha_i + (y_n - y_m)\sin\alpha_i. \tag{6}$$

The complex amplitude spectra measured at each gauge, $a_{i,n}$, along with these assumed separations then allow a reflection analysis procedure to take place. The process in doing this essentially treats each frequency component as a uni-direction problem.

Typical uni-directional reflection analysis can be achieved with a small number of gauges, as demonstrated by Goda and Suzuki (1976) for 2 gauges, and Mansard and Funke (1980), using a least-squares approach with 3 gauges. These methods require the gauge separations to be within a small range to give useful estimates. In this multi-directional work the effective in-line separations are highly variable, and as such require more gauges to ensure useful spacings are available.

Zelt and Skjelbreia (1992) present an extension to the Mansard & Funke method, formulating a weighted least-square approach to estimating incident and reflected wave fields for any number of gauges. This approach is used in this work with some slight modification. The three modifications made are as follows:

1. x-Values are now frequency dependent in-line x-positions, based on the calculated α values.
2. Absolute phases are used rather than phase difference to gauge 1. This eventually allows reconstruction of total, incident, and reflected time-series, and also direct use of the isolated Fourier coefficients.
3. As a weighting function the goodness function presented in Zelt and Skjelbreia (1992) is used in conjunction with the coherence spectra between gauges (dot product). This should enable spacing considerations (goodness function) to be considered in conjunction with a measure of the consistency of the phase differences between gauges. In the results presented here this has made little improvement (<2%). If, however there are particularly noisy signals, or if complex reflections build up throughout a test this may prove more useful. The coherence spectra were calculated using the in-built mscohere MATLAB function.

   The final modified equations used to calculate the complex incident and reflected Fourier coefficients, a_{inc} and a_{ref} are shown below:

$$a_{inc,i} = \sum_{n=1}^{N} C_{i,n} a_{i,n} \tag{7}$$

$$a_{ref,i} = \sum_{n=1}^{N} C^*_{i,n} a_{i,n} \tag{8}$$

where $a_{i,n}$ is the *measured* Fourier coefficients with absolute phase (rather than with phases relative to gauge 1), and

$$C_{i,n} = \frac{2iW_{i,n}}{D} \sum_{m=1}^{N} W_{i,m} \sin(\Delta\Phi_{i,nm}) e^{i\Phi_{i,m}} \tag{9}$$

$$D = 4 \sum_{n=1}^{N} \sum_{m<n} W_{i,n} W_{i,m} \left[\sin(\Delta\Phi_{i,nm})\right]^2 \tag{10}$$

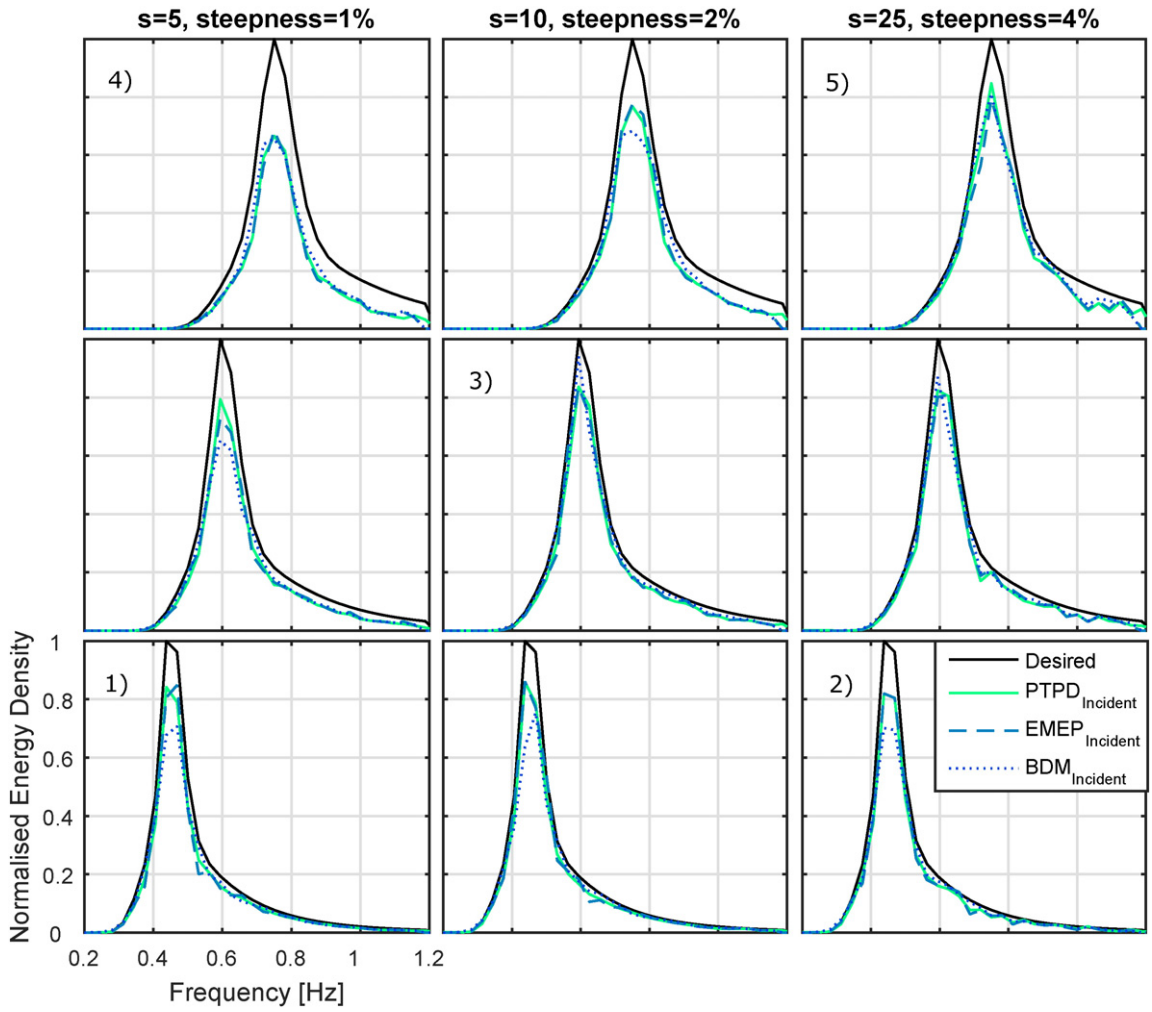

Fig. 9. Example frequency spectra outputs with numbers corresponding to directional spectra in Fig. 10.

where:

$$\Delta\Phi_{i,nm} = k_i[(x_n - x_m)\cos\alpha_i + (y_n - y_m)\sin\alpha_i] = k_i\left(x'_{i,n} - x'_{i,m}\right) \quad (11)$$

$$\Phi_{i,m} = k_i \cdot x'_{i,m}. \quad (12)$$

$W_{i,n}$ is the weighting function for gauge n and frequency i. See Zelt and Skjelbreia (1992) for the goodness function, and Mandel and Wolf (1976) for information on coherence spectra.

These equations allow the incident and reflected amplitude spectra to be resolved for single-summation generated directional spectrum. The incident and reflected wave energy density spectra can now be calculated as:

$$S_{inc,i} = \frac{|a_{inc,i}|^2}{2 \cdot \delta f} \quad (13)$$

$$S_{ref,i} = \frac{|a_{ref,i}|^2}{2 \cdot \delta f}. \quad (14)$$

The frequency-dependent reflection coefficient, $K_{r,i}$, can also be readily calculated as:

$$K_{r,i} = \frac{|a_{ref,i}|}{|a_{inc,i}|}. \quad (15)$$

2.3.3. Calculating the updated incident, and the reflected directional spectrum

Knowledge of the incident and reflected wave frequency spectrum does not allow for an update to be made to the incident directional spectrum directly. The reflections present in the tank cause gauge dependent amplitude and phase deviations. The nature of the PTPD approach means that these can manifest themselves as a directional distribution error, rather than being isolated. This requires the incident propagation directions to be recalculated, using the already isolated incident Fourier coefficients.

In order to fix the measured incident directional spectrum the isolated incident Fourier coefficients can be re-processed using the PTPD approach. This requires the phases for the base Fourier coefficients, $a_{inc,i}$, at [0,0], to be shifted to the in-line apparent gauge positions. This is done noting that:

$$a_{i,n} = a_{inc,i}e^{-i\Phi_{i,n}} + a_{ref,i}e^{i\Phi_{i,n}}. \quad (16)$$

This defines the incident, position shifted Fourier coefficients as:

$$a_{inc,i,n} = a_{inc,i}e^{-i\Phi_{i,n}} = a_{inc,i}e^{-i\left(k_i \cdot x'_{i,n}\right)}. \quad (17)$$

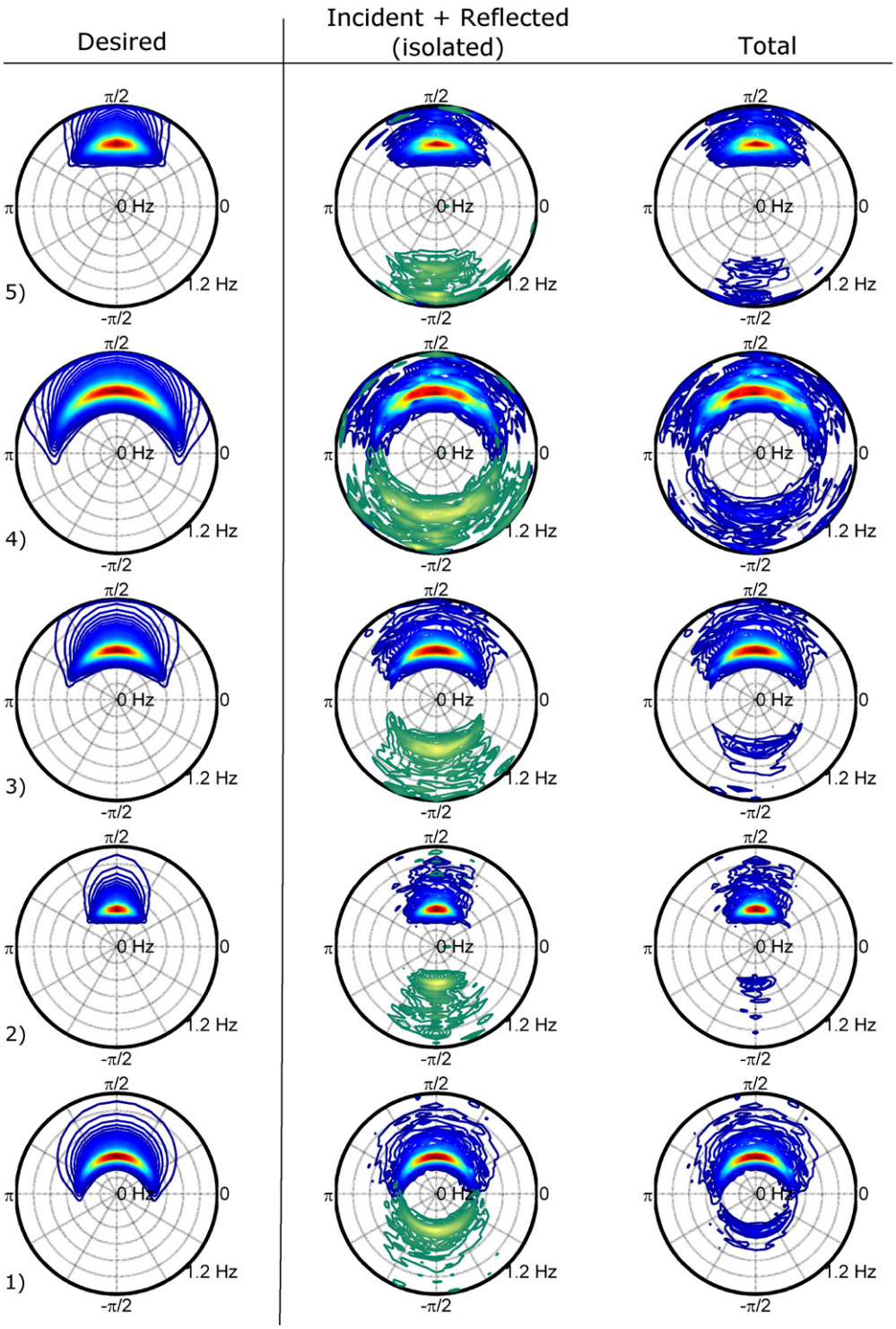

Fig. 10. Example SPAIR reconstructed directional spectra outputs. Energy density [m^2s/rad] is shown by the colour, relative to the peak of the desired spectrum. 1) 0.45 Hz, s = 5, st = 1%, 2) 0.45 Hz, s = 25, st = 4%, 3) 0.6 Hz, s = 10, st = 2% 4) 0.75 Hz, s = 5, st = 1% 5) 0.75 Hz, s = 25, st = 4%.

These Fourier coefficients can now be used directly with the PTPD approach, enabling an estimate of the incident directional spectrum to be made with an attempt to remove the artificial amplitude and phase deviations. The reflected directional spectrum can be calculated similarly, or more easily through knowledge of the reflection coefficients. In addition to this, the incident and reflected time series at the gauge positions can be estimated through an IFFT.

The nature of this combined approach means that incident and reflected spectra can be separated over all directions without requiring prior knowledge of the input angular range. Neither the BDM or EMEP

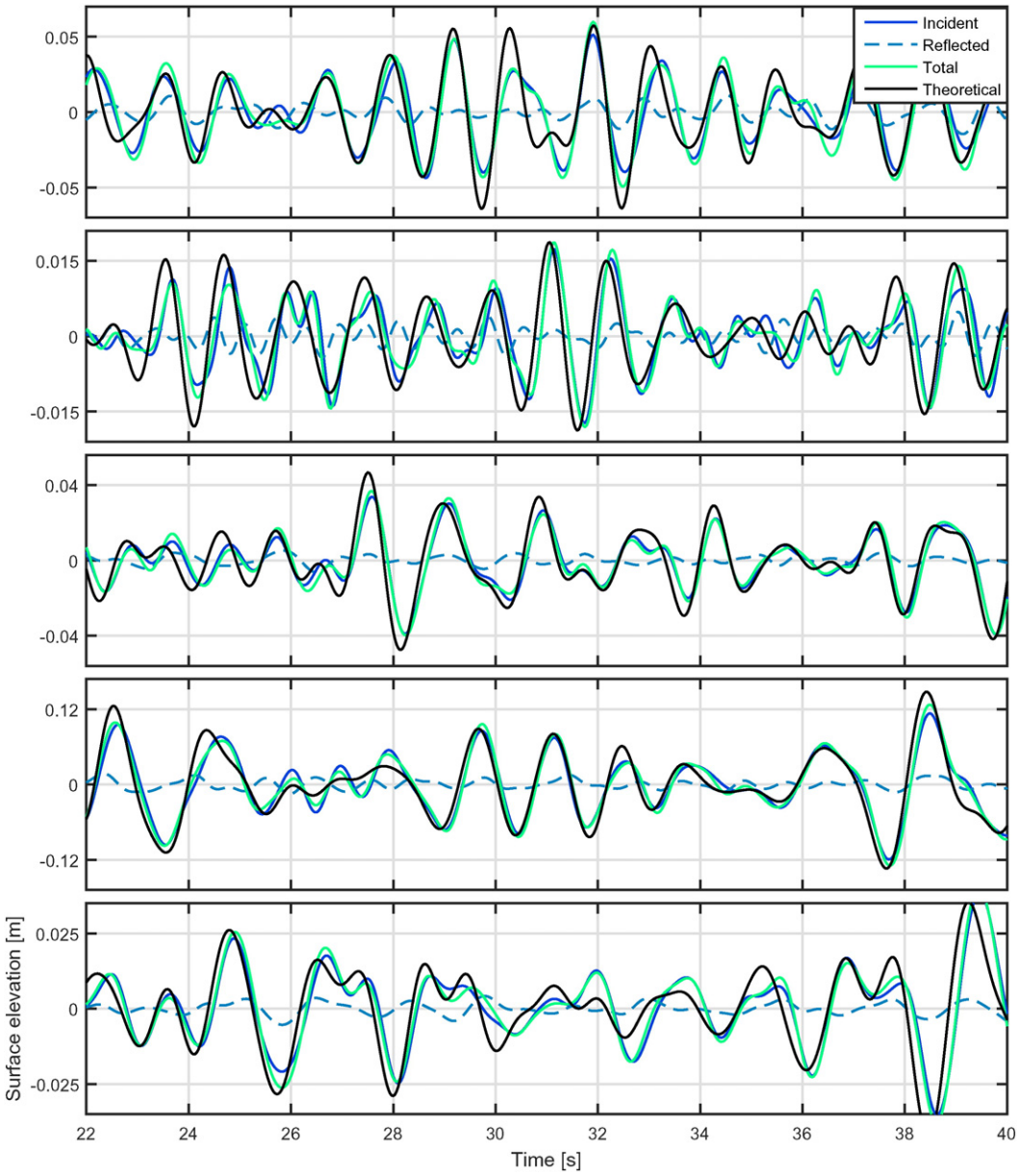

Fig. 11. Example time series outputs for the example spectra shown in Figs. 9 and 10. Theoretical time series as well as measured are shown, in addition to the isolated incident and reflected components for a range of gauges. Sea state 1, gauge 1; sea state 2, gauge 2 etc.

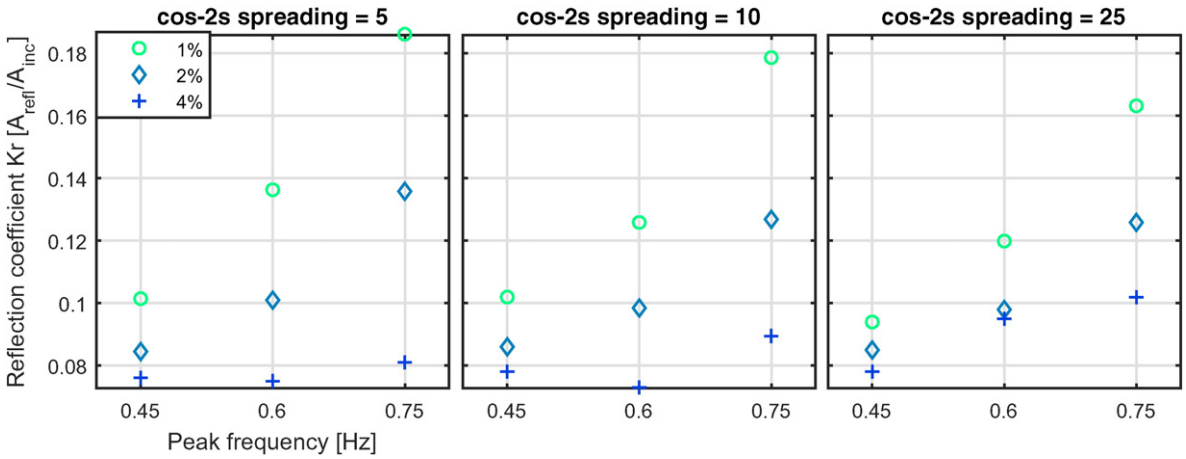

Fig. 12. Overall reflection coefficients for different values of spreading, peak frequency, and wave steepness.

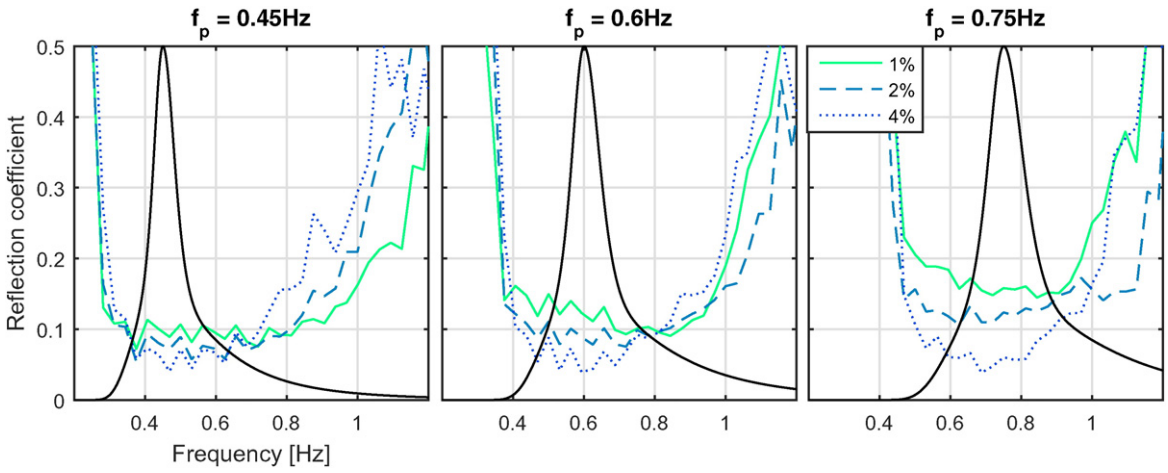

Fig. 13. Mean frequency dependent reflection coefficients for each peak frequency averaged over directional spreading, separated by steepness. Normalised wave spectra overlaid to aid explanation of overall reflection coefficients (Fig. 12).

approaches are capable of achieving this, and even with a defined input range are shown to exhibit much larger uncertainties.

3. Results

3.1. Frequency spectra

Example incident frequency spectra are shown in Fig. 9. These provide results for a range of sea states covering both the highest and lowest reflection conditions, as shown in Fig. 12. There is an apparent tendency to under-produce waves, particularly at the spectral peak, and whilst being more pronounced for sea states with higher peak frequency, and inherently higher reflections, it is prevalent throughout. In general the deviation is much lower for sea states with lower peak frequency, suggesting that, as expected, the tank's generating and absorbing effectiveness reduces above a certain frequency threshold. To demonstrate that this deviation isn't a function of the method, and to allow comparisons to be made in Section 3.5.1, the frequency spectra outputs for the BDM and EMEP approaches are also been shown.

This deviation, despite being consistent, is also easy to rectify. Linear frequency dependent correction factors can be applied as a function of the deviation between the target amplitude spectrum and the isolated incident spectrum. These have proved to be effective in previous tests, bringing down the relative deviation to 1 — 2%. As the current tests are focussed on directional distribution and reflection calculation it was not deemed necessary to apply them for this purpose.

3.2. Incident and reflected directional spectra

Directional spectra relating to the numbered frequency spectra in Fig. 9 are shown in Fig 10, ensuring the extremes of the test programme are still included. The majority of sea states shows good agreement between the input and measured spectra. The difference between the measured incident spectrum from the desired input is generally low, with the exception of sea state 4. Viewing the colour-scale-separated spectra (middle column of Fig. 10) it is apparent that the reflected spectrum has been effectively isolated, generally mirroring the form of the incident distribution.

It is apparent that example sea state 4 demonstrates much larger deviations than the others. Fig. 9 highlights that this is largely due to significant under-generation, whilst in Fig. 12 it is observed that the reflection coefficient is also very high. This re-iterates the findings that high frequency, low amplitude waves are generated, and absorbed less effectively, especially when combined with high directional spreading.

3.3. Time series

Fig. 11 shows the example time series outputs for the spectra in Fig. 10. An IFFT of the complex input amplitude spectra enables the

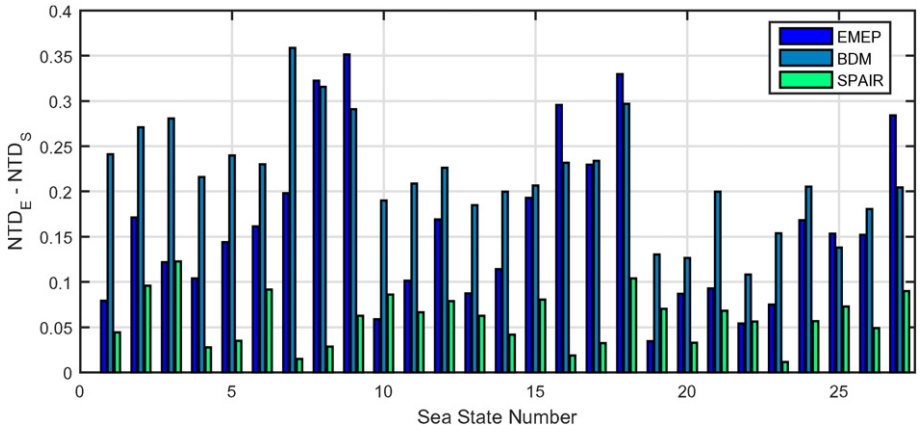

Fig. 14. Comparison of directional distribution error for calculated incident spectra created using the EMEP, BDM and SPAIR approaches.

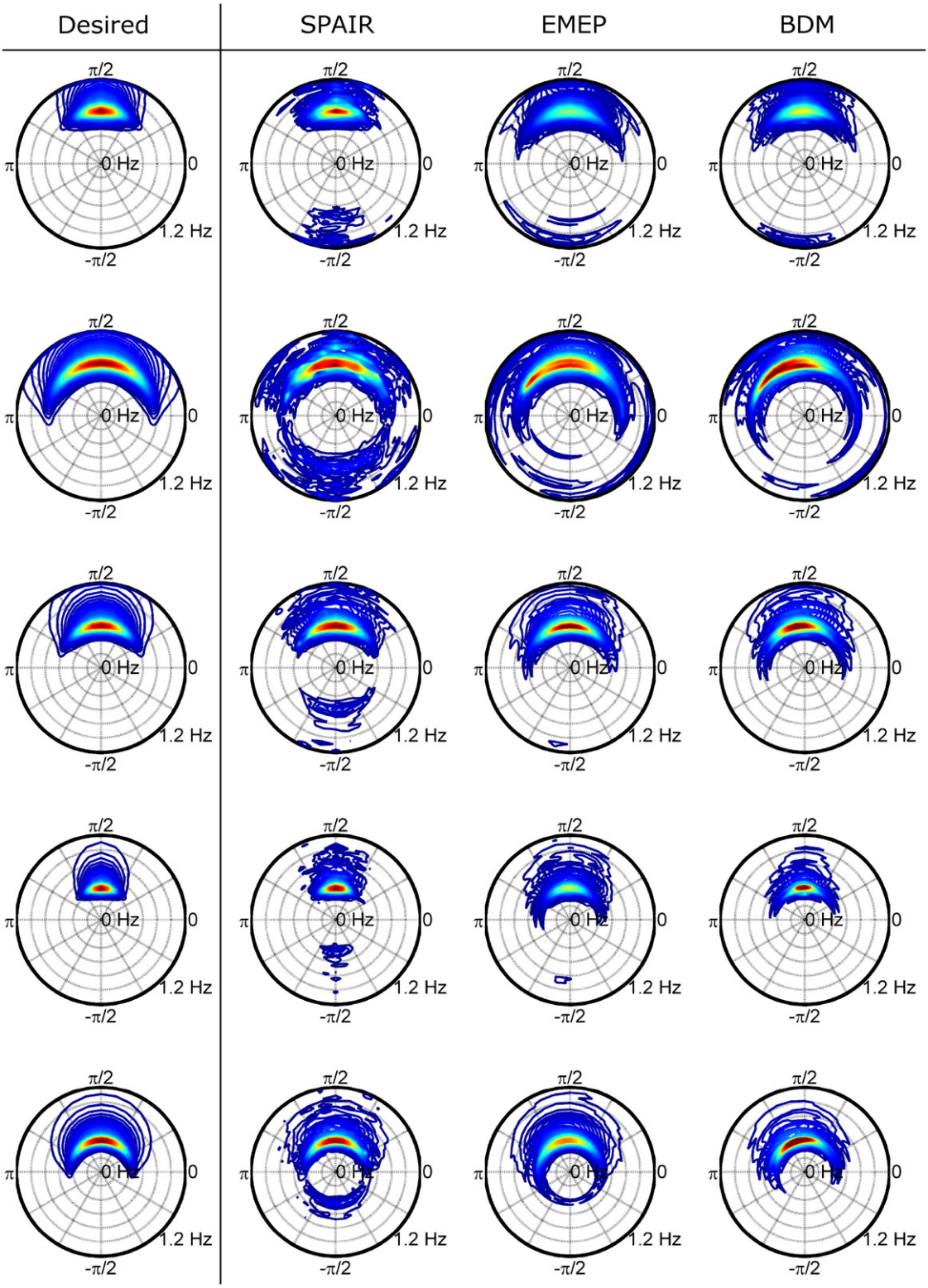

Fig. 15. Comparison of example directional spectrum outputs from SPAIR, EMEP and BDM approaches. Energy density [m^2s/rad] is shown by the colour, relative to the peak of the desired spectrum.

theoretical time series to be computed using linear wave theory, before being compared to the actual measurements. As shown in Section 2.3.3, the presented method also allows for the separation of incident and reflected time series in the tank domain, and as such these have been computed at the gauge locations for comparison.

The measured time series outputs show reasonably good agreement with the theoretical time series calculated using linear wave theory. The removal of the reflected components generally provides a closer match, however, this is not always the case. The isolation of what is unaccounted reflections from non-linear behaviour appears difficult. As expected from

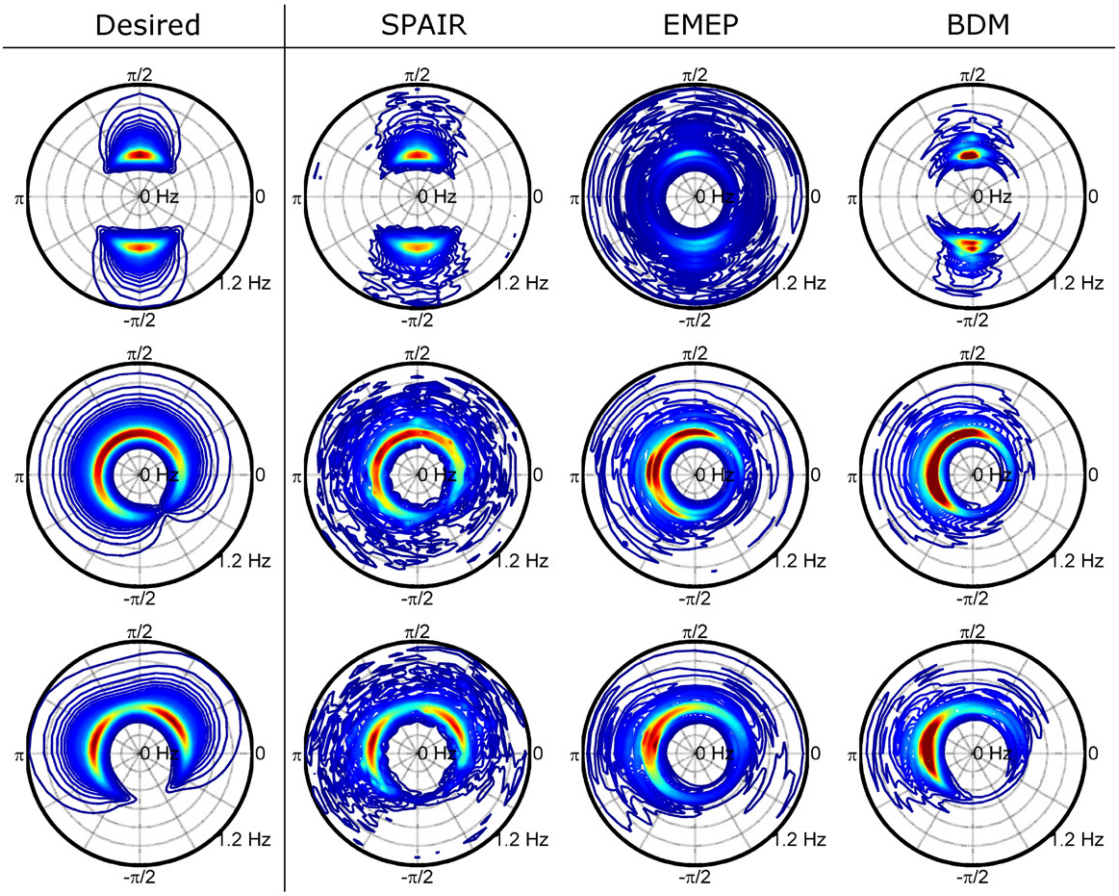

Fig. 16. Complex directional spectra outputs (total) for SPAIR, BDM and EMEP approaches. Energy density [m^2s/rad] is shown by the colour, relative to the peak of the desired spectrum.

the spectral analysis, example sea state 4 shows the largest deviations, and also the largest relative reflected components.

3.4. Reflection analysis

The output of the directional reflection analysis for the $3\times3\times3$ test matrix is shown in Fig. 12. Reflections in the FloWave facility are primarily related to the absorption characteristics of the force-feedback wavemakers, and as such are both frequency and amplitude dependent. This is demonstrated in Fig. 12 where it can be clearly observed that increasing peak frequency, or decreasing wave steepness, causes an increase in the overall wave reflection coefficient. This frequency dependency can be attributed to the paddle characteristics, as well as absorption control scheme, as explored in Gyongy et al. (2014). The reduced sensitivity of the force-feedback mechanism to low wave forces appears to drive the decreased absorption effectiveness for small, low steepness waves.

Fig. 13 shows the mean frequency dependent reflection coefficients for each peak frequency used, averaged over directional spreading. This enables a more detailed frequency dependent exploration of the reflection coefficients, and offers further explanation to the results shown in Fig. 12.

3.5. Method performance

3.5.1. Comparison to other methods

In order to assess combined sea state and method performance, the Normalised Total Difference (NTD) between target and measured spectra can be assessed, defined as:

For directional spectra:

$$NTD_E = \frac{\sum_{p=1}^{N_f}\sum_{q=1}^{N_\theta}|E_{i,pq}-E_{m,pq}|}{\sum_{p=1}^{N_f}\sum_{q=1}^{N_\theta}E_{i,pq}}. \quad (18)$$

For frequency spectra:

$$NTD_S = \frac{\sum_{p=1}^{N_f}|S_{i,p}-S_{m,p}|}{\sum_{p=1}^{N_f}S_{i,p}}. \quad (19)$$

NTD_E provides assessment of the total deviation from target spectra, which includes:

- frequency spectrum error, NTD_S
- directional distribution error, NTD_D
- method reconstruction error, NTD_M
- miscellaneous (other) error, NTD_O e.g. noise, position error.

Ideally the method reconstruction error, NTD_M, would be assessed to gauge method performance. It is not possible, however, to isolate this as the true directional distribution error is not known. Fig. 9 shows that the deviation from target frequency spectra, NTD_S, is mostly tank dependent and not a function of the methodology. For these reasons to assess method performance, NTD_E–NTD_S has been used, noting that it incorporates the method reconstruction error, along with the directional distribution error. As the true distribution error is constant this should allow effective comparisons to be made between methods.

Fig. 14 shows this comparison for the calculated incident spectra (using a fixed input range of 0–180° for BDM and EMEP methods)

Table 4
Directional distribution error, NTD_E–NTD_S, for complex spectra.

NTD_E–NTD_S	Sea state 1	Sea state 2	Sea state 3
SPAIR	0.153	0.127	0.054
EMEP	0.340	0.227	0.454
BDM	0.414	0.344	0.322

over the initial $3\times3\times3$ test plan. The SPAIR approach consistently performs better, with a mean NTD of 5.93%, compared with 16.1 and 21.7% for the EMEP and BDM approaches respectively.

Example directional spectrum outputs from these methods are shown in Fig. 15, for the same sea states as shown in Fig. 10. It can be seen that neither the EMEP or BDM approaches consistently fit a DSF that incorporates reflected components. The EMEP approach appears to incorporate some reflected energy content, but the distribution seems incorrect, likely constrained by the inherent frequency-dependent 'curve-fitting' process.

Visually all of the methods perform reasonably well in terms of characterising the incident wave field, with the SPAIR approach demonstrating the best performance, as shown in Fig. 14. This is also apparent through visual observation, as the high energy components of the incident distribution match up very well with that of the desired. At low energy levels, however, the distribution does appear to be ill-defined, a function of the discretised nature of the solution, and the low energy densities present at these frequencies.

3.5.2. Performance with complex spectra

The complex spectra defined in Table 3 have no defined incident and reflected range and as such the EMEP and BDM approaches cannot resolve the reflected components. Fig. 16 shows the total reconstructed wave field using the three methodologies. It is clear that the EMEP and BDM approaches generally fail to capture the multi-modal and highly spread nature of the input sea states, other than perhaps the BDM approach reconstruction of sea state 3.

The SPAIR approach enables a much more effective characterisation of the input conditions, as demonstrated in Fig. 16 and Table 4. The reflected spectrum and coefficients can also be calculated as no input angular range is required, with the result that the incident and reflected spectra can apparently overlap. The reflected spectra are shown in Fig. 17, and the total reflection calculated coefficients were found to be 8.36, 8.61 and 8.13% respectively.

Each of the unusual spectra have peak frequencies of between 0.45 Hz and 0.5 Hz, around 2–3% steepness, and large spreading. Despite having vastly different spectral forms they have near identical reflection coefficients, consistent with the results shown in Fig. 12. This supports previous findings that peak frequency and steepness are the main parameters to which absorption effectiveness is sensitive to, along with some sensitivity to directional spreading.

4. Discussion

4.1. Method limitations and sensitivity

4.1.1. Effect of in-line reflection level

The presence of in-line reflections alter the phases and phase differences measured at the gauges, and hence causes an apparent angle estimation error through Eq. (3). The effect of this can be understood by looking at the resulting Fourier coefficients in the presence of such reflections.

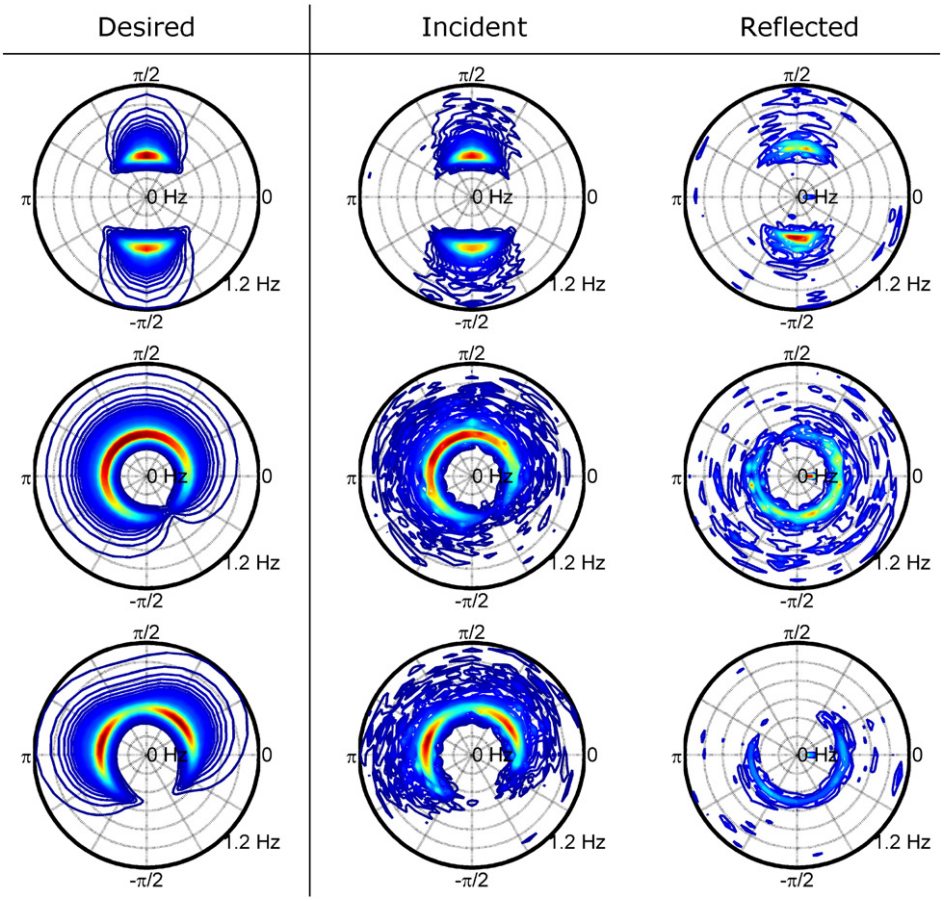

Fig. 17. Incident and reflected directional spectrum outputs for complex spectra defined in Table 3. Energy density [m^2s/rad] is shown by the colour, relative to the peak of each spectrum.

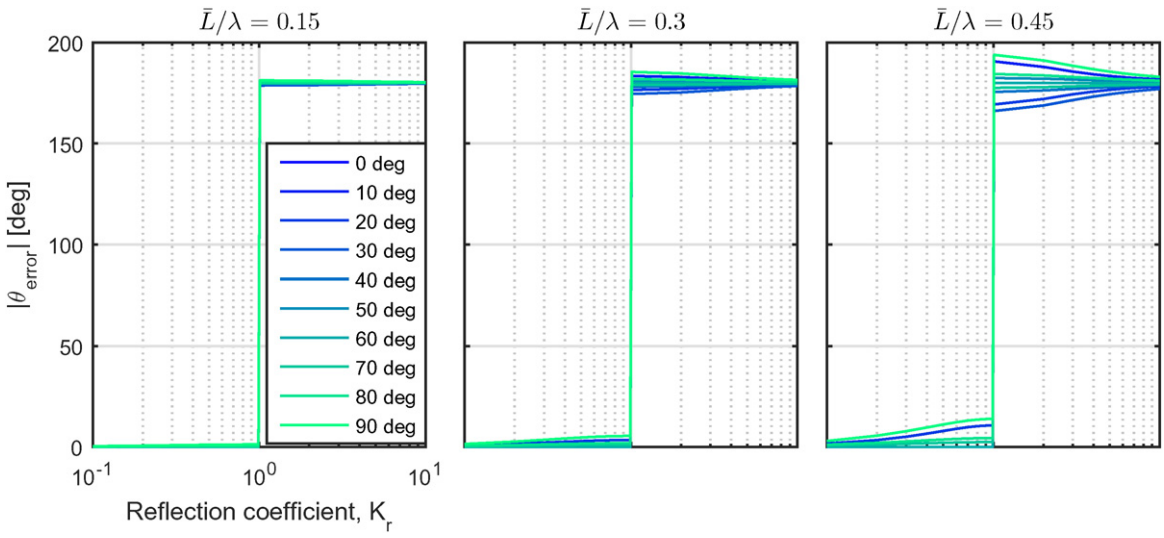

Fig. 18. Effect of in-line reflection coefficient, wave angle and relative separation magnitude on apparent angle calculation.

Surface elevations in the presence of in-line reflections, at [x,y], can be modelled as:

$$\begin{aligned}\eta(x,y,t) = \sum_{n=1}^{N} & A_{inc,i}\cos\left(k_i\left(x\cos\alpha_{inc,i} + y\sin\alpha_{inc,i}\right) + \Phi_{inc,i} + \omega_i t\right) \\ & + K_{r,i}A_{inc,i}\cos\left(-k_i\left(x\cos\alpha_{inc,i} + y\sin\alpha_{inc,i}\right)\right. \\ & \left. + \Phi_{inc,i} + \Phi_{ref,i} + \omega_i t\right).\end{aligned} \tag{20}$$

Defining $k_{i,xy} = k_i(x_n\cos\alpha_{inc,i} + y_n\sin\alpha_{inc,i})$, and $k_{r,i} = K_{r,i}e^{i\Phi_{ref,i}}$, the resulting Fourier coefficients at gauge n can be expressed as:

$$\begin{aligned}a_{i,n} &= a_{inc,i}e^{ik_{i,xy}} + a_{inc,i}k_{r,i}e^{-ik_{i,xy}} \\ &= a_{inc,i}\left[\cos(k_{i,xy}) + i\sin(k_{i,xy})\right] + a_{inc,i}k_{r,i}\left[\cos(k_{i,xy}) - i\sin(k_{i,xy})\right] \\ &= a_{inc,i}(1-k_{r,i})i\sin(k_{i,xy}) + a_{inc,i}(1+k_{r,i})\cos(k_{i,xy}).\end{aligned} \tag{21}$$

The expected phase at gauge n is therefore:

$$\Phi_{n,i} = a\tan\left[\frac{\tan(k_{i,xy})(1-k_{r,i})}{(1+k_{r,i})}\right]. \tag{22}$$

Apparent angle for each gauge triad is calculated using:

$$\alpha_{\text{apparent},i} = \tan^{-1}\frac{\left[(x_1-x_2)\Phi_{i,13} - (x_1-x_3)\Phi_{i,12}\right]/sgn(P)}{\left[(y_1-y_3)\Phi_{i,12} - (y_1-y_2)\Phi_{i,13}\right]/sgn(P)} \tag{23}$$

where:

$$\Phi_{i,mn} = \Phi_{m,i} - \Phi_{n,i}. \tag{24}$$

From Eq. (22) it can be seen that phases and phase differences at the gauge locations are heavily influenced by the magnitude of the reflection coefficient, $K_{r,i}$. However the extent with which this alters the resulting angle estimation depends on the relative change in $\Phi_{i,13}$ to $\Phi_{i,12}$, which is a function of the angle relative to the triad orientation, along with the magnitude of the separations relative to the wavelength.

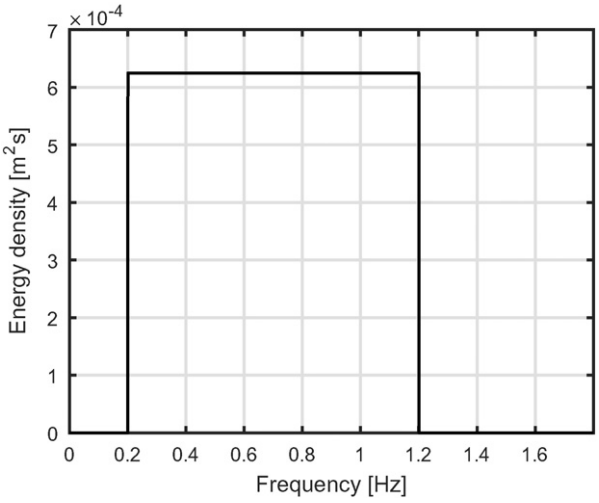

Fig. 19. Uni-directional spectrum for numerical sensitivity analysis. $H_{m0} = 0.2$. For the simulations, an incident angle of $\theta = 22.5°$ has been used.

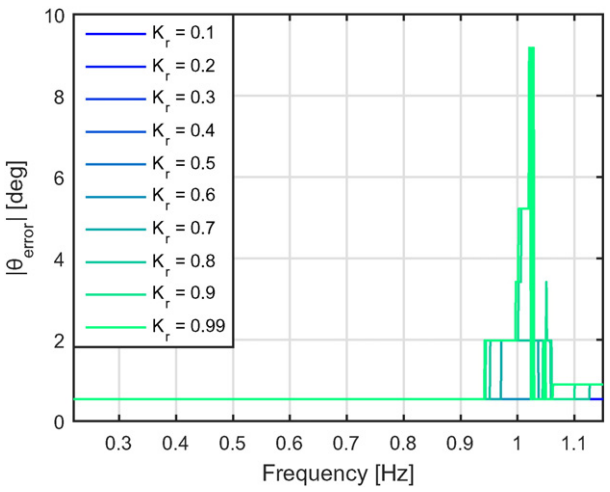

Fig. 20. Angle error for broad-banded spectrum shown in Fig. 19 for various levels of in-line reflection.

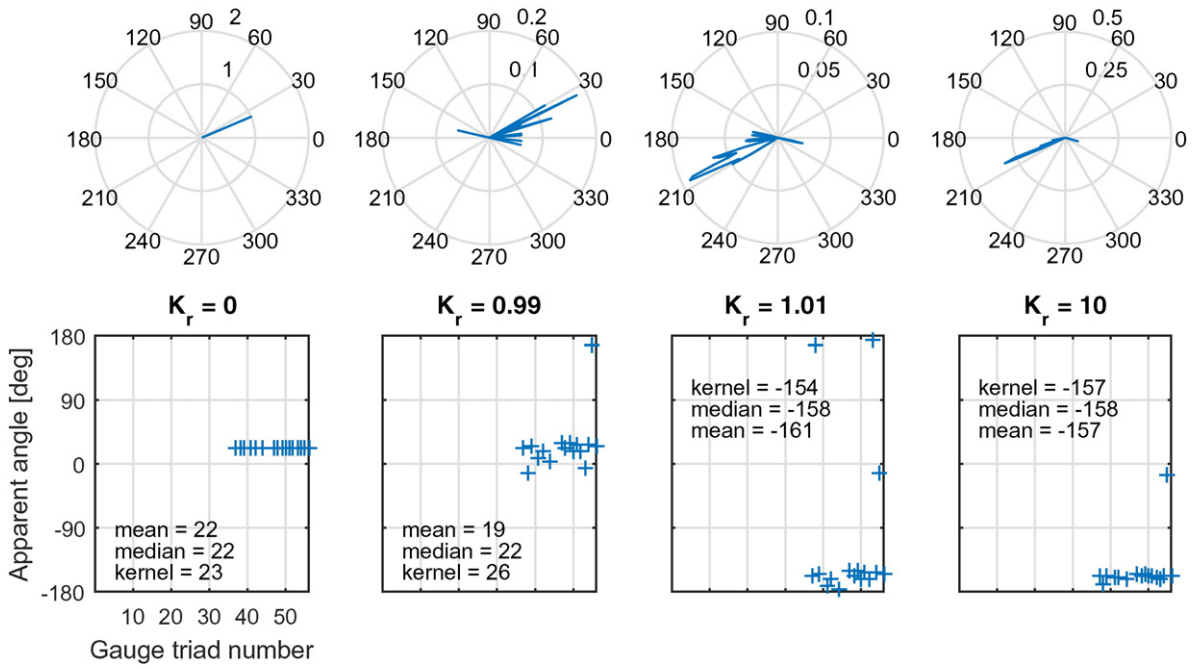

Fig. 21. Individual angle estimates for 1 Hz components of spectrum shown in Fig. 19. Shown with in-line reflection levels of 0, 0.99, 1.01 and 10, along with the resulting kernel density estimates.

Fig. 18 shows the expected angular error for a single equilateral gauge triad as a function of the reflection coefficient, incident angle and relative separation magnitude. K_r values between 0 to 10 have been used to assess whether the PTPD method presented identifies the 'reflected' component as the incident direction if $K_r>1$. From Fig. 18 it is apparent that the method does find the correct 'dominant' angle when $K_r>1$.

It is clear that if gauge separations are small then the angle calculation is relatively unaffected by the level of reflection. Practically, however, if gauge separations are *too* small relative to all frequency components, position error and noise will alter the measured phases more greatly and hence cause increased errors in the apparent angle estimates.

As expected, when reflection levels are low the angular estimates are also largely unaffected. When reflections are large, however, the incident angle relative to the gauge triad orientation becomes important, highly influencing the values of individual angle estimates. Overall the effect of these poor individual estimates can be minimised by designing a wave gauge array so that for each frequency (wavelength) there is a uniform co-array distribution of valid separations. If this is the case, using all of the estimates, the kernel density estimate approach discussed in Section 2.3.1 should be able to provide the correct incident angle.

To assess how the kernel density approach with the array layout shown in Fig. 3 deals with different levels of reflection, a numerical simulation has been carried out, using a uni-directional broad-banded spectrum with frequency independent in-line reflections. This spectrum has been used as it covers the operational frequency range of the tank (0.2→1.2 Hz), whilst enabling easy analysis and viewing of results. This spectrum is shown in Fig. 19 and is also used for the sensitivity analysis shown in Section 4.1.2.

Fig. 20 shows the angular error resulting from the simulation. It is clear that the combination of the array and method used performs very well for frequencies up to 0.95 Hz, regardless of the level of reflection. The error shown is purely a function of the number of bins used for the kernel density estimate (250). When reflection is relatively low ($K_r<0.5$) there is also no perceived error in the angle estimate, at any frequency. This shows that the array-method combination performs very well in general, especially for the level of reflection present in the (empty) FloWave basin. Once this initial angle is effectively identified the subsequent in-line reflection analysis will then be correct, which can be seen in Fig. 23 when the oblique reflection angle is 0°.

Errors arise from 0.95 Hz onwards when the reflection coefficient is over 0.5, due to the smaller number of valid gauge triads (see Fig. 6). This means that poor individual estimates have a greater effect on the final angle calculation, a result of the combined effect of larger reflections, triad orientation and large relative separations. Individual estimates for 1 Hz with a range of reflection scenarios are illustrated in Fig. 21, demonstrating how individual estimates are affected by reflection levels and how the kernel density estimate mitigates the effect of these on the final angle values.

Where large reflections and high wave frequencies are present it may be necessary to use an array with additional gauges placed closer together. This would ensure that there are enough gauge triads with

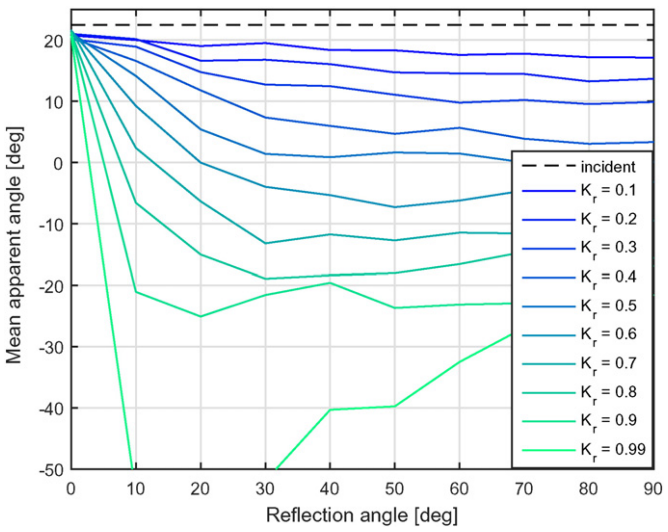

Fig. 22. Effect of reflection level and angle on the mean apparent angle (over all frequencies).

separations less than $0.45\lambda_i$, thus improving the high frequency estimates. For the levels of reflection present in the empty tank the current array layout should be suitable for identifying the correct incident angle regardless of frequency. That is, under the assumption that position error and noise are negligible, and more importantly, that reflections can be assumed to be in-line. This will be discussed in Section 4.1.2.

4.1.2. Effect of reflection angle and curvature

4.1.2.1. Oblique reflections. In Section 4.1.1 it was found that the level of in-line reflection does not greatly affect the correct identification of the incident angle when using the current implementation of the method in combination with the wave gauge array. This additionally enables a correct in-line reflection analysis to take place. If, however, the reflections are not in-line then this is no longer the case.

Introducing a change in reflected angle, $\Delta\alpha_{ref,i}$, the surface elevations become:

$$\begin{aligned}\eta(x,y,t) = \sum_{n=1}^{N} & A_{inc,i}\cos\left(k_i\left(x\cos\alpha_{inc,i} + y\sin\alpha_{inc,i}\right) + \Phi_{inc,i} + w_i t\right) \\ & + K_{r,i}A_{inc,i}\cos\left(-k_i\left(x\cos\left(\alpha_{inc,i} + \Delta\alpha_{ref,i}\right)\right.\right. \\ & \left.\left. + y\sin\left(\alpha_{inc,i} + \Delta\alpha_{ref,i}\right)\right) + \Phi_{inc,i} + \Phi_{ref,i} + w_i t\right).\end{aligned} \tag{25}$$

Defining $k_{i,\alpha,xy} = k_i(x\cos(\alpha_{inc,i} + \Delta\alpha_{ref,i}) + y\sin(\alpha_{inc,i} + \Delta\alpha_{ref,i})$, the resulting phases can be shown to be:

$$\Phi_{n,i} = a\tan\left[\frac{a_{inc,i}\sin\left(k_{i,xy}\right) - k_{r,i}a_{inc,i}\sin\left(k_{i,\alpha,xy}\right)}{a_{inc,i}\cos\left(k_{i,xy}\right) + k_{r,i}a_{inc,i}\cos\left(k_{i,\alpha,xy}\right)}\right]. \tag{26}$$

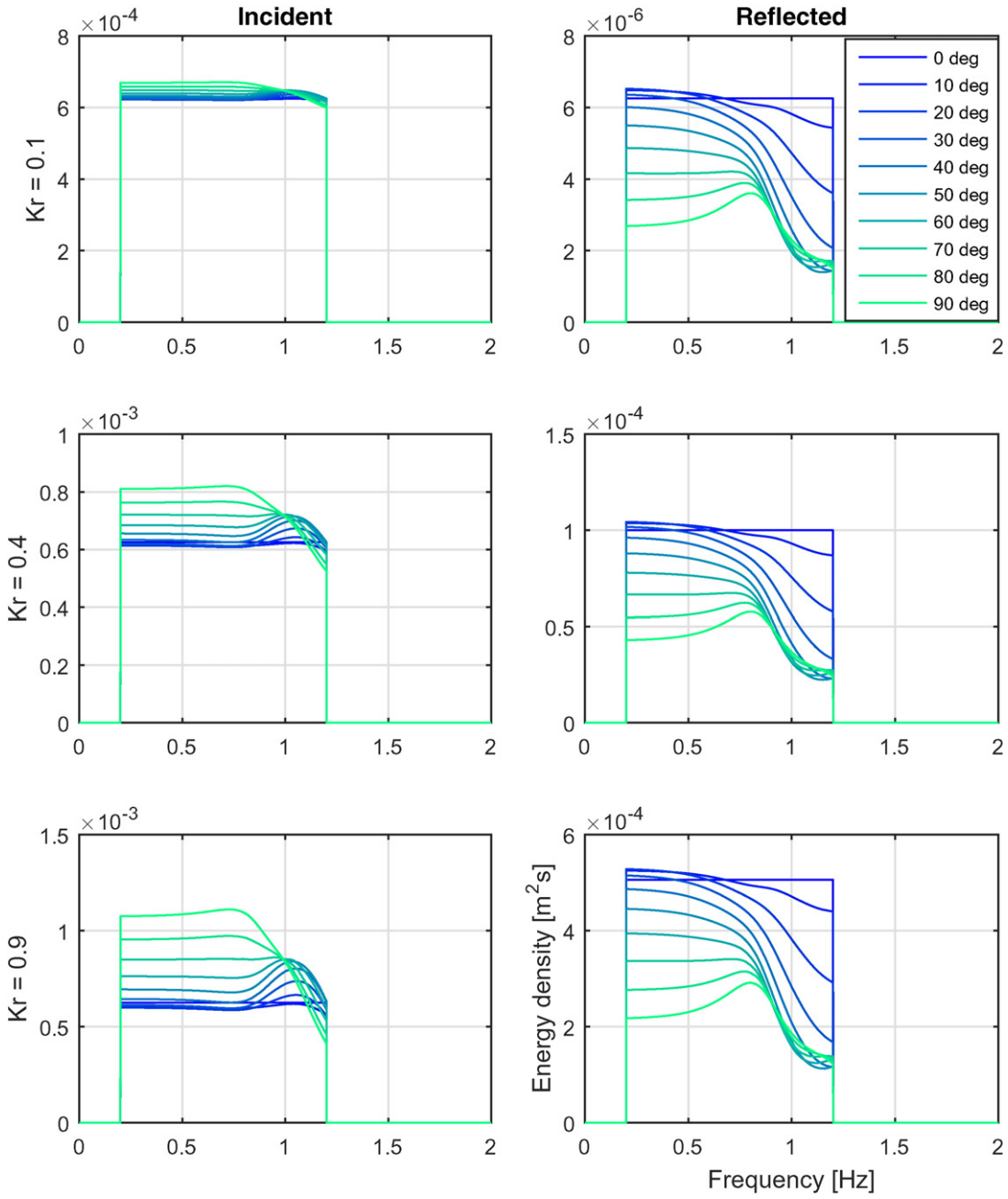

Fig. 23. Effect of reflection level and angle on the separation of incident and reflected spectra.

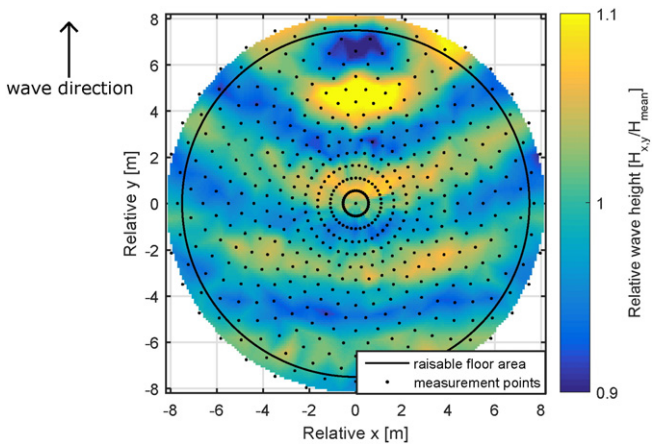

Fig. 24. Spatial map of wave height variation for 0.45 Hz regular waves (2% steepness). Shows reflected wave curvature over the tank operational area (roughly equal to floor area).

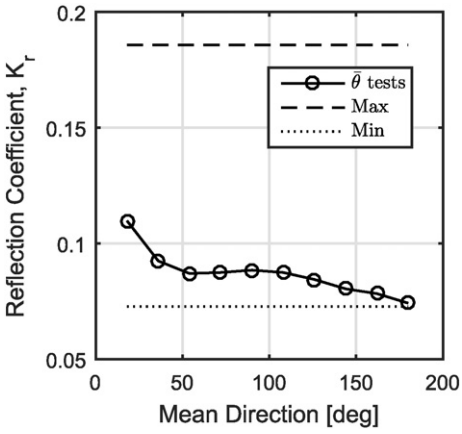

Fig. 26. Effect of mean direction on perceived reflection coefficient. Maximum and minimum values of the test programme shown in dashed lines.

It can be seen from Eq. (26) that the phase differences will be altered by the magnitude of $\Delta\alpha_{ref,i}$ in addition to the level of reflection and array layout. The difference here compared with the in-line reflection analysis, Eq. (22), is that when the angles are calculated using Eq. (3), the 'direction' of the angular error is now no longer solely a function of the triad layout, and as such does not 'average' out over multiple estimates. All angle estimates now contain a consistent error as a function of $\Delta\alpha_{ref,i}$.

Using the spectrum shown in Fig. 19, and simulating the oblique reflections over the array we can observe this consistent shift in angle estimate, shown in Fig. 22. This shows that if there are sizeable reflections with even a small reflection angle then the PTPD approach cannot be used to effectively identify the incident angle.

As discussed in Section 4.2.2 it is not always necessary to estimate the incident angle. To further assess how oblique reflections affect the isolation of incident and reflected spectra the incident angles are assumed to be known. Fig. 23 shows how the level, and angle of reflection, affect the isolation of incident and reflected spectra. As expected, this shows that it is not appropriate to use in-line reflection analysis when the reflections are oblique relative to the incident. This is because the phase differences are no longer a function of the 'in-line' gauge separations assumed in the analysis. It may however be suggested that results are still somewhat useful if the reflection angle is low, perhaps less than 20°.

4.1.2.2. Curved reflections. When reflections are curved or directionally spread, there will be larger variation in the individual angle estimates generated using the gauge triad combinations. If the mean direction of the curved waves is not opposite the incident, then similar behaviour is to be expected to the oblique wave analysis, but with additional scatter. If, however the mean direction of the curved waves opposes the incident, then the correct incident angle can be identified with an appropriate array, and a meaningful representative in-line reflection analysis procedure can take place. This is the case at FloWave.

The circular wave basin at FloWave ensures that the mean direction of reflected components opposes the incident direction. The circular shape also means that the reflected components are curved, as a function of the wave basin geometry and the angular dependency of the tank transfer function.

Reflected wave curvature has been analysed through the spatial variation of measured wave heights. As it is known that the incident waves are long crested and uniform, the variation in wave height is solely a function of the curved reflected components interacting with the incident waves. An example 'spatial map' is shown in Fig. 24 for 0.45 Hz regular waves, noting that from further tests the curvature of these reflections appears to be independent of wave frequency. Over the small array area (1 m^2) the assumption that curvature is negligible for the purpose of reflection analysis seems appropriate.

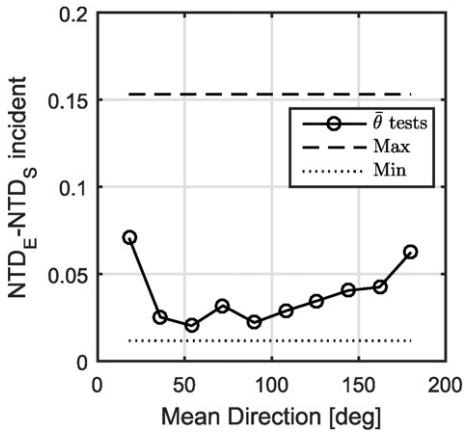

Fig. 25. Effect of mean direction on perceived sea state performance. Maximum and minimum values of the test programme shown in dashed lines.

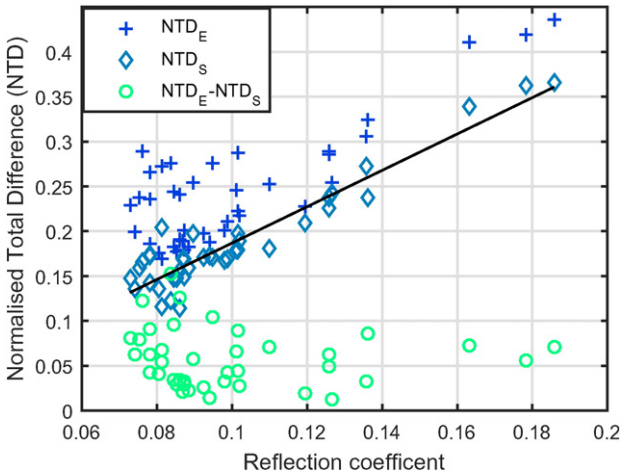

Fig. 27. Normalised total difference for incident spectra as a function of reflection coefficient. Linear fit overlaid for NTD_S v K_r with an r^2 value of 0.89.

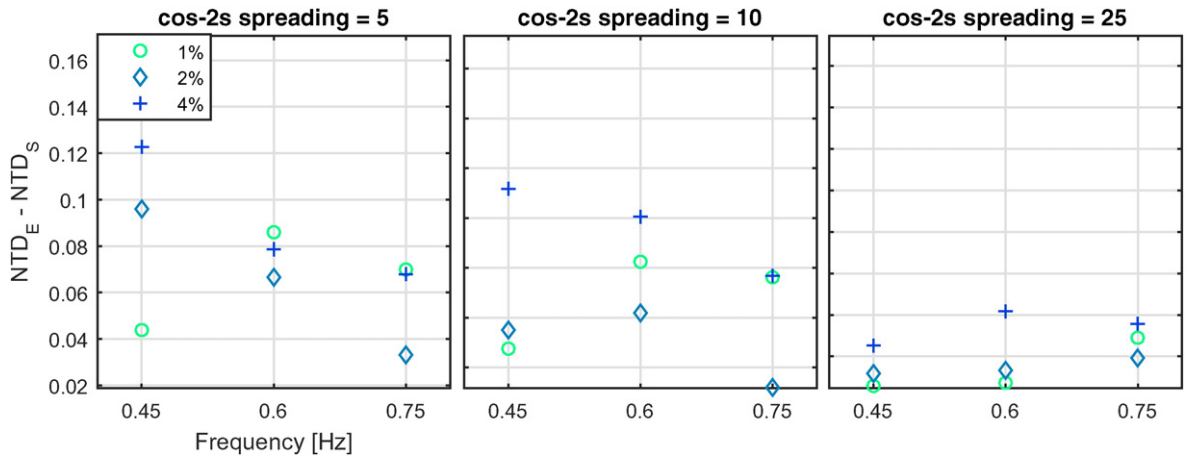

Fig. 28. Directional distribution error as a function of spreading, steepness and peak frequency.

The results presented here clearly shows that for the level of reflection and curvature present, the incident angle can be effectively identified using PTPD approach with the wave gauge array shown in Fig. 3. Once these are identified the co-array uniformity and least squares approach of the reflection analysis should ensure that the representative in-line reflection coefficients are valid despite these small levels of curvature. This should give a very good estimate of the incident and reflected spectra, and time-series, over the array area. This approach means that sea states can be effectively characterised in a particular location (generally in the tank centre), prior to use in a test programme with a model installed.

From Fig. 24, it is apparent that the effective reflection coefficient is not constant, and in fact varies in the in-line direction due to circular focussing effects. As a result of this, and the reflected wave curvature, it is clear that the reflected directional spectrum is spatially variable. This means that although the isolation of incident and reflected spectra, and time-series over the array area gives reliable results, using this 2D approach to extrapolate far from the measurement area will not be accurate. However, through knowledge of the wave curvature and in-line dependency of the reflection coefficient, it should be possible to alter the energy density and angles in the reflected spectrum, and amplitudes and phases in the time-series reconstructions to provide reasonable estimates over the tank area, if desired.

4.1.3. Influence of mean direction

The wave generating capability at FloWave is designed to be directionally independent, meaning that any change in mean wave propagation direction should not influence the sea state performance. Any perceived changes should therefore be attributed to the array layout, and the method itself.

Figs. 25 and 26 show the perceived reflection coefficient and directional NTD variation incurred by varying mean direction for a single sea state. The sea state used is detailed in Table 2. It can be seen in Fig. 26 that when altering the mean direction, the perceived reflections also vary. This is coupled with variation in the perceived directional distribution error.

Without the presence of reflections, noise, or position error, there would be no error in the measured propagation directions, and hence no discrepancy in the directional distribution. Of these factors, the presence of reflections is probably the largest contributor in most circumstances. It is observed to have a consistent effect on both the relative phases, and the amplitudes at the gauge locations.

As the mean direction changes, the array layout plays an important role, as the relative reflection and error-influenced phase differences are dependent on the projected in-line separations. These deviations cause differences in the perceived angles and hence incur a varied and largely unpredictable directional distribution error. A portion of the perceived directional deviation for any sea state is therefore a complex function of the induced phase errors (mostly reflection based), and the array layout.

Table 5
Number of gauge combinations available.

Number of gauges	Number of combinations
3	56
4	70
5	56
6	28
7	8
8	1

4.1.4. Influence of primary sea state parameters on performance

Analysing the variation in NTD, it is difficult to assess what proportion of this difference is the result of actual sea state deviation, and what can be attributed to the array-methodology effectiveness under various conditions. This was one of the reasons for using NTD_E–NTD_S

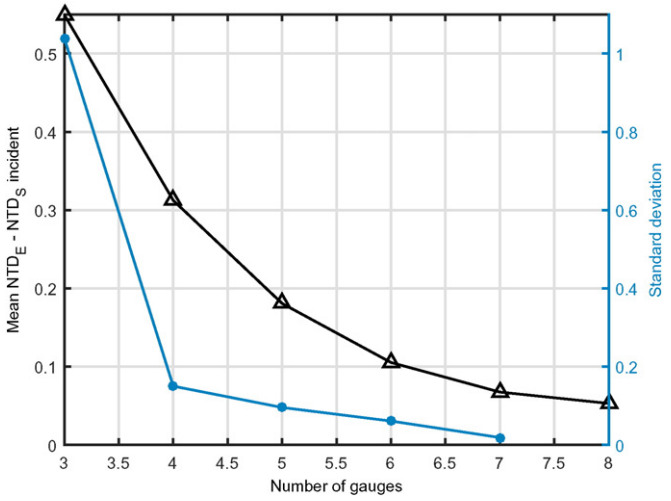

Fig. 29. Influence the number of gauges has on the directional distribution error, along with the standard deviation of this error.

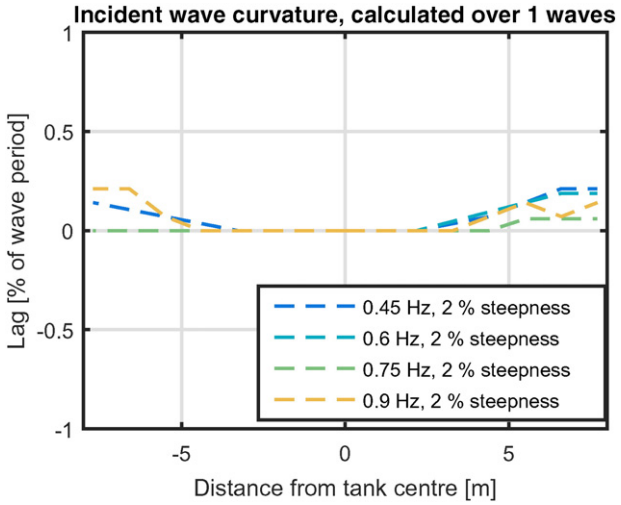

Fig. 30. Phase lag between wave gauges in a line perpendicular to the expected wave propagation direction. Shows that the waves are produced at the correct angle and have negligible curvature.

in Section 3.5.1, removing the frequency spectrum deviation, and focussing on the directional distribution reconstruction.

The total deviation, NTD_E, and the frequency spectrum deviation, NTD_S, essentially show the same dependencies as the reflection coefficient, shown in Fig. 12. It appears that higher peak frequency sea states with low steepness incur both greater reflections, and larger deviations in the incident spectrum simultaneously. The correlation between NTD and reflection coefficient can be seen in Fig. 27.

The directional deviation metric, NTD_E–NTD_S, appears not to have a predictable correlation to reflection coefficient, as discussed in Section 4.1.3. Fig. 28 shows the relationship between the directional distribution component, and the primary sea state parameters. The only apparent relationship appears to be a reduced NTD when spreading is lower (s is higher). This is potentially expected as the only two parameters affecting directionality are spreading and mean direction, of which, mean direction has been fixed for the main $3\times3\times3$ test matrix.

4.1.5. Influence of number of gauges

As discussed in Section 4.1.3 increasing the number of gauges, if positioned correctly, should reduce the sensitivity to wave directionality. In general, additional gauges should give rise to improved estimates and reduced directional discrepancy between target and measured spectra. To explore the effect of the number of gauges all gauge combinations with 3 or more gauges have been assessed under an individual sea state (Table 2, $\overline{\theta} = 36^{\circ}$). The number of combinations for a desired number of gauges is shown in Table 5, whilst the mean directional deviation and the standard deviation of this between array layouts is shown in Fig. 29. As expected, the mean directional deviation reduces with the use of more gauges. The standard deviation of the directional deviation is also shown, describing the expected variation in performance when using different sets of gauges.

Increasing the number of gauges will further reduce both the directional deviation and the variation between hypothetical gauge subsets. As the gauge combination choice is analogous to an effective change in wave direction, this will further reduce the sensitivity of an array to direction, thus improving the reliability of the estimates under a variety of wave conditions.

4.2. Alternative applications

4.2.1. No reflection analysis: PTPD approach only

As demonstrated in Draycott et al. (2015), using the PTPD approach to reconstruct directional spectra at FloWave works effectively without the addition of reflection analysis. This works particularly well at the FloWave facility (or other circular wave basins with active absorption) as the reflections are low, and can be approximated as in-line. It should also be effective for tanks with different geometry, providing reflections are relatively low, and the reflection angle isn't very large (see Fig. 22). If this is the case then the incident directions should be effectively identified, and a more accurate representation of the incident directional spectrum should be attained than when using the EMEP or BDM approaches.

4.2.2. No angle calculation: assumed incident angles

Sections 4.1.1 and 4.1.2 show that under certain conditions the presence of reflections can introduce errors in the incident angle calculation. This, consequently, means that the projected in-line reflection analysis is done at a slightly incorrect angle thus meaning that the reflection coefficients themselves will be incorrectly calculated, along with the incident and reflected spectra. If it can be assumed that the incident wave propagation angles are known, and precisely produced, then reflection coefficients can be calculated more accurately, whilst giving a better representation of the reflected wave field.

Fig. 30 shows the relative time lag between gauges mounted perpendicular to the expected wave propagation direction, for a variety of regular waves with different frequencies. Sampled at 128 Hz, it can be seen that the phase lags are all less than 1 time step. This shows that the

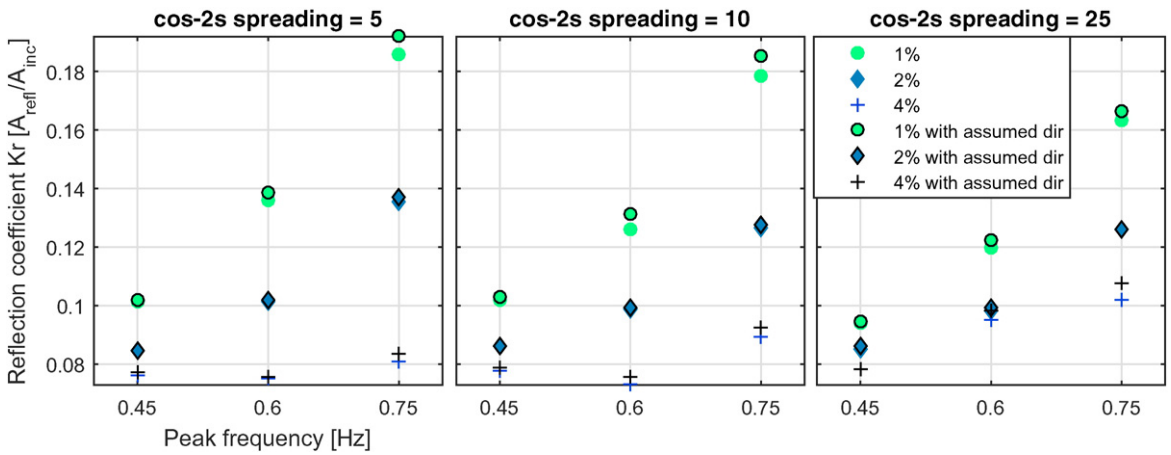

Fig. 31. Influence assuming the incident direction has on the reflection coefficient calculation.

desired angle is precisely produced with negligible curvature, at least from ±8 m from the tank centre. This analysis was done on only the first few regular waves (to avoid reflections), however it is probably a good assumption that the generation capability is not greatly affected by either simultaneous absorption or the generation of multi-directional sea states. Therefore the incident angles can be assumed correct at FloWave.

The resulting overall reflection coefficients when the assumed input angles are used are shown in Fig. 31. It is apparent that when the reflections are larger, the greater the error in the computed reflection coefficient, highlighting this 'feedback loop' problem. In general however, the reflection coefficients agree very well and it is clear that the computations where angle isn't assumed will provide adequate practical reflection estimations in the majority of cases.

4.3. Further work

Further work aims to include an extension to handle oblique reflections, potentially using a procedure similar to Wang et al. (2008). This extension, along with an understanding of the geometry in question would enable directional reflections to be calculated accurately for other objects such as rectangular tanks, or indeed other structures and devices. The idea of enabling of reflections to be resolved using double summation approaches, or as curved components will also be explored, enabling the reflected components to have a spread at each frequency.

5. Conclusions

The directional characteristics of sea states are often relevant to ocean and coastal engineering problems. The capability of wave basins to produce more complex multidirectional sea states has expanded in recent years, with many facilities now having wavemakers along multiple boundaries, or in the case of circular tanks, around the entire circumference. The ability to generate more complex spectra, including those with extreme spreading and multi-modality, brings about challenges in validating and calibrating these sea states and highlights the limitations in the established measurement techniques. To this end the SPAIR method has been developed. A single-summation method of wave generation has been used to generate a range of directional sea state conditions in a circular wave tank, FloWave. A phase-time-path difference approach has then been used to calculate wave propagation angles, before frequency-dependent in-line reflection analysis is performed.

This method, SPAIR, has proved to be highly effective in the measurement of multidirectional sea states within a circular wave tank, providing both incident and reflected directional spectra, and reconstructed time-series. The method has been demonstrated with both standard parametric and more complex multi-modal and extremely spread seas. When this single-summation method of wave generation is used, the PTPD-based reconstruction method has shown to be more effective at validating directional sea states than either the EMEP or BDM approaches, reducing the mean apparent directional deviation from 16.1% (EMEP), and 21.7% (BDM), down to 5.93%.

Sensitivity analysis shows that method itself, in combination with the wave gauge array, has very low sensitivity the level of in-line reflection, particularly for the range expected at the FloWave facility. However, high sensitivity is displayed to the presence of oblique reflections, something which future work aims to deal with.

Acknowledgements

The authors would like to thank the Energy Technology Institute and the Research Council UK Energy Programme for funding this research as part of the IDCORE programme (EP/J500847/1). In addition we would like to thank the UK Engineering and Physical Science Research Council for funding towards the creation of the FloWave Ocean Energy Research Facility (EP/I02932X/1).

References

Benoit, M.P., Frigaard, P., Schaffer, H.A., 1997. Analysing multidirectional wave spectra: a tentative classification of available methods. Assoc. Hydraulic Res. Seminar: Multidirectional Waves.
Draycott, S., Davey, T., Ingram, D.M., Lawrence, J., Day, A., Johanning, L., 2015. Using a Phase-Time-Path-Difference Approach to measure directional wave spectra in FloWave. EWTEC Conference Proceedings.
Esteva, D., 1976. Wave direction computations with three gage arrays. Coastal Engineering Proceedings.
Fernandes, A.A., Sarma, Y.V.B., Menon, H.B., 2000. Directional spectrum of ocean waves from array measurements using phase/time/path difference methods. Ocean Eng. 27 (4), 345–363.
Goda, Y., Suzuki, T., 1976. Estimation of incident and reflected waves in random wave experiments. Coastal Engineering Proceedings, pp. 828–845.
Gyongy, I., Bruce, T., Bryden, I., 2014. Numerical analysis of force-feedback control in a circular tank. Appl. Ocean Res. 47, 329–343 (August).
Hashimoto, N., Konbune, K., 1988. Directional spectrum estimation from a Bayesian approach. Coastal Engineering Proceedings, pp. 62–76.
Hashimoto, N., Nagai, T., Asai, T., 1994. Extension of the maximum entropy principle method for directional wave spectrum estimation. Coastal Engineering Proceedings, pp. 232–246.
Haubrich, R.A., 1968. Array Des. 58 (3), 977–991.
Ingram, D., Wallace, R., Robinson, A., Bryden, I., 2014. The design and commissioning of the first, circular, combined current and wave test basin. Flow3d.com.
Krogstad, H.E., 1988. Maximum likelihood estimation of ocean wave spectra from general arrays of wave gauges. Modeling, Identification and Control.
Mandel, L., Wolf, E., 1976. Spectral coherence and the concept of cross-spectral purity. J. Opt. Soc. Am. 66 (6), 529.
Mansard, E.P.D., Funke, E.R., 1980. The measurement of incident and reflected spectra using a least squares method. Coastal Engineering Proceedings, pp. 154–172.
Miles, M.D., Funke, E.R., 1989. A Comparison of Methods for Synthesis of Directional Seas.
Pascal, R.C.R., 2012. Quantification of the Influence of Directional Sea State Parameters Over the Performances of Wave Energy Converters.
Wang, S.K., Hsu, T.W., Weng, W.K., Ou, S.H., 2008. A three-point method for estimating wave reflection of obliquely incident waves over a sloping bottom. Coast. Eng. 55 (2), 125–138 (February).
Zelt, J.A., Skjelbreia, J., 1992. Estimating incident and reflected wave fields using an arbitrary number of wave gauges. Coast. Eng. Proc. 1, 777–789.

Using a Phase-Time-Path-Difference Approach to Measure Directional Wave Spectra in FloWave

S.Draycott[#1], T.Davey[#2], D.M.Ingram[*3], J.Lawrence[^4], A.Day[~5], L.Johanning[+6]

[#] FloWave Ocean Energy Research Facility, Max Born Crescent, King's Buildings, Edinburgh, UK, EH9 3BF, S.Draycott@ed.ac.uk [1], Tom.Davey@ed.ac.uk [2]

[*]Institute for Energy Systems, School of Engineering, The University of Edinburgh, Edinburgh, UK, EH9 3JL, David.Ingram@ed.ac.uk [3]

[^]The European Marine Energy Centre (EMEC) Ltd, Old Academy Business Centre, Stromness, Orkney, UK, KW16 3AW, John.Lawrence@emec.org.uk [4]

[~]Naval Architecture and Marine Engineering, The University of Strathclyde, Glasgow, UK, G4 0LZ, sandy.day@strath.ac.uk [5]

[+]Renewable Energy Research Group, University of Exeter, UK TR10 9E, L.Johanning@exeter.ac.uk [6]

Abstract— **The realism of wave tank testing can be increased by the use of complex directional seas states. The measurement and validation of these wave conditions, however, comes with inherent difficulty and uncertainty. In this work we aim to reduce this uncertainty. A variety of directional sea states are generated in a unique circular wave tank, the FloWave Ocean Energy Research Facility. Two standard directional spectrum reconstruction methods are then used, in addition to an implementation of the Phase-Time-Path-Difference approach, taking advantage of knowledge about the wave generation method. We show that this PTPD approach is significantly quicker, whilst also reducing the perceived directional deviation down from 17.8% (BDM), and 34.2% (EMEP), to 4%. The method is also shown to be effective with resolving complex multi-modal sea states, and despite having some sensitivity to wave reflection, demonstrates how this method can be used to improve confidence in the validation of directional seas.**

Keywords— **Tank Testing, Directional Spectrum Measurement, Resource Assessment, FloWave, Phase/Time/Path/Difference**

I. Introduction

Wave tank testing enables complex sea conditions to be generated in a controlled and repeatable manner. This allows the dynamics of Wave Energy Converters (WECs) and other offshore structures to be assessed under a range of desired conditions, at scale. As devices may be sensitive to wave directionality, it is important to use realistic directional wave spectra if possible. Equally, it is important to be able to measure these complex sea states and validate their performance.

The FloWave facility, based at the University of Edinburgh, is a unique, circular, combined wave and current test basin. It has primarily been designed to test wave and tidal energy devices at around 1:20th to 1:40th scale, and enables waves and current to be generated in any direction, either independently, or in combination. The ability to generate and absorb waves from all directions simultaneously removes directional constraints on the generation of complex spectra.

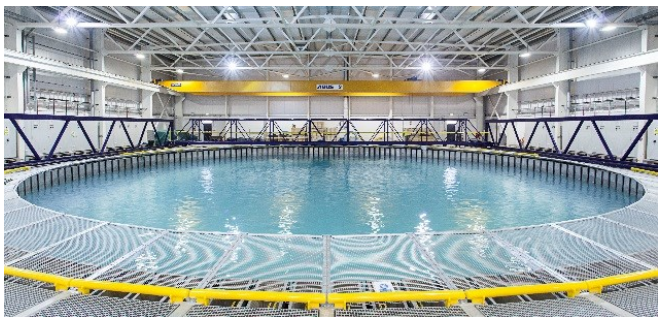

Figure 1: The FloWave facility

Measuring and validating directional spectra can be challenging. Most directional spectrum reconstruction methods aim to resolve the Directional Spreading Function (DSF), describing the distribution of wave energy with direction for each frequency band. This essentially uses the inter-gauge cross-spectra of the measured time series, along with the known gauge positions, to fit a directional distribution. There are a number of approaches to achieving this, including the Maximum Likelihood Method (MLM) [1][2], the Extended Maximum Entropy Principal (EMEP) [3], and the Bayesian Directional Method (BDM) [4].

The DSF-based reconstruction methods can be used for both laboratory and ocean measurement. In this work we explore the use of a tank specific method of directional spectrum measurement, taking advantage of the knowledge of how the waves have been produced. Seas are synthesised using the single-summation method [5], such that each distinct wave frequency only has one propagation direction. This means that the Phase-Time-Path-Difference (PTPD) method [6] can be used effectively to calculate the wave direction, without making the normally inappropriate assumption that each frequency band can be represented by a single propagation direction.

II. Methodology

A. Sea State Input and Generation

1) *Input Sea States*

Five parametric directional spectra are generated using JONSWAP frequency spectra in combination with cos-2s spreading functions. A random selection of values are used to give a good range, shown in Table I, with the resulting directional spectra shown in Figure 10.

TABLE I
INPUT SEA STATES

Sea State	Hm0 [m]	Tp [s]	JONSWAP peak enhancement factor, γ	cos-2s spreading factor, s	MDIR [rad]
1	0.05	3	3	25	π/2
2	0.1	2	2	20	π
3	0.15	3.3	3.3	30	3π/2
4	0.15	4	4	5	0
5	0.2	3.5	3.5	15	π/4

2) *Wave Generation*

In line with the approach historically adopted by the University of Edinburgh, FloWave's wave generation is achieved using a deterministic approach. This enables complete

repeatability, allowing changes to devices to be assessed independently of sea state variations.

The two main approaches of deterministic wave generation are the single and double summation methods. The double summation method creates multiple waves at the same frequency with differing amplitudes, phases and directions. Using the single summation method, however, means that each frequency only has one propagation direction associated with it, avoiding a phenomenon called phase-locking. Phase-locking happens when waves at the same frequency but different directions constructively interact and cause spatial patterns across the tank [5]. This results in a spatial non-homogeneity of the wave field, and it is therefore preferable to use the single summation method for wave tank sea generation.

In order to use the single-summation method the nominal directional spectrum form must be altered so that it has sub-frequencies, and new frequency increments (δf) equal to the original frequency increments divided by the number of discrete directions being used, i.e. $\delta f = \Delta F/NDIR$. This is demonstrated in Figure 2.

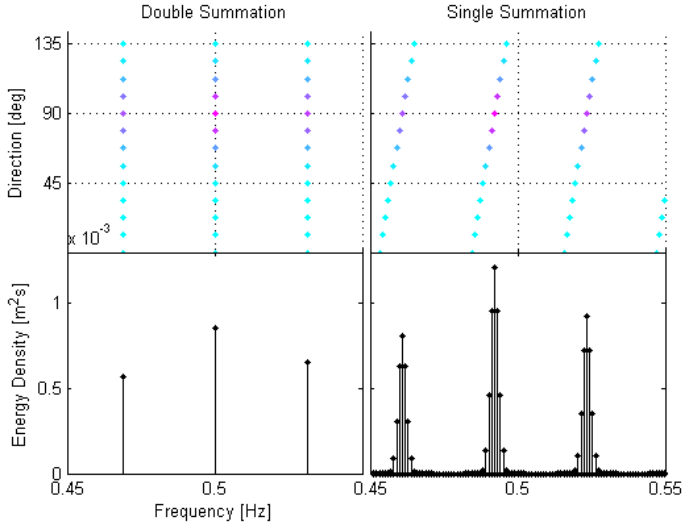

Figure 2: Illustration of the double and single summation methods

Once the spectrum is redefined, an Inverse Fast Fourier Transform (IFFT), or summation, can be used to calculate both the paddle motion (with transfer function) and the time series of surface elevations. The surface elevation can be described by:

$$\eta(x,y,t) = \sum_{i=0}^{NF.NDIR-1} A_i \cos(-\omega_i t + k_i[x\cos\theta_i + y\sin\theta_i] + \Phi_i)$$

B. Directional Spectrum Estimation Methods

1) DSF Based Methods

To compare the performance of the PTPD approach to the standard approaches some DSF-based methods have been implemented. The WaveLab software package, developed by Aalborg University uses the BDM approach by default, whilst the DIWASP Matlab® toolbox uses the EMEP method. These two methods have been used in this work for comparison and benchmarking against the PTPD technique.

2) The Combined Single-Summation PTPD Method

The PTPD method of calculating wave direction has been used previously, such as in [6] and [10], primarily in the field of ocean directional spectrum measurement.

The PTPD approach essentially uses triads of gauges, their known positions, and their phase differences to infer wave direction for each frequency band. The limitation with this method is that it is assumed that each frequency band can be represented by a single propagation direction. This trait means the has limited application for directional spectrum reconstruction in the ocean, or when employing the double summation method of wave generation in tanks, as the phase differences will encompass a range of different waves travelling in different directions.

The PTPD approach can, however, be used effectively to re-construct a directional spectrum if it is known that each wave frequency only has one direction. This is essentially the case with the single-summation method, and enables the directional spectrum to be estimated quickly and without model fitting.

After the spectrum has been altered for use with the single summation method, the wave generation frequency domain, and frequency increments are set. This defines the repeat time of the sea state but also defines the number of Fast Fourier Transform (FFT) points required for appropriate spectral analysis. Once this is known along with the gauge positions and the time series of surface elevations, a PTPD reconstruction method can be implemented. The method used here is as follows:

- Calculate $A(f)$ and $\Phi_{absolute}(f)$ from the FFT outputs for each gauge
- Find all 3 probe combinations from the array e.g. for the 8 gauge array used here , ${}^{8}C_{3}=56$ combinations

For every triad, m, and all frequency components, i:

- Check if inter-gauge separations, $L_{m,12}$ *and* $L_{m,13} < \lambda_i(f)/2$ (to avoid aliasing in high frequency waves)

If so:

- Calculate relative phases, $\Phi i_{,12}$ and $\Phi i_{,13}$
- Calculate perceived angle,α_i , (for that triad and frequency) by Esteva's method [6], [11]. The final equations of which are shown below:

$$\alpha_{i,m} = \tan^{-1}\frac{[(x_{m,1}-x_{m,2})\Phi_{i,13} - (x_{m,1}-x_{m,3})\Phi_{i,12}]/sgn(P_m)}{[(y_{m,1}-y_{m,3})\Phi_{i,12} - (y_{m,1}-y_{m,2})\Phi_{i,13}]/sgn(P_m)}$$

$$P_m = [(x_{m,1}-x_{m,2})(y_{m,1}-y_{m,3}) - (x_{m,1}-x_{m,3})(y_{m,1}-y_{m,2})]$$

- Take the mean angle, or the peak of a circular kernel density estimate, over all valid triad combinations, as the representative angle for that frequency (kernel density used here, shows slight improvement when dealing with outliers)

Can now reconstruct directional spectrum

- Choose desired directional and frequency bins (usually equal to input ΔF and Δθ for comparison of target spectrum)
- Assign each representative direction to a bin
- Calculate the sum of wave energy density in each frequency-directional bin, from mean amplitudes over all gauges, from the FFT. Energy density calculated as:

$$E_i = {A_i^2}/{(2\Delta F \Delta\theta)} = {A_i^2}/{(4\pi\delta f)}$$

C. *Wave Gauge Array Design*

A directional wave gauge array is required for this work. As the directions will be inferred from the known vector array spacings, it is important that these separations cover as many directions and magnitudes as possible. For the DSF based methods this will enable directional distributions to be inferred at a range of frequencies and angles with greater resolution. The PTPD method requires a minimum of 3 gauges but a larger number of points and vector separations allows for reduced errors.

Inter-array separations can be represented by their co-array, describing the vector separations between all points [7]. Good wave gauge arrays are those with a uniform co-array, spanning a range of magnitudes relative to the wavelengths present in the tank. For this reason wave gauge arrays have been designed with the co-array uniformity in mind.

Two methods have been used to create arrays that can be placed on the reconfigurable rig shown in Figure 3, and contrasted with classical arrays, shown in [8] . One of these methods aims to use Costas arrays, shown in [9], and take advantage of the naturally good co-array properties that arise from using these permutation matrices as array configurations. The other method is a random probe placement tool that places the probes many times and chooses the best array based on the uniformity of the resulting co-arrays.

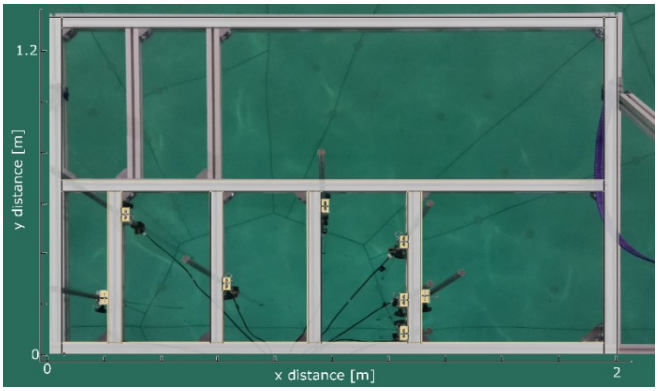

Figure 3: Final wave gauge array design

A number of 8 gauge arrays have been generated and tested numerically to explore the assumed practical performance, identifying sensitivity to frequency, direction, directional spreading and spectral width. It was found that arrays generated using the random probe placement tool generally showed improved performance over both the use of Costas arrays, and the use of standard arrays. After analysing a range of arrays under a variety of conditions, a final design was chosen, shown in Figure 3, with its co-array separations shown in Figure 4.

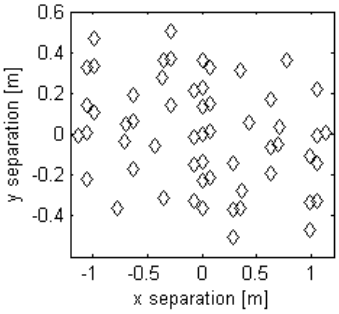

Figure 4: Co-array of final gauge design

III. RESULTS

A. *General Sea State Performance*

1) *Spectral Outputs*

The measured wave frequency spectra are shown in Figure 5. On average the deviation from the target spectrum was 15.2% showing that there is a tendency to under-generate the desired waves. This can be corrected for when re-running these sea states by applying a frequency dependent correction factor, and from previous experience it is expected that this can be brought down to less than 1% after the first iteration.

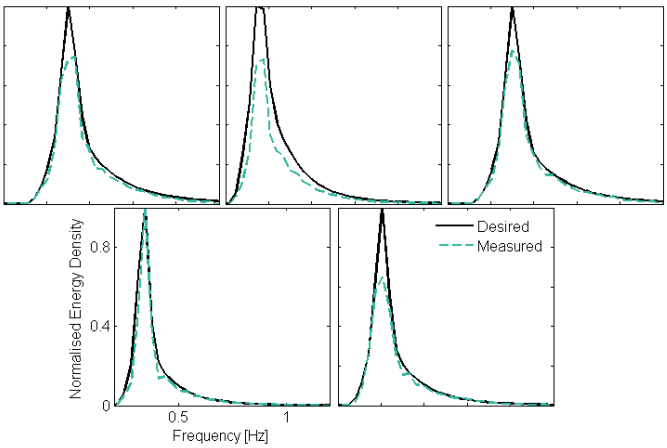

Figure 5: Comparison between desired and measured spectra for all 5 tests

2) *Time Series Outputs*

Using an IFFT the surface elevations can be calculated at the gauge positions. Example outputs of this are shown in Figure 6, and compared to the measured time series at some of the gauge locations. In general they show good agreement, however, in the first time series, relating to the first spectrum, it is obvious that these low amplitude waves are being affected by unpredicted surface noise in the tank.

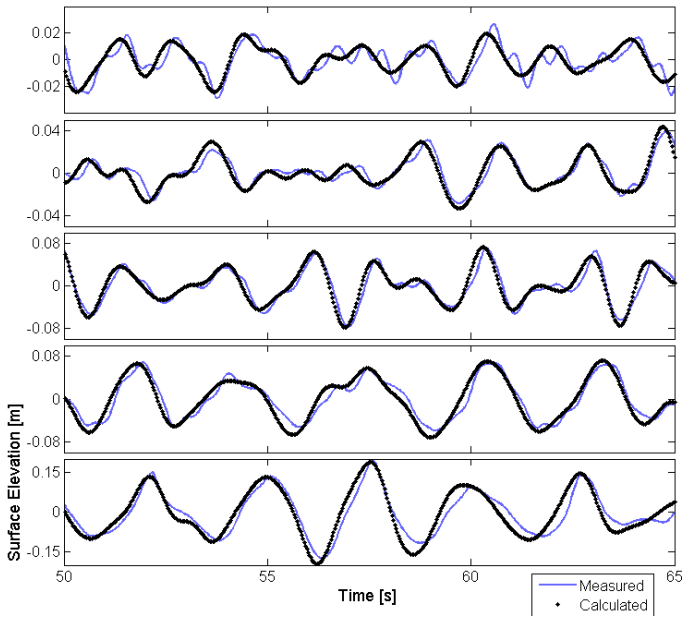

Figure 6: Example time series outputs. S1G1, S2G5, S3G4, S4G3, S5G8

3) *Statistical Outputs*

Desired and measured H_{m0}-T_E combinations are shown in Figure 7. They show the deviation expected from the discrepancy between the produced and desired wave spectra, Figure 5. The tendency to under-produce the peak of the spectrum means that not only will H_{m0} reduce, but so will T_E due to the high-frequency tail of the JONSWAP spectrum. If the peak is under-produced there is relatively more wave energy above the peak, and hence the effective wave frequency increases, and period decreases. This can also be viewed in terms of the spectral moment calculation for T_E.

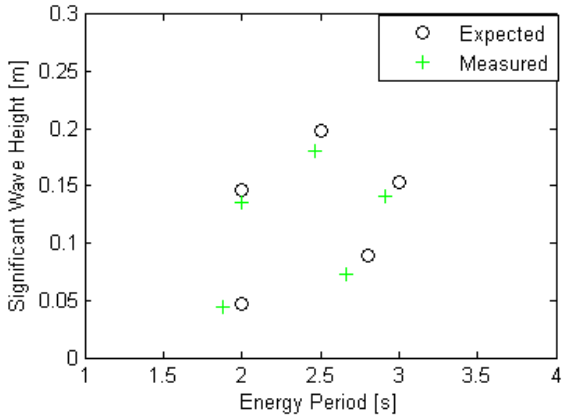

Figure 7: Expected vs measured wave statistics

B. *Directional Spectrum and Method Performance*

The reconstructed directional spectra are shown in Figure 10. Visually it can be seen that the PTPD estimates are much closer to the desired spectrum than the BDM, and especially EMEP outputs. To quantify the deviation the Normalised Total Difference, NTD, describing the total relative difference between target and measured spectra can be examined.

This NTD encompasses a number of potential deviations:

- Frequency spectrum deviation, S_{NTD}
- Directional distribution deviation, E_{NTD}
- Reconstruction method error, M_{NTD}

Removing the frequency spectrum deviation, which can mostly be corrected for, the combined effect of the reconstruction method induced error and the directional distribution error can be observed, shown in Figure 8. This gives the mean combined deviation for the PTPD approach to be 4.0%, BDM 17.8%, and EMEP 34.2%. In addition, for the current tests, the PTPD solution took nearly two order of magnitudes less time to compute than the BDM approach (one order of magnitude difference in comparison to EMEP).This shows that it is a much quicker and more effective method for the reconstruction of directional spectrum when the single-summation method of wave generation is used.

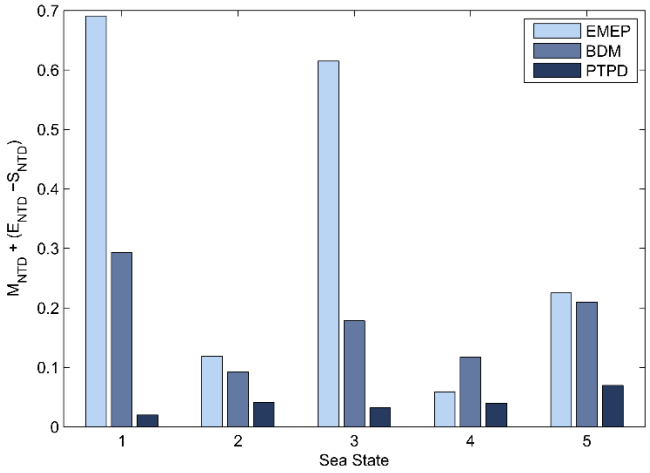

Figure 8: Performance of directional spectrum reconstruction methods

Figure 9 shows the DSF at the peak frequency as calculated by each of the methods, providing an illustration of the relative performance. This highlights the sensitivity of the EMEP method to the sea state properties, especially to mean direction. For the PTPD approach, however, it is clear that there is very little deviation.

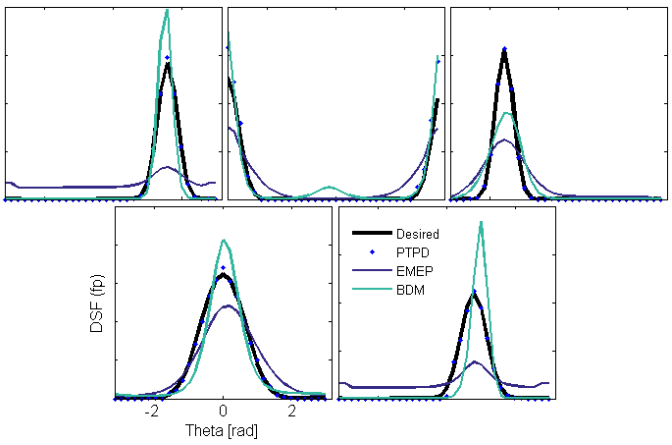

Figure 9: Calculated DSF at peak frequency for reconstruction methods for all 5 tests

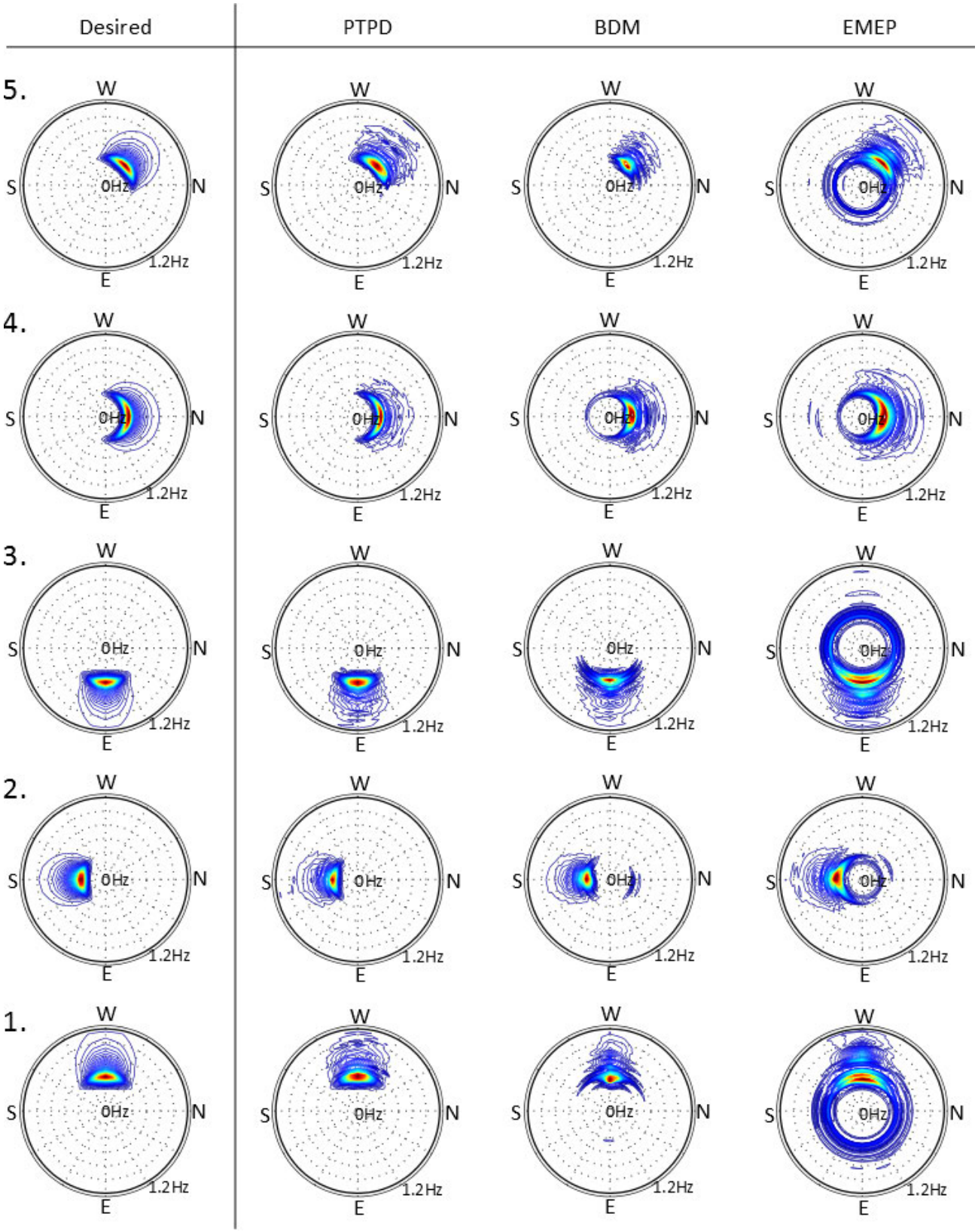

Figure 10: Directional spectrum outputs from the 5 test spectra, created using parametric spreading functions. Desired spectra compared to the outputs of the three reconstruction techniques considered

C. *Example Complex 'Representative' Spectra*

In addition to the parametric test spectra a number of measured sea stated were examined. These sea states have been derived from buoy data made available by the European Marine Energy Centre, Orkney, UK, from their full scale wave test site, Billia Croo. The methodologies used to create these seas is explained in [12], and the spectrum are shown in Figure 11 and Figure 12. The spectra shown have been chosen specifically because they display multi-modal features.

It can be seen, despite the BDM performing well, that the two peaks displayed in Figure 12 are only properly captured using the PTPD approach. These results highlight the ability of the tank to produce complex realistic directional spectra, as well as the ability of the presented PTPD approach at resolving such spectra, and aiding in the validation of such sea states.

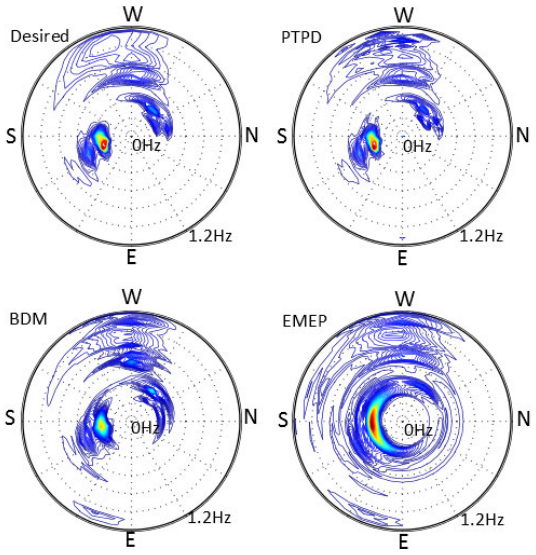

Figure 11: Example directional spectrum output 1: swell with complex features

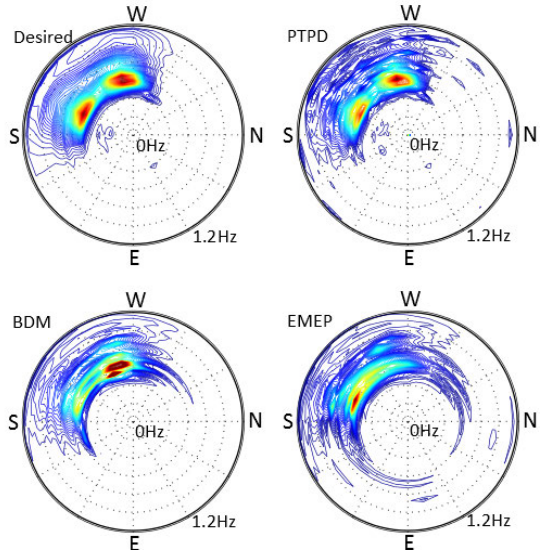

Figure 12: Example directional spectrum output 2: two peaks at same frequency

IV. DISCUSSION

A. *General Sea State Performance*

In general the sea states were generated well, with most of the deviation coming from an apparent under-production of the peak of the frequency spectra. This deviation can be reduced when these sea states are regenerated, by means of a frequency dependent correction factor.

It is evident from the first time series in Figure 6 that there is some tank noise, either from insufficient settling time after the previous test, or from the presence of reflections. Despite the paddles being very effective at wave absorption, some reflections do occur, especially at the high frequency end.

B. *PTPD Method Performance*

The PTPD method significantly outperforms both the BDM and EMEP methods trialled in this work, and demonstrates that complex directional spectra can be effectively measured and validated at FloWave with a high degree of confidence. Despite this, the method still has some uncertainty associated with it, largely due to the high sensitivity to gauge position error and wave reflection.

The PTPD approach relies on the relative phases calculated at each of the gauges, along with the assumed gauge positions, to infer wave propagation direction. If reflections are present then the assumption that each wave frequency only has one direction is incorrect. However, rather than being shown in the directional spectrum outputs, this occurrence manifests itself as a phase error, and hence a directional distribution error. Having more gauges in this case is advantageous, as either the peak of a probability density function, or simply the mean of the calculated directions, for all of the triad combinations, can be used to estimate direction. This should average over both positive and negative phase deviations to help reduce the perceived directional error.

The sensitivity of the method to reflection is highlighted in Figure 13. From this it can be seen that the reflections in the tank are likely to be around 5%, but also that the method over-exaggerates reflection-based error. For example a 10% reflection, should equal a 1% change in NTD, due to $E \propto A^2$. However, in this case a 1% actual NTD error appears as a 9% apparent NTD error. Future extensions to this method may be able to isolate the reflected components, providing estimates for both the incident and reflected spectra.

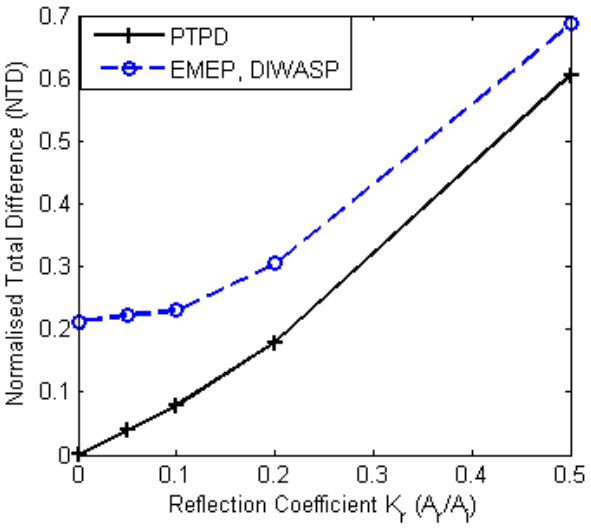

Figure 13: Simulated effect of reflection coefficient on NTD

V. CONCLUSIONS

To conclude, a variety of parametric directional spectra have been created in the FloWave tank and measured using a specially designed wave gauge array. The BDM and EMEP methods have been used to resolve the directional spectrum, along with a unique application of the PTPD approach. The PTPD method proved to have a lower computational cost, whilst also reducing the perceived directional error from 17.8% (BDM), and 34.2% (EMEP), down to 4%. Despite increasing confidence in the generated directional distributions, sensitivity to gauge position error and wave reflection means that some uncertainty is still present, leaving scope for improvement. In addition, more complex directional spectra have been generated, showing the added benefit of the PTPD approach when analysing multi-modal sea states.

REFERENCES

[1] H. Krogstad, "Maximum likelihood estimation of ocean wave spectra from general arrays of wave gauges," *Model. Identif. Control*, 1988.

[2] M. Benoit, H. Frigaard, P. Frigaard, and H. Sch, "Analysing multidirectional wave spectra: a tentative classification of available methods," *... Assoc. Hydraul. Res. Semin. Multidirectional Waves ...*, 1997.

[3] N. Hashimoto, T. Nagai, and T. Asai, "Extension of the maximum entropy principle method for directional wave spectrum estimation," *Coast. Eng. Proc.*, pp. 232–246, 1994.

[4] N. Hashimoto and K. Konbune, "Directional spectrum estimation from a Bayesian approach," *Coast. Eng. Proc.*, pp. 62–76, 1988.

[5] M. D. Miles and E. R. Funke, "A Comparison of Methods for Synthesis of Directional Seas," *Journal of Offshore Mechanics and Arctic Engineering*, vol. 111. p. 43, 1989.

[6] D. Esteva, "Wave direction computations with three gage arrays," *Coast. Eng. Proc.*, 1976.

[7] R. . Haubrich, "Array Design," vol. 58, no. 3, pp. 977–991, 1968.

[8] Y. Goda, *Random seas and design of maritime structures*, vol. 15. 2000, p. 443.

[9] C.-C. Yang, "New extended Costas sequences with ideal auto-and cross-ambiguity functions," *2009 Int. Conf. Commun. Circuits Syst.*, pp. 156–159, Jul. 2009.

[10] A. Fernandes, Y. Sarma, and H. Menon, "Directional spectrum of ocean waves from array measurements using phase/time/path difference methods," *Ocean Eng.*, vol. 27, no. 4, pp. 345–363, 2000.

[11] A. Fernandes, A. Gouveia, and R. Nagarajan, "Determination of wave direction from linear and polygonal arrays," *Ocean Eng.*, vol. 15, no. 4, pp. 345–357, 1988.

[12] S. Draycott, T. Davey, D. M. Ingram, J. Lawrence, A. Day, and L. Johanning, "Applying Site-Specific Resource Assessment : Replicating and Measuring Real Seas in FloWave," *Expect. ISOPE Conf. Proc. 2015*, 2015.

Applying Site-Specific Resource Assessment: Emulation of Representative EMEC seas in the FloWave Facility

S.Draycott[1], T.Davey[1], D.M.Ingram[2], J.Lawrence[3], A.Day[4], L.Johanning[5]

[1] FloWave Ocean Energy Research Facility, Edinburgh

[2]Institute for Energy Systems, School of Engineering, The University of Edinburgh

[3]The European Marine Energy Centre (EMEC) Ltd, Stromness, Orkney

[4]Naval Architecture and Marine Engineering, The University of Strathclyde, Glasgow

[5]Renewable Energy Research Group, University of Exeter

ABSTRACT

The realism of wave tank tests can be improved by the use of site-specific buoy data. However, representing and reproducing vast quantities of complex wave buoy data within practical time constraints can be challenging. In this paper the process of classifying, generating and measuring 'representative' directional spectra in FloWave is presented. Two years of buoy data, from the European Marine Energy Centre, Orkney, UK, is manipulated to give a small number of groups. It is shown that the resulting complex representative sea states can be generated effectively in the FloWave tank.

KEY WORDS: Resource assessment; wave site characterisation; tank testing; directional spectrum measurement

NOMENCLATURE

Hm0	Significant wave height [m]
E(f,θ)	Wave energy directional spectrum [m^2/Hz/Rad]
S(f)	Wave energy frequency spectrum [m^2/Hz]
T_E	Energy period [s]
L	Wavelength [m]
v	Spectral width
MDIR	Mean direction [rad]

INTRODUCTION

Physical model tests facilitate the understanding of how man-made devices interact with complex sea conditions. It is therefore important that the wave test conditions incorporate as much of the underlying complexity, and realism of a device deployment site as possible. Equally, it is essential that a facility aiming to replicate such conditions is capable of doing so.

In order to 'emulate' a site of interest practically, under the inherent time and cost constraints, site data must be characterised and reduced to a reasonable level. These sea states then need to be scaled appropriately and generated in a wave tank, before being measured and validated.

The Facility

The FloWave facility, based at the University of Edinburgh, is a unique, circular, combined wave and current test basin. It has primarily been designed to test wave and tidal energy devices, at around 1:20th to 1:40th scale. 168 independently controlled force-feedback absorbing wavemakers, along with 28 impeller units, allow both wave and current to be generated in any direction, with a high degree of control (Ingram et al. 2014).

Figure 1: The FloWave facility

This work focusses on the re-creation of complex realistic wave conditions derived from site data. Of importance here is the circular design, enabling 360° wave generation and absorption. This removes any intrinsic directional limitations and enables the creation of complex multi-modal, and multidirectional sea states, like those found in reality.

The Site

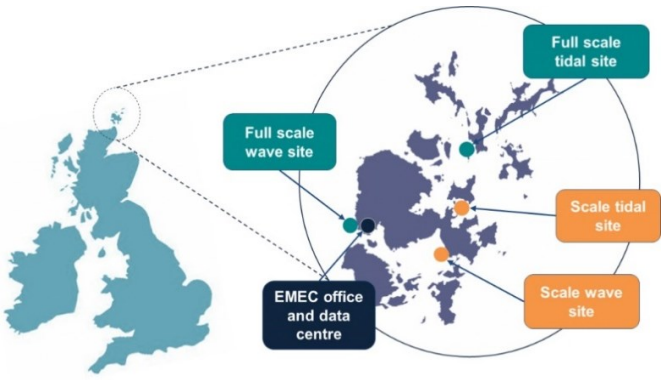

Figure 2: EMEC site location (EMEC 2015)

The European Marine Energy Centre (EMEC), based in Orkney, UK, operates both sheltered and full scale grid-connected wave and tidal test sites. EMEC boasts an energetic wave site exposed to the North Atlantic at Billia Croo, as well as high tidal flows in the Fall of Warness tidal site. EMEC has vast experience of both installing devices and measuring the resource. Of importance for this work is the directional wave buoy dataset available, enabling a vast quantity of directionally complex buoy data to be used for classification, and emulation in the FloWave facility.

The Process

Two years of EMEC buoy data has been manipulated, using a number of different methodologies, to characterise EMEC's Billia Croo wave test site. The most favourable methodology has been chosen, and the resulting sea states ran at scale in the FloWave tank. The data obtained from a directional wave gauge array is then analysed in order to assess the performance of the sea states.

The process shown here, used to replicate and measure EMEC-based sea states in FloWave is as follows:

- Classification of the site
  - Estimate directional spectrum
  - Group the data by various measures of similarity, including:
    - Binning on statistical parameters
    - Clustering on spectra
  - Assess classification performance using a grouping performance metric
  - Choose best method based on metric and create representative sea states
- Sea State Creation
  - Choose appropriate scale(s) to run representative sea states in the tank
  - Choose method of wave creation
- Measurement Strategies
  - Create wave gauge array
  - Reconstruct directional spectrum
- Assess Sea State Performance

SITE CLASSIFICATION METHODOLOGY

The idea behind the site characterisation is to represent the wave site through a small number of 'representative' sea states. These sea states should embody the site's true characteristics, whilst picking out the interesting and important sea states for device performance. Data must therefore be classified, and sea states grouped by similarity. Taking advantage of the tanks directional capabilities, the resulting sea states should then be derived from the directional spectra belonging to each group.

Directional Spectrum Estimation

The directional spectra of the source buoy data has to be estimated in order to use them in the classification process. As wave buoys tend to only give directional Fourier coefficients a model must be used to estimate the full directional spectrum. It has been shown that using the Maximum Entropy Principal (MEP) provides the most reliable results from a single point measurement system (Benoit 1992), and as such was used in the current work. However, the solution to the MEP is nonlinear, computationally challenging, and often results in non-convergence (Kim et al. 1994). To aid the convergence problem Newton's technique of local linearisation has been employed, outlined in Hashimoto (1997), and replaced by approximate solutions shown in Kim et al. (1994) if the problem persists.

Classification Methodologies

Six different methodologies have been used to classify the EMEC dataset. These methods have been based on Hamilton (2010), and Draycott et al (2014), focusing on exploring the merits in using statistical clustering techniques directly on wave spectra to classify the data. Building on Draycott et al. (2014), less effective methodologies have been excluded, whilst additional methodologies have been explored, incorporating wave steepness as a grouping parameter. The range of methods explored here are shown in Table 1.

The binning methods identify group membership by partitioning the dataset using regular sized bins applied to their respective grouping parameters. These methods are contrasted with the use of clustering algorithms applied directly to wave spectra.

The motivation driving the use of statistical clustering methods is that the whole spectral form can be used to characterise the data, meaning that the true underlying energy distribution is considered rather than a proxy set of derived wave statistics. The aim is that the resulting representative wave spectra incorporate more of the true complexity inherent at the site.

Table 1: Classification methodologies

	Method Name	Grouping Parameters
A	H-T binning	H_{m0}, T_E
B	H-T-MDIR binning	H_{m0},T_E,$MDIR$
C	Frequency spectrum clustering	$S(f)$
E	Directional spectrum clustering	$E(f,\theta)$
G	Steepness-spectral width binning	H/L, ν
H	Steepness-Power binning	H/L, $Power$
I	S(f) clustering with H-T bin outputs as start point	$S(f)$

Classification Performance

It is difficult to identify a metric that defines good groupings for all applications. Indeed in 1964, Bonner was the first to argue that there is no all-encompassing criteria, and that the evaluation was application specific. For this work two main criteria were considered important; that the groups are both 'compact', and 'distinct'.

In this work representative sea states are created by taking the mean of each resulting group. If these groups are compact, the spectra/statistics of those sea states in the group are similar, and hence the mean sea state should end up representative of real conditions. In tank testing, however, it is also important to test as many different conditions as possible, given the time constraints, and as such the resulting groups should be as distinct as possible from each other. The problem here is that for a fixed number of desired groups forcing them to more distinct is likely to reduce compactness and vice versa. In addition to this we want the resulting groups to be compact, and distinct, with respect to a range of important variables.

Compactness and distinctness can be described by the resulting groupings intra- and inter-cluster scatter matrices, shown in Rokach & Maimon (2001) as S_W and S_B. respectively. As we want to create compact and distinct groups, this could approached by maximizing $S_W^{-1}S_B$. This metric can be applied to both single and multidimensional data, allowing it to be applied effectively to a range of variables deemed important for device performance.

Final Choice of Sea States

The final choice of sea states depends on both the desired number of sea states and the classification method used to produce them. The desired number of sea states in this case is largely dominated by the time constraints, taken here to be 2 days in the tank. Generally tests of between 500-1000 waves are considered acceptable for irregular seas, giving a good representation of extremes (McCombes et al. 2010). For this particular tank, optimized for 0.5Hz waves, this relates to an individual test length of 1000-2000s. For ease of spectral analysis this practically relates to 20×2048s tests, or 40×1024s tests. Using 40 sea states allows the site to be characterised significantly more effectively, increasing $S_W^{-1}S_B$ values on average by a ratio of 1.9. In addition, the frequency resolution remains comparable with that of the source buoy data equated at the relevant scale factors.

Methods A to I have been tasked to produce 40 sea states, with their relative $S_W^{-1}S_B$ values shown in Table 2. Ideally, if we characterised the sea states by the directional spectrum (method E), describing the wave energy distribution with respect to both frequency and direction, it would automatically partition well with respect to other parameters. However, this is not the case, and Table 2 shows the inherent trade-offs when trying to classify such multi-characteristic datasets.

Table 2: Relative performance metric, $S_W^{-1}S_B$, for a range of variables. Methods as shown in Table 1

	Methods						
Variable	**A**	**B**	**C**	**E**	**G**	**H**	**I**
E(f,θ)	0.83	1.03	1.00	1.96	0.56	0.61	0.98
S(f)	1.07	0.75	1.81	1.11	0.54	0.72	1.74
H_{m0}	1.11	0.44	0.95	0.54	0.67	2.29	1.14
T_E	3.08	1.14	0.41	0.28	0.26	0.82	0.44
v	0.37	0.28	0.12	0.07	4.84	0.32	0.14
Power	1.85	0.73	1.64	0.60	0.38	0.79	1.77
Steepness	0.57	0.24	0.33	0.21	1.94	2.71	0.37

For this work method I was chosen as it was considered to produce the most desirable results, providing a good classification with respect to the directional and frequency spectra, H_{m0}, and wave power. This method used the resulting representative frequency spectra generated through method A as the starting point for *k-means* clustering, providing improvements on method C with respect to the classification on statistical parameters.

SEA STATE CREATION

Choice of Scale

Once the final sea states have been defined, an appropriate Froude scale, or scales, need to be chosen for generation of these waves in the tank. Despite not having any limitations with respect to wave propagation direction, frequency-height limits exist due to a combination of the shape characteristics of the paddles (Dalrymple & Dean 1984), along with inherent limitations of the wavemaker motors. This combination sets the wave generation range to be 0.2-2Hz. At this time, however, the FloWave tank relies solely on active wave absorption from the paddles to control the wave field, and as the absorption performance reduces significantly after about 1.2Hz, this gives a practical frequency range of 0.2-1.2Hz.

Ideally the scale would be based on the depth ratio from tank (2m) to full (~50m) scale, i.e. ~1/25th. However if this is implemented, significant spectral wave energy content is unable to be produced for the low frequency dominated sea states. Due to this, two scales have been chosen based on minimizing the combined relative energy out with the tank bounds, whilst taking into account wave height limitations. This gives 1/26th and 1/68th to be the two optimal scales, practically (<1% spectral energy loss) enabling complete generation and measurement of all of the representative sea states. The scaled frequency spectra are shown in Figure 3.

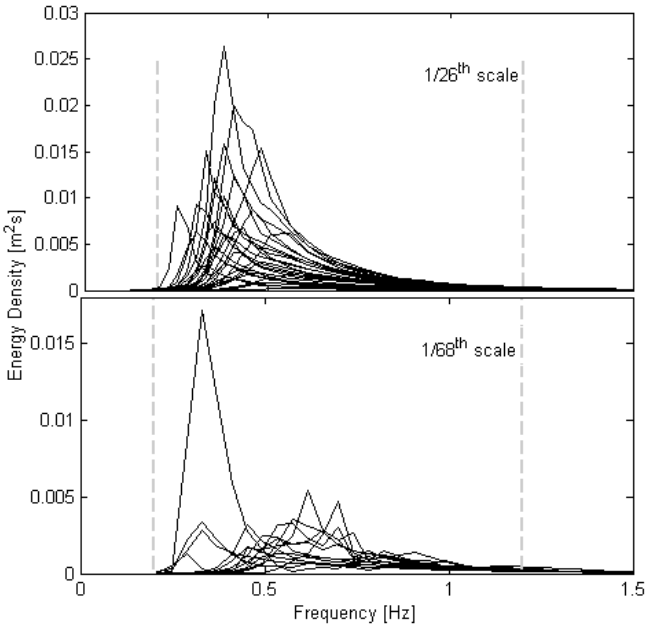

Figure 3: Final dual-scaled frequency spectra with limits in dashed grey

The scales chosen have been optimized for the measurement and validation of the sea states, but these sea states could be run at a range of scales without significant energy loss. In reality it is likely that the model scale will determine the sea state scale and not vice-versa. In this instance, compromises may need to be made, perhaps taking into account the frequency response of the device itself. Alternatively the addition of passive beaches that absorb generated waves above 1.2Hz would also enable a more suitable single-scale test program to be implemented.

Wave Creation

Deterministic waves are generated at the FloWave facility in alignment with the approach historically adopted by the University of Edinburgh. This approach enables repeatability, a key attribute of tank testing which enables device iterations to be assessed independently of sea state variations.

The representative directional spectra created using method I can be represented, and generated deterministically, in a number of ways. The two main approaches being the single and double summation methods. The double summation method mimics the form of the directional spectrum; each wave frequency having a range of wave directions, amplitudes and phases associated with it. This approach, however, leads to a phenomenon called phase-locking, whereby waves travelling at the same frequency but different directions, constructively interact and cause spatial patterns across the tank (Miles & Funke 1989) .

To avoid phase-locking the single summation method can be employed, whereby each distinct frequency only has one direction associated with it, as shown in Figure 4. This requires sub-frequencies to be created within each original band equal to the number of discrete propagation directions being used.

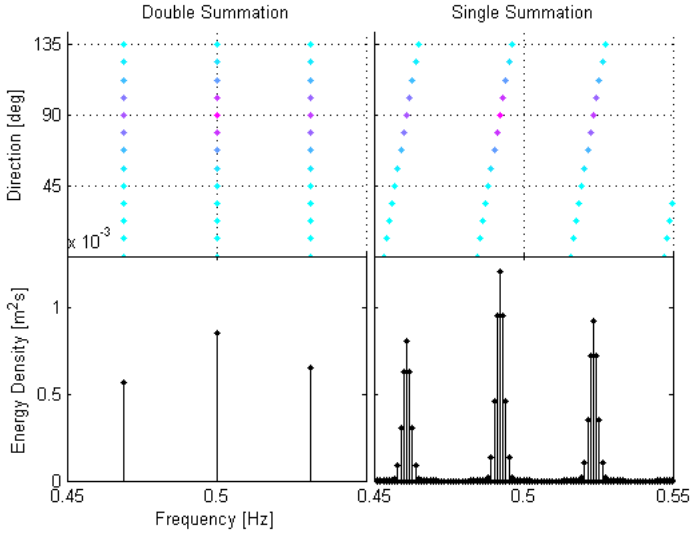

Figure 4: The single summation method

Another tank-related phenomenon, tooth-breeding (Salter 1981), must also be avoided. This phenomenon occurs when two unidirectional waves of very close frequency interact, forming additional frequency components. In order to minimize this effect, an approach similar to Pascal (2012) has been used, creating wave repartitions inside each original frequency band, forcing waves propagating in the same direction to be distanced in frequency as much as possible. This single summation approach should enable a wave field that is spatially homogenous and ergodic (Payne 2008).

EXPERIMENTAL SET-UP

A directional wave gauge array has been designed for a reconfigurable rig, shown in Figure 5. The chosen spacings should enable the generated directional spectrum to be estimated using a method of reconstruction. Hashimoto & Konbune (1988) suggest that the Bayesian Directional Method (BDM) is most accurate, and as WaveLab, created by Aalborg University uses this method as default, it was used in this work.

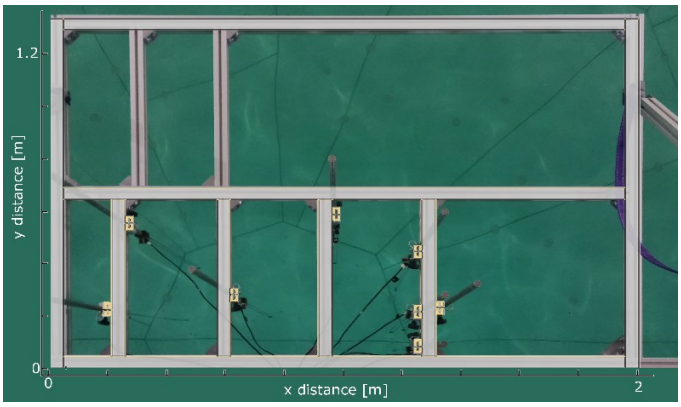

Figure 5: Wave gauge array overlaid with desired positions

RESULTS AND EXAMPLE OUTPUTS

Example Spectral Inputs and Outputs

Method I groups the data by clustering on the frequency spectra, meaning that similar spectra should be grouped together. Some of the resulting representative spectra, and their group members are shown in Figure 6. These representative spectra have then been generated in the tank, and measured, shown in Figure 7. The deviations between target and measured spectra are generally low, and show a less than 10% deviation on average. This deviation can largely be overcome when these spectra are run again by applying a frequency dependent correction factor.

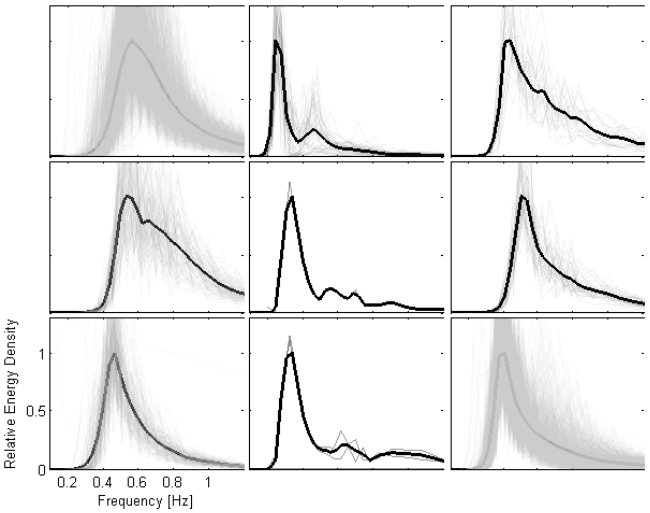

Figure 6: Normalised representative (mean) spectra, shown with group members in grey

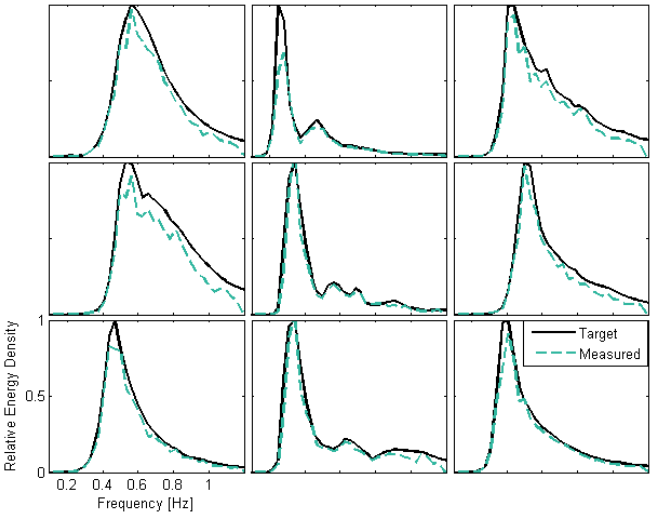

Figure 7: Normalised example spectral inputs and tank measurements

Statistical Outputs (Relating back to full scale)

Statistical outputs, at the relevant full-scale equivalent are shown in Figure 8. This essentially shows the resulting H_{m0}-T_E combinations generated through method I, as well as the re-scaled statistical outputs from the subsequent tank tests. It is interesting how the lack of distinctness in T_E shown in Table 2 is clearly visible here, but equally, important to note that these are not the only variables that have been considered during the characterisation, and that these values have been derived from the frequency spectra, S(f), explicitly considered in method I.

There is some deviation between the desired and measured values. This is in part due to the frequency limitations, however is mostly the result of deviations in the produced spectra, with a tendency to under-generate, highlighted in Figure 7.

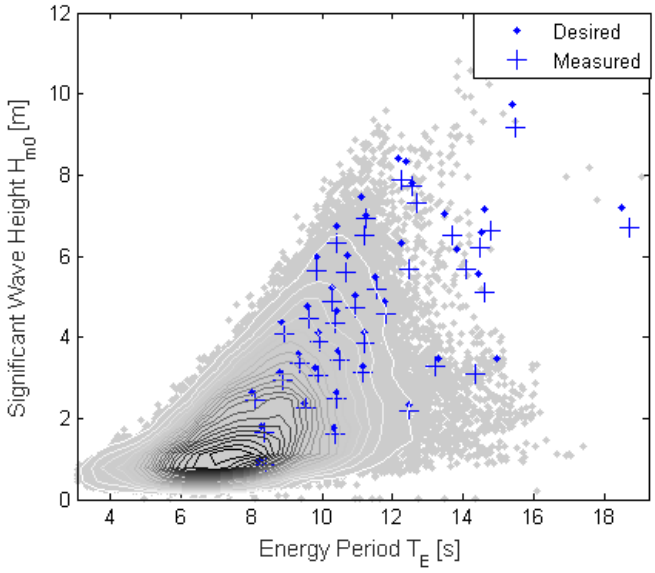

Figure 8: Statistical outputs from characterisation and from tank tests, shown overlaid onto kernel density map of original buoy data

Time Series Comparisons

Time series of surface elevations have been measured at all 8 gauges for each of the 40 representative sea states. Using an Inverse Fast Fourier Transform (IFFT), accounting for the phase relationships as a function of wave direction and gauge position, the time series can also be estimated at the gauge locations. This aids in assessing the wave generation performance. Figure 9 shows some examples of the deviation between target and measured time series, and demonstrates good agreement.

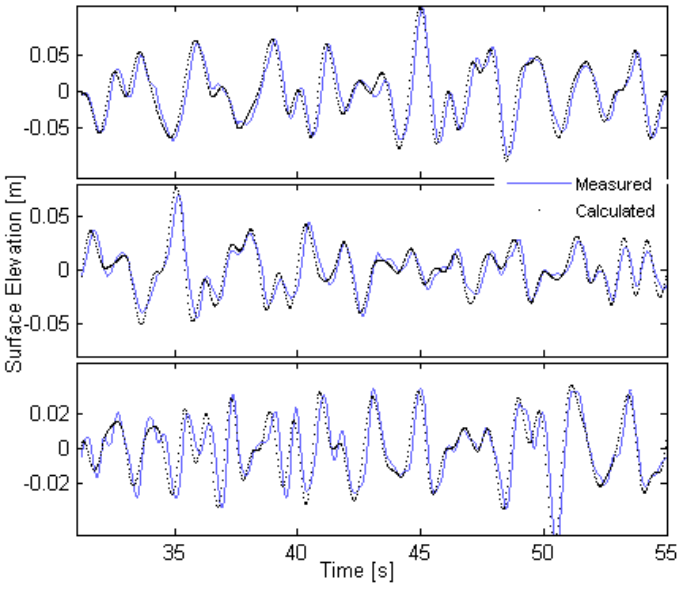

Figure 9: Example time series comparisons a) sea state 12, gauge 4 b) sea state 24, gauge 1 c) sea state 32, gauge 5

Example Directional Spectrum Outputs and Directional Spectrum Performance

Example directional spectrum outputs are shown in Figure 10. These have been generated from the output of method I's site characterisation, with the measured spectrum compared. It can be seen that generally there is good agreement, and complex directional spectra are being successfully generated in the tank.

The BDM method aims to fit a Directional Spreading Function (DSF) to each frequency band, describing the spread of energy with direction. This distribution fitting still has a degree of uncertainty associated with it. This means that the measured spectrum in Figure 10, despite giving a fairly good idea of the wave directionality generated, fails to resolve the wave field with any certainty.

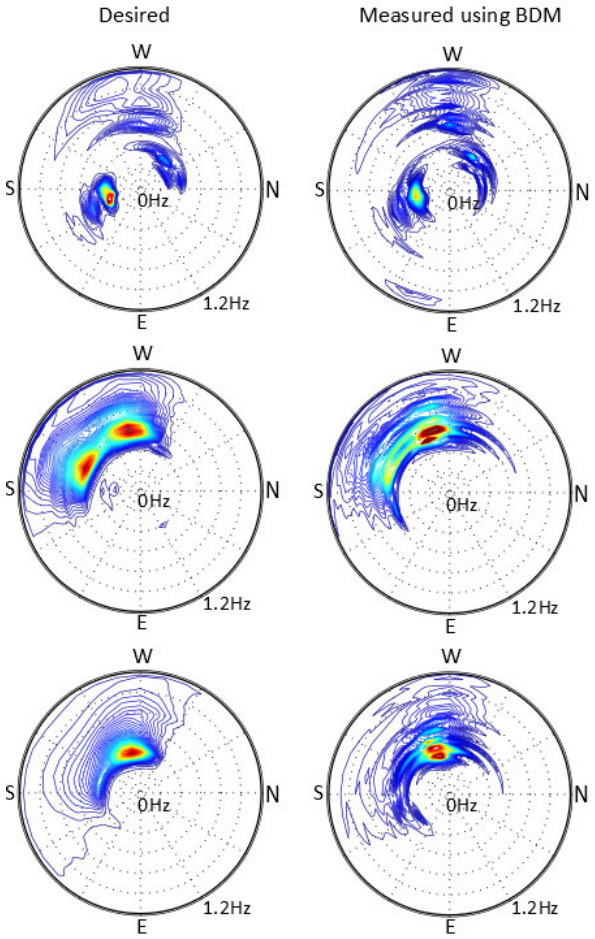

Figure 10: Example desired and measured directional spectrum

In order to assess the deviation from the target spectrum, the Normalised Total Difference, NTD, can been used, describing the total relative difference between the target and measured spectra.

This NTD encompasses a number of potential deviations:

- Frequency spectrum deviation, S_{NTD}
- Directional distribution deviation, E_{NTD}
- Reconstruction method error, M_{NTD}

Removing the frequency spectrum deviation, which can mostly be corrected for, we can observe the combined effect of the reconstruction method induced error, with the directional distribution error. This gives a mean combined deviation of 25.6%, ranging between 15.5 and 42.4% over the 40 tests. It is difficult, however, to assess how much the total NTD can be attributed to the actual directional distribution, and how

much is down to reconstruction error. Idealised numerical simulations suggest that a reconstruction error of around 15-20% may be expected, and as such it is likely that the directional spectra have been well produced.

DISCUSSION

Site Classification

The most subjective element in this whole process is probably the site classification aspect. Which variables are seen to be of importance is dependent on the device sensitivity, the purpose of the test, and some subjective reasoning. In addition, variables such as the length of time available to the test programme, and hence number of sea states may also influence not only the desired method of choice, but also the resulting sea states significantly. The metric used here, $S_W^{-1}S_B$, is also somewhat subjective as it assumes that the distinctness and compactness are equally important for all variables. This may not be the case, for example, you may want distinct T_E and H_{m0} groups but compact spectral partitions.

Method I was chosen in the end for these tests as it was felt it gave the best overall characterisation without knowing any device specific frequency and directional sensitivity. The characterisation of the frequency spectrum is probably the most important variable as it describes the full distribution of wave energy with frequency, something all Wave Energy Converters (WECs), and other structures are highly sensitive to. For example WEC performance is often described by power matrices. However, the true response of the device is a product of the Response Amplitude Operator(s) (RAO) with the wave frequency spectra, as shown in Veritas (2011).

Figure 8 shows method I's resulting sea states plotted in H_{m0}-T_E space. Despite having a good $S_W^{-1}S_B$ value for H_{m0} characterisation it is clear that the T_E, and combined H_{m0}-T_E distinctness is low. This combined distinctness is something that developers value when validating power matrices, e.g. Lavelle & Kofoed (2011). As a result of this, it might be beneficial to force this part of the solution, without losing a good characterisation with respect to S(f) and other parameters. This may be achieved by a coarse H_{m0}-T_E partitioning prior to the use of a clustering algorithm on the spectra.

Sea State Creation

The scale that the sea states have been generated at has been based on the ease of measurement and validation. The Billia Croo site itself is located, for most wavelengths, in what would be considered intermediate water. This means that if ~1/25th scale is not chosen that the wavelength will differ from its desired Froude scale value, altering the wave profile, demonstrated in Figure 11. As the actual scale these type of seas will be generated at is most likely to be determined by the model scale, this is something that will need to be accounted for. If models, as expected, are between 1/20th and 1/40th scale then the wavelength deviation is likely to be around 5-10%.

The tank's frequency-height limitations impose a slightly different preference on scale. The optimal single scale choice, minimising tank level energy losses is 1/30th giving a total wave energy loss throughout the tests of 1.9%, and a wavelength error of 3.6%. Going to 1/25th scale increases the energy loss to 3.2%, so if the model scale is to be designed for the tests a compromise may need to be made.

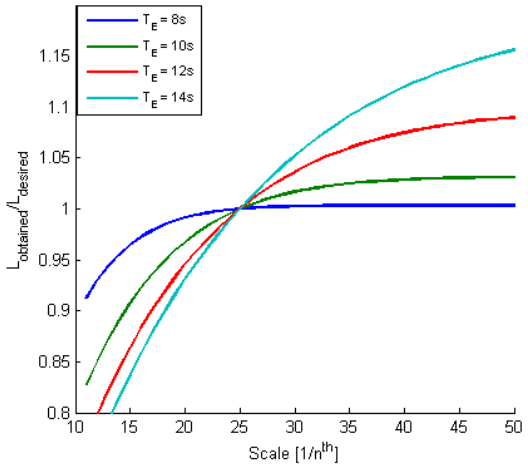

Figure 11: Scaled wavelength deviation for a 12s wave at 50m full scale, to 2m tank scale

Sea State Performance

In general the sea state performance was good. Frequency spectrum deviations are a little high, giving rise to a 10% deviation. Wave height-period combinations show the expected level of error as a result of this. From correcting previous spectra it is thought that this could be brought down to less than 1% after a frequency dependent correction factor is applied. This should improve both the total NTD, and the comparisons between target and measured wave statistics significantly.

CONCLUSIONS

To conclude, the whole process of site-specific wave resource simulation has been carried out. Buoy data has been analysed and classified by a number of methods, including assessing the implementation of using clustering algorithms to partition the data. A final method, using a combined binning-clustering approach, method I, has been chosen as most preferable using a combined compactness and distinctness metric as guidance. This chosen method defines 40 site-specific representative directional spectrum, which have then been scaled and ran successfully in the tank using the single-summation method.

The resulting sea states have been measured using a specially designed wave gauge array, and compared to the target time series, frequency and directional spectrum. Overall it was found that the sea states were generated well, however, deviations from target frequency spectra still require improvement by means of a correction factor. Measured directional distributions using the BDM method show good agreement with those of the desired spectra, however as there is still significant reconstruction error it is difficult to isolate the true directional spectrum.

REFERENCES

Benoit, M., 1992. Practical comparative performance survey of methods used for estimating directional wave spectra from heave-pitch-roll data. *Coastal Engineering Proceedings*, pp.62–75.

Bonner, R.E., 1964. On Some Clustering Techniques. *IBM Journal of Research and Development*, 8, pp.22–32.

Dalrymple, R. & Dean, R., 1984. *Water wave mechanics for engineers and scientists*,

Draycott, S. et al., 2014. Applying Site Specific Resource Assessment: Methodologies for Replicating Real Seas in the FloWave facility. *ICOE Conference Proceedings*.

EMEC, 2015. Facilities. Available at: http://www.emec.org.uk/facilities/ [Accessed January 5, 2015].

Hamilton, L.J., 2010. Characterising spectral sea wave conditions with statistical clustering of actual spectra. *Applied Ocean Research*, 32(3), pp.332–342.

Hashimoto, N., 1997. Analysis of the Directional Wave Spectrum from Field Data. *Advances in Coastal and Ocean Engineering*.

Hashimoto, N. & Konbune, K., 1988. Directional spectrum estimation from a Bayesian approach. *Coastal Engineering Proceedings*, pp.62–76.

Ingram, D. et al., 2014. The design and commissioning of the first, circular, combined current and wave test basin. *flow3d.com*.

Kim, T., Lin, L. & Wang, H., 1994. Application of maximum entropy method to the real sea data. *Coastal Engineering Proceedings*, pp.340–355.

Lavelle, J. & Kofoed, J.P., 2011. *Power Production Analysis of the OE Buoy WEC for the CORES Project*. Aalborg University.

McCombes, T. et al., 2010. Equitable Testing and Evaluation of Marine Energy Extraction Devices in terms of Performance, Cost and Environmental Impact: Devliverable D3.4 Best practice for tank testing of small marine energy devices. *EU FP7 Project*, pp.1–48.

Miles, M.D. & Funke, E.R., 1989. A Comparison of Methods for Synthesis of Directional Seas. *Journal of Offshore Mechanics and Arctic Engineering*, 111, p.43.

Pascal, R., 2012. Quantification of the influence of directional sea state parameters over the performances of wave energy converters.

Payne, G., 2008. Guidance for the experimental tank testing of wave energy converters. *SuperGen Marine, Dec*.

Rokach, L. & Maimon, O., 2001. *Data Mining and Knowledge Discovery Handbook*,

Salter, S.H., 1981. Absorbing wave-makers and wide tanks. In *Directional Wave Spectra Applications*. pp. 182–202.

Veritas, D.N., 2011. MODELLING AND ANALYSIS OF MARINE OPERATIONS. *DNV*, (April).

APPLYING SITE SPECIFIC RESOURCE ASSESSMENT: METHODOLOGIES FOR REPLICATING REAL SEAS IN THE FLOWAVE FACILITY

S.Draycott[1*], T.Davey[1], D.M.Ingram[2], J.Lawrence[3] A.Day[4], L.Johanning[5], J.Steynor[1], D.Noble[1]

[1]FloWave Ocean Energy Research Facility, Max Born Crescent, King's Buildings, Edinburgh, EH9 3BF
[2]Institute for Energy Systems, School of Engineering, The University of Edinburgh, Edinburgh, EH9 3JL
[3]The European Marine Energy Centre (EMEC) Ltd, Old Academy Business Centre, Stromness, Orkney, KW16 3AW
[4]Naval Architecture and Marine Engineering, The University of Strathclyde, Glasgow, G4 0LZ
[5]Renewable Energy Research Group, College of Engineering, Mathematics and Physical Science, University of Exeter, TR10 9EZ

Abstract

FloWave is the world's first combined current and wave test basin with a circular design that provides the capability to generate waves from all directions. This makes possible the production of realistic site-specific sea states, with no intrinsic limitations on the creation of multi-directional wave fields. In order to do this effectively, real site data must be used and manipulated in order to preserve both the sites characteristics and the directional complexity. A variety of methods are trialled here for reducing a wave buoy dataset to a subset of representative sea states. Using a year of half-hourly sea states (17520 in total) provided by the European Marine Energy Centre (EMEC), Orkney, UK, six methods have been evaluated, with the aim of producing twenty representative directional spectra. After defining a group 'compactness' metric, it was found that clustering either directly on the wave frequency spectra or on the directional spectra yielded the most favourable results with respect to a range of key variables. These approaches enable the groupings to be based on complex spectral shapes, and thus have the capability to yield complex statistically representative directional spectra suitable for replication in the FloWave facility.

1 INTRODUCTION

Physical model tests continue to play an important role in the development of offshore structures and vessels, facilitating the understanding of how complex sea conditions interact with man-made devices.

The FloWave facility, based at the University of Edinburgh, is a unique, circular, combined wave and current basin. This facility has been designed primarily to test scale models of marine renewable energy devices, and is optimised for around 1:20th to 1:40th scale. The 360° wave generation capabilities of the facility enable the production of complex multidirectional wave conditions, allowing realistic multi-modal sea states to be simulated and their interactions with devices understood.

FIGURE 1: THE FLOWAVE FACILITY

In order to take advantage of these directional capabilities it is important to create sea states that not only contain complex directional information, but are also based on realistic wave conditions. These could be developed by parametric wave spectra, with parametric

* Corresponding author. Tel: +44 (0)131 651 3554
Email address: S.Draycott@ed.ac.uk

directional spreading functions. This technique will not, however, capture the true complexity of how wave energy is distributed across both frequency and direction in real seas.

The aim of this work is to explore the potential merits and methodologies in classifying site-specific buoy data to create a set of representative sea states. A key element in this classification is the incorporation of directional information, so that when these sea states are simulated in FloWave, they preserve as much of the directional complexity as possible. A collaboration agreement with the European Marine Energy Centre (EMEC) allows the use of extensive directional wave buoy datasets from their full-scale wave test site, Billia Croo, to make this a possibility.

2 THE OVERALL PROCESS

The overall process of creating statistically representative, validated site-specific sea states involves a number of components. The buoy data must be processed effectively to provide test inputs. However, it must also be recognised that without well-defined tank characterisation, measurement strategies and analysis tools, the validation aspect cannot be achieved.

This paper will focus on the process of creating representative sea states from buoy data, outlined in Figure 2. Throughout each of the stages depicted it is important to preserve as much of the key information as possible, choosing the methodology carefully so that the waves produced in the tank accurately represent the site they were derived from.

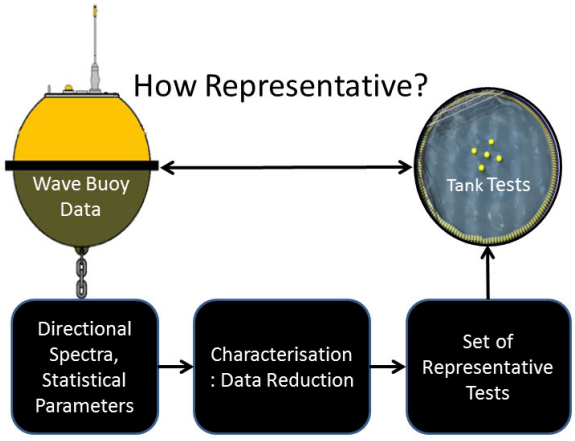

FIGURE 2: CLASSIFICATION PROCESS

One of the key aspects here is the data classification methodology. An annual dataset from a single measurement buoy will contain thousands of sea states, and as such it is very impractical to simulate each one individually. This necessitates a method of data reduction to classify the sea states into groups of similar properties. The aim is produce a small dataset for deployment in the wave tank which is representative of annual conditions at the target site. The choice of grouping method, and the properties that they operate on will vastly alter the resulting 'representative' sea states designed to embody each group's characteristics.

3 METHODOLOGY

3.1 CREATION OF DIRECTIONAL SPECTRA

Directional wave buoys exist in a variety of forms and measure a range of values. The Datawell Waverider® buoys used here measure heave, pitch and roll.

Inferring meaningful directional information from point measurements is difficult, however through cross-spectral analysis of the three signals, the first four Fourier coefficients of the directional spreading function (DSF) can be calculated (Longuet-Higgins et al. 1963). These coefficients begin to describe the distribution of wave energy across direction, for each frequency, but cannot be used directly as they tend to produce negative values (e.g. Figure 3, TFS (Truncated Fourier Series)). This means a distribution model is required to be used to create the DSF, which in turn creates the assumed directional spectrum, $E(f,\theta)$.

The difficulty arises in the choice of model, as the true directional spectrum remains unknown, while each of the potential DSFs satisfy the known Fourier coefficients. Figure 3 shows an example of the discrepancy in the DSF, for several models at a given frequency.

It has been shown that the maximum entropy principal (MEP) provides the most reliable results from a single point measurement system (Benoit, 1992). However, the solution to the MEP is non-linear, computationally challenging, and often results in non-

convergence (Kim et al. 1994). To aid the convergence problem Newton's technique of local linearisation has been employed, outlined in Hashimoto (1997).

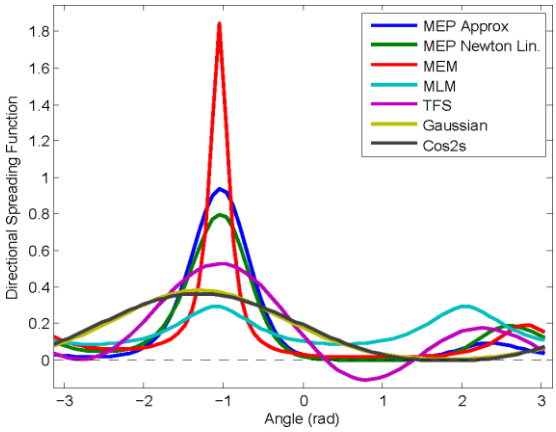

FIGURE 3: EXAMPLE DSF OUTPUT

The local linearisation method still fails to converge roughly 10% of the time on the dataset available, and in this case is replaced by the approximate solutions shown in Kim et al. (1994). The approximate MEP DSF generally shows good agreement with the full MEP solutions, and as such this combined approach has been deemed most effective for this work.

An example output from the applied MEP method is shown in Figure 4 iii. This highlights the increase in directional complexity achieved by using this approach when compared to simpler approaches commonly employed in tank tests. Using this more representative form of the directional spectrum will enable the consideration of higher quality directional information when grouping the data. This should lead to the preservation, and eventual simulation of this information.

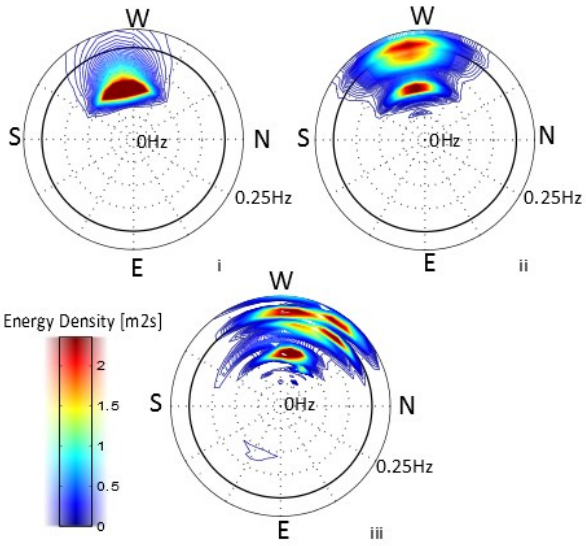

FIGURE 4: EXAMPLE DIRECTIONAL SPECTRA

Polar plots of energy density, with frequency increasing from centre. i) Parametric fitted spectrum and frequency independent cos-2s spreading function, ii) Actual frequency spectrum with frequency independent cos-2s spreading function, iii) MEP fitted directional spectrum

3.2 SITE CLASSIFICATION METHODOLOGY

In order to reduce the vast amount of buoy data to a sub-set of meaningful sea states the data must be grouped by similarity. Each sea state has a number of parameters that can potentially be utilised for this purpose:

- Statistical parameters e.g. significant wave height, H_{m0}, and peak period, T_p or energy period, T_E
- Frequency dependent parameters e.g. wave energy spectra, $S(f)$
- Frequency-direction dependent parameters; the directional spectrum, $E(f,\theta)$.

The methodology needs to be driven primarily by the parameters that are important to preserve for the purpose of the testing, i.e. those that are deemed influential in device response, and estimated power production.

For the purposes of this work the most significant parameter is the energy in the sea state, which can be described by either H_{m0}-T_E combinations, frequency spectra, or directional spectra. Each descriptor including a differing level of detail, as can be shown in Figure 4

where each of the spectra have the same H_{m0} and T_p, whilst ii) and iii) are also derived from the same measured frequency spectrum.

Hamilton (2010) describes a method of effective site characterisation using statistical clustering on the actual spectral form, S(f). This enables the consideration of the entire spectral shape, describing the frequency distribution of wave energy, when creating data partitions. As wave energy converter (WEC) performance tends to be highly frequency dependent, this sort of approach could provide a valuable increase in detail in the resulting representative seas.

This work aims to build on the work from Hamilton (2010), to explore the merits in using clustering techniques to create a set of representative directional spectra. The full range of methods being explored are shown in Table 1. Each method creates a set of representative directional spectra, taken as the mean of the spectra in each partition. These methods were chosen because they differ significantly in how they create the resulting groups, and how they try to incorporate directional characteristics.

TABLE 1: METHODS UNDER COMPARISON

	Method Name	Grouping Parameters
A	2 parameter binning	H_{m0}, T_E
B	3 parameter binning	H_{m0}, T_E, MDIR
C	Spectral clustering	S(f)
D	Partitioning by MDIR then clustering	S(f)
E	Directional spectral clustering	E(f,θ)
F	Clustering on statistical parameters	H_{m0}, T_E, v, MDIR, UI

3.2.1 Clustering

Cluster analysis is a method of grouping objects by similarity, using a clustering algorithm and a distance metric to make decisions on group membership. Parametric clustering algorithms such as the *k*-means algorithm enable the user to input the desired number of output clusters, *K*, making it useful as an effective data partitioning tool, as well as for data exploration.

For the purpose of this work the *k*-means algorithm has been used, with a square Euclidean distance metric, defining the objective function to minimise to be:

$$\sum_{k=1}^{K}\sum_{m=1}^{M(K)}\left|\boldsymbol{v_{k,m}}-\boldsymbol{\mu_k}\right|^2 \qquad (1)$$

In other words the aim is to minimise the sum of the within-cluster distances. Where M is the number of objects in cluster k, and μ_k is the cluster mean. This is done by randomly initialising the K clusters with members, calculating the means, and then re-assigning each object to the 'nearest' cluster centroid. This is repeated until re-assigning objects no longer benefits the objective function. As this process has an element of randomness, especially in the initialisation, this can be repeated multiple times and the output with the lowest sum of within-cluster distances chosen as the preferred result.

3.2.2 Performance Metric

As the aim of this work is to explore different characterisation methodologies it is necessary to create a performance metric that enables comparison. Each classification method outputs a number of groups, $k = 1 \dots K$, each with a different number of members, $m = 1 \dots M(k)$. The metric should be able to assess how well a method has grouped with respect to a certain variable, $v = 1 \dots V$, with discrete values $d = 1 \dots D(V)$.

For a given method and variable of interest the following metric has been proposed:

$$\boldsymbol{Met} = \sum_{k=1}^{K}\frac{1}{K}\sum_{m=1}^{M}\frac{1}{M(k)}\sum_{d=1}^{D}\frac{\left|\boldsymbol{v_{k,m,d}}-\boldsymbol{\mu_{k,d}(v)}\right|}{\sum_{d=1}^{D}\boldsymbol{\mu_{k,d}(v)}} \qquad (2)$$

This metric gives the mean absolute relative error incurred by representing a sea state's variable of interest by the cluster mean, essentially defining the 'compactness' of the resulting group with respect to variable v.

3.2.3 Methodologies Overview

A sample year was extracted from the EMEC data from Billia Croo, consisting of 17520 half-

hourly sea states. The data was then filtered under the assumption that no device would produce any power under a significant wave height of 0.5m. This then removes the influence of these low energy sea states from the characterisation, although they could easily be included for the purpose of a more general site characterisation. The desired additional wave statistics were then calculated, such as spectral bandwidth, ϑ, and mean directional spread, $Mspread$, and then the directional spectra were calculated using the approach detailed in 3.1.

Each method was then tasked to produce K=20 representative sea states.

A: 2 parameter binning

2 parameter binning was achieved simply by creating a number of regularly spaced H_{m0} - T_E bins, and altering the number of bins appropriately until there was K, or very close to K non-empty bins. The idea of using irregular bin sizes based on the probability density was explored. However, it was felt that this approach would give more weighting to the abundant, similar sea states, rather than classifying the sea states by their underlying characteristics.

It was found that 7 H_{m0} and 5 T_E regular bins provided 21 non-empty partitions on the current dataset. These non-empty bins then define the resulting definition of the groups, and group membership, shown in Figure 5.

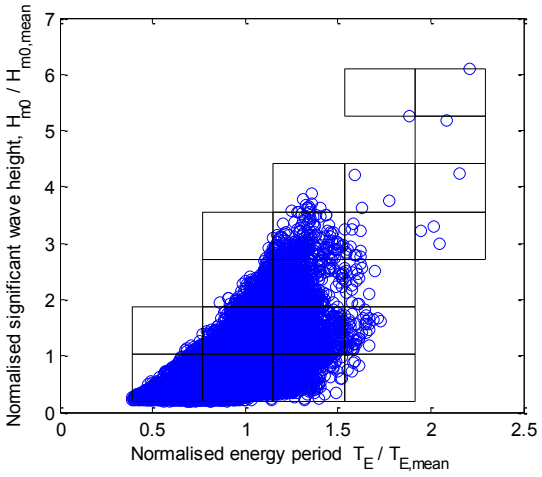

FIGURE 5: 2 PARAMETER BINS

B: 3 parameter binning

3 parameter binning was done in exactly the same way as the H_{m0}-T_E binning, but mean direction, *MDIR*, was also included as a tertiary membership condition. It was found that 4 H_{m0}, 4 T_E and 3 *MDIR* bins provided the desired, K=20, non-empty partitions. The new H_{m0}-T_E bins are shown in Figure 6, noting that there are up to three additional *MDIR* partitions for each bin shown.

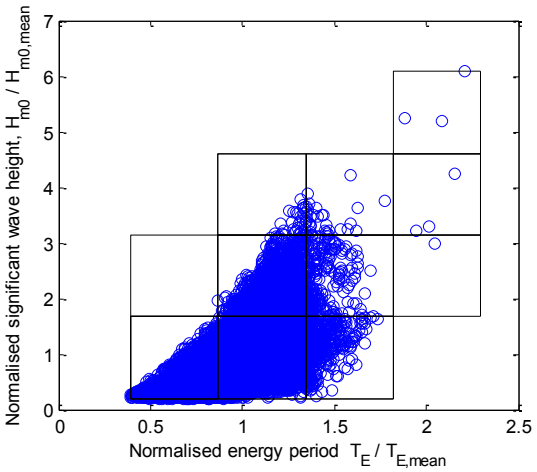

FIGURE 6: 3 PARAMETER H_{M0}-T_E BINS

C: Clustering of wave spectra

The *k*-means algorithm used to cluster spectra was defined in 3.2.1 and was used to partition the data using the whole frequency spectra form, $S(f)$. This was implemented in MATLAB®, using their built-in function *kmeans*. Solver info: *Number of replicates=10, Maximum Iterations=400.*

D: Partitioning by MDIR then clustering

To create coarse starting partitions, the data was initially grouped using 4 *MDIR* bins. Then each group was further partitioned using the *k*-means algorithm, acting on $S(f)$, to produce a further 5 sub-groups. Solver info: *same as for C.*

E: Directional Spectra Clustering

The *k*-means algorithm was used here to act on the full directional wave energy spectrum $E(f,\theta)$. The number of iterations was increased to allow the high-dimensional problem to converge, although the number of algorithm replicates was reduced due to computing power and time constraints. Solver

info: *Number of replicates=5, Maximum Iterations=1000.*

F: Clustering on statistical parameters

Each of the statistical parameters shown in Table 1 were normalised. These new variables are then treated equally by the *k*-means algorithm and gives an output based on this assumed weighting. Mean direction was initially included in this, however, as yet no effective method of normalising and clustering appropriately on circular data had been found. Solver info: *same as for C.*

4 RESULTS & EXAMPLE OUTPUTS

4.1 METHODOLOGY PERFORMANCE

Once the group members had been defined through methods A to F, the representative directional spectra were taken from each of the 1..K groups. Each of the remaining representative wave statistics were then derived from this to give $\mu_k(v)$, and the mean relative error calculated from Equation 2.

The mean relative error is shown in Table 2, noting how the scale of the error increases significantly with $S(f)$ and $E(f,\theta)$ due to the higher number of discrete values (dimensions). In order to visualise the relative performance more easily, the mean relative error for a given variable has been normalised across the methodologies, shown in Figure 7. Although each variable has been presented on the same scale, it is important to note that this doesn't mean that each variable is equally significant.

It is clear from both Figure 7 and Table 2 that clustering directly on either the frequency or directional spectra gives the best overall groupings. Partitioning the data by mean direction beforehand proved to be highly ineffective, as did clustering directly on statistical parameters with respect to most variables. Although the binning methods trialled here perform relatively well with respect to certain variables, these approaches are both significantly outperformed by either of the spectral clustering methods.

Determining which method is best overall is device dependent and a little subjective. For example, a point absorber WEC may be uninfluenced by directional characteristics, leading to the conclusion that clustering on the wave frequency spectra is the best approach. An articulated attenuator type device may, however, be highly influenced by the spread of wave energy with direction, and conclude that clustering on the directional spectra is the only option that characterises the site effectively with respect to that variable.

It may be desirable to create a set of representative seas that are effective for all device types, creating a standard set of site-specific seas that can be used to contrast and compare. In this instance it may be wise to cluster using the directional spectra as it significantly outperforms frequency spectra clustering with respect to directional spectra 'compactness', whilst being close to equal effectiveness with respect to other variables.

TABLE 2: MEAN RELATIVE ERROR FOR A RANGE OF VARIABLES

Method / Variable	2 parameter binning	3 parameter binning	Clustering on spectra	Partitioning by MDIR then clustering	Directional spectral clustering	Clustering on statistical parameters
Hm0	13%	16%	9.8%	16%	11%	21%
Te	8.1%	6.5%	5.3%	10%	5.2%	7.2%
Power	38%	36%	20%	40%	22%	45%
v	8.6%	8.1%	6.5%	10%	6.4%	6.4%
MDIR	11%	16%	7.8%	20%	9.7%	7.4%
S	50%	50%	40%	57%	41%	63%
E	72%	72%	87%	82%	66%	106%

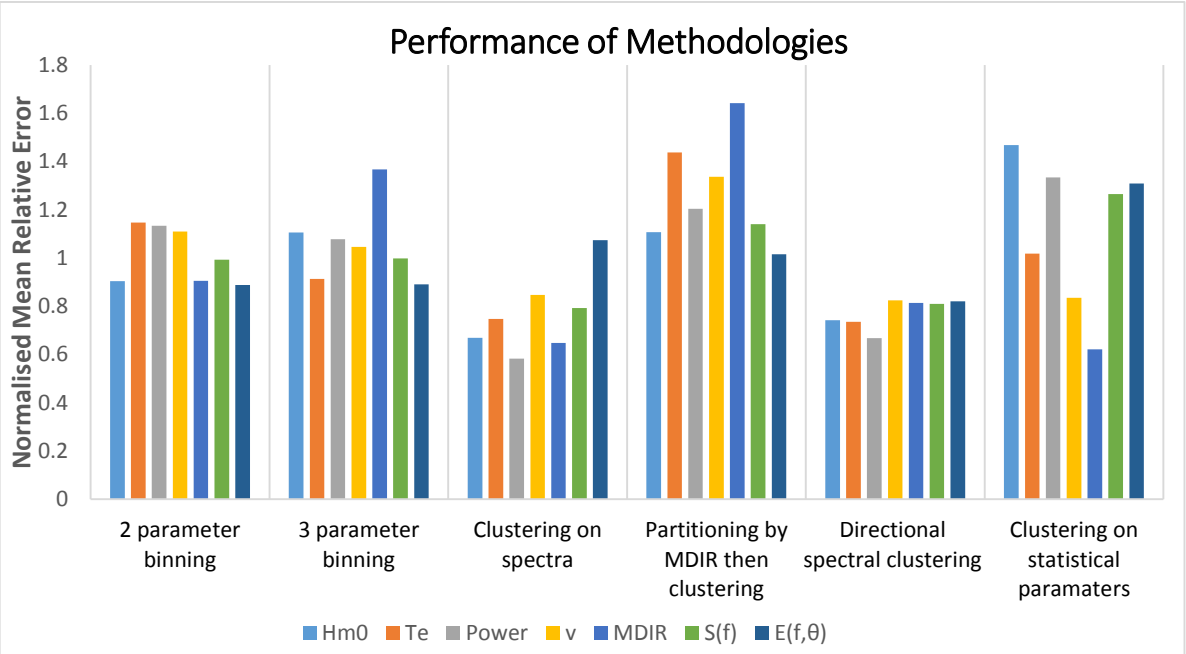

FIGURE 7: NORMALISED MEAN RELATIVE ERROR

4.2 EXAMPLE OUTPUTS

4.2.1 Spectral Outputs

Each of the methods have created approximately 20 representative sea states, all of which have corresponding directional spectra, frequency spectra and wave statistics. Due to this it is difficult to show a significant amount of the spectral outputs and so only a small sample will be shown. Figure 8 and 9 show roughly equivalent representative sea states from methods C and E, as these methods performed most favourably. This was done by sorting by H_{m0} and picking out 4 sea states that had the same relative ranking.

It is evident that despite the large amount of data, the more energetic, low abundance sea states still feature within the 20 representative seas, and still contain the directional complexity, and in some cases multi-modality that was present in the original dataset, and indeed reality. One feature of clustering in general is that is incurs a greater cost to the objective function to cluster large valued objects with other dissimilar objects, thus for this application, the algorithm naturally picks out the larger sea states. Those sea states with higher abundance tend to lose some distinctive features due to being highly averaged, however from visual observation it appears that they still represent their relatively large groups effectively.

4.2.2 Statistical Outputs

Some of the representative wave statistics are shown in Figure 10 and 11. This provides an easy means of comparison between the methods. It is interesting to note that how method F, clustering on statistical parameters, is the only method that picks out low energy, wide bandwidth sea states. This is due to the relatively high weighting placed on partitioning by spectral bandwidth used in this method, and those seas with high spectral bandwidth tend to have low energy content.

The high value bias of the clustering methods, C and E, is also evident here, with neither method producing many representative sea states with low power. The binning methods, and the clustering on statistical parameters, however, have a more even spread of representative wave statistics.

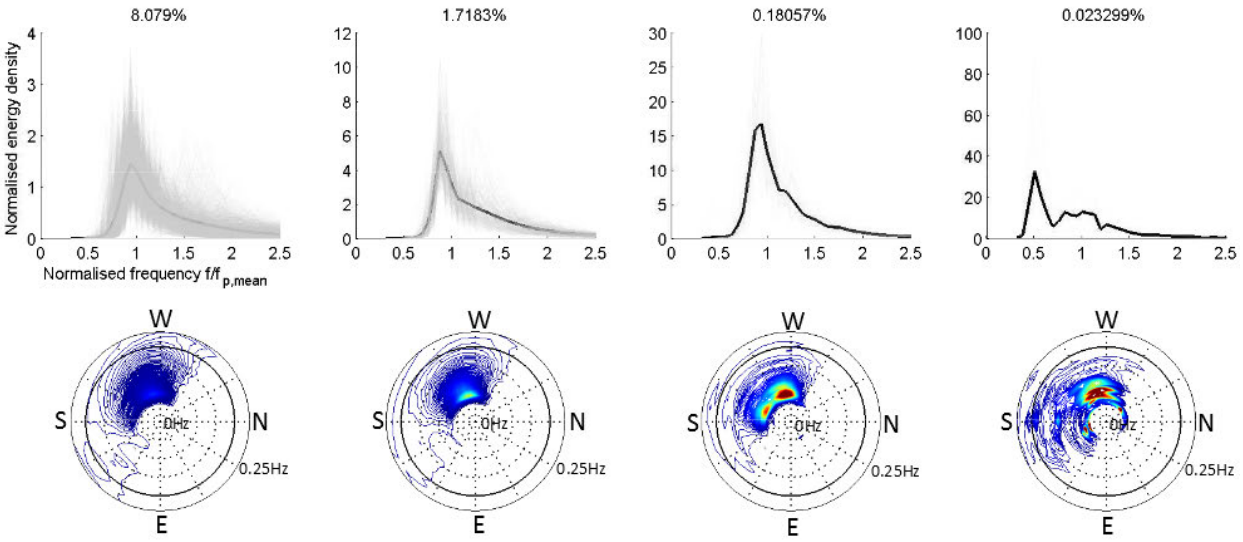

FIGURE 8: EXAMPLE SEA STATES FROM METHOD C

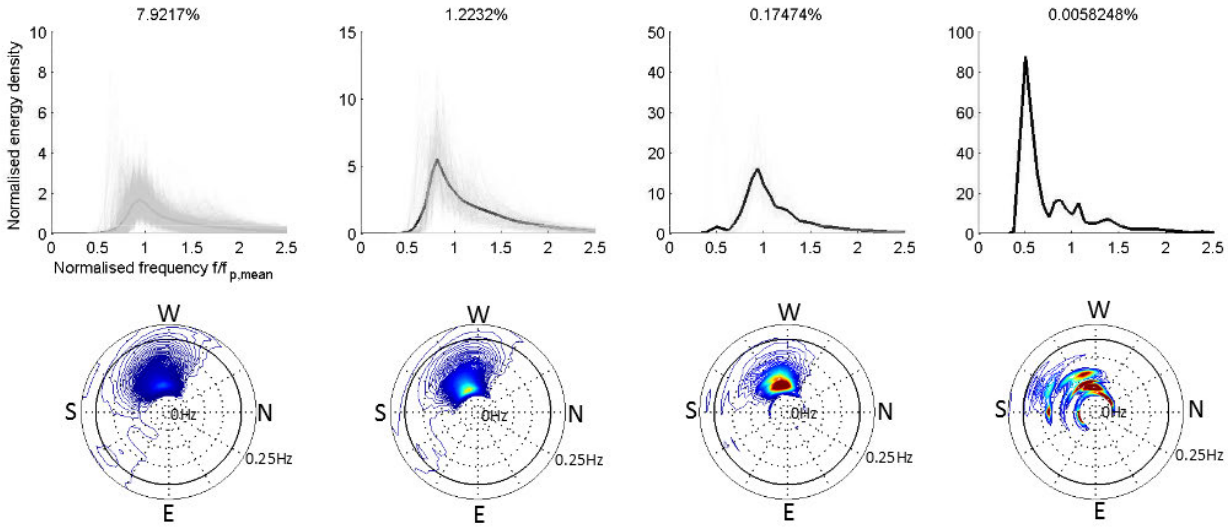

FIGURE 9: EXAMPLE SEA STATES FROM METHOD E

Figure 8 and 9 show example representative spectra normalised with respect to the peak of the mean spectrum. Their relative abundance in the sample dataset is displayed as a percentage above.

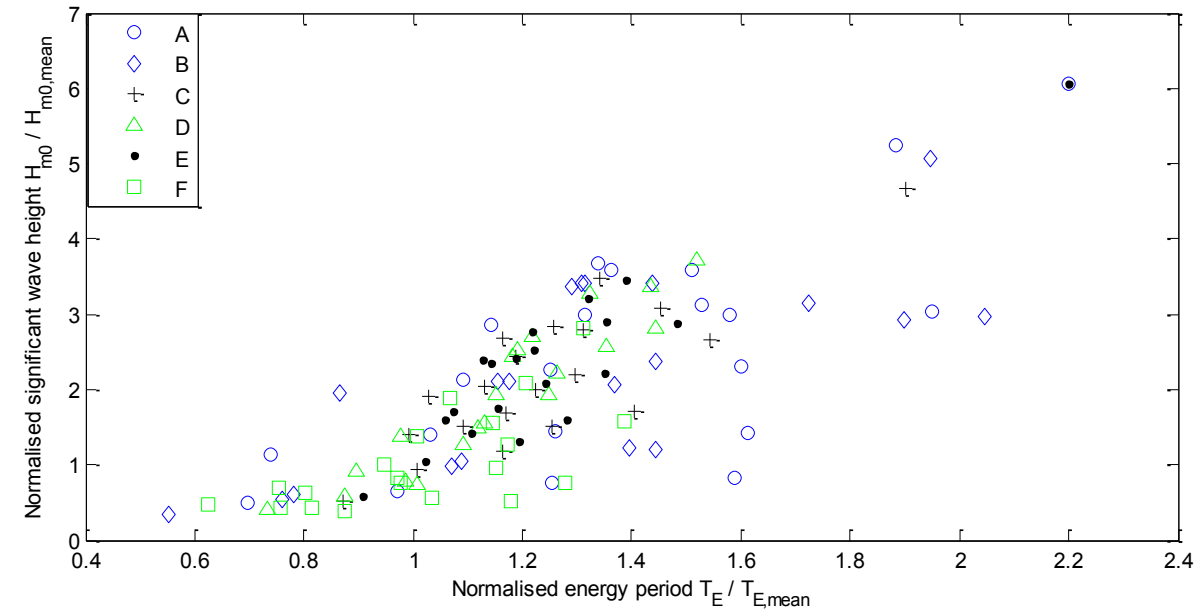

FIGURE 10: H_{M0}-T_E SCATTER PLOT FOR REPRESENTATIVE SEA STATES

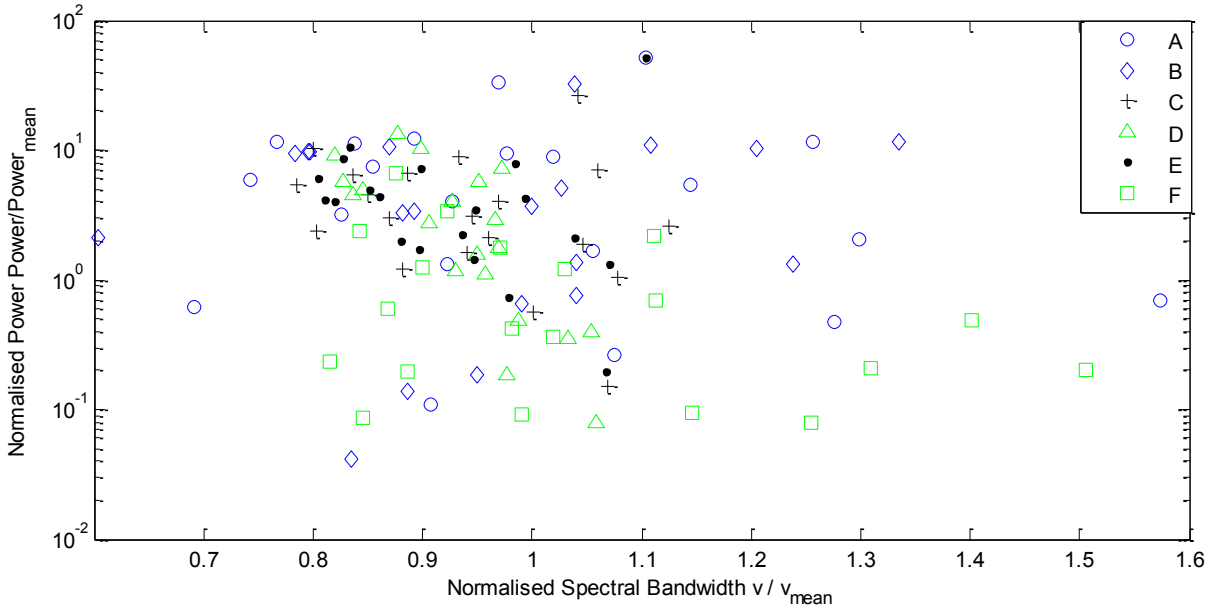

FIGURE 11: V-POWER SCATTER PLOT FOR REPRESENTATIVE SEAS

5 DISCUSSION

5.1 SUBJECTIVITY

One of the main things discovered here was that key elements of the methods trialled here are highly subjective, other than for the direct clustering approaches, methods C and E. Methods A and B both have a choice of number of bins in addition to the choice of bin widths. With method D, the number of pre-clustering partitions, and method of grouping by mean direction is another choice to be made. Method F requires a decision to be made on the relative weighting of the statistical parameters. Here they have been assumed equal, but this may not provide the best approach with respect to the defined metric. For this reason it would be advantageous to explore how each of these methods could be optimised by varying these parameters, and assessing their relative performance.

Another element of subjectivity is the prioritisation of certain variables in the resulting characterisation. This may be mostly determined by device type, but introduces an

issue when determining the most effective methodology overall.

5.2 INCLUSION OF MEAN DIRECTION

For method D, clustering on statistical parameters, it would have been interesting to explore the inclusion of mean direction. However, it was found difficult to normalise and effectively cluster on circular data. This is because, for example, 2π and 0 (or π and $-\pi$) radians are effectively equal. However, when trying to normalise, or cluster on this data, they will be treated as the two most different values.

This problem has also meant that the metric defined in equation 2 has been applied incorrectly when used on mean direction, and as such the values will be unreliable. Fortunately most of the wave energy in this dataset is between 0 and π radians, and as such the metric computation may remain largely unaffected.

A solution may be to convert these circular values onto an equivalent linear scale, or use circular statistics. This should enable mean direction to be treated like all of the other variables in the characterisation.

6 CONCLUSIONS

In order to simulate realistic site-specific wave fields it is important to accurately represent the directional spectrum. The maximum entropy principal seems to provide the most reliable results, with a combination of Newton's method of local linearisation, outlined in Hashimoto (1997), and the approximate solutions outlined in Kim et al. (1994), providing an effective solution.

Reducing a large dataset down to a small number of representative sea states inevitably loses detail and can be a highly subjective process. With respect to an error related 'compactness' metric, using statistical clustering algorithms directly on the wave frequency spectra, or the directional spectra yields the most favourable results. These methods also have the additional advantage in that they are significantly less subjective, with only the solution paramaters and the 'k-value' being open to specification.

It appears that as an overall most favourable method, clustering on the directional spectrum yields the best results. Although additional methods and parameters need to be explored it apprears to be a highly effective method for creating a set of statistically representative directional spectra, suitable for replication in the FloWave facility.

References

Benoit, M., 1992. Practical comparative performance survey of methods used for estimating directional wave spectra from heave-pitch-roll data. *Coastal Engineering Proceedings*, pp.62–75.

Hamilton, L.J., 2010. Characterising spectral sea wave conditions with statistical clustering of actual spectra. *Applied Ocean Research*, 32(3), pp.332–342.

Hashimoto, N., 1997. Analysis of the Directional Wave Spectrum from Field Data. *Advances in Coastal and Ocean Engineering*.

Kim, T., Lin, L. & Wang, H., 1994. Application of maximum entropy method to the real sea data. *Coastal Engineering Proceedings*, pp.340–355.

Longuet-Higgins, M., Cartwright, D. & Smith, N., 1963. Observations of the directional spectrum of sea waves using the motions of a floating buoy.